3D MODELLING OF MAMMALIAN EMBRYOS AND ORGANS

EDITED BY: Silvia Garagna, Juan Aréchaga, Elisa Cebral and Maurizio Zuccotti

PUBLISHED IN: Frontiers in Cell and Developmental Biology

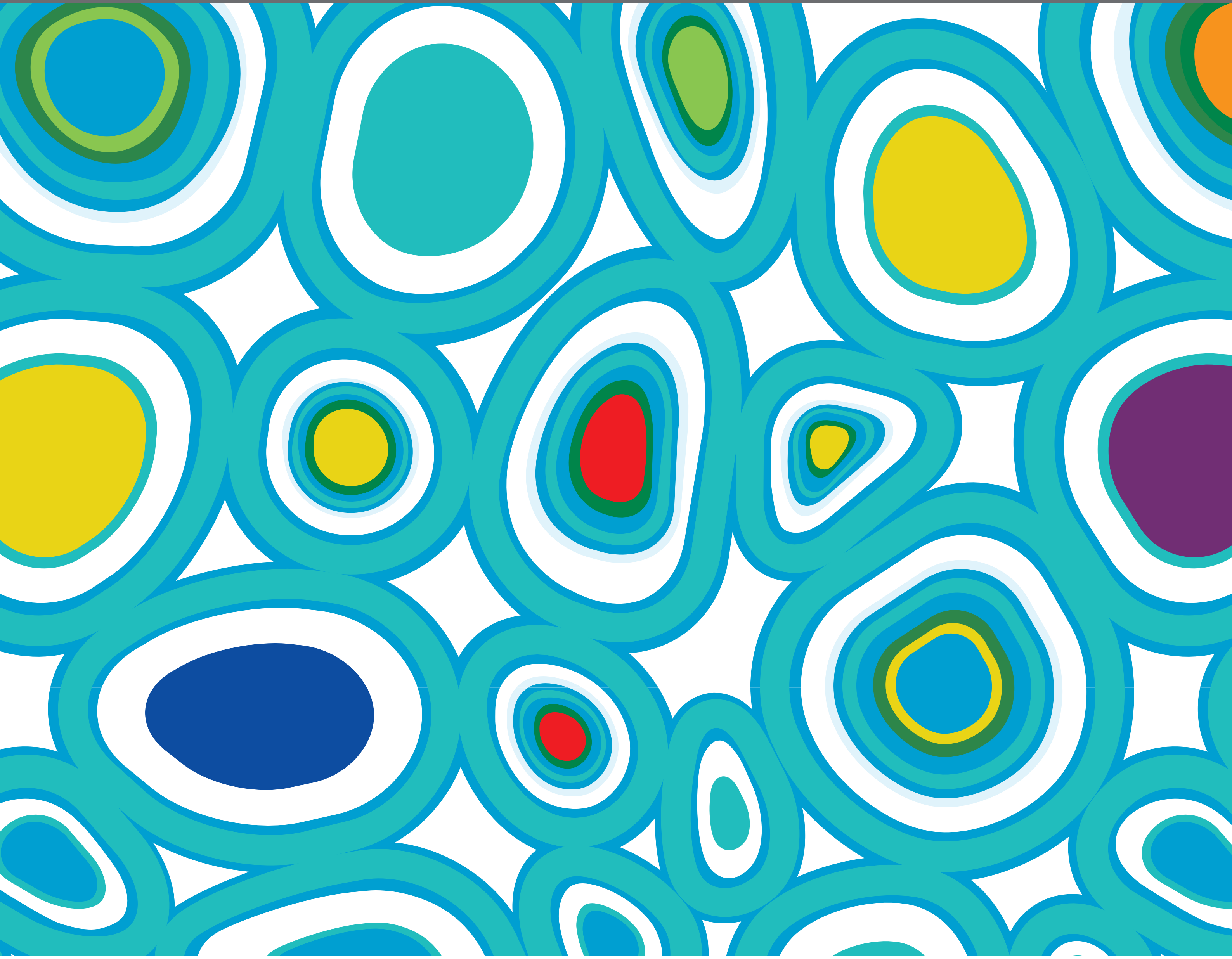

frontiers Research Topics

ISSN 1664-8714
ISBN 978-2-88971-607-4
DOI 10.3389/978-2-88971-607-4

About Frontiers

Frontiers is more than just an open-access publisher of scholarly articles: it is a pioneering approach to the world of academia, radically improving the way scholarly research is managed. The grand vision of Frontiers is a world where all people have an equal opportunity to seek, share and generate knowledge. Frontiers provides immediate and permanent online open access to all its publications, but this alone is not enough to realize our grand goals.

Frontiers Journal Series

The Frontiers Journal Series is a multi-tier and interdisciplinary set of open-access, online journals, promising a paradigm shift from the current review, selection and dissemination processes in academic publishing. All Frontiers journals are driven by researchers for researchers; therefore, they constitute a service to the scholarly community. At the same time, the Frontiers Journal Series operates on a revolutionary invention, the tiered publishing system, initially addressing specific communities of scholars, and gradually climbing up to broader public understanding, thus serving the interests of the lay society, too.

Dedication to Quality

Each Frontiers article is a landmark of the highest quality, thanks to genuinely collaborative interactions between authors and review editors, who include some of the world's best academicians. Research must be certified by peers before entering a stream of knowledge that may eventually reach the public - and shape society; therefore, Frontiers only applies the most rigorous and unbiased reviews.
Frontiers revolutionizes research publishing by freely delivering the most outstanding research, evaluated with no bias from both the academic and social point of view.
By applying the most advanced information technologies, Frontiers is catapulting scholarly publishing into a new generation.

What are Frontiers Research Topics?

Frontiers Research Topics are very popular trademarks of the Frontiers Journals Series: they are collections of at least ten articles, all centered on a particular subject. With their unique mix of varied contributions from Original Research to Review Articles, Frontiers Research Topics unify the most influential researchers, the latest key findings and historical advances in a hot research area! Find out more on how to host your own Frontiers Research Topic or contribute to one as an author by contacting the Frontiers Editorial Office: frontiersin.org/about/contact

3D MODELLING OF MAMMALIAN EMBRYOS AND ORGANS

Topic Editors:
Silvia Garagna, University of Pavia, Italy
Juan Aréchaga, University of the Basque Country, Spain
Elisa Cebral, CONICET Institute of Biodiversity and Experimental and Applied Biology (IBBEA), Argentina
Maurizio Zuccotti, University of Pavia, Italy

Citation: Garagna, S., Aréchaga, J., Cebral, E., Zuccotti, M., eds. (2021). 3D Modelling of Mammalian Embryos and Organs. Lausanne: Frontiers Media SA. doi: 10.3389/978-2-88971-607-4

Table of Contents

frontiers
in Cell and Developmental Biology

EDITORIAL
published: 22 September 2021
doi: 10.3389/fcell.2021.763008

Editorial: 3D Modelling of Mammalian Embryos and Organs

Silvia Garagna[1]*, *Elisa Cebral*[2]*, *Juan Aréchaga*[3]* *and Maurizio Zuccotti*[1]*

[1] *Department of Biology and Biotechnology Lazzaro Spallanzani, University of Pavia, Pavia, Italy,* [2] *Departamento de Biodiversidad y Biología Experimental, Facultad de Ciencias Exactas y Naturales, Universidad de Buenos Aires, Buenos Aires, Argentina,* [3] *Department of Cell Biology and Histology, School of Medicine and Nursing, University of the Basque Country, Leioa, Spain*

Keywords: embryos, organs, organogenesis, organoids, 3D imaging, 3D modeling, gastruloids

Editorial on the Research Topic

3D Modelling of Mammalian Embryos and Organs

The main scope of this Special issue was to gain understanding on how tissues and organs are arranged into integrative hierarchical levels of complexity, from the molecular to the morphological organization. To understand the underlying complexity of the relationships among these levels during morphogenesis or in the adult we must learn how to resolve single-cell spatial relationships in the three-dimensional (3D) organization of tissues, organs, and even of the whole organisms.

Each paper in this "Frontiers" special issue contributes to deepen our understanding on the dynamics and mechanisms of development and differentiation in the complexity of the 3D architecture of embryos, intact organs, or organoids.

Five out of 13 contributions, which include Original articles, Reviews, Perspectives, Hypothesis and Theories, focused on intact tissues or organs. In the other eight papers, 3D stem cell culture systems, coupled with advanced microscopy approaches, are exploited to recapitulate morphogenesis and differentiation with the creation of gastruloids, spheroids, or organoids where the cellular organization and function of specific tissues and organs are mimicked. A main content of each contribution is briefly described below starting with those papers focusing on organs and then with those that have used stem cell cultures in 3D.

The use of focused-ion beam-scanning electron microscopic (FIB-SEM) tomography applied to resin-embedded rat adult cortex kidney, allowed Kawasaki et al. to reconstruct, with unprecedented accuracy, the first ultrastructural 3D organization of glomerular endothelial cells (GEnCs). In their paper, entitled "Three-Dimensional Architecture of Glomerular Endothelial Cells Revealed by FIB-SEM Tomography," these cells are made of three major subcellular compartments -the cell body, cytoplasmic ridges, and sieve plates—in addition to the globular protrusions and the reticular porous structures). Moreover, GEnCs organize, without obvious joints, in a tubular shape. This paper reveals the mystery of the capillaries of the rat kidney and sets the bases for 3D structural studies on the glomerular capillary system during development, in physiological or pathological conditions and in different species.

In their elegant study "Three-Dimensional Analysis of Busulfan-Induced Spermatogenesis Disorder in Mice" Nakata et al. adopted a conventional histological approach to perform a 3D reconstruction of all the seminiferous tubules present in the mouse testis treated with busulfan to impair spermatogenesis. They found that impaired tubule segments increased in length, but not in number, in a dose-dependent manner and that the severity of busulfan-induced spermatogenesis disorder is not fixed in location among individuals.

The architecture of intact organs at the single cell level was addressed in two articles where limitations of traditional histology were overcome by the use of an iDISCO-based clearing approach coupled with light-sheet microscopy or micro-computed tomography.

Edited and reviewed by:
Philipp Kaldis,
Lund University, Sweden

****Correspondence:***
Silvia Garagna
silvia.garagna@unipv.it
Elisa Cebral
ecebral@hotmail.com
Juan Aréchaga
juan.arechaga@ehu.eus
Maurizio Zuccotti
maurizio.zuccotti@unipv.it

Specialty section:
This article was submitted to Cell Growth and Division, a section of the journal Frontiers in Cell and Developmental Biology

Received: *23 August 2021*
Accepted: *27 August 2021*
Published: *22 September 2021*

Citation:
Garagna S, Cebral E, Aréchaga J and Zuccotti M (2021) Editorial: 3D Modelling of Mammalian Embryos and Organs.
Front. Cell Dev. Biol. 9:763008.
doi: 10.3389/fcell.2021.763008

In their paper “3D reconstruction of the clarified rat hindbrain choroid plexus” Perin et al. reconstructed the rat hindbrain choroid plexus macro-and microstructure, using markers for epithelium, arteries, microvasculature, and macrophages, and found its association with 4th ventricle-related neurovascular structures.

On formalin-fixed intact ovaries, Fiorentino et al. in their “Three-Dimensional Micro-Computed Tomography of the Adult Mouse Ovary” determined the number of follicles, from pre-antral secondary to antral, of *corpora lutea*, and described the major vasculature, defining their precise 3D localization within the organ volume. They suggest that follicle recruitment is homogeneously distributed all-over the cortex and that follicles grow within the less stiff environment of the medulla until when they re-emerge on the cortex surface of the same tissue region, ready to be eventually ovulated.

The importance of a 3D analysis of the ovary is well-underlined in the Review “Ovary Development: Insights From a Three-Dimensional Imaging Revolution” where Soygur and Laird stress how 3D modeling has evidenced new relationships and levels of organization among follicles during the dynamic tissue remodeling at each hormonal cycle and, also, suggest to exploit ovarian architecture toward therapeutic applications.

Ismagulov et al. in their inspiring Review entitled “Epithelial-Mesenchymal Transition Drives Three-Dimensional Morphogenesis in Mammalian Early Development” present a model in which cellular morphogenesis is the driving force of embryonic 3-D organization. They suggest that the use of *in vitro* platforms where cells grow and differentiate on biomaterials capable of dynamic modulation of their physical properties will make possible to study the integration between mechanical signals and downstream effectors of pathways leading to cell specification and tissue patterning.

The importance of a 3D modeling approach extended to organoids is nicely summarized by Susaki and Takasato in their Perspective “Extending the Utility of Three-Dimensional Organoids by Tissue Clearing Technologies” which contributes with a wide panorama of basic research applications on organoids and provides a toolbox for the study of 3D alterations occurring during either drug administration or deviation from homeostasis to pathology.

On the same line, Kwon et al. in their Review “Intestinal Morphogenesis in Development, Regeneration, and Disease: The Potential Utility of Intestinal Organoids for Studying Compartmentalization of the Crypt-Villus Structure” explore how the current technology of 3D intestinal organoids contributes to the understanding of the regulatory factors and signaling pathways acting during development, maintenance, and regeneration of crypt-villi in the intestinal epithelium.

Organoids are also an innovative technique to study human brain development, but limitations due to heterogeneity and long-term differentiation still hinder their application in disease modeling and drug discovery. In their study “Simplified Brain Organoids for Rapid and Robust Modeling of Brain Disease,” Ha et al. developed homogeneous simplified brain organoids generated in only 2 weeks and made hPSC-derived mature neurons and astroglial cells that can be applied to large-scale disease models and alternative drug-testing platforms.

A rapid and robust protocol to induce neural rosette formation from monolayer cultures of human pluripotent stem cell-derived neural progenitor cells (NPC) was developed by Townshend et al. and described in their original article “Effect of Cell Spreading on Rosette Formation by Human Pluripotent Stem Cell-Derived Neural Progenitor Cells.” The Authors by demonstrating that NPC rosette morphogenesis requires basal spreading activity tightly regulated by Rho/ROCK signaling, provide a cell platform for further investigations on the cellular and molecular mechanisms underlying NPC rosette morphogenesis.

Telencephalon patterning was investigated by Nasu et al. in their “Two-Phase Lineage Specification of Telencephalon Progenitors Generated From Mouse Embryonic Stem Cells” using a 3D *in vitro* differentiation embryonic stem cell model, verifying the contribution of the ventralizing Shh, the dorsalizing BMP and WNT signals. The study reveals a novel developmental mechanism that depends on a dose- and time-dependent signaling interplay which includes a time lag for specification and a temporal shift in cellular Shh sensitivity.

By differentiating patient-derived microtic cartilage stem/progenitor cells using a 3D spheroid culture platform, Zucchelli et al. in “Modeling Normal and Pathological Ear Cartilage *in vitro* Using Somatic Stem Cells in Three-Dimensional Culture” showed that microtic spheroids were asymmetric, hyper-cellularized, the inner, and outer regions did not develop properly with an organization similar to that of native microtic cartilage. Importantly, they observed that microtic cartilages are vascularized. The use of a 3D self-organizing *in vitro* system allowed to identify novel features of microtic ears demonstrating the value of this type of approach for both understanding differentiation and for disease modeling.

Lung epithelial morphogenesis and differentiation were studied by Rabata et al. and described in their paper “3D Cell Culture Models Demonstrate a Role for FGF and WNT Signaling in Regulation of Lung Epithelial Cell Fate and Morphogenesis” employing mouse lung epithelial stem/progenitor cells differentiated in lungospheres (in non-adherent cultures) or lung organoids (using a 3D extracellular matrix culture system). The Results obtained from the two different culture systems revealed distinct roles for FGF ligands in regulating lung morphogenesis and differentiation.

Overall, we believe that the topic of this collection of papers is both relevant and timely. Although limited to specific examples, it overwhelmingly emerges that a significant understanding of development, differentiation, homeostasis, or pathogenesis will be possible when these processes will be studied in the 3D organization of the biological structures.

AUTHOR CONTRIBUTIONS

All authors listed have made a substantial, direct and intellectual contribution to the work, and approved it for publication.

Conflict of Interest: The authors declare that the research was conducted in the absence of any commercial or financial relationships that could be construed as a potential conflict of interest.

frontiers
in Cell and Developmental Biology

ORIGINAL RESEARCH
published: 21 July 2020
doi: 10.3389/fcell.2020.00574

3D Cell Culture Models Demonstrate a Role for FGF and WNT Signaling in Regulation of Lung Epithelial Cell Fate and Morphogenesis

Anas Rabata*[1], *Radek Fedr*[2,3], *Karel Soucek*[2,3], *Ales Hampl*[1,3]* and *Zuzana Koledova*[1]

[1] Department of Histology and Embryology, Faculty of Medicine, Masaryk University, Brno, Czechia, [2] Department of Cytokinetics, Institute of Biophysics of the Czech Academy of Sciences, Brno, Czechia, [3] International Clinical Research Center, St. Anne's University Hospital Brno, Brno, Czechia

Edited by:
Maurizio Zuccotti,
University of Pavia, Italy

Reviewed by:
Soula Danopoulos,
Children's Hospital Los Angeles,
United States
Saverio Bellusci,
University of Giessen, Germany

***Correspondence:**
Ales Hampl
ahampl@med.muni.cz
Zuzana Koledova
koledova@med.muni.cz

Specialty section:
This article was submitted to Cell Growth and Division, a section of the journal Frontiers in Cell and Developmental Biology

Received: *04 April 2020*
Accepted: *15 June 2020*
Published: *21 July 2020*

Citation:
Rabata A, Fedr R, Soucek K, Hampl A and Koledova Z (2020) 3D Cell Culture Models Demonstrate a Role for FGF and WNT Signaling in Regulation of Lung Epithelial Cell Fate and Morphogenesis. Front. Cell Dev. Biol. 8:574. doi: 10.3389/fcell.2020.00574

FGF signaling plays an essential role in lung development, homeostasis, and regeneration. We employed mouse 3D cell culture models and imaging to study *ex vivo* the role of FGF ligands and the interplay of FGF signaling with epithelial growth factor (EGF) and WNT signaling pathways in lung epithelial morphogenesis and differentiation. In non-adherent conditions, FGF signaling promoted formation of lungospheres from lung epithelial stem/progenitor cells (LSPCs). Ultrastructural and immunohistochemical analyses showed that LSPCs produced more differentiated lung cell progeny. In a 3D extracellular matrix, FGF2, FGF7, FGF9, and FGF10 promoted lung organoid formation. FGF9 showed reduced capacity to promote lung organoid formation, suggesting that FGF9 has a reduced ability to sustain LSPC survival and/or initial divisions. FGF7 and FGF10 produced bigger organoids and induced organoid branching with higher frequency than FGF2 or FGF9. Higher FGF concentration and/or the use of FGF2 with increased stability and affinity to FGF receptors both increased lung organoid and lungosphere formation efficiency, respectively, suggesting that the level of FGF signaling is a crucial driver of LSPC survival and differentiation, and also lung epithelial morphogenesis. EGF signaling played a supportive but non-essential role in FGF-induced lung organoid formation. Analysis of tissue architecture and cell type composition confirmed that the lung organoids contained alveolar-like regions with cells expressing alveolar type I and type II cell markers, as well as airway-like structures with club cells and ciliated cells. FGF ligands showed differences in promoting distinct lung epithelial cell types. FGF9 was a potent inducer of more proximal cell types, including ciliated and basal cells. FGF7 and FGF10 directed the differentiation toward distal lung lineages. WNT signaling enhanced the efficiency of lung organoid formation, but in the absence of FGF10 signaling, the organoids displayed limited branching and less differentiated phenotype. In summary, we present lung 3D cell culture models as useful tools to study the role and interplay of signaling pathways in postnatal lung development and homeostasis, and we reveal distinct roles for FGF ligands in regulation of mouse lung morphogenesis and differentiation *ex vivo*.

Keywords: 3D cell culture, epithelial cell, FGF signaling, lung, morphogenesis, organoid, WNT signaling

INTRODUCTION

Mammalian lung is a complex, stereotypically branched organ, whose development is strictly regulated by multiple signaling pathways. They include fibroblast growth factor (FGF) (Lebeche et al., 1999; Ohuchi et al., 2000; Tichelaar et al., 2000; del Moral et al., 2006; Cardoso and Lü, 2006), WNT (Shu et al., 2005; Yin et al., 2008), bone morphogenetic protein (Weaver et al., 1999; Lu et al., 2001; Shu et al., 2005), Sonic Hedgehog (Miller et al., 2004; White et al., 2006), epidermal growth factor (EGF) (Kheradmand et al., 2002), retinoic acid (Malpel et al., 2000), and HIPPO (Volckaert et al., 2019) pathways. Tight interplay of these pathways is essential also for lung epithelial homeostasis, regeneration, and repair (Volckaert and De Langhe, 2015; Volckaert et al., 2017).

FGF signaling plays an essential role in lung development from the very earliest stages. FGF4 is involved in organ-specific domain formation along the anteroposterior axis of the early endoderm (Wells and Melton, 2000; Dessimoz et al., 2006). Later, FGF10-FGFR2b signaling is essential for lung bud formation and to control branching morphogenesis of the lung. Deletion of either *Fgf10* or *Fgfr2b* results in complete distal lung agenesis (Min et al., 1998; Sekine et al., 1999; De Moerlooze et al., 2000), while *Fgf10* hypomorphic lungs display decreased ramifications (Ramasamy et al., 2007). *Fgf10* gain-of-function prevents differentiation of epithelial tip cells toward the bronchial progenitor lineage and disrupts lung morphogenesis (Nyeng et al., 2008; Volckaert et al., 2013). Furthermore, FGF1, FGF2, FGF7, and FGF9 were found in fetal rodent lung, too (Han et al., 1992; Cardoso et al., 1997; Powell et al., 1998; Colvin et al., 2001; Jones et al., 2019). FGF7 acts as a proliferative factor for lung epithelium during lung development (Lebeche et al., 1999), and together with FGF2, it induces expression of surfactant proteins (Matsui et al., 1999). FGF9 is responsible for mesenchymal cell proliferation, and it is also involved in lung epithelium regulation (del Moral et al., 2006).

The role of FGF signaling in lung development and homeostasis is interwoven with WNT signaling. FGF and WNT signaling regulate proximal/distal patterning and fate of lung progenitor cells (Volckaert and De Langhe, 2015). Canonical WNT signaling is required for mesenchymal expression of FGF10 and primary lung bud formation (Goss et al., 2009). Furthermore, mesenchymal WNT signaling regulates amplification of *Fgf10* expressing airway smooth muscle cell progenitors in the distal mesenchyme (Volckaert and De Langhe, 2015). In adult lung, FGF10 and WNT signaling regulate the activity of basal cells, the lung epithelial stem/progenitor cells (LSPCs) that ensure lung epithelial homeostasis and repair after injury (Volckaert et al., 2013). However, the exact functions of FGF and WNT signaling in LSPCs have not been fully elucidated.

In this study, we investigated the role of FGF and WNT signaling in the regulation of postnatal lung epithelial morphogenesis and homeostasis from LSPCs. To this end, we developed and used several 3D cell culture techniques, including lungosphere and lung organoid assays, and we investigated the ability of various FGF ligands and WNT signaling to support LSPC survival and differentiation to epithelial structures.

RESULTS

Lungosphere Assay Demonstrates the Existence of Cells With Capacity for Anchorage-Independent Growth and Self-Renewal

Stem and progenitor cells are defined by their capacities to self-renew (i.e., to replicate and form more of the same cells), as well as to produce more differentiated progeny (Fuchs and Chen, 2013). On top of that, one of the distinctive characteristics of stem and progenitor cells is their ability to resist anoikis and to survive in non-adherent conditions (Pastrana et al., 2011). These characteristics have been applied in sphere formation assays, such as neurosphere (Reynolds and Weiss, 1992) or mammosphere (Shaw et al., 2012) formation assays and, to some extent, also in lung cancer sphere formation assays (Zhao et al., 2015). We applied this approach to isolate LSPCs. Single epithelial cells from mouse lung were seeded in non-adherent plates in a defined serum-free medium with epidermal growth factor (EGF) and FGF2 and cultured for 10–14 days, with the addition of a fresh medium every 3 days (Shaw et al., 2012; Rabata et al., 2017). Because FGF2 rapidly loses its biological activity at 37°C, we tested the use of FGF2-wt, as well as FGF2 with increased thermal stability (FGF2-STAB) (Dvorak et al., 2018) and sustained FGFR specificity (Koledova et al., 2019) for their capacity to support lungosphere formation. With FGF2-wt, the lungosphere formation efficiency (LFE) was 0.088 ± 0.006% (**Supplementary Figures 1A,B**), and the lungospheres were of three different phenotypes: grape-like, cystic with a clearly defined lumen, and compound with regions resembling both the grape-like and the cystic phenotype. With FGF2-STAB, lungospheres were formed with the same phenotypes as with FGF2-wt; however, they formed with significantly higher LFE (0.132 ± 0.015%) (**Figures 1A,B** and **Supplementary Figure 1B**).

To test the capacity of these spheres to self-renew, we performed a secondary lungosphere assay. Primary lungospheres were disintegrated to single cells and seeded again in non-adherent conditions. After 14 days of cultivation, secondary lungospheres of similar phenotypes as the primary lungospheres were formed at LFE 0.150 ± 0.055% (**Figures 1A,B**), whereas the LFE in the presence of FGF2-wt was lower (0.100 ± 0.029%) (**Supplementary Figure 1C**).

To investigate what cells of the lung epithelium are capable of lungosphere formation, we sorted the lung epithelial cells by FACS according to markers for adult lung stem cells

---

Abbreviations: AQP5, aquaporin 5; ATI, alveolar type I cell; ATII, alveolar type I cell; CC10, club cells specific 10 protein; ECM, extracellular matrix; EGF, epithelial growth factor; EMT, epithelial to mesenchymal transition; FACS, fluorescence-activated cell sorting; FGF, fibroblast growth factor; FGF2-STAB, stabilized FGF2; FGF2-wt, wild-type FGF2; FGFR, fibroblast growth factor receptor; K5, keratin 5; K8, keratin 8; LFE, lungosphere forming efficiency; LSPC, lung epithelial stem/progenitor cells; OFE, organoid forming efficiency; pro-SPB, pro-surfactant protein B; pro-SPC, pro-surfactant protein C; WCM, WNT3A-conditioned medium.

(McQualter and Bertoncello, 2015) and cultured them in non-adherent conditions. The adult lung stem cell-enriched population characterized by EpCAM$^+$, CD49f$^+$, CD24^{low}, CD104$^+$ status (McQualter and Bertoncello, 2015) formed primary and secondary lungospheres of similar phenotypes as unsorted cells and with LFE 1.475 ± 0.150% for primary and 1.967 ± 0.208% for secondary lungospheres, respectively (**Figures 1C,D**). In contrast, EpCAM$^+$, CD49f$^+$, CD24^{hi}, CD104$^+$ and EpCAM$^+$, CD49f$^+$, CD24^{neg}, CD104^{neg} cells formed only primary lungospheres with LFE 1.4% and 0.2%, respectively, and failed to form secondary lungospheres (**Figures 1E,F**). These results indicated that the self-renewing lungosphere-forming stem cells are present in the EpCAM$^+$, CD49f$^+$, CD24^{low}, CD104$^+$ population.

To test whether the lungospheres were clonal and formed by the division of single stem cells rather than being formed by cell aggregation, we sorted single EpCAM$^+$, CD49f$^+$, CD24^{low}, CD104$^+$ cells directly in 96-well plates at only one cell per well in non-adherent conditions. We observed the formation of lungospheres with LFE 1.733 ± 0.153% (**Figure 1D**), which was similar to the primary LFE when thousands of cells were cultured together in one well, suggesting that the lungospheres were clonal.

Histological analysis of primary lungospheres grown from unsorted cells in non-adherent conditions revealed that lungospheres formed lung-like structures, with both alveolar-like and airways-like morphologies (**Figure 1G**). Using immunofluorescence analysis of the lungospheres, we detected cells positive for lung epithelial cell markers cytokeratin 8 (K8) and E-cadherin, basal cell markers cytokeratin 5 (K5) and cytokeratin 14 (K14), club cell marker CC10, mucous cell marker MUC5AC, marker of secretory serous cells in the respiratory pathway lysozyme, markers of ATII cells prosurfactant protein B (pro-SPB) and prosurfactant protein C (pro-SPC), and the marker of the ATI cells aquaporin 5 (AQP5) (**Figure 1H**). Ultrastructural analysis by transmission electron microscopy showed that a lungosphere is composed of a group of cells connected by tight junctions (**Supplementary Figure 2A**). Some of the lungosphere cells have a dense cytoplasm that is rich in mitochondria and lamellar bodies (**Supplementary Figure 2A**).

In summary, our observations suggest that postnatal lung epithelium contains LSPCs with the ability to resist anoikis, to self-renew, and to form clonal spheres containing both stem/progenitor cells and more differentiated cells, and that the LSPCs can be efficiently isolated from the lung using the lungosphere assay without the requirement for FACS.

Lung Epithelial Cells Form Organoids in 3D Matrigel

Extracellular matrix (ECM) provides regulatory signals for epithelial tissue growth and patterning (De Arcangelis and Georges-Labouesse, 2000). Therefore, we embedded lungospheres formed in non-adherent conditions in 3D Matrigel and cultured them for over 30 days to investigate the morphogenesis of lungospheres in a physiologically more relevant setting. We observed the formation of large cystic and/or branched organoids (**Figure 1I**). These organoids had a complex lung-like structure (**Figure 1J**). Ultrastructural analysis by transmission electron microscopy revealed different types of cells present in the lungosphere-derived organoids (**Supplementary Figure 2B**). They included ATI cell-like simple squamous cells with central nucleus and a thin cytoplasm, ATII cell-like cuboidal cells with central nucleus and cytoplasm rich in mitochondria and lamellar bodies, and club cell-like columnar cells with basally located nucleus and lamellar bodies within the cytoplasm (**Supplementary Figure 2B**). This cell diversity was further supported by the presence of a variety of epithelial and lung cell markers, including K5, K8, Pro-SPC, CC10, and AQP5 (**Figure 1K**), as found by immunofluorescence.

Next, we investigated the ability of unsorted lung epithelial cells to form lung organoids directly in Matrigel from single cells. The cells were cultured in 3D Matrigel in the same medium as lungospheres. We observed the formation of organoids with efficiency (organoid forming efficiency, OFE) of 0.110 ± 0.007% (**Figure 2A**), which was similar to the LFE of unsorted lung epithelial cells. Control experiments with FGF2-wt showed the formation of lung organoids with similar phenotype but at lower OFE (0.067 ± 0.008%) (**Supplementary Figures 3A,B**). The organoids, which had developed in the presence of FGF2-wt, did not show any significant difference in branching efficiency in comparison to organoids developed in the presence of FGF2-STAB (**Supplementary Figure 3C**). However, we observed a significantly higher proportion of K8-positive to K5-positive cells in the FGF2-STAB organoids (**Supplementary Figures 3D,E**).

Different FGF Ligands Contribute Differently to Lung Organoid Formation

During lung development, different FGFs are differently required at specific stages of lung specification and morphogenesis (Volckaert and De Langhe, 2015). Therefore, we investigated the effect of different FGFs on lung organoid formation. To this end, we cultured unsorted lung epithelial cells in 3D Matrigel with EGF (20 ng/ml) and FGF2, FGF7, FGF9, or FGF10 (all at 1 nM). We found that with the different FGFs tested, the organoids formed with similar efficiencies as with FGF2, except for FGF9 with which the organoids formed with significantly lower efficiency (0.110 ± 0.007%, 0.117 ± 0.006%, 0.053 ± 0.017%, and 0.123 ± 0.017% for FGF2, FGF7, FGF9, and FGF10, respectively) (**Figures 2A,C**). Analysis of the organoid morphology revealed that FGF7 and FGF10, respectively, supported the formation of more complex, branched structures in a significantly higher proportion of organoids (**Figure 2B** and **Supplementary Figure 4A**). For all FGFs tested, the increase in their concentration to 2 nM has led to at least twofold increase in numbers of produced organoids (**Figure 2D**).

Next, we tested the requirement of EGF for lung organoid formation. To this end, we cultured the lung epithelial cells in 3D Matrigel with media containing different FGFs (2 nM)

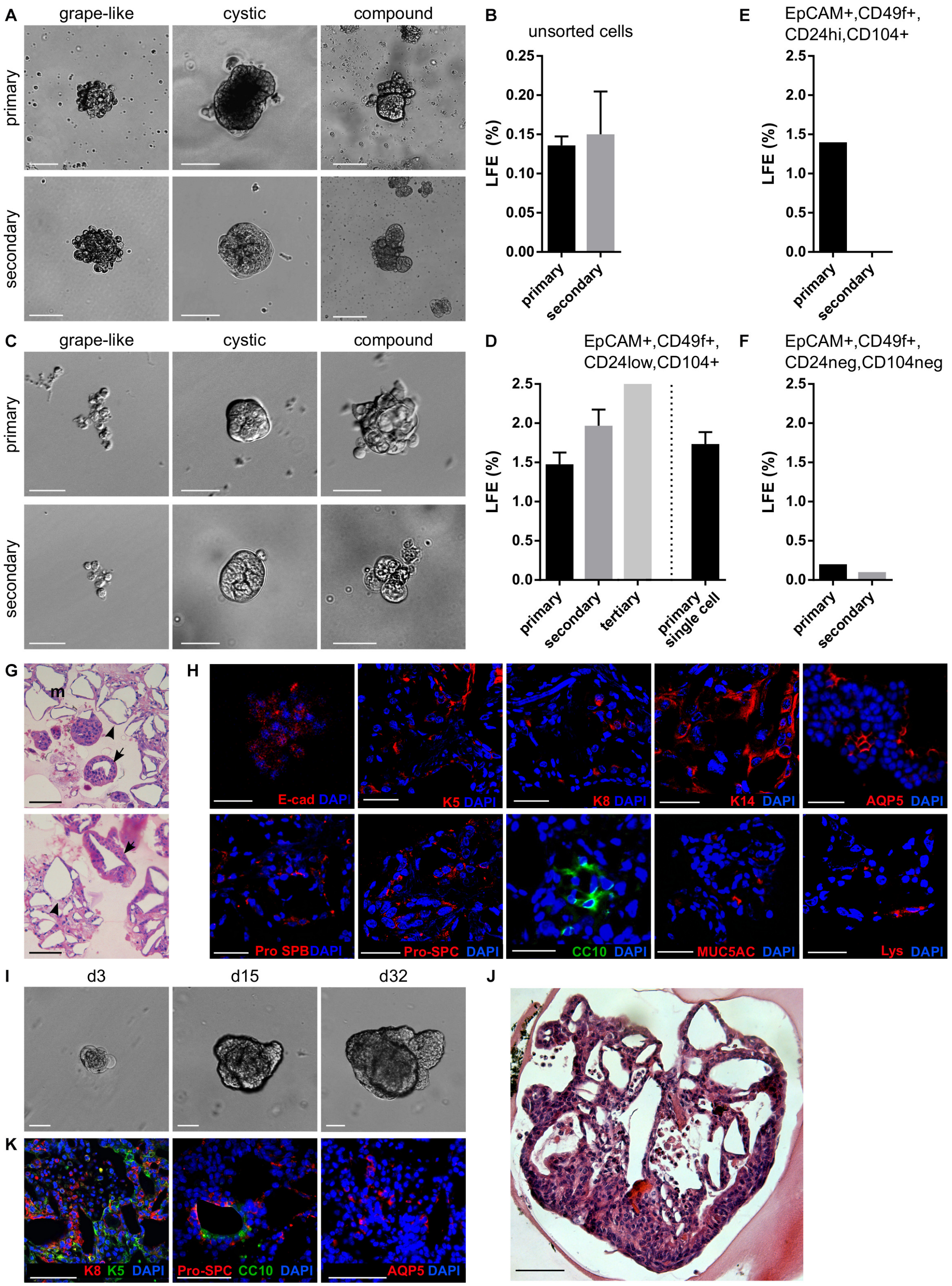

FIGURE 1 | Lung epithelium contains LSPCs that form lungospheres with the capacity for self-renewal and differentiation. **(A,B)** Lungospheres formed from unsorted lung epithelial cells in non-adherent conditions with EGF and FGF2. **(A)** Representative photographs of primary and secondary lungospheres. Scale bar, 100 μm. **(B)** The efficiency of primary and secondary lungosphere formation with EGF and FGF2. The plots show mean + SD; *n* = 5. **(C,D)** Lungospheres formed from FACS-sorted EpCAM$^+$, CD49f$^+$, CD24^{low}, CD104$^+$ cells in non-adherent conditions with EGF and FGF2**(C)** Representative photographs of primary and secondary lungospheres. Scale bar, 100 μm. **(D)** The efficiency of primary and secondary lungosphere formation with EGF and FGF2.The plots show mean + SD;

(Continued)

FIGURE 1 | Continued
$n = 3$ ($n = 1$ for tertiary lungospheres). The columns left from the dashed vertical line show LFE from cells cultured at thousands of cells per well; the column right from the line shows LFE from cells cultured individually – a single cell per well. **(E,F)** The efficiency of primary and secondary lungosphere formation of FACS-sorted EpCAM$^+$, CD49f$^+$, CD24^{hi}, CD104$^+$ **(E)** and EpCAM$^+$, CD49f$^+$, CD24^{neg}, CD104^{neg} **(F)** cells in non-adherent conditions with EGF and FGF2. The plots show mean + SD; $n = 1$. **(G,H)** Primary lungospheres grown in non-adherent conditions form lung-like structures. **(G)** The photographs of hematoxylin/eosin-stained paraffin sections show alveolar-like structures (arrowheads) and airways-like structures (arrows). **(H)** Immunofluorescence staining of paraffin sections for E-cadherin, keratin 5 (K5), keratin 8 (K8), keratin 14 (K14), Pro-SPB, Pro-SPC, aquaporin 5 (AQP5), CC10, MUC5AC, lysozyme (Lys), and nuclei (DAPI). **(I–K)** Lungospheres embedded in 3D Matrigel and cultured with EGF and FGF2 proliferate and form large organoids with lung-like structure. **(I)** The photographs show morphogenesis of a lungosphere-derived organoid over 32 days. **(J)** Hematoxylin/eosin-stained section of lungosphere-derived organoid. **(K)** Immunofluorescence staining of paraffin sections of lungosphere-derived organoids for keratin 5 (K5), cytokeratin 8 (K8), Pro-SPC, CC10, AQP5, and nuclei (DAPI). **(G–K)** Scale bar, 100 μm.

in the presence (20 ng/ml) or absence of EGF. We found that lung organoids formed also in the absence of EGF (**Figure 2E**). However, removal of EGF from the cell culture media significantly reduced primary lung organoid formation in the case of culture with FGF2 and FGF9, and reduced secondary OFE in the case of FGF9 (**Figures 2F,G**). No organoids formed in the absence of both EGF and FGF. However, EGF on its own was capable of supporting lung organoid formation at low OFE (**Figures 2F,G**).

Analysis of the organoid morphology revealed that organoids that formed in the absence of EGF were significantly smaller compared to those formed with EGF (**Figure 2H**). Also, organoids formed with FGF7 and/or FGF10 were significantly bigger than the organoids formed with FGF2 and/or FGF9 (**Figure 2H**). Moreover, FGF7 and FGF10 induced organoid branching in a significantly higher proportion of organoids than FGF2 or FGF9, irrespective of EGF presence (**Supplementary Figures 4B,C**). The absence of EGF significantly reduced branching of organoids formed with FGF9 (**Supplementary Figure 4B**). The most complex organoids with the highest number of branches were then produced by treatment with FGF7 or FGF10 (**Supplementary Figures 4B,C**).

We then investigated whether preculturing of lung epithelial cells with FGF2, followed by cultivation with different FGFs, would affect organoid formation and branching. We first cultured the lung epithelial cells for 7 days with 1 nM FGF2 only and then continued with the culture in media containing 1 nM FGF2, or FGF7, or FGF9, or FGF10 (**Figure 2I**). Overall, the preculture with FGF2 had a positive effect on organoid formation. It rescued the inability of FGF9 to efficiently support organoid formation and also significantly increased organoid formation in a medium with FGF7, FGF9, and FGF10, respectively (**Figures 2I,J**). In contrast to its effect on organoid formation, 7-day preculture with FGF2 did not influence organoid branching (**Figure 2K**). Still, the organoids cultured in FGF7 and FGF10, respectively, were superior in their branching capability compared to those cultured continuously in only FGF2 (**Figure 2K**). This observation suggests that in the initial phase of lung organoid formation, cell survival and/or proliferation, which is efficiently supported by FGF2, might be the deciding factors for further organoid development. Then, in the later stage of lung organoid growth and patterning, organoid morphogenesis may be more driven by signals from FGF7, FGF9, and FGF10.

Collectively, our data indicate that at least *ex vivo,* FGF ligands assayed here may have partially redundant functions. An intriguing role seems to be played by FGF9 that has minimal capacity to promote organoid formation from single cells but is a strong organoid-stimulating signal in later stages of their morphogenesis.

Lung Organoids Contain Both of Alveolar-Like and Airway-Like Structures

Next, we characterized the overall histological structure and cell type composition of lung organoids using hematoxylin-eosin staining and immunohistochemistry. Because FGF10 plays an important role during lung specification and morphogenesis (Ramasamy et al., 2007; Volckaert et al., 2013), and because it acted as one of the most effective inducers of lung organoid formation and branching in our experiments, we focused our attention primarily to the organoids formed with FGF10. Typically, we detected the presence of basally localized K5-positive cells and luminally localized K8-positive cells, in both more cystic-like and branched organoids (**Figures 3A,B**). The organoids contained airway-like regions with ciliated cells (positive for acetylated tubulin) (**Figure 3C**) and club cells (positive for CC10), as well as alveolar-like regions with cells expressing ATII and ATI cell markers pro-SPC and AQP5, respectively (**Figure 4**). Distal lung patterning (indicated by positivity for NKX2-1) was more prominent in the organoids than the proximal patterning (SOX2) (**Figure 4** and **Supplementary Figure 5**). Organoids formed in the presence of FGF2, FGF7, or FGF9 showed cellular composition similar to the organoids formed with FGF10 according to histological and immunofluorescence analysis (**Figure 4**). However, qPCR analysis revealed several interesting differences in the expression of lung epithelial cell genes in organoids treated with different FGF ligands. Overall, organoids formed with FGF7 showed very similar gene expression profile to organoids formed with FGF10. They both showed downregulated expression of proximal lung marker *Sox2*, and increased expression of distal lung markers *Sox9* and *Nkx2-1*, ATI marker *Aqp5, Calca* (neuro-endocrine cell marker), *Foxi* (pulmonary ionocyte marker), *Muc5ac* and *Muc5b*, surfactant genes *Sftpa1, Sftpb*, and *Sftpc*, and club cell marker *Scgb1a1.* Organoids formed with FGF9 demonstrated markedly decreased expression of surfactant genes and *Calca,* but increased expression of *Foxj* (marker of ciliated cells) and *Krt5* (**Figure 5**).

These results indicate that the lung organoid system, elaborated and used here, achieves cell differentiation to a wide range of lung epithelial cell lineages and that FGF

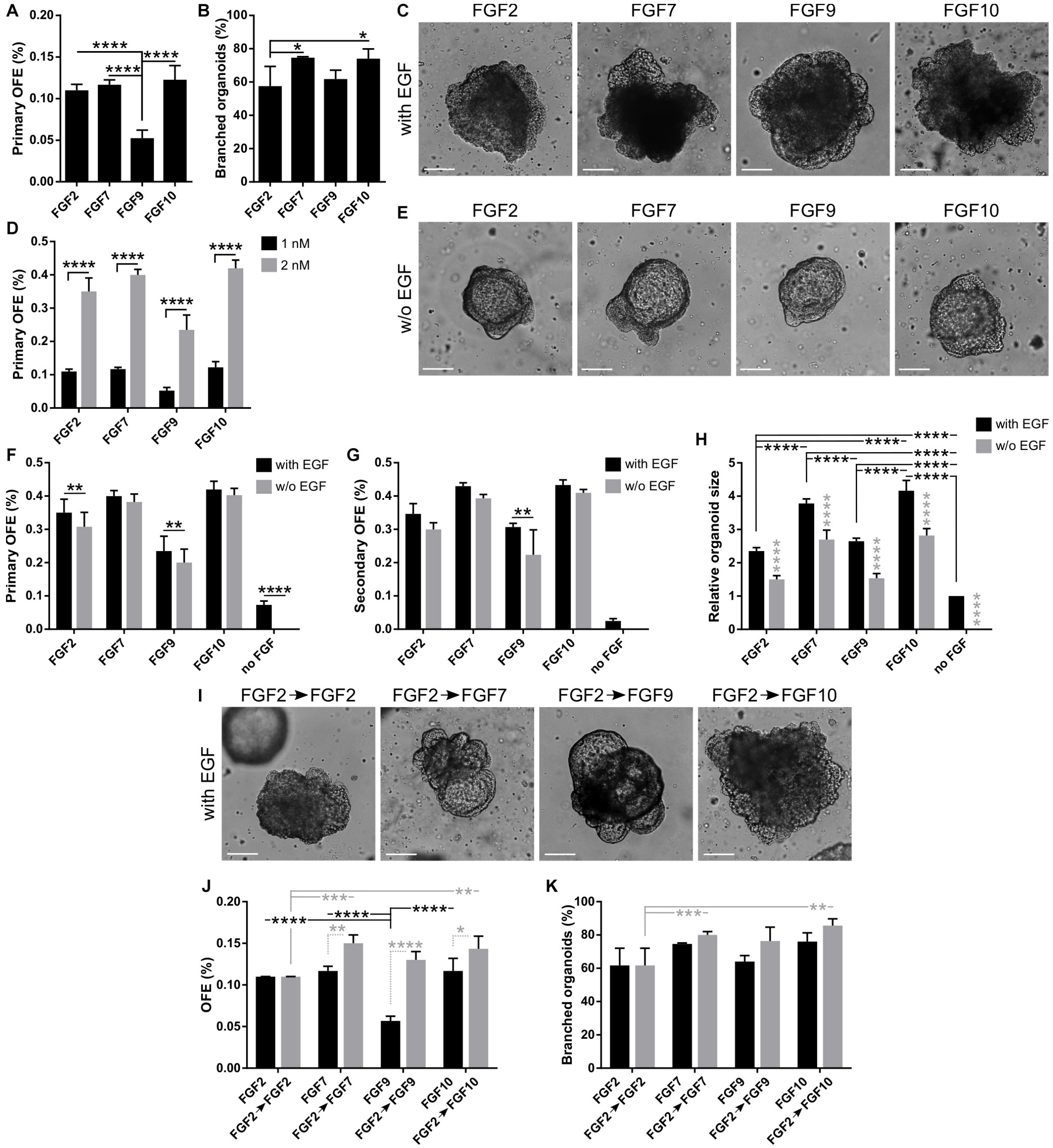

FIGURE 2 | FGFs promote formation, proliferation, and branching of lung organoids. **(A–C)** In 3D Matrigel, lung organoids are efficiently formed in response to different FGFs. **(A)** Primary lung organoid forming efficiency (OFE). The plot shows mean + SD; *n* = 3–5. ****$P < 0.0001$ (one-way ANOVA). **(B)** Branching efficiency (%) of lung organoids on day 21 of culture, shown as mean + SD; *n* = 3–4. *$P < 0.05$ (one-way ANOVA). **(C)** Representative photographs of primary lung organoids formed in 3D Matrigel in response to different FGFs (1 nM). Scale bar, 100 μm. **(D)** Increased concentration of FGFs increases organoid forming efficiency. The plot shows primary lung OFE as mean + SD; *n* = 3–5. ****$P < 0.0001$ (two-way ANOVA). **(E–H)** EGF is not essential for lung organoid formation in the presence of FGFs. **(E)** Representative photographs of primary lung organoids formed in 3D Matrigel in the presence of different FGFs (2 nM) and in the absence of EGF. Scale bar, 100 μm. **(F,G)** The plots show primary **(F)** and secondary **(G)** lung organoid forming efficiency as mean + SD; *n* = 3–4. **$P < 0.01$; ****$P < 0.0001$ (two-way ANOVA). **(H)** Analysis of organoid size. The sizes are relative to organoids formed in a medium with EGF and no FGF. The plots show mean + SD; *n* = 3, *N* = 15–20 organoids/treatment. The gray symbols indicate significance between the culture with and without EGF for the respective FGF. ****$P < 0.0001$ (two-way ANOVA). **(I–K)** Initial treatment with FGF2 for 7 days increases lung organoid formation and branching efficiency in response to FGF7, FGF9, and FGF10. **(I)** Representative photographs of primary lung organoids formed in 3D Matrigel after 7 days of culture with 1 nM FGF2, followed by culture with different FGFs (1 nM). The pictures are from day 20 of culture. Scale bar, 100 μm. **(J,K)** The plots show primary lung OFE **(J)** and branching efficiency of lung organoids **(K)** as mean + SD; *n* = 3. *$P < 0.05$; **$P < 0.01$; ***$P < 0.001$; ****$P < 0.0001$ (two-way ANOVA).

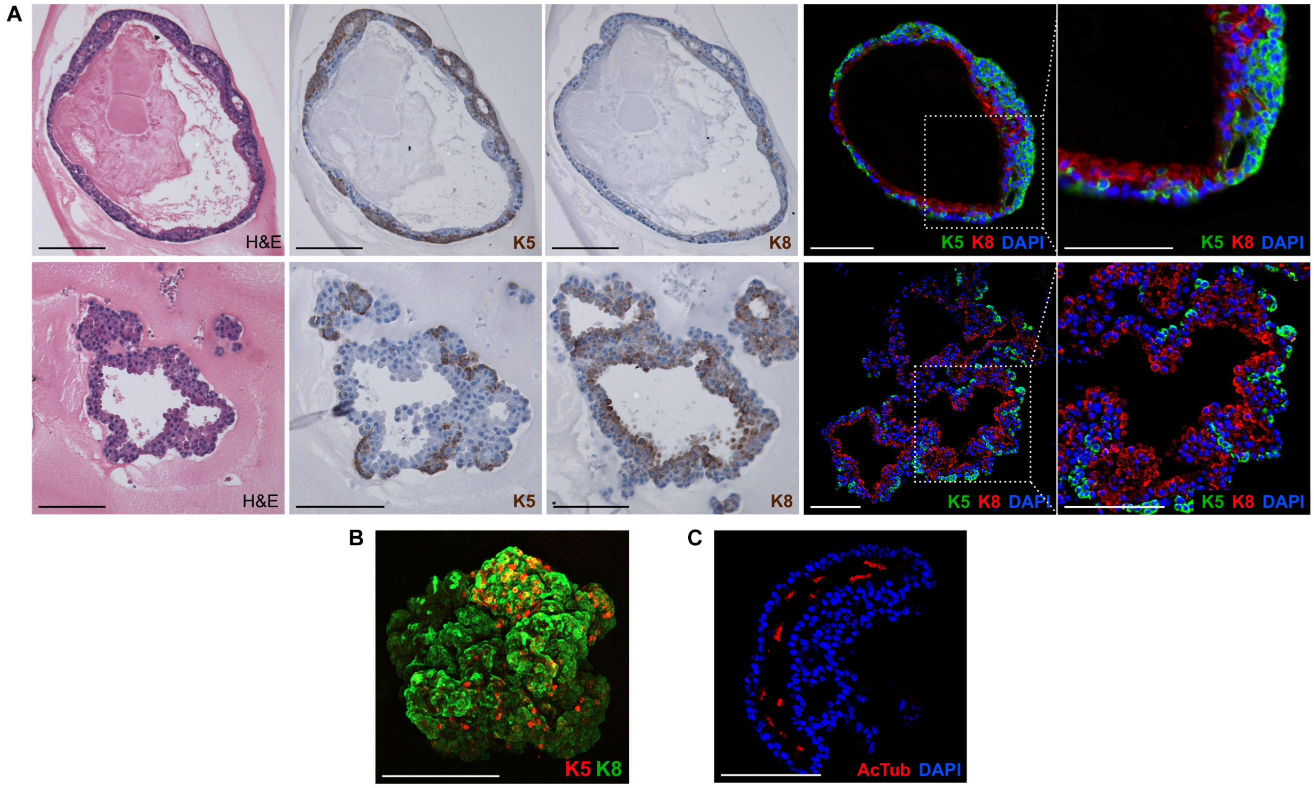

FIGURE 3 | Lung organoids recapitulate cellular composition and organization of the lung. **(A,B)** Lung organoids have complex organization with basally localized keratin 5 positive cells and luminally localized keratin 8 positive cells. The photographs show paraffin sections of an organoid cultured in 3D Matrigel with FGF10, stained with hematoxylin/eosin (H&E) or by immunohistochemistry for keratin 5 (K5) or 8 (K8). Scale bar, 100 μm. **(B)** A whole-mount 3D confocal image of an organoid cultured in 3D Matrigel with FGF10, stained by immunofluorescence for keratin 5 (K5) and 8 (K8). Scale bar, 100 μm. **(C)** Immunofluorescence analysis of paraffin sections of lung organoids for acetylated tubulin (AcTub), a marker of ciliated cells. Blue, nuclei (DAPI). Scale bar, 100 μm.

ligands influence differentiation to certain lung epithelial cell types differently.

WNT3A Increases the Efficiency of Lung Organoid Formation and FGF10 Promotes Differentiation to Lung Epithelial Cell Lineages

WNT signaling plays an essential role during lung development (Frank et al., 2016) and repair after injury (Whyte et al., 2012; Lee et al., 2017). Moreover, WNT signaling is critically important for self-renewal and specification of stem cells in multiple organs (Clevers et al., 2014) and has been successfully employed in protocols for the production of organoids from several organs, including lungs (Lee et al., 2017). Therefore, here we also investigated the formation of lung organoids under the conditions involving WNT signals.

The WNT-based protocols typically combine WNT3A, R-Spondin1 (WNT agonist), Noggin (bone morphogenic protein inhibitor), and EGF and, optionally, also FGFs, to support organoid growth in basement membrane ECM. WNT3A can be supplemented to the medium in the form of recombinant protein from a commercial supplier, or in the form of a WNT3A-conditioned medium (WCM; Sugimoto and Sato, 2017). We tested both approaches.

WNT3A efficiently promoted lung organoid formation, but WCM was significantly less effective in this phenomenon (**Figures 6A,B**). Moreover, in the culture variant with WCM, we observed a striking new phenotype – colonies of cells of mesenchymal-like morphology (**Figures 6A,C**). These colonies started off as epithelial structures but changed into mesenchymal-like cells, intriguingly resembling the process of epithelial-to-mesenchymal transition (EMT). We hypothesized that factor(s) responsible for such effect of WCM may originate from the serum contained in WCM preparation as part of the culture medium. Therefore, we prepared also serum-free WCM (WCM-I) by culturing cells in a medium containing ITS (insulin–transferrin–selenium) instead of serum. As expected, the EMT-like phenotype was much less pronounced in the WCM-I compared to serum-containing WCM (WCM-S). Also, WCM-I was superior to WCM-S in the efficiency of organoid production (**Figures 6A–C**).

Because of the important role of FGF10 during lung epithelial development, also demonstrated here, we further investigated

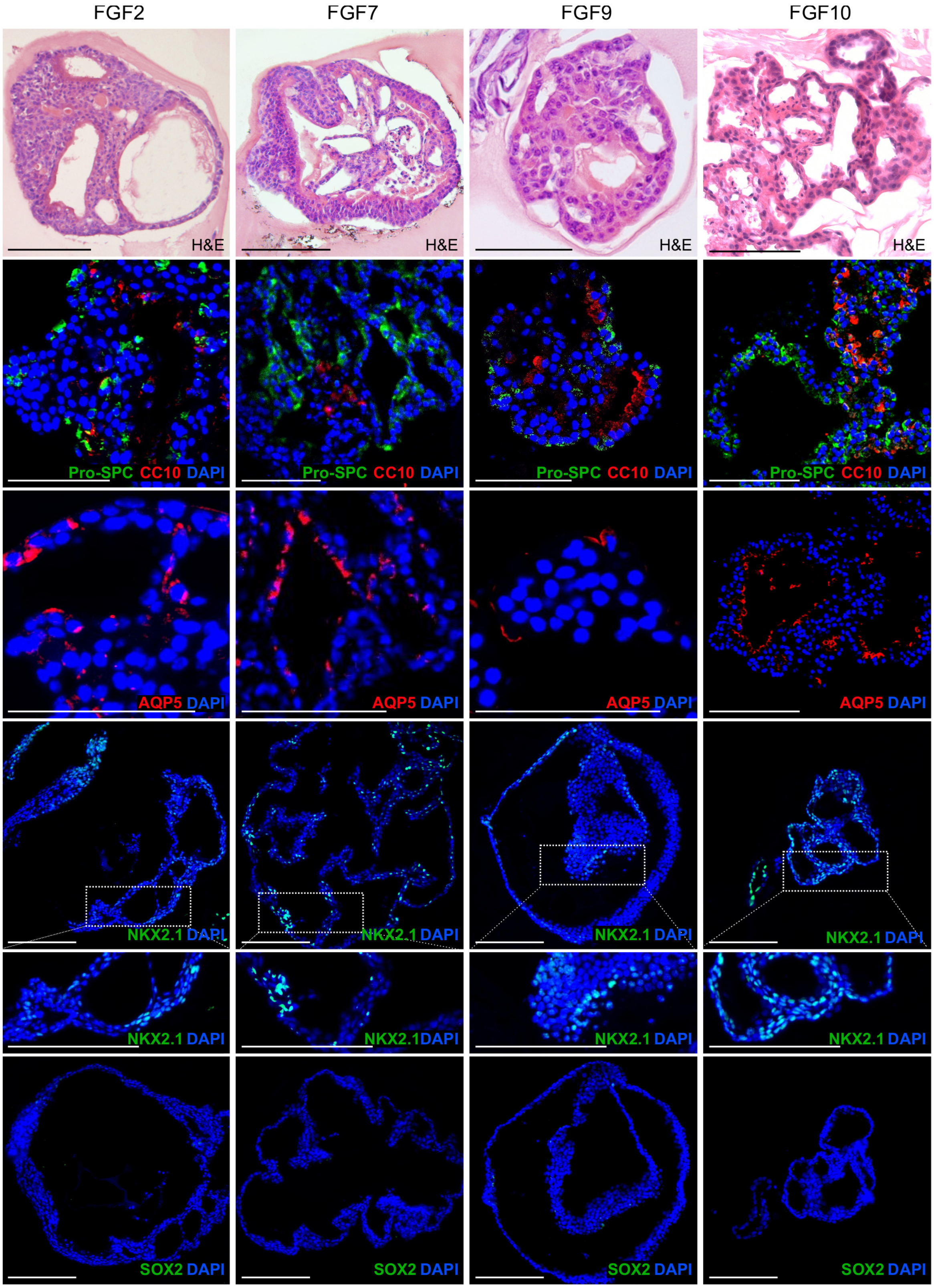

FIGURE 4 | Lung organoids formed with different FGF ligands show similar cellular composition, including both alveolar-like regions and airway-like regions. The photographs show immunofluorescence analysis of paraffin sections of lung organoids for markers of ATII cells (Pro-SPC), club cells (CC10), ATI cells (AQP5), distal lung lineages (NKX2-1), and proximal lung lineages (SOX2). Blue, nuclei (DAPI). Scale bar, 100 μm.

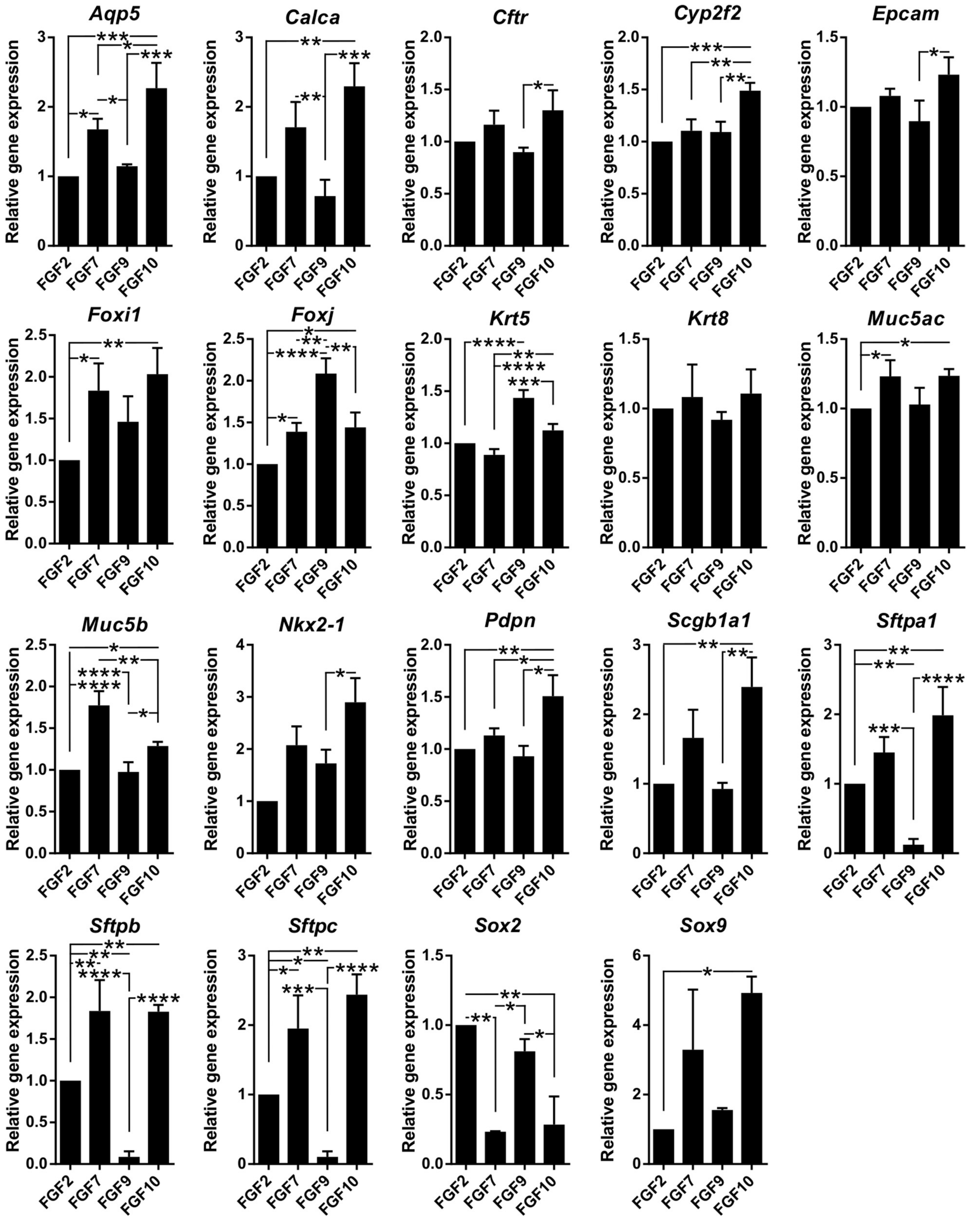

FIGURE 5 | FGF ligands demonstrate differences in promoting certain lung epithelial cell types. Results from qPCR analysis of expression of candidate genes in organoids grown with different FGF ligands (1 nM). The plots show mean + SD, $n = 3$ (2 for *Sox2, Sox9,* and *Nkx2-1*). $^{*}P < 0.05$; $^{**}P < 0.01$; $^{***}P < 0.001$; $^{****}P < 0.0001$ (one-way ANOVA).

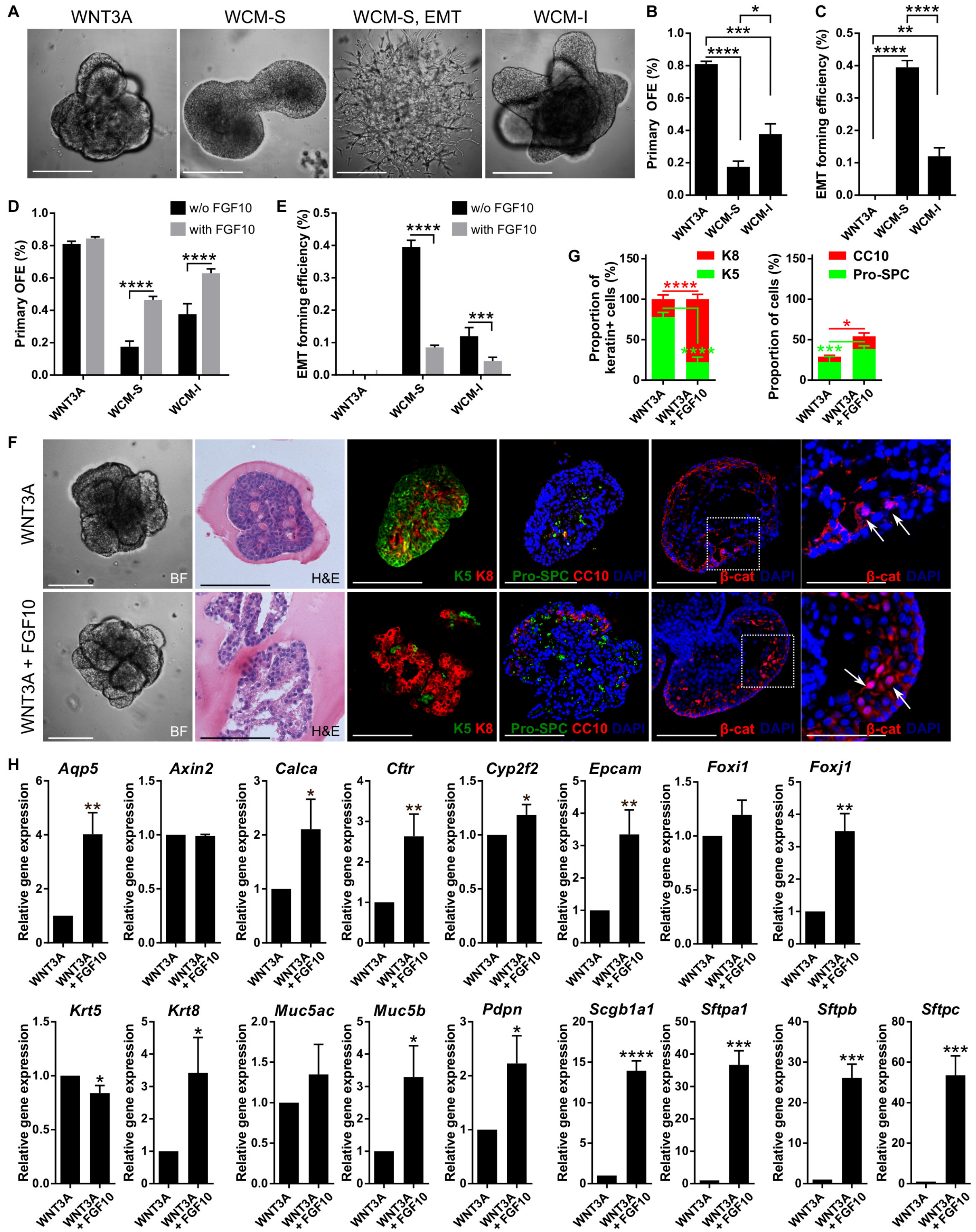

FIGURE 6 | WNT3A enhances the efficiency of lung organoid formation and addition of FGF10 promotes organoid differentiation. **(A)** Representative photographs of lung organoids formed with WNT-based protocol in 3D Matrigel. WCM-S, WNT3A-conditioned medium with serum; WCM-I, serum-free WNT3A-conditioned medium (with ITS); EMT, epithelial to mesenchymal transition. **(B,C)** Primary lung organoid forming efficiency (OFE; **B**) and efficiency of formation of EMT colonies **(C)**. The plots show mean + SD; *n* = 3. $^{*}P < 0.05$; $^{**}P < 0.01$; $^{***}P < 0.001$; $^{****}P < 0.0001$ (one-way ANOVA). **(D,E)** FGF10 increases lung organoid formation efficiency and decreases EMT occurrence in the cultures with WCM-based media. The plots show mean + SD; *n* = 3. $^{***}P < 0.001$; $^{***}P < 0.001$ (two-way ANOVA).

(Continued)

FIGURE 6 | Continued
(F) Brightfield images (BF), histological analysis (H&E), and immunofluorescence staining of lung organoids.Scale bar, 100 μm. The area marked by white dashed line is magnified in the picture on the right; scale bars represent 50 μm in the magnified picture. The arrows indicate nuclear localization of β-catenin. **(G)** The plots show proportion of K5 positive (+) or K8 + cells in the total number of keratin + (sum of K5 + and K8 + cells) cells, and CC10 + and Pro-SPC + cells in the total number of cells in the organoid sections as mean + SD; $n = 4$, $N = 3$ organoids per experiment. $^*P < 0.05$; $^{***}P < 0.001$; $^{****}P < 0.0001$ (one-way ANOVA). **(H)** Results from qPCR analysis of expression of candidate genes of WNT3A treatment with or without FGF10. *Actb* and *Eef1g* were used as reference genes for normalization. The plots show mean + SD, $n = 3$. $^*P < 0.05$; $^{**}P < 0.01$; $^{***}P < 0.001$; $^{****}P < 0.0001$ (Student's *t*-test).

the effect of FGF10 on the formation of lung organoids under conditions utilizing WNT signaling. Curiously, while FGF10 did not potentiate organoid forming efficiency when combined with WNT3A, it did significantly increase organoid formation in cultures containing either type of WCM (**Figure 6D**). FGF10 also significantly reduced the occurrence of EMT-like phenotype in WCM-containing cultures (**Figure 6E**).

Histological and immunohistochemical analysis of lung organoids produced under conditions containing WNT3A alone or WNT3A plus FGF10, respectively, demonstrated that the presence of FGF10 dramatically increased a degree of organoid differentiation. Specifically, organoids grown under the influence of FGF10 contained expanded lung-like regions (**Figure 6F**) and typically expressed much higher numbers of K8-, Pro- SPC-, and CC10-positive cells (**Figures 6F,G**). The organoids formed with WNT3A only were more compact and contained several layers of less differentiated basal cells (**Figure 6F**). It is of note that organoids produced under conditions containing WNT3A showed nuclear localization of β-catenin, thus documenting activation of the WNT signaling pathway (**Figure 6F**).

We have further approached the regulatory significance of WNT and FGF10 by quantifying the expression of 16 genes that define specific types of cells and/or stages of development of lung epithelial cell lineages (**Figure 6H**). To this end, the organoids were cultured in the media containing WNT3A with or without FGF10. The key findings were as follows. The organoids expressed all the genes assayed, however, the expression levels were influenced by the presence and absence of FGF10. Although the statistical significance of the differences varied among the individual genes, overall, the expression of genes associated with differentiated cell phenotypes was higher in organoids formed in an FGF10-containing medium. Specifically, this difference was very highly pronounced for genes encoding AQP5 (*Aqp5*; ATI cells), CFTR (*Cftr*; anion secretory cells), EpCAM (*Epcam*; epithelial cells), forkhead box protein J1 (*Foxj1*; ciliated cells), CC10 (*Scgb1a1*; club cells), SP-A (*Sftpa1*; ATII cells), SP-B (*Sftpb*; ATII cells), and SP-C *(Sftpc*; ATII cells); less pronounced for CGRP (*Calca*; neuroendocrine cells), P450 (*Cyp2f2*; club cells), K8 (*Krt8*; epithelial cells), mucin 5B (*Muc5b*; mucosa cells), and podoplanin (*Pdpn*; ATI cells); and statistically insignificant for forkhead box protein I1 (*Foxi1;* pulmonary ionocytes) and mucin 5A/C (*Muc5ac*; mucosa cells). Importantly, FGF10 decreased the expression of stemness-associated K5 gene (*Krt5;* basal cells). Comparison of the gene expression in the presence of WNT3A, WNT3A + FGF10, or FGF10 only revealed that these genes were indeed regulated by FGF10 (**Supplementary Figure 6**). FGF10 did not influence intracellular action of WNT3A, as indicated by sustained expression of WNT target *Axin2* (**Figure 6H** and **Supplementary Figure 6**). Together, this set of data identifies WNT3A as a factor that preferentially enhances organoid formation, whereas FGF10 drives differentiation of cells within the organoids.

DISCUSSION

FGF and WNT signaling pathways are essential components of the gene regulatory network in the lungs. They coordinate maintenance of stem/progenitor cells, epithelial/mesenchymal patterning, and branching morphogenesis during lung development and repair (Volckaert and De Langhe, 2015). In this study, we investigated the roles of FGF ligands and also WNT3A in lung epithelial morphogenesis using 3D cell culture models that we have developed. Our main findings are summarized in **Figure 7**.

Our study revealed that unsorted lung epithelial cells as well as sorted LSPCs (EpCAM$^+$ CD49f$^+$ CD24$^{\text{low}}$ CD104$^+$) are capable of proliferation, self-renewal, and differentiation in non-adherent conditions to form spheres, similar to epithelial stem cells from other organs (Reynolds and Weiss, 1992; Shaw et al., 2012; Zhao et al., 2015). The lungospheres formed structures that could be categorized into three phenotypes, which were similar to the phenotypes described for LSPC-derived organoids grown in ECM (McQualter et al., 2010), suggesting that the mechanisms underlying these phenotypes are independent of the ECM. However, embedding of the lungospheres in 3D ECM (Matrigel) supported further development, including growth and morphological changes of the lungospheres into lung organoids with branched lung-like structures.

Direct seeding of unsorted lung epithelial cells into Matrigel promoted organoid formation at similar efficiency as culture in non-adherent conditions, suggesting that the lungospheres and lung organoids come from the same type of cells. Importantly, while several studies reported that co-culture with stromal cells is required for distal LSPCs to form lung-like epithelial structures (McQualter et al., 2010; Chen et al., 2012; Barkauskas et al., 2013; Lee et al., 2014; Hegab et al., 2015), our cell culture method in the defined medium with EGF and FGF ligands enables lung organoid formation without the need for stromal cells. Several studies reported the ability of FGF ligands to replace the requirement for stromal support (McQualter et al., 2010; Hegab et al., 2015). Interestingly, in these studies, 5–10 times higher concentration of FGF was used than in our study, suggesting that our cell culture protocol is more effective. Our study also

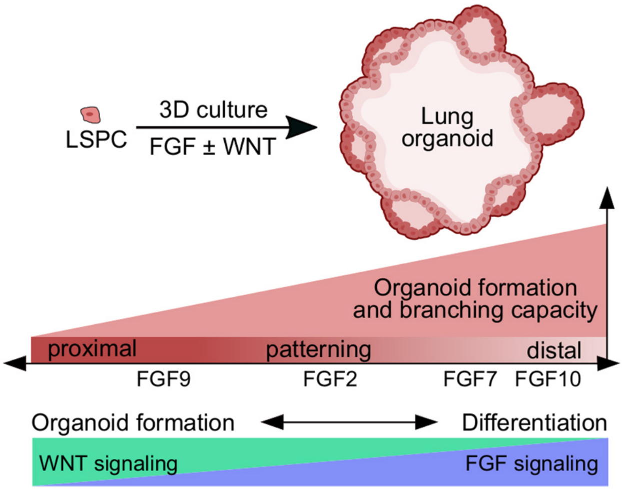

FIGURE 7 | Schematic presentation of the role of FGF and WNT signaling in lung organoid formation and differentiation. FGF ligands differ in their capacity to promote lung organoid formation and branching, and in directing cell differentiation toward proximal or distal lung lineages. FGF9 has the lowest capacity for lung organoid formation and branching, and higher capacity for directing cells toward proximal lung lineages. FGF7 and FGF10 have the highest capacity to promote lung organoid formation, branching, and differentiation toward distal lung lineages. WNT signaling is a very potent inducer of lung organoid formation and growth, but FGF signaling is required for efficient differentiation to lung lineages. LSPC, lung stem/progenitor cell.

shows the advantage of using hyperstable growth factor variants, such as FGF2-STAB, for lung organoid culture, and extends the cell culture potential of FGF2-STAB beyond the reported use in human embryonic stem cell culture (Dvorak et al., 2018).

Our experiments addressing organoid forming efficiency and organoid morphology revealed that FGF ligands FGF2, FGF7, FGF9, and FGF10 act only partially redundantly *ex vivo*. All tested FGF ligands were capable of supporting organoid formation and branching, with FGF9 showing a significantly lower capacity to promote lung organoid formation compared to other FGF ligands (**Figure** 7). However, preculture with FGF2 followed by further culture with FGF9 was able to rescue the low organoid formation, typical for treatment with only FGF. Moreover, preculture with FGF2 further increased the organoid forming efficiency of FGF7, FGF9, and FGF10, suggesting that FGF2 supported cell survival and/or proliferation more efficiently than other FGF ligands. In contrast to our *ex vivo* observations, only FGF10 is essential for lung development *in vivo*. FGF10 null mice show complete lung agenesis (Min et al., 1998; Sekine et al., 1999), whereas inactivation of FGF2, FGF7, or FGF9 affects only lung patterning and branching morphogenesis (Guo et al., 1996; Zhou et al., 1998; White et al., 2006). In concordance with different roles for FGF ligands in lung patterning *in vivo*, we found that FGF ligands differ in their capacity to direct cell differentiation *ex vivo* toward proximal or distal lung lineages (**Figure** 7).

WNT signaling plays important roles in self-renewal and differentiation of stem cell in adults as well as during embryonic development (Mucenski et al., 2003; Clevers et al., 2014; Bhavanasi and Klein, 2016). WNT3A was reported to potentiate alveolar organoid formation from ATII cells and also expansion of ATII cells *ex vivo* (Frank et al., 2016; Lee et al., 2017). Furthermore, WNT activation promotes clonal expansion of ATII cells during alveologenesis *in vivo* (Frank et al., 2016). In this study, we showed that WNT3A significantly increases organoid forming efficiency of unsorted lung epithelial cells in comparison to WNT3A-free conditions (**Figure** 7). Importantly, we report on major differences in organoid forming efficiency depending on the source of WNT3A. Recombinant WNT3A demonstrated the highest capacity to promote organoid formation, while conditioned media from cells expressing WNT3A showed lower capacity to promote organoid formation. While the lower capacity to support organoid formation could, in theory, be compensated by increasing the proportion of the WNT3A-conditioned medium in the organoid medium, it would not bring much advantage. That is because the WNT3A-conditioned medium also induces formation of disorganized colonies of mesenchymal-like cells. These colonies arise probably through epithelial-to-mesenchymal transition (EMT) of lung epithelial cells because we frequently observed transition of smooth, epithelial-like organoid structures to mesenchymal-like colonies of spiky morphology. The L-cell-derived factors that induce such EMT-like behavior remain to be determined.

When FGF10 was added to the WCM-based medium, it increased the efficiency of organoid formation and decreased the incidence of mesenchymal-like structures. However, when FGF10 was added to the medium with recombinant WNT3A, it did not increase the formation of organoids any further, suggesting that WNT3A saturated organoid formation to its maximum. Still, we observed significantly higher expression of markers of all lung cell lineages, suggesting that FGF10 promoted organoid differentiation to both airway and distal lung epithelium. This is consistent with the reported role of FGF10 in the regulation of lung progenitor differentiation based on the developmental context (Volckaert et al., 2013) as well as during homeostasis and in regeneration (Volckaert et al., 2017; Yuan et al., 2019).

3D culture models of the lung, including lung organoids, represent an invaluable tool for developmental biology, cancer biology, pharmacology, and disease modeling (Barkauskas et al., 2017; Rabata et al., 2017). They offer a wide range of modalities and can be adjusted according to research needs. In this work, we developed and utilized a lung organoid model based on unsorted lung epithelial cells cultured in Matrigel in a defined medium to assess the role of FGF and WNT signaling in lung epithelial morphogenesis. Our findings contribute to better understanding of the complex signaling pathways involved in lung organogenesis with potential applications in tissue engineering and regenerative medicine. Furthermore, as demonstrated, our model can be used for testing of growth factor variants created by protein engineering and potentially other proteins or bioactive substances, providing that the targeted pathways are involved in lung epithelial morphogenesis, including cell survival, proliferation, or differentiation.

MATERIALS AND METHODS

Mice

Female ICR mice of 6–10 weeks of age were used as donors of the lung tissue. The mice were housed, handled, and sacrificed in accordance with the Czech and European laws for the use of animals in research, under a valid project license at the Laboratory Animal Breeding and Experimental Facility of Masaryk University.

Isolation of Lung Epithelial Cells by Differential Centrifugation

Lung epithelial cells were isolated as described previously (Rabata et al., 2017). Briefly, the lungs were mechanically disintegrated using scalpels and digested by a solution of collagenase and trypsin [2 mg/ml collagenase A, 2 mg/ml trypsin, 5 μg/ml insulin, 50 μg/ml gentamicin (all Sigma/Merck), 5% fetal bovine serum (FBS; Hyclone/GE Healthcare) in DMEM/F12 (Thermo Fisher Scientific)] for 45 min at 37°C with shaking. The resulting tissue suspension was centrifuged, and the pellet was treated with a red blood cell lysis buffer [155 mM NH_4Cl (Penta), 12 mM $NaHCO_3$ (Fluka), 0.1 mM EDTA (Merck) in distilled H_2O, pH 7.4, filter sterilized]. After washing with DMEM/F12 and centrifugation, the cell pellet was treated by DNase I (20 U/ml; Merck). After a final wash with DMEM/F12, the cell pellet was exposed to five rounds of differential centrifugation to remove mesenchymal cells. The resulting pellet of primary lung epithelial organoids was further processed by incubation in HyQTase (Hyclone/GE Healthcare) and repetitive pipetting to produce single-celled suspension.

Isolation of Lung Epithelial Stem/Progenitor Cells by FACS

LSPCs were isolated as described previously (McQualter and Bertoncello, 2015; Rabata et al., 2017). Briefly, the lungs were chopped up using scalpels, and the resulting mince was digested by Liberase (0.048 mg/ml; Roche) and incubated for 45 min at 37°C with shaking. The suspension was passed through 18G and 21G needles and treated with DNase I (20 U/ml). Next, the suspension was passed through a 100 μm cell strainer, treated with a red blood cell lysis buffer, and passed through a 40 μm cell strainer. The resulting single-celled suspension was centrifuged to collect the cells. The pellet was suspended in a blocking buffer [1% BSA in HBSS (both Merck)] and incubated for 20 min at room temperature. After centrifugation, the cells were resuspended at 1×10^7 cells/ml in a FACS buffer containing the selection antibody cocktail (anti-CD104, anti-EpCAM, anti-CD24, anti-CD49f, anti-CD45; see **Supplementary Table 1**) and incubated in ice in the dark for 20 min. The cells were washed with HBSS, passed through a 30 μm cell strainer, and incubated with 10 μl/ml 7-ADD (BD Biosciences) for 5 min in ice in the dark. Cells were then sorted using FACSAria II SORP (BD Biosciences).

Lungosphere Culture in Non-adherent Conditions

Lung epithelial cells were cultured in non-adherent conditions as described previously (Rabata et al., 2017). Briefly, for primary lungosphere assay, unsorted lung epithelial cells were seeded in polyHEMA-treated six-well plates at 2.5×10^4 to 5×10^4 cells in 2 ml/well of a lungosphere medium [1 × B-27 without vitamin A, 100 U/ml penicillin, 100 μg/ml streptomycin (all Thermo Fisher Scientific), 4 μg/ml heparin (Sigma/Merck), 20 ng/ml murine EGF (#315-09, Peprotech), 10 ng/ml FGF2-STAB (thermostable FGF2 based on human FGF2 sequence; Enantis), or 10 ng/ml human FGF2-wt (#100-18C, Peprotech), 10 μM Y-27632 (Merck) in phenol red-free DMEM/F12 (Thermo Fisher Scientific)]; or 500–1000 FACS-sorted cells were seeded in polyHEMA-treated 24-well plates in 1 ml/well of a lungosphere medium. The plates were incubated in a humidified atmosphere at 37°C, 5% CO_2. A fresh lungosphere medium (without Y-27632) was added every 3 days. Lungospheres were counted after 10–15 days of culture. To passage lungospheres (for secondary and tertiary lungosphere assay), the lungospheres were collected from the plates and processed to single-celled suspension by HyQTase digestion and repetitive pipetting. Resulting single cells were reseeded in polyHEMA-treated plates in a lungosphere medium at the same density as for primary assay. Lungosphere forming efficiency (LFE,%) was calculated as (number of lungospheres formed)/(number of cells seeded) × 100.

Embedded Culture of Lungospheres in 3D Matrigel

The lungospheres were collected from the polyHEMA-treated plates, washed with DMEM/F12 and then with a basal culture medium [1 × ITS (10 μg/ml insulin, 5.5 μg/ml transferrin, 6.7 ng/ml selenium), 100 U/ml penicillin, 100 μg/ml streptomycin in DMEM/F12 (all Thermo Fisher Scientific)]. Then the lungospheres were mixed with Matrigel (growth factor reduced; Corning) and plated into a Matrigel-coated 24-well plate in domes. The plate was incubated at 37°C for 30–45 min before adding a basal culture medium supplemented with growth factors as needed. The plate was incubated in a humidified atmosphere of a cell culture incubator (37°C, 5% CO_2). The medium was changed every 2–3 days.

Lung Organoid Culture in 3D Matrigel

The unsorted or sorted lung epithelial cells were resuspended in Matrigel and plated into a Matrigel-coated 24-well plate in domes (1–2 × 10^4 cells in 50 μl Matrigel/well). The plate was incubated at 37°C for 30–45 min before adding 1 ml of medium per well. The cells were incubated in a humidified atmosphere of a cell culture incubator (37°C, 5% CO_2). The medium was changed every 3 days. The media used were the following: Lungosphere medium [1 × B-27 without vitamin A, 100 U/ml penicillin, 100 μg/ml streptomycin, in phenol red-free DMEM/F12], supplemented with EGF (20 ng/ml) and/or FGFs [1 or 2 nM FGF2-STAB, FGF2-wt, murine FGF7 (#450-60, Peprotech), murine FGF9 (#450-30, Peprotech), or human FGF10 (#100-26, Peprotech)] as needed according to experiment, and 10 μM Y-27632 (only for the first 3 days of culture); a WNT lung organoid medium (Lee et al., 2017): 50 ng/ml murine WNT3A (#315-20, Peprotech) or 50% WNT3A-conditioned medium,100 ng/ml murine Noggin (#250-38, Peprotech), 500 ng/ml human R-spondin 1 (#120-44, Peprotech), and 40 ng/ml EGF in lungosphere medium, with or without 40 ng/ml FGF10. Organoid forming efficiency (OFE,%) was calculated as (number of organoids formed)/(number of cells seeded) × 100. Organoid size was measured from organoid photographs using ImageJ (NIH) as the area occupied by the organoid.

Production of WNT3A-Conditioned Medium

A WNT3A-conditioned medium (WCM) was prepared using the cell line L WNT3A (ATCC®, CRL-2647™) (Sugimoto and Sato, 2017). The L cells were cultured in a DMEM (Thermo Fisher Scientific), 100 U/ml penicillin, and 100 μg/ml streptomycin with 10% FBS or 1× ITS. The medium was collected and sterile filtered after 3 days of culture (first batch), then a fresh medium was added to the cells for another 2 days until the medium was collected and sterile filtered (second batch). The first and second batches of the medium were mixed (1:1), resulting in the WCM. The WCM was aliquoted and stored at −20°C until use.

Histological and Immunohistochemical Analysis

The lungospheres formed in non-adherent conditions or organoids formed in 3D Matrigel were fixed with 4% paraformaldehyde in PBS for 30 min, washed with PBS, and embedded in 3% low melting point agarose (Merck). Then the samples were processed via standard procedure for paraffin embedding. Paraffin sections were cut (2 μm thickness), deparaffinized using xylene, and rehydrated. For histological analysis, the sections were stained with hematoxylin and eosin, dehydrated, and mounted in Pertex (Histolab Products). For immunohistochemistry analysis, antigens were retrieved using a Citrate buffer (Dako) for 30 min, and endogenous peroxidase activity was blocked using 3% hydrogen peroxide. The sections were blocked in PBS with 10% FBS and incubated with primary antibody (**Supplementary Table 1**) for 1 h at RT. After washing, sections were incubated with secondary antibody (anti-mouse, EnVision + Dual Link System-HRP; Dako) for 30 min at RT. After washing, bound secondary antibody was detected using Liquid DAB + Substrate Chromogen System (Dako). The nuclei were stained with Mayer's hematoxylin, dehydrated, and mounted in Pertex. The photographs were taken using a Leica DM5000B microscope equipped with a Leica DFC480 camera. For immunofluorescence analysis, the sections were immersed in a citrate buffer and blocked with PBS with 10% FBS. Then the sections were incubated with primary antibodies (**Supplementary Table 1**) overnight at 4°C. After washing, the sections were incubated with secondary antibodies (**Supplementary Table 1**) for 2 h at RT. Then the sections were washed, stained with DAPI (1 μg/ml; Merck) for 10 min, and mounted in Mowiol (Merck). Fluorescence was detected and documented using a Nikon Eclipse Ti2 inverted microscope or using an Olympus FV500 and FV3000 confocal laser scanning microscope.

Real-Time Quantitative PCR (qPCR)

RNA was isolated using an RNeasy Mini Kit (Qiagen) according to the manufacturer's instruction. cDNA was prepared using a High Capacity RNA-to-cDNA kit (Thermo Fisher Scientific). Real-time qPCR was performed using 5 ng cDNA, 5 pmol of the forward and reverse gene-specific primers each (primer sequences shown in **Supplementary Table 2**) in Light Cycler SYBR Green I Master mix (Roche) on LightCycler 480 II (Roche). Relative gene expression was calculated using the $\Delta\Delta$Ct method and normalization to two housekeeping genes, β-actin (*Actb*) and Eukaryotic elongation factor 1 γ (*Eef1g*).

Statistics

Statistical analysis was performed using the Prism software (GraphPad) using Student's *t*-test and ANOVA. $^{*}P < 0.05$, $^{**}P < 0.01$, $^{***}P < 0.001$, and $^{****}P < 0.0001$. The number of independent biological replicates is indicated as *n*.

DATA AVAILABILITY STATEMENT

All datasets presented in this study are included in the article/**Supplementary Material**.

ETHICS STATEMENT

The animal study was reviewed and approved by Ministry of Agriculture of the Czech Republic Expert Committee for Laboratory Animal Welfare at the Faculty of Medicine, Masaryk University.

AUTHOR CONTRIBUTIONS

AR performed the experiments, analyzed the data, and drafted the manuscript. ZK conceptualized the study, designed the experiments, analyzed the data, and wrote the manuscript. RF and KS performed sorting of cells by FACS. AH secured funding and revised the manuscript. All authors approved the final manuscript.

FUNDING

This study was supported by funds from the Ministry of Health of the Czech Republic (Grant 16-31501A to AH), the Ministry of Education, Youth, and Sports of the Czech Republic (National Program of Sustainability II, project no. LQ1605 to AH and KS), the Grant Agency of Masaryk University (project no. MUNI/A/1382/2019), and the Faculty of Medicine, Masaryk University to junior researcher (ZK, ROZV/28/LF/2020).

ACKNOWLEDGMENTS

We thank Prof. Vitezslav Bryja for providing WNT3A-producing L cells, Dr. Jana Dumkova for help with electron microscopy, Jakub Sumbal for helping with animals, and Katarina Mareckova for excellent histology service. We are thankful to Veronika Stepankova, Radka Chaloupkova, and Jiri Damborsky for providing the FGF2-STAB. We acknowledge the core facility CELLIM of CEITEC supported by the Czech-BioImaging large RI project (LM2015062 funded by MEYS CR) for their support with obtaining scientific data presented in this paper.

SUPPLEMENTARY MATERIAL

The Supplementary Material for this article can be found online at: https://www.frontiersin.org/articles/10.3389/fcell.2020.00574/full#supplementary-material

REFERENCES

Barkauskas, C. E., Chung, M.-I., Fioret, B., Gao, X., Katsura, H., and Hogan, B. L. M. (2017). Lung organoids: current uses and future promise. *Development* 144, 986–997. doi: 10.1242/dev.140103

Barkauskas, C. E., Cronce, M. J., Rackley, C. R., Bowie, E. J., Keene, D. R., Stripp, B. R., et al. (2013). Type 2 alveolar cells are stem cells in adult lung. *J. Clin. Invest.* 123, 3025–3036. doi: 10.1172/JCI68782

Bhavanasi, D., and Klein, P. S. (2016). Wnt signaling in normal and malignant stem cells. *Curr. Stem Cell Rep.* 2, 379–387. doi: 10.1007/s40778-016-0068-y

Cardoso, W. V., Itoh, A., Nogawa, H., Mason, I., and Brody, J. S. (1997). FGF-1 and FGF-7 induce distinct patterns of growth and differentiation in embryonic lung epithelium. *Dev. Dyn. Off. Publ. Am. Assoc. Anat.* 208, 398–405. doi: 10.1002/(sici)1097-0177(199703)208:3<398::aid-aja10>3.0.co;2-x

Cardoso, W. V., and Lü, J. (2006). Regulation of early lung morphogenesis: questions, facts and controversies. *Development* 133:1611. doi: 10.1242/dev.02310

Chen, H., Matsumoto, K., Brockway, B. L., Rackley, C. R., Liang, J., Lee, J.-H., et al. (2012). Airway epithelial progenitors are region specific and show differential responses to bleomycin-induced lung injury. *Stem Cells Dayt. Ohio* 30, 1948–1960. doi: 10.1002/stem.1150

Clevers, H., Loh, K. M., and Nusse, R. (2014). An integral program for tissue renewal and regeneration: Wnt signaling and stem cell control. *Science* 346:1248012. doi: 10.1126/science.1248012

Colvin, J. S., White, A. C., Pratt, S. J., and Ornitz, D. M. (2001). Lung hypoplasia and neonatal death in Fgf9-null mice identify this gene as an essential regulator of lung mesenchyme. *Dev. Camb. Engl.* 128, 2095–2106.

De Arcangelis, A., and Georges-Labouesse, E. (2000). Integrin and ECM functions: roles in vertebrate development. *Trends Genet.* 16, 389–395. doi: 10.1016/S0168-9525(00)02074-6

De Moerlooze, L., Spencer-Dene, B., Revest, J. M., Hajihosseini, M., Rosewell, I., and Dickson, C. (2000). An important role for the IIIb isoform of fibroblast growth factor receptor 2 (FGFR2) in mesenchymal-epithelial signalling during mouse organogenesis. *Dev. Camb. Engl.* 127, 483–492.

del Moral, P.-M., De Langhe, S. P., Sala, F. G., Veltmaat, J. M., Tefft, D., Wang, K., et al. (2006). Differential role of FGF9 on epithelium and mesenchyme in mouse embryonic lung. *Dev. Biol.* 293, 77–89. doi: 10.1016/j.ydbio.2006.01.020

Dessimoz, J., Opoka, R., Kordich, J. J., Grapin-Botton, A., and Wells, J. M. (2006). FGF signaling is necessary for establishing gut tube domains along the anterior-posterior axis in vivo. *Mech. Dev.* 123, 42–55. doi: 10.1016/j.mod.2005.10.001

Dvorak, P., Bednar, D., Vanacek, P., Balek, L., Eiselleova, L., Stepankova, V., et al. (2018). Computer-assisted engineering of hyperstable fibroblast growth factor 2. *Biotechnol. Bioeng.* 115, 850–862. doi: 10.1002/bit.26531

Frank, D. B., Peng, T., Zepp, J., Snitow, M., Vincent, T., Penkala, I. J., et al. (2016). Emergence of a wave of Wnt signaling that regulates lung alveologenesis through controlling epithelial self-renewal and differentiation. *Cell. Rep.* 17, 2312–2325. doi: 10.1016/j.celrep.2016.11.001

Fuchs, E., and Chen, T. (2013). A matter of life and death: self-renewal in stem cells. *EMBO Rep.* 14, 39–48. doi: 10.1038/embor.2012.197

Goss, A. M., Tian, Y., Tsukiyama, T., Cohen, E. D., Zhou, D., Lu, M. M., et al. (2009). Wnt2/2b and beta-catenin signaling are necessary and sufficient to specify lung progenitors in the foregut. *Dev. Cell.* 17, 290–298. doi: 10.1016/j.devcel.2009.06.005

Guo, L., Degenstein, L., and Fuchs, E. (1996). Keratinocyte growth factor is required for hair development but not for wound healing. *Genes Dev.* 10, 165–175. doi: 10.1101/gad.10.2.165

Han, R. N., Liu, J., Tanswell, A. K., and Post, M. (1992). Expression of basic fibroblast growth factor and receptor: immunolocalization studies in developing rat fetal lung. *Pediatr. Res.* 31, 435–440. doi: 10.1203/00006450-199205000-00004

Hegab, A. E., Arai, D., Gao, J., Kuroda, A., Yasuda, H., Ishii, M., et al. (2015). Mimicking the niche of lung epithelial stem cells and characterization of several effectors of their in vitro behavior. *Stem Cell. Res.* 15, 109–121. doi: 10.1016/j.scr.2015.05.005

Jones, M. R., Dilai, S., Lingampally, A., Chao, C.-M., Danopoulos, S., Carraro, G., et al. (2019). A comprehensive analysis of fibroblast growth factor receptor 2b signaling on epithelial tip progenitor cells during early mouse lung branching morphogenesis. *Front. Genet.* 9:746. doi: 10.3389/fgene.2018.00746

Kheradmand, F., Rishi, K., and Werb, Z. (2002). Signaling through the EGF receptor controls lung morphogenesis in part by regulating MT1-MMP-mediated activation of gelatinase A/MMP2. *J. Cell Sci.* 115, 839–848.

Koledova, Z., Sumbal, J., Rabata, A., de La Bourdonnaye, G., Chaloupkova, R., Hrdlickova, B., et al. (2019). Fibroblast growth factor 2 protein stability provides decreased dependence on heparin for induction of FGFR signaling and alters ERK signaling dynamics. *Front. Cell Dev. Biol.* 7:331. doi: 10.3389/fcell.2019.00331

Lebeche, D., Malpel, S., and Cardoso, W. V. (1999). Fibroblast growth factor interactions in the developing lung. *Mech. Dev.* 86, 125–136. doi: 10.1016/S0925-4773(99)00124-0

Lee, J.-H., Bhang, D. H., Beede, A., Huang, T. L., Stripp, B. R., Bloch, K. D., et al. (2014). Lung stem cell differentiation in mice directed by endothelial cells via a BMP4-NFATc1-Thrombospondin-1 axis. *Cell* 156, 440–455. doi: 10.1016/j.cell.2013.12.039

Lee, J.-H., Tammela, T., Hofree, M., Choi, J., Marjanovic, N. D., Han, S., et al. (2017). Anatomically and functionally distinct lung mesenchymal populations marked by Lgr5 and Lgr6. *Cell* 170, 1149.e12–1163.e12. doi: 10.1016/j.cell.2017.07.028

Lu, M. M., Yang, H., Zhang, L., Shu, W., Blair, D. G., and Morrisey, E. E. (2001). The bone morphogenic protein antagonist gremlin regulates proximal-distal patterning of the lung. *Dev. Dyn. Off. Publ. Am. Assoc. Anat.* 222, 667–680. doi: 10.1002/dvdy.1231

Malpel, S., Mendelsohn, C., and Cardoso, W. V. (2000). Regulation of retinoic acid signaling during lung morphogenesis. *Development* 127, 3057–3067.

Matsui, R., Brody, J. S., and Yu, Q. (1999). FGF-2 induces surfactant protein gene expression in foetal rat lung epithelial cells through a MAPK-independent pathway. *Cell. Signal.* 11, 221–228. doi: 10.1016/s0898-6568(98)00070-9

McQualter, J. L., and Bertoncello, I. (2015). "Clonal culture of adult mouse lung epithelial stem/progenitor cells," in *Stem Cell Protocols Methods in Molecular Biology*, ed. I. N. Rich (New York, NY: Springer), 231–241. doi: 10.1007/978-1-4939-1785-3_17

McQualter, J. L., Yuen, K., Williams, B., and Bertoncello, I. (2010). Evidence of an epithelial stem/progenitor cell hierarchy in the adult mouse lung. *Proc. Natl. Acad. Sci. U.S.A.* 107, 1414–1419. doi: 10.1073/pnas.0909207107

Miller, L.-A. D., Wert, S. E., Clark, J. C., Xu, Y., Perl, A.-K. T., and Whitsett, J. A. (2004). Role of Sonic hedgehog in patterning of tracheal-bronchial cartilage and the peripheral lung. *Dev. Dyn. Off. Publ. Am. Assoc. Anat.* 231, 57–71. doi: 10.1002/dvdy.20105

Min, H., Danilenko, D. M., Scully, S. A., Bolon, B., Ring, B. D., Tarpley, J. E., et al. (1998). Fgf-10 is required for both limb and lung development and exhibits striking functional similarity to *Drosophila* branchless. *Genes Dev.* 12, 3156–3161. doi: 10.1101/gad.12.20.3156

Mucenski, M. L., Wert, S. E., Nation, J. M., Loudy, D. E., Huelsken, J., Birchmeier, W., et al. (2003). beta-Catenin is required for specification of proximal/distal cell fate during lung morphogenesis. *J. Biol. Chem.* 278, 40231–40238. doi: 10.1074/jbc.M305892200

Nyeng, P., Norgaard, G. A., Kobberup, S., and Jensen, J. (2008). FGF10 maintains distal lung bud epithelium and excessive signaling leads to progenitor state arrest, distalization, and goblet cell metaplasia. *BMC Dev. Biol.* 8:2. doi: 10.1186/1471-213X-8-2

Ohuchi, H., Hori, Y., Yamasaki, M., Harada, H., Sekine, K., Kato, S., et al. (2000). FGF10 acts as a major ligand for FGF receptor 2 IIIb in mouse multi-organ development. *Biochem. Biophys. Res. Commun.* 277, 643–649. doi: 10.1006/bbrc.2000.3721

Pastrana, E., Silva-Vargas, V., and Doetsch, F. (2011). Eyes wide open: a critical review of sphere-formation as an assay for stem cells. *Cell Stem Cell* 8, 486–498. doi: 10.1016/j.stem.2011.04.007

Powell, P. P., Wang, C. C., Horinouchi, H., Shepherd, K., Jacobson, M., Lipson, M., et al. (1998). Differential expression of fibroblast growth factor receptors 1 to 4 and ligand genes in late fetal and early postnatal rat lung. *Am. J. Respir. Cell Mol. Biol.* 19, 563–572. doi: 10.1165/ajrcmb.19.4.2994

Rabata, A., Hampl, A., and Koledova, Z. (2017). "Lungosphere assay: 3D culture of lung epithelial stem/progenitor cells," in *3D Cell Culture: Methods and Protocols Methods in Molecular Biology*, ed. Z. Koledova (New York, NY: Springer), 149–165. doi: 10.1007/978-1-4939-7021-6_11

Ramasamy, S. K., Mailleux, A. A., Gupte, V. V., Mata, F., Sala, F. G., Veltmaat, J. M., et al. (2007). Fgf10 dosage is critical for the amplification of epithelial cell progenitors and for the formation of multiple mesenchymal lineages during lung development. *Dev. Biol.* 307, 237–247. doi: 10.1016/j.ydbio.2007.04.033

Reynolds, B. A., and Weiss, S. (1992). Generation of neurons and astrocytes from isolated cells of the adult mammalian central nervous system. *Science* 255, 1707–1710. doi: 10.1126/science.1553558

Sekine, K., Ohuchi, H., Fujiwara, M., Yamasaki, M., Yoshizawa, T., Sato, T., et al. (1999). Fgf10 is essential for limb and lung formation. *Nat. Genet.* 21, 138–141. doi: 10.1038/5096

Shaw, F. L., Harrison, H., Spence, K., Ablett, M. P., Simões, B. M., Farnie, G., et al. (2012). A detailed mammosphere assay protocol for the quantification of breast stem cell activity. *J. Mammary Gland Biol. Neoplasia* 17, 111–117. doi: 10.1007/s10911-012-9255-3

Shu, W., Guttentag, S., Wang, Z., Andl, T., Ballard, P., Lu, M. M., et al. (2005). Wnt/β-catenin signaling acts upstream of N-myc, BMP4, and FGF signaling to regulate proximal–distal patterning in the lung. *Dev. Biol.* 283, 226–239. doi: 10.1016/j.ydbio.2005.04.014

Sugimoto, S., and Sato, T. (2017). "Establishment of 3D intestinal organoid cultures from intestinal stem cells," in *3D Cell Culture: Methods and Protocols Methods in Molecular Biology*, ed. Z. Koledova (New York, NY: Springer), 97–105. doi: 10.1007/978-1-4939-7021-6_7

Tichelaar, J. W., Lu, W., and Whitsett, J. A. (2000). Conditional expression of fibroblast growth factor-7 in the developing and mature lung. *J. Biol. Chem.* 275, 11858–11864. doi: 10.1074/jbc.275.16.11858

Volckaert, T., Campbell, A., Dill, E., Li, C., Minoo, P., and De Langhe, S. (2013). Localized Fgf10 expression is not required for lung branching morphogenesis but prevents differentiation of epithelial progenitors. *Dev. Camb. Engl.* 140, 3731–3742. doi: 10.1242/dev.096560

Volckaert, T., and De Langhe, S. P. (2015). Wnt and FGF mediated epithelial mesenchymal crosstalk during lung development. *Dev. Dyn. Off. Publ. Am. Assoc. Anat.* 244, 342–366. doi: 10.1002/dvdy.24234

Volckaert, T., Yuan, T., Chao, C.-M., Bell, H., Sitaula, A., Szimmtenings, L., et al. (2017). Fgf10-hippo epithelial-mesenchymal crosstalk maintains and recruits lung basal stem cells. *Dev. Cell* 43, 48.e5–59.e5. doi: 10.1016/j.devcel.2017.09.003

Volckaert, T., Yuan, T., Yuan, J., Boateng, E., Hopkins, S., Zhang, J.-S., et al. (2019). Hippo signaling promotes lung epithelial lineage commitment by curbing Fgf10 and β-catenin signaling. *Dev. Camb. Engl.* 146:dev166454. doi: 10.1242/dev.166454

Weaver, M., Yingling, J. M., Dunn, N. R., Bellusci, S., and Hogan, B. L. (1999). Bmp signaling regulates proximal-distal differentiation of endoderm in mouse lung development. *Dev. Camb. Engl.* 126, 4005–4015.

Wells, J. M., and Melton, D. A. (2000). Early mouse endoderm is patterned by soluble factors from adjacent germ layers. *Dev. Camb. Engl.* 127, 1563–1572.

White, A. C., Xu, J., Yin, Y., Smith, C., Schmid, G., and Ornitz, D. M. (2006). FGF9 and SHH signaling coordinate lung growth and development through regulation of distinct mesenchymal domains. *Dev. Camb. Engl.* 133, 1507–1517. doi: 10.1242/dev.02313

Whyte, J. L., Smith, A. A., and Helms, J. A. (2012). Wnt signaling and injury repair. *Cold Spring Harb. Perspect. Biol.* 4:a008078. doi: 10.1101/cshperspect.a008078

Yin, Y., White, A. C., Huh, S.-H., Hilton, M. J., Kanazawa, H., Long, F., et al. (2008). An FGF–WNT gene regulatory network controls lung mesenchyme development. *Dev. Biol.* 319, 426–436. doi: 10.1016/j.ydbio.2008.04.009

Yuan, T., Volckaert, T., Redente, E. F., Hopkins, S., Klinkhammer, K., Wasnick, R., et al. (2019). FGF10-FGFR2B signaling generates basal cells and drives alveolar epithelial regeneration by bronchial epithelial stem cells after lung injury. *Stem Cell Rep.* 12, 1041–1055. doi: 10.1016/j.stemcr.2019.04.003

Zhao, C., Setrerrahmane, S., and Xu, H. (2015). Enrichment and characterization of cancer stem cells from a human non-small cell lung cancer cell line. *Oncol. Rep.* 34, 2126–2132. doi: 10.3892/or.2015.4163

Zhou, M., Sutliff, R. L., Paul, R. J., Lorenz, J. N., Hoying, J. B., Haudenschild, C. C., et al. (1998). Fibroblast growth factor 2 control of vascular tone. *Nat. Med.* 4, 201–207. doi: 10.1038/nm0298-201

Conflict of Interest: The authors declare that the research was conducted in the absence of any commercial or financial relationships that could be construed as a potential conflict of interest.

frontiers
in Cell and Developmental Biology

ORIGINAL RESEARCH
published: 28 July 2020
doi: 10.3389/fcell.2020.00666

Modeling Normal and Pathological Ear Cartilage *in vitro* Using Somatic Stem Cells in Three-Dimensional Culture

***Eleonora Zucchelli*[1]*, Martin Birchall*[2]*, Neil W. Bulstrode*[3] *and Patrizia Ferretti*[1]**

[1] Stem Cells and Regenerative Medicine Section, UCL Great Ormond Street Institute of Child Health, University College London, London, United Kingdom, [2] UCL Ear Institute, University College London, London, United Kingdom, [3] Department of Plastic Surgery, Great Ormond Street Hospital for Children NHS Foundation Trust, London, United Kingdom

Edited by:
Silvia Garagna,
University of Pavia, Italy

Reviewed by:
Yilin Cao,
Shanghai Jiao Tong University, China
Hang Lin,
University of Pittsburgh, United States

***Correspondence:**
Patrizia Ferretti
p.ferretti@ucl.ac.uk

Specialty section:
This article was submitted to Cell Growth and Division, a section of the journal Frontiers in Cell and Developmental Biology

Received: *16 April 2020*
Accepted: *01 July 2020*
Published: *28 July 2020*

Citation:
Zucchelli E, Birchall M, Bulstrode NW and Ferretti P (2020) Modeling Normal and Pathological Ear Cartilage in vitro Using Somatic Stem Cells in Three-Dimensional Culture. Front. Cell Dev. Biol. 8:666. doi: 10.3389/fcell.2020.00666

Microtia (underdeveloped ear) is a rare congenital dysmorphology affecting the development of the outer ear. Although human microtic cartilage has not been fully characterized, chondrogenic cells derived from this tissue have been proposed as a suitable source for autologous auricular reconstruction. The aim of this study was to further characterize native microtic cartilage and investigate the properties of cartilage stem/progenitor cells (CSPCs) derived from it. Two-dimensional (2D) systems are most commonly used to assess the chondrogenic potential of somatic stem cells *in vitro*, but limit cell interactions and differentiation. Hence here we investigated the behavior of microtic CSPCs in three-dimensional spheroid cultures. Remarkable similarities between human microtic cartilages from five patients, as compared to normal cartilage, were observed notwithstanding possibly different etiologies of the disease. Native microtic cartilage displayed poorly defined perichondrium and hyper-cellularity, an immature phenotype that resembled that of the normal developing human auricular cartilage we studied in parallel. Crucially, our analysis of microtic ears revealed for the first time that, unlike normal cartilage, microtic cartilages are vascularized. Importantly, CSPCs isolated from human microtic and normal ear cartilages were found to recapitulate many characteristics of pathological and healthy tissues, respectively, when allowed to differentiate as spheroids, but not in monolayer cultures. Noteworthily, starting from initially homogeneous cell pellets, CSPC spheroids spontaneously underwent a maturation process in culture, and formed two regions (inner and outer region) separated by a boundary, with distinct cell types that differed in chondrogenic commitment as indicated by expression of chondrogenic markers. Compared to normal ear-derived spheroids, microtic spheroids were asymmetric, hyper-cellularized and the inner and outer regions did not develop properly. Hence, their organization resembled that of native microtic cartilage. Together, our results identify novel features of microtic ears and highlight the importance of 3D self-organizing *in vitro* systems for better understanding somatic stem cell behavior and disease modeling. Our observations of ear-derived chondrogenic stem cell behavior have implications for choice of cells for tissue engineered reconstructive purposes and for modeling the etiopathogenesis of microtia.

Keywords: cartilage, development, ear, human, mesenchymal stem cells, microtia, spheroid cultures, tissue engineering

INTRODUCTION

Microtia (small ear) and anotia (absent external ear) are rare congenital defects affecting development of the outer ear (Luquetti et al., 2012; Cox et al., 2014). They can occur as part of a syndrome, such as hemifacial microsomia, Goldenhar syndrome, Treacher Collins, Nager, and CHARGE, or independently, with the mechanisms underlying the defect largely unknown (Luquetti et al., 2012). Different degrees of reduction in size and malformed shape are observed among microtic ears depending on the severity of the malformation, with anotia and the most severe cases of microtia requiring surgical reconstruction. Development of tissue engineering approaches would circumvent the use of autologous rib cartilage, currently the most successful reconstructive approach, but associated with high morbidity and in some cases respiratory complications (Ohara et al., 1997; Walton and Beahm, 2002; Kusuhara et al., 2009; Baluch et al., 2014; Pappa et al., 2014; Gu et al., 2018).

Notwithstanding much clinical interest in microtia, both normal and microtic ear cartilages remain under-characterized, and so are the stem/progenitor cells present in these tissues, which may be of value for autologous cell therapy (Anthwal and Thompson, 2016). Hence there is a need for carrying out a more systematic analysis of microtic cartilages both *in vivo* and *in vitro*.

It is well established that, although cartilage lacks intrinsic reparative ability, a unique population of cartilage stem/progenitor cells (CSPCs) is present in the superficial zone (SZ) of mature avascular cartilage and in the tissues immediately surrounding it (inner perichondrium) in both animals and humans (Engkvist and Wilander, 1979; Dowthwaite et al., 2004; Shirasawa et al., 2006; Togo et al., 2006; Kobayashi et al., 2011a,b; Kagimoto et al., 2016; Xue et al., 2016). These cells are thought to be involved in the maintenance of tissue homeostasis. CSPCs isolated from normal ear cartilage exhibit typical features of mesenchymal stem cells (MSCs), such as adherence to plastic, spindle-like morphology and three-mesenchymal lineage differentiation potential *in vitro* (Kobayashi et al., 2011a; Jiang and Tuan, 2015; Zhang et al., 2017).

Previous studies have demonstrated that CSPCs can be isolated also from the human microtic ear, and have the ability to proliferate and undergo chondrogenic differentiation; in addition, it has been proposed that microtic CSPCs can be used for cartilage reconstruction (Yanaga et al., 2009; Kobayashi et al., 2011a; Yanaga et al., 2012; Zhou et al., 2018). However, there are discrepancies on how “normally” microtic CSPCs behave, and studies directly comparing microtic cells with normal CSPCs from normal auricular cartilage or other sources are very limited. In addition, potential differences between normal and microtic cartilages *in vivo* have not been fully explored. A better understanding of microtic cells is important to fully establish their potential for cartilage engineering and may help to elucidate causes of the disease. It is also important to note that most studies of microtic cells have been carried out in 2-dimensional (2D) culture systems, that prevent the more complex cell interactions occurring in tissues (Laschke and Menger, 2017). Hence, we hypothesized that potential differences between normal and microtic ear cartilage may be obscured in standard 2D cultures but become apparent in 3D cultures where the cells are allowed to self-organize (spheroids).

To test this hypothesis, we assessed chondrogenic differentiation of microtic ear derived cells, both in 2D and in spheroid cultures, and compared them with chondrogenic cells derived from normal ear cartilage, and with other MSCs with chondrogenic differentiation ability, such as pediatric adipose-tissue derived stem cells (ADSCs). In parallel, we compared changes in human auricular cartilage with development and in microtic ears to gain further understanding of normal and microtic cartilage traits, and assess whether the spheroids modeled some aspects of the disease.

In addition to differences in cellularity and cytoarchitecture between healthy and microtic native cartilages, our analysis has demonstrated for the first time the presence of blood vessels in the chondrium layer of microtic cartilages. This is in contrast to healthy cartilages, that are always avascular, and identifies a new important landmark of the disease.

This study has also shown that following chondrogenic differentiation in 3D cultures, CSPCs derived from microtic ear cartilage remnants display differences in their spontaneous spatial organization as compared to normal ear CSPCs, which are not readily apparent in 2D cultures. Significantly, comparative analysis of differentiated spheroids and native cartilage has indicated that normal ear CSPC-derived spheroids display a structural organization resembling that of developing normal ear cartilage, including a chondrium layer and an inner and outer perichondrium (OP). In contrast, microtic ear CSPC-derived spheroids appear to reproduce some morphological features of pathological tissues, such as hyper-cellularization of cartilage nodules and disruption of the typical multi-layered architecture of cartilage suggesting they provide a suitable system for modeling the disease.

MATERIALS AND METHODS

All chemicals were from Sigma-Aldrich (United Kingdom), unless otherwise stated.

All procedures involving human tissue were carried out in accordance to the UK Human Tissue Act 2006.

Human Fetal Ear Tissues

External ear tissues from human fetuses at different developmental stages used for tissue analysis were provided by a tissue bank, the Human Developmental Biology Resource[1] (HDBR) under ethical approval (NRES Committee London – Fulham, United Kingdom). Dissected tissues were fixed in 4% PFA, dehydrated in ascending ethanol solutions, and embedded in paraffin using a Sakura Tissue-Tek TEC embedding machine (Sakura Tissue Tek). Sections (3 μm) were dewaxed in Histo-clear II (National Diagnostics, Atlanta, GA, United States) and then rehydrated by descending ethanol solutions, prior to histological staining and protein expression analysis by immunohistochemistry. Embryos at 16 and 22 post conception weeks (PCW) were used in this study.

Human Pediatric Adipose and Ear Tissues

All abdominal adipose tissue and auricular cartilage used for tissue analysis and cell line generation (**Supplementary Table 1**), were collected from consenting patients under ethical approval from the Camden and Islington Community Local Research Ethics Committee (London, United Kingdom). Microtic ear tissues were obtained from surplus cartilage of patients undergoing autologous costal to ear graft reconstruction, whereas normal ear cartilage was obtained from a healthy donor, undergoing otoplasty as an aesthetic procedure. Dissected tissues were fixed in 4% PFA prior to cryo- or paraffin embedding and sectioning for histological staining and protein expression analysis by immunohistochemistry.

Cell Growth and Differentiation

All cells were grown at 37°C with 5% CO_2 in a humidified incubator.

Human Pediatric Adipose Tissue-Derived Stem Cells (ADSCs)

Adipose tissue-derived stem cells were isolated from lipoaspirates of pediatric patients as previously described (Guasti et al., 2012). Isolated ADSCs were cultured in high glucose Dulbecco's modified Eagle's medium (DMEM; Life Technologies) containing GlutaMAX^{TM} and supplemented with 10% embryonic stem cell-qualified fetal bovine serum (ES-FBS; ES-009-B, Merk Millipore, Burlington, MA, United States) and 1% penicillin/streptomycin.

Human Pediatric Normal and Microtic Ear Cartilage-Derived Cells (Normal and Microtic CSPCs)

Human normal and microtic CSPCs were derived using the primary explant technique, as previously described (Guasti et al., 2012). Explants and isolated cartilage precursor cells were cultured in DMEM containing GlutaMAX^{TM} and supplemented with 10% ES-FBS and 1% penicillin/streptomycin. After collection, all cartilages were extensively washed in phosphate buffer saline (PBS, pH 7.4) and cut into approximately 2 mm^3 pieces following careful removal of fat and connective tissues. Two to three explants were plated onto each well of a 12 well culture plastic plate. Explants were allowed to adhere to the plastic for a few minutes before covering each of them with one drop of medium (approximately 100 μl). After 24–48 h, if the explants had attached to the plastic, more medium was added. Explants were handled carefully and fed very gently to prevent them from detaching and floating until the cells started to migrate out. Once the cells had become confluent, the explants were removed, and the cells were passaged and expanded in the same medium.

Adipogenic Differentiation

Adipogenic differentiation was induced in confluent cells by the addition of DMEM containing GlutaMAX^{TM}, 1% penicillin/streptomycin, 10% ES-FBS, 10 ng/ml insulin, 500 μM 3-isobutyl-1-methylxanthine, 1 μM dexamethasone, and 1 μM rosiglitazone (Molekula, Gillingham, United Kingdom). After 3 weeks, cells were fixed in 4% PFA, and stained with Oil Red O working solution to visualize lipid droplets, as previously described (Guasti et al., 2012).

Chondrogenic Differentiation

Chondrogenic differentiation was induced in confluent cells by the addition of DMEM containing GlutaMAX^{TM}, 1% penicillin/streptomycin, 10% ES-FBS, 0.1 μM dexamethasone, 50 μg/ml ascorbate, 10 ng/ml transforming growth factor β 1 (TGF β 1), and insulin-transferrin-selenium supplement (ITS, Sigma). After 3 weeks, cells were fixed in 4% PFA and stained with Alcian Blue dye for semi-quantitative analysis, as previously described (Guasti et al., 2012). Fold changes relative to chondrogenic measurements were calculated taking undifferentiated controls as reference (value 1).

Osteogenic Differentiation

Osteogenic differentiation was induced in confluent cells by the addition of DMEM containing GlutaMAX^{TM}, 1% penicillin/streptomycin, 10% ES-FBS, 0.1 μM dexamethasone, 100 μg/ml ascorbate, and 10 mM β-glycerophosphate. After 3 weeks, cells were fixed in ice-cold 70% ethanol and stained with Alizarin Red solution as previously described (Guasti et al., 2012).

Spheroid Cultures

For 3D spheroid cell cultures, 3×10^5 cells were resuspended in 100–150 μl of DMEM containing GlutaMAX^{TM}, 1% penicillin/streptomycin, 10% ES-FBS, collected in 1.5 ml conical tubes with screw caps, allowed to settle down to the bottom of the tube for around 10 min, and centrifuged at 300 *g* for 5 min. Aggregates were incubated at 37°C in 5% CO2 overnight. After spheroid formation (usually within 24–48 h after centrifugation), the medium was replaced with either control or chondrogenic medium, and cells were fed 3–4 times a week. In each experiment at least four samples per treatment were used. After either 4 or 6 weeks, spheroids were fixed in 4% PFA prior to cryo-embedding and sectioning (10 μm sections) for histological staining and protein expression analysis by immunofluorescence.

---

[1] http://hdbr.org

Spheroid Diameter Measurement

Spheroids were imaged using a Leica MZ FL III Fluorescence Stereomicroscope (Leica) and their diameter measured using Fiji software. In undifferentiated spheroids that were less compact and had a less well-defined shape than the differentiated ones, the width was measured only considering the core of the samples, as shown in **Figure 5A**.

Reverse Transcription-Polymerase Chain Reaction

RNA was extracted from cells and tissues using TRIzol reagent (Life Technologies) according to the manufacturer's protocol. After treating with DNase I, Amplification Grade (Life Technology), RNA was retrotranscribed with Moloney murine leukemia virus reverse transcriptase (Promega, Madison, WI, United States). cDNA was amplified using GoTaq® DNA Polymerase kit (Promega), in a Veriti® Thermal Cycler (Applied Biosystems, Life Technology). Primers and conditions used are listed in **Supplementary Table 2**. No template controls containing water instead of cDNA were included in each PCR run. Glyceraldehyde 3-phosphate dehydrogenase (*GAPDH*) and 60s ribosomal protein L19 (*RPL19*) housekeeping genes were used as internal controls. After PCR amplification, the PCR product was analyzed by electrophoresis in agarose gels, with SYBR® Safe DNA Gel Stain (10,000×) (Thermo Fisher Scientific) and visualized using a Gel Doc system (ChemiDoc™ XRS + System, Bio-Rad).

Western Blot Analysis

Proteins were extracted either from fresh or frozen cell pellets by homogenization for 15 min on ice in RIPA buffer (50 mM Tris-HCl pH 7.4, 150 mM NaCl, 1 mM phenylmethylsulfonyl fluoride (PMSF), 1 mM EDTA, 1% Triton X-100, 0.1% SDS, 1% sodium deoxycholate, containing one tablet of total protease inhibitor (cOmplete™, Mini Protease Inhibitor Cocktail, Roche, Switzerland)/10 ml of buffer). The lysates were centrifuged at 11,000 *g* at 4°C for 15 min, and the supernatants containing the solubilized proteins were transferred to a new tube.

Whole protein extracts from porcine auricular cartilage were used as a positive control. Ears of adult pigs were collected from the Royal Veterinary College, University of London (Royal College Street, London, United Kingdom). First, pig auricles were extensively washed in 1× PBS and dissected to remove all skin and fat. The ear cartilage was then cut into stripes and snap–frozen in liquid nitrogen. Frozen cartilage was pulverized using mortar and pestle cooled with liquid nitrogen. The cartilage powder was weighed and proteins extracted in RIPA buffer (1 g of tissue powder/3 ml extraction buffer) overnight at 4°C on a roller shaker. The protein extract was centrifuged at 11,000 *g*, at 4°C for 30 min and the supernatant containing the solubilized proteins was transferred to a new tube. Centrifugation was repeated until the supernatant appeared clear.

Proteins were quantified using the BCA assay, with Pierce BCA Protein Assay Kit (Life Technology), following the manufacturer's instructions. Protein extracts (20 μg/lane) were denatured and reduced by boiling for 10 min at 99°C in Loading Buffer (NuPAGE® LDS Sample Buffer, Thermo Fisher Scientific), supplemented with 10% β-mercaptoethanol and loaded onto 10% sodium-dodecyl-sulfate polyacrylamide gel electrophoresis (SDS-PAGE) gels. A protein ladder (Precision Plus Protein™ Dual Colour Standards, #1610374, Bio-Rad) was run alongside the samples for molecular weight estimation. Proteins from the gel were transferred onto a nitrocellulose membrane (Hybond-C Extra, GE Healthcare, Life Sciences, Amersham, United States) at 15 V overnight at 4°C, then blocked with 5% milk powder in 0.5% Tween 20 in TBS (TBS-T) for 1 at room temperature, and incubated with an anti-Collagen 2 rabbit polyclonal Ab (**Supplementary Table 3**) overnight at 4°C. Membranes were washed for 3 × 10 min with TBS-T, incubated with the horseradish peroxidase (HRP)-conjugated polyclonal goat anti-rabbit IgG for 1 h at room temperature and washed again. The bound antibody was detected using ECL Western Blotting reagents (GE Healthcare, Life Science) following the manufacturer's instructions.

Histological Analysis

Tissue and spheroid sections were stained for hematoxylin and eosin (H&E), Alcian Blue (glycosaminoglycans), Alcian Blue/Periodic Acid – Schiff (acidic and neutral mucins) and Alizarin Red (calcium deposition) using standard histological methods. Stained sections were imaged using the Zeiss Axioplan 2IE Mot Microscope System (Carl Zeiss, Jena, Germany) and the Axiovision software (Carl Zeiss). Cell nuclei and vessel counts were performed with ImageJ/Fiji, using the automatic Particle Analysis tool or the manual Cell Counter plugin, considering only those found in the chondrium layer. For each tissue, cell nuclei were counted in three independent fields, in at least 4 sections; for vessel quantification, at least 12 sections per tissue were imaged. The average numbers of cell nuclei and vessels in each tissue was expressed per unit area. Phase contrast pictures of tissues were taken using an inverted microscope Olympus IX71 equipped ORCA-R2 digital camera (Hamamatsu Corp., Bridgewater, NJ, United States). Differential interference contrast (DIC) pictures of spheroid sections were acquired using the Zeiss Axioplan 2IE Mot Microscope System (Carl Zeiss).

Immunofluorescence

Cells or spheroid sections were fixed in 4% PFA prior to immunofluorescence protein detection. After incubation for 30 min with a blocking/permeabilizing buffer (10% FBS, 3% BSA, and 0.2% Triton X-100 in PBS), samples were incubated with primary antibodies for 2 h at room temperature and then for 1 h with fluorescent dye-conjugated secondary antibodies and Hoechst 33258 (2 μg/ml) at room temperature. All antibodies used are listed in **Supplementary Table 3**. Negative controls were incubated with the secondary antibody only. When tissue sections were permeabilized, 1% Triton X-100 was supplemented to the blocking buffer, and samples were incubated for 1 h. When sections were stained with anti-Collagen 1, -Collagen 2 and -Elastin (ELN) antibodies, samples were pre-treated with 0.1% trypsin for 20 min at 37°C, followed by washes in deionized H_2O and PBS. Images were acquired either using an inverted microscope Olympus IX71 equipped ORCA-R2 digital camera (Hamamatsu Corp., Bridgewater, NJ, United States) or by confocal laser scanning microscopy (LSM 710, Carl Zeiss, Jena, Germany). Image analysis was performed using Fiji/ImageJ software.

Horseradish Peroxidase (HRP) Staining

Horseradish peroxidase staining was performed using the Vectastain Elite ABC kits (Vector Laboratories, Burlingame, CA, United States), according to manufacturer's protocols. All antibodies used are listed in **Supplementary Table 3**. Antigen retrieval was performed via trypsin digestion (0.1% trypsin for 20 min at 37°C, followed by washes in deionized H_2O and PBS). Primary antibody was incubated overnight at 4°C, followed by incubation in 0.3% hydrogen peroxide in methanol for 30 min at room temperature and 3 × 10 min washes in 1× PBS, to inactivate endogenous peroxidases. A 1 h biotin-conjugated secondary antibodies incubation, at room temperature was followed by a 30 min incubation with ABC mixture solution containing biotinylated HRP (Vectastain Elite ABC kits, Vector Laboratories, Burlingame, CA, United States) at room temperature, and finally the color was developed using DAB (3,3′-diaminobenzidine) solution (DAB Peroxidase substrate, Vector Laboratories). Stained sections were dehydrated through ascending ethanol solutions, mounted using DPX Mounting Medium (Thermo Fisher Scientific), and imaged using the Zeiss Axioplan 2IE Mot Microscope System (Carl Zeiss) and the Axiovision software (Carl Zeiss).

Statistical Analysis

Data are expressed as mean ± standard error of the mean (S.E.M). Statistical analysis was performed using GraphPad Prism 7 (GraphPad software Inc., La Jolla, CA, United States). Each experiment was performed on cells or tissues from one to five patients (N), and replicates in each experimental group were $n \geq 3$. Statistical significance was evaluated by Mann–Whitney test or Kruskal–Wallis, followed by a Dunn's *post hoc* test. A p value equal to or less than 0.05 was considered as statistically significant.

RESULTS

Comparison of Native Human Normal and Microtic Ear Cartilages

Microtic ear cartilages were compared with developing normal ear and pediatric auricular cartilage to assess whether microtic cartilages display an immature phenotype. Developing human fetal external ears at 16 and 22 PCW ($N = 1$) were analyzed by histology and immunohistochemistry on paraffin sections (**Figure 1**). At both 16 and 22 PCW, two zones were identified in the developing cartilage layer: (i) a central layer, highly cellularized, containing immature chondroblasts with round nuclei and a few small peri-cellular cavities, identifiable as the chondrium, and (ii) the inner perichondrium, a thin, regular layer which contained spindle-like/fibroblastic shaped cells (we define these cells as CSPCs, according to Kobayashi et al., 2011a; Jiang and Tuan, 2015; Zhang et al., 2017). In many areas of the 16 PCW ear cartilage, the inner perichondrium appeared irregular (**Figure 1A**). In the 22 PCW ear, peri-cellular cavities and a few chondrocytes embedded in lacunae were apparent in the cartilage layer at high magnification (**Figure 1B**). Cells were sparser in the developing cartilage layer of 22 PCW ear sections compared to 16 PCW, as demonstrated by quantification of cell nuclei per unit area in tissue sections (**Figure 1C**). At 22 PCW, the cartilage layer was surrounded by an abundant OP containing fibers, small blood vessels, and sparse cells. Elastic cartilage proteins such as ELN and Collagen 2 (COL2) were already expressed in the inner perichondrium and developing cartilage by 16 PCW, but increased accumulation of COL2 in the inner perichondrium, where CSPCs are located, was observed at 22 PCW. Collagen 1 (COL1) reactivity was detected in the inner and OP, but not in the developing chondrium layer, both at 16 and 22 PCW (**Figures 1D–F** and **Supplementary Figures 1A,B**, for negative controls).

By 9 year of age, the normal external ear cartilage, was hard and elastic with a typical white and translucent appearance. Histological examination by H&E and Alcian Blue staining of this biopsy showed a thin and regular layer of cartilage tissue with a high GAG content, as indicated by the staining intensity, surrounded by a fibrous OP (**Figures 2A,B,D**). As evident at high magnification, normal elastic cartilage presented a multi-layered architecture including: (i) the OP, consisting of connective fibers and vessels, (ii) the inner perichondrium, a thin, regular layer containing CSPCs (spindle-like cells), (iii) the transitional layer, containing chondroblasts, and (iv) the chondrium or mature cartilage layer, containing chondrocytes (**Figures 2C,D**). Chondrocytes were in lacunae and organized in vertical columns (**Figures 2B–D**). Several isogenous groups were identified, each containing two–three chondrocytes (**Figure 2B**).

In contrast to normal ears, microtic cartilages ($N = 5$) were amorphic with high variability in shape and size observed between patients. An example of the gross anatomy of microtic cartilage is shown in **Figure 2E**. Histological analysis showed that although microtic cartilages contained chondrocytes in lacunae that produced GAGs, there was major disruption of the structural organization typical of normal ears (**Figures 2F–I**). A key feature of microtic cartilage was the presence of unshaped islets of cartilage surrounded by abundant fibrous connective tissue and fat instead of a regular, thin layer of elastic cartilage (**Figure 2F**). In many areas the multi-layered architecture of cartilage was missing, and the inner perichondrium and chondrium appeared very irregular compared to normal elastic cartilage (**Figures 2G,H**). Furthermore, microtic ear cartilage appeared hyper-cellular compared to normal ear cartilage (**Figures 2G,J,K**), and chondrocytes were not organized in vertical columns as in normal cartilage (**Figures 2H,I,J**). The interterritorial matrix was present only in some areas and in small patches, whereas it was completely absent in other parts of the chondrium. Very large isogenous groups, including up to 10–12 chondrocytes, were found in the chondrium of microtic cartilage (**Figure 2I**). Finally, small vessels were found in the chondrium layer of microtic ear cartilage, in addition to the OP, but not in the chondrium of normal ear cartilage (**Figures 2J,L**, **3A**).

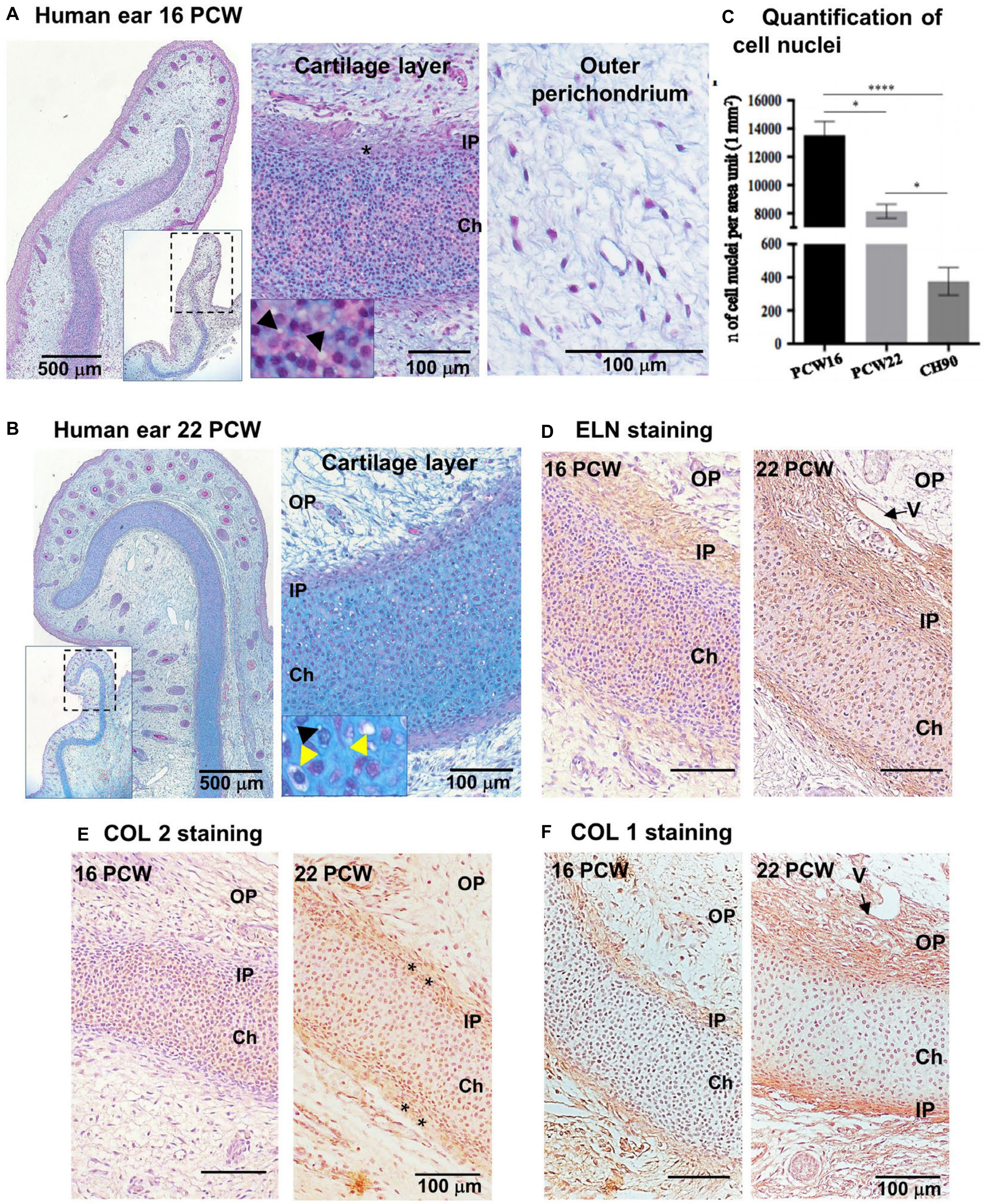

FIGURE 1 | Characterization of human developing normal ear cartilage. Morphology and expression of ELN, COL2, and COL1 in 16 and 22 post-conception weeks (PCW) human ear cartilage sections. **(A,B)** Alcian Blue/Periodic Acid – Schiff (PAS) staining sections showing the developing ear and high magnification of the cartilage layer (chondrium) with developing chondroblasts (black arrowheads = peri-cellular cavities) ad chondrocytes (yellow arrowhead = lacunar space), and the surrounding outer perichondium (OP), at 16 **(A)** and 22 **(B)** PCW. Insets show lower magnification pictures of the ear section, and dashed rectangles indicate the field enlarged in the correspondent pictures. Asterisks indicate thick and irregular, developing inner perichondrium (IP). **(C)** Quantification of cell nuclei in the chondrium layer of fetal (PCW16 and PCW22) and pediatric ear normal cartilage sections ($n = 4$, in which at least three independent fields were analyzed). Data are expressed as mean ± SEM. Significance of differences (Kruskal–Wallis test and Dunn's *post hoc* test, confidence level = 95%): $^{*}p < 0.05$ and $^{****}p < 0.0001$; n = number. **(D)** Elastin, **(E)** COL2, and **(F)** COL1 expression by HRP immunohistochemistry shown by brown staining, in 16 and 22 PCW. Nuclei counterstained by hematoxylin. V = vessel.

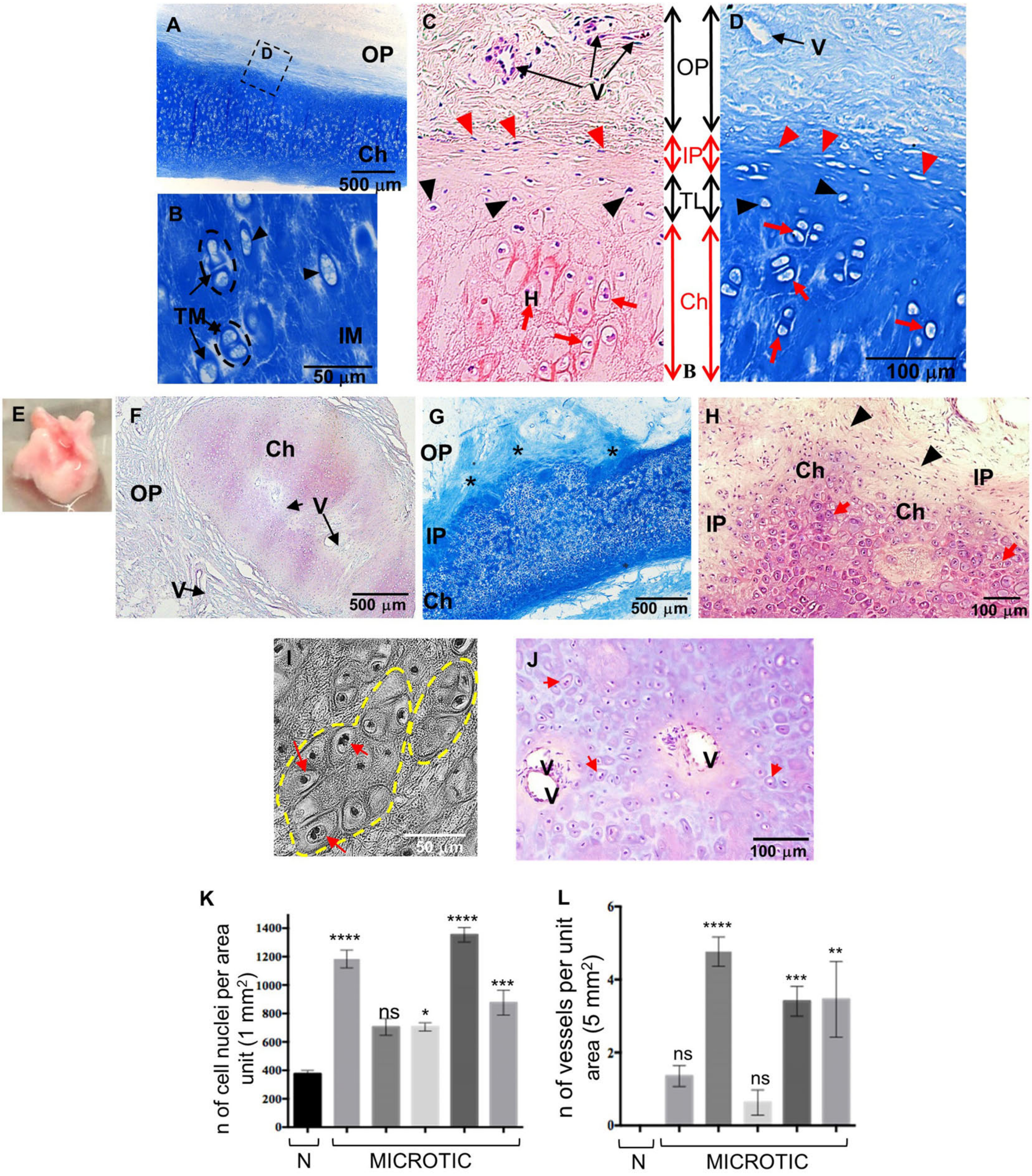

FIGURE 2 | Histology of human normal and microtic pediatric ear cartilage. **(A–D)** Sections of normal auricular cartilage from a 9-year-old individual stained with Alcian Blue **(A,B,D)** or H&E **(C)**. Note that the chondrium layer (Ch) enlarged in **(B)** contains chondrocytes in lacunae (black arrowheads) surrounded by territorial matrix (TM), and small isogenous groups (black dashed circles). **(C,D)** Multi-layered tissue architecture. Outer perichondrium containing fibers and vessels (V); inner perichondrium containing cartilage stem/progenitor cells (CSPCs, red arrowheads); transitional layer containing chondroblasts (black arrowheads); mature chondrium containing chondrocytes in lacunae (red arrows). **(E)** Example of a biopsy of microtic cartilage. **(F–J)** Representative sections of microtic auricular cartilage from a 9-year-old individual stained with H&E **(F,H,J)** or Alcian Blue **(G)**. **(F)** Amorphic islet of cartilage containing vessels (V) in the chondrium (also shown in **I**) and surrounded by outer perichondrium. **(G)** Cartilage multi-layered architecture is disrupted, and IP is irregular (asterisks) in many areas. **(H)** At high magnification chondrium (with round cells) and IP (with CSPCs) are found in the same layer. **(I)** Phase contrast image of big isogenous groups (yellow dashed circles). **(J)** Vessels in the chondrium layer of microtic ear cartilage. Red arrows, chondrocytes in lacunae; IP, inner perichondrium; OP, outer perichondrium; TM, territorial matrix; IM, interterritorial matrix. **(K)** Quantification of cell nuclei in the chondrium layer of normal ($N = 1$) and microtic ear cartilage patients ($N = 5$). **(L)** Quantification of vessels in the chondrium layer of normal and microtic ear cartilage patients. Data are expressed as mean ± SEM. Significance of differences (Kruskal–Wallis test and Dunn's *post hoc* test, confidence level = 95%): $^{*}p < 0.05$, $^{**}p < 0.01$, $^{***}p < 0.001$, and $^{****}p < 0.0001$ vs normal ear. *n* = number; ns = non-significant. *N* = normal.

Analysis of ECM proteins, ELN and COL2, in pediatric normal and microtic cartilages showed comparable expression patterns (**Figure 3** and **Supplementary Figures 1C–F**, for negative controls). In normal ear cartilage, ELN was detected in the inner perichondrium, translational layer and mature chondrium layer, and elastic fibers were also present in the OP. Similarly, in microtic ear cartilage, ELN was expressed in both amorphic cartilage islets and the surrounding OP. COL2 was found in the inner perichondrium and translational layer, where CSPCs and chondroblasts were present, both in normal and microtic ear cartilage. In contrast, COL1 expression pattern differed in microtic and normal ear cartilages. While in normal cartilage COL1 expression was restricted to the inner and OP, in microtic ear cartilage it was found also within the amorphic cartilage islets.

Characterization and Differentiation Potential of Human Pediatric Precursor Cells From Normal and Microtic Ear Cartilage and Adipose Tissue in 2-Dimensional (2D) Cultures

The behavior and differentiation potential of cells derived from either normal or microtic cartilages was investigated in 2D cultures. Cells from both microtic and healthy ear cartilage explants migrated out within 5–7 days after plating and displayed the same fibroblast-like morphology (spindle-shaped cells) with multiple, long protrusions (**Figure 4A** and **Supplementary Figure 2**). Based on their morphology and properties shown below, we will refer to these cells as CSPCs. In monolayer cultures, these cells expressed typical MSCs markers such as Vimentin (VIM) and COL1 as well as cartilage-associated proteins, such as COL2 and ELN, as assessed by immunofluorescence. COL1 and COL2 staining was intracellular and punctuated, and mainly localized around the cell nuclei. This is likely to reflect accumulation of procollagens in the endoplasmic reticulum and Golgi network in undifferentiated cells, as reported in previous studies (Bonfanti et al., 1998; Unlu et al., 2014). A similar pattern of expression was observed in ADSC primary cultures (**Supplementary Figure 2**), which were used for comparison. COL2 protein expression in microtic ear cells and ADSCs was also confirmed by Western Blotting (**Supplementary Figure 3**). Expression of *VIM*, *COL1*, and *ELN* in microtic and normal ear CSPCs and in ADSCs was detected also at the transcriptional level (**Supplementary Figure 4**). In contrast, the *COL2* (71 and 125 bp) transcript was barely detectable in the CSPCs. This could be explained by the long half-live and very slow turnover of ECM proteins. Therefore, these proteins can be still detected by immunohystochemistry when gene expression has been already down-regulated (Verzijl et al., 2000; Decaris et al., 2014). The cartilage-specific transcript Aggrecan (*ACAN*) was clearly detected in all cell lines, except for one microtic ear- and one ADSC line where it was barely detectable. Both CSPCs and ADSCs expressed Nestin (*NES*) gene, usually considered a marker of neural stem cells, but more recently found expressed also by pluripotent MSCs (Mendez-Ferrer et al., 2010). Other chondrogenesis markers, such as SRY-Box Transcription Factor 9 (*SOX9*), Runt-related transcription factor 2 (*RUNX2*), and collagen 10 (*COL10*) were detected in all cell lines tested, but *COL10* was not observed in ear cartilage, as expected in non-hypertrophic tissue (**Supplementary Figure 4**).

Normal and microtic CSPCs were cultured in 2D in adipogenic, chondrogenic or osteogenic media to assess their differentiation potential along three-mesenchymal lineages. ADSCs were used as positive control. Tri-lineage differentiation was observed in all CSPCs, as demonstrated by Oil Red O (lipid droplets: adipogenic), Alcian Blue (GAGs, glycosaminoglycans: chondrogenic) and Alizarin Red (calcium deposits: osteogenic) staining, similarly to ADSCs (**Figure 4B**). When grown in 2D in chondrogenic differentiation media, CSPCs condensed and spontaneously formed 3D aggregates by 10–15 days of culture. Undifferentiated cultures grew as monolayers and never aggregated (data not shown). Quantification of GAGs produced upon chondrogenic differentiation was assessed in microtic and normal CSPCs (**Figure 4C**), and ADSCs (**Supplementary Figure 5**), by semiquantitative analysis of Alcian Blue staining. After 3 weeks of differentiation, GAG levels in differentiated ear-derived cultures were all increased compared to undifferentiated ($^*p < 0.05$ and were found around 3.5 times higher than in chondrogenic ADSCs).

Characterization of Chondrogenically Differentiated Ear CSPC and ADSC Spheroids

We initially used normal CSPCs to set up a high-density spheroid culture system (**Figure 5A**), and then used this model to investigate the response of microtic CSPCs to a 3D environment. ADSCs were used for comparison. For simplicity we will refer to the spheroids generated using normal and microtic ear CSPCs and ADSCs, as normal and microtic spheroids, and ADSC spheroids, respectively. After 4 weeks in culture, both undifferentiated and differentiated normal spheroids showed a round shape and ivory-white color. Chondrogenically differentiated spheroids were around 2.5-fold bigger (mean diameter of differentiated/mean diameter of undifferentiated, $n = 3$, $^*p < 0.05$), compared to the undifferentiated ones (**Supplementary Table 4**). Undifferentiated spheroids maintained a round shape up to the fourth week in culture. However, when maintained in culture for up to 6 weeks, they gradually lost contours and became very fragmented, with a small central core surrounded by loose matrix (**Figure 5A**). In contrast, differentiated spheroids maintained a well-defined, round shape and a firm consistency, and they were 3.3-fold bigger (mean diameter of differentiated/mean diameter of undifferentiated, $n = 4$, $p < 0.05$) than the undifferentiated ones (**Supplementary Table 4**).

Undifferentiated and chondrogenically differentiated normal spheroids were cryosectioned and analyzed by histological and immunofluorescence staining. The diagram in **Figure 5B** shows a schematic view of the spheroid and indicates the terms used for the analysis of the spheroid sections. Undifferentiated and differentiated normal spheroid cryosections displayed a very different morphology. In 4 weeks, undifferentiated spheroid sections stained with H&E and Alcian Blue, cells appeared

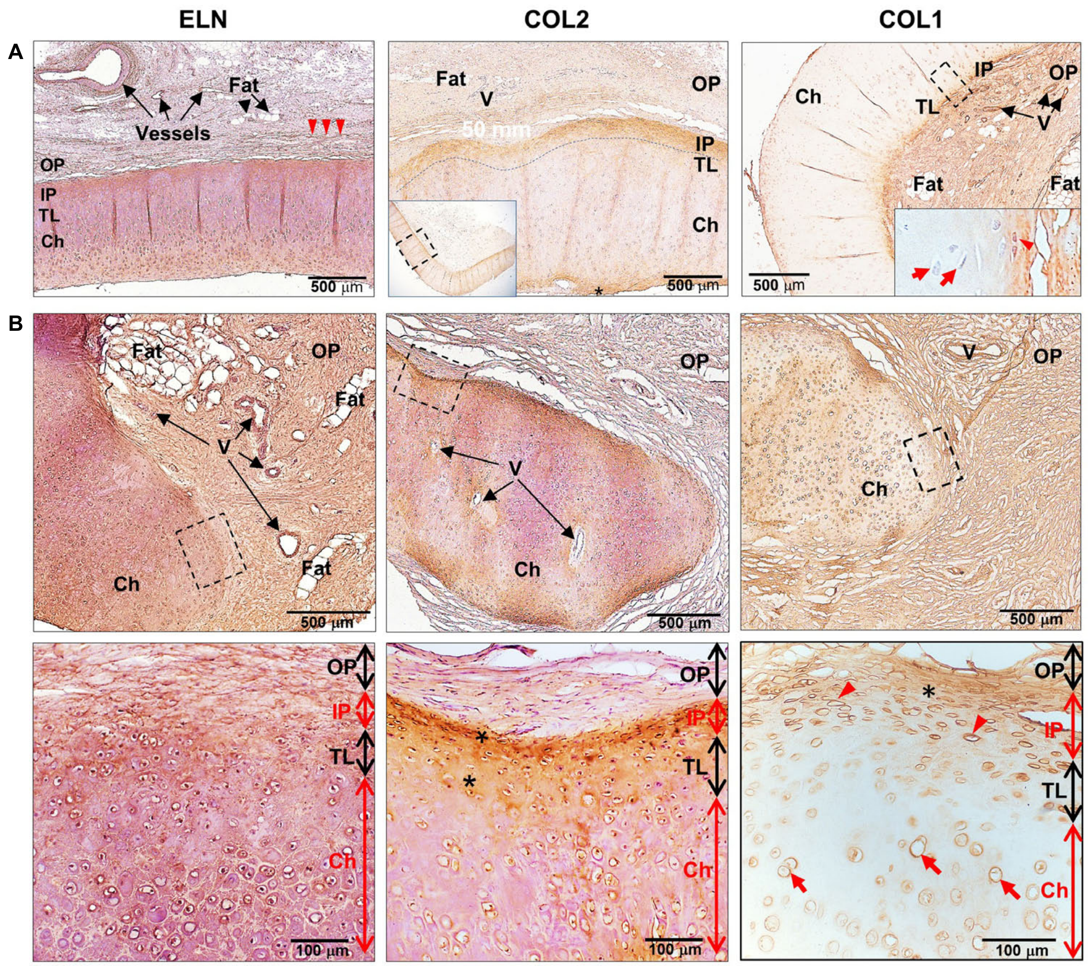

FIGURE 3 | Expression of extracellular matrix proteins in human healthy and microtic ear cartilage. ELN, COL2, and COL1 expression in **(A)** human pediatric normal (*N* = 1) and (B) microtic (*N* = 2, *N* = 4, and *N* = 4, respectively) ear cartilage, by HRP immunohistochemistry shown by brown staining. Nuclei counterstained by hematoxylin. **(A)** COL2 panel: the inset shows the tissue section at low magnification, and the dashed rectangle indicates the area enlarged in the panel; COL1 panel: the inset shows the enlarged area indicated by the dashed rectangle. **(B)** The dashed rectangles in the top panels indicate enlarged areas shown in the bottom panels. For each tissue, at least three sections were examined, in which at least four independent regions were analyzed. Red arrowheads, cartilage stem/progenitor cells (CSPCs); red arrows, chondrocytes; arrowheads, elastin fibers in the outer perichondrium; OP, outer perichondrium; IP, inner perichondrium; TL, transitional layer; Ch, developing chondrium; V, vessels.

homogeneously distributed both at the surface and in the core (**Supplementary Figure 6A** and **Figure 6A**); they produced GAGs and expressed COL2 and VIM throughout (**Figure 6B**). In contrast, the 4 weeks differentiated normal spheroids contained different regions with diverse cellular and matrix organization (**Figure 6C**). On the spheroid surface, cells appeared to have formed a tight and homogenous layer (**Supplementary Figure 6B**). In contrast, sections in the middle (**Supplementary Figure 6C**) and in the core (**Figures 6C–I**) of the spheroids contained distinct regions: (i) a spherical inner region with a low GAG content (**Figures 6C,D**), surrounded by (ii) a ring-like outer region, with a high GAG content as indicated by the strong AB staining (**Figures 6C,E**) separated by (iii) a boundary zone (**Figures 6C,F,G**). Cell density was significantly lower in the outer region than in the inner region (**Supplementary Figure 8D**). The external ring contained some cartilage nodules which stained intensely for Alcian Blue and COL2 (arrows in **Figures 6C,E–G**). Cells that formed the boundary zone were strongly COL2-positive (asterisks in **Figures 6C,F,G**). ACAN staining was detected only within the outer region (**Figure 6I**). In 6 weeks differentiated normal spheroids (**Figure 7**), these features appeared even more pronounced. We observed a more clearly defined boundary at the interface between the inner and outer regions (asterisks in **Figures 7A,B**), and the presence of two zones within the outer region, indicated as internal zone (IZ) and SZ, containing spindle-like and round cells, respectively (**Figure 7C**). Interestingly, (iii) cartilage nodules were only found within the SZ (**Figures 7B,D,E**); they were more numerous and more mature compared to those present in 4 weeks differentiated spheroids, as they

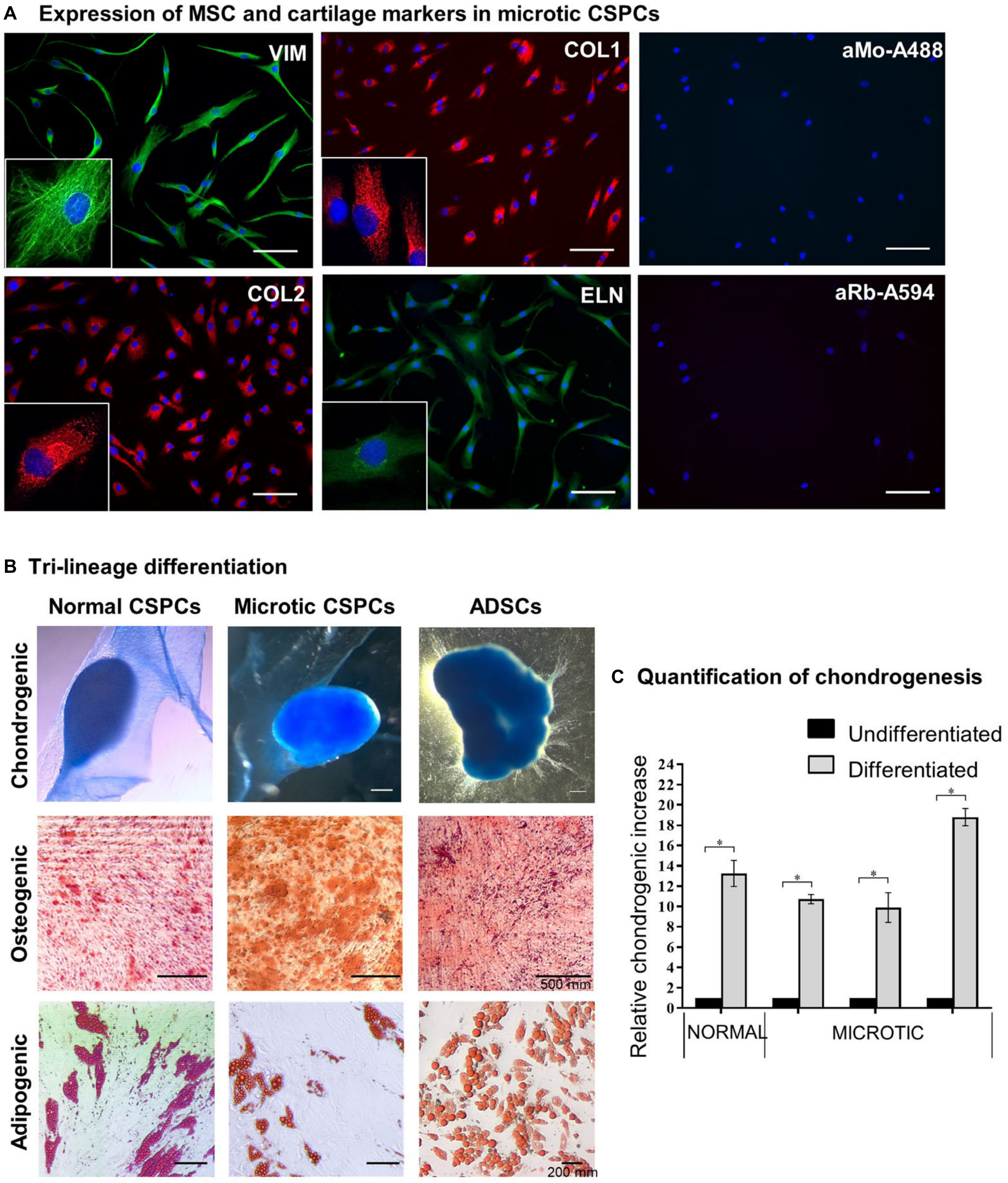

FIGURE 4 | Characterization of microtic cartilage stem progenitor cells. **(A)** Immunofluorescence staining of mesenchymal stem cell (Nestin, NES; Vimentin, VIM; Collagen 1, COL1) and cartilage-associated proteins (Collagen 2, COL2; Elastin, ELN) in microtic CSPCs (cartilage stem/precursor cells). aMo-A488 (Anti-mouse Alexa Fluor® 488) and aRa-594 (Anti-rabbit Alexa Fluor® 594) are negative controls of staining, in which the cells were incubated with secondary Abs only. Scale bars = 100 μm. **(B)** Normal CSPCs (*N* = 1), microtic CSPCs (*N* = 3), and ADSCs (*N* = 3) stained with Oil Red O (adipogenic), Alcian Blue (chondrogenic) and Alizarin Red (osteogenic) after 3 weeks in differentiation media. All pictures are representative of at least *n* = 3 biological replicates, in which four independent fields were examined. **(C)** Quantification of chondrogenesis in normal (*N* = 1) and microtic (*N* = 3) CSPCs, cultured for 3 weeks in either proliferation (undifferentiated) or chondrogenic medium (differentiated), based on Alcian Blue measurement at OD_{595}. Data are expressed as fold difference, taking undifferentiated control as 1; data are mean (*n* = 4) ± SEM Mann–Whitney test, $^{*}p < 0.05$.

contained developing chondrocytes in lacunae (**Figure 7E**'). In some regions of big nodules and in smaller nodules, COL1 expression was detected (**Figure 7E**). Finally, the protein transcribed by the master regulator gene of chondrogenesis, *SOX9*, was expressed only by cells in the external ring of the spheroid, but not in the inner region, both in 4 weeks

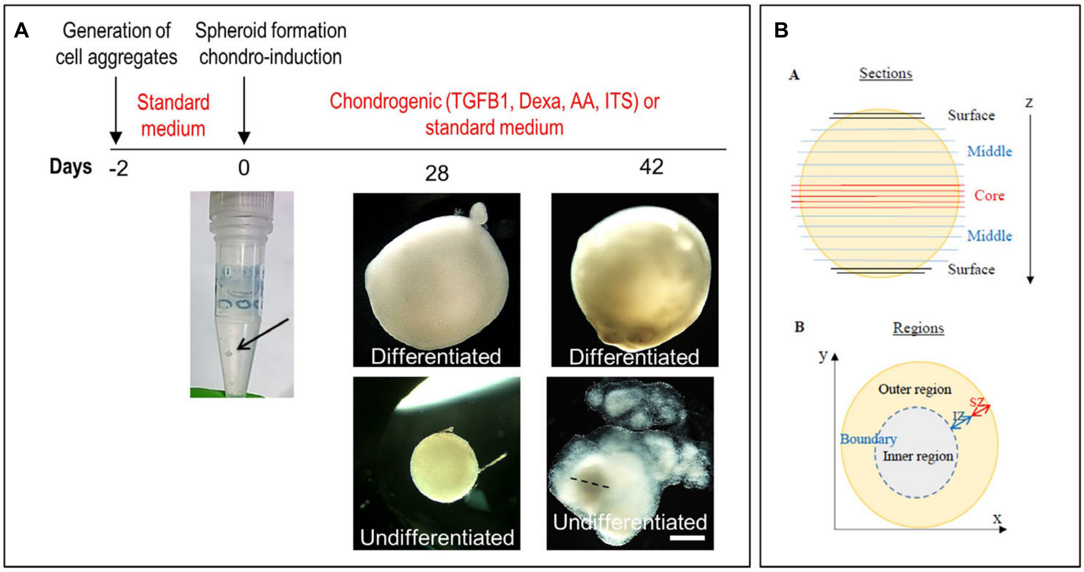

FIGURE 5 | Generation of spheroids and induction of chondrogenic differentiation. **(A)** Timeline of the differentiation of ear CSPCs (cartilage stem/progenitor cells) into cartilage spheroids. The arrows at day 0 points at the cell aggregate after formation. Gross pictures show normal CSPCs cultured for 6 weeks in either standard (undifferentiated) or chondrogenic (differentiated) medium, imaged at 28 and 42 days of culture. The dashed line in 6 weeks undifferentiated spheroid indicates the core, considered to measure the diameter width. Pictures are representative of four undifferentiated/differentiated spheroids (*N* = 1). Scale bar = 500 µm. **(B)** Schematic representation of the spheroids. Spheroid sections are defined as surface, middle and core sections in relation to their position on the *z* axes. Different areas were identified in differentiate spheroid sections, referred to as: (i) inner region: area located in the inner part; (ii) outer region: area from the external surface to the core; and (iii) boundary: interface between the inner and outer region. In some samples, within the outer region two zones were identified, referred to as internal (IZ) and superficial zone (SZ).

(**Supplementary Figure 7**) and 6 weeks differentiated normal spheroids (**Figure 7F**).

The spheroid culture system was then used to study the behavior of microtic spheroids and assess whether this was consistent across patients. To this purpose we compared microtic spheroids from three independent patients (31, 32, and 34 of **Supplementary Table 1**). As the more mature structure was observed in normal spheroids after 6 weeks compared to 4 weeks in culture, we focused on the later time point for the analysis of microtic spheroids. After 6 weeks, all undifferentiated microtic spheroids were very fragile, and much smaller than the differentiated samples (**Figures 8A–C**). In some undifferentiated samples the cells did not form a sphere but remained as discoidal pellets (**Figure 8A**). In contrast, all microtic spheroids maintained in chondrogenic medium had a white color, a glossy and translucent appearance, and a firm texture, similar to differentiated normal spheroids (data not shown). However, they displayed irregular shapes rather than being spherical. Various morphologies were observed in differentiated microtic spheroid sections (**Figures 8D–H**). Spheroids from all lines contained numerous cartilage nodules (**Figures 8D–H**) and discrete areas of ECM deposition (**Figures 8D',E'**), as demonstrated by histological analysis and COL2 staining. Differentiated spheroids from two microtic CSPC lines (32 and 34, **Figures 8G,H**) presented a very different morphology from normal spheroids, with no well-defined ring-like outer region or boundary zone, and cartilage nodules present within the inner-like region. Although spheroids from the third microtic line investigated, 31, had an identifiable circular inner region and outer region like control spheroids (**Figure 8D**), they contained a higher number of cartilage nodules than controls (**Figure 8I**) very close to the inner region (**Figures 8E,F**), and the boundary was discontinuous (**Supplementary Table 5**), with a lack of definition within the outer zone between IZ and SZ (**Figures 8D,F**). No evidence of endochondral ossification was observed in the differentiated CSPC spheroids, as indicated by negative staining for alkaline phosphatase and lack of calcium deposition (**Supplementary Figures 8A–C**).

Adipose-tissue derived stem cells chondrogenic spheroids were generated for comparison. They also showed a firm consistency and a round shape, with white color and a glossy appearance after 6 weeks differentiation (**Supplementary Figure 8A**). Multiple cartilage nodules were observed throughout the differentiated ADSC spheroids, both in surface and core sections, as demonstrated by both Alcian Blue staining and COL2 immunostaining (**Supplementary Figures 8B,C**). However, no stereotyped structure was observed in ADSC spheroid sections.

DISCUSSION

Here, we characterized the macroscopic and microscopic structure of microtic ear cartilage and systematically compared it to normal fetal and postnatal auricular cartilage, revealing

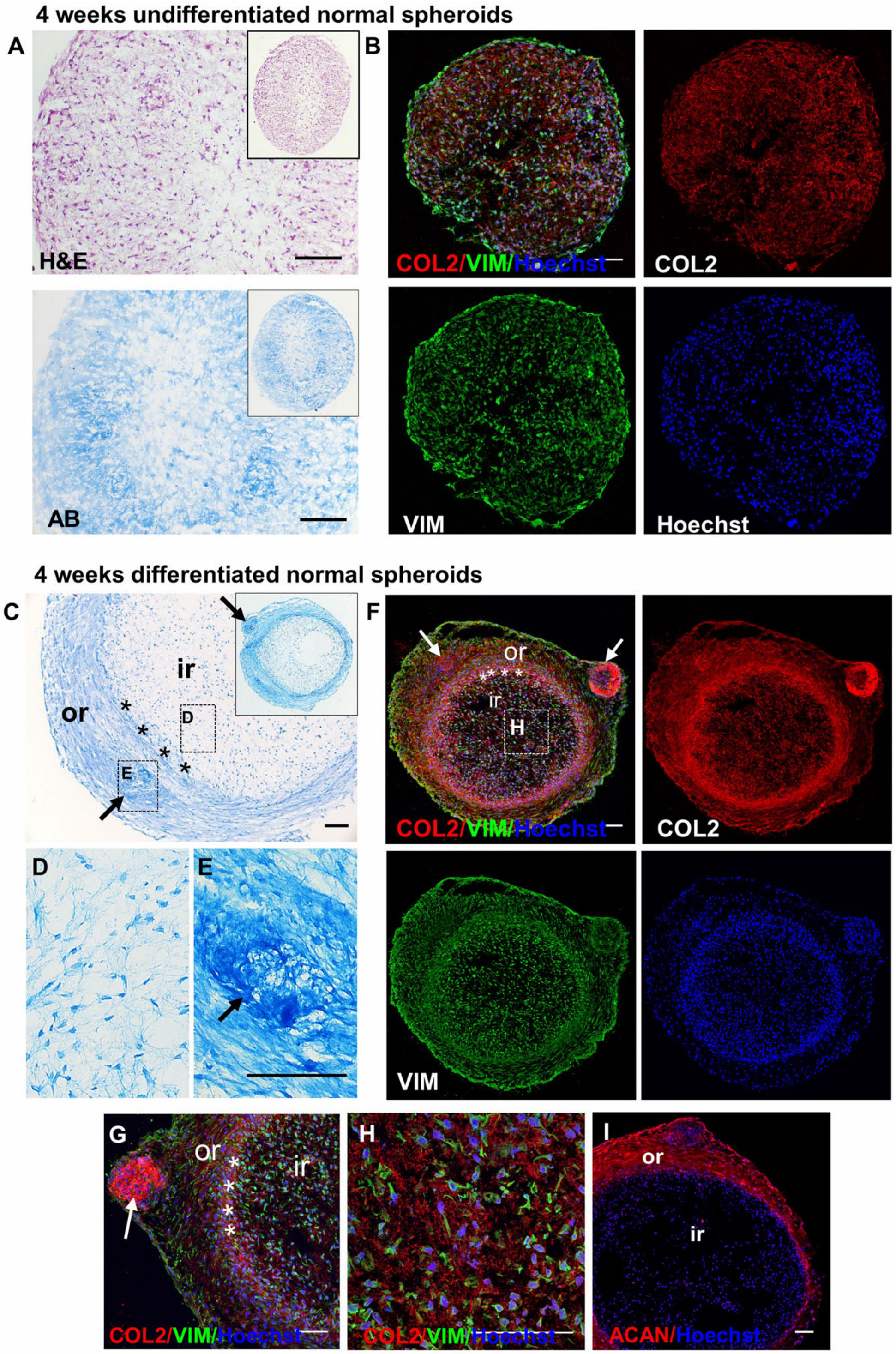

FIGURE 6 | Detection of GAGs, chondrogenic and MSC markers in normal spheroids after 4 weeks of chondrogenic differentiation. Histological and immunofluorescence staining in core section from 4 week undifferentiated **(A,B)** and differentiated **(C–I)** normal CSPC spheroids. Sections were stained for Collagen 2 (COL2), Elastin (ELN), Vimentin (VIM) and Aggrecan (ACAN). Nuclei counterstained with Hoechst (blue). **(A,B)** Undifferentiated spheroid core sections stained by Hematoxylin and Eosin (H&E), Alcian Blue (AB) and **(B)** fluorescent antibodies. **(C–E)** Differentiated spheroid core sections stained by AB. Note the presence of a self-organizing structure, with a ring-like structure (outer region, or) and an inner region (ir), separated by a boundary region (asterisks), in the differentiated samples, but not in the undifferentiated controls. **(F–I)** Differentiated spheroid core sections stained by fluorescent antibodies. The insets in **(A)** and **(C)** show the low magnifications of the same section shown in the correspondent figure. The dashed rectangles in **(C)** and **(F)** show the areas enlarged in panels **(D,E,H)**. Arrows = cartilage nodules. Pictures are representative of *n* spheroids = 4, in which at least six sections were examined (*N* = 1). All scale bars = 100 μm.

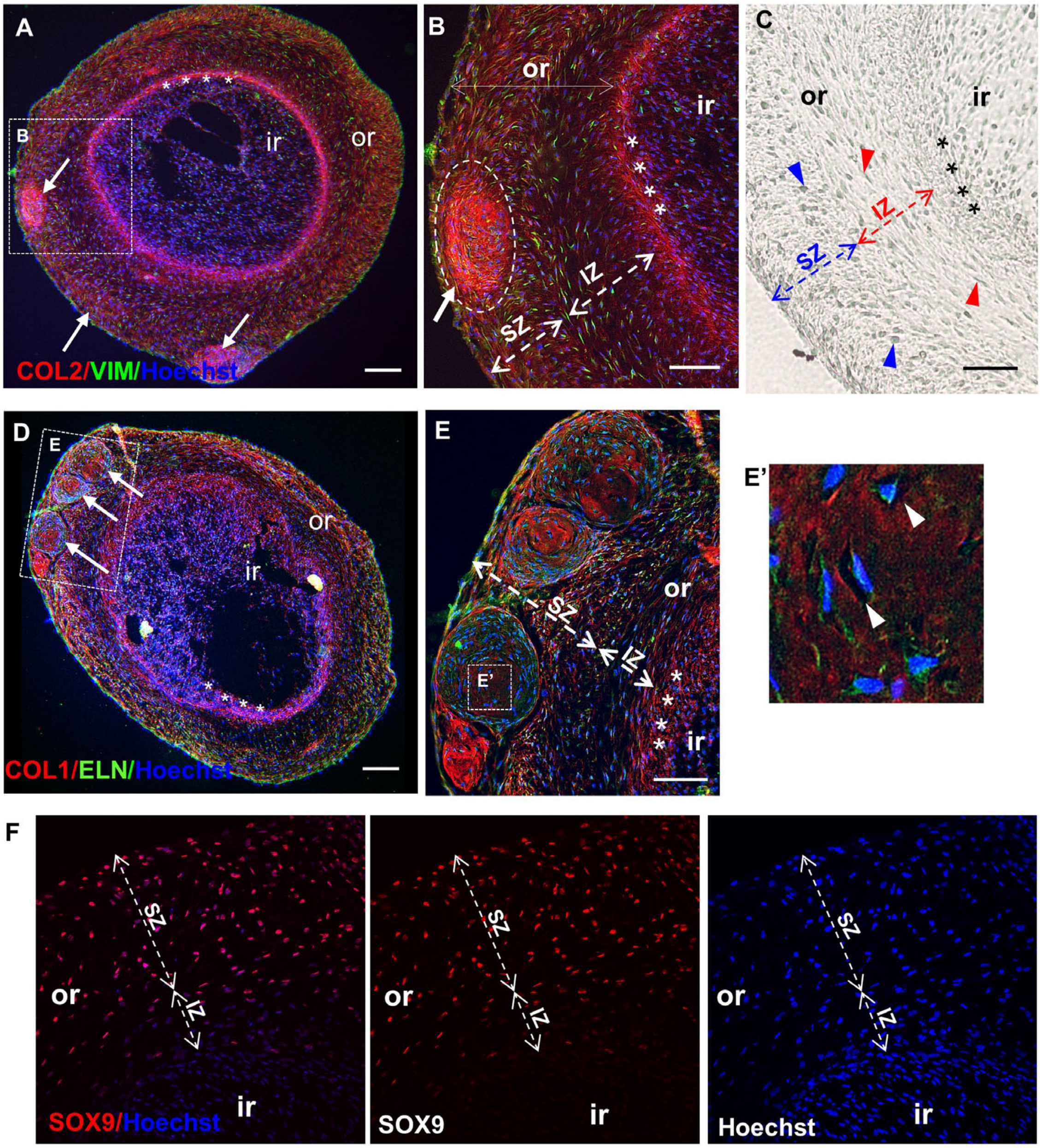

FIGURE 7 | Maturation of normal spheroids after 6 weeks of chondrogenic differentiation. Immunofluorescence **(A,B,D–F)** and differential interference contrast (DIC) **(C)** pictures of core sections from normal CSPC spheroids, after 6 weeks in chondrogenic medium. Sections are stained for Collagen 2 (COL 2), Vimentin (VIM), Elastin (ELN), Collagen 1 (COL 1), and SRY-Box 9 (SOX 9). Nuclei are counterstained with Hoechst dye (blue). **(A,D)** Differentiated spheroids at low magnification show typical self-organizing structure, with an inner (ir) and outer region (or, dashed lines), where cartilage nodules (white arrows) are present, and a definite boundary (asterisks) between the inner (ir) and the outer region (or) (also shown enlarged in **B**). **(C,E)** Note the presence of two zones within the outer region in 6 weeks differentiated spheroids: a more superficial zone (SZ) containing round cells (blue arrowheads), and a more internal zone (IZ) located next to the boundary, containing spindle-like cells (red arrowheads). **(E,E')** Cartilage nodules in the SZ containing developing chondrocytes in lacunae (white arrowheads in **E'**). **(F)** Staining for SOX9 was detected only in the outer region, but not in the internal region. Representative sections from the analysis of three spheroids where ≥6 sections and four independent fields/section were examined (*N* = 1). All scale bars = 100 µm.

previously undescribed features of the pathology. Furthermore, we compared CSPCs from human normal and microtic ears in 2D and 3D high density culture systems, called spheroids, for the first time. Assessment of microtic spheroids against normal developing auricular cartilage and postnatal microtic cartilage suggested that they recapitulate many characteristics of microtic ears, which were not apparent when microtic CSPCs were studied in 2D systems.

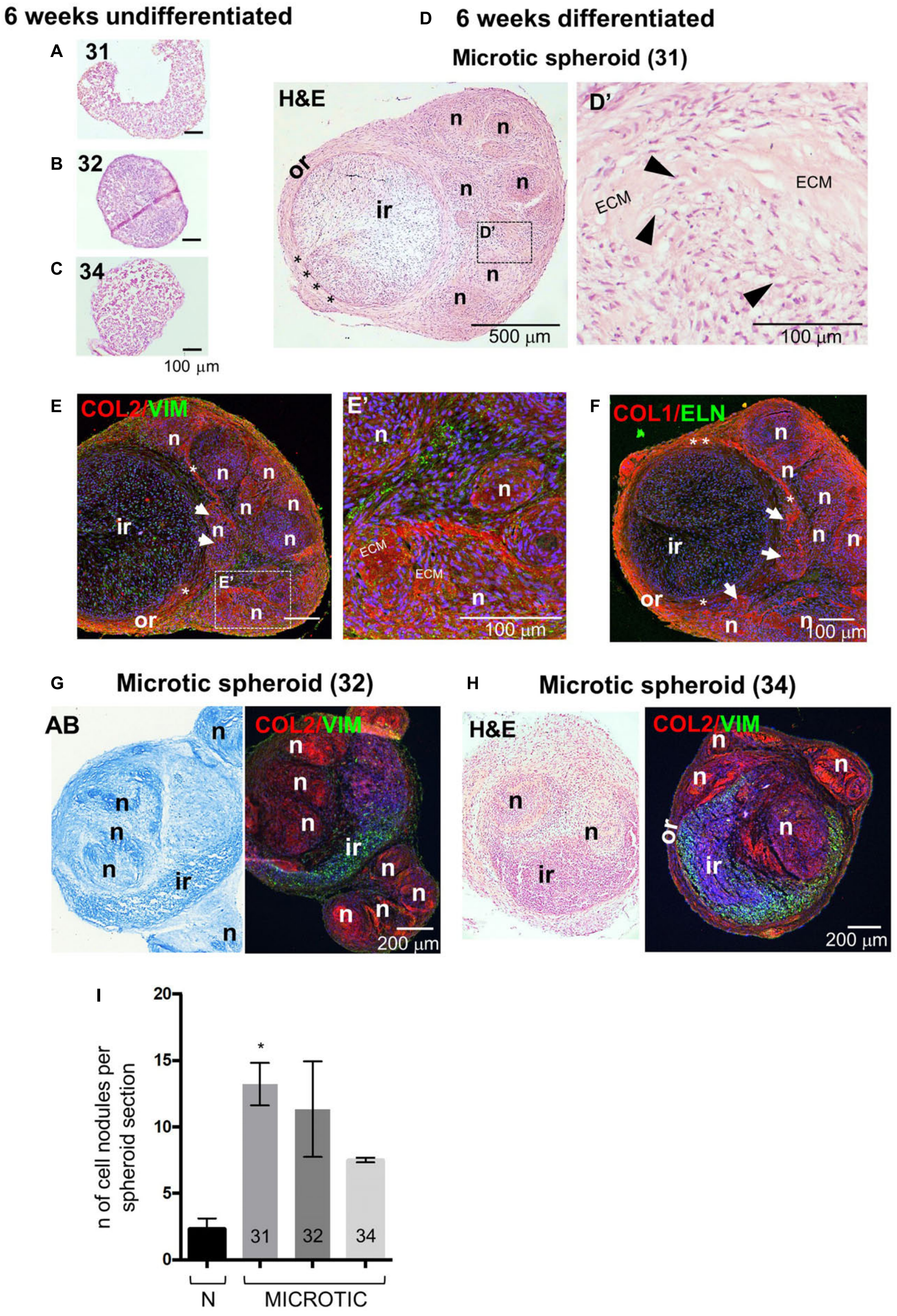

FIGURE 8 | Histology, protein expression and nodule formation in microtic spheroids after 6 weeks of chondrogenic differentiation. **(A–C)** Hematoxylin and Eosin (H&E) staining in core section from microtic spheroids from cartilage stem/progenitor cell (CSPC) lines CSPC-31 **(A)**, CSPC-32 **(B)**, and CSPC-34 **(C)**, cultured for 6 weeks in standard proliferation (Undifferentiated) medium. **(D–H)** Sections from microtic spheroids cultured for 6 weeks in chondrogenic (Differentiated) medium. Sections are stained for Collagen 2 (COL 2), Vimentin (VIM), Elastin (ELN), and Collagen 1 (COL 1). Nuclei are counterstained with Hoechst dye (blue). **(D–F)** Microtic spheroids, line CSPC-31. Hematoxylin and Eosin (H&E) **(D,D')** and immunofluorescent **(E,E',F)** staining in middle **(D,D')** and core **(E,E',F)** sections, showing the **(D–F)** stereotyped structure of CSPC-31-differentiated spheroids. Or, outer region; Ir, inner region; asterisks, boundary; *n*, cartilage nodules; white arrows in **(E,F)**, cartilage nodules close to the ir. **(D',E')** High magnification pictures show cartilaginous nodules, highly cellularized, containing patches of deposited extracellular matrix (ECM), and chondrocytes in lacunae (black arrowheads). **(G)** Alcian Blue (AB) and immunofluorescent pictures of core sections from microtic ear-derived cell spheroids, line CSPC-32. **(H)** H&E and immunofluorescent pictures of core sections from microtic ear-derived cell spheroids, line CSPC-34. **(I)** Quantification of cartilage nodules in normal and microtic spheroid sections from three lines (31, 32, and 34). Data represent analysis of three spheroids per line, apart from line 34 (two spheroids) with nodules counted in three sections/spheroid in three independent fields/section. Data are expressed as mean ± SEM. Significance of differences (Kruskal–Wallis test and Dunn's *post hoc* test, confidence level = 95%): $^*p < 0.05$.

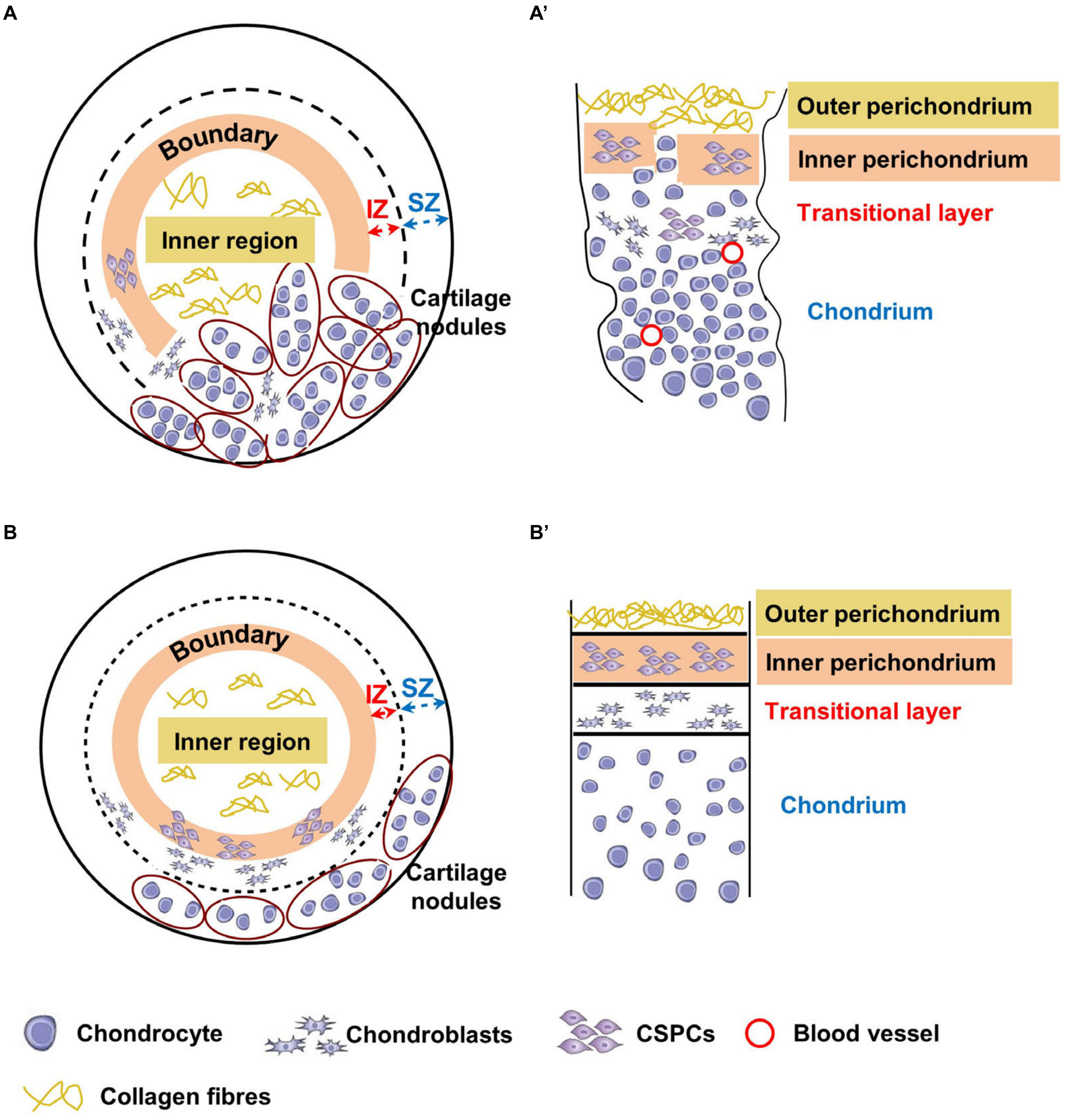

FIGURE 9 | Schematic representation of chondrogenically differentiated spheroids and native cartilages from microtic and normal ears. Corresponding tissue layers in spheroids and native cartilages are indicated by the same color coding. The inner region of the spheroids **(A,B)** corresponds to the outer perichondrium in native tissues **(A',B')**, the boundary between the inner and outer region to the inner perichondrium, the internal zone (IZ) to the transitional layer, and the superficial zone (SZ) to the chondrium. **(A,A')** *In microtic spheroids and microtic tissue, the boundary*/IZ and inner perichondrium/transitional layer, respectively, are discontinuous with mature chondrocytes present across these boundaries. The densely cellularized cartilage nodules accumulated to one side of the spheroid resemble amorphic islets of cartilage present in native microtic cartilage. **(B,B')** *In normal spheroids, boundaries are maintained, with cartilage nodules restricted to the SZ, where they form a layer similar* to the chondrium of normal native ear cartilage.

Microtic Ear Cartilage Appears Underdeveloped *in vivo*

As shown here, the inner perichondrium in developing normal ear cartilage appears as an irregular layer at 16 PCW and has become thinner and more defined by 22 PCW, resembling more closely postnatal cartilage. Also, cell density changes with development, progressively decreasing, and in mature cartilage chondrocytes are interspersed within abundant and homogenous ECM. Notwithstanding some inter-patient variability and possibly different etiologies of the disease, there are remarkable similarities between human microtic cartilages as compared to normal cartilage. These include disruption of the typical multi-layered structural organization of elastic cartilage, presence of unshaped islets of cartilage, hyper-cellularity, expression of COL1 in the chondrium (as shown also by Dahl et al., 2011;

Pappa et al., 2014) and, most surprisingly, the presence of blood vessels in the chondrium. Many of these features are consistent with the hypotheses that in microtia ear cartilage maturation are arrested at an intermediate stage, and neural crest cell patterning into the first and second pharyngeal arch during ear development is defective, as previously suggested (Luquetti et al., 2012). Infiltration of collagen fibers from the perichondrium into the lacunar cartilage of microtic ears has been briefly mentioned only in one study (Gu et al., 2018), whereas other studies reported an overall good preservation of the microtic cartilage structure (Dahl et al., 2011; Pappa et al., 2014). Discrepancies with previous studies may depend on the rather small number of patient samples they analyzed. Together, our analysis of microtic cartilage from five patients is more in agreement with observations by Gu et al. (2018), suggesting abnormalities in perichondrium and lacunae organization, and support the view that at the cellular level microtic cartilage is not simply a smaller normal cartilage, but a cartilage that is unable to reach the maturity and organization of healthy auricular cartilage.

Chondrium Vascularization Is a Landmark of Microtic Ear Cartilage

A novel and unexpected finding that has emerged from our analysis of microtic ears is the presence of small blood vessels in the chondrium. To our knowledge, presence of blood vessels has never been reported in the chondrium of normal cartilage, neither in fetal, nor pediatric (this study), nor adult ear, consistent with the notion that cartilage is an avascular tissue (Chung and Burdick, 2008; Akkiraju and Nohe, 2015; Bernhard and Vunjak-Novakovic, 2016). The only cartilaginous tissue that becomes vascularized in a controlled physiological manner is the hypertrophic cartilage in the growth plates of long bones, ribs, and vertebrae during endochondral ossification (Hattori et al., 2010). Nevertheless, no sign of trabecular bone formation and mineralization were found in microtic cartilages or spheroids, neither in ours (data not shown) nor in previous studies. While at present we do not know what causes microtic cartilage to become vascularized, nor whether it is the cause or a consequence of the disease, we believe this is an important finding that can guide investigation into the pathology of microtia. For example, comparing the expression of vascular endothelial growth factor (*VEGF*), the master regulator gene of angiogenesis, and other cartilage-derived angiogenic and antiangiogenic molecules (such as the angiogenic cartilage-derived inhibitor, CDI; Moses et al., 1990), as well as endothelial cell stimulating angiogenic factor (ESAF) (Brown and Weiss, 1988) in microtic and normal ear tissues, may help to elucidate the molecular mechanisms of aberrant vascularization, and its potential role in the etiogenesis of the disease.

Auricular CSPCs Are Akin to Mesenchymal Stem Cells and Achieve a Stereotyped Organization in 3D

We have shown that human microtic CSPCs can be easily isolated and expanded to large numbers as previously reported (Kobayashi et al., 2011a; Zhou et al., 2018). Our additional characterization in 2D cultures supports the view that auricular CSPCs behave like MSCs. In addition to expressing the typical MSC surface markers, CD73, CD90, and CD105 (Gardner et al., in preparation), they express intracellular markers typical of MSCs as well as chondrogenic/osteogenic lineage markers and display three-mesenchymal lineage differentiation capability. Similar results were obtained with CSPCs derived from normal ear cartilage.

Consistent with other studies, NES, VIM, COL1 and ELN were detected both at the mRNA and protein levels in CSPCs as well as in ADSCs (Schaffler and Buchler, 2007; Guasti et al., 2012; Guasti et al., 2014). Non-secreted COL2 protein was detected in undifferentiated cells, whereas expression of the transcript, previously demonstrated by RT-qPCR both in ADSCs and CSPCs, was below the sensitivity of RT-PCR. This is consistent with the long half-life of COL2 and suggests a very low turnover of the protein in the undifferentiated cells (Verzijl et al., 2000; Decaris et al., 2014; Guasti et al., 2014). This is the first report of COL2 expression also at the protein level in undifferentiated auricular CSPC and ADSC cultures and parallels a study where COL2 protein was detected in undifferentiated human umbilical cord derived-MSCs (Ahn et al., 2015).

All precursor cells analyzed in this study also expressed *SOX9*, *RUNX2*, and *ACAN* genes. Low level of *ACAN* mRNA in undifferentiated cultures was previously shown in ADSCs, and in human MSCs from either umbilical cord blood (UCB-MSCs) or bone-marrow (BM-MSCs) (Mwale et al., 2006a,b; Guasti et al., 2012; Gomez-Leduc et al., 2016). This is not surprising, as *ACAN* is detected in several tissues, including in the brain parenchyma, and not restricted to mature cartilage (Hering et al., 2020; Hermann et al., 2020; Mitlohner et al., 2020). Also, *RUNX2* expression was previously shown in undifferentiated hBM-MSCs (Mwale et al., 2006a). Together, results from ours and other studies suggest that MSCs are multipotent cells that express constitutively a broad set of genes, which are selectively upregulated or downregulated upon differentiation, depending on the stimuli provided in culture. Importantly, expression of a few genes in isolation is not sufficient to determine the extent of chondrogenic differentiation and needs to be combined with assessment at the morphological and protein level.

In 2D cultures microtic cell behavior upon induction of chondrogenic differentiation appears fairly similar to normal CSPCs. Undifferentiated 3D CSPC spheroids were also quite homogeneous and tended to disaggregate and fall apart over time. This is consistent with the only study on microtic spheroid cultures published so far, where spheroids were maintained in growth medium and not exposed to a chondrogenic medium (Zhang et al., 2014). In contrast, as shown here, when CSPC spheroids are induced to undergo chondrogenic differentiation, a more complex and stereotyped organization becomes apparent. Together, this highlights the self-organization capability of CSPCs upon chondrogenic induction and the importance of using more complex systems for human tissue modeling *in vitro*. To some extent, microtic CSPCs grown in 3D replicated the behavior observed in previous studies, where CSPCs could self-renew and reconstitute cartilage chondrium and perichondrium after *in vivo* grafting (Yanaga et al., 2009; Kobayashi et al., 2011a; Yanaga et al., 2012; Zhou et al., 2018).

Microtic Ear Cell-Derived Spheroids Show Similar Features to Immature Developing Ear Cartilage and Microtic Ear Cartilage *in vivo*

Remarkably, microtic chondrogenic spheroids *in vitro* appear to recapitulate some abnormal features observed in the microtic cartilage *in vivo*. Although they can clearly undergo chondrogenic differentiation, the numerous cartilage nodules that accumulate to one side of the spheroids are highly cellularized and contain only small areas of ECM. Moreover, the cartilage nodules in microtic spheroids appear to be in close contact with the inner region, and the boundary between the inner and outer region was missing, as the inner perichondrium and transitional layer in microtic cartilage (**Figure 9A**).

Our observations of normal CSPCs chondrogenic spheroids, although not as extensive as that of microtic ones because of tissue availability, suggest a more even distribution of cartilage nodules, and formation of an organized multi-layered structure. This includes an inner region with low GAG content, a boundary with spindle like-cells, and an outer region with high GAG content and chondrogenic cells (Sox9 positive), which closely resemble the outer, inner perichondrium and chondrium of native cartilage, respectively (**Figure 9B**). In normal spheroids the inner region contained more cells than the outer region, and in microtic spheroids the inner region often formed off-centre beneath a thin outer region. Furthermore, such compartmentalization was never observed in chondrogenically differentiated ADSC spheroids of a comparable size. For these reasons, it seems unlikely that formation of the inner region is due to limited nutrient diffusion to the core of the spheroids rather than to a spontaneous ability of CSPCs to self-organize in 3D cultures. Finally, no cartilage hypertrophy-associated markers were detected either in normal or in microtic spheroids, ruling out the occurrence of chondrocyte hypertrophy and mineralization. Hence, it could be inferred that the spheroid system can be used to mimic the behavior of normal and abnormal ear cartilage.

CONCLUSION

Together, our study suggests that in 3D spheroids, microtic and normal CSPCs undergo a chondrogenic differentiation process, which results in tissues morphologically similar to native microtic and normal cartilage, respectively. The similarity we have observed between microtic and normal CSPCs with their tissues of origin were not apparent in 2D cultures, which are therefore not sufficient to validate the suitability of microtic cells for cartilage engineering for auricle reconstruction. Furthermore, the similarity between microtic 3D spheroids and native microtic cartilage suggest they can provide a very valuable model to investigate cellular and molecular mechanisms underlying the disease. Recently, microtic ear-derived cells seeded in bioabsorbable scaffolds have been used for auricle reconstruction in patients (Zhou et al., 2018). However, more extended analysis is required to understand whether microtic cells will be able to maintain the appropriate biological and mechanical properties over time once the scaffold is degraded.

DATA AVAILABILITY STATEMENT

The raw data supporting the conclusions of this article will be made available by the authors, without undue reservation, to any qualified researcher.

ETHICS STATEMENT

The studies involving human participants were reviewed and approved by NRES Committee London, UK – Fulham Research Ethics Committee (fetal tissue) and Camden and Islington Community Local Research Ethics Committee (pediatric tissue). Written informed consent to participate in this study was provided by the participants' legal guardian/next of kin.

AUTHOR CONTRIBUTIONS

EZ designed and performed experiments, analyzed data, wrote the manuscript, and obtained funding. MB supervised research, obtained funding, and provided critical reading of the manuscript. NB obtained patient consent, collected tissues, and provided critical reading of the manuscript. PF supervised research, analyzed data, obtained funding, and wrote the manuscript. All authors contributed to the article and approved the submitted version.

FUNDING

This work was supported by UCL Impact Studentship, Microtia UK, and in particular Hana Thalova Salussolia, GOSH NIHR Biomedical Research Centre, NIHR, The Wellcome Trust, and EPSRC.

ACKNOWLEDGMENTS

We are most grateful to Dr. Dale Moulding at the GOS-ICH Microscopy Facility for his advice on data acquisition and analysis. We also wish to thank Alex Virasami at the GOS-ICH Histopathology Facility for the preparation of histological samples, and Dr. Oliver Gardner for critical reading of the manuscript.

SUPPLEMENTARY MATERIAL

The Supplementary Material for this article can be found online at: https://www.frontiersin.org/articles/10.3389/fcell.2020.00666/full#supplementary-material

REFERENCES

Ahn, J., Park, E. M., Kim, B. J., Kim, J. S., Choi, B., Lee, S. H., et al. (2015). Transplantation of human Wharton's jelly-derived mesenchymal stem cells highly expressing TGFbeta receptors in a rabbit model of disc degeneration. *Stem Cell Res. Ther.* 6:190. doi: 10.1186/s13287-015-0183-1

Akkiraju, H., and Nohe, A. (2015). Role of chondrocytes in cartilage formation, progression of osteoarthritis and cartilage regeneration. *J. Dev. Biol.* 3, 177–192. doi: 10.3390/jdb3040177

Anthwal, N., and Thompson, H. (2016). The development of the mammalian outer and middle ear. *J. Anat.* 228, 217–232. doi: 10.1111/joa.12344

Baluch, N., Nagata, S., Park, C., Wilkes, G. H., Reinisch, J., Kasrai, L., et al. (2014). Auricular reconstruction for microtia: A review of available methods. *Plast. Surg.* 22, 39–43. doi: 10.1177/229255031402200102

Bernhard, J. C., and Vunjak-Novakovic, G. (2016). Should we use cells, biomaterials, or tissue engineering for cartilage regeneration? *Stem Cell Res. Ther.* 7:56. doi: 10.1186/s13287-016-0314-3

Bonfanti, L., Mironov, A. A. Jr., Martinez-Menarguez, J. A., Martella, O., Fusella, A., et al. (1998). Procollagen traverses the Golgi stack without leaving the lumen of cisternae: evidence for cisternal maturation. *Cell* 95, 993–1003. doi: 10.1016/s0092-8674(00)81723-7

Brown, R. A., and Weiss, J. B. (1988). Neovascularisation and its role in the osteoarthritic process. *Ann. Rheum. Dis.* 47, 881–885. doi: 10.1136/ard.47.11.881

Chung, C., and Burdick, J. A. (2008). Engineering cartilage tissue. *Adv. Drug Deliv. Rev.* 60, 243–262. doi: 10.1016/j.addr.2007.08.027

Cox, T. C., Camci, E. D., Vora, S., Luquetti, D. V., and Turner, E. E. (2014). The genetics of auricular development and malformation: new findings in model systems driving future directions for microtia research. *Eur. J. Med. Genet.* 57, 394–401. doi: 10.1016/j.ejmg.2014.05.003

Dahl, J. P., Caballero, M., Pappa, A. K., Madan, G., Shockley, W. W., and van Aalst, J. A. (2011). Analysis of human auricular cartilage to guide tissue-engineered nanofiber-based chondrogenesis: implications for microtia reconstruction. *Otolaryngol. Head. Neck. Surg.* 145, 915–923. doi: 10.1177/0194599811419092

Decaris, M. L., Gatmaitan, M., FlorCruz, S., Luo, F., Li, K., Holmes, W. E., et al. (2014). Proteomic analysis of altered extracellular matrix turnover in bleomycin-induced pulmonary fibrosis. *Mol. Cell Proteomics* 13, 1741–1752. doi: 10.1074/mcp.M113.037267

Dowthwaite, G. P., Bishop, J. C., Redman, S. N., Khan, I. M., Rooney, P., Evans, D. J., et al. (2004). The surface of articular cartilage contains a progenitor cell population. *J. Cell Sci.* 117(Pt 6), 889–897. doi: 10.1242/jcs.00912

Engkvist, O., and Wilander, E. (1979). Formation of cartilage from rib perichondrium grafted to an articular defect in the femur condyle of the rabbit. *Scand. J. Plast. Reconstr. Surg.* 13, 371–376. doi: 10.3109/02844317909013085

Gomez-Leduc, T., Hervieu, M., Legendre, F., Bouyoucef, M., Gruchy, N., Poulain, L., et al. (2016). Chondrogenic commitment of human umbilical cord blood-derived mesenchymal stem cells in collagen matrices for cartilage engineering. *Sci. Rep.* 6:32786. doi: 10.1038/srep32786

Gu, Y., Kang, N., Dong, P., Liu, X., Wang, Q., Fu, X., et al. (2018). Chondrocytes from congenital microtia possess an inferior capacity for *in vivo* cartilage regeneration to healthy ear chondrocytes. *J. Tissue Eng. Regen. Med.* 12, e1737–e1746. doi: 10.1002/term.2359

Guasti, L., Prasongchean, W., Kleftouris, G., Mukherjee, S., Thrasher, A. J., Bulstrode, N. W., et al. (2012). High plasticity of pediatric adipose tissue-derived stem cells: too much for selective skeletogenic differentiation? *Stem Cells Transl. Med.* 1, 384–395. doi: 10.5966/sctm.2012-0009

Guasti, L., Vagaska, B., Bulstrode, N. W., Seifalian, A. M., and Ferretti, P. (2014). Chondrogenic differentiation of adipose tissue-derived stem cells within nanocaged POSS-PCU scaffolds: a new tool for nanomedicine. *Nanomedicine* 10, 279–289. doi: 10.1016/j.nano.2013.08.006

Hattori, T., Muller, C., Gebhard, S., Bauer, E., Pausch, F., Schlund, B., et al. (2010). SOX9 is a major negative regulator of cartilage vascularization, bone marrow formation and endochondral ossification. *Development* 137, 901–911. doi: 10.1242/dev.045203

Hering, T. M., Beller, J. A., Calulot, C. M., and Snow, D. M. (2020). Contributions of Chondroitin Sulfate, Keratan Sulfate and N-linked Oligosaccharides to Inhibition of Neurite Outgrowth by Aggrecan. *Biology* 9:29. doi: 10.3390/biology9020029

Hermann, M., Reumann, R., Schostak, K., Kement, D., Gelderblom, M., Bernreuther, C., et al. (2020). Deficits in developmental neurogenesis and dendritic spine maturation in mice lacking the serine protease inhibitor neuroserpin. *Mol. Cell Neurosci.* 102:103420. doi: 10.1016/j.mcn.2019.103420

Jiang, Y., and Tuan, R. S. (2015). Origin and function of cartilage stem/progenitor cells in osteoarthritis. *Nat. Rev. Rheumatol.* 11, 206–212. doi: 10.1038/nrrheum.2014.200

Kagimoto, S., Takebe, T., Kobayashi, S., Yabuki, Y., Hori, A., Hirotomi, K., et al. (2016). Autotransplantation of Monkey Ear Perichondrium-Derived Progenitor Cells for Cartilage Reconstruction. *Cell Transpl.* 25, 951–962. doi: 10.3727/096368916X690917

Kobayashi, S., Takebe, T., Inui, M., Iwai, S., Kan, H., Zheng, Y. W., et al. (2011a). Reconstruction of human elastic cartilage by a CD44+ CD90+ stem cell in the ear perichondrium. *Proc. Natl. Acad. Sci. U.S.A.* 108, 14479–14484. doi: 10.1073/pnas.1109767108

Kobayashi, S., Takebe, T., Zheng, Y. W., Mizuno, M., Yabuki, Y., Maegawa, J., et al. (2011b). Presence of cartilage stem/progenitor cells in adult mice auricular perichondrium. *PLoS One* 6:e26393. doi: 10.1371/journal.pone.0026393

Kusuhara, H., Isogai, N., Enjo, M., Otani, H., Ikada, Y., Jacquet, R., et al. (2009). Tissue engineering a model for the human ear: assessment of size, shape, morphology, and gene expression following seeding of different chondrocytes. *Wound Repair. Regen.* 17, 136–146. doi: 10.1111/j.1524-475X.2008.00451.x

Laschke, M. W., and Menger, M. D. (2017). Life is 3D: Boosting Spheroid Function for Tissue Engineering. *Trends Biotechnol.* 35, 133–144. doi: 10.1016/j.tibtech.2016.08.004

Luquetti, D. V., Heike, C. L., Hing, A. V., Cunningham, M. L., and Cox, T. C. (2012). Microtia: epidemiology and genetics. *Am. J. Med. Genet. A* 158A, 124–139. doi: 10.1002/ajmg.a.34352

Mendez-Ferrer, S., Michurina, T. V., Ferraro, F., Mazloom, A. R., Macarthur, B. D., Lira, S. A., et al. (2010). Mesenchymal and haematopoietic stem cells form a unique bone marrow niche. *Nature* 466, 829–834. doi: 10.1038/nature09262

Mitlohner, J., Kaushik, R., Niekisch, H., Blondiaux, A., Gee, C. E., Happel, M. F. K., et al. (2020). Dopamine receptor activation modulates the integrity of the perisynaptic extracellular matrix at excitatory synapses. *Cells* 9:60. doi: 10.3390/cells9020260

Moses, M. A., Sudhalter, J., and Langer, R. (1990). Identification of an inhibitor of neovascularization from cartilage. *Science* 248, 1408–1410. doi: 10.1126/science.1694043

Mwale, F., Girard-Lauriault, P. L., Wang, H. T., Lerouge, S., Antoniou, J., and Wertheimer, M. R. (2006a). Suppression of genes related to hypertrophy and osteogenesis in committed human mesenchymal stem cells cultured on novel nitrogen-rich plasma polymer coatings. *Tissue Eng.* 12, 2639–2647. doi: 10.1089/ten.2006.12.2639

Mwale, F., Stachura, D., Roughley, P., and Antoniou, J. (2006b). Limitations of using aggrecan and type X collagen as markers of chondrogenesis in mesenchymal stem cell differentiation. *J. Orthop. Res.* 24, 1791–1798. doi: 10.1002/jor.20200

Ohara, K., Nakamura, K., and Ohta, E. (1997). Chest wall deformities and thoracic scoliosis after costal cartilage graft harvesting. *Plast. Reconstr. Surg.* 99, 1030–1036. doi: 10.1097/00006534-199704000-00017

Pappa, A. K., Caballero, M., Dennis, R. G., Skancke, M. D., Narayan, R. J., Dahl, J. P., et al. (2014). Biochemical properties of tissue-engineered cartilage. *J. Craniofac. Surg.* 25, 111–115. doi: 10.1097/SCS.0b013e3182a2eb56

Schaffler, A., and Buchler, C. (2007). Concise review: adipose tissue-derived stromal cells–basic and clinical implications for novel cell-based therapies. *Stem Cells* 25, 818–827. doi: 10.1634/stemcells.2006-0589

Shirasawa, S., Sekiya, I., Sakaguchi, Y., Yagishita, K., Ichinose, S., and Muneta, T. (2006). In vitro chondrogenesis of human synovium-derived mesenchymal stem cells: optimal condition and comparison with bone marrow-derived cells. *J. Cell Biochem.* 97, 84–97. doi: 10.1002/jcb.20546

Togo, T., Utani, A., Naitoh, M., Ohta, M., Tsuji, Y., Morikawa, N., et al. (2006). Identification of cartilage progenitor cells in the adult ear perichondrium: utilization for cartilage reconstruction. *Lab. Invest.* 86, 445–457. doi: 10.1038/labinvest.3700409

Unlu, G., Levic, D. S., Melville, D. B., and Knapik, E. W. (2014). Trafficking mechanisms of extracellular matrix macromolecules: insights from vertebrate development and human diseases. *Int. J. Biochem. Cell Biol.* 47, 57–67. doi: 10.1016/j.biocel.2013.11.005

Verzijl, N., DeGroot, J., Thorpe, S. R., Bank, R. A., Shaw, J. N., Lyons, T. J., et al. (2000). Effect of collagen turnover on the accumulation of advanced glycation end products. *J. Biol. Chem.* 275, 39027–39031. doi: 10.1074/jbc.M006700200

Walton, R. L., and Beahm, E. K. (2002). Auricular reconstruction for microtia: Part II. Surgical techniques. *Plast. Reconstr. Surg.* 110, 234–249. doi: 10.1097/00006534-200207000-00041

Xue, K., Zhang, X., Qi, L., Zhou, J., and Liu, K. (2016). Isolation, identification, and comparison of cartilage stem progenitor/cells from auricular cartilage and perichondrium. *Am. J. Transl. Res.* 8, 732–741.

Yanaga, H., Imai, K., Fujimoto, T., and Yanaga, K. (2009). Generating ears from cultured autologous auricular chondrocytes by using two-stage implantation in treatment of microtia. *Plast. Reconstr. Surg.* 124, 817–825. doi: 10.1097/PRS.0b013e3181b17c0e

Yanaga, H., Imai, K., Koga, M., and Yanaga, K. (2012). Cell-engineered human elastic chondrocytes regenerate natural scaffold in vitro and neocartilage with neoperichondrium in the human body post-transplantation. *Tissue Eng. Part A* 18, 2020–2029. doi: 10.1089/ten.TEA.2011.0370

Zhang, L., He, A., Yin, Z., Yu, Z., Luo, X., Liu, W., et al. (2014). Regeneration of human-ear-shaped cartilage by co-culturing human microtia chondrocytes with BMSCs. *Biomaterials* 35, 4878–4887. doi: 10.1016/j.biomaterials.2014.02.043

Zhang, Z., Duan, Y., Wu, Z., Zhang, H., Ren, J., and Huang, L. (2017). PPARD is an Inhibitor of Cartilage Growth in External Ears. *Int. J. Biol. Sci.* 13, 669–681. doi: 10.7150/ijbs.19714

Zhou, G., Jiang, H., Yin, Z., Liu, Y., Zhang, Q., Zhang, C., et al. (2018). In vitro regeneration of patient-specific ear-shaped cartilage and its first clinical application for auricular reconstruction. *EBioMedicine* 28, 287–302. doi: 10.1016/j.ebiom.2018.01.011

Conflict of Interest: The authors declare that the research was conducted in the absence of any commercial or financial relationships that could be construed as a potential conflict of interest.

frontiers
in Cell and Developmental Biology

ORIGINAL RESEARCH
published: 15 October 2020
doi: 10.3389/fcell.2020.588941

Effect of Cell Spreading on Rosette Formation by Human Pluripotent Stem Cell-Derived Neural Progenitor Cells

Ryan F. Townshend[1†], Yue Shao[2†‡], Sicong Wang[2], Chari L. Cortez[1], Sajedeh Nasr Esfahani[2], Jason R. Spence[3], K. Sue O'Shea[1], Jianping Fu[2], Deborah L. Gumucio[1*] and Kenichiro Taniguchi[1,4,5*]

[1] Department of Cell & Developmental Biology, University of Michigan Medical School, Ann Arbor, MI, United States, [2] Department of Mechanical Engineering, University of Michigan, Ann Arbor, MI, United States, [3] Department of Internal Medicine, University of Michigan Medical School, Ann Arbor, MI, United States, [4] Department of Cell Biology, Neurobiology, and Anatomy, Medical College of Wisconsin, Milwaukee, WI, United States, [5] Department of Pediatrics, Medical College of Wisconsin, Milwaukee, WI, United States

Edited by:
Silvia Garagna,
University of Pavia, Italy

Reviewed by:
Phillip Karpowicz,
University of Windsor, Canada
Paris Alexander Skourides,
University of Cyprus, Cyprus

***Correspondence:**
Deborah L. Gumucio
dgumucio@med.umich.edu;
dgumucio@umich.edu
orcid.org/0000-0001-8883-383X
Kenichiro Taniguchi
ktaniguchi@mcw.edu
orcid.org/0000-0002-4531-7197

† These authors have contributed equally to this work

‡ Present address:
Yue Shao,
Mong Man-Wei Sci. and Technol.
Bldg., Tsinghua University, Beijing,
China

Specialty section:
This article was submitted to Cell Growth and Division, a section of the journal Frontiers in Cell and Developmental Biology

Received: *31 July 2020*
Accepted: *14 September 2020*
Published: *15 October 2020*

Citation:
Townshend RF, Shao Y, Wang S, Cortez CL, Esfahani SN, Spence JR, O'Shea KS, Fu J, Gumucio DL and Taniguchi K (2020) Effect of Cell Spreading on Rosette Formation by Human Pluripotent Stem Cell-Derived Neural Progenitor Cells. Front. Cell Dev. Biol. 8:588941. doi: 10.3389/fcell.2020.588941

Neural rosettes (NPC rosettes) are radially arranged groups of cells surrounding a central lumen that arise stochastically in monolayer cultures of human pluripotent stem cell (hPSC)-derived neural progenitor cells (NPC). Since NPC rosette formation is thought to mimic cell behavior in the early neural tube, these rosettes represent important *in vitro* models for the study of neural tube morphogenesis. However, using current protocols, NPC rosette formation is not synchronized and results are inconsistent among different hPSC lines, hindering quantitative mechanistic analyses and challenging live cell imaging. Here, we report a rapid and robust protocol to induce rosette formation within 6 h after evenly-sized "colonies" of NPC are generated through physical cutting of uniformly polarized NESTIN$^+$/PAX6$^+$/PAX3$^+$/DACH1$^+$ NPC monolayers. These NPC rosettes show apically polarized lumens studded with primary cilia. Using this assay, we demonstrate reduced lumenal size in the absence of *PODXL,* an important apical determinant recently identified as a candidate gene for juvenile Parkinsonism. Interestingly, time lapse imaging reveals that, in addition to radial organization and apical lumen formation, cells within cut NPC colonies initiate rapid basally-driven spreading. Further, using chemical, genetic and biomechanical tools, we show that NPC rosette morphogenesis requires this basal spreading activity and that spreading is tightly regulated by Rho/ROCK signaling. This robust and quantitative NPC rosette platform provides a sensitive system for the further investigation of cellular and molecular mechanisms underlying NPC rosette morphogenesis.

Keywords: neural rosette, human pluripotent stem cells, cell spreading, neural progenitor cells, actin cytoskeletal network, RhoA, neural tube, microcontact printing

INTRODUCTION

The radial organization of cells into rosette-like structures containing a central apical lumen is a fundamental developmental hallmark of neuroepithelial tissue (Tomooka et al., 1993; Deglincerti et al., 2016). Recent methodological advances in the directed differentiation of human pluripotent stem cells (hPSC) have resulted in a variety of neural differentiation methods to generate monolayers of apico-basally polarized neural stem cell (NPC) types (Chambers et al., 2009; Shi et al., 2012; Lukovic et al., 2017). Interestingly, in some neural differentiation culture systems, NPC monolayers undergo spontaneous radial morphogenesis and apical constriction, forming NPC rosettes, or neural rosettes, which are apico-basally polarized pseudostratified structures similar to the embryonic neural tube (Haigo et al., 2003; Curchoe et al., 2012; Christodoulou and Skourides, 2015; Deglincerti et al., 2016; Nikolopoulou et al., 2017).

Rosette formation from NPC *in vitro* provides an important model to study the underpinnings of normal and defective human neural tube morphogenesis and defects in this *in vitro* process have been documented in several neurological disorders, including bipolar disorder, autism spectrum disorder and schizophrenia (Ladran et al., 2013; Chen et al., 2014; Kim et al., 2014; Yoon et al., 2014; Madison et al., 2015; O'Shea and McInnis, 2016; Valensisi et al., 2017). Recently, abnormal rosette formation was demonstrated in patients with schizophrenia and traced to haploinsufficiency of CYFIP1, a WAVE complex component that regulates Arp2/3 and controls apico-basal polarity (Yoon et al., 2014). Additionally, deletion of *Crb2*, also a cell polarity protein, in mouse NPC results in defective neural rosette formation, even though *Crb2*$^{-/-}$ NPC monolayers show normal polarization (Boroviak and Rashbass, 2011), emphasizing that rosette structures have apico-basal properties that are distinct from those of polarized monolayers. Interestingly, recent genetic studies implicate *Podocalyxin like* (*PODXL*), a gene encoding a sialyated apical glycoprotein that is highly expressed in neural tissue, as a causal gene in autosomal-recessive juvenile onset Parkinsonism (Sudhaman et al., 2016). PODXL has been well studied in early mouse embryogenesis and in kidney for its role in apical polarization and lumen formation (Takeda et al., 2000; Bryant et al., 2014; Yang et al., 2016; Shahbazi et al., 2017; Christodoulou et al., 2018), but the role of this protein in rosette formation has not been reported.

Although NPC rosette formation *in vitro* can be a powerful tool for detection and investigation of molecular pathways important in human neurological disease, a major limitation to current methods for rosette generation is that rosettes arise in a sporadic and uncoordinated manner. This makes it difficult to reproducibly, systematically and quantitatively study the molecular and cellular requirements of this process using live-imaging, biomechanical platforms, small molecule screens and/or genetic manipulation. Finally, while current assays can measure attributes of individual mature rosettes, a complete mechanistic understanding of the dynamics of NPC rosette morphogenesis, starting from a polarized monolayer and ending in a fully-formed rosette, is currently limited.

Here, we report a protocol that efficiently induces near synchronous rosette organization, even from hPSC-derived NPC monolayers that do not generally exhibit rosette formation using previously existing protocols. Robust radial organization is seen within 6 h after induction; this rapid response lends itself to mechanistic and quantitative analyses. Using this assay, we document lumenal size defects in NPC carrying loss-of-function mutations of *PODXL,* a feature that may have implications for early onset Parkinson's disease caused by loss of PODXL activity (Sudhaman et al., 2016). Further, we trace the cellular dynamics of NPC rosette formation using live cell imaging. These data reveal that an early aspect of rosette formation is dynamic spreading of the basal portions of cells within NPC colonies. Using chemical, genetic and engineering tools, we show that this basal colony spreading is required for successful NPC rosette morphogenesis. Thus, this novel NPC rosette induction system enables robust mechanistic analyses that reveal new cellular and molecular details about NPC rosette formation and polarization. Such a reproducible assay is critical requirement for quantitative examination of alterations in rosette formation that might accompany a variety of human diseases and could be diagnosed using induced pluripotent stem cells (hiPSC).

RESULTS

Development of a Simple and Robust Neural Differentiation Protocol in an Extracellular Matrix-Based, Feeder-Free Condition

Multiple protocols exist for the generation of NPC rosettes (Dhara and Stice, 2008; Chambers et al., 2009; Shi et al., 2012; Knight et al., 2018); these differ in multiple aspects (e.g., 3D vs. 2D, presence or absence of feeder cells, differing growth media). We employed the dual SMAD inhibitor-based NPC monolayer induction protocol (using 2Si, SB-431542 and LDN-193189 to inhibit TGFβ and BMP receptor kinase activity, respectively) originally developed by Chambers et al. (2009), rather than another commonly utilized embryoid body system that has inherent heterogeneity and also gives rise to non-neural cell types (Zhang et al., 2001; Reinhardt et al., 2013). We utilized a feeder-free substrate coated with Geltrex extracellular matrix, since this substrate is routinely used to culture a variety of hPSC lines (**Figure 1A**; Shao et al., 2017a; Shao et al., 2017b; Taniguchi et al., 2017). While a laminin-511 feeder-free substrate had previously been shown to support neural differentiation (Nakagawa et al., 2014), the Geltrex feeder-free system had not been previously tested. This 2Si-based neural differentiation was performed using mTeSR medium to provide additional pro-neural factors (such as FGF2 and LiCl, (Taupin et al., 2000; Elkabetz et al., 2008; Qi et al., 2017)). This culture method results in the formation of a dense apicobasally polarized monolayer of neural cells that exhibit expression of neural markers, NESTIN and N-CADHERIN (**Figures 1B,C**) as well as significantly reduced expression of *OCT4* (also known as *POU5F1*) and *NANOG* within 10 days (**Figure 1D**). Thus, this Geltrex feeder-free system, in combination with 2Si and mTeSR, can be utilized to support efficient differentiation of hPSC toward the neural lineage.

Development of a Robust NPC Rosette Formation System

Using this mTeSR/2Si neural differentiation method, NPC monolayers generated from H9 hESC exhibit abundant rosette morphogenesis (**Supplementary Figure 1A**, H9 hESC 10 days) as previously seen in other 2Si culture

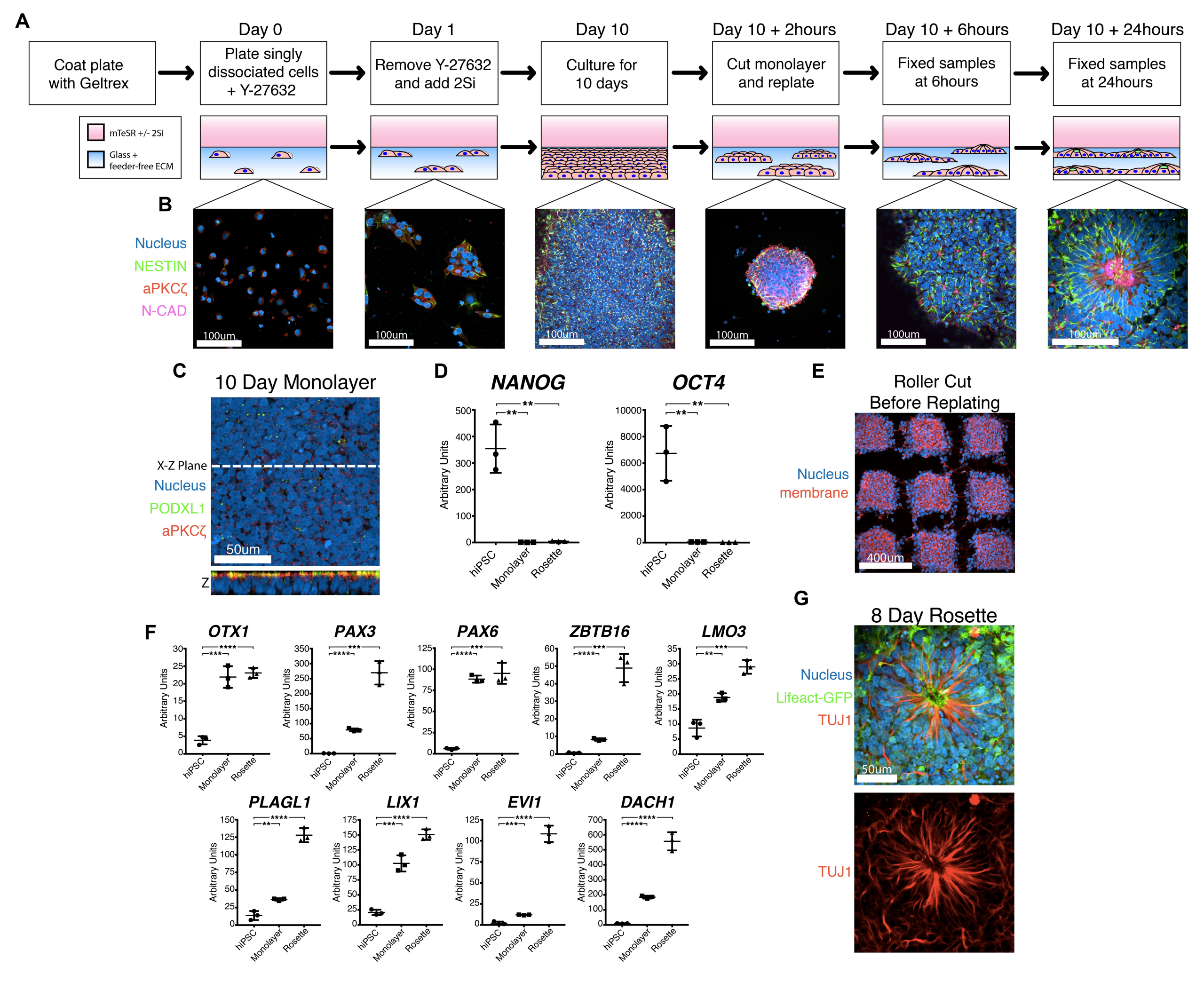

FIGURE 1 | A novel robust and quantitative method for NPC rosette induction. **(A,B)** Overview of the NPC rosette induction protocol, using a Geltrex-based feeder-free ECM substrate and mTeSR medium with dual SMAD inhibitors (2Si). Singly dissociated cells were grown for 10 days to allow the formation of a tightly packed NPC monolayer. At d10, the NPC monolayer was cut into small pieces, scraped off the substrate and re-plated to allow the formation of NPC rosettes. Cells were stained with antibodies to NESTIN (green), aPKCξ (red) and N-CAD (purple). DAPI = Nuclei (Blue). **(C)** Apical surface of the d10 NPC monolayer. An optical section along X–Z-plane reveals that the monolayer formed a uniformly polarized apical membrane. Apical markers: PODXL (green) and aPKCξ (red). **(D)** Relative expression of pluripotency markers (*NANOG* and *OCT4*) as determined by quantitative PCR (qPCR). hiPSC = 1196a hiPSC monolayer (no neural induction), Monolayer = d10 NPC monolayer, and Rosette = NPC rosettes, 24 h after cutting and re-plating. RNA expression is normalized (to *GAPDH*); mean and standard deviation (SD) is shown. **(E)** Confocal section of the roller-cut d10 NPC monolayer, stained with DAPI (Nucleus) and WGA (membrane), revealing colonies with highly consistent sizes. **(F)** qPCR analysis of neural markers: *OTX1*, *PAX3*, *PAX6*, *ZBTB16*, *LMO3*, *PLAGL1*, *LIX1*, *EVI1*, *DACH1*. For all qPCR analyses: hiPSC = 1196a hiPSC monolayer (no neural induction), Monolayer = d10 NPC monolayer, and Rosette = NPC rosettes 24 h after cutting and re-plating. Relative RNA expression is normalized (to *GAPDH*); mean and standard deviation (SD) is shown for all qPCR analyses. **(G)** Immunolocalization of TUJ1, a neuron-specific Class III γ-tubulin, in a rosette generated from cells carrying Lifeact-GFP, cultured for 8 days after roller-dissociation. Student's *t*-test was used for all statistical analyses: ns = $p > 0.05$; **$p \leq 0.01$; ***$p \leq 0.001$; ****$p \leq 0.0001$.

conditions using Essential 6 (E6)/2Si medium (Lippmann et al., 2014). However, two tested hiPSC lines (1196a – **Figures 1B,C**, Day 10; and iPSC20-1 – **Supplementary Figure 1A**, iPSC20-1 10 days) failed to form radially organized colonies under mTeSR/2Si or E6/2Si conditions (**Supplementary Figure 1B**). Others have reported that dissociation of NPC monolayers by manual scraping and re-plating the cells as small clumps or "colonies" induces radial patterning using hESC and hiPSC lines (Shi et al., 2012). The culture conditions previously described by Shi et al. (2012) readily induced formation of radially patterned structures when H9 hESC were manually scraped, and re-plated as small clumps (**Supplementary Figure 1C**, top, H9 hESC 24-hour colony). However, when using 1196a hiPSC, rosette morphogenesis was rarely seen with the (Shi et al., 2012) protocol (**Supplementary Figure 1C**, bottom, see 1196a 24-hour colony), demonstrating cell line-specific variability of this system to induce rosette morphogenesis.

Interestingly, when 2Si/mTeSR conditions were used and NPC monolayers derived from 1196a and iPSC20-1 were manually dissociated and re-plated as small colonies (manual-dissociation), rosette formation was seen in the majority (69.44% ± 1.338, $n = 360$) of the colonies (**Supplementary Figure 1A**, 1196a and iPSC20-1 24-hour colony). However, such manually dissociated colonies were highly variable in size (**Supplementary Figure 1D**, scraped), preventing reproducible quantitative analyses. To generate colonies with more consistent sizes, we used a roller-based StemPro EZPassage Disposable Stem Cell Passaging Tool (Thermo-Fisher, schematics of this tool shown in **Supplementary Figure 1E**) to roller-cut NPC monolayers (roller-dissociation) into approximately 0.022 $mm^2 \pm 0.003$ SD ($N = 35$) colonies (**Figure 1E** and **Supplementary Figure 1D**, see Roller Cut, and S1F for size quantitation). After attachment for 1 h, colony size variation was significantly reduced, compared to the manual dissociation method (**Supplementary Figure 1F**, F-test: $p < 0.01$): colony size at the 1-hour time-point was 0.016 $mm^2 \pm 0.007$ SD ($N = 38$) in size for roller cut and 0.010 $mm^2 \pm 0.016$ SD ($N = 68$) for manually scraped cells.

Radial morphogenesis of roller-cut NPC colonies is very rapid; rosettes can be observed as early as 6 h after plating cut colonies (**Figure 1B**, see Day 10 +6 h, see **Supplementary Figure 1G** for a large field-of-view image). Mature rosettes are formed by 24 h (**Figure 1B**, Day 10 +24 h). Importantly, cutting alone is not sufficient to induce radial morphogenesis, since no signs of radial organization are seen in 12-hr colonies that were roller-cut, but not replated (**Supplementary Figure 1H**). NPC rosettes exhibit expression of several markers of neural differentiation, including *OTX1, PAX3, PAX6, ZBTB16, LMO3, PLAGL1, LIX1, EVI1*, and *DACH1* (**Figure 1F**; Elkabetz et al., 2008; Reinhardt et al., 2013; Deglincerti et al., 2016). Within 7 days of extended culture, cells within the NPC rosettes display a highly elongated morphology with processes that extend beyond the radial core; in fact, these cells express TUJ1, neuron-specific Class III γ-tubulin (**Figure 1G**, see **Supplementary Figure 1I** for large-field of view). Thus, combined with roller-dissociation, this 2Si/mTeSR-based system reproducibly triggers rapid and robust generation of NPC rosette formation as well as subsequent differentiation of $TUJ1^+$ neurons from hPSC lines that do not show radially organized phenotypes using existing protocols.

We next tested the ability of this system to effectively detect aberrancies in rosette formation after exposure of cells to compounds known to affect rosette morphogenesis. Yoon et al. (2014) previously showed that *CYFIP1*, a component of the WAVE complex, is critical for NPC rosette formation through its regulation of Arp2/3-dependent actin polymerization. Thus, we allowed roller cut colonies to attach for 2 h and then treated them with CK-666, a small molecule inhibitor of Arp2/3, for 10 h. Indeed, this relatively short exposure of cells to the inhibitor significantly altered rosette formation, reducing total NPC $aPKC\zeta^+$ lumenal area (∼3.4-fold reduction, $p < 0.1$, **Supplementary Figures 2A–C**) as well as radial organization, as measured by nuclear aspect ratio (1.44-fold reduction, $p < 0.01$, **Supplementary Figure 2D**). However, colony size and number of lumens per colony do not significantly change with CK-666 treatment (**Supplementary Figures 2E,F**). Thus, the system is sensitive to rosette perturbation by small molecule inhibitors of actin polymerization.

Characteristics of the Apical Domain of Roller-Dissociated NPC Rosettes

Neural progenitor cell rosettes are described as polarized structures with a central apically constricted domain surrounded by radially organized cells (Boroviak and Rashbass, 2011; Deglincerti et al., 2016); these features are also seen in roller-dissociated 2Si/mTeSR NPC rosettes (**Figures 2A,B**). Additional immunolocalization analyses reveal that recycling (RAB11) and early (RAB5) endosomes are localized adjacent to the apical cortex, and Golgi (GM130) and centrosomes (γ-TUBULIN) are localized at the apical pole of the cells (**Figure 2C**), further confirming the apical nature of the central domain. Interestingly, 3D reconstruction of NPC rosettes stained for the apical marker PODXL reveals that cells completely surround the lumen (**Figure 2D**), confirming recent studies (Hribkova et al., 2018). Indeed, the apical region of each cell is studded with a single primary cilium (ARL13B, **Figure 2E**); this is in accord with the localization of the centrosomes (γ-TUBULIN, **Figure 2C**). This polarized organization of organelles is topologically similar to *in vitro* lumenal cyst models documented in cell types such as MDCK.2, Caco-2, and hPSC (Rodriguez-Boulan and Macara, 2014; Taniguchi et al., 2015) that show apical localization of endosomes, Golgi, centrosomes and cilia.

In other systems of apical polarization, it has been demonstrated that PODXL is necessary for apical actin cytoskeletal organization and lumen expansion (Takeda et al., 2000; Bryant et al., 2014; Shahbazi et al., 2017; Christodoulou et al., 2018). To test this requirement in the rosette system, we generated a loss-of-function mutation in *PODXL* in 1196a hiPSC (**Figures 2F–H**, see **Supplementary Figure 3** for genotyping information) and examined rosette formation using two independent lines of successfully targeted cells. Quantitation shows that, 12 h after plating, *PODXL* mutant rosettes exhibit fewer rosettes/colony and reduced lumenal sizes (quantified using $aPKC\zeta^+$ area as shown in **Supplementary Figure 2B**) while exhibiting largely intact radial organization (**Figures 2G–I**). Thus, *PODXL*, which is abundant in the developing brain (Nowakowski et al., 2010; Vitureira et al., 2010; Sudhaman et al., 2016), is important for lumenal initiation and expansion in neural rosettes.

Colony Dynamics During NPC Rosette Formation

The robust and rapid nature of NPC rosette formation, as well as consistent colony size produced by roller-dissociation of the NPC monolayer, allowed us to perform quantitative live imaging to investigate the morphogenic steps that characterize the formation of NPC rosettes. We utilized live tracking of hiPSC, stably expressing Lifeact (live-actin)- or PODXL-GFP fusion proteins (**Figures 3A–C**; Taniguchi et al., 2017). F-actin (visualized using Lifeact-GFP) is initially localized uniformly across the entire apical surface of recently cut NPC colonies. However, by 6 h after plating, localized apical constriction

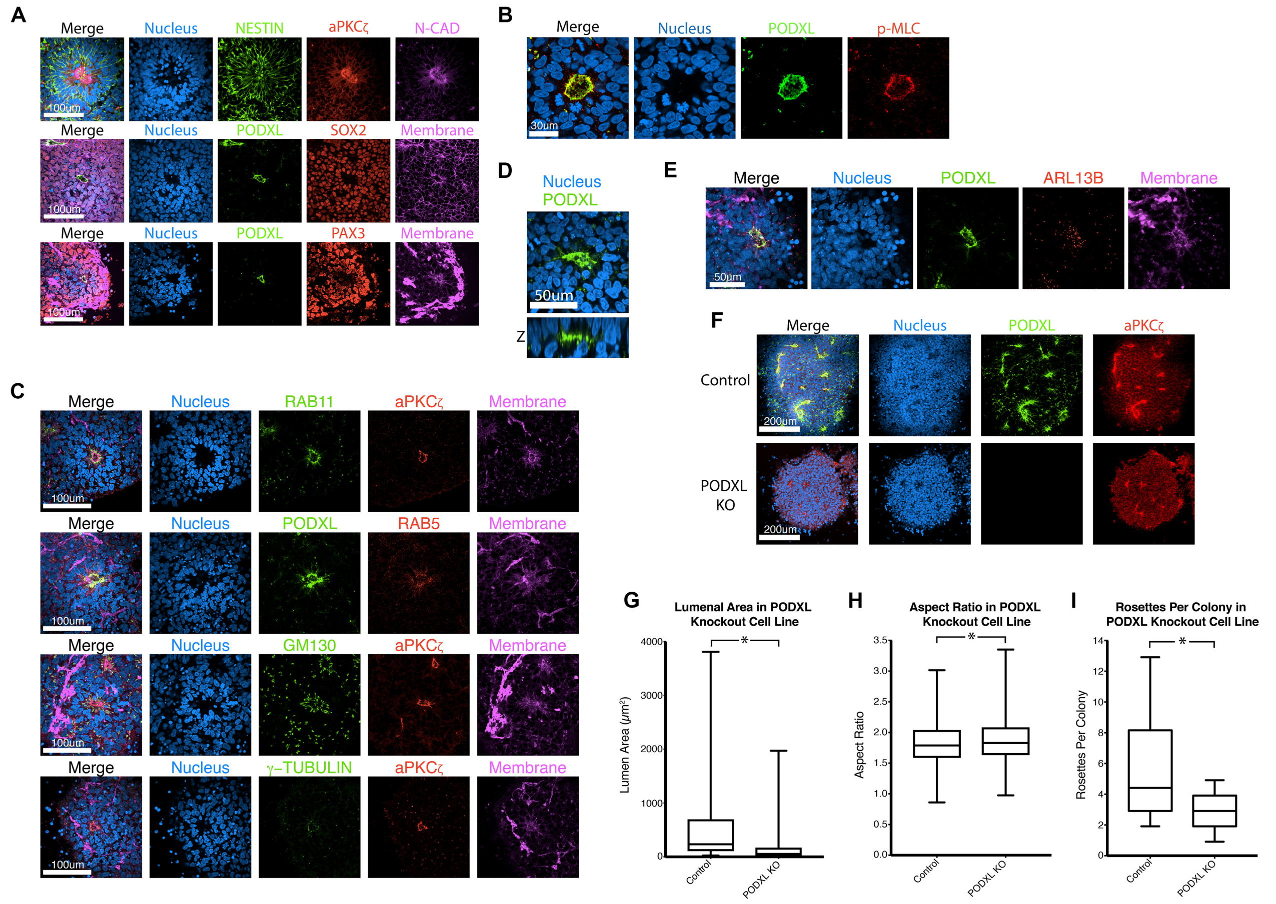

FIGURE 2 | Characterization of NPC rosettes. **(A–E)** Immunolocalization analyses of NPC rosettes with indicated markers: neural markers = NESTIN, N-CADHERIN (N-CAD), SOX2 and PAX3; apical markers = aPKCζ and PODXL; myosin activity marker = p-MLC; and organelle markers = RAB11 (recycling endosome), RAB5 (early endosome), GM130 (Golgi), γ-TUBULIN (centrosome) and ARL13B (primary cilium). In **(D)**, the X-Z plane is shown to reveal the internalized $PODXL^+$ apical domain. Note that the rosette that is stained for NESTIN, aPKCζ, N-CAD and DNA is identical to the Day 10 + 24 hr sample in **Figure 1B**. **(F)** Confocal fluorescent images of control and *PODXL*-KO NPC rosettes stained with indicated markers. **(G–I)** Quantitation of lumenal area **(G)**, aspect ratio **(H)** and number of rosettes per colony **(I)** of control and *PODXL*-KO cells. Student's *t*-test was used for statistical analyses: ns = $p > 0.05$; $*p \leq 0.05$.

produces multiple Lifeact-GFP foci (rosette lumens), surrounded by radially organized NPC (**Figure 3A** and **Supplementary Movie 1**, see 06:20 and 12:00).

As a more specific label of the apical domain, we next utilized PODXL-GFP (**Figures 3B,C** and **Supplementary Movie 2**). Again, freshly cut colonies show abundant fluorescence across the apical surface of all cells, consistent with the fact that the initial NPC monolayer is uniformly apically polarized (**Figure 1C**). However, within hours after plating the cut colonies, PODXL-GFP is localized in multiple distinct foci that are shared by groups of radially oriented cells (**Figure 3C** and **Supplementary Movie 2**). Additionally, while some rosettes continue radial organization, others undergo previously unreported progressive fission of established radial domains to give rise to secondary NPC rosettes (**Supplementary Movie 2** center, see 9:00 to 11:00). Together, these data reveal a dramatic re-organization of the apical domain as rosettes are formed.

Basal Cell Spreading Is an Early Feature of NPC Rosette Organization

Interestingly, live imaging using both Lifeact-GFP and PODXL-GFP reveals that cut NPC colonies quickly increase in size as soon as they attach to the substrate (**Figures 3A,C** and **Supplementary Movies 1, 2**). This colony expansion precedes radial organization and continues during radial morphogenesis. Detailed quantitation shows that these colonies expand 4-fold in size by 8 h after plating (6-hour timepoint in **Figure 4A**, live imaging initiated 2 h after plating, red dotted line) and 6-fold by 12 h (**Figure 4A**).

Given this unexpected finding, cell expansion was further examined at the cellular level using hiPSC stably expressing Lifeact-GFP, 5 h after plating, when colonies had attached and were beginning to initiate radial organization. Under these conditions, continuous colony spreading is seen during 200 min of imaging, at 5-minute intervals (**Figure 4B**, control, and **Supplementary Movies 3–5**). At the cellular level, two types

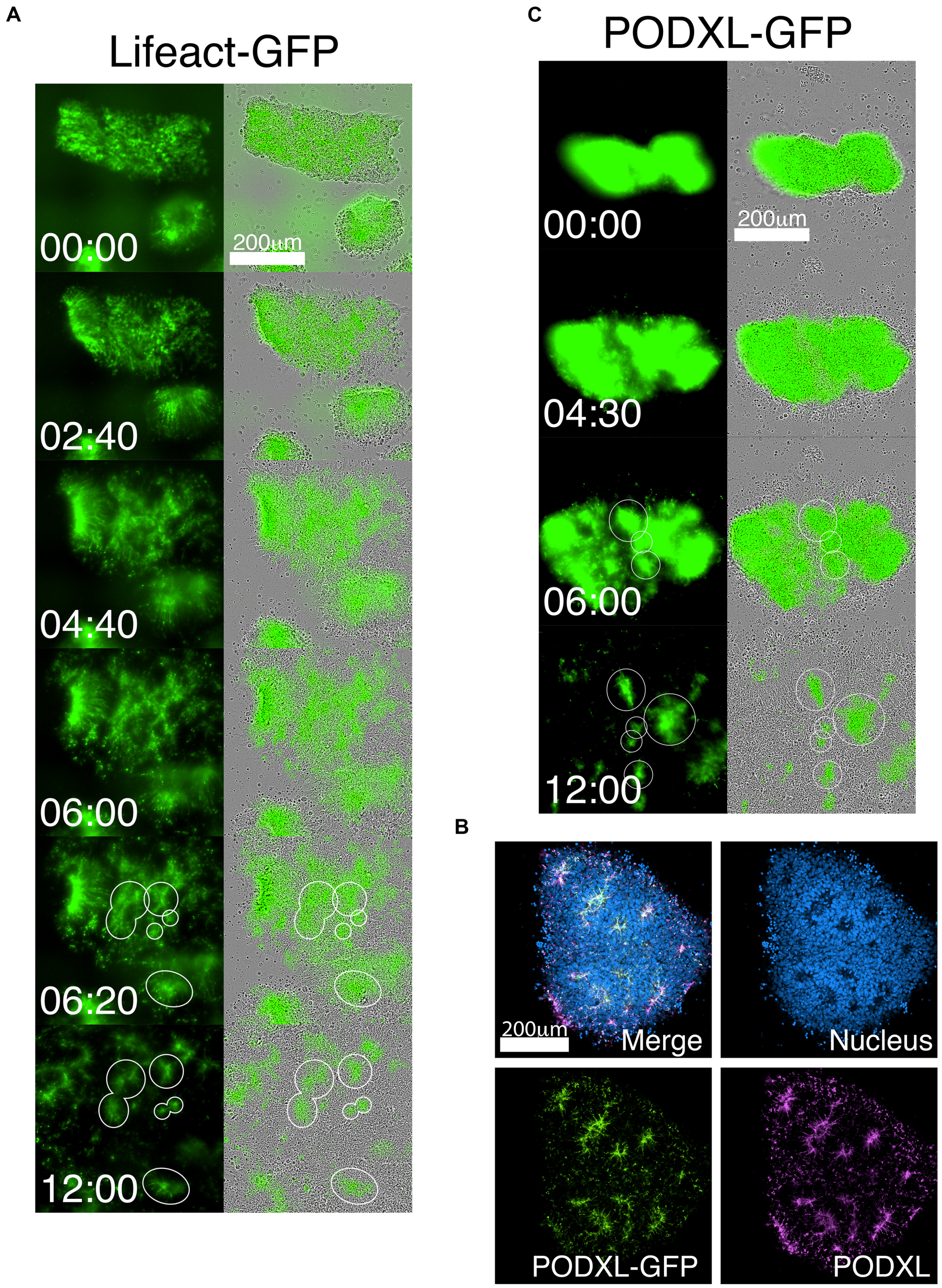

FIGURE 3 | Live-tracking of NPC rosette morphogenesis. **(A–C)** Live imaging of 1196a hiPSC expressing Lifeact-GFP **(A)** or PODXL-GFP **(C)** for 12 h after colonies were allowed to reattach for 2 h. **(B)** Confocal images of PODXL-GFP NPC rosettes stained with anti-PODXL. GFP localization mirrors endogenous PODXL localization. Note that, while a uniform prominent GFP signal is initially seen throughout the apical surface of the recently plated colony, at later time points, GFP-enriched regions are concentrated at the constricted centers of the rosettes (lumen). It is likely that, as the colony expands rapidly, the apical surface area of non-rosette cells dramatically increases, resulting in reduced GFP signal intensity per unit area. Scales as indicated.

of spreading are detectable. Cells at the edge of the colony exhibit dynamic protrusion and retraction of filopodia and lamellipodia, visible by Lifeact staining of these organized actin-rich protrusions (**Figure 4Bi**, control, **Supplementary Movie 4**). Despite the increased basal protrusive activity, these edge cells maintain cell membrane localization of N-CADHERIN directly adjacent to neighboring cells (**Figure 4C**), indicating that cell-cell contacts are maintained. Interestingly, cells in the inner portion of the colony, which are organizing into rosettes, do not form lamellipodia and filopodia (**Figure 4Bii**, control,

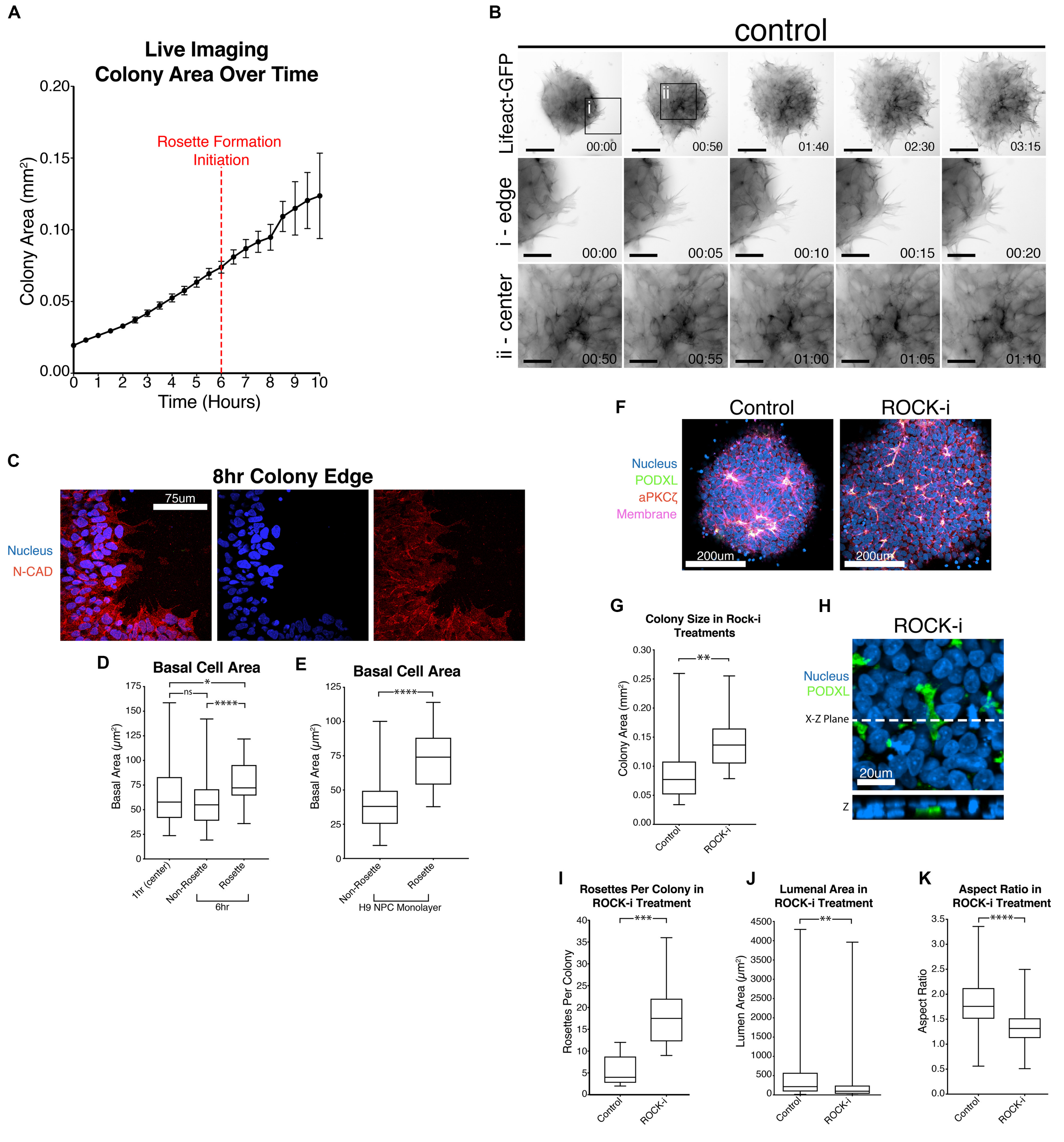

FIGURE 4 | Colony spreading regulates NPC rosette formation. **(A)** Quantitation of the growth of PODXL-GFP colonies over time. Imaging initiated 2 h after plating. Red dotted line at the 6-hr time point (8 h after plating) indicates the start of rosette morphogenesis. **(B)** Live imaging of 1196a hiPSC expressing Lifeact-GFP 2 h after roller cutting and re-plating. Imaging was started 5 h after re-plating. Top panels show images of whole colonies. (i) and (ii) panels show magnified images at the colony edge (i) or at the center (ii). Scales indicate 150 μm for whole colony, 50 μm for magnified images in i and ii. **(C)** Confocal images of 8 h NPC rosette colony edge cells stained with indicated markers. **(D)** Quantitation of basal cell area (based on N-CADHERIN membrane staining) of roller-dissociated 1196a hiPSC-derived NPC colonies 1 h after plating at the center (1 h (center)) and 6 h after plating in cells that are inside (Rosette) and outside (Non-Rosette) of rosettes. **(E)** Quantitation of basal cell area of H9 hESC-derived day 10 NPC monolayer (no roller-cut) in cells that are inside (Rosette) and outside (Non-Rosette) of rosettes. **(F)** Confocal images of NPC rosettes treated with DMSO (control) or ROCK-i, stained with indicated markers. **(G)** Quantitation of colony size from samples in panel **(F)**. **(H)** Immunolocalization analysis of PODXL$^+$ domain in ROCK-i treated samples: the X–Z plane is shown to reveal the internalized PODXL$^+$ apical domain. **(I–K)** Quantitation of number of rosettes per colony **(I)**, individual lumen area **(J)** and nuclear aspect ratio **(K)** from samples in panel **(F)**. Scales as indicated. Student's *t*-test was used for statistical analyses: $*p \leq 0.05$; $**p \leq 0.01$; $***p \leq 0.001$; $***p < 0.0001$.

and **Supplementary Movie 5**), but do appear to spread basally. To quantify basal spreading during NPC-rosette formation, we assessed the basal membrane area (based on N-CADHERIN staining, **Supplementary Figure 4A**) of cells at the colony center at 1-hour (prior to rosette formation) and at 6-hour (the time of apical constriction initiation) time points (**Figure 4D**). These measurements were taken by confocal microscopy, focusing on the most basal surface. Interestingly, cells associated with forming rosettes at 6-hour show a clear increase in basal surface area. In contrast, central cells of the 6-hour colonies that are not associated with rosettes show a basal surface area that is similar to their basal area at 1 h (**Figure 4D**). Thus, rosette initiation is accompanied by basal spreading of the rosette-forming cells. This was not an artifact of cutting, since basal areas of cells forming spontaneous rosettes in H9 hESC-derived NPC monolayers (10 days 2Si treatment, **Supplementary Figure 1A**, top) are also significantly larger (**Figure 4E**) than the basal areas of non-rosette forming cells. Together, these results demonstrate that rapid basal expansion is an early step in rosette organization.

Enhancement of Cell Spreading Increases Rosette Number, but Reduces Rosette Organization and Lumenal Size

Since basal spreading likely relies on the actin network of the cell, we next explored how modulating the activity of this network affects basal spreading and rosette formation. Lowering actomyosin contractility in an hPSC-derived neuroectoderm model was recently shown to expand cell area, leading to an increased colony area (Xue et al., 2018). Thus, we first tested the effect of further enhancing spreading, using Y-27632, a small molecule inhibitor of Rho-associated kinase, or ROCK (ROCK-i). Roller-dissociated colonies of 1196a hiPSC were allowed to attach for 2 h, then treated with ROCK-i. This treatment significantly increases colony area (**Figures 4F,G**), as expected. Interestingly, compared to controls, ROCK-i treatment leads to rosette formation in all colonies, and these colonies show an increased number of PODXL$^+$ apical domains that maintain apical constriction as demonstrated by phosphorylated-MLC and closely spaced tight junctions (ZO-1) (**Figures 4F,H,I** and **Supplementary Figure 4B**). However, average lumenal size is decreased and cells surrounding the PODXL$^+$ apical foci display significantly reduced radial organization (**Figures 4J,K** and **Supplementary Movie 6**), indicating that enhancing spreading with ROCK-i increases rosette initiation, but impairs NPC-radial morphogenesis and lumenal expansion.

Colony Confinement Improves Rosette Organization

To further explore the role of active basal spreading in NPC rosette formation, we manipulated the degree of spreading by physically confining roller-dissociated segments on micropatterned surfaces of various sizes. To accomplish this, Geltrex solution (1%) was micro-printed onto otherwise non-stick PDMS surfaces. Three different sizes (small - 0.008 mm^2, medium - 0.049 mm^2 and large - 0.196 mm^2) of Geltrex spots were tested; small and medium patterns were smaller than the average size of 12 h colonies from non-patterned conditions (0.124 mm^2, **Figure 4A**). Plating cut colonies on these small and medium patterns limits the degree to which they can spread, while colonies can spread on larger patterns in an uninhibited manner. Notably, for all pattern sizes, the original size of the plated colony was the same, as determined by standard roller cutting of the 10-day monolayer. Thus, the relative number and density of cells initially plated on each Geltrex spot was the same for all pattern sizes.

Marker analyses confirm that apical foci, surrounded by radially organized cells, are present in all colony sizes (**Figure 5A**). However, quantitation reveals that the number of apical foci per colony is significantly reduced in small patterns in which colony spreading is limited when compared to colonies grown on unpatterned Geltrex-coated substrates (**Figure 5A**, see DMSO group of rosette per colony in **Figure 5B**; and graphs including all conditions in **Supplementary Figure 5**). Colonies on the smallest patterns also exhibit a significant increase in lumenal size and slightly improved radial organization over the 12-hour culture period (see DMSO group in **Figure 5B**). Thus, confinement appears to reduce rosette initiation, but improve maturation of forming rosettes. This finding is in accordance with recently published results suggesting that plating neuronal progenitor cells on small micropatterns optimizes the formation of single, well-organized rosettes (Knight et al., 2018).

The data above suggest that colony confinement produces fewer but more well-organized rosettes, while enhancing colony spreading does the opposite. However, ROCK-i treatment likely perturbs other cellular processes in addition to its effect on spreading. Therefore, to specifically address the role of excessive spreading *per se* in the impaired radial organization phenotype, we tested whether colony confinement can rescue the phenotype imposed by ROCK-i (increased rosette number, but decreased lumen size and reduced radial organization). To do this, roller cut segments were cultured on small (0.008 mm^2), medium (0.049 mm^2) or large (0.196 mm^2) circular patterns and treated with ROCK-i (**Figure 5A**). While colonies grown on large patterns show the full spectrum of the ROCK-i treatment phenotype, confining segments on small patterns rescues this phenotype: fewer PODXL$^+$ apical foci are seen per colony, while radial organization and lumenal size are significantly increased, to levels similar to the “no pattern - DMSO” condition (**Figures 5A,C**, ROCK-i, compare to differences seen on non-patterned substrates, **Figures 4I–K**); data for all conditions are presented in **Supplementary Figure 5**). Together, these data suggest that basal cell spreading promotes rosette formation (apical foci per colony) and that the degree of spreading modulates overall NPC-rosette organization (lumenal area and radial organization).

Genetic or Small Molecule-Induced Activation of Rho/ROCK Signaling Impairs Rosette Initiation

To further examine the relationship between cell spreading and rosette initiation, we inhibited spreading using a small molecule inhibitor as well as genetic perturbation. First, colonies

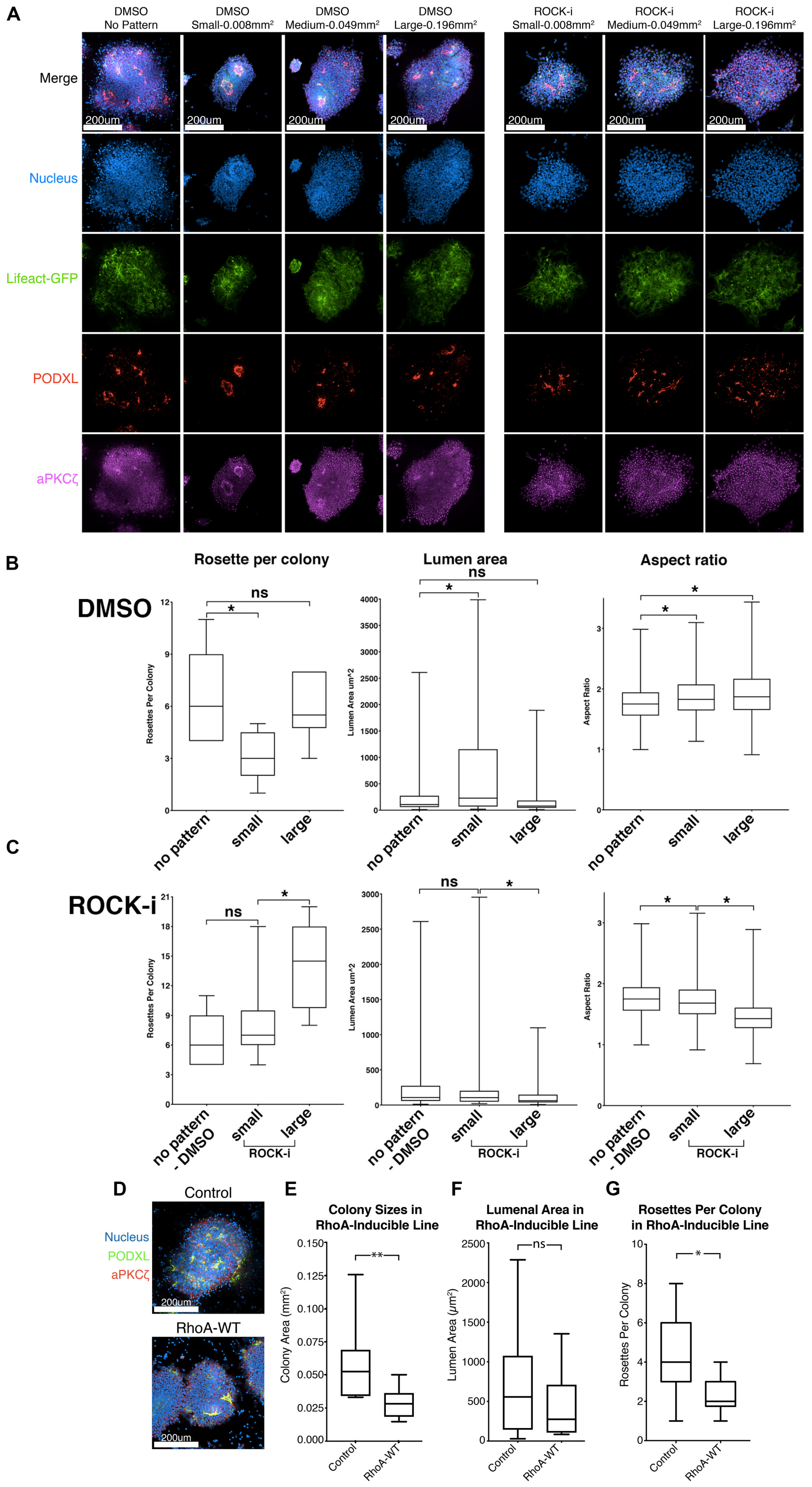

FIGURE 5 | Effects of colony confinement on NPC rosette morphogenesis. **(A)** Confocal images of NPC rosettes, 12 h after culturing on un-patterned PDMS, or on small (0.008 mm^2), medium (0.049 mm^2) or large (0.196 mm^2) circular patterns coated with 1% Geltrex in the absence (control, DMSO) or presence of ROCK-i, stained with indicated markers. **(B,C)** Quantitation of number of rosettes per colony (left), individual lumen area (middle) and nuclear aspect ratio (right) from DMSO (B) and ROCK-i **(C)** treated samples in panel **(A)**. Graphs containing all conditions are shown in **Supplementary Figure 5**. **(D)** Confocal images of control and RhoA-WT expressing NPC rosettes stained with apical markers, PODXL (green) and aPKCζ (red). **(E–G)** Quantitation of colony sizes **(E)**, individual lumen area **(F)**, and rosettes per colony **(G)** in control and RhoA-WT colonies. Scales as indicated. Student's *t*-test was used for statistical analysis: ns = $p > 0.05$; *$p \leq 0.05$; **$p \leq 0.01$.

were treated with 10 μM lysophosphatidic acid (LPA), an activator of Rho/ROCK signaling. Indeed, LPA-treated colonies fail to show signs of colony spreading, and NPC rosette morphogenesis is greatly reduced (**Supplementary Figures 6A–E** and **Supplementary Movie 7**). Next, to genetically test the influence of increased Rho signaling, we generated hiPSC carrying doxycycline-inducible RhoA. While, consistent with the LPA treatment, colony spreading is significantly reduced in cells treated with doxycycline and colonies exhibit reduced number of NPC rosettes per colony, RhoA-WT colonies show largely intact lumens demarcated by PODXL and aPKCξ, suggesting that increased RhoA activity does not completely disrupt NPC rosette morphogenesis (**Figures 5D,E–G**). These results confirm that active cell spreading is important for rosette initiation and point to an important role for proper levels of Rho/ROCK signaling in NPC rosette morphogenesis.

DISCUSSION

We report a simple and robust protocol that triggers the formation of NPC rosettes from hPSC-derived NPC monolayers within 6 h after induction. Using this system as a platform for highly efficient quantitative and mechanistic analyses, we demonstrate that Rho/ROCK-dependent basal NPC spreading promotes NPC-rosette initiation, and that NPC-rosette organization is modulated by the efficiency of basal spreading which also controls the size of NPC colonies.

NPC rosette morphogenesis is sensitive to culture conditions and is highly variable among hPSC lines; it is difficult to induce NPC rosette formation in some hPSC lines. In this study, we demonstrate the effects of different culture conditions on NPC rosette formation among multiple hPSC lines and establish an NPC rosette induction method that can robustly induce radial organization in hPSC lines that do not generally exhibit NPC rosette-forming property. We speculate that culture medium-based variability might be caused by differences in neural progenitor cell types; it will be of future interest to perform a systematic comparison of RNA expression profiles between hPSC grown in N2B27 supplements (Shi et al., 2012) vs. the mTeSR-based neural induction media used here. Furthermore, cellular mechanisms that control the propensity of hPSC to form NPC rosettes are not understood, though we as well as others have identified Rho/ROCK signaling as an important determinant (Knight et al., 2018). Since heterogeneity among hPSC lines has been recently noted (Rouhani et al., 2014; DeBoever et al., 2017; Kilpinen et al., 2017), a large-scale analysis using NPC derived from multiple hPSC lines with defined genetic backgrounds is needed to underpin variables that might control this propensity. Indeed, the 2Si/mTeSR-based NPC rosette induction protocol with roller-dissociation described here expands the ability of researchers to perform such mechanistic analyses in hPSC lines that could not have been used previously.

A major advantage of this protocol is its efficiency and reproducibility, as rosette organization is seen in the majority of colonies within 6 h after roller-dissociation, allowing for quantitative live imaging as well as small molecule, genetic and physical perturbations. Additionally, dozens of similarly sized colonies can be analyzed as independent units, permitting efficient statistical analyses of perturbations. Using these tools, we demonstrate that proper rosette formation requires basal spreading, ensured by inhibition of Rho/ROCK activity, while maturation of rosette organization (improved radial organization and lumenal expansion) is favored by confinement. Robust activation of Rho/ROCK, however, is detrimental to rosette formation, revealing a need for control of proper levels of signaling from this pathway. Importantly, detection of the phenomenon of colony spreading was enabled by high-resolution live cell imaging. Although Ziv et al. (2015) used live imaging to quantify nuclear movements within established mature rosettes, to our knowledge, ours is the first study to characterize morphological parameters surrounding NPC rosette initiation.

We provide strong evidence for a link between basally-driven cell spreading and apical organization of neural rosettes. Using live imaging, we show that basal cell spreading accompanies rosette organization. Physical confinement analyses, using circular micropatterned substrates combined with small molecule inhibitors, reveal that final neural rosette organization (apical foci per colony, lumen area and radial organization) is determined by the degree to which cells can spread. It will be of future interests to directly pursue whether cell spreading *per se*, or increased colony size (caused by spreading) is the most important factor for controlling NPC-rosette organization. Additionally, it is important to address whether rosette number within a colony affects rosette maturation and lumen formation since it might be speculated that when excess rosettes are present, fewer cells may be available for each rosette.

Interestingly, a recent study of rosette formation during *Drosophila* germ-band extension also concluded that basolaterally-driven cell movements precede the formation of apical rosette structures (Sun et al., 2017), similar to what we see in NPC rosettes. However, in that system, rosette morphogenesis is thought to be driven by planar cell polarity rather than apical constriction as in NPC, and basal protrusion activity is toward the rosette center rather than cell spreading toward the colony periphery. Nevertheless, basal cell movements appear to be key elements of this morphogenic process in both settings. These results show that proper apical organization of NPC rosettes is dependent on basal cell spreading, and that spreading must be tightly controlled to generate the single neural tube structure seen *in vivo*. It should also be noted that basal cell spreading may be a consequence of a previously described cell volume conservation mechanism involved in tissue morphogenesis (Gelbart et al., 2012), as reduction in apical surface area during apical construction must result in increased basal cell surface area (or *vice versa*) if cell volume is unchanged. These data also suggest a mechanistic explanation for the recent finding by Knight et al. (2018), that controlling the morphology of differentiating NPC colonies on micropatterns permits the generation of colonies with single rosettes and an organization that is more reminiscent of the *in vivo* neural tube.

We also confirm the need for Arp2/3 activity in rosette morphogenesis and show for the first time that the abundant neural sialoglycoprotein, PODXL, is necessary for lumenal expansion, as it is in MDCK cysts (Rodriguez-Boulan and Macara, 2014). PODXL, a transmembrane protein, has been shown to act both on the lumenal side, by forcing opposing membranes apart due to its heavy negative charge and on the cytosolic side, by affecting the apical actin network (Nielsen and McNagny, 2008). Indeed, the lumen in MDCK cysts arises by trafficking of apically charged vesicles to the cytokinetic plane and negatively charged PODXL is thought to be important in further expansion of the resulting lumen (Mangan et al., 2016; Mrozowska and Fukuda, 2016; Roman-Fernandez and Bryant, 2016). However, it is interesting to consider that NPC rosettes form in the context of a monolayer that is already polarized and they undergo lumen formation via apical constriction; thus PODXL may be utilized differently in NPC rosette formation vs. MDCK cysts. This remains to be tested. It will also be of interest to examine whether the previously described role of PODXL-dependent cell-cell adhesion is relevant to reduced lumenal expansion of rosettes in PODXL null cells (Takeda et al., 2000). Though the exact mechanism underlying the link between reduced or impaired PODXL activity and Juvenile Parkinsonism remains to be elucidated, we speculate that lumenal expansion during early neural tube morphogenesis may be impaired and that this in turn could perturb the forming neural epithelium. Consistent with this notion, *Podxl* deficient mouse hippocampal explants and primary hippocampal neurons display defective neurite outgrowth (Vitureira et al., 2010) and pan-neural *Podxl* loss produces malformation of ventricular spaces (Nowakowski et al., 2010).

Overall, the robust NPC rosette formation protocol described here, combined with a micropattern-based confinement method to generate NPC rosettes, provides a novel *in vitro* avenue to perform mechanistic analyses of rosette morphogenesis using neural progenitor cells derived from hESC or hiPSC.

MATERIALS AND METHODS

Stem Cell Maintenance and Passaging

Human hPSC used in this work included H9 hESC (WA09) as well as 1196a and 20-1 iPSC. All protocols for the use of the hPSC lines were approved by the Human Pluripotent Stem Cell Research Oversight Committee at the University of Michigan. The hESC and hiPSC lines were cultured and maintained as described (Ludwig et al., 2006), using lactate dehydrogenase-elevating virus (LDEV)-free hESC-qualified Geltrex (Thermo Fisher, derived from reduced growth factor ECM, extracted from murine Engelbreth-Holm-Swarm sarcoma cells similar to Matrigel) to prepare ECM-coated plates. All cell lines tested negative for mycoplasma contamination (LookOut Mycoplasma PCD Detection kit; Sigma-Aldrich).

Neural Rosette Induction

Cells cultured in maintenance conditions were disassociated using 1 mL of Accutase (Sigma-Aldrich) and incubated at 37°C for 10 min. Cells were agitated thoroughly with a P1000 pipetman to ensure complete dissociation, then resuspended in DMEM-F12 and spun down to pellet. The supernatant was removed and cells were resuspended in mTeSR containing 10 μM Y-27632, a ROCK inhibitor necessary to inhibit dissociation mediated apoptosis of hPSC (Watanabe et al., 2007). Cells were plated at a density of 6.67×10^4 cells per cm^2 or approximately 600,000 cells per well of a 6-well plate in 1% Geltrex coated wells and incubated for 24 h. Y-27632 was then removed by washing with DMEM;F12 and cells were incubated in mTeSR containing 10 μM SB-431542 and 0.5 μM LDN-193189 (2Si). Cells were maintained in mTeSR/2Si for 9 days with daily medium change. A tightly packed monolayer appeared by the end of day 10. A StemPro® EZPassage™ Disposable Stem Cell Passaging Tool was used to cut the monolayer into 0.022 mm^2 sections and these sections were removed by scraping (roller-dissociation). Cut and scraped sections were re-plated onto a glass coverslip coated with 1% Geltrex. Rosettes began to appear 6 h after replating, and continued to mature for approximately 12 h. Samples were fixed using 4% PFA for 30 min, then washed with PBS solution prior to immunostaining. For micropattern assays, the roller-cut colonies in mTeSR/2Si were detached from substrates by scraping, which were re-plated onto micropatterned substrates. After 2 h, colony attachment to substrates was confirmed and unattached colonies were washed off (3× washes using DMEM;F12). Medium (mTeSR/2Si) was added for an additional 10 h. This method reproducibly allows for the attachment of a single colony per micropattern. Since colonies are of similar size, this means that all micropatterns contain approximately the same number of plated cells. For ROCK inhibition (Y-27632) and Rho activation assays (LPA), ROCK-i was added 2 h after plating.

Immunostaining and Characterization

Assays were induced to make neural rosettes as described above and fixed at varying time points from 6 to 72 h. Antibodies for immunofluorescence staining were: anti-Nestin (1:100, Santa-Cruz Biotechnologies, sc-23927), anti-PKC-ζ (1:250, sc-216, Santa-Cruz), N-cadherin (1:500, MNCD2-c, DSHB), anti-Podxl (1:2000, MAB1658, R&D Systems), anti-Sox2 (1:1000, 09-0024, Stemgent), anti-Pax3 (1:200, R&D Systems, NBP1-32944), anti-Rab11 (1:500, #610656, BD), E-cadherin (1:500, #610182, BD), anti-GM130 (1:500, #610822, BD), Arl13B (1:500, 17711-1-AP, Proteintech), ZO-1 (1:200, sc-33725, Santa-Cruz Biotechnologies) phosphorylated myosin light chain (Ser19) (1:400, 3671S, Cell Signaling Technologies). DNA and membrane was labeled using Hoechst 33258 (Life Technologies) and wheat germ agglutinin (1:250, Life Technologies), respectively. Goat-raised secondary antibodies labeled with various fluorophores (1:500, Life Technologies) were used. Imaging was done using a Nikon A-1 confocal microscope, and images were analyzed and generated using Imaris (Bitplane), Photoshop CS6 (Adobe) or ImageJ (National Institute of Health). The free hand tool on ImageJ was used to outline lumenal area demarcated by anti-PODXL immunostaining and total pixel area was measured. Aspect ratio was quantified by measuring the perpendicular length of the nuclei bordering the apical surface of the rosette and dividing this by the parallel width of the nuclei.

Small Molecule Drug Inhibitor Assays

Colonies were cultured with or without indicated small molecule modulators, CK-666 (500 μM, Arp2/3 inhibitor, EMD Millipore), Y-27632 (10 μM, Rho inhibitor, Stem Cell Technologies) and lysophosphatidic acid (Rho activator, Cayman). DMSO was added in control groups. The amount of DMSO added to the experimental condition is the same as that of added to the control condition.

Microcontact Printing

We used a two-step micropatterning technique using a standard microcontact printing process to pattern ECM protein on the substrate and then recoated the patterned substrate with 1% Geltrex to improve protein attachment. For microcontact printing, patterned stamps were generated using replica molding from a silicon mold fabricated by standard photolithography and deep reactive ion etching (DRIE) (Fu et al., 2010). A flat 1:15 PDMS stamp was prepared and inked with Geltrex for 24 h at 4°C to absorb protein via hydrophilic interactions between the stamp and the Geltrex. The PDMS stamp was then thoroughly rinsed with distilled water and blown dry with a stream of nitrogen. In parallel, the PDMS coated coverslips were treated with ultraviolet (UV) ozone (UV-ozone cleaner; Jelight, Irvine, CA, United States) for 7 min to oxidize the PDMS surface and change the PDMS surface from hydrophobic to hydrophilic, allowing complete transfer of Geltrex from the PDMS stamp to the coverslip. The PDMS stamp was placed in contact with the coverslip for about 5 s to complete the Geltrex transfer process. To avoid protein adsorption to non-functionalized regions of the coverslip, the coverslip surface was treated with pluronics F127 NF dissolved in PBS (0.2%, w/v; BASF, Ludwigshafen, Germany) for 30 min at room temperature and then washed three times with distilled water. To recoat the patterned substrate with Geltrex, coverslips patterned by microcontact printing were first immersed in mTeSR for at least 2 h to prevent protein adsorption to PDMS surfaces not coated with Geltrex and then recoated with 1% Geltrex for an additional hour. The substrate was then washed with PBS several times to remove any protein attached to unpatterned regions (Nasr Esfahani et al., 2019).

Live Imaging

Lifeact- or PODXL-GFP expressing 1196a hiPSC (see cloning in the Constructs and cell lines section) were plated on six-well plates (Nunc) in mTeSR1/2Si medium, and time-lapse images were taken at 37°C using the IncuCyte Zoom live cell imaging (Sartorius). Alternatively, cells were plated on a glass bottom culture dish (MatTek), and were imaged in a live-cell imaging chamber (Tokai HIT) configured for Olympus IX-83 at 37°C.

Constructs and Cell Lines

The piggyBac transposon system was used to prepare cell lines expressing PODXL-EGFP and Lifeact-EGFP using a procedure previously described (Taniguchi et al., 2015). PODXL-EGFP constructs have been described previously (Taniguchi et al., 2017). Lifeact-EGFP (46356; Addgene; Iain Cheeseman) was PCR amplified (forward: 5′-GCGAATTCGCCACCATGGGTGTCGCAG-3′; reverse: 5′-CGGCGGCCGCTTACTTGTACA GCTCGTC-3′). The amplified product was then subcloned into the pPBCAG-GFP piggyBac transposon vector (Chen and LoTurco, 2012) which was digested with *EcoRI* and *NotI*. Transfection was done as previously described (Taniguchi et al., 2015). Fluorescence-activated cell sorting was performed to collect cells stably expressing specific fluorophores. Inducible expression of RhoA-EGFP constructs was performed using an Inducible All-in-One piggyBac Transposon System (Kim et al., 2016). RhoA-WT and –CA constructs (12965 and 12968; Addgene) (Subauste et al., 2000) were PCR amplified (forward: 5′-CACC-GCCACC-ATGGTGAGCAAGGGC-3′; reverse: 5′-TCACAAGACAAGGCACCC-3′) and subcloned into pENTR-dTOPO (Thermo Fisher). Lastly, using the Gateway L-R clonase II system (Invitrogen), RhoA constructs were subcloned into the PB-TA-ERP2 piggyBac All-in-One inducible destination vector (80477; Addgene) (Kim et al., 2016).

Genome Editing for *PODXL* Knockout

PODXL knockout 1196a hiPSC were generated using a piggyBac transposon-CRISPR/Cas9-based genome editing construct as previously described (Shao et al., 2017b). To introduce insertion/deletion (indel) mutations into exon 1 of the human *PODXL* locus (as shown in **Supplementary Figure 2**) via non-homologous end joining (NHEJ), a gRNA targeting sequence (GCGTCGAAGTGGGTTGTCGG) was designed (using published algorithms)[1]. The annealed oligo containing the gRNA sequence (sense: 5′- CACCGGCGTCGAAGTGGGTTGTCGG-3′; anti-sense: 5′- AAACCCGACAACCCACTTCGACGCC-3′) was subcloned into *BbsI* sites to generate the piggyBac-CRISPR/Cas9 construct containing the *PODXL* gRNA targeting sequence (piggyBac-CRISPR/Cas9-*PODXL*). This construct was transfected into 1196a hiPSC, sorted for GFP$^+$ cells using fluorescence-activated cell sorting (FACS). Resulting clonally purified cells were genotyped as previously described (Shao et al., 2017b). In control cells, a piggyBac-CRISPR/Cas9 vector lacking the gRNA targeting sequence was used.

RNA Isolation and RT-PCR

RNA was extracted from hiPSC monolayer cultures, at 10d of neural induction (immediately before roller-dissociation), or 24 h after roller-dissociation, using RNeasy Micro Kit (Qiagen). RNA quality and quantity were determined spectrophotometrically using NanoDrop 2000 (Thermo). Reverse transcription was conducted using the SuperScript VILO kit (Life Technologies). qRTPCR was performed using Quantitect Sybr Green MasterMix (Qiagen) on a Step One Plus Real-Time PCR system (Life Technologies). Primers specific to *OCT4*, *NANOG*, *OTX1*, *PAX3*, *PAX6*, *ZBTB16*, *LMO3*, NR2F1, *PLAGL1*, *LIX1*, *EVI1*, and *DACH1* were used. Resulting values were then normalized to GAPDH. A standard curve of GAPDH control with 90% efficiency was generated to determine relative abundance of tested messages.

---

[1] http://crispr.mit.edu

List of RT-PCR Primers

h-Otx1-F	GCGTCGTCGCTGAGTACAC
h-Otx1-R	ACATGGGATAAGAGGCTGCTG
h-Pax3-F	AGCTCGGCGGTGTTTTTATCA
h-Pax3-R	CTGCACAGGATCTTGGAGACG
h-Pax6-F	TGGGCAGGTATTACGAGACTG
h-Pax6-R	ACTCCCGCTTATACTGGGCTA
h-Tuj1-F (TUBB3)	GGCCAAGGGTCACTACACG
h-Tuj1-R (TUBB3)	GCAGTCGCAGTTTTCACACTC
h-Dach1-F	ATGTGGAACAAGTTCGCATCC
h-Dach1-R	TGCAGTCATTGTAGAGGGTCT
h-ZBTB16-F (PLZF)	GAGATCCTCTTCCACCGCAAT
h-ZBTB16-R (PLZF)	CCGCATACAGCAGGTCATC
h-LMO3-F	GACACCAAGCCGAAAGGTTG
h-LMO3-R	ATGCCAGTATTTGTCCAGTGC
h-PLAGL1-F	AAAGATGCTTCTACACCCGGA
h-PLAGL1-R	AGTGGGTCTTCTTGGTATGCC
h-Lix1-F	CACAGAGATCCGGCTCTAGTC
h-Lix1-R	CACGTAACTCACAAAGGGAGG
h-Evi1-F (MECOM)	TATCCACGAAGAACGGCAATATC
h-Evi1-R (MECOM)	CATGGAAACTTTTGGTGATCTGC
h OCT4 F	GTGGAGGAAGCTGACAACAA
h OCT4 R	GGTTCTCGATACTGGTTCGC
h NANOG F	GATTTGTGGGCCTGAAGAAA
h NANOG R	ATGGAGGAGGGAAGAGGAGA
hGAPDH-F	CTCTGCTCCTCCTGTTCGAC
hGAPDH-R	TTAAAAGCAGCCCTGGTGAC

DATA AVAILABILITY STATEMENT

The raw data supporting the conclusions of this article will be made available by the authors, without undue reservation.

AUTHOR CONTRIBUTIONS

RT, YS, DG, and KT designed the experiments. RT, YS, SW, CC, and KT performed the experiments. JS established the 20-1 hiPSC line. KO'S derived the 1196a hiPSC line. YS, SN, and JF designed the Geltrex-ECM micropattern system. RT, YS, DG, and KT analyzed the data and wrote the manuscript. All authors read and edited the manuscript.

FUNDING

This work was supported by the University of Michigan Mechanical Engineering Startup Fund (JF) and the National Institutes of Health (R01 DK089933, DG; T32 HD007505, KT). YS was partially supported by a University of Michigan Rackham Predoctoral Fellowship. RT was partially supported by the University of Michigan Phi-Kappa-Phi Honor Society Student Grant.

ACKNOWLEDGMENTS

pTK_93-Lifeact-EGFP was a gift from Iain Cheeseman (plasmid 46356; Addgene). pcDNA3-EGFP-RhoA constructs were from Gary Bokoch (plasmid 12965 and 12968; Addgene). We also thank the Prechter Fund for the derivation of 1196a hiPSC line (KO'S), the Tam Fund for the Incucyte.

SUPPLEMENTARY MATERIAL

The Supplementary Material for this article can be found online at: https://www.frontiersin.org/articles/10.3389/fcell.2020.588941/full#supplementary-material

Supplementary Figure 1 | **(A)** H9 hESC, 1196a hiPSC or 20-1 hiPSC, cultured in mTeSR/2Si neural differentiation media, were examined in 10-day (d10) monolayers, prior to dissociation (left, 10 day), or were examined 24 h after roller-dissociation and re-plating of d10 monolayers (right, 24-hour colony). Cells were stained for apical markers, PODXL (green) and aPKCζ (red). X-Z planes reveal polarized monolayers. **(B)** 1196a hiPSC cultured in E6/2Si and examined in a d10 monolayer. Cells were apically polarized as shown by staining for apical markers, PODXL (green) and aPKCζ (red). **(C)** H9 hESC and 1196a hiPSC, cultured in neural differentiation conditions outlined by Shi et al. (2012) were harvested on d10, prior to dissociation (left, 10 day), or were harvested 24 h after roller-dissociation and re-plating of d10 monolayers (right, 24-hour colony). Cells were stained for indicated apical markers. X–Z planes reveal polarized monolayer morphology. While PODXL^{+}/membrane^{+} foci are seen using 1196a hiPSC (24-hour colony) using a method described by Shi et al., these foci are not surrounded by radially organized NPC (see "i"). **(D)** Confocal micrographs of roller-cut (left) and manually dissociated (right) colonies stained with indicated markers, 1 h after plating. **(E)** Schematic of the roller-based StemPro$^{®}$ EZPassage$^{\mathrm{TM}}$ Disposable Stem Cell Passaging Tool. **(F)** Colony size quantitation of roller-cut and scraped colonies. The roller-cut method shows significantly less variability in colony size (*F*-test: $p < 0.05$). **(G)** Wide-field confocal images of roller-dissociated colonies 6 h after plating, stained with indicated markers, revealing the formation of multiple aPKCζ^{+} apical foci throughout the colony. **(H)** Confocal images of three representative colonies 12 h after roller-cutting without replating. Orange dotted boxes indicate the size of colonies after roller-cut. White dotted boxes indicate the edge of colonies after expansion. No PODXL^{+} foci were seen, even when neighboring colonies were removed to provide additional space to spread (middle, right panels). **(I)** Immunolocalization of TUJ1, a neuron-specific Class III β-tubulin, in a rosette generated from cells carrying Lifeact-GFP, cultured for 8 days after roller-dissociation. Wide-field image is shown to reveal the formation of abundant TUJ1^{+} rosettes.

Supplementary Figure 2 | **(A–F)** Confocal images of NPC colonies treated with DMSO (control) and 500 μM CK-666 for 10 h after colonies were allowed to attach for 2 h **(A)**. A representative image of NPC-rosettes in control samples is used to show how nuclear aspect ratio (nuclear length per width, dotted white cross, (i) and lumenal area (dotted white shape, (ii) are measured **(B)**. Upon CK-666 treatment, significant reduction in lumenal area and nuclear aspect ratio are seen **(C,D)**, while colony size and number of rosettes per colony are not significantly different **(E,F)**. Scales as indicated. Student's *t*-test was used for statistical analysis: $^{*}p \leq 0.05$.

Supplementary Figure 3 | **(A)** The sequence of human *PODXL* exon 2. gRNA target and PAM sequence are shown in red and green, respectively. **(B)** The edited sequence of *PODXL*-KO #1 (middle) and *PODXL*-KO #2 (bottom) are shown with respect to the *PODXL*-wild-type sequence. **(C)** Chromatographs for edited alleles are shown. Red underscore – target sequence after editing; green underscore – PAM sequence after editing; red box – inserted sequence.

Supplementary Figure 4 | **(A)** A representative confocal micrograph near the basal surface of cells stained for N-CADHERIN in control samples is used to show how basal cell area (dotted white shape) was measured. **(B)** Confocal images of DMSO and ROCK-i treated samples 12 h after roller-dissociation stained with indicated markers. Some degree of apical constriction (p-MLC) as well as tight junction (ZO-1) formation was maintained in ROCK-i samples. **(C)** Immunolocalization analysis of p-MLC in colony edge of DMSO and ROCK-i treated samples, 12 h after roller-dissociation. Scales as indicated.

Supplementary Figure 5 | **(A–C)** Quantitation [rosette per colony **(A)**, lumenal area **(B)** and nuclear aspect ratio **(C)**] in all conditions in **Figure 5A**.

Supplementary Figure 6 | **(A)** Confocal images of NPC rosettes treated with DMSO (control), ROCK-i or LPA, stained with indicated markers. **(B–E)** Quantitation for colony size **(B)**, number of rosettes per colony **(C)**, lumenal area **(D)**, and nuclear aspect ratio **(E)** from DMSO (control), ROCK-i and LPA treated samples in panel **(A)**. Control and ROCK-i images in panel **(A)** are from **Figure 4G**. Control and ROCK-i quantitation data in panels **(B–E)** are identical to **Figures 4H–L**. Scales as indicated. Student's *t*-test was used for statistical analysis: $^{*}p \leq 0.05$; $^{**}p \leq 0.01$; and $^{***}p \leq 0.001$.

Supplementary Movie 1 | Live imaging of roller-cut 1196a Lifeact-GFP colonies. Imaging was started 2 h after roller-dissociating the d10 NPC monolayer.

Supplementary Movie 2 | Live imaging of roller-cut 1196a colonies expressing PODXL-GFP. Imaging was started 2 h after roller-dissociating the d10 NPC monolayer.

Supplementary Movie 3 | Live imaging of colony spreading of 1196a hiPSC colony stably expressing Lifeact-GFP. Imaging was started 5 h after roller-dissociation of the d10 NPC monolayer.

Supplementary Movie 4 | Live imaging of colony edge (as shown in **Figure 4Bi**, control) during spreading of 1196a Lifeact-GFP hiPSC in **Supplementary Movie 3**.

Supplementary Movie 5 | Live imaging of colony center (as shown in **Figure 4Bii**, control) during spreading of 1196a Lifeact-GFP hiPSC in **Supplementary Movie 3**.

Supplementary Movie 6 | Live imaging of roller-cut 1196a PODXL-GFP colonies treated with 10 μM ROCK-i (Y-27632). Imaging and ROCK-i treatment were initiated 2 h after roller-dissociation of the d10 NPC monolayer.

Supplementary Movie 7 | Live imaging of roller-cut 1196a PODXL-GFP colonies treated with 10 μM LPA (lysophosphatidic acid). Imaging and LPA treatment were initiated 2 h after roller-dissociation of the d10 NPC monolayer.

REFERENCES

Boroviak, T., and Rashbass, P. (2011). The apical polarity determinant Crumbs 2 is a novel regulator of ESC-derived neural progenitors. *Stem Cells* 29, 193–205. doi: 10.1002/stem.567

Bryant, D. M., Roignot, J., Datta, A., Overeem, A. W., Kim, M., Yu, W., et al. (2014). A molecular switch for the orientation of epithelial cell polarization. *Dev. Cell* 31, 171–187. doi: 10.1016/j.devcel.2014.08.027

Chambers, S. M., Fasano, C. A., Papapetrou, E. P., Tomishima, M., Sadelain, M., and Studer, L. (2009). Highly efficient neural conversion of human ES and iPS cells by dual inhibition of SMAD signaling. *Nat. Biotechnol.* 27, 275–280. doi: 10.1038/nbt.1529

Chen, F., and LoTurco, J. (2012). A method for stable transgenesis of radial glia lineage in rat neocortex by piggyBac mediated transposition. *J. Neurosci. Methods* 207, 172–180. doi: 10.1016/j.jneumeth.2012.03.016

Chen, H. M., Delong, C. J., Bame, M., Rajapakse, I., Herron, T. J., Mcinnis, M. G., et al. (2014). Transcripts involved in calcium signaling and telencephalic neuronal fate are altered in induced pluripotent stem cells from bipolar disorder patients. *Transl. Psych.* 4:e375. doi: 10.1038/tp.2014.12

Christodoulou, N., Kyprianou, C., Weberling, A., Wang, R., Cui, G., Peng, G., et al. (2018). Sequential formation and resolution of multiple rosettes drive embryo remodelling after implantation. *Nat. Cell Biol.* 20, 1278–1289. doi: 10.1038/s41556-018-0211-3

Christodoulou, N., and Skourides, P. A. (2015). Cell-Autonomous Ca(2+) Flashes Elicit Pulsed Contractions of an Apical Actin Network to Drive Apical Constriction during Neural Tube Closure. *Cell Rep.* 13, 2189–2202. doi: 10.1016/j.celrep.2015.11.017

Curchoe, C. L., Russo, J., and Terskikh, A. V. (2012). hESC derived neuro-epithelial rosettes recapitulate early mammalian neurulation events; an in vitro model. *Stem Cell Res.* 8, 239–246. doi: 10.1016/j.scr.2011.11.003

DeBoever, C., Li, H., Jakubosky, D., Benaglio, P., Reyna, J., Olson, K. M., et al. (2017). Large-Scale Profiling Reveals the Influence of Genetic Variation on Gene Expression in Human Induced Pluripotent Stem Cells. *Cell Stem Cell* 20:e537.

Deglincerti, A., Etoc, F., Ozair, M. Z., and Brivanlou, A. H. (2016). Self-Organization of Spatial Patterning in Human Embryonic Stem Cells. *Curr. Top Dev. Biol.* 116, 99–113. doi: 10.1016/bs.ctdb.2015.11.010

Dhara, S. K., and Stice, S. L. (2008). Neural differentiation of human embryonic stem cells. *J. Cell Biochem.* 105, 633–640.

Elkabetz, Y., Panagiotakos, G., Al Shamy, G., Socci, N. D., Tabar, V., and Studer, L. (2008). Human ES cell-derived neural rosettes reveal a functionally distinct early neural stem cell stage. *Genes Dev.* 22, 152–165. doi: 10.1101/gad.1616208

Fu, J., Wang, Y.-K., Yang, M. T., Desai, R. A., Yu, X., Liu, Z., et al. (2010). Mechanical regulation of cell function with geometrically modulated elastomeric substrates. *Nat. Methods* 7:733. doi: 10.1038/nmeth.1487

Gelbart, M. A., He, B., Martin, A. C., Thiberge, S. Y., Wieschaus, E. F., and Kaschube, M. (2012). Volume conservation principle involved in cell lengthening and nucleus movement during tissue morphogenesis. *Proc. Natl. Acad. Sci. U. S. A.* 109, 19298–19303. doi: 10.1073/pnas.1205258109

Haigo, S. L., Hildebrand, J. D., Harland, R. M., and Wallingford, J. B. (2003). Shroom induces apical constriction and is required for hingepoint formation during neural tube closure. *Curr. Biol.* 13, 2125–2137. doi: 10.1016/j.cub.2003.11.054

Hribkova, H., Grabiec, M., Klemova, D., Slaninova, I., and Sun, Y. M. (2018). Calcium signaling mediates five types of cell morphological changes to form neural rosettes. *J Cell Sci* 131:jcs206896. doi: 10.1242/jcs.206896

Kilpinen, H., Goncalves, A., Leha, A., Afzal, V., Alasoo, K., Ashford, S., et al. (2017). Common genetic variation drives molecular heterogeneity in human iPSCs. *Nature* 546, 370–375.

Kim, D. S., Ross, P. J., Zaslavsky, K., and Ellis, J. (2014). Optimizing neuronal differentiation from induced pluripotent stem cells to model ASD. *Front. Cell Neurosci.* 8:109. doi: 10.3389/fncel.2014.00109

Kim, S. I., Oceguera-Yanez, F., Sakurai, C., Nakagawa, M., Yamanaka, S., and Woltjen, K. (2016). Inducible Transgene Expression in Human iPS Cells Using Versatile All-in-One piggyBac Transposons. *Methods Mol. Biol.* 1357, 111–131. doi: 10.1007/7651_2015_251

Knight, G. T., Lundin, B. F., Iyer, N., Ashton, L. M., Sethares, W. A., Willett, R. M., et al. (2018). Engineering induction of singular neural rosette emergence within hPSC-derived tissues. *Elife* 7:e37549.

Ladran, I., Tran, N., Topol, A., and Brennand, K. J. (2013). Neural stem and progenitor cells in health and disease. *Wiley Interd. Rev. Syst. Biol. Med.* 5, 701–715.

Lippmann, E. S., Estevez-Silva, M. C., and Ashton, R. S. (2014). Defined human pluripotent stem cell culture enables highly efficient neuroepithelium derivation without small molecule inhibitors. *Stem Cells* 32, 1032–1042. doi: 10.1002/stem.1622

Ludwig, T. E., Bergendahl, V., Levenstein, M. E., Yu, J., Probasco, M. D., and Thomson, J. A. (2006). Feeder-independent culture of human embryonic stem cells. *Nat. Methods* 3, 637–646.

Lukovic, D., Diez Lloret, A., Stojkovic, P., Rodriguez-Martinez, D., Perez Arago, M. A., Rodriguez-Jimenez, F. J., et al. (2017). Highly Efficient Neural Conversion of Human Pluripotent Stem Cells in Adherent and Animal-Free Conditions. *Stem Cells Transl. Med.* 6, 1217–1226. doi: 10.1002/sctm.16-0371

Madison, J. M., Zhou, F., Nigam, A., Hussain, A., Barker, D. D., Nehme, R., et al. (2015). Characterization of bipolar disorder patient-specific induced pluripotent stem cells from a family reveals neurodevelopmental and mRNA expression abnormalities. *Mol. Psych.* 20, 703–717. doi: 10.1038/mp.2015.7

Mangan, A. J., Sietsema, D. V., Li, D., Moore, J. K., Citi, S., and Prekeris, R. (2016). Cingulin and actin mediate midbody-dependent apical lumen formation during polarization of epithelial cells. *Nat. Commun.* 7:12426.

Mrozowska, P. S., and Fukuda, M. (2016). Regulation of podocalyxin trafficking by Rab small GTPases in 2D and 3D epithelial cell cultures. *J. Cell Biol.* 213, 355–369. doi: 10.1083/jcb.201512024

Nakagawa, M., Taniguchi, Y., Senda, S., Takizawa, N., Ichisaka, T., Asano, K., et al. (2014). A novel efficient feeder-free culture system for the derivation of human induced pluripotent stem cells. *Sci. Rep.* 4:3594.

Nasr Esfahani, S., Shao, Y., Resto Irizarry, A. M., Li, Z., Xue, X., Gumucio, D. L., et al. (2019). Microengineered human amniotic ectoderm tissue array for high-content developmental phenotyping. *Biomaterials* 216:119244. doi: 10.1016/j.biomaterials.2019.119244

Nielsen, J. S., and McNagny, K. M. (2008). Novel functions of the CD34 family. *J. Cell Sci.* 121, 3683–3692. doi: 10.1242/jcs.037507

Nikolopoulou, E., Galea, G. L., Rolo, A., Greene, N. D., and Copp, A. J. (2017). Neural tube closure: cellular, molecular and biomechanical mechanisms. *Development* 144, 552–566. doi: 10.1242/dev.145904

Nowakowski, A., Alonso-Martin, S., Gonzalez-Manchon, C., Larrucea, S., Fernandez, D., Vilar, M., et al. (2010). Ventricular enlargement associated with the panneural ablation of the podocalyxin gene. *Mol. Cell Neurosci.* 43, 90–97. doi: 10.1016/j.mcn.2009.09.011

O'Shea, K. S., and McInnis, M. G. (2016). Neurodevelopmental origins of bipolar disorder: iPSC models. *Mol. Cell Neurosci.* 73, 63–83. doi: 10.1016/j.mcn.2015.11.006

Qi, L., Tang, Y., He, W., Pan, H., Jiang, W., Wang, L., et al. (2017). Lithium chloride promotes neuronal differentiation of rat neural stem cells and enhances neural regeneration in Parkinson's disease model. *Cytotechnology* 69, 277–287. doi: 10.1007/s10616-016-0056-1

Reinhardt, P., Glatza, M., Hemmer, K., Tsytsyura, Y., Thiel, C. S., Hoing, S., et al. (2013). Derivation and expansion using only small molecules of human neural progenitors for neurodegenerative disease modeling. *PLoS One* 8:e59252. doi: 10.1371/journal.pone.0059252

Rodriguez-Boulan, E., and Macara, I. G. (2014). Organization and execution of the epithelial polarity programme. *Nat. Rev. Mol. Cell Biol.* 15, 225–242. doi: 10.1038/nrm3775

Roman-Fernandez, A., and Bryant, D. M. (2016). Complex Polarity: Building Multicellular Tissues Through Apical Membrane Traffic. *Traffic* 17, 1244–1261. doi: 10.1111/tra.12417

Rouhani, F., Kumasaka, N., De Brito, M. C., Bradley, A., Vallier, L., and Gaffney, D. (2014). Genetic background drives transcriptional variation in human induced pluripotent stem cells. *PLoS Genet* 10:e1004432. doi: 10.1371/journal.pgen.1004432

Shahbazi, M. N., Scialdone, A., Skorupska, N., Weberling, A., Recher, G., Zhu, M., et al. (2017). Pluripotent state transitions coordinate morphogenesis in mouse and human embryos. *Nature* 552, 239–243. doi: 10.1038/nature24675

Shao, Y., Taniguchi, K., Gurdziel, K., Townshend, R. F., Xue, X., Yong, K. M. A., et al. (2017a). Self-organized amniogenesis by human pluripotent stem cells in a biomimetic implantation-like niche. *Nat. Mater.* 16, 419–425. doi: 10.1038/nmat4829

Shao, Y., Taniguchi, K., Townshend, R. F., Miki, T., Gumucio, D. L., and Fu, J. (2017b). A pluripotent stem cell-based model for post-implantation human amniotic sac development. *Nat. Commun.* 8:208.

Shi, Y., Kirwan, P., and Livesey, F. J. (2012). Directed differentiation of human pluripotent stem cells to cerebral cortex neurons and neural networks. *Nat. Protoc.* 7, 1836–1846. doi: 10.1038/nprot.2012.116

Subauste, M. C., Von Herrath, M., Benard, V., Chamberlain, C. E., Chuang, T. H., Chu, K., et al. (2000). Rho family proteins modulate rapid apoptosis induced by cytotoxic T lymphocytes and Fas. *J. Biol. Chem.* 275, 9725–9733. doi: 10.1074/jbc.275.13.9725

Sudhaman, S., Prasad, K., Behari, M., Muthane, U. B., Juyal, R. C., and Thelma, B. K. (2016). Discovery of a frameshift mutation in podocalyxin-like (PODXL) gene, coding for a neural adhesion molecule, as causal for autosomal-recessive juvenile Parkinsonism. *J. Med. Genet* 53, 450–456. doi: 10.1136/jmedgenet-2015-103459

Sun, Z., Amourda, C., Shagirov, M., Hara, Y., Saunders, T. E., and Toyama, Y. (2017). Basolateral protrusion and apical contraction cooperatively drive Drosophila germ-band extension. *Nat. Cell Biol.* 19, 375–383. doi: 10.1038/ncb3497

Takeda, T., Go, W. Y., Orlando, R. A., and Farquhar, M. G. (2000). Expression of podocalyxin inhibits cell-cell adhesion and modifies junctional properties in Madin-Darby canine kidney cells. *Mol. Biol. Cell* 11, 3219–3232. doi: 10.1091/mbc.11.9.3219

Taniguchi, K., Shao, Y., Townshend, R. F., Cortez, C. L., Harris, C. E., Meshinchi, S., et al. (2017). An apicosome initiates self-organizing morphogenesis of human pluripotent stem cells. *J. Cell Biol.* 216, 3981–3990. doi: 10.1083/jcb.201704085

Taniguchi, K., Shao, Y., Townshend, R. F., Tsai, Y. H., Delong, C. J., Lopez, S. A., et al. (2015). Lumen Formation Is an Intrinsic Property of Isolated Human Pluripotent Stem Cells. *Stem Cell Rep.* 5, 954–962. doi: 10.1016/j.stemcr.2015.10.015

Taupin, P., Ray, J., Fischer, W. H., Suhr, S. T., Hakansson, K., Grubb, A., et al. (2000). FGF-2-responsive neural stem cell proliferation requires CCg, a novel autocrine/paracrine cofactor. *Neuron* 28, 385–397. doi: 10.1016/s0896-6273(00)00119-7

Tomooka, Y., Kitani, H., Jing, N., Matsushima, M., and Sakakura, T. (1993). Reconstruction of neural tube-like structures in vitro from primary neural precursor cells. *Proc. Natl. Acad. Sci. U. S. A.* 90, 9683–9687. doi: 10.1073/pnas.90.20.9683

Valensisi, C., Andrus, C., Buckberry, S., Doni Jayavelu, N., Lund, R. J., Lister, R., et al. (2017). Epigenomic Landscapes of hESC-Derived Neural Rosettes: Modeling Neural Tube Formation and Diseases. *Cell Rep.* 20, 1448–1462. doi: 10.1016/j.celrep.2017.07.036

Vitureira, N., Andres, R., Perez-Martinez, E., Martinez, A., Bribian, A., Blasi, J., et al. (2010). Podocalyxin is a novel polysialylated neural adhesion protein with multiple roles in neural development and synapse formation. *PLoS One* 5:e12003. doi: 10.1371/journal.pone.0012003

Watanabe, K., Ueno, M., Kamiya, D., Nishiyama, A., Matsumura, M., Wataya, T., et al. (2007). A ROCK inhibitor permits survival of dissociated human embryonic stem cells. *Nat. Biotechnol.* 25, 681–686. doi: 10.1038/nbt1310

Xue, X., Sun, Y., Resto-Irizarry, A. M., Yuan, Y., Aw Yong, K. M., Zheng, Y., et al. (2018). Mechanics-guided embryonic patterning of neuroectoderm tissue from human pluripotent stem cells. *Nat. Mater.* 17, 633–641. doi: 10.1038/s41563-018-0082-9

Yang, Z., Zimmerman, S. E., Tsunezumi, J., Braitsch, C., Trent, C., Bryant, D. M., et al. (2016). Role of CD34 family members in lumen formation in the developing kidney. *Dev. Biol.* 418, 66–74. doi: 10.1016/j.ydbio.2016.08.009

Yoon, K. J., Nguyen, H. N., Ursini, G., Zhang, F., Kim, N. S., Wen, Z., et al. (2014). Modeling a genetic risk for schizophrenia in iPSCs and mice reveals neural stem cell deficits associated with adherens junctions and polarity. *Cell Stem Cell* 15, 79–91. doi: 10.1016/j.stem.2014.05.003

Zhang, S. C., Wernig, M., Duncan, I. D., Brustle, O., and Thomson, J. A. (2001). In vitro differentiation of transplantable neural precursors from human embryonic stem cells. *Nat. Biotechnol.* 19, 1129–1133. doi: 10.1038/nbt1201-1129

Ziv, O., Zaritsky, A., Yaffe, Y., Mutukula, N., Edri, R., and Elkabetz, Y. (2015). Quantitative Live Imaging of Human Embryonic Stem Cell Derived Neural Rosettes Reveals Structure-Function Dynamics Coupled to Cortical Development. *PLoS Comput. Biol.* 11:e1004453. doi: 10.1371/journal.pcbi.1004453

Conflict of Interest: The authors declare that the research was conducted in the absence of any commercial or financial relationships that could be construed as a potential conflict of interest.

frontiers
in Cell and Developmental Biology

BRIEF RESEARCH REPORT
published: 19 October 2020
doi: 10.3389/fcell.2020.566152

Three-Dimensional Micro-Computed Tomography of the Adult Mouse Ovary

Giulia Fiorentino[1,2], Annapaola Parrilli[3]*, Silvia Garagna[1,2]* and Maurizio Zuccotti[1,2]*

[1] Laboratory of Developmental Biology, Department of Biology and Biotechnology "Lazzaro Spallanzani", University of Pavia, Pavia, Italy, [2] Center for Health Technologies, University of Pavia, Pavia, Italy, [3] Center for X-ray Analytics, Empa–Swiss Federal Laboratories for Materials Science and Technology, Dübendorf, Switzerland

In the mouse ovary, folliculogenesis proceeds through eight main growth stages, from small primordial type 1 (T1) to fully grown antral T8 follicles. Most of our understanding of this process was obtained with approaches that disrupted the ovary three-dimensional (3D) integrity. Micro-Computed Tomography (microCT) allows the maintenance of the organ structure and a true *in-silico* 3D reconstruction, with cubic voxels and isotropic resolution, giving a precise spatial mapping of its functional units. Here, we developed a robust method that, by combining an optimized contrast procedure with microCT imaging of the tiny adult mouse ovary, allowed 3D mapping and counting of follicles, from pre-antral secondary T4 (53.2 ± 12.7 μm in diameter) to antral T8 (321.0 ± 21.3 μm) and *corpora lutea*, together with the major vasculature branches. Primordial and primary follicles (T1–T3) could not be observed. Our procedure highlighted, with unprecedent details, the main functional compartments of the growing follicle: granulosa, antrum, cumulus cells, zona pellucida, and oocyte with its nucleus. The results describe a homogeneous distribution of all follicle types between the ovary dorsal and ventral regions. Also, they show that each of the eight sectors, virtually segmented along the dorsal-ventral axis, houses an equal number of each follicle type. Altogether, these data suggest that follicle recruitment is homogeneously distributed all-over the ovarian surface. This topographic reconstruction builds sound bases for modeling follicles position and, prospectively, could contribute to our understanding of folliculogenesis dynamics, not only under normal conditions, but, importantly, during aging, in the presence of pathologies or after hormones or drugs administration.

Keywords: mouse, ovary, follicles, oocyte, vasculature, micro-computed tomography, three-dimensional rendering

Edited by:
Guido Macchiarelli,
University of L'Aquila, Italy

Reviewed by:
Alberto Maria Luciano,
University of Milan, Italy
Danielle Monniaux,
Institut National de la Recherche Agronomique (INRA), France

****Correspondence:***
Maurizio Zuccotti
maurizio.zuccotti@unipv.it
Silvia Garagna
silvia.garagna@unipv.it
Annapaola Parrilli
annapaola.parrilli@empa.ch

Specialty section:
This article was submitted to Cell Growth and Division, a section of the journal Frontiers in Cell and Developmental Biology

Received: *27 May 2020*
Accepted: *28 September 2020*
Published: *19 October 2020*

Citation:
Fiorentino G, Parrilli A, Garagna S and Zuccotti M (2020) Three-Dimensional Micro-Computed Tomography of the Adult Mouse Ovary. Front. Cell Dev. Biol. 8:566152. doi: 10.3389/fcell.2020.566152

INTRODUCTION

In the adult ovary, folliculogenesis is a hormonally regulated process of growth and maturation from small primordial to fully grown antral follicles. The gonadotropin-independent initial recruitment of primordial follicles is followed, at puberty, by Follicle Stimulating Hormone (FSH) cyclic recruitment of early antral follicles (Hsueh et al., 2015), the latter enveloped within a calyx of capillaries arising from a branch of the ovarian artery (Fraser, 2006). Of these follicles, only a few, in polytocic species like the mouse, or one, in monotocic species like humans, complete their growth and are eventually ovulated. Follicle growth and correct acquisition of developmental competence occur thanks to a continuous, bi-directional, exchange of information both between the oocyte and its surrounding cumulus cells and among separate follicles (Zuccotti et al., 2011; Russell et al., 2016).

Most of our understanding of this process has been obtained with approaches that lead to the loss of the three-dimensional (3D) integrity of the organ. The ovary is disaggregated into its follicular units, which are either directly analyzed with molecular biology techniques, further matured *in vitro*, or cultured in media containing matrices with the aim of maintaining the follicle 3D organization (Belli et al., 2012; Telfer, 2019). Alternatively, the female gonad is fixed and sectioned for histological or immunohistochemical 2D studies.

A 3D reconstruction of the mammalian ovary would not only further improve our understanding of its tissue architecture, but, when combined with specific functional markers, it would help to reveal the multi-layered flow of molecular information that contributes to its biological function.

Up to date, tissue clearing combined with optical imaging allowed the acquisition of molecular details on the inside 3D organization of the ovary (Cordeiro et al., 2015; Faire et al., 2015; Feng et al., 2017; Kagami et al., 2018; Oren et al., 2018; McKey et al., 2020). However, a major drawback of this procedure remains the production of a distorted 3D model of the organ, stretched out along the *z*-axis, due to the lack of an equal resolution on the three axes (Schermelleh et al., 2010; Cremer et al., 2017).

On the contrary, tomographic methods produce a true 3D reconstruction of an object, with cubic voxels (i.e., image elements) and isotropic resolution, in other words, the space between two tomographic sections (*z*-axis) equals the resolution of the xy plane (Flannery et al., 1987; Mizutani and Suzuki, 2012). In order to reconstruct the folliculogenetic process inside the volume of the ovary, different attempts have been made using ultrasonography (Mircea et al., 2009; Ginther et al., 2014; Migone et al., 2016), micro-Magnetic Resonance Imaging (μ-MRI) (Hensley et al., 2007), laboratory-based X-ray micro-Computed Tomography (microCT) (Paulini et al., 2017), synchrotron radiation Computed Tomography (SR-CT) (Kim et al., 2012), and phase contrast Computed Tomography (PC-CT) (Pascolo et al., 2019). However, none of them, with the exception of SR-CT–a technique difficult to access–were capable to identify ovarian follicles smaller in size than those present in the pre-ovulatory compartment on the organ surface (e.g., 450 μm in diameter in rat; 10 mm in bovine). The main limit of ultrasonography, μ-MRI and PC-CT is an insufficient spatial resolution of these instruments, which is in the order of 10–100 μm/pixel; instead, whilst microCT and SR-CT can reach higher resolutions in the range of 0.35–10 μm/pixel, they mainly work when there is a marked contrast generated by differences in tissue radiopacity. For these reasons, it is not surprising that microCT has been extensively used with hard tissues, such as bones (Mussmann et al., 2017; Song et al., 2018) and teeth (Chałas et al., 2017; Batool et al., 2018; Velozo and Albuquerque, 2019), whose histological composition makes them naturally radiopaque to X-rays. On the other hand, its application on soft tissues is often restricted by the need to employ contrast agents that are largely unspecific with a partial capacity to highlight the presence of different structures within organs (Metscher, 2009; Pauwels et al., 2013; de S e Silva et al., 2015; de Bournonville et al., 2019).

In this study, we describe a method that, by combining an optimized contrast procedure with microCT imaging, allowed, for the first time, the 3D mapping and counting of follicles, from pre-antral secondary type 4 (T4) to fully grown antral type 8 (T8), together with the identification of the major vasculature branches inside the adult mouse ovary, one of the smallest among Mammals.

MATERIALS AND METHODS

Animals

CD1 female mice were purchased from Charles River (Como, Italy). Animals were maintained under controlled conditions of 21°C, 60% air humidity and a light/dark cycle of 12:12 h. Research on mice was conducted with permission from the Ministry of Health (No. 1100/2016-PR) in accordance with the guiding principles of European (No. 2010/63/UE) and Italian (No. 26/2014) laws protecting animals used for scientific research.

Ovaries Fixation

Ovaries of 8-week-old females were isolated and, after removal of the fat residuals, individually fixed in either Carnoy's solution (60% Ethanol, 30% Chloroform, and 10% Glacial acetic acid) for 8 h at room temperature, or Bouin's solution (15 mL Picric acid, 5 mL 40% Formaldehyde, 1 mL Glacial acetic acid) for 2 h at room temperature, or 4% Paraformaldehyde (PFA; 4 gr Paraformaldehyde in 100 mL 1× PBS) overnight at 4°C. The excess of fixative was washed out with its specific solvent.

Contrast Agent Treatment

Following fixation, ovaries were individually treated at room temperature with one of the following contrast agent: Iodine tincture [70% Ethanol and 1% Iodine Tincture (10% in distilled water)], 25% Lugol's solution (2.5 gr Potassium iodide and 1.25 gr Iodine in 100 mL distilled water), Phosphotungstic acid (0.2 gr PTA in 100 mL distilled water), or Uranyl acetate (1 gr in 100 mL distilled water). Different treatment times were tested, ranging from a minimum of 15 min up to a maximum of 8 h. Each contrast agent was washed out with its respective solvent, for a period ranging from 30 s to 15 h.

Micro-CT Imaging

Following contrast treatment, ovaries were placed in an open nest created with orthodontic wax at the bottom of a 0.5 mL Eppendorf tubes filled with distilled water to avoid organ dehydration and shrinkage. Then, samples were scanned by microtomographic system Skyscan 1172 (Bruker MicroCT, Kontich, Belgium). To determine the best preparation protocol, comparative studies of the different preparations were performed, at a source voltage of 60 kV, 165 μA current and using a 0.5 mm aluminum filter, adopting a scanning resolution of 5 μm/pixel for nearly 25 min. Samples were rotated to 180° with a rotation step of 0.4°. Terminated the cone beam acquisition, the dataset acquired was of approximately 500 images in 16-bit tiff format. Three ovaries from three different females were fixed in 4% PFA, treated with Lugol's solution for 3 h, washed for 15 h and scanned at a source voltage of 59 kV, 167 μA current, with a resolution of 1.5 μm/pixel for nearly 5 h. Samples were rotated to 180° with a rotation step of 0.1°. The scanning dataset consisted of about 2000 images in 16-bit tiff format. The final microCT sections were reconstructed using the NRecon software (Bruker MicroCT, Kontich, Belgium) in 8-bit jpg format (2000 × 2000 pixels). Sections were visualized with Fiji ImageJ (NIH) (Schindelin et al., 2012) and follicles and blood vessels were manually segmented and isolated, combing the use of regions of interest (ROIs) manager, thresholding and logical operations. 3D rendering of the follicular and vascular components was obtained with the volren module of the Avizo-9 software (Thermo Fisher Scientific) that approximates the organ isosurface from the segmented perimeters, resulting in a final model with a shaded surface and optimized transparency/opacity values.

Histology

Histology was used as a cross-checking technique to validate the results of the microCT analysis. After microCT scanning, samples were individually dehydrated through an ascending ethanol series, clarified with xylene and embedded in paraffin wax (Paraplast Plus, Merck). Sagittal serial 6-μm cross sections of the whole ovary were prepared using a RM2125RT microtome (Leica Biosystems) and, then, were stained with Hematoxylin and Eosin. Sections were examined and digitalized at 63× magnification, using a Leica DMi6 light microscope equipped with a motorized XY scanning stage controlled by the LAS X Navigator stitching software (Leica Biosystems).

Follicle Classification, Counting and 3D Localization

Based on a combination of morphological parameters and the size in diameter, follicular structures observed through the microCT sections of each ovary were individually counted and assigned to a specific follicle type (T4, T5, T6, T7, or T8) or *corpus luteum*. The morphological features considered were the presence/absence and size of the antrum and the thickness of the follicle cells layer surrounding the oocyte (Pedersen and Peters, 1968), but also the presence/absence of a well-visible zona pellucida space. Using Fiji ImageJ software on microCT sections, the follicle size was recorded at the major diameter and compared to that measured on histological sections prepared after microCT acquisition. More specifically, follicles were classified as T8 when they showed a size in diameter within the range of 321.0 ± 21.3 μm, combined with the presence of a large single antrum cavity, a cumulus stalk, and a well-visible zona pellucida space in between the oocyte and the surrounding cumulus cells; T7 displayed a 218.9 ± 36.9 μm diameter, a single antrum cavity smaller than T8, the presence of a cumulus oophorus and a zona pellucida space; T6 exhibited a 137.0 ± 24.9 μm diameter, several scattered small antral cavities and a zona pellucida space; T5 showed a 89.0 ± 11.2 μm diameter, the absence of antrum cavities, and the presence of a zona pellucida space separating the oocyte from the surrounding granulosa cell layers; T4, the smallest identifiable follicles by microCT, had a size in diameter of 53.2 ± 12.7 μm, they lacked of a zona pellucida space and showed a lower radiopacity compared to that of the other follicle types.

The spatial reference system used for follicle localization within each ovary was the anatomical orientation of the organ in relation to the anterior–posterior and dorsal-ventral body axes. The series of microCT sections of each ovary was divided into two halves along the dorsal-ventral axis, obtaining a dorsal and a ventral subset. Using Fiji ImageJ, each subset was partitioned into four, equally distributed, sectors, of which I and IV were positioned on the anterior region, while II and III on the posterior. A follicle was attributed to a specific sector when >50% of its volume belonged to that sector.

Statistical Analysis

Differences in total follicles number or in the distribution of each follicle type along the anterior–posterior or dorsal-ventral axes were evaluated using the Student's *t*-test. Differences in total follicles number or in the number of each follicle type present in the eight dorsal and ventral sectors were estimated using the one-way ANOVA followed by the Bonferroni's *post-hoc* test. All statistical analyses were performed using the RStudio software (RStudio, Inc., version 1.1.423). Data were considered significantly different when $p < 0.05$.

RESULTS

Three different fixative types [Carnoy, Bouin's solution or 4% Paraformaldehyde (PFA)] and four contrast agents (Iodine tincture, Phosphotungstic acid, Uranyl acetate or Lugol's solution) were tested in preparation to microCT analysis. Of the three fixatives, independently of the contrast agent used, Carnoy caused a shrinkage of the ovary, which persisted even during the microCT scanning period and led to the acquisition of fuzzy images (data not shown). The Bouin's solution, although it well preserved the histological organization, reduced tissue accessibility, resulting in an uneven contrast agent penetration and patchy images (data not shown). On the contrary, 4% PFA, a water-based fixative, turned out to be the best compromise as it maintained a good histology and it enabled an optimal contrast agent diffusion.

Following PFA fixation, treatment with the contrast agent was performed for different incubation periods, ranging from 15 min to 8 h, followed by a washing period ranging from 30 s to 15 h. Compared to either Iodine tincture (**Supplementary Figure S1A**), Phosphotungstic acid (**Supplementary Figure S1B**) or Uranyl acetate (**Supplementary Figure S1C**), treatment with Lugol's solution for 3 h, followed by a washing period of 15 h, produced the best results (**Supplementary Figure S2A**). Contrast was homogeneous throughout the whole organ volume, highlighting, on microCT images acquired at 5 μm/pixel resolution, distinctly marked follicles. **Supplementary Figure S2B** shows the corresponding histological cross-section, and **Supplementary Figures S2C,D** are enlargements of microCT and histological images, respectively.

Using this latter protocol, we prepared a new group of three ovaries, isolated from three adult females, and performed microCT scanning at 1.5 μm/pixel resolution, the highest obtainable with the instrument used (**Supplementary Movie S1**). This resolution allowed the identification of all the phases of follicle growth. **Figure 1A** shows the eight main stages of mouse folliculogenesis (Pedersen and Peters, 1968; Peters, 1969), from the resting pool of tiny primordial type 1 (T1) and type 2 (T2), followed by the primary type 3 (T3), the secondary T4 through to fully grown antral T8 follicles.

Figure 1B shows a representative microCT image of an ovary in which we could pinpoint equatorially sectioned follicles ranging from the small secondary T4, with 60 μm size in diameter, through all the growing stages until the largest T8 and the *corpora lutea* (CL). In T8 follicles, the Lugol's radiopacity brought up differences in density among the follicle's internal components (**Figure 1B**, enlargement), thus allowing microCT imaging of the layers of granulosa cells, antrum, cumulus cells, zona pellucida, and of the oocyte with its nucleus. Nuclei regions were clearly seen when watched through a sequence of microCT images (**Supplementary Movie S2**).

A further observation that the proposed protocol allowed was the identification of the main ovarian vasculature branches, ranging from the largest vessels at the ovarian hilum site (150 μm in diameter; **Figure 1C**) to smaller present in the medulla region (35 μm in diameter; **Figure 1D**).

These digital microCT images were further analyzed to visualize each single follicle along the three orthogonal sections (**Figures 2A–D**) and to reconstruct, with a volume rendering software, a 3D model of the ovary which combined both follicular and vascular components (**Figures 2E,F**).

The possibility to rapidly watch through the entire sequence of thin 1.5 μm sagittal images offered the opportunity not only to draw, on each single section, a detailed territorial map of the follicles, from the small T4 to the largest T8 and CL (**Figure 3A**), but also to render their spatial 3D localization (**Figure 3B**) and perform a precise follicle counting.

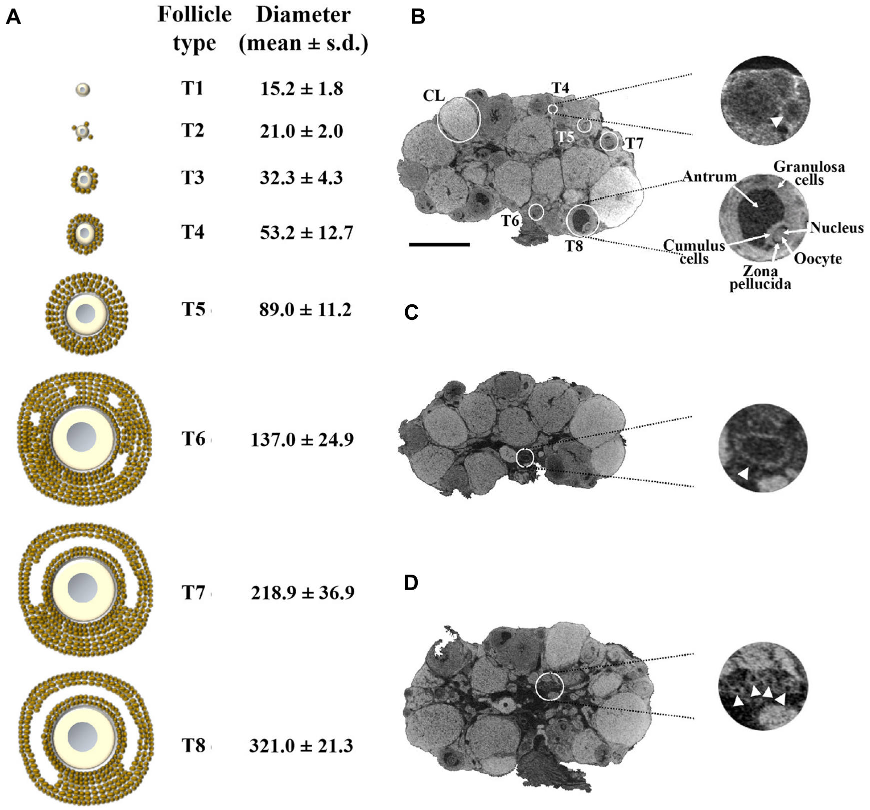

FIGURE 1 | Representative 1.5 μm/pixel microCT image of the mouse ovary. **(A)** Schematic representation of the eight main stages of the mouse folliculogenesis, with their corresponding size in diameter (mean ± s.d.), during the pre-antral (T1–T5) and antral (T6–T8) growth phases. **(B)** A representative microCT section highlighting follicles from T4 to T8 and *corpora lutea* (CL). On the right-hand side (top), an enlargement of a secondary T4 follicle (arrow); on the right-hand side (bottom), an enlargement of a fully grown T8 follicle, in which the different cytological components (granulosa cells, antrum, cumulus cells, zona pellucida space, oocyte with its nucleus) are clearly visible. **(C)** microCT section with an enlargement of a vessel (arrowhead; 150 μm in diameter) at the ovarian hilum site. **(D)** microCT section with an enlargement of a group of small vessels (arrowheads; 35 μm in diameter) in the medulla region. Bar, 500 μm.

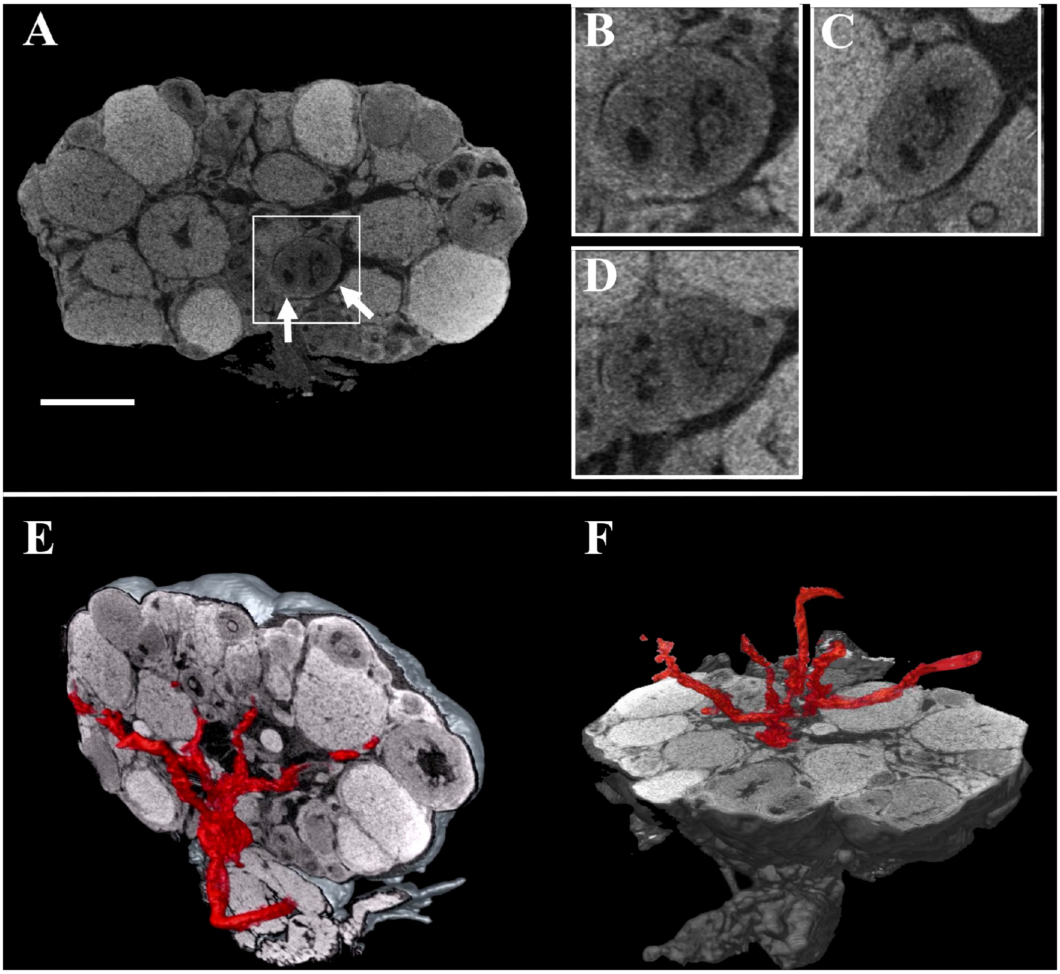

FIGURE 2 | Combined three-dimensional rendering of microCT sections of the ovary and of the main vasculature. **(A)** A representative equatorial microCT slice. Inset, two T7 follicles (arrows). **(B–D)** coronal, sagittal, and axial planes of the two T7 follicles shown in the inset. **(E,F)** Reconstruction of the main vasculature on the coronal and axial section, respectively. Bar, 500 μm.

The total number of T4-CL follicles counted in the ovary was 334.0 ± 48.8, with T5 and T6 as the most abundant (**Supplementary Table S1**). When the ovary was virtually divided into two equivalent halves along the anterior–posterior axis, we counted the same total number of follicles in the anterior (162 ± 34.4) and posterior (172 ± 14.4) region ($p > 0.05$), and an even distribution ($p > 0.05$) of each follicle type (data not shown). Similarly, when the ovary was halved along the dorsal-ventral axis, the number of both total and of each specific follicle type was equally allocated between the two regions (**Supplementary Table S1**), although dorsally we recorded a slight, but not significant ($p > 0.05$), higher total number.

Then, we proceeded by segmenting both the dorsal (D-I to D-IV) and ventral (V-I to V-IV) region into four, equally partitioned, sectors. Sectors contained an equal total number of follicles (41.7 ± 12.6; $p > 0.05$) and an identical number of each follicle type, with the exception of T5 and T6, which resulted the most numerous ($p < 0.05$), and of fully grown T8, the smallest group (**Supplementary Table S1** and **Figure 3C**).

DISCUSSION

This study describes a microCT procedure which allows the observation of the inside of the tiny mouse ovary with its main ovarian artery branches, and the mapping of the 3D position of all the follicle types from T4 through T8 and *corpora lutea*, with unprecedented precision. This procedure is robust, has the advantage of being faster than other classical methods, like histology or tissue clearing (Cordeiro et al., 2015; Faire et al., 2015; Feng et al., 2017; Kagami et al., 2018; Oren et al., 2018; McKey et al., 2020), and gives a true isotropic 3D reconstruction (Flannery et al., 1987; Mizutani and Suzuki, 2012). A typical experiment requires a total of 35 man/h from ovaries isolation to completion of X-ray scanning, and 24 man/h for follicles classification and mapping.

The reason why we could not identify follicles smaller than T4 may depend on the reduced size of its enclosed oocyte (<20 μm in diameter)–much similar to that of the companion follicle cells–and on the absence around the germ cell of a zona pellucida,

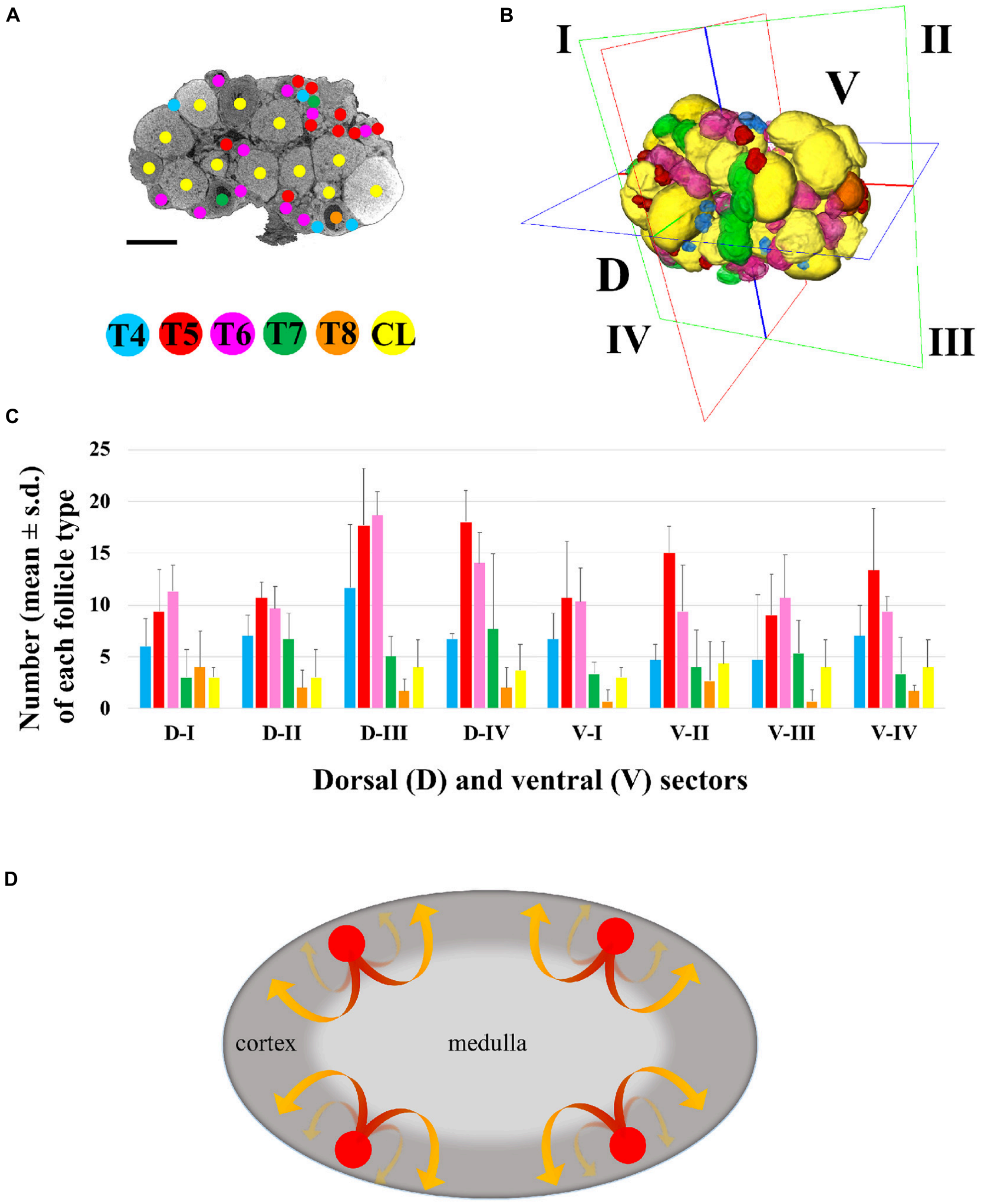

FIGURE 3 | Three-dimensional mapping of growing type 4 to type 8 follicles and *corpora lutea*. **(A)** Representative microCT image of T4-CL mapping procedure, performed through all ovary sections. Bar, 500 μm. **(B)** Volume rendering of T4–T8 follicles and CL present in the ovary, and virtual segmentation of the organ's dorsal (D-I to D-IV) and ventral (V-I to V-IV) side into four equal sectors. **(C)** Histogram describing the distribution of each follicle type and *corpora lutea* into the four dorsal and ventral sectors of three ovaries from three different female mice. **(D)** Graphical model describing the trajectory of follicles recruitment and growth. Follicle recruitment (red circle) occurs simultaneously in the cortex of all the eight sectors in which the ovary was virtually segmented. Then, follicles initiate growth toward the medulla (red segment of the arrow), increasing their size until they re-emerge into the cortical region (yellow segment of the arrow) from where, as fully grown antral follicles, they could undergo ovulation.

which begins to be fully present in T4 follicles, and that, with its glycoprotein layer, may create the right conditions for the contrast agent to be deposited. To this end, we are now working on improving the contrast procedure.

Besides the observation of growing follicles, our tomographic procedure allowed–to the best of our knowledge for the first time–the identification of the main functional cellular and subcellular compartments that constitute the growing follicle. Thus, the granulosa, antrum, cumulus cells, zona pellucida, and oocyte together with its nucleus, were clearly brought up not only in the largest T8 follicles, but also, when present, in smaller follicle types. The observation of a subcellular component such as the nucleus might be explained with an on-site specific contrast created by a differential local density of a tightly dense nucleolus surrounded by centromeric heterochromatin (Longo et al., 2003).

The *in-silico* reconstruction of the ovary with isotropic resolution allowed a 360° observation along the three axes and an accurate counting of each T4 to T8 follicles and CL comprised dorsally and ventrally. Our results highlight a homogeneous distribution of all the different follicle types not only between the dorsal and ventral region, but also among the eight sectors in which they were divided. In other words, each sector houses an equal number of follicles, including CL and, also, each follicle type is equally represented, with T5/T6 and fully grown T8 being the most and least abundant, respectively. Taken as a whole, these data suggest that (i) follicle recruitment is homogeneously distributed all-over the cortex, (ii) it occurs simultaneously in all the eight sectors, and (iii) follicles initiate and terminate their growth within the same sector (**Figure 3D**). After recruitment, biomechanical signals might guide follicles growth toward the less stiff environment of the medulla (Shah et al., 2018) until when they locally re-emerge, tens of folds bigger in size (T8), on the cortex surface from where they could be ovulated, leaving the *corpora lutea* behind.

In conclusion, the quantitative topographic information obtained builds sound bases for modeling follicles position inside the ovary, and, prospectively, could contribute to our understanding of the dynamics of the folliculogenetic process, not only under normal conditions, but, importantly, also during aging, in the presence of pathologies (e.g., polycystic ovary syndrome, hyperstimulation syndrome or ovarian cancer) or after hormones or drugs administration. In addition, our study on the mouse ovary, which is one of the tiniest in Mammals, sets the bases for a comparative 3D anatomy within this class, but also could be extended to a reconstruction of the evolutionary history of the female gonad. Finally, microCT preserves the integrity of the sample and facilitates its further analysis with other approaches. The use of PFA well maintains both tissue histology and protein components, thus allowing additional immunohistochemical investigations into more specific molecular functional markers.

DATA AVAILABILITY STATEMENT

The raw data supporting the conclusions of this article will be made available by the authors, without undue reservation.

ETHICS STATEMENT

The animal study was reviewed and approved by the Animal Welfare Committee of the University of Pavia.

AUTHOR CONTRIBUTIONS

GF prepared all the samples used for microCT and histological analyses, and did the follicle counting. AP designed the microCT analysis and performed the scanning of the samples. GF and AP did the post-microCT software analysis and 3D rendering. SG and MZ designed, followed, and interpreted the experiments and together with GF and AP wrote the manuscript. All authors contributed to the article and approved the submitted version.

FUNDING

This work was made possible thanks to support from the Italian Ministry of Education, University and Research (MIUR) Dipartimenti di Eccellenza Program (2018–2022) to the Department of Biology and Biotechnology "Lazzaro Spallanzani", University of Pavia, and a grant from the University of Pavia (FRG 2018).

ACKNOWLEDGMENTS

The authors thank Merck-MilliQ Laboratory Water Solutions and the IRCCS-Istituto Ortopedico Rizzoli for support.

SUPPLEMENTARY MATERIAL

The Supplementary Material for this article can be found online at: https://www.frontiersin.org/articles/10.3389/fcell.2020.566152/full#supplementary-material

Supplementary Figure 1 | Representative 5 μm/pixel microCT images of PFA-fixed mouse ovaries treated with different contrast agents. **(A)** Iodine tincture. **(B)** Phosphotungstic acid. **(C)** Uranyl acetate. Bar, 500 μ m.

Supplementary Figure 2 | Representative 5 μm/pixel microCT image of the mouse ovary after PFA fixation and contrast with Lugol's solution. **(A)** A representative microCT image acquired at 5 μm/pixel clearly showing various *corpora lutea* (CL), type 7 (T7), type 6 (T6), and type 4 (T4) follicles; Bar, 500 μm. **(B)** Hematoxylin and Eosin stained cross-section corresponding to the microCT image shown in panel **(A)**; Bar, 500 μm. **(C,D)** Enlarged details of panels **(A,B)**, respectively; Bar, 150 μ m.

Supplementary Movie 1 | A representative microCT imaging of an adult mouse ovary.

Supplementary Movie 2 | MicroCT identification of the oocyte's nucleus inside two type 7 follicles.

REFERENCES

Batool, F., Strub, M., Petit, C., Bugueno, I. M., Bornert, F., Clauss, F., et al. (2018). Periodontal Tissues, Maxillary Jaw Bone, and Tooth Regeneration Approaches: From Animal Models Analyses to Clinical Applications. *Nanomaterials* 8:337. doi: 10.3390/nano8050337

Belli, M., Vigone, G., Merico, V., Redi, C. A., Zuccotti, M., and Garagna, S. (2012). Towards a 3D culture of mouse ovarian follicles. *Int. J. Dev. Biol.* 56, 931–937. doi: 10.1387/ijdb.120175mz

Chałas, R., Szlązak, K., Wójcik-Chęcińska, I., Jaroszewicz, J., Molak, R., Czechowicz, K., et al. (2017). Observations of mineralised tissues of teeth in X-ray micro-computed tomography. *Folia Morphol.* 76, 143–148. doi: 10.5603/FM.a2016.0070

Cordeiro, M. H., Kim, S. Y., Ebbert, K., Duncan, F. E., Ramalho-Santos, J., and Woodruff, T. K. (2015). Geography of follicle formation in the embryonic mouse ovary impacts activation pattern during the first wave of folliculogenesis. *Biol. Reprod.* 93:88. doi: 10.1095/biolreprod.115.131227

Cremer, C., Szczurek, A., Schock, F., Gourram, A., and Birk, U. (2017). Super-resolution microscopy approaches to nuclear nanostructure imaging. *Methods* 123, 11–32. doi: 10.1016/j.ymeth.2017.03.019

de Bournonville, S., Vangrunderbeeck, S., and Kerckhofs, G. (2019). Contrast-Enhanced MicroCT for Virtual 3D Anatomical Pathology of Biological Tissues: A Literature Review. *Contr. Med. Mol. Imag.* 2019:8617406. doi: 10.1155/2019/8617406

de S e Silva, J. M., Zanette, I., Noël, P. B., Cardoso, M. B., Kimm, M. A., and Pfeiffer, F. (2015). Three-dimensional non-destructive soft-tissue visualization with X-ray staining micro-tomography. *Sci. Rep.* 5:14088. doi: 10.1038/srep14088

Faire, M., Skillern, A., Arora, R., Nguyen, D. H., Wang, J., Chamberlain, C., et al. (2015). Follicle dynamics and global organization in the intact mouse ovary. *Dev. Biol.* 403, 69–79. doi: 10.1016/j.ydbio.2015.04.006

Feng, Y., Cui, P., Lu, X., Hsueh, B., Möller Billig, F., Zarnescu Yanez, L., et al. (2017). CLARITY reveals dynamics of ovarian follicular architecture and vasculature in three-dimensions. *Sci. Rep.* 7:44810. doi: 10.1038/srep44810

Flannery, B. P., Deckman, H. W., Roberge, W. G., and D'Amico, K. L. (1987). Three-Dimensional X-ray Microtomography. *Science* 237, 1439–1444. doi: 10.1126/science.237.4821.1439

Fraser, H. M. (2006). Regulation of the ovarian follicular vasculature. *Reprod. Biol. Endocrinol.* 4:18. doi: 10.1186/1477-7827-4-18

Ginther, O. J., Rakesh, H. B., and Hoffman, M. M. (2014). Blood flow to follicles and CL during development of the periovulatory follicular wave in heifers. *Theriogenology* 82, 304–311. doi: 10.1016/j.theriogenology.2014.04.009

Hensley, H., Quinn, B. A., Wolf, R. L., Litwin, S. L., Mabuchi, S., Williams, S. J., et al. (2007). Magnetic resonance imaging for detection and determination of tumor volume in a genetically engineered mouse model of ovarian cancer. *Cancer Biol. Ther.* 6, 1717–1725. doi: 10.4161/cbt.6.11.4830

Hsueh, A. J., Kawamura, K., Cheng, Y., and Fauser, B. C. (2015). Intraovarian control of early folliculogenesis. *Endocr. Rev.* 36, 1–24. doi: 10.1210/er.2014-1020

Kagami, K., Shinmyo, Y., Ono, M., Kawasaki, H., and Fujiwara, H. (2018). Three-dimensional evaluation of murine ovarian follicles using a modified CUBIC tissue clearing method. *Reprod. Biol. Endocrinol.* 16:72. doi: 10.1186/s12958-018-0381-7

Kim, J., Choi, Y. H., Chang, S., Kim, K. T., and Je, J. H. (2012). Defective folliculogenesis in female mice lacking Vaccinia-related kinase 1. *Sci. Rep.* 2:468. doi: 10.1038/srep00468

Longo, F., Garagna, S., Merico, V., Orlandini, G., Gatti, R., Scandroglio, R., et al. (2003). Nuclear localization of NORs and centromeres in mouse oocytes during folliculogenesis. *Mol. Reprod. Dev.* 66, 279–290. doi: 10.1002/mrd.10354

McKey, J., Cameron, L. A., Lewis, D., Batchvarov, I. S., and Capel, B. (2020). Combined iDISCO and CUBIC tissue clearing and lightsheet microscopy for in toto analysis of the adult mouse ovary. *Biol. Reprod.*, 102, 1080–1089. doi: 10.1093/biolre/ioaa012

Metscher, B. D. (2009). MicroCT for comparative morphology: simple staining methods allow high-contrast 3D imaging of diverse non-mineralized animal tissues. *BMC Physiol.* 9:11. doi: 10.1186/1472-6793-9-11

Migone, F. F., Cowan, R. G., Williams, R. M., Gorse, K. J., Zipfel, W. R., and Quirk, S. M. (2016). In vivo imaging reveals an essential role of vasoconstriction in rupture of the ovarian follicle at ovulation. *Proc. Natl. Acad. Sci. U S A* 113, 2294–2299. doi: 10.1073/pnas.1512304113

Mircea, C. N., Lujan, M. E., Jaiswal, R. S., Singh, J., Adams, G. P., and Pierson, R. A. (2009). Ovarian imaging in the mouse using ultrasound biomicroscopy (UBM): a validation study. *Reprod. Fertil. Dev.* 21, 579–586. doi: 10.1071/RD08295

Mizutani, R., and Suzuki, Y. (2012). X-ray microtomography in biology. *Micron* 43, 104–115. doi: 10.1016/j.micron.2011.10.002

Mussmann, B., Overgaard, S., Torfing, T., Traise, P., Gerke, O., and Andersen, P. E. (2017). Agreement and precision of periprosthetic bone density measurements in micro-CT, single and dual energy CT. *J. Orthop. Res.* 35, 1470–1477. doi: 10.1002/jor.23417

Oren, R., Fellus-Alyagor, L., Addadi, Y., Bochner, F., Gutman, H., and Blumenreich, S. (2018). Whole Organ Blood and Lymphatic Vessels Imaging (WOBLI). *Sci. Rep.* 8:1412. doi: 10.1038/s41598-018-19663-w

Pascolo, L., Sena, G., Gianoncelli, A., Cernogoraz, A., Kourousias, G., and Metscher, B. D. (2019). Hard and soft X-ray imaging to resolve human ovarian cortical structures. *J. Synchr. Rad.* 26, 1322–1329. doi: 10.1107/S1600577519003680

Paulini, F., Chaves, S. B., Rôlo, J., Azevedo, R. B., and Lucci, C. M. (2017). Evaluation of ovarian structures using computerized microtomography. *An. Acad. Bras. Cienc.* 89, 2131–2139. doi: 10.1590/0001-3765201720150864

Pauwels, E., Van Loo, D., Cornillie, P., Brabant, L., and Van Hoorebeke, L. (2013). An exploratory study of contrast agents for soft tissue visualization by means of high resolution X-ray computed tomography imaging. *J. Microsc.* 250, 21–31. doi: 10.1111/jmi.12013

Pedersen, T., and Peters, H. (1968). Proposal for a classification of oocytes and follicles in the mouse ovary. *J. Reprod. Fertil.* 17, 555–557. doi: 10.1530/jrf.0.0170555

Peters, H. (1969). The development of the mouse ovary from birth to maturity. *Acta Endocrinol.* 62, 98–116. doi: 10.1530/acta.0.0620098

Russell, D. L., Gilchrist, R. B., Brown, H. M., and Thompson, J. G. (2016). Bidirectional communication between cumulus cells and the oocyte: Old hands and new players? *Theriogenology* 86, 62–68. doi: 10.1016/j.theriogenology.2016.04.019

Schermelleh, L., Heintzmann, R., and Leonhardt, H. (2010). A guide to super-resolution fluorescence microscopy. *J. Cell. Biol.* 190, 165–175. doi: 10.1083/jcb.201002018

Schindelin, J., Arganda-Carreras, I., Frise, E., Kaynig, V., Longair, M., Pietzsch, T., et al. (2012). Fiji: an open-source platform for biological-image analysis. *Nat. Methods* 9, 676–682. doi: 10.1038/nmeth.2019

Shah, J. S., Sabouni, R., Cayton Vaught, K. C., Owen, C. M., Albertini, D. F., and Segars, J. H. (2018). Biomechanics and mechanical signaling in the ovary: a systematic review. *JARG* 35, 1135–1148. doi: 10.1007/s10815-018-1180-y

Song, Y., Zhu, F., Lin, F., Zhang, F., and Zhang, S. (2018). Bone quality, and the combination and penetration of cement-bone interface: A comparative micro-CT study of osteoarthritis and rheumatoid arthritis. *Medicine* 97:e11987. doi: 10.1097/MD.0000000000011987

Telfer, E. E. (2019). Future developments: In vitro growth (IVG) of human ovarian follicles. *Acta Obstet. Gynecol. Scand.* 98, 653–658. doi: 10.1111/aogs.13592

Velozo, C., and Albuquerque, D. (2019). Microcomputed Tomography Studies of the Effectiveness of XP-endo Shaper in Root Canal Preparation: A Review of the Literature. *Sci. World J.* 2019:3570870. doi: 10.1155/2019/3570870

Zuccotti, M., Merico, V., Cecconi, S., Redi, C. A., and Garagna, S. (2011). What does it take to make a developmentally competent mammalian egg? *Hum. Reprod. Update* 17, 525–540. doi: 10.1093/humupd/dmr009

Conflict of Interest: The authors declare that the research was conducted in the absence of any commercial or financial relationships that could be construed as a potential conflict of interest.

frontiers
in Cell and Developmental Biology

REVIEW
published: 23 October 2020
doi: 10.3389/fcell.2020.593969

Intestinal Morphogenesis in Development, Regeneration, and Disease: The Potential Utility of Intestinal Organoids for Studying Compartmentalization of the Crypt-Villus Structure

Ohman Kwon[1], Tae-Su Han[1] and Mi-Young Son[1,2]**

[1] *Korea Research Institute of Bioscience and Biotechnology, Daejeon, South Korea,* [2] *KRIBB School of Bioscience, Korea University of Science and Technology, Daejeon, South Korea*

OPEN ACCESS

Edited by:
Silvia Garagna,
University of Pavia, Italy

Reviewed by:
Elena Goncharova,
University of California, Davis,
United States
Rajprasad Loganathan,
Johns Hopkins University,
United States

***Correspondence:**
Tae-Su Han
tshan@kribb.re.kr
Mi-Young Son
myson@kribb.re.kr

Specialty section:
This article was submitted to
Cell Growth and Division,
a section of the journal
Frontiers in Cell and Developmental
Biology

Received: *12 August 2020*
Accepted: *05 October 2020*
Published: *23 October 2020*

Citation:
Kwon O, Han T-S and Son M-Y
(2020) Intestinal Morphogenesis
in Development, Regeneration,
and Disease: The Potential Utility
of Intestinal Organoids for Studying
Compartmentalization of the
Crypt-Villus Structure.
Front. Cell Dev. Biol. 8:593969.
doi: 10.3389/fcell.2020.593969

The morphology and structure of the intestinal epithelium are rearranged dynamically during development, tissue regeneration, and disease progression. The most important characteristic of intestinal epithelial morphogenesis is the repetitive compartmentalized structures of crypt-villus units, which are crucial for maintaining intestinal homeostasis and functions. Abnormal structures are known to be closely associated with disease development and progression. Therefore, understanding how intestinal crypt-villus structures are formed and grown is essential for elucidating the physiological and pathophysiological roles of the intestinal epithelium. However, a critical knowledge gap in understanding the compartmentalization of the crypt-villus axis remains when using animal models, due to obvious inter-species differences and difficulty in real-time monitoring. Recently, emerging technologies such as organoid culture, lineage tracing, and single cell sequencing have enabled the assessment of the intrinsic mechanisms of intestinal epithelial morphogenesis. In this review, we discuss the latest research on the regulatory factors and signaling pathways that play a central role in the formation, maintenance, and regeneration of crypt-villus structures in the intestinal epithelium. Furthermore, we discuss how these factors and pathways play a role in development, tissue regeneration, and disease. We further explore how the current technology of three-dimensional intestinal organoids has contributed to the understanding of crypt-villus compartmentalization, highlighting new findings related to the self-organizing-process-driven initiation and propagation of crypt-villus structures. We also discuss intestinal diseases featuring abnormalities of the crypt-villus structure to provide insights for the development of novel therapeutic strategies targeting intestinal morphogenesis and crypt-villus formation.

Keywords: intestine, development, morphogenesis, regeneration, crypt, villus, organoid

INTRODUCTION

The human small intestine is the primary organ responsible for the absorption and metabolism of nutrients or drugs and plays an important role in controlling diverse physiological functions such as commensal bacterium colonization and immune system regulation. The adult small intestine requires a large surface area for efficient metabolism and nutrient absorption, and the inner surface area of the adult small intestine is approximately 30 m^2 on average (Helander and Fandriks, 2014). To form a large surface area, unique structures such as villi and microvilli are developed in the small intestine. The villi, which have a finger-shaped structure protruding toward the intestinal lumen, enormously expand the surface area of the small intestine (Walton et al., 2016). Moreover, microvilli within the brush border further amplify the surface area of the small intestine by approximately 9–16-fold (Crawley et al., 2014a; Helander and Fandriks, 2014). Appropriate development of the fingerlike protruding villus structure on the intestinal surface is crucial for nutrient and fluid absorption, allowing maintenance of homeostasis in adults and growth in children. Therefore, the reduction in inner surface area due to the defective development of villi and microvilli causes intestinal failure, including short bowel syndrome, Hirschsprung disease, and chronic intestinal pseudo-obstruction syndrome (Goulet et al., 2004).

The intestinal epithelium is rapidly self-renewing to repair damages caused by exposure to a hostile environment (Barker et al., 2007; Sato et al., 2009). To support rapid regeneration of the intestine, actively cycling intestinal stem cells (ISCs) are housed at the base of the crypt between the differentiated secretory Paneth cells (Clevers, 2013; Tan and Barker, 2014). The crypt has a flask-shaped structure located in the intervillus region and is embedded in the mesenchyme, and the actively proliferating ISCs are crypt base columnar cells that strongly express $Lgr5^+$ (Barker et al., 2007). For the sustainable maintenance of the intestinal epithelium, the ISCs continuously undergo self-renewal and produce transit-amplifying cells. These cells move up the crypt-villus axis and generate every type of differentiated cell comprising the intestinal epithelium, such as enterocytes, Paneth cells, goblet cells, enteroendocrine cells, and tuft cells (Marshman et al., 2002; Clevers, 2013). After reaching the tips of the villi, cells are extruded into the lumen upon apoptosis and are replaced by new cell populations, ensuring intestinal homeostasis (Barker, 2014). Although the crypt-villus is the basic architectural unit of the intestine, there is still a lack of understanding of crypt-villus structure formation, in addition to the physiological and pathological implications of the crypt-villus structure from the perspective of functionality.

In this review, we highlight the processes responsible for the specific compartmentalization of cells into crypt-villus units in the intestinal epithelium during vertebrate intestinal development and tissue regeneration. In addition, we discuss the molecular and cellular mechanisms underlying crypt-villus morphogenesis and the pathological correlation between the compartmentalized crypt-villus structure and disease incidence.

VILLUS MORPHOGENESIS DURING INTESTINAL DEVELOPMENT

In vertebrates, villus morphogenesis is initiated by the synchronized development of the intestinal epithelium and mesenchyme during early embryonic development. At E14.5 in mice (weeks 8–10 in humans), the flat pseudostratified intestinal epithelium initiates morphogenesis and gives rise to villi that protrude into the intestinal lumen (**Figure 1A**; Spence et al., 2011a; Walton et al., 2016). To initiate villus morphogenesis, cluster formation must be carried out through mesenchymal cell condensation under the intestinal epithelium. The intestinal epithelium remains flat when mesenchymal cell clusters are formed, and villus formation is severely interrupted by the inhibition of mesenchymal cell clustering (Karlsson et al., 2000; Madison et al., 2005; Walton et al., 2012). Mesenchymal cell cluster formation is promoted by soluble ligands such as bone morphogenetic protein (Bmp), hedgehog (Hh), and platelet-derived growth factor A (Pdgf-A) secreted from the intestinal epithelium, and mesenchymal cells express receptors such as Pdgfr-α for Pdgf-A and Ptch1/2 for Hh (Karlsson et al., 2000; Madison et al., 2005; Kolterud et al., 2009; Grosse et al., 2011; Walton et al., 2012; Freddo et al., 2016). Genetic ablation of either Pdgf-A or Pdgfr-α does not inhibit the initial emergence of mesenchymal cell clusters, but subsequent mesenchymal cell cluster formation is suppressed by decreased proliferative activity of PDGFR-α-expressing mesenchymal cells (Karlsson et al., 2000). Unlike the PDGF pathway, mesenchymal cell cluster formation is severely disrupted by Hh pathway inhibition, while cluster size is increased by Hh pathway enhancement (Madison et al., 2005; Mao et al., 2010; Walton et al., 2012). This suggests that the Hh pathway is critical for the initiation of mesenchymal cell clustering and that the Pdgf pathway is necessary for cluster propagation through the activation of subsequent proliferation. Consistent with this notion, genetic deletion of the transcription factors Foxf1, Foxf2, and Foxl1, which are known to be Hh target genes, in mesenchymal cells also results in significantly reduced villus development (Kaestner et al., 1997; Ormestad et al., 2006; Madison et al., 2009).

Although the molecular mechanisms of mesenchymal cell clustering are not fully understood, increased cell adhesion and planar cell polarity (PCP) by Hh signaling are required for mesenchymal cell clustering via oriented cell movement and collective cell migration (Rao-Bhatia et al., 2020). PCP genes, including *Fat4* and *Dchs1,* were recently identified as direct target genes of Hh downstream of glioma-associated oncogene (GLI) transcription factors (Coquenlorge et al., 2019; Rao-Bhatia et al., 2020). Moreover, the activation of the *Fat4*-PCP pathway in Hh-responsive mesenchymal cells augments the formation of mesenchymal cell clustering, as this pathway controls the orientation and directional migration of mesenchymal cells toward chemoattractants such as WNT5A (Rao-Bhatia et al., 2020). The expression level of *Wnt5a* gradually increases toward

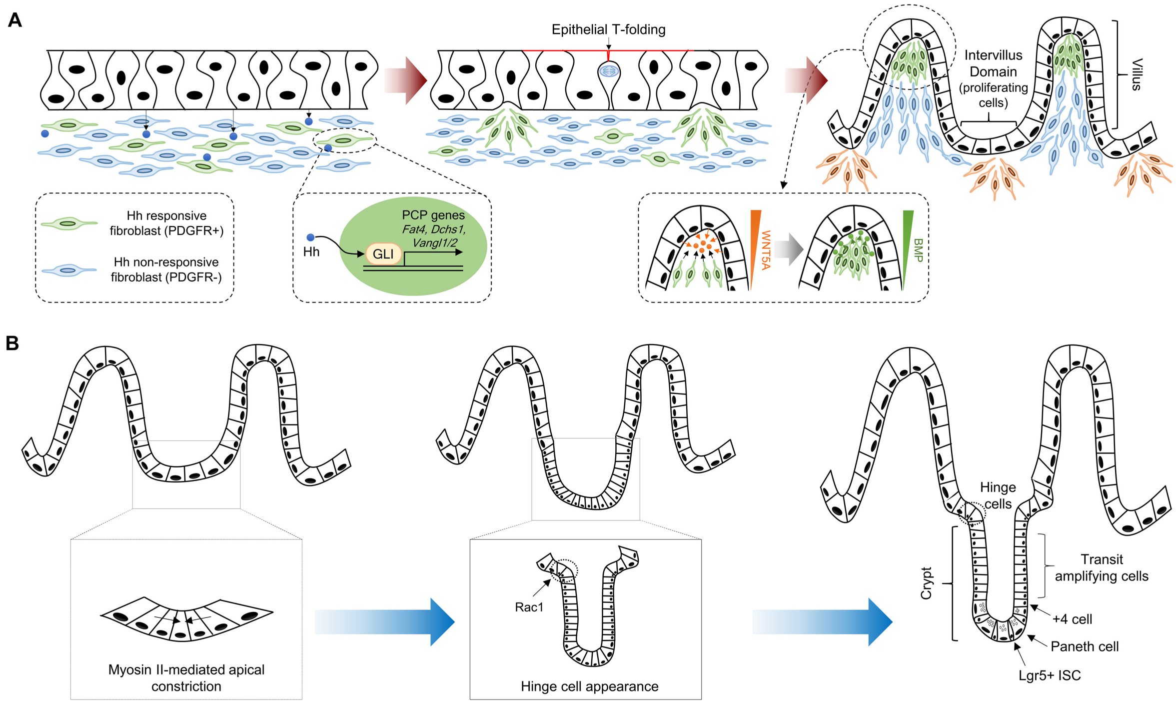

FIGURE 1 | Crypt-villus morphogenesis during mouse development. **(A)** The pseudostratified intestinal epithelium secretes Hh ligands that induce expression of PCP genes, such as *Fat4*, *Dchs1*, *Vangl1*, and *Vangl2*, via GLI transcriptional factor activation. Clustered mesenchymal cells (green color) cause deformation of intestinal epithelium through apical membrane invagination with the emergence of epithelial T-folding. The clustered mesenchymal cells underneath the tip of the villus, which are formed by directional migration toward chemoattractants such as WNT5A, enforce villification and differentiation of intestinal epithelium via secretion of soluble ligands including BMPs. New mesenchymal clusters (orange color) beneath the intervillus domain lead to the second round of villification processes. **(B)** Intervillus proliferating cells transform into crypts. The initiation of crypt formation is driven by myosin II-mediated apical constriction and invagination of the crypt cells. Subsequently, hinge formation in the crypt neck is initiated to compartmentalize crypts and villus, and Rac1 controls this process through the wedge-shaped hinge cell formation. These crypts contain Lgr5 + ISCs intercalated between Paneth cells at the crypt base, and transit amplifying cells.

the villus core, and the expression pattern of WNT5A along the villus is maintained until the late stage of development (Gregorieff et al., 2005; Rao-Bhatia et al., 2020). In addition, severe villus fusions were observed at E15.5 in both *Fat4* knockout (KO) and *Wnt5a* KO mice. Villus fusion is a requirement for *Fat4*-PCP for appropriate villus development via mesenchymal cell clustering (Cervantes et al., 2009; Rao-Bhatia et al., 2020). The mesenchymal clusters underneath the intestinal epithelial cells subsequently induce apical membrane invagination on epithelial cells, which is required for villus formation via fingerlike protrusions toward the luminal side. Intestinal epithelial cells between mesenchymal clusters form T-shaped membrane invaginations (T-folds) due to apical side constriction, which occurs via mitotic cell rounding and circumferential pressure (Nishimura et al., 2007; Kondo and Hayashi, 2013; Freddo et al., 2016). The invagination of the intestinal epithelium converts flat pseudostratified epithelium into a clearly demarcated villus structure.

After the appearance of the villus structure, proliferating cells are collected in the intervillus pockets and are subsequently confined to the crypt base (Crosnier et al., 2006; Shyer et al., 2015). The villus length is continuously increased by intervillus cell proliferation, and newly formed mesenchymal clusters between existing villi facilitate the formation of new villi. This process is repeated for several rounds, and the number of villi is approximately doubled each round (Walton et al., 2012, 2016). The architecture of the intestinal epithelium is changed by the emergence of nascent villi; therefore, the local concentration of soluble ligands for the Hh and Bmp pathways is elevated in the mesenchyme under the area of the epithelial curvature (Shyer et al., 2015). In particular, the expression levels of Bmp ligands are strongly increased in the inter-villus mesenchymal cells (Shyer et al., 2015; Walton et al., 2016). Bmp pathway activation in the intestinal epithelium suppresses Wnt signaling to promote differentiation of the progeny of proliferating cells into functional cell types, such as absorptive enterocytes, goblet cells, and enteroendocrine cells (He et al., 2004; Crosnier et al., 2006). Collectively, villification of the intestinal epithelium is regulated by the combined effects of both signaling molecules and biomechanical forces, which involve the simultaneous development of the intestinal epithelium and mesenchyme.

CRYPT MORPHOGENESIS DURING INTESTINAL DEVELOPMENT

In mice, crypt formation is initiated from the first week after birth (**Figure 1B**; Dehmer et al., 2011), but in humans, crypt formation has occurred in the intervillus regions in early gestation (weeks 11–12) (Trier and Moxey, 1979). The proliferating precryptic cells in the intervillus region are arranged in a flat sheet at P0–P2, and there is no obvious crypt-like structure (Sumigray et al., 2018). However, the apical area of crypt cells at P1 is decreased by approximately threefold compared to that at P0 (P0: 18.4 ± 0.5 mm^2; P1: 6.2 ± 0.1 mm^2). Additionally, the expression of myosin II-associated contractility genes, such as the myosin light chain *Myl9*, the myosin heavy chain *Myh9*, the Rho GEF *Ect2*, and the actin nucleators *Diaph2* and *Diaph3,* is increased in crypt cells compared to that in villus cells (Sumigray et al., 2018). This means that apical constriction driven by type II myosin-associated genes facilitates reduction of the apical area of crypt cells and eventually causes crypt formation by promoting epithelial sheet bending and invagination. These morphogenetic changes by apical constriction are also observed in *Xenopus* neural tube closure and *Drosophila* gastrulation (Martin et al., 2009; Rolo et al., 2009).

At P3, a broad curvature on the intestinal epithelium appears in approximately 60% of crypts, which is driven by myosin II-mediated apical constriction (Sumigray et al., 2018). The wedge-shaped crypt appearance and crypt depth continuously increase until P6 (Sumigray et al., 2018). However, at P7, an unusually shaped "hinge cell" appears at the crypt-villus boundaries and exhibits basally constricted and apically expanded morphology (Tan and Barker, 2014; Sumigray et al., 2018). Hinge cells appear to be required for maintaining the organization of the intestinal epithelium and adequate distance between villi (Sumigray et al., 2018). Interestingly, genetic ablation of Rac1 in intestinal epithelial cells impairs hinge cell formation. This is because basal constriction does not occur normally, as the attachment to the extracellular matrix (ECM) of crypt cells becomes stronger (Sumigray et al., 2018). In addition, the interaction between the ECM proteins laminin-322 and α6β4 hemidesmosomal integrin is enhanced by the increased expression of α6 and β4 integrin subunits in *Rac1* KO mice (Sumigray et al., 2018). Therefore, Rac1 plays a crucial role in regulating crypt-villus formation, in part by controlling hinge cell formation.

During the early stage of crypt development, the nascent crypts consist of just over 30 ± 9 cells (Sumigray et al., 2018). These crypts undergo continuous elongation and expansion until P14. $Lgr5^+$ ISCs intercalated between Paneth cells are restricted in the crypt base, in accordance with the histological structure of mature crypts (Sato et al., 2011; Shyer et al., 2015; Yanai et al., 2017). The $Lgr5^+$ ISCs undergo continuous division to maintain the morphological and functional properties of the intestinal epithelium, there by rapidly proliferating transit-amplifying (TA) cells. Furthermore, diverse types of differentiated cells are generated by asymmetric cells in a stem cell niche (Potten, 1998; Barker et al., 2007; Umar, 2010; Santos et al., 2018). Paneth cells consist of an ISC niche that excrete growth factors such as Wnt ligands and lateral activation of Notch signaling on neighboring $Lgr5^+$ ISCs required for ISC maintenance (Pellegrinet et al., 2011; Sato et al., 2011). As well as, Paneth cells also contribute to the maintenance of intestinal homeostasis by sensing external stimuli including nutrient availability (Beumer and Clevers, 2016). For example, calorie restriction suppresses mTORC1 activity in Paneth cells, which induces an increase in the number of Paneth cells and $Lgr5^+$ ISCs to maintain intestinal homeostasis (Yilmaz et al., 2012). It is already well-known that mTORC1 activity is important for stem niche maintenance (Kaur and Moreau, 2019), further studies are needed on the molecular mechanism of how mTORC1 activity regulates Paneth cell function needs to be elucidated. Collectively, Paneth cell consist of an essential stem niche that supports $Lgr5^+$ ISCs maintenance at the bottom of the crypt where the stem cell continuously divide to produce intestinal progenitors and differentiated cells for homeostatic maintenance (Clevers, 2013; Van Der Heijden and Vermeulen, 2019).

CRYPT-VILLUS MORPHOGENESIS DURING TISSUE REGENERATION

The intestinal epithelium is a physical and selectively permeable barrier that protects the host from contamination with undesirable luminal contents while simultaneously preserving the ability to absorb nutrients. Disruption of the intestinal epithelium allows the passage of microbes, microbial products, and foreign antigens into the mucosa and the host and is caused by pathogen infection, excessive uncontrolled inflammation, or vascular insults (Wang Y. et al., 2019). In addition, defects in the intestinal epithelial barrier are frequently observed in diverse pathological conditions, including inflammatory disease, ischemic events, or mechanical injuries (Quiros and Nusrat, 2019). In response to epithelial injury and to regain mucosal homeostasis, distinct repair strategies have evolved to restore the epithelial barrier and prevent translocation of undesirable luminal contents across the mucosa (Iizuka and Konno, 2011).

In the intestinal epithelium, specialized repairing cells known as wound-associated epithelial (WAE) cells transiently emerge to establish an epithelial barrier after tissue damage (Seno et al., 2009; Miyoshi et al., 2012). Following intestinal epithelial injuries, WAE cells, which emerge from the crypts adjacent to the wounded area, rapidly migrate to cover the wound surfaces for epithelial restitution. These WAE cells are transformed into monolayer intestinal epithelium during a subsequent repair process (**Figure 2**; Seno et al., 2009; Miyoshi et al., 2012). Recent studies have shown that WAE differentiation and wound repair after epithelial injury are promoted by prostaglandin E2 (PGE_2) signals through the prostaglandin E receptor 4 (EP4) on the crypts adjacent to the wound bed (Manieri et al., 2012, 2015; Miyoshi et al., 2017). In part, the generation of WAE cells by PGE_2-EP4 signaling is due to the activation of the canonical Wnt pathway in crypt cells through nuclear β-catenin accumulation (Miyoshi et al., 2017). WAE cells are attracted by a high local concentration of PGE_2 emanating from crypts adjacent to the wound and migrate to form an array of epithelial channel-like structures by forming a lateral, open extension toward the center of the wound area (Miyoshi et al., 2012). The wound-channel epithelium is composed of highly proliferative cells and express Axin2, a direct target of canonical Wnt signaling. This wound-channel epithelium is converted

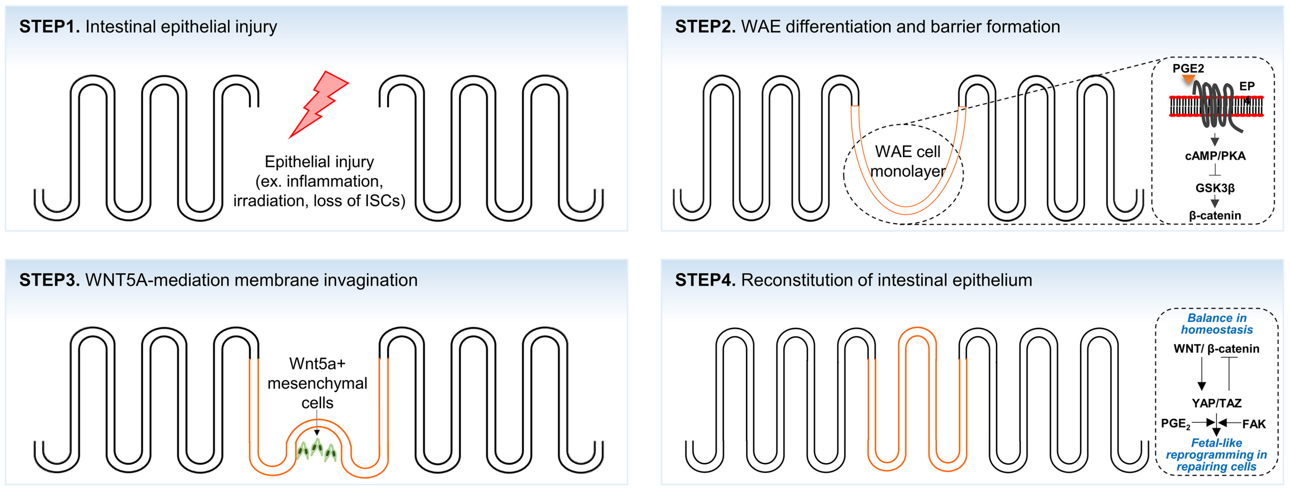

FIGURE 2 | A scheme of the crypt-villus morphogenesis during tissue regeneration. Intestinal epithelium lost by intestinal injuries (STEP1) is rapidly re-epithelialized by wound-associated cell (WAE) monolayer (orange color; STEP2). Morphological transformation of the WAE monolayer into crypt-villus structure is initiated by WNT5A^{+} mesenchymal cells (STEP3) that subsequently develop to fully reconstitute the epithelium (STEP4).

into segmented compartments similar to crypts, and epithelial morphogenesis is modulated by Wnt5a secreted from the subepithelial mesenchyme. Although the exact function of Wnt5a has not been elucidated, it is understood that Wnt5a induces multiple invagination through inhibiting the proliferation of WAE cells (Miyoshi et al., 2012). In *Wnt5a* KO mice, the wound-channel epithelium contains significantly fewer invaginations and defective crypt-like structures. This suggests that Wnt5a plays a crucial role in tissue regeneration through the proper formation and division of the wound-channel epithelium into crypts (Miyoshi et al., 2012).

The overall process of tissue regeneration through wound channel formation and epithelium invagination is similar to the epithelial response accompanied by chronic inflammation, intestinal irradiation, or ablation of Lgr5^{+} ISCs (Metcalfe et al., 2014; Nusse et al., 2018; Yui et al., 2018). Upon crypt disruption by chemical or pathogenic damage, intestinal epithelial cells around the wound area are reprogrammed into fetal-like cells. In addition, fetal signature genes are strongly enriched in repairing epithelium, whereas the expression of adult stem cell markers, such as Lgr5, Olfm4, and Lrig1, is lost (Nusse et al., 2018; Yui et al., 2018). These fetal-like repairing cells are derived from adjacent intestinal cells and migrate to the wound bed to rapidly cover the wound area. Although the molecular mechanism of injury-induced cellular reprogramming is not fully understood, it is known that the activation of the mechanosensor YAP/TAZ signaling, which is controlled by integrin-mediated bidirectional signaling between repairing cells and ECM (Lotz et al., 1997; Koivisto et al., 2014), is required for fetal-like cell reprogramming (Cai et al., 2010; Taniguchi et al., 2015; Yui et al., 2018). Consistent with this notion, transient YAP/TAZ expression has been observed to dedifferentiate committed cells back to expandable tissue-specific stem/progenitor cells (Panciera et al., 2016). Furthermore, it was recently suggested that PGE$_2$ signaling upregulates the expression and transcriptional activities of YAP1 and promotes colon tissue regeneration in mice with colitis (Kim et al., 2017).

MICROVILLI AND BRUSH BORDER MORPHOGENESIS

The brush border on the apical surface of fully differentiated enterocytes consists of highly ordered membrane protrusions, also known as microvilli. These microvilli constitute a biochemical and mechanical interface required for efficient digestion, nutrient absorption, and protection from infectious diseases (Sebe-Pedros et al., 2013; Crawley et al., 2014a; Delacour et al., 2016). While the initiation mechanism of microvilli morphogenesis remains unclear, it seems that actin filament nucleation and elongation are required to generate the force for membrane deformation (**Figure 3**; Pollard and Mooseker, 1981; Mooseker et al., 1982). The formation of polymerized and bundled actin microfilaments provides membrane protrusion force to drive microvillus morphogenesis. A large panel of different actin interacting proteins such as actin-capping proteins, F-actin bundling proteins, membrane-cytoskeleton crosslinking proteins, and intermicrovillar adhesion proteins is required for dense apical arrays of microvilli, known as "brush borders" (Bartles, 2000; Fehon et al., 2010; Tocchetti et al., 2010; Revenu et al., 2012; Edwards et al., 2014).

The microvillar actin bundles are extended and anchored into the terminal web, which plays a critical role in the structural and mechanical stabilization of the brush border (Fath et al., 1993; Grimm-Gunter et al., 2009). In addition, the brush border microvilli have a highly ordered packing structure and uniform microvillar length (Crawley et al., 2014a,b; Delacour et al., 2016). To control brush border assembly, nascent microvilli are incorporated into existing clusters, or small clusters coalesce into larger clusters. These

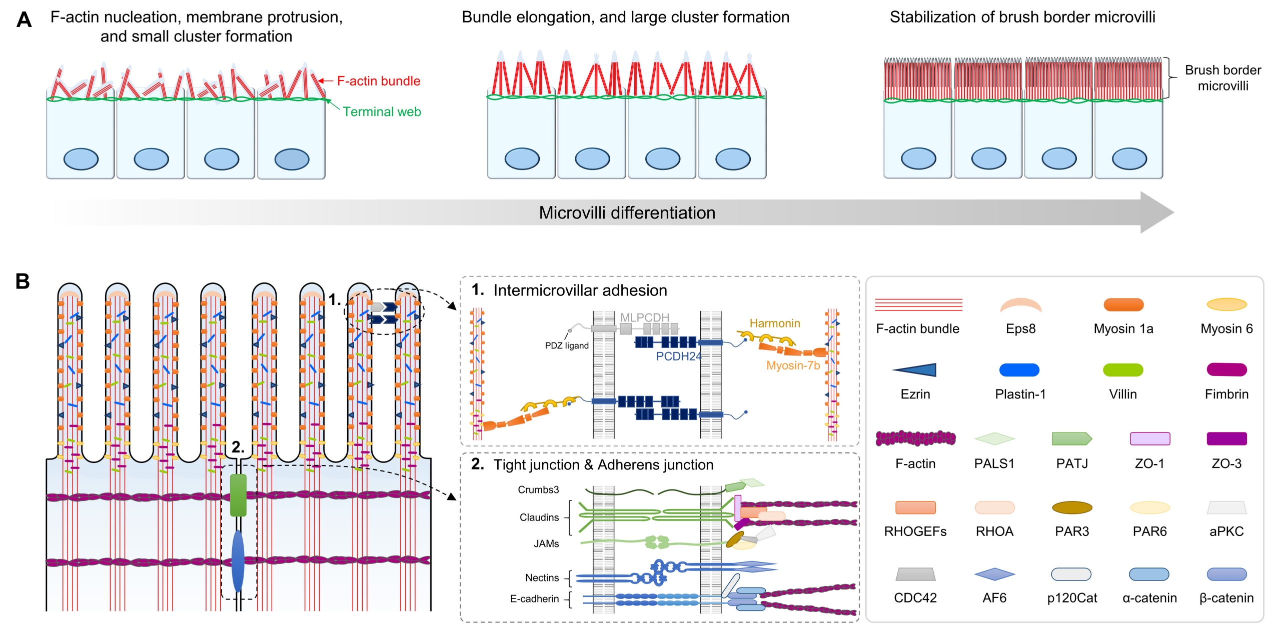

FIGURE 3 | Structure and composition of microvilli during brush border development. **(A)** Small cluster of microvilli on the apical surface is formed by the formation of F-actin bundles beneath the membrane. As microvilli differentiate, clusters elongate and form large cluster, ultimately resulting in stabilized brush border. **(B)** Molecular composition and two distinctive structures of the microvilli are shown. ① Intermicrovillar adhesion between the distal tips of microvilli is mediated by a heterophilic complex between protocadherin-24 (PCDH24) and mucin-like protocadherin (MLPCDH). The protocadherin complex is physically linked to the actin bundle through interaction with harmonin and myosin 7b. ② Molecular composition of tight junctions (TJs) and adherens junction at the lateral membrane of brush border. JAMs, junctional adhesion molecules.

processes are mediated by Ca^{2+}-dependent adhesion between neighboring microvilli. Ca^{2+}-dependent adhesion links are formed by a heterophilic complex between protocadherin-24 (PCDH24) and mucin-like protocadherin (MLPCDH) (Crawley et al., 2014b). The protocadherins PCDH24 and MLPCDH are highly expressed and localized to the tips of microvilli through interaction with the scaffolding protein harmonin-a and the molecular motor myosin-7b. Knockdown of both protocadherins interrupts brush border assembly (Crawley et al., 2014b).

Tight junctions (TJs) are not only part of the epithelial junctional complex but are also essential components for the formation and maintenance of brush border microvilli (Saotome et al., 2004; Casaletto et al., 2011; Whiteman et al., 2014; Tilston-Lunel et al., 2016; Margolis, 2018). Thus, disruptive compositions of cell-to-cell adhesion complexes cause the appearance of short and disorganized microvilli (Saotome et al., 2004; Casaletto et al., 2011; Whiteman et al., 2014; Charrier et al., 2015). For example, *ezr* plays an essential role in assembling TJ protein complexes and linking them to the actomyocin network. *Ezr*-mutant mice exhibit disrupted apical membrane complex formation during both fetal development and adult homeostasis, and the ultrastructure of microvilli shows irregular and fused morphologies (Saotome et al., 2004; Casaletto et al., 2011). In addition, loss of the gene encoding Crumbs3 (Crb3), which is a binding protein of ezrin, also exhibits irregular fused villi and shortened microvilli as a major phenotype (Whiteman et al., 2014; Charrier et al., 2015). These results demonstrate that membrane-cytoskeleton crosslinking plays an important role in nascent microvilli stabilization and elongation.

CRYPT-VILLUS MORPHOGENESIS IN INTESTINAL ORGANOIDS

Intestinal cell lines based on two-dimensional (2D) culture technology grow flat monolayers and attach to the bottom, impeding dynamic morphogenesis such as crypt-villus formation. With the recent development of three-dimensional (3D) organoid culture methods, cell culture conditions more closely resemble *in vivo* cellular activity, and dynamic cell morphogenesis, including crypt-villus formation, is more similar to its *in vivo* counterpart (Ootani et al., 2009; Sato et al., 2009; Spence et al., 2011b; Jung et al., 2018; Wang S. et al., 2019; Zhang et al., 2020). For example, organoids contain a budding structure surrounding the central lumen; this budding domain is structurally and functionally similar to the intestinal crypt domain (Sato et al., 2009; Sato and Clevers, 2013). Similar to *in vivo* intestinal crypt domain, $Lgr5^{+}$ ISCs, which are enriched in the budding domain, continuously divide to generate self-renewing stem cells, as well as cells terminally differentiated into enterocytes, Paneth cells, goblet cells, and enteroendocrine cells. The terminally differentiated cells migrate to the central lumen to form a villus-like domain, and eventually undergo a cell death process as they are extruded into the lumen. Furthermore, cytokines such as EGF, R-Spondin 1, and Noggin, which are

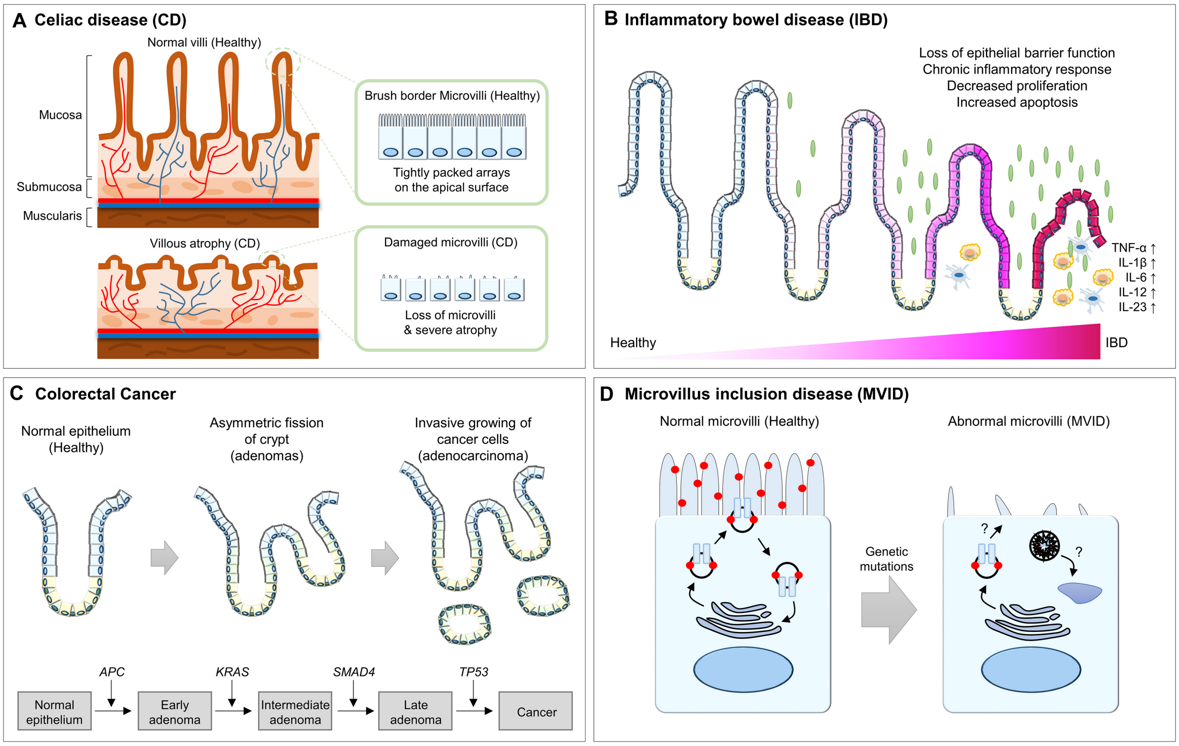

FIGURE 4 | Summary of the abnormalities of intestinal epithelium in human diseases. **(A)** The healthy intestinal epithelium is compartmentalized into crypt-villus structures and consists of a tightly packed array of microvilli. In CD patients, villus atrophy causes the surface area reduction of the intestinal epithelium. **(B)** In IBD patients, chronic inflammation results in architectural abnormalities of the intestinal epithelium, which leads to distinct morphological changes within the intestinal epithelium. **(C)** In CRC patients, hyperplasia of poorly differentiated intestinal epithelial cells and invasion into the submucosal layer for metastasis is frequently observed. **(D)** In MVID patients, microvilli are distorted or absent and are instead accumulated with microvillus inclusions, which are formed by a yet unresolved mechanism. CD, celiac disease; IBD, inflammatory bowel disease; CRC, colorectal cancer; APC, adenomatous polyposis coli; MVID, microvillus inclusion disease.

essential for the formation of intestinal stem niche *in vivo*, should be included in the organoid culture medium to maintain the structural and functional properties of the intestinal organoid as the growth and differentiation of intestinal organoids is carried out by a mechanism similar to that of the intestine *in vivo* (Sato et al., 2009).

The intestinal organoids contain the crypt-villus compartment, allowing the implementation of crypt-villus morphogenesis *in vitro* (Dahl-Jensen and Grapin-Botton, 2017; Serra et al., 2019). Recently, an intestinal organoid culture technique was applied to elucidate the molecular mechanisms associated with self-organization via symmetry breaking. It has been found that these processes also play critical roles in *in vivo* intestinal morphogenesis (Serra et al., 2019). When an intestinal organoid was formed from a single ISC, it remained in a state of equilibrium, with little difference between cells until the four-cell-stage. However, in the eight- and sixteen-cell stages, the localization of YAP1 was changed in a subset of cells, and variability in the nuclear localization of YAP1 initiated symmetry breaking through a Notch-DLL1 lateral inhibition mechanism. Finally, nuclear YAP1-positive cells differentiated into Paneth cells, leading to the formation of asymmetric spheres with initial crypt-like structures. Notably, Lgr5$^+$ ISCs appear by locally induced canonical Wnt signaling, and nascent crypts are reestablished by returning the stem cell niche to homeostasis (Serra et al., 2019). Organoid development from a single stem cell in a 3D culture system is considerably similar to the *in vivo* intestinal tissue regeneration process, and the molecules and signaling pathways involved in organoid development are also conserved. The initial crypt formation process occurs by a symmetry-breaking event; the crypt-villus separation process is also recapitulated in a 3D organoid culture system. When a crypt-like protrusion is generated from a round-shaped organoid, specialized wedge-shaped cells referred to as hinge cells appear at the crypt/villus boundaries (Sumigray et al., 2018; Hartl et al., 2019). These hinge cells also exist in the postnatal mouse intestine at the hinge region, and hinge formation is regulated by Rac1 activity. Upon loss of Rac1 in the mouse intestine, wedge-shaped hinge cells were absent, and the crypt/villus boundaries were ambiguous. Remarkably, genetic ablation of Rac1 in intestinal organoids reproduced abnormal compartmentalization of the crypt and villus region (Sumigray et al., 2018).

In general, 3D organoids are usually cultivated inside 3D matrices such as Matrigel. However, it is difficult to cultivate homogeneous organoids, increase the size on a macroscale, and perform experimental manipulation. In order to overcome these limitations, various types of organoid culture methods that use tissue engineering techniques have been developed (Murrow et al., 2017). For example, a technique for culture standardization of organoid culture using microcavity arrays within a polymer-hydrogel substrate (Brandenberg et al., 2020), and a culture technique to create a 3D crypt/villus structure by applying environmental stimuli (e.g., air-liquid interface) to 2D flat ISC monolayer on the transwell plate or microfluidic chip (Kim et al., 2012; Wang et al., 2015). In addition, it is also possible to generate organoids structurally and functionally similar to the *in vivo* intestinal epithelium by culturing ISCs on a scaffold that mimic crypt/villus structure using micropatterning or bioprinting technology (Wang et al., 2017; Brassard et al., 2020). These new technologies not only simulate the developmental process of crypt/villus itself, but also enable various applied research such as *in vitro* modeling of interaction among the intrinsic genetic factors and extrinsic environmental factors. Furthermore, since organoids are easily genetically manipulated though genome editing technology, genetically engineered intestinal organoids can be used to identify the roles of various genes related to crypt-villus morphogenesis (**Table 1**).

Intestinal organoids can be used in many ways to study crypt/villus morphogenesis, but there are still many limitations to be overcome. First, organoids currently in use consist mostly of epithelial cell. As cell-to-cell interactions with stromal cells including mesenchymal fibroblast are important in crypt/villus morphogenesis (Walton et al., 2016), it is necessary to develop organoid culture method with various cell composition. Recently, as intestinal organoid differentiation methods composed of multi-lineage cells or technologies for co-culture with various cells are actively developed, these limitations are expected to be overcome in the near future (Workman et al., 2017; Holloway et al., 2020). Second, it is necessary to develop organoid culture methods that enable changes to the environmental factors according to the crypt/villus developmental process. Currently, Matrigel is the most widely used matrix for organoid culture given its high efficiency and utility, but the batch-by-batch variation and impossible modification due to unclear chemical composition prevent its application in advanced research. Therefore, it is necessary to develop a matrix that can replace Matrigel; such new matrix should not only have a defined chemical composition and structure that can be easily modified. Currently, various matrices including hydrogel-based macromolecules have been developed (Aisenbrey and Murphy, 2020), including synthetic matrices whose physical properties change according to the crypt/villus morphogenesis of intestinal organoids (Gjorevski et al., 2016). Based on these technologies, diverse application studies have been conducted, but there are still room for improvements including their long-term stability to enable long-term culture of intestinal organoids in the future.

ROLE OF GUT MICROBIOTA DURING INTESTINAL MORPHOGENESIS

Although the basic morphology of the human intestine is formed before birth, structural and functional maturation takes place after birth, and it is known that intestinal microbiota play an important role in the structural and functional development and maturation of the human intestine (Hooper, 2004). Remarkably, germ-free mice exhibit enormous morphological defects including a decreased intestinal surface (Gordon and Bruckner-Kardoss, 1961), abnormal villus formation (Abrams et al., 1963), reduced crypt depth (Yu et al., 2016), impaired shifting of intestinal epithelial glycans (Bry et al., 1996), and poor development of the villus capillaries (Stappenbeck et al., 2002). However, these developmental defects can be compensated in adult germ-free mice upon colonization of a normal gut microbiota or a single member of gut microflora such as *B. thetaiotaomicron* (Bry et al., 1996; Hooper et al., 1999), thus suggesting that gut microbiota is essential for gut development and morphogenesis.

The bi-directional communication between intestinal epithelium and gut microbiota is important for intestinal epithelial morphogenesis, but it is still unclear why colonization of gut microbiota is necessary for intestinal epithelial morphogenesis at the molecular level. Based on recent studies, the most probable cause is that gut microbiota-derived metabolites can control the intestinal epithelial morphogenesis by affecting intestinal epithelial cell differentiation and maturation

TABLE 1 | Summary of gene list related to morphological abnormalities in crypt-villus structure.

Compartment	Ablated gene(s)	Intestinal phenotype	References
Villus	*Pdgf-A KO Pdgfr-α KO*	Abnormal GI mucosal lining misshapen villi loss of pericryptal mesenchyme	Karlsson et al., 2000
	Shh; Ihh dKO	Embryonic lethal reduced mesenchymal cell proliferation	Mao et al., 2010
	Foxf1;Foxf2 dKO	Died shortly after birth large clusters of epithelial cells and club-shaped with multilayered epithelia	Ormestad et al., 2006
	Fat4 KO	improperly patterned villi extensive fused villus regions failure of stromal clustering	Rao-Bhatia et al., 2020
	Wnt5a KO	Shortened and bifurcated intestinal lumen reduced smooth muscle layer fused villi	Rao-Bhatia et al., 2020 Cervantes et al., 2009
Crypt	*MyoIIA;MyoIIC dKO*	Disruption in apical constriction and invagination of crypt cells	Sumigray et al., 2018
	Rac1 KO	Flat surface and short villi crypt cell expansion deep crypts and short villi	Sumigray et al., 2018
Microvillus	*EPS8 KO*	Reduced microvillus length	Tocchetti et al., 2010
	Espn;Vil1;Pls1 tKO	Delay growth of microvilli sparse and misorganized microvillar actin filament bundles	Revenu et al., 2012
	Harmonin KO	Significant disruption in brush border morphology short and disorganized irregular microvilli	Crawley et al., 2014b
	Ezr KO	Short, thick, and Non-uniform architecture of microvilli disorganized and fused villi	Saotome et al., 2004
	Crb3 KO	Irregular and fused villi and apical membrane bleb disrupted microvilli	Whiteman et al., 2014

(Koh et al., 2016). Indeed, the morphological development and functional maturation of intestinal epithelium is deeply related to the diet, and in particular, the intestinal epithelium undergoes an enormous morphological changes and functional maturation during the weaning period, which is a transition from milk feeding to solid food intake (Subramanian et al., 2015). Dietary transition alters the composition and metabolism of the gut microbiota, resulting in dependence of the bi-directional interaction between gut microbiota and intestinal epithelium on dietary intake. Some of the major products from the gut microbiota are short chain fatty acids (SCFAs) including acetate, propionate, and butyrate (Cummings et al., 1987). At the cellular level, SCFAs have direct and indirect effects on the intestinal epithelial cell proliferation, differentiation, and gene expression, and butyrate reportedly suppresses colonic stem cell proliferation through receptors encoded by *Ffar3*, *Ffar2*, and *Niacr1* (Lee and Hase, 2014; Kaiko et al., 2016). Apart from SCFAs, various metabolites such as folate, bile acids, and vitamins can affect intestinal morphogenesis and functional maturation; however, further studies are required to elucidate the underlying molecular mechanisms.

ABNORMALITIES OF THE INTESTINAL EPITHELIUM IN HUMAN DISEASE

The intestinal epithelium is compartmentalized into crypt-villus structures to maintain homeostasis and perform efficient intestinal functions. These crypt-villus units are tightly regulated by complex mechanisms, but if abnormalities occur in the crypt-villus structure, this results in various intestinal dysfunctions and disorders.

Celiac Disease (CD)

CD, also known as celiac sprue or gluten-sensitive enteropathy, is an autoimmune disorder caused by an immune reaction triggered by ingested gluten and is by far the most common cause of villus atrophy (Aziz et al., 2017; Jansson-Knodell et al., 2018). In the small bowel, it is known that an abnormal immune response by gluten exposure causes an inflammatory response and induces villus atrophy or a significant reduction in the number of villi (Fasano, 2005; Vivas et al., 2015). Villus atrophy reduces the surface area of the intestinal epithelium and causes insufficient absorption of nutrients, micronutrients, water, and electrolytes. Therefore, multiple symptoms of intestinal dysfunctions are frequently observed in CD patients, including chronic or recurrent diarrhea, abdominal distention, anorexia, excessive nutrient deficiency, and failure to lose weight (Fasano, 2005; Vivas et al., 2015).

Inflammatory Bowel Disease (IBD)

Although the etiology of IBD is complex, it is believed that dysregulation of the function of the intestinal epithelial barrier triggers an inappropriate immune response, leading to IBD (Kaser et al., 2010; Coskun, 2014). In fact, the loss of intestinal epithelial barrier function by altered expression of and structural changes in the intestinal TJ proteins induces epithelial damage and mucosal inflammation (Schmitz et al., 1999; Heller et al., 2005; Zeissig et al., 2007). Moreover, a disrupted epithelial architecture due to an imbalanced rate of epithelial cell proliferation and apoptosis also increases development of the chronic inflammatory response (Edelblum et al., 2006; Koch and Nusrat, 2012). IBD animal models with chronic tumor necrosis factor-[α] overexpression or dextran sulfate sodium administration exhibit significant villus atrophy and elevated epithelial cell death along the crypt-villus axis, which is most prominent at the villus tip in acute and chronic inflammation (Westbrook and Schiestl, 2010; Gunther et al., 2013; Parker et al., 2019; Lee et al., 2020). This long-lasting chronic inflammation resulting from architectural abnormalities of the intestinal epithelium leads to distinct morphological changes within the intestinal epithelium (Koch and Nusrat, 2012). This feedback loop between disrupted intestinal epithelium and chronic inflammation eventually causes the development of IBD.

Cancer

Colorectal cancer (CRC) initially forms a benign adenoma and then develops into invasive and metastatic adenocarcinoma through the stepwise accumulation of multiple genetic and epigenetic aberrations (Fearon and Vogelstein, 1990; Grady, 2005; Nguyen and Duong, 2018). In many cases, hundreds to thousands of adenomas or adenomatous polyps are formed in CRC patients via an acquired mutation in the adenomatous polyposis coli (*APC*) gene (Fearon and Vogelstein, 1990; Kinzler and Vogelstein, 1996). These adenomas display enlarged crypts and subsequent cryptic fissions, which protrude into the intestinal lumen (Wasan et al., 1998; Taketo, 2006; Barker et al., 2007; Jones et al., 2008). For example, the representative *Apc* mutant mouse strain $Apc^{\Delta 716}$ (truncating mutation at codon 716) develops numerous polyps, not only in the small intestine, but also in the distal colon. Using this mouse model, it was determined that polyp formation is initiated by loss of heterozygosity at the *Apc* locus in proliferative zone cells, followed by the formation of an outpocket in the intestinal crypt. Interestingly, as the adenoma is covered by normal villus epithelium in the intestinal lumen, the growing adenoma does not break the crypt-villus structure. Even in relatively advanced polyps consisting of multiple villi, the normal villus epithelium is still conserved (Oshima et al., 1997; Taketo, 2006). However, malignant transformation and adenocarcinoma progresses due to continuous clonal expansion, with mutations in genes such as *KRAS*, *PIK3CA*, *SMAD4,* and *TP53*. This results in severe structural abnormalities, such as hyperplasia of poorly differentiated intestinal epithelial cells and invasion into the submucosal layer for metastasis (Humphries and Wright, 2008; Jones et al., 2008; Vogelstein et al., 2013).

Brush Border-Related Enteropathies

The brush border on the apical surface of enterocytes consists of a tightly packed array of microvilli, which are required for supporting the apical structure and maintaining intestinal functionalities. Therefore, disrupted integrity, either through inherited or pathogen-induced defects, leads to severe disease of the intestinal epithelium. For example, microvillus inclusion disease (MVID) is a rare human congenital enteropathy that is an autosomal recessive disorder. It is characterized by chronic, severe, watery diarrhea and the insufficient absorption of necessary nutrients in newborn infants, typically beginning in the first hours to days of life. It is known that perturbed apical endosomal trafficking causes many of the abnormalities of MVID, such as defective brush border assembly, increased numbers of subapical vesicles, and the presence of microvillus inclusions in the apical region of villus enterocytes (Cutz et al., 1989; Ameen and Salas, 2000; Sherman et al., 2004; Ruemmele et al., 2006). Since apical endosomal trafficking regulates microvillus development and targeted protein delivery to the apical brush border, mutations in the *RAB8*, *RAB11*, and *MYO5B* genes associated with apical endosomal trafficking result in the MVID-like phenotype (Sato et al., 2007; Muller et al., 2008; Sobajima et al., 2014; Knowles et al., 2015). Another rare human enteropathy, congenital tufting enteropathy, is associated with mutations in the *EPCAM* and *SPINT2* genes, which result in the display of focal stacks of multiple layers of enterocytes and microvilli atrophy (Patey et al., 1997; Slae et al., 2013). In addition, a dominant mutation in *GUGY2C* and recessive mutations in *NHE3* lead to abnormalities in the apical brush border microvilli, resulting in chronic diarrhea (Janecke et al., 2015; Muller et al., 2016).

CONCLUSION AND FUTURE DIRECTIONS

The intestinal epithelium serves as a physical and functional barrier interfacing the external environment and luminal contents, including digestive nutrients, orally administered drugs, the microbiome, and antigens. One of the most important goals of this area of research is to understand how to establish or regenerate a normal and fully functional intestine that can successfully form crypt-villus architecture. However, there is a large gap in the knowledge surrounding morphogenesis during human intestinal development. Recent technical advances, such as the ability to culture primary intestinal tissues or organoids and the use of human PSC-derived intestinal organoids, provide new and exciting avenues for understanding the molecular mechanisms involved in human intestinal morphogenesis. To achieve a comprehensive understanding of intestinal morphogenesis and its dynamic function, multidisciplinary approaches and the development of state-of-the-art model systems offer new ways to further our understanding.

Research on intestinal epithelial morphogenesis and regeneration is rapidly expanding, but further studies related to intestinal epithelial morphogenesis and regeneration are still needed. First, through comparative analysis of normal and abnormal intestinal epithelium, key molecules and signaling pathways that are important for intestinal epithelial morphogenesis and regeneration should be identified. As high-throughput technologies such as single cell RNA sequencing and automated imaging are advancing, the understanding of the molecular mechanism of intestinal epithelial morphogenesis and regeneration is rapidly expanding. Another is the need to figure out the interactions with environmental factors such as nutrition status, mesenchymal cell composition, and gut microbiome colonization that influence intestinal epithelial morphogenesis and regeneration. Recently, bi-directional communication between intestinal epithelium and environmental factors during intestinal epithelial morphogenesis and regeneration can be recapitulated *in vitro* due to the development of the diverse platform technologies including organoid culture and co-culture in microchips. These can help the development of novel therapeutics such as probiotics that can successfully regenerate the intestinal epithelium in patients with intestinal failure or short bowel syndrome.

AUTHOR CONTRIBUTIONS

All authors contributed to the conception, writing, and review of the manuscript.

FUNDING

This work was supported by a grant from the Technology Innovation Program (No. 20008777) and 3D-TissueChip Based Drug Discovery Platform Technology Development Program (No. 20009774) funded by the Ministry of Trade, Industry & Energy (MOTIE, South Korea), grant from the National Research Foundation of Korea (NRF) funded by the Ministry of Science, ICT, and Future Planning (NRF-2018M3A9H3023077 and 2020R1C1C1007431), and the KRIBB Research Initiative Program. The funders had no role in the study design, data collection or analysis, decision to publish, or preparation of the manuscript.

REFERENCES

Abrams, G. D., Bauer, H., and Sprinz, H. (1963). Influence of the normal flora on mucosal morphology and cellular renewal in the ileum. A comparison of germ-free and conventional mice. *Lab. Invest.* 12, 355–364.

Aisenbrey, E. A., and Murphy, W. L. (2020). Synthetic alternatives to Matrigel. *Nat. Rev. Mater.* 5, 539–551. doi: 10.1038/s41578-020-0199-8

Ameen, N. A., and Salas, P. J. (2000). Microvillus inclusion disease: a genetic defect affecting apical membrane protein traffic in intestinal epithelium. *Traffic* 1, 76–83. doi: 10.1034/j.1600-0854.2000.010111.x

Aziz, I., Peerally, M. F., Barnes, J. H., Kandasamy, V., Whiteley, J. C., Partridge, D., et al. (2017). The clinical and phenotypical assessment of seronegative villous atrophy; a prospective UK centre experience evaluating 200 adult cases over a 15-year period (2000-2015). *Gut* 66, 1563–1572. doi: 10.1136/gutjnl-2016-312271

Barker, N. (2014). Adult intestinal stem cells: critical drivers of epithelial homeostasis and regeneration. *Nat. Rev. Mol. Cell Biol.* 15, 19–33. doi: 10.1038/nrm3721

Barker, N., Van Es, J. H., Kuipers, J., Kujala, P., Van Den Born, M., Cozijnsen, M., et al. (2007). Identification of stem cells in small intestine and colon by marker gene Lgr5. *Nature* 449, 1003–1007. doi: 10.1038/nature06196

Bartles, J. R. (2000). Parallel actin bundles and their multiple actin-bundling proteins. *Curr. Opin. Cell Biol.* 12, 72–78. doi: 10.1016/S0955-0674(99)00059-9

Beumer, J., and Clevers, H. (2016). Regulation and plasticity of intestinal stem cells during homeostasis and regeneration. *Development* 143, 3639–3649. doi: 10.1242/dev.133132

Brandenberg, N., Hoehnel, S., Kuttler, F., Homicsko, K., Ceroni, C., Ringel, T., et al. (2020). High-throughput automated organoid culture via stem-cell aggregation in microcavity arrays. *Nat. Biomed. Eng.* 4, 863–874. doi: 10.1038/s41551-020-0565-2

Brassard, J. A., Nikolaev, M., Hubscher, T., Hofer, M., and Lutolf, M. P. (2020). Recapitulating macro-scale tissue self-organization through organoid bioprinting. *Nat. Mater.* doi: 10.1038/s41563-020-00803-5 [Epub ahead of print].

Bry, L., Falk, P. G., Midtvedt, T., and Gordon, J. I. (1996). A model of host-microbial interactions in an open mammalian ecosystem. *Science* 273, 1380–1383. doi: 10.1126/science.273.5280.1380

Cai, J., Zhang, N., Zheng, Y., De Wilde, R. F., Maitra, A., and Pan, D. (2010). The Hippo signaling pathway restricts the oncogenic potential of an intestinal regeneration program. *Genes Dev.* 24, 2383–2388. doi: 10.1101/gad.1978810

Casaletto, J. B., Saotome, I., Curto, M., and Mcclatchey, A. I. (2011). Ezrin-mediated apical integrity is required for intestinal homeostasis. *Proc. Natl. Acad. Sci. U.S.A.* 108, 11924–11929. doi: 10.1073/pnas.1103418108

Cervantes, S., Yamaguchi, T. P., and Hebrok, M. (2009). Wnt5a is essential for intestinal elongation in mice. *Dev. Biol.* 326, 285–294. doi: 10.1016/j.ydbio.2008.11.020

Charrier, L. E., Loie, E., and Laprise, P. (2015). Mouse Crumbs3 sustains epithelial tissue morphogenesis in vivo. *Sci. Rep.* 5:17699. doi: doi.org/10.1038/srep17699

Clevers, H. (2013). The intestinal crypt, a prototype stem cell compartment. *Cell* 154, 274–284. doi: 10.1016/j.cell.2013.07.004

Coquenlorge, S., Yin, W. C., Yung, T., Pan, J., Zhang, X., Mo, R., et al. (2019). GLI2 modulated by SUFU and SPOP induces intestinal stem cell niche signals in development and tumorigenesis. *Cell Rep.* 27, 3006–3018.e3004. doi: 10.1016/j.celrep.2019.05.016

Coskun, M. (2014). Intestinal epithelium in inflammatory bowel disease. *Front. Med.* 1:24. doi: 10.3389/fmed.2014.00024

Crawley, S. W., Mooseker, M. S., and Tyska, M. J. (2014a). Shaping the intestinal brush border. *J. Cell Biol.* 207, 441–451. doi: 10.1083/jcb.201407015

Crawley, S. W., Shifrin, D. A. Jr., Grega-Larson, N. E., Mcconnell, R. E., and Benesh, A. E. (2014b). Intestinal brush border assembly driven by protocadherin-based intermicrovillar adhesion. *Cell* 157, 433–446. doi: 10.1016/j.cell.2014.01.067

Crosnier, C., Stamataki, D., and Lewis, J. (2006). Organizing cell renewal in the intestine: stem cells, signals and combinatorial control. *Nat. Rev. Genet.* 7, 349–359. doi: 10.1038/nrg1840

Cummings, J. H., Pomare, E. W., Branch, W. J., Naylor, C. P., and Macfarlane, G. T. (1987). Short chain fatty acids in human large intestine, portal, hepatic and venous blood. *Gut* 28, 1221–1227. doi: 10.1136/gut.28.10.1221

Cutz, E., Rhoads, J. M., Drumm, B., Sherman, P. M., Durie, P. R., and Forstner, G. G. (1989). Microvillus inclusion disease: an inherited defect of brush-border assembly and differentiation. *N. Engl. J. Med.* 320, 646–651. doi: 10.1056/NEJM198903093201006

Dahl-Jensen, S., and Grapin-Botton, A. (2017). The physics of organoids: a biophysical approach to understanding organogenesis. *Development* 144, 946–951. doi: 10.1242/dev.143693

Dehmer, J. J., Garrison, A. P., Speck, K. E., Dekaney, C. M., Van Landeghem, L., Sun, X., et al. (2011). Expansion of intestinal epithelial stem cells during murine development. *PLoS One* 6:e27070. doi: 10.1371/journal.pone.0027070

Delacour, D., Salomon, J., Robine, S., and Louvard, D. (2016). Plasticity of the brush border - the yin and yang of intestinal homeostasis. *Nat. Rev. Gastroenterol. Hepatol.* 13, 161–174. doi: 10.1038/nrgastro.2016.5

Edelblum, K. L., Yan, F., Yamaoka, T., and Polk, D. B. (2006). Regulation of apoptosis during homeostasis and disease in the intestinal epithelium. *Inflamm. Bowel Dis.* 12, 413–424. doi: 10.1097/01.MIB.0000217334.30689.3e

Edwards, M., Zwolak, A., Schafer, D. A., Sept, D., Dominguez, R., and Cooper, J. A. (2014). Capping protein regulators fine-tune actin assembly dynamics. *Nat. Rev. Mol. Cell Biol.* 15, 677–689. doi: doi.org/10.1038/nrm3869

Fasano, A. (2005). Clinical presentation of celiac disease in the pediatric population. *Gastroenterology* 128, S68–S73. doi: 10.1053/j.gastro.2005.02.015

Fath, K. R., Mamajiwalla, S. N., and Burgess, D. R. (1993). The cytoskeleton in development of epithelial cell polarity. *J. Cell Sci. Suppl.* 17, 65–73.doi: 10.1242/jcs.1993.Supplement_17.10

Fearon, E. R., and Vogelstein, B. (1990). A genetic model for colorectal tumorigenesis. *Cell* 61, 759–767. doi: 10.1016/0092-8674(90)90186-I

Fehon, R. G., Mcclatchey, A. I., and Bretscher, A. (2010). Organizing the cell cortex: the role of ERM proteins. *Nat. Rev. Mol. Cell Biol.* 11, 276–287.doi: 10.1038/nrm2866

Freddo, A. M., Shoffner, S. K., Shao, Y., Taniguchi, K., Grosse, A. S., Guysinger, M. N., et al. (2016). Coordination of signaling and tissue mechanics during morphogenesis of murine intestinal villi: a role for mitotic cell rounding. *Integr. Biol.* 8, 918–928. doi: 10.1039/C6IB00046K

Gjorevski, N., Sachs, N., Manfrin, A., Giger, S., Bragina, M. E., Ordonez-Moran, P., et al. (2016). Designer matrices for intestinal stem cell and organoid culture. *Nature* 539, 560–564. doi: 10.1038/nature20168

Gordon, H. A., and Bruckner-Kardoss, E. (1961). Effect of normal microbial flora on intestinal surface area. *Am. J. Physiol.* 201, 175–178. doi: 10.1152/ajplegacy.1961.201.1.175

Goulet, O., Ruemmele, F., Lacaille, F., and Colomb, V. (2004). Irreversible intestinal failure. *J. Pediatr. Gastroenterol. Nutr.* 38, 250–269. doi: 10.1097/00005176-200403000-00006

Grady, W. M. (2005). Epigenetic events in the colorectum and in colon cancer. *Biochem. Soc. Trans.* 33, 684–688. doi: 10.1042/BST0330684

Gregorieff, A., Pinto, D., Begthel, H., Destree, O., Kielman, M., and Clevers, H. (2005). Expression pattern of Wnt signaling components in the adult intestine. *Gastroenterology* 129, 626–638. doi: 10.1016/j.gastro.2005.06.007

Grimm-Gunter, E. M., Revenu, C., Ramos, S., Hurbain, I., Smyth, N., Ferrary, E., et al. (2009). Plastin 1 binds to keratin and is required for terminal web assembly in the intestinal epithelium. *Mol. Biol. Cell* 20, 2549–2562. doi: 10.1091/mbc.e08-10-1030

Grosse, A. S., Pressprich, M. F., Curley, L. B., Hamilton, K. L., Margolis, B., Hildebrand, J. D., et al. (2011). Cell dynamics in fetal intestinal epithelium: implications for intestinal growth and morphogenesis. *Development* 138, 4423–4432. doi: 10.1242/dev.065789

Gunther, C., Neumann, H., Neurath, M. F., and Becker, C. (2013). Apoptosis, necrosis and necroptosis: cell death regulation in the intestinal epithelium. *Gut* 62, 1062–1071. doi: 10.1136/gutjnl-2011-301364

Hartl, L., Huelsz-Prince, G., Van Zon, J., and Tans, S. J. (2019). Apical constriction is necessary for crypt formation in small intestinal organoids. *Dev. Biol.* 450, 76–81. doi: 10.1016/j.ydbio.2019.03.009

He, X. C., Zhang, J., Tong, W. G., Tawfik, O., Ross, J., Scoville, D. H., et al. (2004). BMP signaling inhibits intestinal stem cell self-renewal through suppression of Wnt-beta-catenin signaling. *Nat. Genet.* 36, 1117–1121. doi: 10.1038/ng1430

Helander, H. F., and Fandriks, L. (2014). Surface area of the digestive tract - revisited. *Scand. J. Gastroenterol.* 49, 681–689. doi: 10.3109/00365521.2014.898326

Heller, F., Florian, P., Bojarski, C., Richter, J., Christ, M., Hillenbrand, B., et al. (2005). Interleukin-13 is the key effector Th2 cytokine in ulcerative colitis that affects epithelial tight junctions, apoptosis, and cell restitution. *Gastroenterology* 129, 550–564. doi: 10.1016/j.gastro.2005.05.002

Holloway, E. M., Wu, J. H., Czerwinski, M., Sweet, C. W., Wu, A., Tsai, Y. H., et al. (2020). Differentiation of human intestinal organoids with endogenous vascular endothelial cells. *Dev. Cell* 54, 516–528.e517.doi: 10.1016/j.devcel.2020.07.023

Hooper, L. V. (2004). Bacterial contributions to mammalian gut development. *Trends Microbiol.* 12, 129–134. doi: 10.1016/j.tim.2004.01.001

Hooper, L. V., Xu, J., Falk, P. G., Midtvedt, T., and Gordon, J. I. (1999). A molecular sensor that allows a gut commensal to control its nutrient foundation in a competitive ecosystem. *Proc. Natl. Acad. Sci. U.S.A.* 96, 9833–9838. doi: 10.1073/pnas.96.17.9833

Humphries, A., and Wright, N. A. (2008). Colonic crypt organization and tumorigenesis. *Nat. Rev. Cancer* 8, 415–424. doi: 10.1038/nrc2392

Iizuka, M., and Konno, S. (2011). Wound healing of intestinal epithelial cells. *World J. Gastroenterol.* 17, 2161–2171. doi: 10.3748/wjg.v17.i17.2161

Janecke, A. R., Heinz-Erian, P., Yin, J., Petersen, B. S., Franke, A., Lechner, S., et al. (2015). Reduced sodium/proton exchanger NHE3 activity causes congenital sodium diarrhea. *Hum. Mol. Genet.* 24, 6614–6623. doi: 10.1093/hmg/ddv367

Jansson-Knodell, C. L., Hujoel, I. A., Rubio-Tapia, A., and Murray, J. A. (2018). Not all that flattens villi is celiac disease: a review of enteropathies. *Mayo Clin. Proc.* 93, 509–517. doi: 10.1016/j.mayocp.2017.10.025

Jones, S., Chen, W. D., Parmigiani, G., Diehl, F., Beerenwinkel, N., Antal, T., et al. (2008). Comparative lesion sequencing provides insights into tumor evolution. *Proc. Natl. Acad. Sci. U.S.A.* 105, 4283–4288. doi: 10.1073/pnas.0712345105

Jung, K. B., Lee, H., Son, Y. S., Lee, M. O., Kim, Y. D., Oh, S. J., et al. (2018). Interleukin-2 induces the in vitro maturation of human pluripotent stem cell-derived intestinal organoids. *Nat. Commun.* 9:3039. doi: 10.1038/s41467-018-05450-8

Kaestner, K. H., Silberg, D. G., Traber, P. G., and Schutz, G. (1997). The mesenchymal winged helix transcription factor Fkh6 is required for the control of gastrointestinal proliferation and differentiation. *Genes Dev.* 11, 1583–1595. doi: 10.1101/gad.11.12.1583

Kaiko, G. E., Ryu, S. H., Koues, O. I., Collins, P. L., Solnica-Krezel, L., Pearce, E. J., et al. (2016). The colonic crypt protects stem cells from microbiota-derived metabolites. *Cell* 167:1137. doi: 10.1016/j.cell.2016.05.018

Karlsson, L., Lindahl, P., Heath, J. K., and Betsholtz, C. (2000). Abnormal gastrointestinal development in PDGF-A and PDGFR-(alpha) deficient mice implicates a novel mesenchymal structure with putative instructive properties in villus morphogenesis. *Development* 127, 3457–3466.

Kaser, A., Zeissig, S., and Blumberg, R. S. (2010). Inflammatory bowel disease. *Annu. Rev. Immunol.* 28, 573–621. doi: 10.1146/annurev-immunol-030409-101225

Kaur, H., and Moreau, R. (2019). Role of mTORC1 in intestinal epithelial repair and tumorigenesis. *Cell Mol. Life Sci.* 76, 2525–2546. doi: 10.1007/s00018-019-03085-6

Kim, H. B., Kim, M., Park, Y. S., Park, I., Kim, T., Yang, S. Y., et al. (2017). Prostaglandin E2 Activates YAP and a positive-signaling loop to promote colon regeneration after colitis but also carcinogenesis in mice. *Gastroenterology* 152, 616–630. doi: 10.1053/j.gastro.2016.11.005

Kim, H. J., Huh, D., Hamilton, G., and Ingber, D. E. (2012). Human gut-on-a-chip inhabited by microbial flora that experiences intestinal peristalsis-like motions and flow. *Lab. Chip.* 12, 2165–2174.doi: 10.1039/c2lc40074j

Kinzler, K. W., and Vogelstein, B. (1996). Lessons from hereditary colorectal cancer. *Cell* 87, 159–170. doi: 10.1016/S0092-8674(00)81333-1

Knowles, B. C., Weis, V. G., Yu, S., Roland, J. T., Williams, J. A., Alvarado, G. S., et al. (2015). Rab11a regulates syntaxin 3 localization and microvillus assembly in enterocytes. *J. Cell Sci.* 128, 1617–1626. doi: 10.1242/jcs.163303

Koch, S., and Nusrat, A. (2012). The life and death of epithelia during inflammation: lessons learned from the gut. *Annu. Rev. Pathol.* 7, 35–60. doi: 10.1146/annurev-pathol-011811-120905

Koh, A., De Vadder, F., Kovatcheva-Datchary, P., and Backhed, F. (2016). From dietary fiber to host physiology: short-chain fatty acids as key bacterial metabolites. *Cell* 165, 1332–1345. doi: 10.1016/j.cell.2016.05.041

Koivisto, L., Heino, J., Hakkinen, L., and Larjava, H. (2014). Integrins in wound healing. *Adv. Wound Care* 3, 762–783.doi: 10.1089/wound.2013.0436

Kolterud, A., Grosse, A. S., Zacharias, W. J., Walton, K. D., Kretovich, K. E., Madison, B. B., et al. (2009). Paracrine Hedgehog signaling in stomach and intestine: new roles for hedgehog in gastrointestinal patterning. *Gastroenterology* 137, 618–628. doi: 10.1053/j.gastro.2009.05.002

Kondo, T., and Hayashi, S. (2013). Mitotic cell rounding accelerates epithelial invagination. *Nature* 494, 125–129. doi: 10.1038/nature11792

Lee, H., Son, Y. S., Lee, M. O., Ryu, J. W., Park, K., Kwon, O., et al. (2020). Low-dose interleukin-2 alleviates dextran sodium sulfate-induced colitis in mice by recovering intestinal integrity and inhibiting AKT-dependent pathways. *Theranostics* 10, 5048–5063. doi: 10.7150/thno.41534

Lee, W. J., and Hase, K. (2014). Gut microbiota-generated metabolites in animal health and disease. *Nat. Chem. Biol.* 10, 416–424. doi: 10.1038/nchembio.1535

Lotz, M. M., Nusrat, A., Madara, J. L., Ezzell, R., Wewer, U. M., and Mercurio, A. M. (1997). Intestinal epithelial restitution. Involvement of specific laminin isoforms and integrin laminin receptors in wound closure of a transformed model epithelium. *Am. J. Pathol.* 150, 747–760.

Madison, B. B., Braunstein, K., Kuizon, E., Portman, K., Qiao, X. T., and Gumucio, D. L. (2005). Epithelial hedgehog signals pattern the intestinal crypt-villus axis. *Development* 132, 279–289. doi: 10.1242/dev.01576

Madison, B. B., Mckenna, L. B., Dolson, D., Epstein, D. J., and Kaestner, K. H. (2009). FoxF1 and FoxL1 link hedgehog signaling and the control of epithelial proliferation in the developing stomach and intestine. *J. Biol. Chem.* 284, 5936–5944. doi: 10.1074/jbc.M808103200

Manieri, N. A., Drylewicz, M. R., Miyoshi, H., and Stappenbeck, T. S. (2012). Igf2bp1 is required for full induction of Ptgs2 mRNA in colonic mesenchymal stem cells in mice. *Gastroenterology* 143, 110–121.e110. doi: 10.1053/j.gastro.2012.03.037

Manieri, N. A., Mack, M. R., Himmelrich, M. D., Worthley, D. L., Hanson, E. M., Eckmann, L., et al. (2015). Mucosally transplanted mesenchymal stem cells stimulate intestinal healing by promoting angiogenesis. *J. Clin. Invest.* 125, 3606–3618. doi: 10.1172/JCI81423

Mao, J., Kim, B. M., Rajurkar, M., Shivdasani, R. A., and Mcmahon, A. P. (2010). Hedgehog signaling controls mesenchymal growth in the developing mammalian digestive tract. *Development* 137, 1721–1729. doi: 10.1242/dev.044586

Margolis, B. (2018). The Crumbs3 polarity protein. *Cold Spring Harb. Perspect. Biol.* 10:a027961. doi: 10.1101/cshperspect.a027961

Marshman, E., Booth, C., and Potten, C. S. (2002). The intestinal epithelial stem cell. *Bioessays* 24, 91–98. doi: 10.1002/bies.10028

Martin, A. C., Kaschube, M., and Wieschaus, E. F. (2009). Pulsed contractions of an actin-myosin network drive apical constriction. *Nature* 457, 495–499. doi: 10.1038/nature07522

Metcalfe, C., Kljavin, N. M., Ybarra, R., and De Sauvage, F. J. (2014). Lgr5+ stem cells are indispensable for radiation-induced intestinal regeneration. *Cell Stem Cell* 14, 149–159. doi: 10.1016/j.stem.2013.11.008

Miyoshi, H., Ajima, R., Luo, C. T., Yamaguchi, T. P., and Stappenbeck, T. S. (2012). Wnt5a potentiates TGF-beta signaling to promote colonic crypt regeneration after tissue injury. *Science* 338, 108–113. doi: 10.1126/science.1223821

Miyoshi, H., Vandussen, K. L., Malvin, N. P., Ryu, S. H., Wang, Y., Sonnek, N. M., et al. (2017). Prostaglandin E2 promotes intestinal repair through an adaptive cellular response of the epithelium. *EMBO J.* 36, 5–24. doi: 10.15252/embj.201694660

Mooseker, M. S., Pollard, T. D., and Wharton, K. A. (1982). Nucleated polymerization of actin from the membrane-associated ends of microvillar filaments in the intestinal brush border. *J. Cell Biol.* 95, 223–233. doi: 10.1083/jcb.95.1.223

Muller, T., Hess, M. W., Schiefermeier, N., Pfaller, K., Ebner, H. L., Heinz-Erian, P., et al. (2008). MYO5B mutations cause microvillus inclusion disease and disrupt epithelial cell polarity. *Nat. Genet.* 40, 1163–1165. doi: /10.1038/ng.225

Muller, T., Rasool, I., Heinz-Erian, P., Mildenberger, E., Hulstrunk, C., Muller, A., et al. (2016). Congenital secretory diarrhoea caused by activating germline mutations in GUCY2C. *Gut* 65, 1306–1313. doi: 10.1136/gutjnl-2015-309441

Murrow, L. M., Weber, R. J., and Gartner, Z. J. (2017). Dissecting the stem cell niche with organoid models: an engineering-based approach. *Development* 144, 998–1007. doi: 10.1242/dev.140905

Nguyen, H. T., and Duong, H. Q. (2018). The molecular characteristics of colorectal cancer: Implications for diagnosis and therapy. *Oncol. Lett.* 16, 9–18. doi: 10.3892/ol.2018.8679

Nishimura, M., Inoue, Y., and Hayashi, S. (2007). A wave of EGFR signaling determines cell alignment and intercalation in the *Drosophila* tracheal placode. *Development* 134, 4273–4282. doi: 10.1242/dev.010397

Nusse, Y. M., Savage, A. K., Marangoni, P., Rosendahl-Huber, A. K. M., Landman, T. A., De Sauvage, F. J., et al. (2018). Parasitic helminths induce fetal-like reversion in the intestinal stem cell niche. *Nature* 559, 109–113. doi: 10.1038/s41586-018-0257-1

Ootani, A., Li, X., Sangiorgi, E., Ho, Q. T., Ueno, H., Toda, S., et al. (2009). Sustained in vitro intestinal epithelial culture within a Wnt-dependent stem cell niche. *Nat. Med.* 15, 701–706. doi: 10.1038/nm.1951

Ormestad, M., Astorga, J., Landgren, H., Wang, T., Johansson, B. R., Miura, N., et al. (2006). Foxf1 and Foxf2 control murine gut development by limiting mesenchymal Wnt signaling and promoting extracellular matrix production. *Development* 133, 833–843. doi: 10.1242/dev.02252

Oshima, H., Oshima, M., Kobayashi, M., Tsutsumi, M., and Taketo, M. M. (1997). Morphological and molecular processes of polyp formation in Apc(delta716) knockout mice. *Cancer Res.* 57, 1644–1649.

Panciera, T., Azzolin, L., Fujimura, A., Di Biagio, D., Frasson, C., Bresolin, S., et al. (2016). Induction of expandable tissue-specific stem/progenitor cells through transient expression of YAP/TAZ. *Cell Stem Cell* 19, 725–737. doi: 10.1016/j.stem.2016.08.009

Parker, A., Vaux, L., Patterson, A. M., Modasia, A., Muraro, D., Fletcher, A. G., et al. (2019). Elevated apoptosis impairs epithelial cell turnover and shortens villi in TNF-driven intestinal inflammation. *Cell Death Dis.* 10:108. doi: 10.1038/s41419-018-1275-5

Patey, N., Scoazec, J. Y., Cuenod-Jabri, B., Canioni, D., Kedinger, M., Goulet, O., et al. (1997). Distribution of cell adhesion molecules in infants with intestinal epithelial dysplasia (tufting enteropathy). *Gastroenterology* 113, 833–843. doi: 10.1016/S0016-5085(97)70178-1

Pellegrinet, L., Rodilla, V., Liu, Z., Chen, S., Koch, U., Espinosa, L., et al. (2011). Dll1- and dll4-mediated notch signaling are required for homeostasis of intestinal stem cells. *Gastroenterology* 140, 1230–1240. doi: 10.1053/j.gastro.2011.01.005

Pollard, T. D., and Mooseker, M. S. (1981). Direct measurement of actin polymerization rate constants by electron microscopy of actin filaments nucleated by isolated microvillus cores. *J. Cell Biol.* 88, 654–659. doi: 10.1083/jcb.88.3.654

Potten, C. S. (1998). Stem cells in gastrointestinal epithelium: numbers, characteristics and death. *Philos. Trans. R. Soc. Lond. B Biol. Sci.* 353, 821–830. doi: 10.1098/rstb.1998.0246

Quiros, M., and Nusrat, A. (2019). Contribution of wound-associated cells and mediators in orchestrating gastrointestinal mucosal wound repair. *Annu. Rev. Physiol.* 81, 189–209. doi: 10.1146/annurev-physiol-020518-114504

Rao-Bhatia, A., Zhu, M., Yin, W. C., Coquenlorge, S., Zhang, X., Woo, J., et al. (2020). Hedgehog-activated Fat4 and PCP pathways mediate mesenchymal cell clustering and villus formation in gut development. *Dev. Cell* 52, 647–658.e646. doi: 10.1016/j.devcel.2020.02.003

Revenu, C., Ubelmann, F., Hurbain, I., El-Marjou, F., Dingli, F., Loew, D., et al. (2012). A new role for the architecture of microvillar actin bundles in apical retention of membrane proteins. *Mol. Biol. Cell* 23, 324–336. doi: 10.1091/mbc.e11-09-0765

Rolo, A., Skoglund, P., and Keller, R. (2009). Morphogenetic movements driving neural tube closure in Xenopus require myosin IIB. *Dev. Biol.* 327, 327–338. doi: 10.1016/j.ydbio.2008.12.009

Ruemmele, F. M., Schmitz, J., and Goulet, O. (2006). Microvillous inclusion disease (microvillous atrophy). *Orphanet. J. Rare Dis.* 1:22. doi: 10.1186/1750-1172-1-22

Santos, A. J. M., Lo, Y. H., Mah, A. T., and Kuo, C. J. (2018). The intestinal stem cell niche: homeostasis and adaptations. *Trends Cell Biol.* 28, 1062–1078. doi: 10.1016/j.tcb.2018.08.001

Saotome, I., Curto, M., and Mcclatchey, A. I. (2004). Ezrin is essential for epithelial organization and villus morphogenesis in the developing intestine. *Dev. Cell* 6, 855–864. doi: 10.1016/j.devcel.2004.05.007

Sato, T., and Clevers, H. (2013). Growing self-organizing mini-guts from a single intestinal stem cell: mechanism and applications. *Science* 340, 1190–1194. doi: 10.1126/science.1234852

Sato, T., Mushiake, S., Kato, Y., Sato, K., Sato, M., Takeda, N., et al. (2007). The Rab8 GTPase regulates apical protein localization in intestinal cells. *Nature* 448, 366–369. doi: 10.1038/nature05929

Sato, T., Van Es, J. H., Snippert, H. J., Stange, D. E., Vries, R. G., Van Den Born, M., et al. (2011). Paneth cells constitute the niche for Lgr5 stem cells in intestinal crypts. *Nature* 469, 415–418. doi: 10.1038/nature09637

Sato, T., Vries, R. G., Snippert, H. J., Van De Wetering, M., Barker, N., Stange, D. E., et al. (2009). Single Lgr5 stem cells build crypt-villus structures in vitro without a mesenchymal niche. *Nature* 459, 262–265. doi: 10.1038/nature07935

Schmitz, H., Barmeyer, C., Fromm, M., Runkel, N., Foss, H. D., Bentzel, C. J., et al. (1999). Altered tight junction structure contributes to the impaired epithelial barrier function in ulcerative colitis. *Gastroenterology* 116, 301–309. doi: 10.1016/S0016-5085(99)70126-5

Sebe-Pedros, A., Burkhardt, P., Sanchez-Pons, N., Fairclough, S. R., Lang, B. F., King, N., et al. (2013). Insights into the origin of metazoan filopodia and microvilli. *Mol. Biol. Evol.* 30, 2013–2023. doi: 10.1093/molbev/mst110

Seno, H., Miyoshi, H., Brown, S. L., Geske, M. J., Colonna, M., and Stappenbeck, T. S. (2009). Efficient colonic mucosal wound repair requires Trem2 signaling. *Proc. Natl. Acad. Sci. U.S.A.* 106, 256–261. doi: 10.1073/pnas.0803343106

Serra, D., Mayr, U., Boni, A., Lukonin, I., Rempfler, M., Challet Meylan, L., et al. (2019). Self-organization and symmetry breaking in intestinal organoid development. *Nature* 569, 66–72. doi: 10.1038/s41586-019-1146-y

Sherman, P. M., Mitchell, D. J., and Cutz, E. (2004). Neonatal enteropathies: defining the causes of protracted diarrhea of infancy. *J. Pediatr. Gastroenterol. Nutr.* 38, 16–26. doi: 10.1097/00005176-200401000-00007

Shyer, A. E., Huycke, T. R., Lee, C., Mahadevan, L., and Tabin, C. J. (2015). Bending gradients: how the intestinal stem cell gets its home. *Cell* 161, 569–580. doi: 10.1016/j.cell.2015.03.041

Slae, M. A., Saginur, M., Persad, R., Yap, J., Lacson, A., Salomon, J., et al. (2013). Syndromic congenital diarrhea because of the SPINT2 mutation showing enterocyte tufting and unique electron microscopy findings. *Clin. Dysmorphol.* 22, 118–120. doi: 10.1097/MCD.0b013e328361d42f

Sobajima, T., Yoshimura, S., Iwano, T., Kunii, M., Watanabe, M., Atik, N., et al. (2014). Rab11a is required for apical protein localisation in the intestine. *Biol Open* 4, 86–94. doi: 10.1242/bio.20148532

Spence, J. R., Lauf, R., and Shroyer, N. F. (2011a). Vertebrate intestinal endoderm development. *Dev. Dyn.* 240, 501–520. doi: 10.1002/dvdy.22540

Spence, J. R., Mayhew, C. N., Rankin, S. A., Kuhar, M. F., Vallance, J. E., Tolle, K., et al. (2011b). Directed differentiation of human pluripotent stem cells into intestinal tissue in vitro. *Nature* 470, 105–109. doi: 10.1038/nature09691

Stappenbeck, T. S., Hooper, L. V., and Gordon, J. I. (2002). Developmental regulation of intestinal angiogenesis by indigenous microbes via Paneth cells. *Proc. Natl. Acad. Sci. U.S.A.* 99, 15451–15455. doi: 10.1073/pnas.202604299

Subramanian, S., Blanton, L. V., Frese, S. A., Charbonneau, M., Mills, D. A., and Gordon, J. I. (2015). Cultivating healthy growth and nutrition through the gut microbiota. *Cell* 161, 36–48. doi: 10.1016/j.cell.2015.03.013

Sumigray, K. D., Terwilliger, M., and Lechler, T. (2018). Morphogenesis and Compartmentalization of the Intestinal Crypt. *Dev. Cell* 45, 183–197.e185. doi: 10.1016/j.devcel.2018.03.024

Taketo, M. M. (2006). Mouse models of gastrointestinal tumors. *Cancer Sci.* 97, 355–361. doi: 10.1111/j.1349-7006.2006.00190.x

Tan, D. W., and Barker, N. (2014). Intestinal stem cells and their defining niche. *Curr. Top. Dev. Biol* 107, 77–107. doi: 10.1016/B978-0-12-416022-4.00003-2

Taniguchi, K., Wu, L. W., Grivennikov, S. I., De Jong, P. R., Lian, I., Yu, F. X., et al. (2015). A gp130-Src-YAP module links inflammation to epithelial regeneration. *Nature* 519, 57–62. doi: 10.1038/nature14228

Tilston-Lunel, A. M., Haley, K. E., Schlecht, N. F., Wang, Y., Chatterton, A. L. D., Moleirinho, S., et al. (2016). Crumbs 3b promotes tight junctions in an ezrin-dependent manner in mammalian cells. *J. Mol. Cell Biol.* 8, 439–455.

Tocchetti, A., Soppo, C. B., Zani, F., Bianchi, F., Gagliani, M. C., Pozzi, B., et al. (2010). Loss of the actin remodeler Eps8 causes intestinal defects and improved metabolic status in mice. *PLoS One* 5:e9468. doi: 10.1371/journal.pone.09468

Trier, J. S., and Moxey, P. C. (1979). Morphogenesis of the small intestine during fetal development. *Ciba Found Symp.* 70, 3–29.

Umar, S. (2010). Intestinal stem cells. *Curr. Gastroenterol. Rep.* 12, 340–348.

Van Der Heijden, M., and Vermeulen, L. (2019). Stem cells in homeostasis and cancer of the gut. *Mol. Cancer* 18:66.

Vivas, S., Vaquero, L., Rodriguez-Martin, L., and Caminero, A. (2015). Age-related differences in celiac disease: Specific characteristics of adult presentation. *World J. Gastrointest. Pharmacol. Ther.* 6, 207–212.

Vogelstein, B., Papadopoulos, N., Velculescu, V. E., Zhou, S., and Diaz, L. A. Jr. (2013). Cancer genome landscapes. *Science* 339, 1546–1558.

Walton, K. D., Freddo, A. M., Wang, S., and Gumucio, D. L. (2016). Generation of intestinal surface: an absorbing tale. *Development* 143, 2261–2272.

Walton, K. D., Kolterud, A., Czerwinski, M. J., Bell, M. J., Prakash, A., Kushwaha, J., et al. (2012). Hedgehog-responsive mesenchymal clusters direct patterning and emergence of intestinal villi. *Proc. Natl. Acad. Sci. U.S.A.* 109, 15817–15822.

Wang, S., Walton, K. D., and Gumucio, D. L. (2019). Signals and forces shaping organogenesis of the small intestine. *Curr. Top. Dev. Biol.* 132, 31–65.

Wang, Y., Chiang, I. L., Ohara, T. E., Fujii, S., Cheng, J., Muegge, B. D., et al. (2019). Long-term culture captures injury-repair cycles of colonic stem cells. *Cell* 179, 1144–1159.e1115.

Wang, X., Yamamoto, Y., Wilson, L. H., Zhang, T., Howitt, B. E., Farrow, M. A., et al. (2015). Cloning and variation of ground state intestinal stem cells. *Nature* 522, 173–178.

Wang, Y., Gunasekara, D. B., Reed, M. I., Disalvo, M., Bultman, S. J., Sims, C. E., et al. (2017). A microengineered collagen scaffold for generating a polarized crypt-villus architecture of human small intestinal epithelium. *Biomaterials* 128, 44–55.

Wasan, H. S., Park, H. S., Liu, K. C., Mandir, N. K., Winnett, A., Sasieni, P., et al. (1998). APC in the regulation of intestinal crypt fission. *J. Pathol.* 185, 246–255.

Westbrook, A. M., and Schiestl, R. H. (2010). Atm-deficient mice exhibit increased sensitivity to dextran sulfate sodium-induced colitis characterized by elevated DNA damage and persistent immune activation. *Cancer Res.* 70, 1875–1884.

Whiteman, E. L., Fan, S., Harder, J. L., Walton, K. D., Liu, C. J., Soofi, A., et al. (2014). Crumbs3 is essential for proper epithelial development and viability. *Mol. Cell. Biol.* 34, 43–56.

Workman, M. J., Mahe, M. M., Trisno, S., Poling, H. M., Watson, C. L., Sundaram, N., et al. (2017). Engineered human pluripotent-stem-cell-derived intestinal tissues with a functional enteric nervous system. *Nat. Med.* 23, 49–59.

Yanai, H., Atsumi, N., Tanaka, T., Nakamura, N., Komai, Y., Omachi, T., et al. (2017). Intestinal stem cells contribute to the maturation of the neonatal small intestine and colon independently of digestive activity. *Sci. Rep.* 7:9891. doi: 10.1038/s41598-017-09927-2

Yilmaz, O. H., Katajisto, P., Lamming, D. W., Gultekin, Y., Bauer-Rowe, K. E., Sengupta, S., et al. (2012). mTORC1 in the Paneth cell niche couples intestinal stem-cell function to calorie intake. *Nature* 486, 490–495. doi: 10.1038/nature11163

Yu, Y., Lu, L., Sun, J., Petrof, E. O., and Claud, E. C. (2016). Preterm infant gut microbiota affects intestinal epithelial development in a humanized microbiome gnotobiotic mouse model. *Am. J. Physiol. Gastrointest. Liver Physiol.* 311, G521–G532. doi: 10.1152/ajpgi.00022.2016

Yui, S., Azzolin, L., Maimets, M., Pedersen, M. T., Fordham, R. P., Hansen, S. L., et al. (2018). YAP/TAZ-dependent reprogramming of colonic epithelium links ECM remodeling to tissue regeneration. *Cell Stem Cell* 22, 35–49.e37. doi: 10.1016/j.stem.2017.11.001

Zeissig, S., Burgel, N., Gunzel, D., Richter, J., Mankertz, J., Wahnschaffe, U., et al. (2007). Changes in expression and distribution of claudin 2, 5 and 8 lead to discontinuous tight junctions and barrier dysfunction in active Crohn's disease. *Gut* 56, 61–72.doi: 10.1136/gut.2006.094375

Zhang, M., Liu, Y., and Chen, Y. G. (2020). Generation of 3D human gastrointestinal organoids: principle and applications. *Cell Regen.* 9:6.

Conflict of Interest: The authors declare that the research was conducted in the absence of any commercial or financial relationships that could be construed as a potential conflict of interest.

frontiers
in Cell and Developmental Biology

ORIGINAL RESEARCH
published: 28 October 2020
doi: 10.3389/fcell.2020.594090

Simplified Brain Organoids for Rapid and Robust Modeling of Brain Disease

Jeongmin Ha[1,2], Ji Su Kang[1,2], Minhyung Lee[1], Areum Baek[1], Seongjun Kim[1,2], Sun-Ku Chung[3], Mi-Ok Lee[1,2]* and Janghwan Kim[1,2]*

[1] Stem Cell Convergence Research Center, Korea Research Institute of Bioscience and Biotechnology (KRIBB), Daejeon, South Korea, [2] Department of Functional Genomics, KRIBB School of Bioscience, Korea University of Science and Technology (UST), Daejeon, South Korea, [3] Mibyeong Research Center, Korea Institute of Oriental Medicine, Daejeon, South Korea

Although brain organoids are an innovative technique for studying human brain development and disease by replicating the structural and functional properties of the developing human brain, some limitations such as heterogeneity and long-term differentiation (over 2 months) impede their application in disease modeling and drug discovery. In this study, we established simplified brain organoids (simBOs), composed of mature neurons and astroglial cells from expandable hPSC-derived primitive neural stem cells (pNSCs). simBOs can be rapidly generated in 2 weeks and have more homogeneous properties. Transcriptome analysis revealed that three-dimensional (3D) environment of simBOs facilitates the conversion of pNSCs to mature neuronal systems compared to a two-dimensional environment in the context of neurotransmitter release, synaptic vesicle formation, ion channels, calcium signaling, axonal guidance, extracellular matrix organization, and cell cycle. This result was correlated with the translocation of YAP1 into the cytoplasm by sensing matrix stiffness on the 3D models. Furthermore, we demonstrated that simBOs could easily be specified into midbrain-like simBOs by treatment with Shh and FGF8. Midbrain-like simBOs from a Parkinson's disease patient (*LRRK2*$^{\mathrm{G2019S}}$)-derived pNSCs and gene-corrected (*LRRK2*^{WT}) control pNSCs represented disease-associated phenotypes in terms of increased LRRK2 activity, decreased dopaminergic neurons, and increased autophagy. Treatment with the LRRK2 inhibitor, PFE-360, relieved the phenotype of Parkinson's disease in midbrain-like simBOs. Taken together, these approaches could be applied to large-scale disease models and alternative drug-testing platforms.

Keywords: brain organoid, neural stem cells, disease modeling, drug screening, Parkinson's disease, LRRK2, gene editing

Edited by:
Silvia Garagna,
University of Pavia, Italy

Reviewed by:
Susanna Narkilahti,
University of Tampere, Finland
Murugan Kalimutho,
The University of Queensland,
Australia

***Correspondence:**
Mi-Ok Lee
molee@kribb.re.kr
Janghwan Kim
janghwan.kim@kribb.re.kr

Specialty section:
This article was submitted to
Cell Growth and Division,
a section of the journal
Frontiers in Cell and Developmental Biology

Received: *12 August 2020*
Accepted: *08 October 2020*
Published: *28 October 2020*

Citation:
Ha J, Kang JS, Lee M, Baek A, Kim S, Chung S-K, Lee M-O and Kim J (2020) Simplified Brain Organoids for Rapid and Robust Modeling of Brain Disease. Front. Cell Dev. Biol. 8:594090. doi: 10.3389/fcell.2020.594090

INTRODUCTION

Neurological disorders, an immense threat to human health, are diseases with psychological and/or physical symptoms characterized by an abnormality in the development, patterning, and maintenance of homeostasis of the human brain or nervous system (Thakur et al., 2016). Besides the complexity of the biological structure and function of the human brain, the difficulty of

---

Abbreviations: simBOs, simplified brain organoids.

obtaining human brain tissues impedes understanding of pathogenesis and drug discovery. Human neuronal tissues can only be obtained from postmortem or surgically removed brain tissues. In addition, primary neurons derived from the brain are post-mitotic cells, which limits *in vitro* expansion (Koo et al., 2019). The experimental animal models have provided considerable insights into the molecular basis of normal brain development, disease pathogenesis, and therapeutic options for neurological disorders, but the inter-species differences in development (Liu et al., 2012; Homem et al., 2015) and pathogenesis (Burbulla et al., 2017; Gitler et al., 2017) make understanding the human brain and disease challenging. Furthermore, recent advances in single-cell transcriptome revealed divergent gene expression between homolog cell types of human versus mouse cortex associated with neuronal connectivity, signaling, neurotransmitters, and cell-type-specific markers, implying functional variations between the two species (Hodge et al., 2019). Thus, new experimental models are required for replicating the characteristics of the human brain and pathological conditions, in order to better understand the human brain development and disease.

Human pluripotent stem cells (hPSCs) (Thomson et al., 1998; Takahashi et al., 2007) have provided tremendous opportunities to study the human brain. The development of neuronal-cell specific differentiation has made it possible to obtain various types of neural cells (Tao and Zhang, 2016). In particular, human induced pluripotent stem cells (hiPSCs) can produce patient-specific neuronal cells and are useful in genome editing, allowing us to understand the pathogenic mechanisms associated with genetic risk factors (Lin et al., 2018; Kim et al., 2019). Despite the advantage of a relatively homogeneous production of high-purity neuronal cells, two-dimensional (2D) cultures, which differ from the human brain environment in terms of cell-to-cell or cell-to-matrix connections and spatial organization (Wang, 2018), have limited ability to replicate human brain development and pathogenesis.

Recently, it was reported that three-dimensional (3D) differentiation into the neuronal lineage from hPSCs could generate brain-like 3D tissue biomimetics, named brain organoids (Lancaster et al., 2013). Various types of brain organoids, such as brain region-specific organoids (Muguruma et al., 2015; Pasca et al., 2015; Sakaguchi et al., 2015; Jo et al., 2016; Qian et al., 2016) and assembloids (Bagley et al., 2017; Birey et al., 2017; Xiang et al., 2017), have been developed. These brain organoids replicate human-specific brain structures (Lancaster et al., 2013) and disease pathology (Jo et al., 2016; Burbulla et al., 2017), suggesting that brain organoids are more physiologically related to the human brain than animal models. Since brain organoids have no blood brain barrier and are difficult to reflect the systemic effects of drugs, brain organoids and animal models can become complementary human brain models. Brain organoid systems have modeled neurodevelopmental and neurodegenerative disorders, such as microcephaly, autism spectrum disorder, Alzheimer's disease, and Parkinson's disease (PD) (Lancaster et al., 2013; Mariani et al., 2015; Jo et al., 2016; Raja et al., 2016).

In this study, we aimed to develop simBOs, which could enable the rapid and robust production of uniform brain organoids for application in disease modeling and drug discovery. To shorten the period of differentiation and reduce the variability of brain organoids, we developed a step-wise differentiation method from hPSC-derived expandable primitive neural stem cells (pNSCs) (Li et al., 2011; Liu et al., 2012) to organoids. Transcriptome analysis was performed to establish the neuronal characteristics of simBOs and to understand the molecular differences between 2D and 3D environments in neuronal differentiation. Furthermore, we generated midbrain-like simBOs, which could replicate PD phenotype and drug response.

MATERIALS AND METHODS

hiPSCs Maintenance and Differentiation Into pNSCs

Human-induced pluripotent stem cells (hiPSCs) were obtained from a healthy donor and generated from fibroblasts (AG02261, Coriell Cells Repositories, Camden, NJ, United States) as previously described (Lee M. et al., 2019) and PD-patient (*LRRK2*^{G2019S})-derived induced pluripotent stem cells (iPSCs) (Son et al., 2017) and gene-corrected iPSCs (Lee and Chung, 2019) were used for PD modeling. hiPSCs were maintained in TeSR-E8 medium (STEMCELL Technologies, Vancouver, Canada) and subcultured with ReLeSR (STEMCELL Technologies) according to the manufacturer's instructions. For reprogramming purposes, human fibroblasts were exempted from IRB review by the Public Institutional Review Board designated by the Ministry of Health and Welfare (P01-201802-31-001).

Primitive neural stem cells (pNSCs) were induced and maintained as previously described (Liu et al., 2012). Briefly, hiPSCs were seeded onto Geltrex (Thermo Fisher Scientific, Waltham, MA, United States)-coated 35 mm dishes (Corning, NY, United States) for 20% confluence. The next day, the medium was switched to Neural Induction Medium-I [NIM-I: 50% Advanced DMEM/F12 (Gibco, Invitrogen, Waltham, MA, United States), 50% Neurobasal (Gibco), 1× N2 (Gibco), 1× B27 (Gibco), 1% Glutamax (Gibco), 0.5% Albumax (Thermo Fisher Scientific), and 10 ng/mL hLIF (PeproTech, Rocky Hill, NJ, United States) supplemented with 4 μM CHIR99021 (GSK3 inhibitor; Tocris Bioscience, Bristol, United Kingdom), 3 μM SB431542 (TGF-β receptor inhibitor; Tocris), 2 μM Dorsomorphin (Tocri), and 0.1 μM Compound E (Tocris)] for 2 days. The medium was then switched to NIM-II (NIM-I excluding Dorsomorphin) for another 5 days. The cells were transferred onto Geltrex-coated dishes with Accutase (MilliporeSigma, Billerica, MA, United States) and maintained in Neural Stem Cell Maintenance Medium (NSMM: 50% Advanced DMEM/F12, 50% Neurobasal, 1× N2, 1× B27, 1% Glutamax, 0.5% Albumax, 10 ng/mL hLIF, 3 μM CHIR99021, and 2 μM SB431542).

Spontaneous Differentiation of pNSCs in 2D Culture Dishes

pNSCs were dissociated into single cells using Accutase. 80,000 cells were plated on Geltrex-coated 24- or 4-well tissue culture plates (Corning) and cultured in NSMM for 4 days. Then, the medium was switched to differentiation medium [DMEM/F12, 1× N2, 1× B27, 200 ng/mL dbcAMP (Enzo Life Sciences, Basel, Switzerland) and 5 μM DAPT (Tocris)] with 10 ng/mL BDNF (PeproTech), 10 ng/mL GDNF (PeproTech), and fed every other day for 10–20 days.

Generation of Simplified Brain Organoids (simBOs)

To permit pNSCs self-organization, single-cell-dissociated pNSCs were seeded on wells of ultra-low attachment 96-well plates (Corning Incorporated, Kennebunk, ME, United States) and cultured in NSMM. 100,000 cells and 50,000 cells were used for self-organization of simBOs and midbrain-like simBOs, respectively. After 4 days, 96 spheres of pNSCwere transferred into a bioreactor (ABLE Corporation, Tokyo, Japan) and maintained in 5–10 ml of spontaneous differentiation medium (differentiation medium with 10 ng/mL BDNF and 10 ng/mL GDNF) or midbrain-specification medium [differentiation medium with 100 ng/mL Shh (R&D systems, Minneapolis, MN, United States) and 100 ng/mL FGF8 (PeproTech, TX, United States)] for 10–20 days. The culture medium was changed every 3 days. To check the efficacy of LRRK2 kinase inhibitors in PD patient-derived midbrain-like simBOs, 5 μM PFE-360 (MedChem Express, Sollentuna, Sweden) was used for 3 days.

Size Measurement of simBOs

The size of simBOs was determined using phase contrast images by measuring the diameter of 10 to 25 organoids with the ImageJ software (National Institutes of Health, Bethesda, MD, United States). The area was calculated using the following equation:

$$\text{Area} = \left(\frac{\text{major axis}}{2}\right) \times \left(\frac{\text{minor axis}}{2}\right) \times \pi$$

RNA Preparation, cDNA Synthesis, and Quantitative Real-Time PCR

Twelve organoids were lysed for each sample using Easyblue (iNtRON Biotechnology, Seongnam-si, South Korea) and total RNA was extracted according to the manufacturer's instructions. cDNA was synthesized from 1 μg of total RNA using the iScript cDNA synthesis kit (Bio-Rad, Hercules, CA, United States). Quantitative real-time PCR was performed using a 1/50 concentration of the obtained cDNA with iQ SYBR Green Supermix (Bio-Rad) on an Applied Biosystems 7500 Fast Real-Time PCR instrument system (Thermo Fisher Scientific). The cycle threshold (*C*t) value for each target gene was determined using the software provided by the manufacturer. The expression data were normalized to the *C*t value of *RPL7* (Efe et al., 2011). The primer sequences used in this study are shown in **Supplementary Table 1**.

Immunohistochemistry and Immunocytochemistry

Eight to 12 organoids of each sample were fixed with 4% paraformaldehyde (Electron Microscopy Sciences, Hatfield, PA, United States) and incubated overnight at 4°C. Fixed samples were incubated with sucrose solutions of an increasing gradient (10, 20, and 30%) prepared in Dulbecco's phosphate-buffered saline (DPBS; WELGENE, Daegu, South Korea) for cryoprotection. Samples were embedded in optimal cutting temperature (O.C.T.) compound (Sakura Finetek, Tokyo, Japan) and frozen in liquid nitrogen. The organoids were sectioned using a cryostat microtome into 10–15 μm-thick sections. The cells cultured in 2D were grown in 24- or 4-well tissue culture plates and fixed with 4% paraformaldehyde and 0.15% picric acid (Sigma-Aldrich, St. Louis, MO, United States) in DPBS for 15 min.

For immunostaining, samples were blocked and permeabilized with 3% bovine serum albumin (BSA; Thermo Fisher Scientific) and 0.3% Triton X-100 (Sigma-Aldrich) in DPBS for 1 h at room temperature, as previously described (Lee et al., 2020). All primary antibodies were diluted in 1% BSA and incubated overnight at 4°C. After iterative washing with 0.1% BSA in DPBS, the samples were incubated with Alexa-594- or Alexa-488-conjugated secondary antibodies (Thermo Fisher Scientific) for 1 h at room temperature. All fluorescent images were acquired using an Evos FL auto 2 imaging system (Thermo Fisher Scientific). The antibodies used in this study are listed in **Supplementary Table 2**.

Microarray Analysis

For comprehensive gene expression analysis, 12 organoids were used for each sample and cDNA microarray was performed at e-biogen (ebiogen, Seoul, South Korea) using an Agilent Human GE 4 × 44K v2 Microarray Kit (Agilent, Santa Clara, CA, United States), as described previously (Lee M.O. et al., 2019). Data normalization was performed with GeneSpring software (Agilent) and differentially expressed genes were sorted by fold-change of gene expression and heat map was presented using the Multi Experiment Viewer software (MeV version 4.9.0[1]). Gene set enrichment analysis was performed with GSEA (GSEA[2]) (Mootha et al., 2003; Subramanian et al., 2005) and pathway enrichment in the Reactome Database[3] was performed using Cytoscape software[4].

Western Blotting

Whole-cell extracts of 8 to 12 organoids were prepared using RIPA buffer (Sigma-Aldrich) containing 1 mM PMSF (Sigma-Aldrich), a cocktail of protease inhibitors, and 1× phosSTOPTM (Roche Applied Science, Basel, Switzerland). Protein concentrations were determined using a Pierce BCA protein assay kit (Thermo Fisher Scientific). Equal amounts of total protein were separated on MP TGX Precast Gels (Bio-Rad) and transferred to polyvinylidene fluoride membranes (Bio-Rad). The membranes were blocked in Tris-buffered saline (LPS Solution, Daejeon, South Korea) containing 0.05% Tween-20 (TBST; Sigma-Aldrich) and 1.5% BSA for 1 h at room

---

[1] http://mev.tm4.org/

[2] http://software.broadinstitute.org/gsea/index.jsp

[3] https://reactome.org/

[4] www.cytoscape.org

temperature and then incubated with specific primary antibodies overnight at 4°C. After washing with TBST, the samples were incubated for 1 h at room temperature with horseradish peroxidase-conjugated secondary antibodies (Cell Signaling Technology, Danvers, MA, United States; 1:5000). The antibodies used in this study are listed in **Supplementary Table 2**. The blots were developed using ECL Select Western Blotting Detection Reagent (GE Healthcare, Little Chalfont, United Kingdom) and band images were acquired using the luminescent image analyzer LAS-3000 (Fuji Photo Film GMBH, Tokyo, Japan). The band intensity was quantified using ImageJ software.

Dopamine Secretion

To determine the amount of dopamine released from simBOs, 24 h-culture medium was harvested from 24-well containing 8 organoids at 13 days post-differentiation and subjected to enzyme-linked immunoassay with the Dopamine Research ELISA kit (LDN, Nordhorn, Germany) according to the manufacturer's instructions. In brief, dopamine was extracted, acylated, and enzymatically converted. Once the antibody bound to the bottom of the plates captured the converted dopamine, the first was detected using an anti-rabbit IgG-peroxidase conjugate with the substrates. Samples were quantified by comparing their absorbance values with a standard curve prepared with known standard concentrations.

Statistical Analysis

Statistical significance was calculated with the unpaired *t*-test or analysis of variance (ANOVA) in GraphPad Prism version 8 for windows (GraphPad Software, Inc., CA, United States). Bar-charts (in **Figures 1C**, **3C**, **5C**, **6B**, **7C,G,H**) are presented as means ± standard error (SE) and the box-and-whisker plots in **Figures 1G**, **7I** are presented as min to max with all points. Size similarity of simBOs (**Supplementary Figures 2B, S3B, S6A,B**) was presented by calculating the standard deviation/average. Experimental replicates of each experiment was indicated in the figure legend.

RESULTS

Generation of simBOs From hPSC-Derived pNSCs

Given that pNSCs differentiated from hPSCs are highly proliferative, cryopreservable, and capable of producing various cell types present in the brain and nervous system (Li et al., 2011; Liu et al., 2012), we hypothesized that self-organization of pNSCs and subsequent differentiation in a stirred bioreactor could rapidly generate simBOs. To address this idea, we differentiated pNSCs from hiPSCs derived from healthy human somatic cells following a previously reported procedure (**Supplementary Figures 1A,B**) (Liu et al., 2012). pNSCs showed high expression of neuronal stem cell markers (PAX6, NESTIN, and SOX2), marginal expression of pan-neuronal marker (TUJ1), and no expression of mature neuronal marker (MAP2), implying that pNSCs harboring the characteristics of neural stem cells (**Supplementary Figure 1C**).

To generate simBOs, pNSCs were self-organized in ultra-low attachment 96-well plates with the indicated number of cells (30,000 to 200,000 cells per organoid). Four days later, the cell aggregates were transferred to a bioreactor and differentiated in spontaneous differentiation medium for 10–20 days (**Figure 1A**). To analyze morphological homogeneity and growth, the size of each organoid was measured on days 0, 10, and 20 (**Figure 1B** and **Supplementary Figures 2A,B**). Up to a seeding density of 100,000 cells per organoid, simBOs were homogeneously produced and showed less than 2% of standard deviation/average (STDEV) of spheroid size. However, at a seeding density of 200,000 cells, STDEV was over 2–7% (**Supplementary Figures 2A,B**). Additionally, this seeding density significantly impaired the induction of mature neuronal marker (*NEUN*) (**Supplementary Figure 2C**) and facilitated apoptosis (**Supplementary Figure 2D**). Thus, we set up a protocol with an initial number of 100,000 cells for the self-organization of pNSCs.

To verify the robust reproducibility of the system, we produced up to 96 simBOs at a time, and these were cultured in one bottle with 5–10 mL of differentiation medium. Since the capacity of the bottle was of 30 mL, increasing the amount of medium is expected to increase the number of simBOs that can be cultured in a bottle. The bioreactor can accommodate up to six bottles, suggesting that at least are 576 simBOs (minimum) can be produced and cultured at each time (**Supplementary Figure 3A**). Importantly, given that the pNSCs used as starting cells for organoid production are highly proliferative and stable, we were able to culture a large number of simBOs with the established bioreactor system. Analysis of three independent batches of simBOs production confirmed very similar size distribution within each batch (STDEV/AVG < 5%) (**Supplementary Figures 3B,C**).

To characterize simBOs, we first examined the expression of neuronal markers in the levels of transcripts and proteins to evaluate time-dependent neuronal differentiation. Quantitative real-time PCR (qRT-PCR) analysis revealed reduced expression of the neural progenitor marker gene (*PAX6*) and enhanced expression of neuronal marker genes (*TUBB3*, *DCX*, *MAP2*, and *NEUN*) during spontaneous differentiation until day 20 (**Figure 1C**). Homogenous expression of neuronal markers (*PAX6*, *DCX*, *MAP2*, *and NEUN*) was showed in distinct batches of simBOs (**Supplementary Figure 4**). Consistently, immunofluorescence analysis also showed a decrease in neural stem cell marker (PAX6) and an increase in neuronal markers (TUJ1, MAP2, and NEUN) with a homogeneous pattern between organoids through differentiation (**Figure 1D** and **Supplementary Figures 5A,B**). In particular, the proliferation marker (Ki67) was substantially reduced after differentiation, implying differentiation into post-mitotic neurons. Moreover, the staining of cell death marker (cCASP3) indicated no significant formation of apoptotic bodies in simBOs (**Figure 1D**). We also observed the expression of a synaptic marker (SYN1), suggesting that our simBOs contained functionally mature neurons (**Figure 1E**). Next, we analyzed the distribution of neuron and astroglia in simBOs. $MAP2^+$ neuronal cells were evenly distributed throughout the organoids, whereas $GFAP^+$

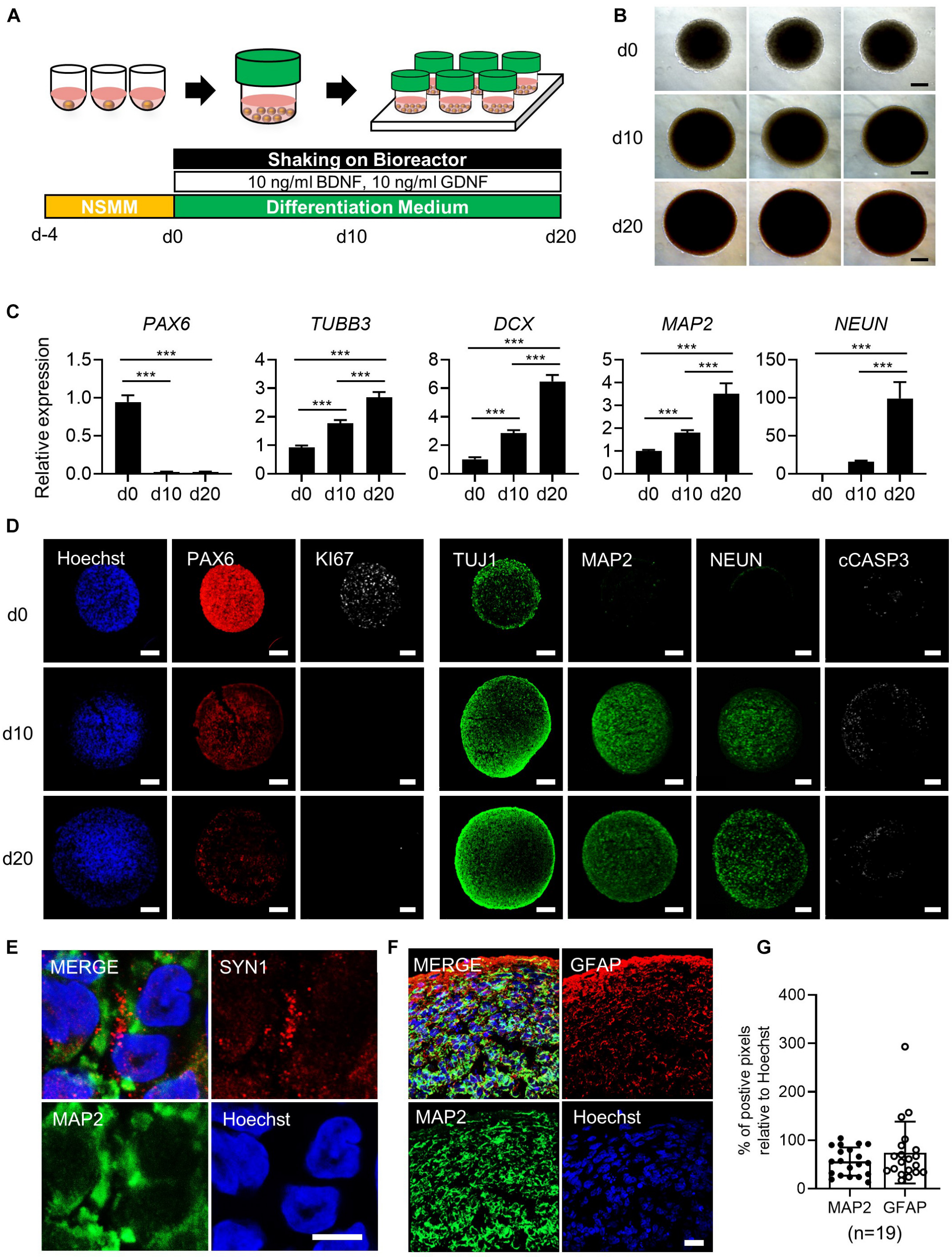

FIGURE 1 | Generation of simplified brain organoids (simBOs) from human primitive neural stem cells (pNSC). **(A)** Graphical schematics for the generation of pNSCs into simBOs. **(B)** Phase contrast images of simBOs at days 0, 10, and 20 of spontaneous differentiation. Scale bars represent 200 μm. **(C)** Quantitative reverse transcription polymerase chain reaction (qRT-PCR) analysis for neural progenitor (*PAX6*) and neuronal (*TUBB3*, *DCX*, *MAP2*, and, *NEUN*) markers in simBOs at days 0, 10, and 20 of spontaneous differentiation. Expression value was normalized to those of day 0 (d0). Data represent mean ± standard error (SE) from three technical replicates. Statistical significance of Turkey's multiple comparisons $^{***}p < 0.001$ after one-way ANOVA. **(D)** Immunofluorescence analysis of simBOs with proliferating neural progenitor markers (PAX6 and Ki67), neuronal markers (TUJ1, MAP2, and NEUN), and apoptotic cell marker (cleaved caspase III; cCASP3) at indicated times. Scale bars represent 100 μm. **(E)** Immunofluorescence analysis of simBOs with a mature neuronal marker (MAP2) and a synaptic marker (SYN1) in simBOs after day 10 of spontaneous differentiation. Scale bar represents 5 μm. **(F)** Immunofluorescence analysis of simBOs with mature neuronal marker (MAP2) and astroglial cell marker (GFAP) after day 10 of spontaneous differentiation. Scale bar represents 20 μm. **(G)** Quantitative graph of the percentage (%) of positive pixels of each marker relative to Hoechst. Data represent mean ± standard error (SE) (*n* = 19). No significant differences were observed.

astroglial cells were enriched at the edges of organoids, and were also observed around neurons on day 10 simBOs (**Figure 1F**). Comparing the content of the two cells through pixel analysis of immunostained images, $GFAP^{+}$ astroglial cells were distributed in a similar amount of $MAP2^{+}$ neurons. To confirm the reproducible production of simBOs from various pNSC lines, we generated simBOs from two independent pNSCs [Parkinson disease (PD)-patient derived LRRK2G2019S pNSCs and gene-corrected control pNSCs] (**Supplementary Figure 6**). The result demonstrated that simBOs can be uniformly produced form a variety of human pNSCs. Taken together, these data demonstrated that simBOs are rapidly and homogenously produced brain organoids, which are structurally simple but uniform.

Molecular Characteristics of the simBOs

To access the molecular characteristics of simBOs, we performed a comprehensive gene expression analysis. Gene set enrichment analysis (GSEA) between pNSCs and simBOs indicated that pNSCs have a molecular signature of neocortex basal radial glia (**Figure 2A**) and simBOs of the neuronal system (**Figure 2B**). To further analyze transcriptional changes during the step-wise differentiation (hiPSCs-pNSCs-simBOs), differentially expressed genes were selected by a fourfold or higher change and clustered into five groups (clusters A–E) (**Figures 2C,D**). The 524 genes in cluster E were decreased in both pNSCs and simBOs compared to hiPSCs, which were involved in the transcriptional regulation of pluripotent stem cells, signaling by nodal, and signaling by receptor tyrosine kinases. On the other hand, the 270 genes in cluster D, associated with cell cycle, DNA synthesis, and telomere extension, were only decreased in simBOs, implying that iPSCs and pNSCs consisted of proliferative cells, but simBOs were post-mitotic.

The pNSC-specific genes were grouped in cluster C, involving the signaling by NOTCH and heparin sulfate/heparin metabolism, and the 459 genes (in cluster B) related to neuronal development in terms of axon guidance, activation of HOX genes during differentiation, and NCAM signaling for neurite out-growth, were increased in both pNSCs and simBOs. In contrast, the 589 genes in cluster A related to neuronal functionality (e.g., transmission across chemical synapses, neurotransmitter release cycle, GABA receptor activation, glutamate binding, potassium channels, and ion homeostasis) were increased only in simBOs. These data suggest that pNSCs have the properties of NOTCH signaling-dependent proliferative neural stem cells and 3D differentiation induces rapid conversion into post-mitotic functional neurons.

Enhanced Neuronal Differentiation in the simBOs

Next, we assessed whether a 3D environment could promote enhanced neuronal differentiation of simBOs. To directly compare the neuronal differentiation pattern between 2D cultures and simBOs, pNSCs were differentiated in a 2D environment with the same differentiation medium used for simBOs. Immunofluorescence analysis showed that neurons differentiated in 2D cultures had higher level of TUJ1, a neurofilament protein, but lower expression of mature neuronal markers (MAP2 and NEUN) than simBOs (**Figures 3A,B**). Consistent with this result, rapid reduction of the neural stem cell marker (*PAX6*) and robust induction of immature (*DCX*) and mature (*MAP2*, *NEUN*, and *SYN1*) neuronal markers in the simBOs was confirmed via qRT-PCR (**Figure 3C**). Moreover, *GRIN1* and *GRIN2B*, which play a crucial role in excitatory glutamatergic and inhibitory GABAergic synapses, respectively, also dramatically increased in the simBOs. However, *S100B*, the glial-specific protein, showed no difference between 2D cultures and simBOs, suggesting that the 3D environment could trigger neuron-specific maturation within 10 days.

A comparison of transcriptome data between the differentiation in 2D and 3D environments showed that there were 1,490 and 1,839 genes enriched in simBOs (clusters I and II) and 2D (clusters III and IV) cultures, respectively (**Figure 4A**). Gene ontology analysis according to cellular components showed that both environments markedly increased the expression of genes encoding proteins that act at different intracellular locations (**Supplementary Figure 7**). The simBOs were promoted genes encoding proteins of the cellular component related to neuronal functionality such as neuron projection, synapse, axon, dendritic spine, voltage-gated potassium, or calcium channel complex (clusters I and II). On the other hand, the 2D cultures were enhanced the expression of genes related to the extracellular space, elastic fiber, midbody, and kinetochore (clusters III and IV).

By analyzing the enriched pathway of 4 cluster gene sets, we found that simBOs were improved neuronal characteristics and the extracellular environment with higher similarity to the human brain (**Figure 4B**). In detail, cluster I consisted of 987 genes that increased in 2D cultures and further increased in simBOs. These differentially expressed genes corresponded to a representative enrichment in the pathways associated with differentiation into functional neurons such as glutamatergic synapses, GABAergic synapses, neurotransmitter release cycles, axon guidance, and potassium channels. Furthermore, the 459 genes in cluster II were only increased in simBOs and partly included genes belonging to pathways of calcium signaling, potassium channels, cholinergic synapses, and glutamatergic synapses (**Figure 4B** and **Supplementary Figure 8**).

In contrast, the 2D cultures were increased the expression of 924 genes (cluster III) involved in the extracellular matrix (ECM) organization and focal adhesion, whereas these genes were decreased in simBOs (**Figure 4B** and **Supplementary Figure 9**). Fibrous proteins such as collagen and fibronectin are barely present in the extracellular space of the brain, which gives the brain its soft properties (Hong and Do, 2019). To verify whether simBOs created an ECM environment closer to the *in vivo* brain, we compared 74 differentially expressed genes related to ECM organization during *in vitro* neural differentiation or *in vivo* human brain development. As shown in the **Supplementary Figure 10**, simBOs showed a similar expression pattern of ECM-related genes to that of the *in vivo* brain development,

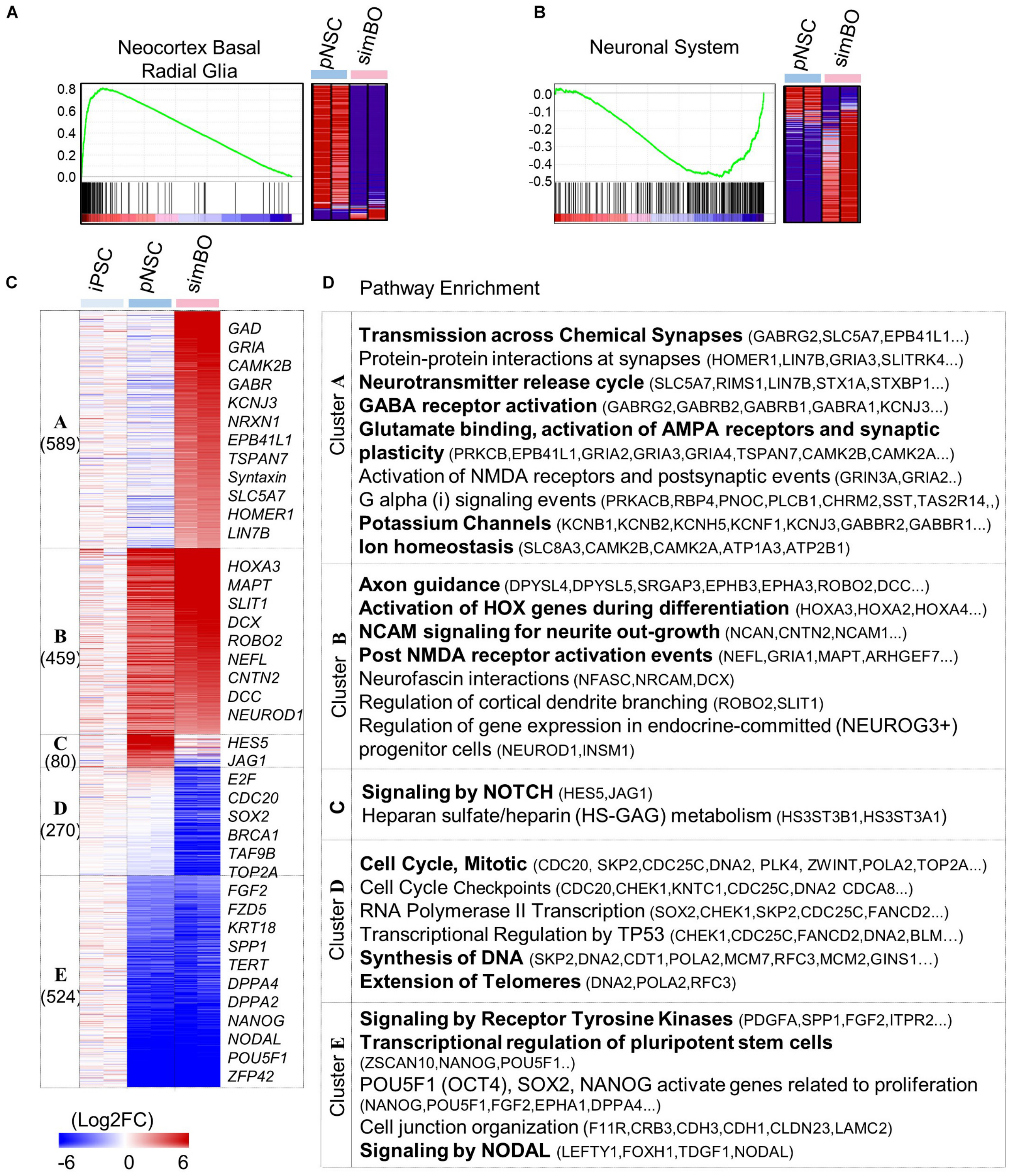

Cluster A	**Transmission across Chemical Synapses** (GABRG2,SLC5A7,EPB41L1...) Protein-protein interactions at synapses (HOMER1,LIN7B,GRIA3,SLITRK4...) **Neurotransmitter release cycle** (SLC5A7,RIMS1,LIN7B,STX1A,STXBP1...) **GABA receptor activation** (GABRG2,GABRB2,GABRB1,GABRA1,KCNJ3...) **Glutamate binding, activation of AMPA receptors and synaptic plasticity** (PRKCB,EPB41L1,GRIA2,GRIA3,GRIA4,TSPAN7,CAMK2B,CAMK2A...) Activation of NMDA receptors and postsynaptic events (GRIN3A,GRIA2..) G alpha (i) signaling events (PRKACB,RBP4,PNOC,PLCB1,CHRM2,SST,TAS2R14,,) **Potassium Channels** (KCNB1,KCNB2,KCNH5,KCNF1,KCNJ3,GABBR2,GABBR1...) **Ion homeostasis** (SLC8A3,CAMK2B,CAMK2A,ATP1A3,ATP2B1)
Cluster B	**Axon guidance** (DPYSL4,DPYSL5,SRGAP3,EPHB3,EPHA3,ROBO2,DCC...) **Activation of HOX genes during differentiation** (HOXA3,HOXA2,HOXA4...) **NCAM signaling for neurite out-growth** (NCAN,CNTN2,NCAM1...) **Post NMDA receptor activation events** (NEFL,GRIA1,MAPT,ARHGEF7...) Neurofascin interactions (NFASC,NRCAM,DCX) Regulation of cortical dendrite branching (ROBO2,SLIT1) Regulation of gene expression in endocrine-committed (NEUROG3+) progenitor cells (NEUROD1,INSM1)
C	**Signaling by NOTCH** (HES5,JAG1) Heparan sulfate/heparin (HS-GAG) metabolism (HS3ST3B1,HS3ST3A1)
Cluster D	**Cell Cycle, Mitotic** (CDC20, SKP2,CDC25C,DNA2, PLK4, ZWINT,POLA2,TOP2A...) Cell Cycle Checkpoints (CDC20,CHEK1,KNTC1,CDC25C,DNA2 CDCA8...) RNA Polymerase II Transcription (SOX2,CHEK1,SKP2,CDC25C,FANCD2...) Transcriptional Regulation by TP53 (CHEK1,CDC25C,FANCD2,DNA2,BLM…) **Synthesis of DNA** (SKP2,DNA2,CDT1,POLA2,MCM7,RFC3,MCM2,GINS1…) **Extension of Telomeres** (DNA2,POLA2,RFC3)
Cluster E	**Signaling by Receptor Tyrosine Kinases** (PDGFA,SPP1,FGF2,ITPR2...) **Transcriptional regulation of pluripotent stem cells** (ZSCAN10,NANOG,POU5F1..) POU5F1 (OCT4), SOX2, NANOG activate genes related to proliferation (NANOG,POU5F1,FGF2,EPHA1,DPPA4...) Cell junction organization (F11R,CRB3,CDH3,CDH1,CLDN23,LAMC2) **Signaling by NODAL** (LEFTY1,FOXH1,TDGF1,NODAL)

FIGURE 2 | Transcriptomic analysis of simBOs. **(A,B)** Enrichment plot and Heat map for the molecular signature of Neocortex Basal radial glia **(A)** and neuronal system **(B)** analyzing by gene set enrichment analysis of pNSC and simBOs. **(C)** Heat map of differentially expressed genes among iPSCs, pNSCs, and simBOs. Expression value was normalized to those of iPSCs. Cluster name and gene number in each cluster were indicated in left panel and representative gene names in each cluster were indicated in the right panel. Color scale of expression value were presented in lower panel. **(D)** Chart describing representative enrichment reactome pathways and entities related to differentially expressed genes in each cluster.

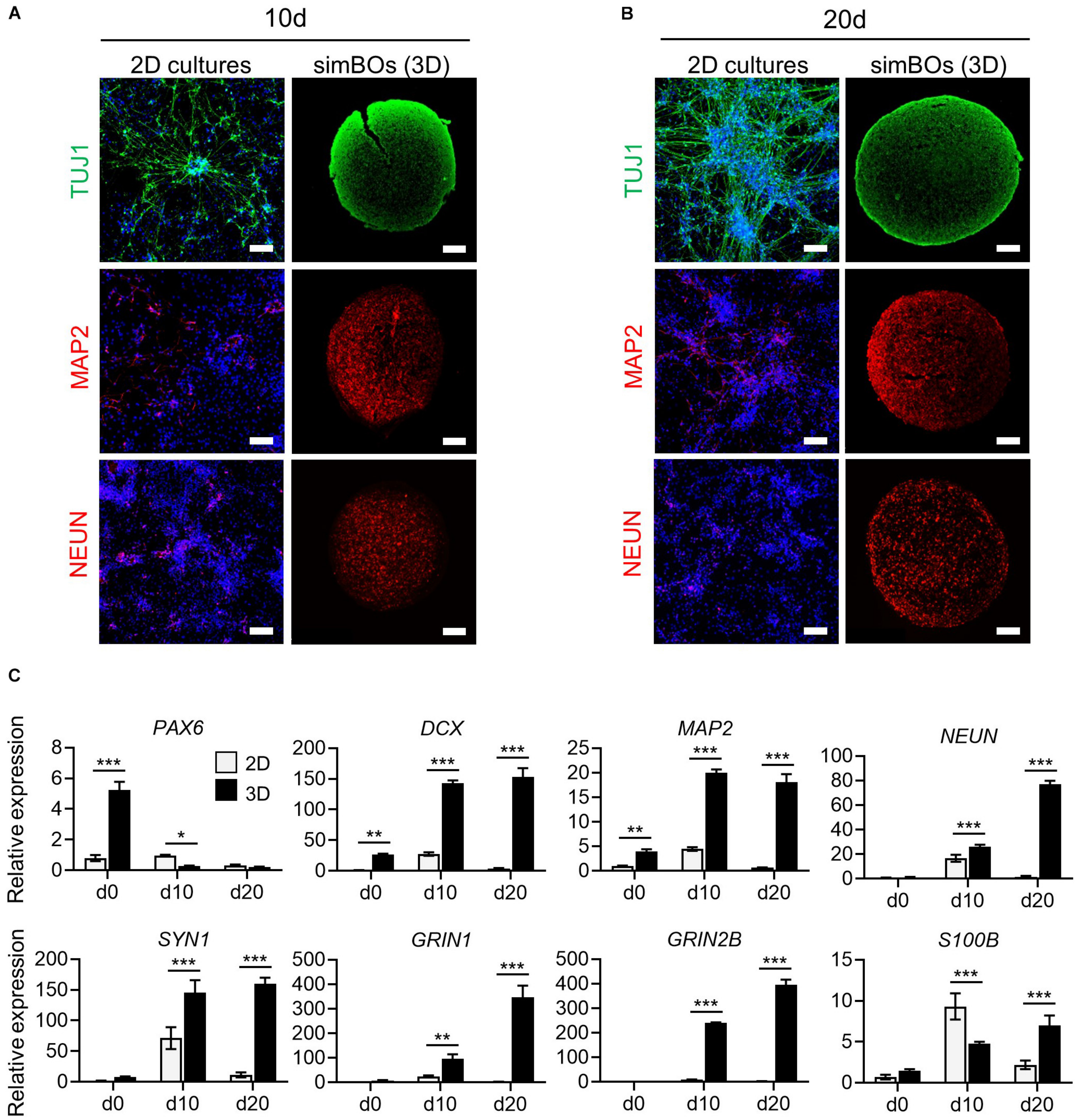

FIGURE 3 | Comparison of neuronal differentiation potential in 2D vs. 3D. **(A,B)** Immunofluorescence analysis to compare neuronal differentiation potential between 2D and 3D with neuronal markers (TUJ1, MAP2, and, NEUN) in simBOs at day 10 **(A)** and 20 **(B)** of spontaneous differentiation. Scale bars represent 100 μm. **(C)** Quantitative reverse transcription polymerase chain reaction (qRT-PCR) analysis for neural progenitor marker (*PAX6*), pan-neuronal markers (*DCX*, *MAP2*, *NEUN*, and *SYN1*), glutamatergic neuronal marker (*GRIN1*), GABAergic neuronal marker (*GRIN2B*) and glial marker (*S100B*) in simplified brain organoids (simBOs; 3D) and 2D differentiation samples. Expression value was normalized to those of human primitive neural stem cells (pNSC) in 2D (d0). Data represent mean ± standard error (SE) from three technical replicates. Statistical significance of Sidak's multiple comparisons $^{*}p < 0.05$, $^{**}p < 0.01$, $^{***}p < 0.001$ after two-way ANOVA.

with reduced number of fibrous ECM organization genes. In addition, the cluster IV genes, which were reduced in the 2D cultures and further decreased in the simBOs, are involved in cell cycles, signaling by rho GTPase, and S phase (**Figure 4B** and **Supplementary Figure 9**). Interestingly, genes involved in the Hippo signaling pathway were enriched in clusters III and IV (**Figure 4B**), implying a possible role in differentiation of simBO. Taken together, these results suggest that the 3D environment

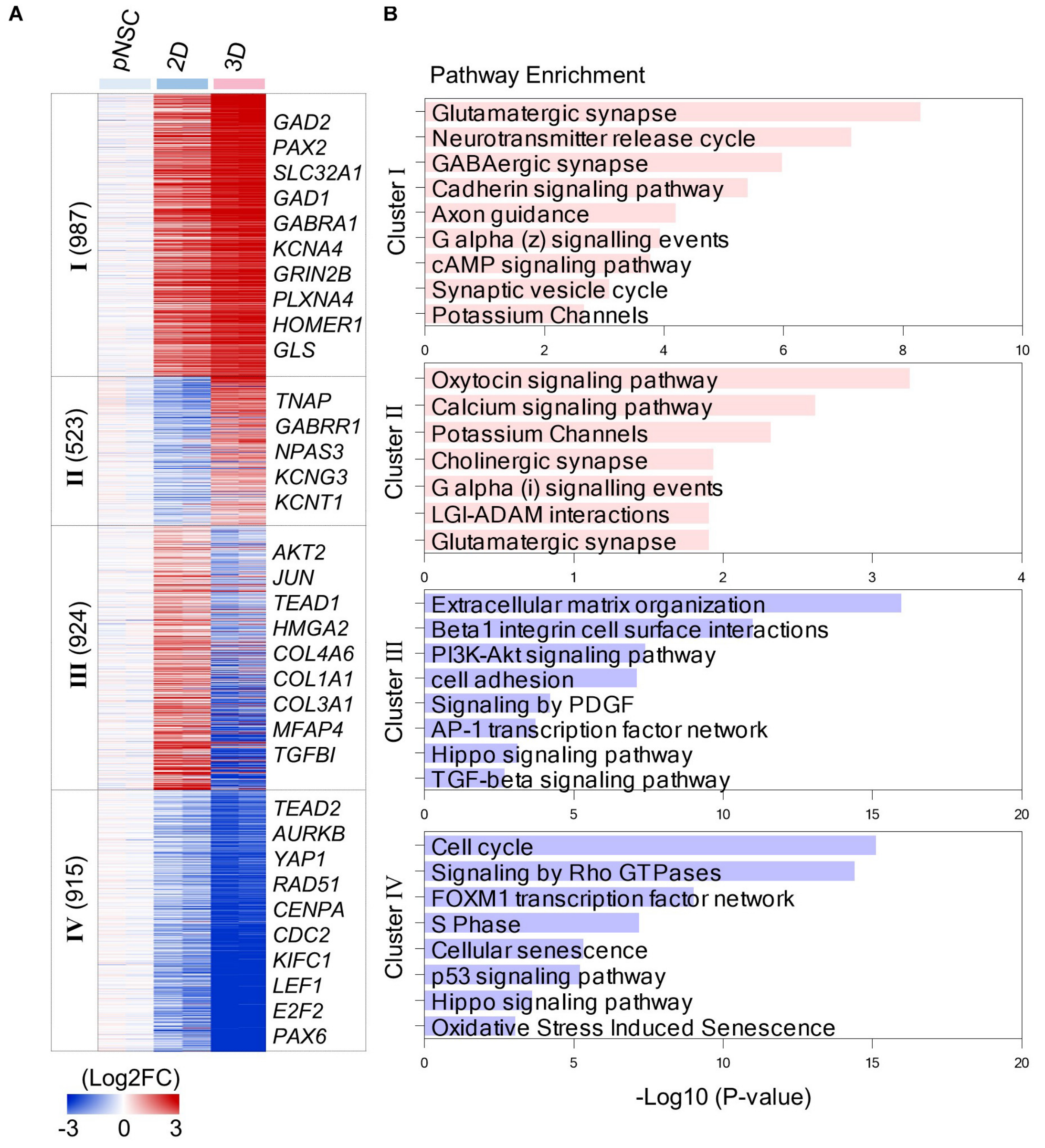

FIGURE 4 | Transcriptomic analysis of simBOs and 2D differentiation. **(A)** Heat map of differentially expressed genes between 2D and 3D differentiation. Expression value was normalized to those of iPSCs. Cluster name and gene number in each cluster were indicated in left panel and representative gene names in each cluster were indicated in the right panel. Color scale of expression value were presented in lower panel. **(B)** Bar chart for the –Log10(*p*.value) of representative enriched pathway calculated by reactome pathway enrichment analysis.

during neuronal differentiation enhanced differentiation into post-mitotic mature neurons and brain-like ECM.

Cytoplasmic Translocation of YAP1 in the 3D Environment

Next, we explored how the 3D environment can enhance rapid neuronal differentiation in the same differentiation medium. The 3D environment provides a relatively low-stiffness matrix closer to that of tissues than the plastic surface of culture dishes (Baker and Chen, 2012) and Yes-associated protein 1 (YAP1), a transcription co-activator of the Hippo signaling pathway, is a well-known mechanosensor that modulates cellular behavior through cytoplasmic-nuclear translocation by responding to stimuli from the mechanical environment (Dupont et al., 2011). Moreover, YAP1 promotes the proliferation of neural stem cells and inhibits neuronal differentiation (Cao et al., 2008; Zhang et al., 2012). Thus, we hypothesized that low stiffness in a 3D environment could translocate YAP1 proteins into the cytoplasm, and this could promote neuronal differentiation by inhibiting the function of YAP1 as a transcriptional co-activator. To test this hypothesis,

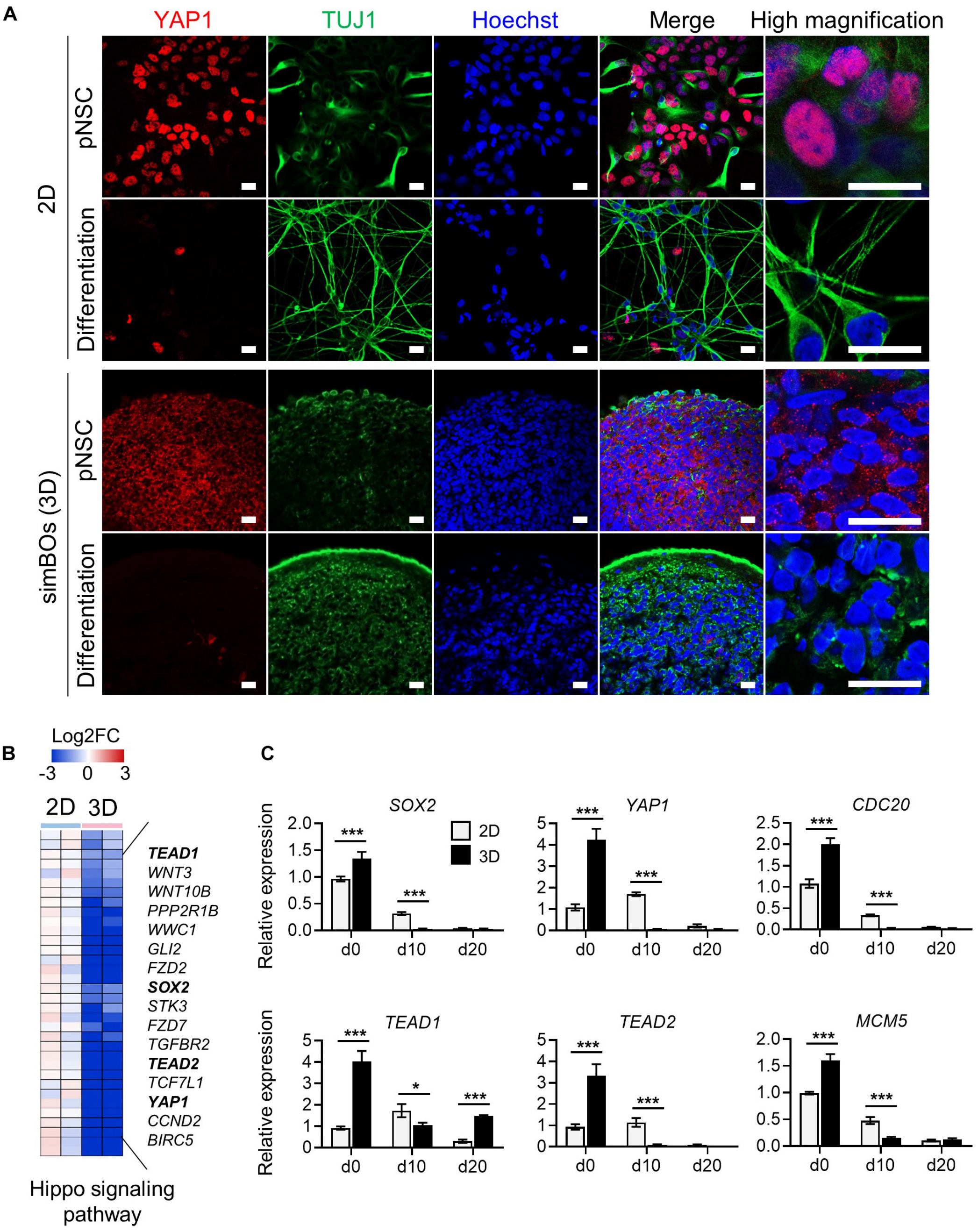

FIGURE 5 | Subcellular localization and transcription regulation of YAP1. **(A)** Subcellular localization of YAP1 and TUJ1. Scale bars represent 20 μm. **(B)** Heat map for the Hippo signaling pathway genes differentially expressed during 2D and 3D differentiation. Representative gene names were presented in right panel and color scale was presented upper panel. **(C)** Quantitative reverse transcription polymerase chain reaction (qRT-PCR) analysis for *YAP1* and direct targets of YAP1 (*SOX2*, *TEAD1*, *TEAD2*, *CDC20*, and *MCM5*) in simplified brain organoids (simBOs; 3D) and 2D differentiation samples. Expression value was normalized to those of human primitive neural stem cells (pNSCs) in 2D (d0). Data represent mean ± standard error (SE) from three technical replicates. Statistical significance of Sidak's multiple comparisons $^{*}p < 0.05$, $^{***}p < 0.001$ after two-way ANOVA.

we examined the subcellular localization of YAP1 in the pNSCs and differentiated neuronal cells depending on the 2D or 3D environment. As expected, **Figure 5A** shows that YAP1 is mainly located in the nucleus in the 2D environment, whereas it is detected in the cytoplasm in the simBOs, suggesting functional impairment of YAP1. In addition, neuronal differentiation rapidly diminished YAP1 expression in differentiated neurons (**Figure 5A**).

Furthermore, transcriptome data showed that 3D differentiation further decreased genes related to the Hippo

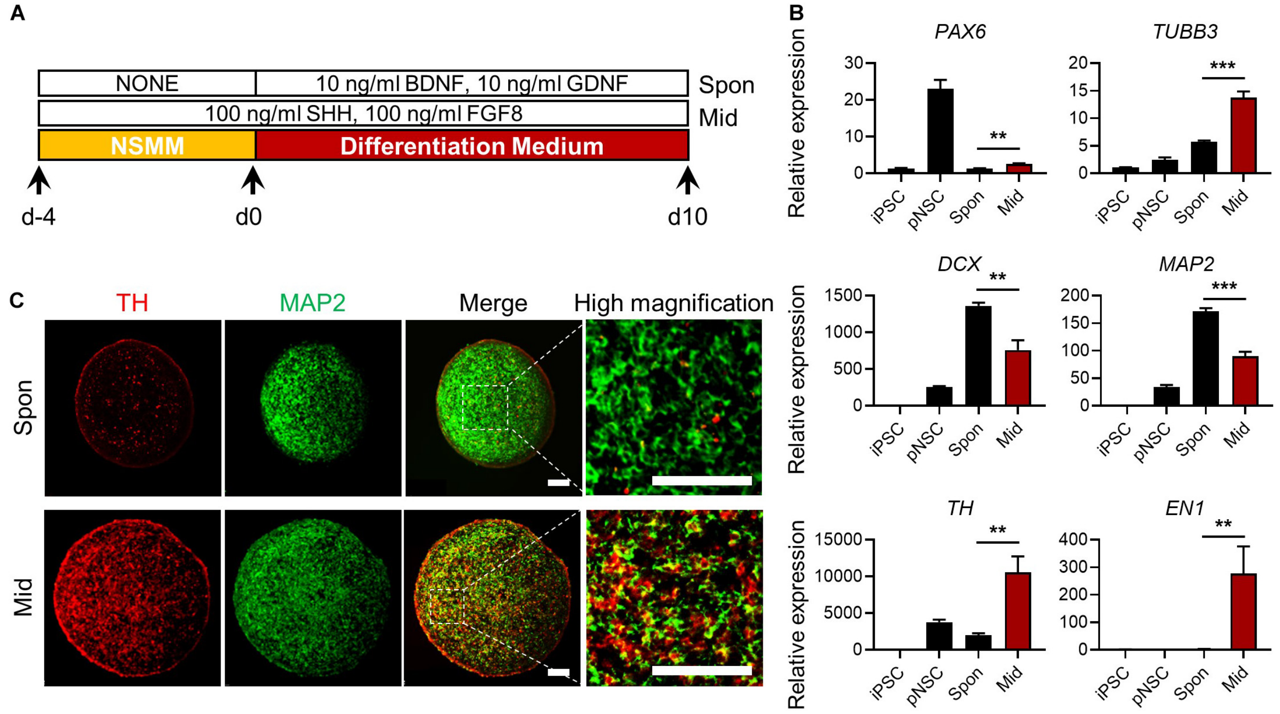

FIGURE 6 | Generation of midbrain-like simplified brain organoids (simBOs). **(A)** Graphical schematics for midbrain-like simBOs. **(B)** Quantitative reverse transcription polymerase chain reaction (qRT-PCR) analysis for neural progenitor marker (*PAX6*), pan-neuronal markers (*TUBB3*, *DCX*, and *MAP2*) and dopaminergic neuron markers (*TH* and *EN-1*) in induced pluripotent stem cells (iPSCs), human primitive neural stem cells (pNSCs), spontaneously differentiated-simBOs (Spon), and midbrain-like simBOs (Mid). Expression value was normalized to those of iPSCs. Data represent mean ± standard error (SE) from three technical replicates. Statistical significance of $^{**}p < 0.01$, $^{***}p < 0.001$ was calculated by unpaired *t*-test. **(C)** Immunofluorescence analysis with pan-neuronal markers (MAP2) and dopaminergic neuronal marker (TH) in Spon-simBOs and Mid-simBOs. Scale bars represent 100 μm.

signaling pathway including *YAP1*, *TEAD1*, and *TEAD2*, and transcription factors directly bound to YAP1 and mediated YAP1-dependent transcription regulations (Cao et al., 2008) (**Figure 5B**). To confirm the expression of *YAP1* and its targets, we performed RT-PCR in the pNSCs and differentiated cells in the 2D or 3D environment (**Figure 5C**). *YAP1*, *TEAD1*, *and TEAD2* expression decreased more rapidly during differentiation in the 3D environment, comparably to the expression pattern of the neural stem cell marker *SOX2*. Moreover, *CDC20* and *MCM5*, which are direct targets of the YAP1-TEADs complex and regulators of the cell cycle, also had their expression decreased more rapidly during differentiation in the 3D environment compared to the 2D environment. These data suggest that the rapid differentiation of simBOs is related to the dysfunction of YAP1 by translocation.

Generation of Midbrain-Like simBOs and PD Modeling

Next, we examined whether simBOs could be specified into midbrain-like organoids, which can replicate the pathology and drug response of PD. Because sonic hedgehog (Shh) and fibroblast growth factor 8 (FGF8) are key signaling molecules for midbrain specification (Arenas et al., 2015), we treated simBOs with Shh and FGF8 during differentiation (**Figure 6A**). Compared to spontaneously differentiated simBOs, the dopaminergic neuronal markers (*TH* and *EN1*) were robustly up-regulated in the midbrain-like simBOs (**Figure 6B**). In contrast, neuronal markers (*TUBB3*, *DCX*, and *MAP2*) were highly expressed in both spontaneously differentiated simBOs and midbrain-like simBOs. Immunofluorescence staining showed that TH^{+}(tyrosine hydroxylase)/$MAP2^{+}$ dopaminergic neurons were distributed throughout the midbrain-like simBOs (**Figure 6C**).

For PD modeling, we used PD patient-derived iPSCs harboring *LRRK2*^{G2019S} point mutation (PD-iPSCs) and gene-corrected control iPSCs (Control-iPSCs) by BAC-based homologous recombination (Son et al., 2017; Lee and Chung, 2019) (**Figure 7A**). We performed DNA sequencing and confirmed a heterozygous *LRRK2*^{G2019S} mutation in PD-iPSCs and corrected this mutation in control-iPSCs (**Figure 7B**). These iPSCs were fully characterized in the context of alkaline phosphatase activity, expression of pluripotency markers (OCT-3/4 and NANOG) (**Supplementary Figure 11A**), and embryonic body formation (**Supplementary Figure 11B**). Additionally, both iPSCs showed a normal karyotype (**Supplementary Figure 11C**) and the same genotype on short tandem repeat (STR), proving to be isotype-paired cells from an identical person (**Supplementary Figure 11D**). Finally, we obtained expandable pNSCs from these iPSCs

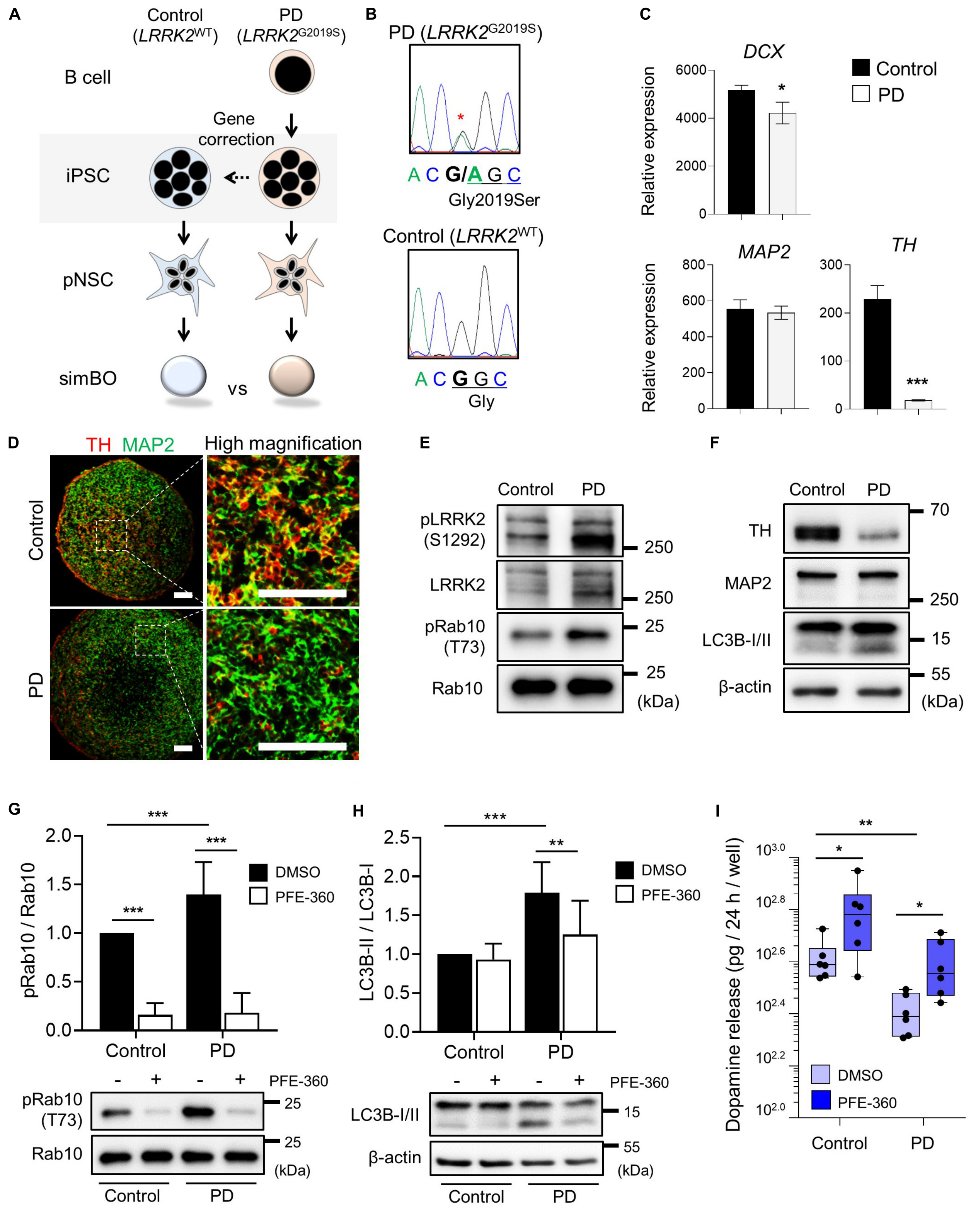

FIGURE 7 | Parkinson's modeling with midbrain-like simplified brain organoids (simBOs). **(A)** Schematic flow diagram to depict the establishment of PD patient-derived simBOs from harboring *LRRK2* G2019S mutation (PD) and gene-corrected control iPSCs (Control). **(B)** DNA sequencing data for the *LRRK2* G2019S (Gly to Ser) mutation and correction of this gene in the iPSCs. **(C)** Quantitative reverse transcription polymerase chain reaction (qRT-PCR) analysis for pan-neuronal

(Continued)

FIGURE 7 | Continued
markers (DCX and MAP2) and dopaminergic neuronal marker (TH). Expression value was normalized to those of induced pluripotent stem cells (iPSCs). Data represent mean standard error (SE) from three technical replicates. Statistical significance of $^{*}p < 0.05$, $^{***}p < 0.001$ was calculated by unpaired *t*-test.
(D) Immunofluorescence analysis with pan-neuronal marker (MAP2) and dopaminergic neuronal marker (TH). Scale bars represent 100 μm. **(E,F)** Western blotting for indicated proteins in PD-simBOs. β-actin was used as loading control. **(G,H)** Representative western blotting and quantitative graph for LC3B-II normalized to LC3B-I. **(G)** and pRab10 normalized to total Rab10 **(H)** at day 13 with or without LRRK2 kinase inhibitor (PFE-360) treatment for 3 days. β-actin was used as loading control. Data represent mean ± SE from three batches, two technical replicates. Statistical significance of Turkey's multiple comparisons $^{**}p < 0.01$, $^{***}p < 0.001$ after two-way ANOVA. **(I)** Dopamine secretion of simBOs was measured in the presence of DMSO or PFE-360. For analysis, cultured media for 24-h were obtained from the wells containing eight simBOs each. Data represent mean ± SE from two batches, three technical replicates. Statistical significance of $^{*}p < 0.05$, $^{**}p < 0.01$ was calculated by unpaired *t*-test.

and characterized them by immunofluorescence analysis of neural markers (NESTIN) and neurofilament protein (TUJ1) (**Supplementary Figure 11E**).

Generation of PD Patient-Derived (*LRRK2*$^{\text{G2019S}}$) and Gene-Corrected Control Midbrain-Like simBOs

Next, we generated midbrain-like simBOs from PD patient-derived (*LRRK2*$^{\text{G2019S}}$)-pNSCs (PD-simBOs) and gene-corrected control-pNSCs (Control-simBOs). These midbrain-like simBOs showed no differences in the expression of neuronal marker genes (*DCX* and *MAP2*), but the mDA neuronal marker gene (*TH*) expression was substantially decreased in PD-simBOs (**Figure 7C**). Consistently, we observed that dopaminergic neurons (TH^{+}/MAP2^{+}) were decreased in PD-simBOs compared to control-simBOs (**Figure 7D**). Moreover, to confirm LRRK2 kinase activity in these midbrain-like simBOs, we examined phosphorylation sites of LRRK2 kinase substrates, Ser1292 in LRRK2 (Sheng et al., 2012) and Thr73 in Rab10 (Thirstrup et al., 2017). The phosphorylation of LRRK2 kinase substrates was increased in PD-simBOs compared to control-simBOs (**Figure 7E**), demonstrating that PD-simBOs replicated the molecular signatures of familial PD. Consistently with previous results, MAP2 expression was quite similar between PD- and control-simBOs, but TH was decreased in PD-simBOs (**Figure 7F**). Additionally, the levels of LC3B-II, an autophagy marker, were increased in PD-simBOs (**Figure 7F**). Previously, it was reported that the *LRRK2*$^{\text{G2019S}}$ mutation caused autophagy, which resulted in neurite autophagy and shortening (Plowey et al., 2008; Bravo-San Pedro et al., 2013). Thus, we hypothesized that the elevated autophagy in PD-simBOs could be rescued by suppression of LRRK2 kinase activity. When we treated PD models of midbrain-like simBOs with LRRK2 kinase inhibitor, PFE-360, Rab10 phosphorylation was significantly suppressed in both PD- and control-simBOs (**Figure 7G**) and the LC3B-II levels were rescued in PD-simBOs (**Figure 7H**), suggesting autophagy are regulated by LRRK2 kinase activity in PD-simBOs.

Furthermore, we demonstrated that reduced dopamine release in PD-simBOs could be rescued by treatment with PFE-360 (**Figure 7I**), implying functional improvement of dopaminergic neurons by the LRRK2 inhibitor. These data indicate that midbrain-like simBOs from PD-iPSC-derived pNSCs could replicate the phenotype of PD and drug response.

DISCUSSION

Brain organoids are a breakthrough technology for studying embryonic development and disease pathology in the human brain. In particular, brain organoid models replicating various brain disorders are expected to be used as a model for drug screening (Wang, 2018). However, the heterogeneity between organoids and the need for long-term differentiation hinders their further application. Recently, several brain organoids with homogeneous properties in cellular composition have been reported (Velasco et al., 2019; Yoon et al., 2019; Kwak et al., 2020; Sivitilli et al., 2020), but these brain organoids still require long-term differentiation because they use iPSCs as a starting material. In this study, we generated homogeneous simBOs in 2 weeks using expandable pNSCs as a starting material.

Consistently with our results, Nickels et al. (2020) have shown that the use of more committed cells as a starting material not only induces homogeneous properties between organoids but also shortens the differentiation period. The neuronal layer formation seen in cerebral organoids was not observed in simBOs, but they consisted of diverse types of neurons and astrocytes. This approach allowed us to obtain structurally simple, but fast and robustly producible simBOs. Moreover, we demonstrated that pNSCs could be also specified into midbrain-like simBOs for PD modeling and established a pair of isogenic simBOs with an *LRRK2*$^{\text{G2019S}}$ point mutation replicating the pathology of familial PD. We found that PD-simBOs showed elevated LRRK2 kinase activity and reduction of TH^{+} dopaminergic neurons, while these disease phenotypes were rescued in the gene-corrected isogenic control simBOs, indicating that our simBOs are useful models for studying the pathogenesis of familial PD harboring an *LRRK2*$^{\text{G2019S}}$ mutation and discovering novel therapeutic targets for this disease.

After the generation of midbrain organoids (Jo et al., 2016; Qian et al., 2016), various organoid models that replicate familial, sporadic, and toxin-induced PD have been developed (Kim et al., 2019; Smits et al., 2019; Chlebanowska et al., 2020; Kwak et al., 2020). These brain organoids may be suitable models, successfully replicating the midbrain-specific phenotypes, for example, neuromelanin granules or midbrain-specific electrophysiology, and the pathological signatures of PD, for example, aggregation of alpha-synuclein or mDA neuron-specific cell death. However, they still have limitations in terms of time and cost to be used for drug discovery based on high-throughput screening (HTS). Our midbrain-like simBOs are not an advanced midbrain-like organoid model, but they are a more suitable model for HTS, as we were able to achieve rapid and robust production of homogeneous organoids. Moreover, we observed that elevated PD phenotypes were rescued by treatment with the LRRK2 kinase inhibitor, demonstrating that our simBOs are a ready-to-use model for screening drug candidates for PD.

Interestingly, we found enhanced neuronal maturity in simBOs, compared to that in 2D differentiation. It had been previously shown that cellular and extracellular signatures of human brain tissue are promoted in 3D culture environment (Simao et al., 2018). Consistently with these data, our transcriptome data showed that the 3D environment decreased fibrous ECM in the extracellular space and increased synapse and membrane ion-channel complex formation. Brain tissues have a unique composition of ECM compared to other organs: they have relatively low levels of fibrous proteins such as collagen and high levels of glycoproteins and proteoglycans, corresponding to the soft properties of the brain (Hong and Do, 2019). Thus, the decreased fibrous ECM organization in simBOs confers them more similar characteristics to those of the *in vivo* brain. The ECM serves not only as an essential structural scaffold but also provides significant biomechanical and biochemical stimulations for morphogenesis, cellular differentiation, and tissue homeostasis (Frantz et al., 2010). In particular, ECM influences brain development, homeostasis, and disease (Barnes et al., 2017). Thus, the dysregulation of ECM shown in 2D environment may act as a drawback in neuronal differentiation and disease modeling. In addition, enhanced neuronal maturation in simBOs could be associated with the improved ECM environment.

The differentiation and behavior of cells are stiffly regulated not only by biochemical signals (chemical composition and ligand density) but also by biophysical cues (matrix stiffness, topography, and geometry) (Yao et al., 2013; Bao et al., 2019). We observed that the 3D environment differentiates pNSCs faster into mature neurons under the same medium composition. Analysis of differentially expressed genes between samples differentiated in 2D and 3D environments revealed that the transcriptional co-activator YAP1, a mechanosensitive protein, was robustly and more rapidly downregulated during 3D differentiation, similar to the expression pattern of the neural stem cell marker SOX2. These results are consistent with a previous report indicating that SOX2 is a direct transcription regulator of YAP1 (Seo et al., 2013). Previous studies have shown that YAP1 enhances the proliferation of neural progenitors and negatively regulates neuronal differentiation (Cao et al., 2008; Zhang et al., 2012; Chighizola et al., 2019). During neuronal differentiation, YAP1 is excluded from nuclei and undergoes proteasomal degradation (Zaltsman et al., 2019). Interestingly, the subcellular localization of YAP1 was already promoted in our simBOs before neuronal differentiation, suggesting that 3D environment promoted translocation of YAP1. Given that different extracellular features were observed between 2D and 3D environments (Simao et al., 2018) and the stiffness of 3D environment affect the localization and expression of YAP1 (Molina et al., 2019), we could postulate that the altered extracellular features in the 3D environment might promote neuronal differentiation via suppression of YAP1. Although it still remains elusive as to which 3D culture environmental cues modulate the expression and localization of YAP1, our data support that 3D models more closely replicate the physiological relevance of the *in vivo* brain.

CONCLUSION

Our results demonstrate that simBOs present the minimum-sufficient specification for the brain organoid model for HTS and can be a useful platform for modeling various brain disease.

DATA AVAILABILITY STATEMENT

The datasets generated for this study can be found in Gene Expression Omnibus (GSE156396).

ETHICS STATEMENT

The studies involving human participants were reviewed and approved by the Public Institutional Review Board designated by the Ministry of Health and Welfare (P01-201802-31-001). The patients/participants provided their written informed consent to participate in this study.

AUTHOR CONTRIBUTIONS

JH, M-OL, and JK: conceptualization. AB, ML, and S-KC: validation. JSK and SK: formal analysis. JH and M-OL: writing—original draft preparation. M-OL and JK: writing—review and editing. All authors have read and agreed with the published version of the manuscript.

FUNDING

This research was supported by grants from the National Research Foundation of Korea (2015M3A9C7030128 and 2019R1A2C2087606), the 3D-TissueChip Based Drug Discovery Platform Technology Development Program (No. 20009209) funded by the Ministry of Trade, Industry and Energy (MOTIE, South Korea), and KRIBB Research Initiative Program funded by the Ministry of Science and ICT. The funders had no role in the study design, data collection or analysis, decision to publish, or preparation of the manuscript.

SUPPLEMENTARY MATERIAL

The Supplementary Material for this article can be found online at: https://www.frontiersin.org/articles/10.3389/fcell.2020.594090/full#supplementary-material

REFERENCES

Arenas, E., Denham, M., and Villaescusa, J. C. (2015). How to make a midbrain dopaminergic neuron. *Development* 142, 1918–1936. doi: 10.1242/dev.097394

Bagley, J. A., Reumann, D., Bian, S., Levi-Strauss, J., and Knoblich, J. A. (2017). Fused cerebral organoids model interactions between brain regions. *Nat. Methods* 14, 743–751. doi: 10.1038/nmeth.4304

Baker, B. M., and Chen, C. S. (2012). Deconstructing the third dimension: how 3D culture microenvironments alter cellular cues. *J. Cell Sci.* 125, 3015–3024. doi: 10.1242/jcs.079509

Bao, M., Xie, J., Katoele, N., Hu, X., Wang, B., Piruska, A., et al. (2019). Cellular Volume and Matrix Stiffness Direct Stem Cell Behavior in a 3D Microniche. *ACS Appl. Mater Interf.* 11, 1754–1759. doi: 10.1021/acsami.8b19396

Barnes, J. M., Przybyla, L., and Weaver, V. M. (2017). Tissue mechanics regulate brain development, homeostasis and disease. *J. Cell Sci.* 130, 71–82. doi: 10.1242/jcs.191742

Birey, F., Andersen, J., Makinson, C. D., Islam, S., Wei, W., Huber, N., et al. (2017). Assembly of functionally integrated human forebrain spheroids. *Nature* 545, 54–59. doi: 10.1038/nature22330

Bravo-San Pedro, J. M., Niso-Santano, M., Gomez-Sanchez, R., Pizarro-Estrella, E., Aiastui-Pujana, A., Gorostidi, A., et al. (2013). The LRRK2 G2019S mutant exacerbates basal autophagy through activation of the MEK/ERK pathway. *Cell Mol. Life Sci.* 70, 121–136. doi: 10.1007/s00018-012-1061-y

Burbulla, L. F., Song, P., Mazzulli, J. R., Zampese, E., Wong, Y. C., Jeon, S., et al. (2017). Dopamine oxidation mediates mitochondrial and lysosomal dysfunction in Parkinson's disease. *Science* 357, 1255–1261. doi: 10.1126/science.aam9080

Cao, X., Pfaff, S. L., and Gage, F. H. (2008). YAP regulates neural progenitor cell number via the TEA domain transcription factor. *Genes Dev.* 22, 3320–3334. doi: 10.1101/gad.1726608

Chighizola, M., Dini, T., Lenardi, C., Milani, P., Podesta, A., and Schulte, C. (2019). Mechanotransduction in neuronal cell development and functioning. *Biophys. Rev.* 11, 701–720. doi: 10.1007/s12551-019-00587-2

Chlebanowska, P., Tejchman, A., Sulkowski, M., Skrzypek, K., and Majka, M. (2020). Use of 3D Organoids as a Model to Study Idiopathic Form of Parkinson's Disease. *Int. J. Mol. Sci.* 21:694. doi: 10.3390/ijms21030694

Dupont, S., Morsut, L., Aragona, M., Enzo, E., Giulitti, S., Cordenonsi, M., et al. (2011). Role of YAP/TAZ in mechanotransduction. *Nature* 474, 179–183.

Efe, J. A., Hilcove, S., Kim, J., Zhou, H., Ouyang, K., Wang, G., et al. (2011). Conversion of mouse fibroblasts into cardiomyocytes using a direct reprogramming strategy. *Nat. Cell Biol.* 13, 215–222. doi: 10.1038/ncb2164

Frantz, C., Stewart, K. M., and Weaver, V. M. (2010). The extracellular matrix at a glance. *J. Cell Sci.* 123, 4195–4200.

Gitler, A. D., Dhillon, P., and Shorter, J. (2017). Neurodegenerative disease: models, mechanisms, and a new hope. *Dis. Model Mech.* 10, 499–502. doi: 10.1242/dmm.030205

Hodge, R. D., Bakken, T. E., Miller, J. A., Smith, K. A., Barkan, E. R., Graybuck, L. T., et al. (2019). Conserved cell types with divergent features in human versus mouse cortex. *Nature* 573, 61–68.

Homem, C. C., Repic, M., and Knoblich, J. A. (2015). Proliferation control in neural stem and progenitor cells. *Nat. Rev. Neurosci.* 16, 647–659.

Hong, Y. J., and Do, J. T. (2019). Neural Lineage Differentiation From Pluripotent Stem Cells to Mimic Human Brain Tissues. *Front. Bioeng. Biotechnol.* 7:400. doi: 10.3389/fbioe.2019.00400

Jo, J., Xiao, Y., Sun, A. X., Cukuroglu, E., Tran, H. D., Goke, J., et al. (2016). Midbrain-like Organoids from Human Pluripotent Stem Cells Contain Functional Dopaminergic and Neuromelanin-Producing Neurons. *Cell Stem Cell* 19, 248–257. doi: 10.1016/j.stem.2016.07.005

Kim, H., Park, H. J., Choi, H., Chang, Y., Park, H., Shin, J., et al. (2019). Modeling G2019S-LRRK2 Sporadic Parkinson's Disease in 3D Midbrain Organoids. *Stem Cell Rep.* 12, 518–531. doi: 10.1016/j.stemcr.2019.01.020

Koo, B., Choi, B., Park, H., and Yoon, K. J. (2019). Past, Present, and Future of Brain Organoid Technology. *Mol. Cells* 42, 617–627.

Kwak, T. H., Kang, J. H., Hali, S., Kim, J., Kim, K. P., Park, C., et al. (2020). Generation of homogeneous midbrain organoids with in vivo-like cellular composition facilitates neurotoxin-based Parkinson's disease modeling. *Stem Cells* 38, 727–740. doi: 10.1002/stem.3163

Lancaster, M. A., Renner, M., Martin, C. A., Wenzel, D., Bicknell, L. S., Hurles, M. E., et al. (2013). Cerebral organoids model human brain development and microcephaly. *Nature* 501, 373–379.

Lee, H., Son, Y. S., Lee, M. O., Ryu, J. W., Park, K., Kwon, O., et al. (2020). Low-dose interleukin-2 alleviates dextran sodium sulfate-induced colitis in mice by recovering intestinal integrity and inhibiting AKT-dependent pathways. *Theranostics* 10, 5048–5063. doi: 10.7150/thno.41534

Lee, M., Ha, J., Son, Y. S., Ahn, H., Jung, K. B., Son, M. Y., et al. (2019). Efficient exogenous DNA-free reprogramming with suicide gene vectors. *Exp. Mol. Med.* 51:82.

Lee, M. O., Jung, K. B., Jo, S. J., Hyun, S. A., Moon, K. S., Seo, J. W., et al. (2019). Modelling cardiac fibrosis using three-dimensional cardiac microtissues derived from human embryonic stem cells. *J. Biol. Eng.* 13:15.

Lee, S. Y., and Chung, S. K. (2019). Generation of gene-corrected iPSC line, KIOMi002-A, from Parkinson's disease patient iPSC with LRRK2 G2019S mutation using BAC-based homologous recombination. *Stem Cell Res.* 41:101649. doi: 10.1016/j.scr.2019.101649

Li, W., Sun, W., Zhang, Y., Wei, W., Ambasudhan, R., Xia, P., et al. (2011). Rapid induction and long-term self-renewal of primitive neural precursors from human embryonic stem cells by small molecule inhibitors. *Proc. Natl. Acad Sci. U S A* 108, 8299–8304. doi: 10.1073/pnas.1014041108

Lin, Y. T., Seo, J., Gao, F., Feldman, H. M., Wen, H. L., Penney, J., et al. (2018). APOE4 Causes Widespread Molecular and Cellular Alterations Associated with Alzheimer's Disease Phenotypes in Human iPSC-Derived Brain Cell Types. *Neuron* 98:e1147.

Liu, G. H., Qu, J., Suzuki, K., Nivet, E., Li, M., Montserrat, N., et al. (2012). Progressive degeneration of human neural stem cells caused by pathogenic LRRK2. *Nature* 491, 603–607. doi: 10.1038/nature11557

Mariani, J., Coppola, G., Zhang, P., Abyzov, A., Provini, L., Tomasini, L., et al. (2015). FOXG1-Dependent Dysregulation of GABA/Glutamate Neuron Differentiation in Autism Spectrum Disorders. *Cell* 162, 375–390. doi: 10.1016/j.cell.2015.06.034

Molina, E. R., Chim, L. K., Salazar, M. C., Mehta, S. M., Menegaz, B. A., Lamhamedi-Cherradi, S. E., et al. (2019). Mechanically tunable coaxial electrospun models of YAP/TAZ mechanoresponse and IGF-1R activation in osteosarcoma. *Acta Biomater.* 100, 38–51. doi: 10.1016/j.actbio.2019.09.029

Mootha, V. K., Lindgren, C. M., Eriksson, K. F., Subramanian, A., Sihag, S., Lehar, J., et al. (2003). PGC-1alpha-responsive genes involved in oxidative phosphorylation are coordinately downregulated in human diabetes. *Nat. Genet.* 34, 267–273. doi: 10.1038/ng1180

Muguruma, K., Nishiyama, A., Kawakami, H., Hashimoto, K., and Sasai, Y. (2015). Self-organization of polarized cerebellar tissue in 3D culture of human pluripotent stem cells. *Cell Rep.* 10, 537–550. doi: 10.1016/j.celrep.2014.12.051

Nickels, S. L., Modamio, J., Mendes-Pinheiro, B., Monzel, A. S., Betsou, F., and Schwamborn, J. C. (2020). Reproducible generation of human midbrain organoids for in vitro modeling of Parkinson's disease. *Stem Cell Res.* 46:101870. doi: 10.1016/j.scr.2020.101870

Pasca, A. M., Sloan, S. A., Clarke, L. E., Tian, Y., Makinson, C. D., Huber, N., et al. (2015). Functional cortical neurons and astrocytes from human pluripotent stem cells in 3D culture. *Nat. Methods* 12, 671–678. doi: 10.1038/nmeth.3415

Plowey, E. D., Cherra, S. J. III, Liu, Y. J., and Chu, C. T. (2008). Role of autophagy in G2019S-LRRK2-associated neurite shortening in differentiated SH-SY5Y cells. *J. Neurochem.* 105, 1048–1056. doi: 10.1111/j.1471-4159.2008.05217.x

Qian, X., Nguyen, H. N., Song, M. M., Hadiono, C., Ogden, S. C., Hammack, C., et al. (2016). Brain-Region-Specific Organoids Using Mini-bioreactors for Modeling ZIKV Exposure. *Cell* 165, 1238–1254. doi: 10.1016/j.cell.2016.04.032

Raja, W. K., Mungenast, A. E., Lin, Y. T., Ko, T., Abdurrob, F., Seo, J., et al. (2016). Self-Organizing 3D Human Neural Tissue Derived from Induced Pluripotent Stem Cells Recapitulate Alzheimer's Disease Phenotypes. *PLoS One* 11:e0161969. doi: 10.1371/journal.pone.0161969

Sakaguchi, H., Kadoshima, T., Soen, M., Narii, N., Ishida, Y., Ohgushi, M., et al. (2015). Generation of functional hippocampal neurons from self-organizing human embryonic stem cell-derived dorsomedial telencephalic tissue. *Nat. Commun.* 6:8896.

Seo, E., Basu-Roy, U., Gunaratne, P. H., Coarfa, C., Lim, D. S., Basilico, C., and Mansukhani, A. (2013). SOX2 regulates YAP1 to maintain stemness and determine cell fate in the osteo-adipo lineage. *Cell Rep.* 3, 2075–2087. doi: 10.1016/j.celrep.2013.05.029

Sheng, Z., Zhang, S., Bustos, D., Kleinheinz, T., Le Pichon, C. E., Dominguez, S. L., et al. (2012). Ser1292 autophosphorylation is an indicator of LRRK2 kinase activity and contributes to the cellular effects of PD mutations. *Sci. Transl. Med.* 4:164ra161. doi: 10.1126/scitranslmed.3004485

Simao, D., Silva, M. M., Terrasso, A. P., Arez, F., Sousa, M. F. Q., Mehrjardi, N. Z., et al. (2018). Recapitulation of Human Neural Microenvironment Signatures in iPSC-Derived NPC 3D Differentiation. *Stem Cell Rep.* 11, 552–564. doi: 10.1016/j.stemcr.2018.06.020

Sivitilli, A. A., Gosio, J. T., Ghoshal, B., Evstratova, A., Trcka, D., Ghiasi, P., et al. (2020). Robust production of uniform human cerebral organoids from pluripotent stem cells. *Life Sci. Alliance* 3:e202000707. doi: 10.26508/lsa.202000707

Smits, L. M., Reinhardt, L., Reinhardt, P., Glatza, M., Monzel, A. S., Stanslowsky, N., et al. (2019). Modeling Parkinson's disease in midbrain-like organoids. *NPJ. Parkinsons Dis.* 5:5.

Son, M. Y., Sim, H., Son, Y. S., Jung, K. B., Lee, M. O., Oh, J. H., et al. (2017). Distinctive genomic signature of neural and intestinal organoids from familial Parkinson's disease patient-derived induced pluripotent stem cells. *Neuropathol. Appl. Neurobiol.* 43, 584–603. doi: 10.1111/nan.12396

Subramanian, A., Tamayo, P., Mootha, V. K., Mukherjee, S., Ebert, B. L., Gillette, M. A., et al. (2005). Gene set enrichment analysis: a knowledge-based approach for interpreting genome-wide expression profiles. *Proc. Natl. Acad. Sci. U S A* 102, 15545–15550. doi: 10.1073/pnas.0506580102

Takahashi, K., Tanabe, K., Ohnuki, M., Narita, M., Ichisaka, T., Tomoda, K., et al. (2007). Induction of pluripotent stem cells from adult human fibroblasts by defined factors. *Cell* 131, 861–872. doi: 10.1016/j.cell.2007.11.019

Tao, Y., and Zhang, S. C. (2016). Neural Subtype Specification from Human Pluripotent Stem Cells. *Cell Stem Cell* 19, 573–586. doi: 10.1016/j.stem.2016.10.015

Thakur, K. T., Albanese, E., Giannakopoulos, P., Jette, N., Linde, M., Prince, M. J., et al. (2016). "Neurological Disorders," in *Mental, Neurological, and Substance Use Disorders: Disease Control Priorities, Third Edition*, eds V. Patel, D. Chisholm, T. Dua, R. Laxminarayan, and M. E. Medina-Mora (Washington,DC: The International Bank for Reconstruction and Development), 4.

Thirstrup, K., Dachsel, J. C., Oppermann, F. S., Williamson, D. S., Smith, G. P., Fog, K., et al. (2017). Selective LRRK2 kinase inhibition reduces phosphorylation of endogenous Rab10 and Rab12 in human peripheral mononuclear blood cells. *Sci. Rep.* 7:10300.

Thomson, J. A., Itskovitz-Eldor, J., Shapiro, S. S., Waknitz, M. A., Swiergiel, J. J., Marshall, V. S., et al. (1998). Embryonic stem cell lines derived from human blastocysts. *Science* 282, 1145–1147. doi: 10.1126/science.282.5391.1145

Velasco, S., Kedaigle, A. J., Simmons, S. K., Nash, A., Rocha, M., Quadrato, G., et al. (2019). Individual brain organoids reproducibly form cell diversity of the human cerebral cortex. *Nature* 570, 523–527. doi: 10.1038/s41586-019-1289-x

Wang, H. (2018). Modeling Neurological Diseases With Human Brain Organoids. *Front. Synaptic Neurosci.* 10:15. doi: 10.3389/fnsyn.2018.00015

Xiang, Y., Tanaka, Y., Patterson, B., Kang, Y. J., Govindaiah, G., Roselaar, N., et al. (2017). Fusion of Regionally Specified hPSC-Derived Organoids Models Human Brain Development and Interneuron Migration. *Cell Stem Cell* 21, 383–398.e7.

Yao, X., Peng, R., and Ding, J. (2013). Cell-material interactions revealed via material techniques of surface patterning. *Adv. Mater* 25, 5257–5286. doi: 10.1002/adma.201301762

Yoon, S. J., Elahi, L. S., Pasca, A. M., Marton, R. M., Gordon, A., Revah, O., et al. (2019). Reliability of human cortical organoid generation. *Nat. Methods* 16, 75–78. doi: 10.1038/s41592-018-0255-0

Zaltsman, Y., Masuko, S., Bensen, J. J., and Kiessling, L. L. (2019). Angiomotin Regulates YAP Localization during Neural Differentiation of Human Pluripotent Stem Cells. *Stem Cell Rep.* 12, 869–877. doi: 10.1016/j.stemcr.2019.03.009

Zhang, H., Deo, M., Thompson, R. C., Uhler, M. D., and Turner, D. L. (2012). Negative regulation of Yap during neuronal differentiation. *Dev. Biol.* 361, 103–115. doi: 10.1016/j.ydbio.2011.10.017

Conflict of Interest: The authors declare that the research was conducted in the absence of any commercial or financial relationships that could be construed as a potential conflict of interest.

frontiers
in Cell and Developmental Biology

ORIGINAL RESEARCH
published: 17 December 2020
doi: 10.3389/fcell.2020.609278

Three-Dimensional Analysis of Busulfan-Induced Spermatogenesis Disorder in Mice

Hiroki Nakata[1], Taito Nakano[2], Shoichi Iseki[3] and Atsushi Mizokami[2]*

[1] Department of Histology and Cell Biology, Graduate School of Medical Sciences, Kanazawa University, Kanazawa, Japan, [2] Department of Integrative Cancer Therapy and Urology, Graduate School of Medical Sciences, Kanazawa University, Kanazawa, Japan, [3] Department of Clinical Engineering, Faculty of Health Sciences, Komatsu University, Komatsu, Japan

We examined if the distribution of impaired or normal spermatogenesis differs along the length of seminiferous tubules in disorders of spermatogenesis. For this purpose, three-dimensional (3D) reconstruction of seminiferous tubules was performed in mice with experimental spermatogenesis disorder induced by intraperitoneal injection of busulfan, and the areas of impaired and normal spermatogenesis were analyzed microscopically. The volume of the testis and length of seminiferous tubules decreased, and the proportion of tubule areas with impaired spermatogenesis increased depending on the dose of busulfan. With the highest dose of busulfan, although the proportion of impaired spermatogenesis was similar among individual seminiferous tubules, it was slightly but significantly higher in shorter tubules and in tubule areas near branching points. The tubule areas with impaired and normal spermatogenesis consisted of many segments of varying lengths. With increasing doses of busulfan, the markedly impaired segments increased in length without changing in number, whereas normal segments, although reduced in number and length, remained even with the highest dose of busulfan. Individual remaining normal segments consisted of several different stages, among which stage I and XII were found at higher frequencies, and stage VI at a lower frequency than expected in normal seminiferous tubules. We also examined if the distribution of impaired or normal spermatogenesis differs among different 3D positions in the testis without considering the course of seminiferous tubules. Although the proportions of impaired spermatogenesis with the minimum dose of busulfan and normal spermatogenesis with the highest dose of busulfan greatly varied by location within a single testis, there were no 3D positions with these specific proportions common to different testes, suggesting that the factors influencing the severity of busulfan-induced spermatogenesis disorder are not fixed in location among individual mice.

Keywords: spermatogenesis, seminiferous tubule, 3D reconstruction, testis, busulfan

Edited by:
Silvia Garagna,
University of Pavia, Italy

Reviewed by:
Paola Grimaldi,
University of Rome Tor Vergata, Italy
Carla Boitani,
Sapienza University of Rome, Italy

****Correspondence:***
Hiroki Nakata
hnakata@staff.kanazawa-u.ac.jp

Specialty section:
This article was submitted to Cell Growth and Division, a section of the journal Frontiers in Cell and Developmental Biology

Received: *23 September 2020*
Accepted: *30 November 2020*
Published: *17 December 2020*

Citation:
Nakata H, Nakano T, Iseki S and Mizokami A (2020) Three-Dimensional Analysis of Busulfan-Induced Spermatogenesis Disorder in Mice. Front. Cell Dev. Biol. 8:609278. doi: 10.3389/fcell.2020.609278

INTRODUCTION

Approximately 15% of couples trying to conceive are infertile, with a male factor involved in 50% of cases (Corona et al., 2019). The most severe form of male infertility is non-obstructive azoospermia (NOA), which accounts for 5% of infertile couples (Krausz, 2011; Tournaye et al., 2017; Pan et al., 2018). Spermatozoa in NOA can usually only be isolated from the testes, thus the most effective treatment is testicular sperm extraction. However, sperm retrieval in NOA is successful only in approximately 50% of cases due to partial and heterogeneous preserved focal spermatogenesis. Therefore, an accurate predictor for sperm retrieval is desired.

Many clinical factors, such as testicular volume, serum follicle-stimulating hormone, and serum inhibin B, have been investigated as an accurate predictor, but none were useful. Recently, the ultrasonographically measured size of seminiferous tubules was reported as a strong predictor (Nariyoshi et al., 2020). Identifying the focal areas containing mature sperm by ultrasonography mostly depends on the skill of the technician, and if the probable areas were known in advance, the success rate of the identification may increase. Therefore, clarification of the distribution of spermatogenesis in the testis with NOA is required.

It is generally believed that the sites of preserved spermatogenesis in the testis with NOA are multi-focal and distributed diffusely and homogenously rather than being patch-like and distributed heterogeneously in particular regions (Silber et al., 1997; Schwarzer et al., 2013). On the other hand, several groups reported a correlation between testicular blood supply and focal spermatogenesis in NOA (Har-Toov et al., 2004; Herwig et al., 2004). These studies were conducted in human therapy, but morphological analysis of spermatogenesis disorder in the whole human testis is practically difficult. Therefore, studies using animal models of the disorder are needed to confirm the three-dimensional (3D) distribution of impaired or normal spermatogenesis in the whole testis.

Our group recently reported the high-resolution 3D structure of all seminiferous tubules in animal testes using serial paraffin sections and high-performance 3D reconstruction software (Nakata et al., 2015a, 2017a, 2021; Nakata, 2019). Moreover, we found that the sites where spermatogenesis first occurs postnatally are distributed preferentially in the upper and medial areas of the testis close to the rete testis in mice (Nakata et al., 2017a). Our procedure was thought to be applicable to analyzing the distribution of spermatogenesis in the testis with spermatogenesis disorders. In the present study, we prepared mice with different degrees of spermatogenesis disorder by changing the doses of busulfan injection, which is known to cause extensive degeneration of seminiferous tubules (de Rooij and Kramer, 1970; Bucci and Meistrich, 1987). Then, the 3D-reconstructed seminiferous tubules were analyzed to examine if the impaired or normal spermatogenesis was distributed preferentially in particular sites in seminiferous tubules or in the testis.

MATERIALS AND METHODS

Animals

The present animal study was approved by Kanazawa University (approval number: AP-173897) and conducted in accordance with the Guidelines for the Care and Use of Laboratory Animals of Kanazawa University. C57BL/6 strain male mice were purchased from Nippon SLC, Inc. (Hamamatsu, Japan), and reared under standard 12-h light/12-h dark laboratory conditions with free access to standard food and water.

Busulfan Treatment

Busulfan (B2635; Sigma, St. Louis, MO, United States) was dissolved in DMSO and diluted in an equal volume of sterile distilled water to a final concentration of 0, 1, 2, or 3 mg/mL immediately before injection. Six-week-old male mice (body weight approximately 20 g) received a single intraperitoneal injection of 0, 10, 20, or 30 mg/kg of busulfan (IP-0, IP-10, IP-20, or IP30).

Tissue Preparation and Periodic Acid-Schiff-Hematoxylin Staining

At 12 weeks after busulfan treatment, the mice were sacrificed by cervical dislocation. The testis and epididymis were dissected out en bloc, fixed in Bouin's solution or 10% formalin neutral buffer solution overnight, dehydrated in a graded ethanol series, and embedded in paraffin. Using the Bouin's-fixed paraffin blocks, serial 5-μm-thick sections with intervals of 40 or 50 μm were made by cutting the specimen longitudinally in parallel to the plane involving both the testis and epididymis using a microtome, and then mounted on glass slides. The sections were treated with periodic acid-Schiff-hematoxylin (PAS-H) to stain the basement membrane of seminiferous tubules, as previously described (Nakata and Iseki, 2019). The sections were digitized using a whole-slide scanner (Nanozoomer 2.0-HT; Hamamatsu Photonics, Hamamatsu, Japan) with a 20-fold objective lens, and the resulting digital images of the sections were visualized with viewer software (NDP.view2; Hamamatsu Photonics).

Immunohistochemistry

Using the formalin-fixed paraffin sections, immunohistochemistry (IHC) was performed as described previously (Nakata et al., 2015b, 2017b). The sections were incubated with antibodies against ZBTB16 (1:200 dilution; HPA001499, Sigma-Aldrich, St. Louis, MO, United States), GATA4 (1:50; sc-1237, Santa Cruz Biotechnology, Dallas, TX, United States), or SYCP3 (1:400; ab15093, Abcam, Cambridge, United Kingdom) followed by secondary antibodies labeled with Alexa Fluor 488 or 594 (1:400, Molecular Probes, Eugene, OR, United States), or with Alexa Fluor 488-conjugated lectin PNA (1:400, Molecular Probes). All sections were counterstained with DAPI (300 nM; Molecular Probes), mounted on glass slides with Fluoromount (Diagnostic BioSystems, Pleasanton, CA, United States), and examined with a fluorescence microscope (BX51; Olympus, Tokyo, Japan). Fluoromount was then removed and the sections were washed and stained with hematoxylin and eosin (HE).

Reconstruction Processing

The 3D reconstruction was performed as previously described (Nakata et al., 2017a) with slight modification. Briefly, extraction of the PAS-H-stained basement membrane in digital images was performed using ImageJ software (NIH; Bethesda, MD, United States[1]) and Adobe Photoshop 2020 software (Adobe Systems, Inc., Mountain View, CA, United States). After extraction, the images were converted into gray scale in JPEG format with Adobe Photoshop 2020 software at a resolution of 1,816 nm·pixel^{-1}. Using Amira 6.3.0 software (Visage Imaging GmbH, Berlin, Germany), the serial images were aligned

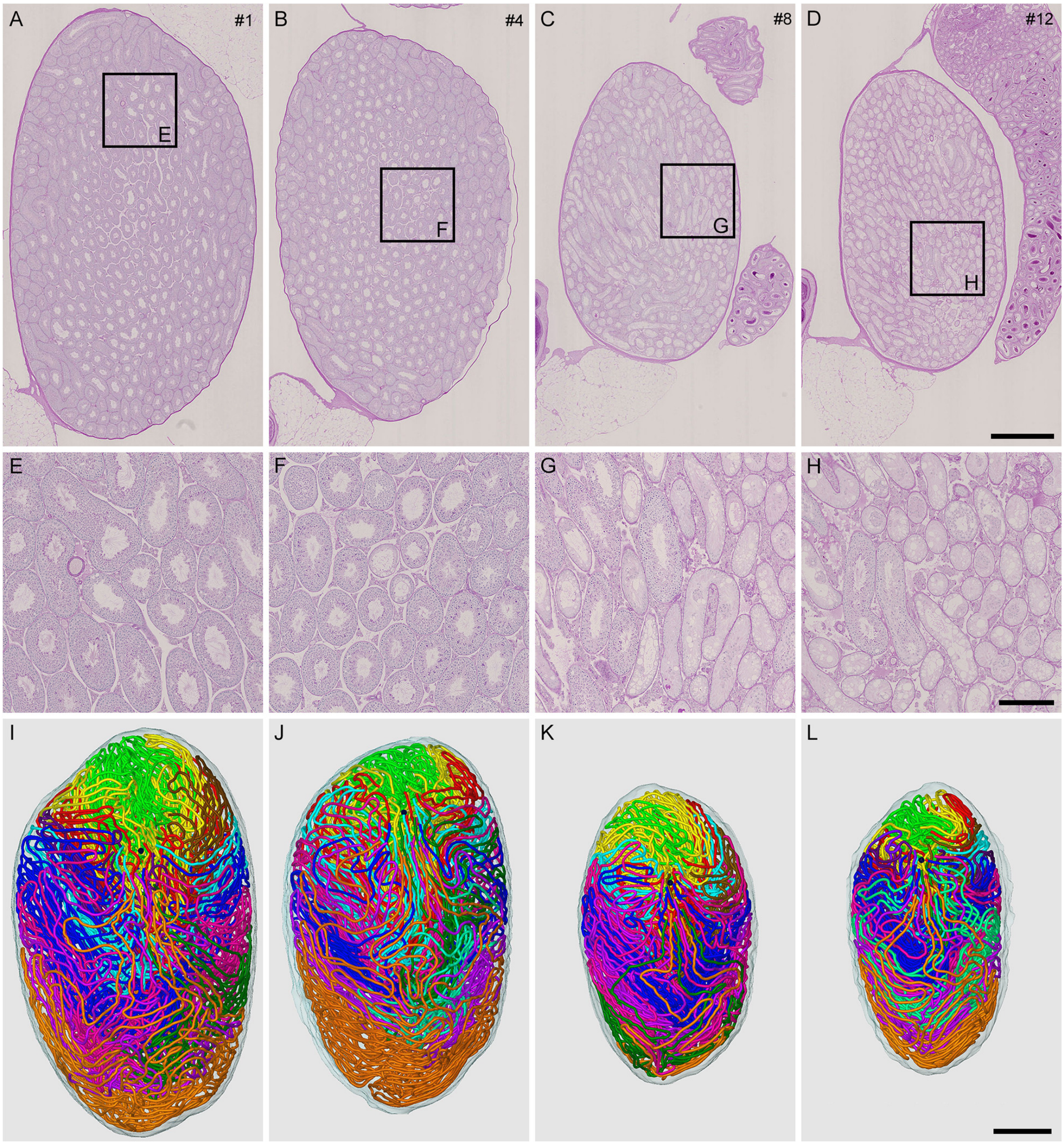

FIGURE 1 | Reconstruction of all seminiferous tubules in mice treated with different busulfan doses (IP-0, 10, 20, and 30 for intraperitoneal injections of 0, 10, 20, and 30 mg/kg, respectively). PAS-H-stained longitudinal sections of testes from mouse #1 **(A,E)**, 4 **(B,F)**, 8 **(C,G)**, and 12 **(D,H)**, which represent IP-0, 10, 20, and 30, respectively, are shown at low **(A–D)** and high magnification (**E–H**, the framed areas in **A–D**). The 3D core lines of all reconstructed seminiferous tubules marked with different colors are shown (**I–L** for mouse #1, 4, 8, and 12, respectively) with the position of the rete testis (black sphere). Scales, 1 mm (**A–D** and **I–L**), 250 μm **(E–H)**.

---

[1] http://imagej.nih.gov/ij/

automatically followed by manual adjustment, and the inside of the outlines of a selected tubule was colored in using threshold processing and traced from section to section. This procedure was repeatedly applied to all seminiferous tubules with different colors and they were then 3D reconstructed. To draw the core lines of seminiferous tubules, individual traced tubules in cross-sections were shrunk concentrically by 16 pixels in all directions, their resolution was changed to 29,056 nm·pixel^{-1}, and they were then reconstructed into thin tubules, in which the core lines were drawn using the same software. The whole testis was also 3D reconstructed by filling the inside of their outlines by threshold processing. The position of the rete testis was defined as the mean coordinate of the connections of all reconstructed seminiferous tubules with the rete testis and shown with a black sphere.

Assessment of the Degree of Spermatogenesis Disorder

Spermatogenesis is routinely divided into 12 stages in mice based on changes in the morphology of the acrosome and nucleus (Oakberg, 1956a; Hess and Franca, 2008; Ahmed and de Rooij, 2009; Meistrich and Hess, 2013; Nakata et al., 2015b; Nakata, 2019). The degree of spermatogenesis disorder in each section of seminiferous tubules in busulfan-treated mice

TABLE 1 | Summary of reconstructed seminiferous tubules in busulfan-induced spermatogenesis disorder in mouse testes.

Testis	IP*	Number				Testis volume (mm^3)		Total tubule length (mm)	
		Total tubules	Terminating points**	Branching points	Blind ends		Group average***		Group average***
#1	0	11	36	16	0	63.2	55.8 ± 5.4	1,815	1, 701 ± 82
#2	0	10	38	18	0	50.4		1,629	
#3	0	13	42	16	0	53.8		1,659	
#4	10	10	36	16	0	55.6	49.2 ± 4.8	1,704	1, 630 ± 67
#5	10	13	47	24	3	47.9		1,646	
#6	10	14	39	11	0	44.2		1,541	
#7	20	11	41	19	0	29.0	25.3 ± 2.8†	1,314	1, 174 ± 103†
#8	20	11	36	14	0	24.7		1,138	
#9	20	13	43	19	0	22.4		1,071	
#10	30	12	41	21	0	24.0	22.1 ± 2.0†	1,074	1, 049 ± 17†
#11	30	13	39	14	1	22.8		1,034	
#12	30	14	41	13	0	19.3		1,040	

**Intraperitoneal injection of busulfan (mg/kg); **Connections with the rete testis; ***Mean ± SD; †Significantly different from IP-0.*

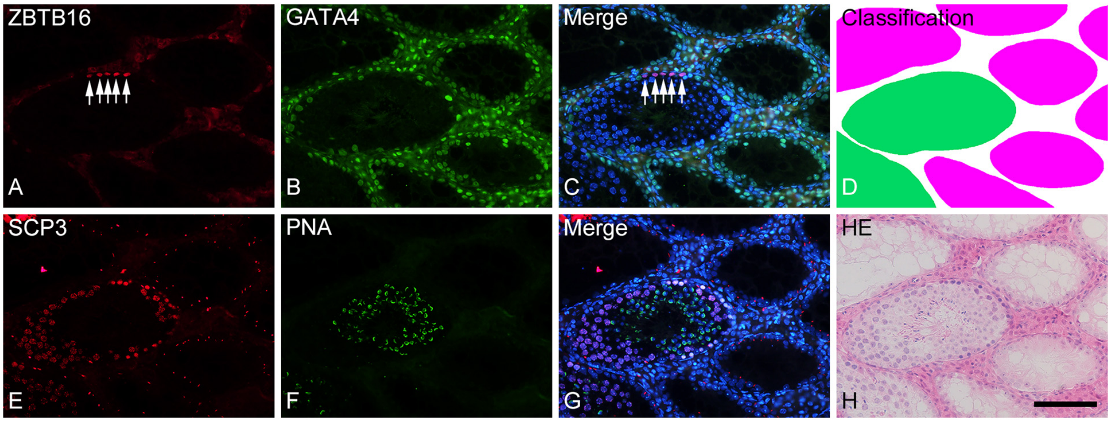

FIGURE 2 | Photographs of a representative cross-section **(A–D)** and the adjacent cross-section **(E–H)** of a formalin-fixed IP-30 testis shown with double-fluorescence staining for ZBTB16 [**(A)**; red] and GATA4 [**(B)**; green] and for SCP3 [**(E)**; red] and PNA-lectin [**(F)**; green], respectively. **(C,G)** are merged pictures of **(A,B)** and **(E,F)**, respectively, together with nuclear staining with DAPI (blue). **(D)** represents classification of tubule areas with normal (green) and markedly impaired (red) spermatogenesis in the same section as **(A–C)**. **(H)** represents HE staining of the same section as **(E–G)**. In the normal tubules, type A spermatogonia (arrows) are stained in nuclei for ZBTB16 **(A)**, Sertoli cells are stained in nuclei for GATA4 **(B)**, spermatocytes are stained in nuclei for SCP3 **(E)**, and spermatids are stained in acrosomes for PNA **(F)**. In contrast, in the markedly impaired tubules, only Sertoli cells but no other cell types are stained with the respective markers. Scale, 100 μm.

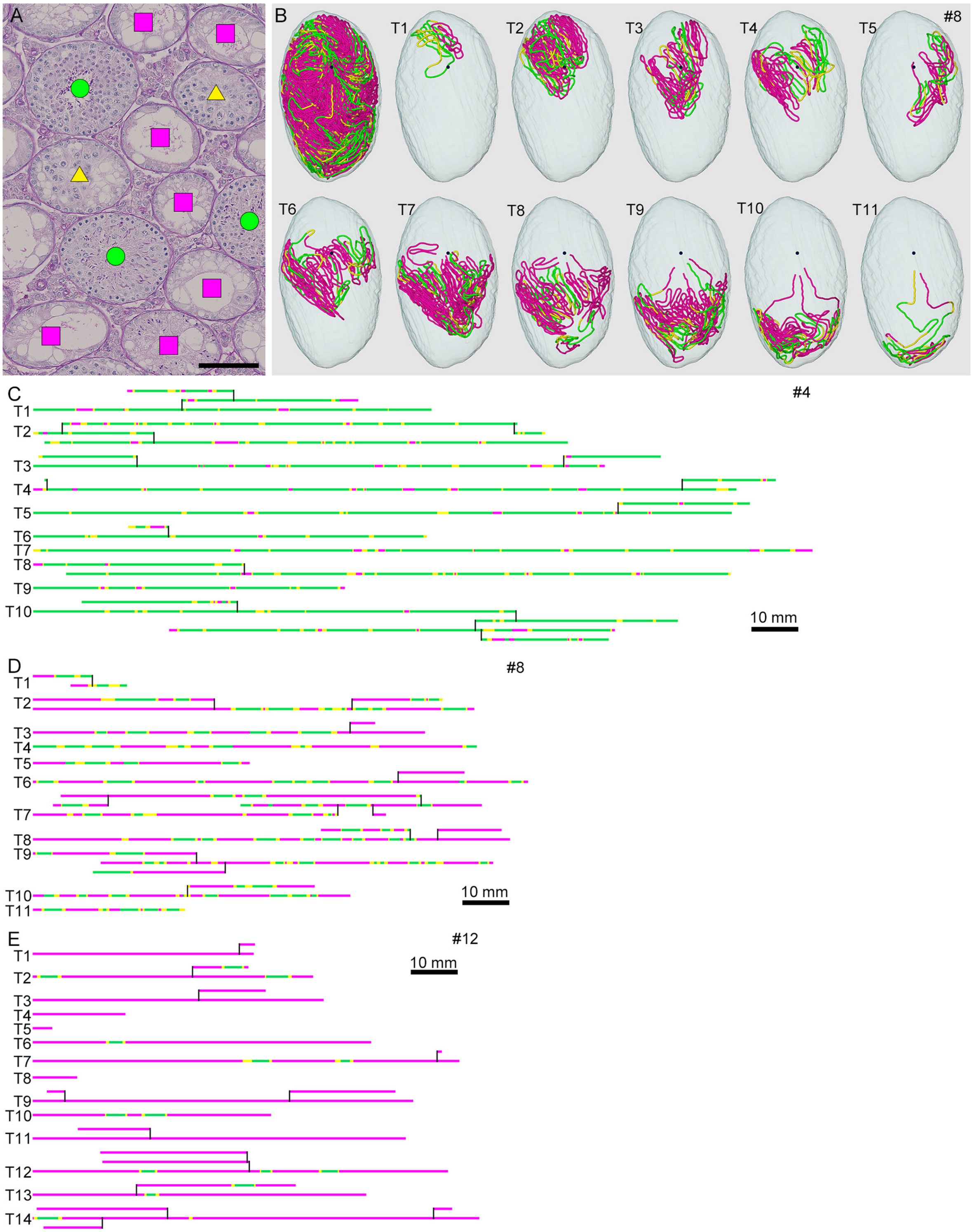

FIGURE 3 | Classification of the degrees of spermatogenesis disorder in mice treated with different busulfan doses. All seminiferous tubules in each section are divided into three types: normal tubules (green circle), abnormal tubules with spermatocytes (yellow triangle), and abnormal tubules without spermatocytes (red square) [**(A)** for mouse #8]. The core lines of all reconstructed seminiferous tubules in #8, with areas belonging to the above three types marked with the corresponding colors, are shown in a vertical view with the position of the rete testis (black sphere) **(B)**. The scheme of all individual seminiferous tubules in mouse #4 (IP-10), #8 (IP-20), and #12 (IP-30) is shown in **(C–E)**. The segments composed of tubule areas belonging to the three types are marked with the corresponding colors. The branching points are shown with vertical bars. All free extremities of the tubules in these cases are connected to the rete testis in terminal points without forming blind ends. Scales, 100 μm **(A)**, 10 mm **(C–E)**.

was assessed by histological observations of cell associations using NDP.view2., and the tubule portions were classified into three types according to the degrees of spermatogenesis disorder: normal, in which all germ cells that define one or more stages are arranged; abnormal with spermatocytes, in which all germ cells that define any one stage are not arranged, but spermatocytes are present; and abnormal without spermatocytes, in which only Sertoli cells are present in most cases, but spermatids are occasionally present. These three types represented normal, moderately impaired, and markedly impaired spermatogenesis, respectively.

Statistical Analysis

Data are presented as the mean ± standard deviation (SD). Comparisons among multiple data were performed with one-way or one-way repeated measures analysis of variance (ANOVA) followed by Bonferroni's or Dunnet's *post hoc* test, respectively, and differences with a P-value of less than 0.05 were considered to be significant. Pearson's correlation coefficient test was performed to assess the magnitude and direction of the proportionality between two parameters, and a positive or negative relationship was acknowledged when the absolute r-value was greater than 0.2.

RESULTS

3D Reconstruction of All Seminiferous Tubules

To generate mice with different degrees of spermatogenesis disorder, 12 mice were divided into four groups of three mice each: IP-0 (#1, 2, 3), IP-10 (#4, 5, 6), IP-20 (#7, 8, 9), and IP-30 (#10, 11, 12), which received a single intraperitoneal injection of 0, 10, 20, and 30 mg/kg of busulfan, respectively. All seminiferous tubules were reconstructed in 12 testes, one from each mouse, at 12 weeks after busulfan treatment. Results in four representative testes, one from each group, are shown in **Figure 1**. As expected, the testis became smaller and seminiferous tubules appeared degenerated with higher doses of busulfan. The quantitative data of the testis and seminiferous tubules are shown in **Table 1**. None of the values for the numbers of seminiferous tubules, terminating points, and branching points per testis were significantly different among the four groups ($P = 0.56$, 0.92, and 0.98, respectively). On the other hand, the testis volume and total length of seminiferous tubules per testis significantly decreased in IP-20 and IP-30 ($P < 0.05$ between IP-0 and IP-20 or IP-30).

Analysis of Spermatogenesis Disorder in Seminiferous Tubules

To analyze the degree of spermatogenesis disorder, all seminiferous tubule areas observed in each testis section were classified into three types as described in section "Materials and Methods," i.e., normal, abnormal with spermatocytes, and abnormal without spermatocytes, which were represented by green, yellow, and red, respectively. Moreover, the normal tubule areas were confirmed to undergo a complete spermatogenesis by immunofluorescence staining for specific markers of type A spermatogonia, spermatocytes, and spermatids (**Figure 2**). Thus, the three colors represented tubule areas with normal, moderately impaired, and markedly impaired spermatogenesis, respectively (**Figure 3A**). According to this typing, the core lines of all seminiferous tubules in 12 testes were divided into three different color segments (**Figures 3B–E**). As the busulfan concentration increased, the proportion of normal segments (green) decreased ($P < 0.05$ between IP-0 and IP-10; between IP-10 and IP20 or IP30) and that of abnormal segments without spermatocytes (red) increased ($P < 0.05$ between IP-0 and IP-10; between IP-10 and IP-20; between IP-20 and IP-30) (**Figure 4**). On the other hand, the proportion of abnormal segments with spermatocytes (yellow) in IP-10 or IP-20 increased in comparison with that in IP-0, but that in IP-30 remained the same as in IP-0 and decreased in comparison with that in IP-10 or IP-20

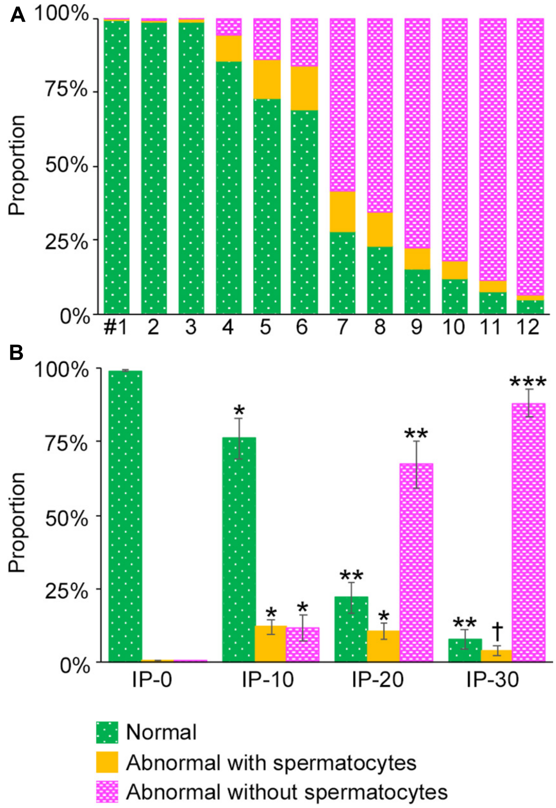

FIGURE 4 | Proportions of different degrees of spermatogenesis disorder in the whole seminiferous tubules in mice treated with different busulfan doses. The proportions of tubule areas belonging to the three types marked with the corresponding colors are shown in individual mice **(A)** and in groups of mice (IP-0, 10, 20, and 30) **(B)**. Each value represents the mean ± SD of three samples. Statistical analysis was performed in **(B)** between values for the same colors. *Significantly different from IP-0 ($P < 0.05$). **Significantly different from IP-0 and IP-10 ($P < 0.05$). ***Significantly different from IP-0, IP-10, and IP-20 ($P < 0.05$). †Significantly different from IP-10 and IP-20 ($P < 0.05$), but not from IP-0.

($P < 0.05$ between IP-0 and IP-10 or IP-20; between IP-30 and IP-10 or IP-20).

We next examined if the degree of spermatogenesis disorder differs among different seminiferous tubules in a testis that were numbered in the order of their connection with the rete testis from the top toward the bottom, or among different seminiferous tubules of varying lengths in IP-10 and IP-30 (three mice each) (**Figure 5**). There was no notable relationship between the proportions of the three color segments and the tubule orders in IP-10 and IP-30. On the other hand, between the proportions of the three color segments and the lengths of individual seminiferous tubules, no correlation existed in IP-10 ($|r| < 0.2$), but weak positive correlations ($r = 0.24$ and 0.32 for green and yellow, respectively) and a weak negative correlation ($r = -0.27$ for red) existed in IP-30.

As shown in **Figures 3C–E**, the areas of seminiferous tubules with different degrees of spermatogenesis disorder were distributed as many segments of varying lengths. We thus examined the changes in the length and number of these segments according to the different doses of busulfan. The total lengths and numbers of green, yellow, and red segments were measured in IP-10, IP-20, and IP-30 (**Figure 6**). The length of the green segments was significantly shorter in IP-20 than in IP-10 ($P < 0.05$), but remained unchanged in IP-30 compared with that in IP-20. The length of the red segments slightly increased in IP-20 compared with that in IP-10, although not significantly, and increased further significantly in IP-30 ($P < 0.05$). In contrast, the length of the yellow segments remained unchanged from IP-10 to IP-30 ($P = 0.80$). The number of green segments decreased significantly in IP-20 compared with that in IP-10 ($P < 0.05$) and slightly decreased further in IP-30, although not significantly. The number of red segments remained unchanged from IP-10 to IP-30 ($P = 0.06$). In contrast, the number of yellow segments significantly decreased in IP-20 compared with that in IP-10 and decreased further in IP-30 ($P < 0.05$).

As described above, the normal (green) segments remained in markedly damaged seminiferous tubules of IP-30 without a significant reduction in length or number from those in IP-20. We then examined which stages of spermatogenesis are preferentially involved in these remaining normal segments. A total of 87 normal segments remaining in the three testes in IP-30 were analyzed for their cell associations to determine the stage (**Figure 7**). The average length of the normal segments was 2.9 ± 1.2 mm, with the longest segment being 6.45 mm and the

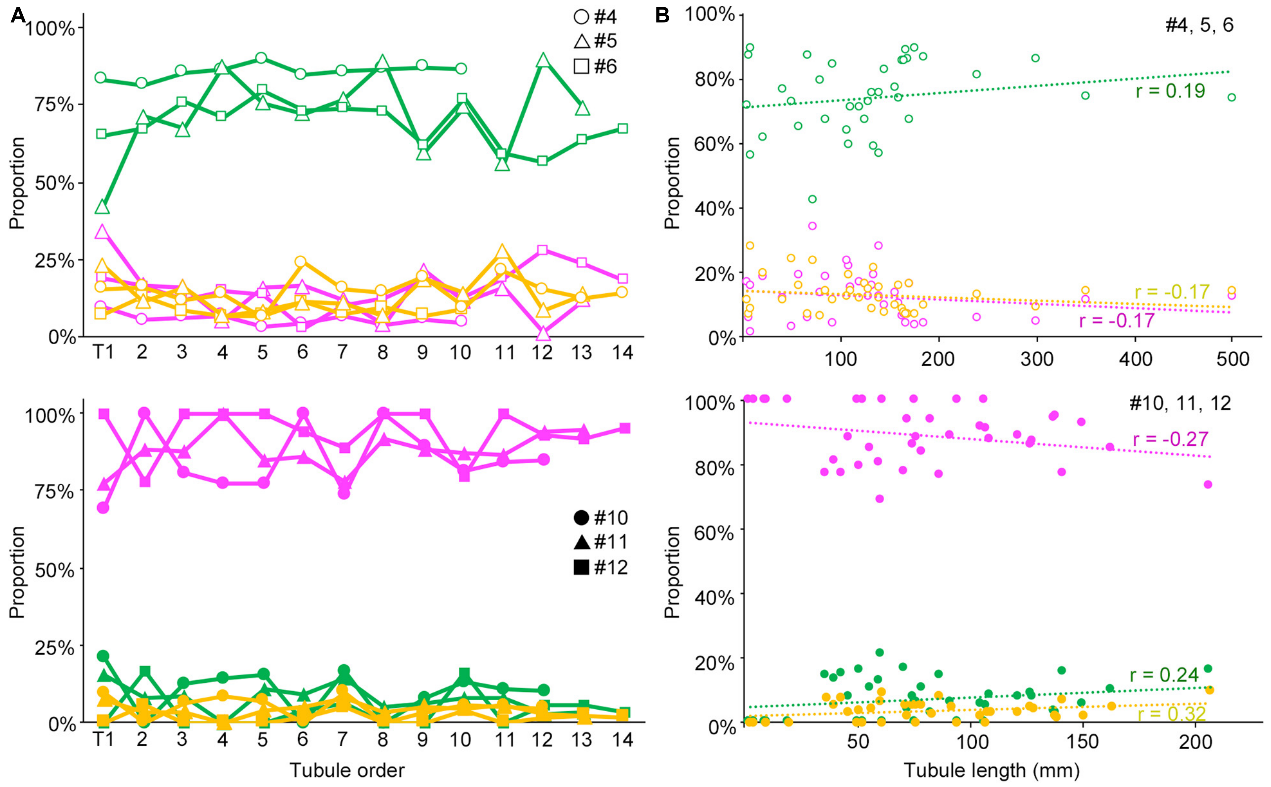

FIGURE 5 | Relationships of the proportions of different degrees of spermatogenesis disorder with the order of all seminiferous tubules expressed as a line graph **(A)** and with the length of individual seminiferous tubules expressed as a scatterplot **(B)**. The upper figures are for IP-10 (#4, 5, and 6) and the lower figures for IP-30 (#10, 11, and 12). The colors represent normal tubules (green), abnormal tubules with spermatocytes (yellow), and abnormal tubules without spermatocytes (red). In **(A)**, the tubules are numbered from T1 to T10 (#4), to T12 (#10), to T13 (#5, 11), and to T14 (#6, 12) in the order of their connection with the rete testis from the top toward the bottom in the testis. The values are expressed with hollow circles, hollow triangles, and hollow squares for #4, 5, and 6, respectively, and with filled circles, filled triangles, and filled squares for #10, 11, and 12, respectively. In **(B)**, the values are expressed as hollow circles for #4, 5, and 6, and with filled circles for #10, 11, and 12. The *r* values of the regression lines are indicated.

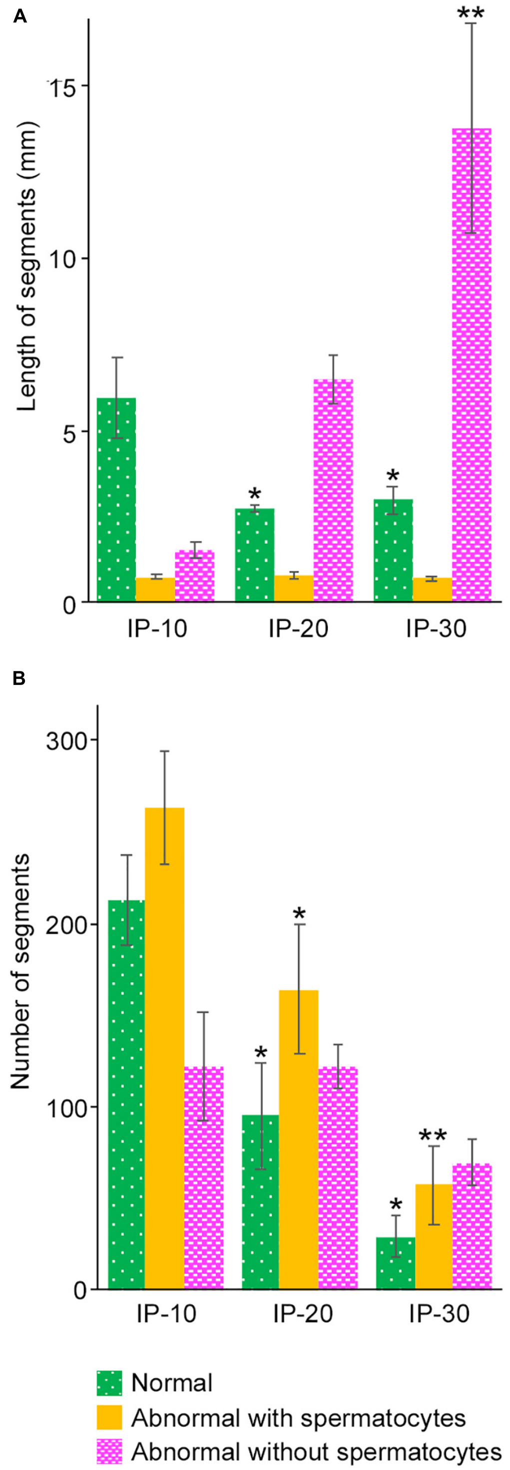

FIGURE 6 | Mean lengths **(A)** and numbers **(B)** of the segments of seminiferous tubules with different degrees of spermatogenesis disorder in mice treated with different busulfan doses (IP-10, -20, and -30). The colors represent normal tubules (green), abnormal tubules with spermatocytes (yellow), and abnormal tubules without spermatocytes (red). Each value represents the mean ± SD of three samples. Statistical analysis was performed between values for the same colors. *Significantly different from IP-10 ($P < 0.05$). **Significantly different from IP-10 and IP-20 ($P < 0.05$).

shortest being 0.70 mm. The average number of stages involved in one segment was 4.1 ± 2.4, with the maximum number being 11 and the minimum being 1. There was no correlation between the segment length and the number of stages involved in the segment ($r = 0.19$) (data not shown). The observed proportions of individual stages were compared with those expected, which were deduced from the duration of these stages in the total cycle of mouse spermatogenesis (35 days) reported previously (Oakberg, 1956b). The proportions of stage I and XII were higher, and the proportion of stage VI was lower than the corresponding expected proportions (**Table 2**). In addition, the average length of the individual segment areas in stage I areas were 1.1 ± 0.9 mm, which was longer than that in any other stages (data not shown).

Localization of the Sites of Spermatogenesis Disorder

Next, we examined if the degrees of spermatogenesis disorder differ among different 3D positions in seminiferous tubules. The proportions of the three color segments were measured in three different areas of seminiferous tubules, i.e., Rete (positions within 10 mm from the terminating points with the rete testis), Branch (positions within 10 mm from the branching points), and Others (positions more than 10 mm apart from the terminating points and branching points), and compared with those in the whole seminiferous tubules (Whole) (**Figure 8**). In IP-10 and IP-20, none of the proportions of the three colors in Rete, Branch, and Others were significantly different from those in Whole. On the other hand, in IP-30, the proportion of red segments was slightly but significantly higher in Branch than in Whole, and the proportion of green segments was slightly but significantly lower in Branch than in Whole.

Lastly, we examined if the degree of spermatogenesis disorder differs among different 3D positions in a testis without considering the course of seminiferous tubules. Using the 3D reconstruction software, each testis was divided into 200-μm-thick serial slices along the perpendicular planes formed by the *X-Y-Z*-axes, and the proportions of green, yellow, and red segments in all seminiferous tubule areas involved in each slice were measured. In the present study, special attention was paid to the distribution of red (abnormal without spermatocytes) segments in IP-10 and green (normal) segments in IP-30 (**Figure 9**). There was a large difference in the proportion of red and green segments among individual slices in all directions. However, on comparison of three testes from three different mice belonging to the same IP-10 or IP-30 group, the positions in the slices with higher or lower proportions of red or green segments, respectively, were distributed randomly and not fixed among different testes.

DISCUSSION

In the present study, we reconstructed seminiferous tubules in 12 mice treated with varying doses of busulfan and analyzed the 3D distribution of spermatogenesis, in order to examine if

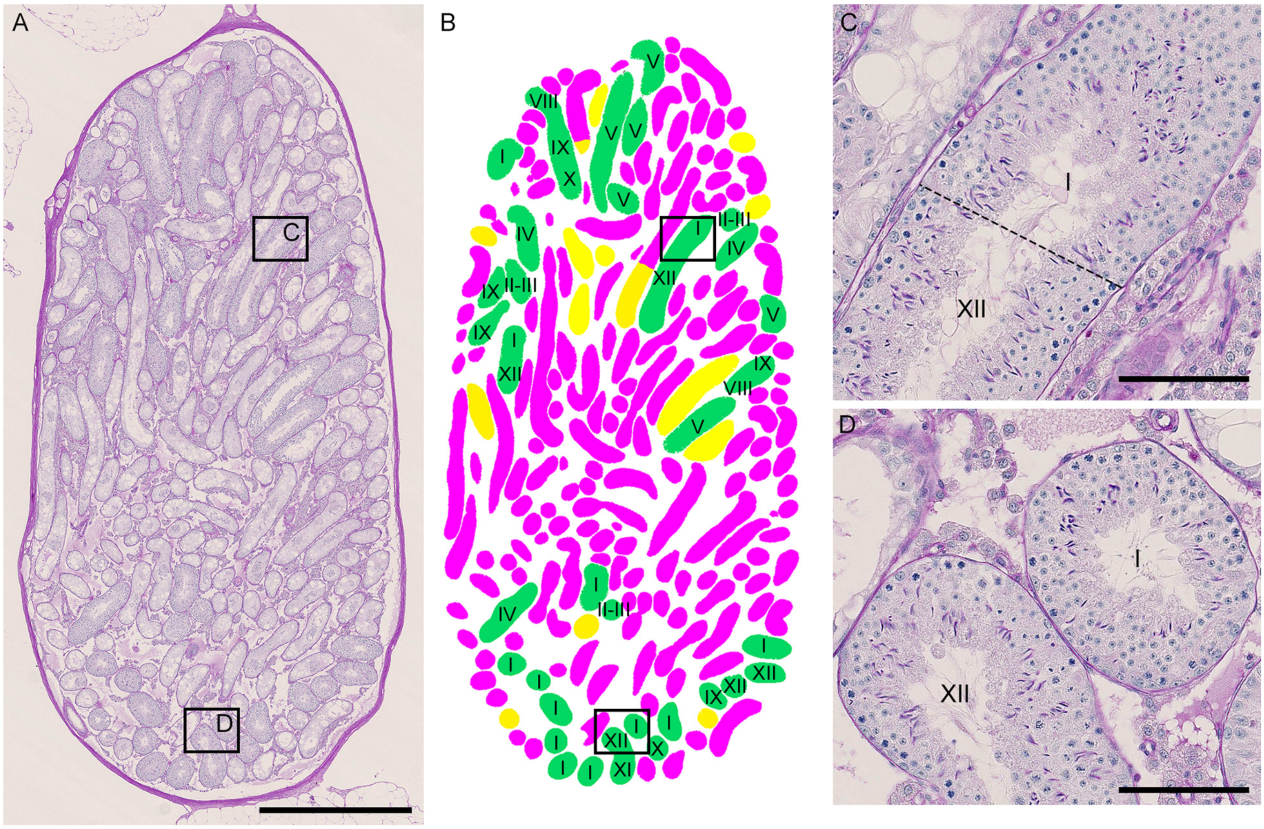

FIGURE 7 | Photographs of a representative cross-section of IP-30 testis from #10 mouse shown with PAS-H staining **(A)** and with assessment of the degree of spermatogenesis disorder and identification of stages in individual tubule sections **(B)**. The framed areas in **(A)** are shown at a high magnification **(C,D)**. The colors in **(B)** represent normal tubules (green), abnormal tubules with spermatocytes (yellow), and abnormal tubules without spermatocytes (red). The roman numerals in **(B–D)** represent stages I–XII. Scales, 1 mm **(A)**, 100 μm **(C,D)**.

spermatogenesis disorder occurs preferentially at specific sites in seminiferous tubules. The testis volume and total length of seminiferous tubules were reduced depending on the dose of busulfan. The positive correlation between the tubule length and the proportion of markedly impaired spermatogenesis with the highest dose of busulfan suggests that the length of seminiferous tubules is shortened due to massive degeneration. However, busulfan treatment caused no change in the basic structure of seminiferous tubules, including the numbers of tubules, terminating points, branching points, and blind ends.

Although the proportion of markedly impaired spermatogenesis increased and that of normal spermatogenesis decreased in a busulfan dose-dependent manner in all seminiferous tubules, the increased proportion of markedly impaired spermatogenesis with the highest dose of busulfan was accompanied by a decreased proportion of moderately impaired spermatogenesis and unchanged proportion of normal spermatogenesis when compared with a moderate dose of busulfan. Furthermore, analysis of the length and number of segments revealed that when the dose of busulfan increased from moderate to the highest, the segments with markedly impaired spermatogenesis increased in length, but not in number, those with moderately impaired spermatogenesis decreased in number, but not in length, and those with normal spermatogenesis remained unchanged in length and only slightly decreased in number. These phenomena

TABLE 2 | Proportion of stages in normal segments in IP-30.

Stage	**Mouse**			**Average (%)**	**Expectation* (%)**
	#10 (%)	**#11 (%)**	**#12 (%)**		
I	39	26	15	27 ± 10	11
II–III	12	13	8	11 ± 3	13
IV	7	12	5	8 ± 3	9
V	7	1	1	3 ± 3	5
VI	1	2	0	1 ± 1	9
VII	4	8	8	7 ± 2	10
VIII	14	8	19	14 ± 5	10
IX	16	8	8	11 ± 4	7
X	8	2	9	6 ± 3	5
XI	4	2	10	5 ± 3	10
XII	14	18	18	16 ± 2	10

**Relative duration of each stage to that of a cycle in normal mouse spermatogenesis. Values are taken from Oakberg (1956b).*

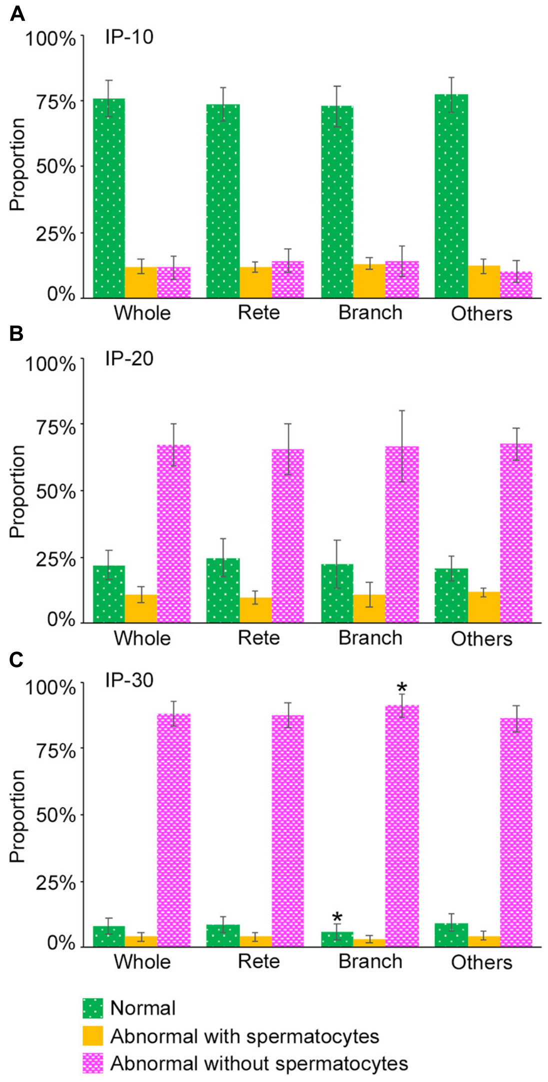

FIGURE 8 | Proportions of different degrees of spermatogenesis disorder at different 3D positions in the seminiferous tubules in mice treated with different busulfan doses, IP-10 **(A)**, −20 **(B)**, and −30 **(C)**. The colors represent normal tubules (green), abnormal tubules with spermatocytes (yellow), and abnormal tubules without spermatocytes (red). The abbreviations of the positions in seminiferous tubules are as follows: whole for all tubule areas, Rete for areas within 10 mm from the terminating points, Branch for areas within 10 mm from the branching points, and Others for areas more than 10 mm apart from the terminating points and branching points. Each value represents the mean ± SD of three samples. Statistical analysis was performed between the values of Whole and those of Rete, Branch, or Others for the same colors. *Significantly different from Whole ($P < 0.05$).

suggest that the markdly damaged segments fuse with each other, whereas the moderately damaged segments further impair spermatogenesis and fuse with neighboring markedly damaged segments, resulting in an increased length of segments with markedly impaired spermatogenesis at the highest dose of busulfan. Furthermore, weakly damaged segments do not further impair spermatogenesis and instead recover and remain as segments of a certain length and number with normal spermatogenesis even at the highest dose of busulfan.

Busulfan is an alkylating agent that kills differentiated spermatogonia and spermatogonial stem cells (de Rooij and Kramer, 1970; Bucci and Meistrich, 1987). Wang et al. (2010) reported normal spermatogenesis in 93% of the seminiferous tubules in mice treated with a low dose of busulfan (10 mg/kg), but it was scarcely found with higher doses of busulfan (20 or 30 mg/kg) at 4 weeks after treatment. In the present study, approximately 76, 22, and 8% of tubule segments exhibited normal spermatogenesis at 12 weeks after treatment with 10, 20, and 30 mg/kg of busulfan, respectively. This suggested that these normal segments result from the expansion of remaining spermatogenesis or recovery of spermatogenesis from surviving stem cells that proceeded between 4 and 12 weeks. The present study also revealed that the normal segments with the highest dose of busulfan preferentially involve stages I and XII, suggesting that the seminiferous epithelia recovered from the initial damage and spermatogenesis proceeded to these stages by 12 weeks after treatment.

Regarding the 3D localization of the sites of spermatogenesis disorder, the proportion of markedly impaired spermatogenesis, although not notably different among individual ordered seminiferous tubules in a testis, was slightly but significantly higher in the tubule areas near the branching points, suggesting that these positions in the seminiferous tubules are more vulnerable to busulfan-induced damage. On the other hand, analysis of the whole testis without considering the course of seminiferous tubules revealed that both the sites of markedly impaired spermatogenesis with the lowest dose of busulfan and those of normal spermatogenesis with the maximum dose of busulfan largely differed among different positions in a testis. These sites are considered to represent the most vulnerable portions of the testis where degeneration of tubules preferentially occurs and the least vulnerable portions of testis where regeneration of tubules preferentially occurs, respectively. However, these sites were not consistent in location among different testes from individual mice.

The factors responsible for the site-specific disorder of spermatogenesis may reside outside of seminiferous tubules. In the human testis with NOA, several groups reported that the least vulnerable positions, i.e., the sperm containing-regions, receive more abundant blood supply (Har-Toov et al., 2004; Herwig et al., 2004). In the mouse testis, seminiferous tubules are uniformly surrounded by capillaries (Suzuki, 1982), thus it is unlikely that the density of capillaries influences the damage of tubules. However, the higher permeability of local capillaries may increase or ameliorate the damage by increasing the testicular concentration of busulfan or serum factors that promote recovery of tubules, respectively. Our present study suggested that the tubule areas near the rete testis, from which blood vessels enter the testis and around which tissue perfusion is considered most abundant, do not have higher or lower proportions of impaired or normal spermatogenesis. This result is consistent with the previous study by Schwarzer et al. (2013), which reported no relationship between biopsy sites near the main testicular vessels

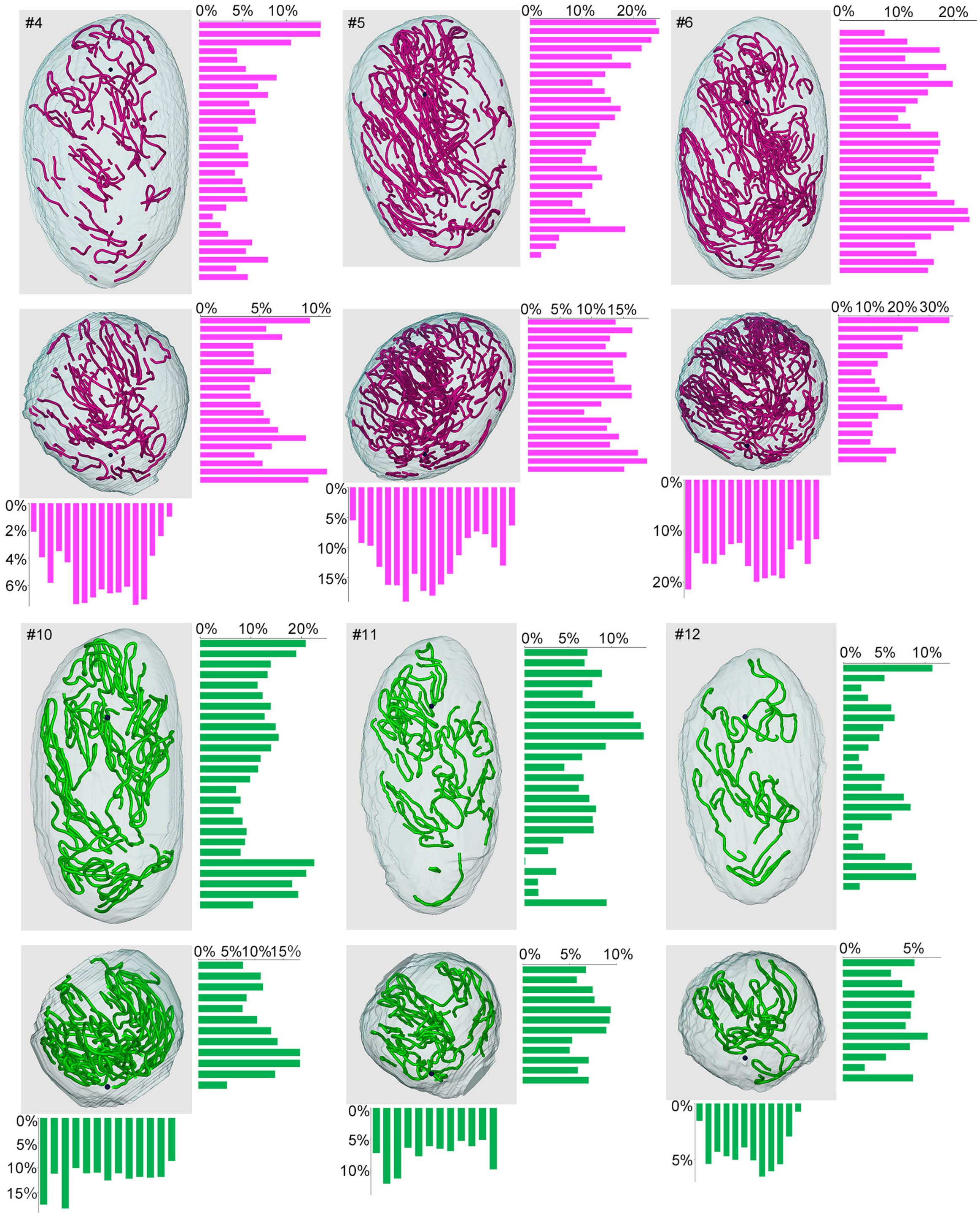

FIGURE 9 | Proportions of different degrees of spermatogenesis disorder at different 3D positions in the testes from mice treated with different busulfan doses. The relative lengths of abnormal segments without spermatocytes (red) in IP-10 (#4, 5, 6) and those of normal segments (green) in IP-30 (#10, 11, 12) were measured in all tubule areas involved in 200-μm-thick serial slices of each testis parallel to the three planes formed by the *X*, *Y*, and *Z*-axes. The 3D core lines of all red or green segments in each testis, and the bars representing the proportions (%) of segments with respective colors in each slice are shown.

or rete testis and successful sperm retrieval in 220 cases of NOA. In addition to the factors from blood vessels, those from nerve terminals and cells surrounding seminiferous tubules, such as Leydig cells and macrophages, may be responsible for the regional difference in the degree of spermatogenesis disorder in the testis.

The present study revealed the detailed 3D structure of seminiferous tubules in busulfan-induced experimental disorder of spermatogenesis in mice. The present methods can be readily applicable to investigating other types of mouse spermatogenesis disorder, including that due to aging, which may have different mechanisms from those in the busulfan model. Although there are large limitations for comparing the mouse models with human NOA that has unknown mechanisms, our ultimate goal is application of the present methods to the study of human NOA. The structure of the testis differs between humans and mice in several aspects: the human testis, which is approximately 150-times larger in volume than the mouse testis, is divided into many lobules by connective tissue septa that separate individual seminiferous tubules, whereas no such septa exist in the mouse testis; human seminiferous tubules are considered to be composed of numerous anastomosed thin loops and run in random directions (Johnson, 1934), whereas mouse seminiferous tubules have limited anastomosis and run in zig-zag curves locally but concentrically as a whole along the circumference of the testis (Nakata et al., 2015a, 2017a). It will be of interest to examine if the degree of spermatogenesis disorder differs from lobule to lobule in human NOA, and if the tubule areas with impaired or normal spermatogenesis are preferentially located near the branching points, which are expected to exist in higher frequencies than in mice. However, obtaining the whole testis from NOA patients is difficult. Therefore, our group is currently conducting studies using human testis specimens obtained through surgery to examine the detailed and precise 3D structure of normal human seminiferous tubules. We are also planning to examine the 3D distribution of gene products inside or outside of seminiferous tubules that may control the initiation and/or expansion of spermatogenesis using normal and disordered mice of different ages. These approaches will help to elucidate the mechanism of NOA and effective clinical treatments for NOA.

DATA AVAILABILITY STATEMENT

The original contributions presented in the study are included in the article/supplementary material, further inquiries can be directed to the corresponding author/s.

ETHICS STATEMENT

The animal study was reviewed and approved by the Kanazawa University.

AUTHOR CONTRIBUTIONS

HN designed the project and performed the study. HN, TN, and SI analyzed the data. HN and SI wrote the manuscript. All authors discussed the data and commented on the manuscript.

FUNDING

This work was supported by JSPS KAKENHI Grant Number JP19K16743 and Ube Industries Foundation.

ACKNOWLEDGMENTS

We thank Itsuro Kamimura (Maxnet Co., Ltd.) for advice on using Amira software, and Toshihisa Hatta (Kanazawa Medical University) and Satoru Honma (Kanazawa Medical University) for the use of Nanozoomer 2.0-HT. We also thank Shuichi Yamazaki for technical assistance in making paraffin sections.

REFERENCES

Ahmed, E. A., and de Rooij, D. G. (2009). Staging of mouse seminiferous tubule cross-sections. *Methods Mol. Biol.* 558, 263–277. doi: 10.1007/978-1-60761-103-5_16

Bucci, L. R., and Meistrich, M. L. (1987). Effects of busulfan on murine spermatogenesis: cytotoxicity, sterility, sperm abnormalities, and dominant lethal mutations. *Mut. Res.* 176, 259–268. doi: 10.1016/0027-5107(87)90057-1

Corona, G., Minhas, S., Giwercman, A., Bettocchi, C., Dinkelman-Smit, M., Dohle, G., et al. (2019). Sperm recovery and ICSI outcomes in men with non-obstructive azoospermia: a systematic review and meta-analysis. *Hum. Reprod. Update* 25, 733–757. doi: 10.1093/humupd/dmz028

de Rooij, D. G., and Kramer, M. F. (1970). The effect of three alkylating agents on the seminiferous epithelium of rodents. I. Depletory effect. *Virchows Arc. B Cell Pathol.* 4, 267–275. doi: 10.1007/BF02906082

Har-Toov, J., Eytan, O., Hauser, R., Yavetz, H., Elad, D., and Jaffa, A. J. (2004). A new power Doppler ultrasound guiding technique for improved testicular sperm extraction. *Fertil. Steril.* 81, 430–434. doi: 10.1016/j.fertnstert.2003.07.020

Herwig, R., Tosun, K., Pinggera, G. M., Soelder, E., Moeller, K. T., Pallwein, L., et al. (2004). Tissue perfusion essential for spermatogenesis and outcome of testicular sperm extraction (TESE) for assisted reproduction. *J. Assist. Reprod. Genet.* 21, 175–180. doi: 10.1023/b:jarg.0000031251.57848.04

Hess, R. A., and Franca, L. R. (2008). Spermatogenesis and cycle of the seminiferous epithelium. *Adv. Exp. Med. Biol.* 636, 1–15. doi: 10.1007/978-0-387-09597-4_1

Johnson, F. P. (1934). Dissections of human seminiferous tubules. *Anat. Rec.* 59, 187–199. doi: 10.1002/ar.1090590205

Krausz, C. (2011). Male infertility: pathogenesis and clinical diagnosis. *Best Pract. Res. Clin. Endocrinol. Metab.* 25, 271–285. doi: 10.1016/j.beem.2010.08.006

Meistrich, M. L., and Hess, R. A. (2013). Assessment of spermatogenesis through staging of seminiferous tubules. *Methods Mol. Biol.* 927, 299–307. doi: 10.1007/978-1-62703-038-0_27

Nakata, H. (2019). Morphology of mouse seminiferous tubules. *Anat. Sci. Int.* 94, 1–10. doi: 10.1007/s12565-018-0455-9

Nakata, H., and Iseki, S. (2019). Three-dimensional structure of efferent and epididymal ducts in mice. *J. Anat.* 235, 271–280. doi: 10.1111/joa.13006

Nakata, H., Sonomura, T., and Iseki, S. (2017a). Three-dimensional analysis of seminiferous tubules and spermatogenic waves in mice. *Reproduction* 154, 569–579. doi: 10.1530/REP-17-0391

Nakata, H., Wakayama, T., Asano, T., Nishiuchi, T., and Iseki, S. (2017b). Identification of sperm equatorial segment protein 1 in the acrosome as the primary binding target of peanut agglutinin (PNA) in the mouse testis. *Histochem. Cell Biol.* 147, 27–38. doi: 10.1007/s00418-016-1478-8

Nakata, H., Wakayama, T., Sonomura, T., Honma, S., Hatta, T., and Iseki, S. (2015a). Three-dimensional structure of seminiferous tubules in the adult mouse. *J. Anat.* 227, 686–694. doi: 10.1111/joa.12375

Nakata, H., Wakayama, T., Takai, Y., and Iseki, S. (2015b). Quantitative analysis of the cellular composition in seminiferous tubules in normal and genetically modified infertile mice. *J. Histochem. Cytochem.* 63, 99–113. doi: 10.1369/0022155414562045

Nakata, H., Yoshiike, M., Nozawa, S., Sato, Y., Iseki, S., Iwamoto, T., et al. (2021). Three-dimensional structure of seminiferous tubules in the Syrian hamster. *J. Anat.* (in press). doi: 10.1111/joa.13287

Nariyoshi, S., Nakano, K., Sukegawa, G., Sho, T., and Tsuji, Y. (2020). Ultrasonographically determined size of seminiferous tubules predicts sperm retrieval by microdissection testicular sperm extraction in men with nonobstructive azoospermia. *Fertil. Steril* 113, 97.e2–104.e2. doi: 10.1016/j.fertnstert.2019.08.061

Oakberg, E. F. (1956a). A description of spermiogenesis in the mouse and its use in analysis of the cycle of the seminiferous epithelium and germ cell renewal. *Am. J. Anat.* 99, 391–413. doi: 10.1002/aja.1000990303

Oakberg, E. F. (1956b). Duration of spermatogenesis in the mouse and timing of stages of the cycle of the seminiferous epithelium. *Am. J. Anat.* 99, 507–516. doi: 10.1002/aja.1000990307

Pan, M. M., Hockenberry, M. S., Kirby, E. W., and Lipshultz, L. I. (2018). Male Infertility Diagnosis and Treatment in the Era of In Vitro Fertilization and Intracytoplasmic Sperm Injection. *Med. Clin. North Am.* 102, 337–347. doi: 10.1016/j.mcna.2017.10.008

Schwarzer, J. U., Steinfatt, H., Schleyer, M., Köhn, F. M., Fiedler, K., von Hertwig, I., et al. (2013). No relationship between biopsy sites near the main testicular vessels or rete testis and successful sperm retrieval using conventional or microdissection biopsies in 220 non-obstructive azoospermic men. *Asian J. Androl.* 15, 795–798. doi: 10.1038/aja.2013.98

Silber, S. J., Nagy, Z., Devroey, P., Tournaye, H., and Van Steirteghem, A. C. (1997). Distribution of spermatogenesis in the testicles of azoospermic men: the presence or absence of spermatids in the testes of men with germinal failure. *Hum. Reprod.* 12, 2422–2428. doi: 10.1093/humrep/12.11.2422

Suzuki, F. (1982). Microvasculature of the mouse testis and excurrent duct system. *Am. J. Anat.* 163, 309–325. doi: 10.1002/aja.1001630404

Tournaye, H., Krausz, C., and Oates, R. D. (2017). Concepts in diagnosis and therapy for male reproductive impairment. *Lancet Diab. Endocrinol.* 5, 554–564. doi: 10.1016/S2213-8587(16)30043-2

Wang, D. Z., Zhou, X. H., Yuan, Y. L., and Zheng, X. M. (2010). Optimal dose of busulfan for depleting testicular germ cells of recipient mice before spermatogonial transplantation. *Asian J. Androl.* 12, 263–270. doi: 10.1038/aja.2009.67

Conflict of Interest: The authors declare that the research was conducted in the absence of any commercial or financial relationships that could be construed as a potential conflict of interest.

frontiers
in Cell and Developmental Biology

HYPOTHESIS AND THEORY
published: 11 February 2021
doi: 10.3389/fcell.2021.639244

Epithelial-Mesenchymal Transition Drives Three-Dimensional Morphogenesis in Mammalian Early Development

*Galym Ismagulov†, Sofiane Hamidi† and Guojun Sheng**

International Research Center for Medical Sciences (IRCMS), Kumamoto University, Kumamoto, Japan

From fertilization to onset of gastrulation, a mammalian embryo goes through several rounds of cellular morphogenesis resembling phenomena of epithelial-mesenchymal transition (EMT) and mesenchymal-epithelial transition (MET), collectively referred to as EMTs. How these EMT events play a role in shaping the three-dimensional (3-D) architecture of the developing embryo is not well-understood. In this review, we present a model in which cellular morphogenesis, represented primarily by dynamic changes in its epithelialization status, is the driving force of embryonic 3-D organization. This is achieved through the integration of three key components of mammalian early development, the pluripotency regulation, morphogenetic signaling, and biomechanical force anisotropy. Although cells in an early embryo do not exhibit full mesenchymal characteristics, our model underscores the importance of investigating molecular regulation of epithelial cell polarity and partial EMT/MET in understanding mammalian early development.

Keywords: EMT, epiblast, pluripotency, polarity, gastrulation

Edited by:
Silvia Garagna,
University of Pavia, Italy

Reviewed by:
Maria Cecilia Cirio,
CONICET Institute of Physiology, Argentina
Isabelle Migeotte,
Université libre de Bruxelles, Belgium
Alexandre Francou,
Sloan Kettering Institute, United States

****Correspondence:***
Guojun Sheng
sheng@kumamoto-u.ac.jp

†These authors have contributed equally to this work

Specialty section:
This article was submitted to Cell Growth and Division, a section of the journal Frontiers in Cell and Developmental Biology

Received: *08 December 2020*
Accepted: *06 January 2021*
Published: *11 February 2021*

Citation:
Ismagulov G, Hamidi S and Sheng G (2021) Epithelial-Mesenchymal Transition Drives Three-Dimensional Morphogenesis in Mammalian Early Development. Front. Cell Dev. Biol. 9:639244. doi: 10.3389/fcell.2021.639244

INTRODUCTION

After fertilization, a mammalian embryo undergoes several rounds of early cleavages before acquisition of apicobasal polarity through compaction and segregation of inner and outer cells through asymmetric divisions (Humiecka et al., 2017). Cells inheriting the apical cortical domain at 8-cell to 16-cell division will reestablish polarity and position themselves in the outer layer of the embryo and will be biased to become trophectoderm (TE) progenitors. The rest of the blastomeres lack apical surface and apicobasal polarity and will be positioned in the inner part of the embryo and eventually contribute to the inner cell mass (ICM) (Maître et al., 2016). The ICM cells will then sort out, in an actin-dependent manner, to give rise to an epithelialized primitive endoderm (hypoblast) (Bedzhov and Zernicka-Goetz, 2014), whereas the remaining epiblast precursors maintain their non-epithelial characteristics. Those epiblast precursors will then undergo an MET process to form an apicobasally polarized epiblast epithelium and generate a pro-amniotic cavity as a consequence of this process. The epithelialized epiblast subsequently goes through an EMT process during gastrulation, generates the mesoderm and definitive endoderm, and lays down the foundation of the three-germ layer and three-dimensional (3-D) mammalian body plan.

Up till the onset of gastrulation, the architecture of a mammalian embryo largely reflects morphogenetic features of its constituent cells, whereas more complex interactions involving cells, tissues, and tissue compartments govern gastrulation and post-gastrulation morphogenesis. In this review, we aim to synthesize published data on early mammalian development with respect to the regulation of cellular morphogenesis and an embryo's 3-D organization, with an emphasis on the interplay between epithelial (E) and/or mesenchymal (M) status, pluripotency, biomechanical forces and morphogen signaling.

INTER-DEPENDENCY BETWEEN CELLULAR MORPHOLOGY AND PLURIPOTENCY

Cellular potency is defined by its ability to differentiate into various cell types either *in vivo* or *in vitro*, varying from totipotency, corresponding to the status of blastomeres before lineage segregation between the TE and ICM, to unipotency which corresponds to cells that can differentiate only into a single cell type (**Figure 1**). Status of a cell's potency in early development reflects both the embryo's developmental stage and the cell's morphogenetic status. For instance, loss of totipotency of early blastomeres is associated with segregation of TE and ICM cells, and the restriction of potency is more pronounced for the outer, apicobasally polarized cells (TE) than the non-polarized ICM cells, which remain pluripotent and can give rise to all cell lineages in an adult body.

Pluripotency was conceptualized based on differentiation capacity (either *in vitro* or *in vivo*) of cells isolated *in vivo* and maintained *in vitro*. Recent efforts have been made to associate pluripotency with features of either the original developmental stage during pluripotent cell derivation or the putative developmental stage after those pluripotent cells have achieved a steady state under a given culture condition. Four pluripotency states have so far been characterized using cell morphological and molecular criteria. The first one is termed "naïve pluripotency," which corresponds to the ICM cell after TE specification and segregation. Naive pluripotent cells do not have apicobasal polarity. They express a particular set of associated genes (e.g., REX1) (Ghimire et al., 2018). The second type is termed "formative pluripotency," which corresponds to epithelializing epiblast precursors at the time of primitive endoderm specification and segregation. The formative pluripotent cells retain germline differentiation capability and are defined molecularly by OTX2 upregulation (Stumpf and MacArthur, 2019; Kinoshita et al., 2020). The third type is "primed pluripotency," corresponding to a partially epithelialized epiblast prior to gastrulation. These cells have many epithelial characteristics (although they are not fully epithelialized) and have lost the capacity to contribute to the germline or to make chimeras (a phenomenon likely related to their epithelial status). Primed pluripotent cells have a differentiation bias toward specific cell linages that reflects their developmental progression along the antero-posterior axis of the embryo (Shahbazi et al., 2017). Finally, the fourth stage is the "pluripotency exit." Cells at this stage are on the verge of differentiation (Thakurela et al., 2019) and are characterized by a progressive reduction of the core pluripotency factors such as OCT4, NANOG and SOX2. These cells can still reverse their pluripotent status upon changes in culture conditions (Hamidi et al., 2020) or developmental cues (Tian et al., 2019).

In human development, these transitions are also supported by progressive epithelialization of the epiblast and its segregation into the embryonic epiblast (giving rise to future three-germ layers) and the amniotic epiblast (contributing to the ectoderm portion of the amnion), and the appearance of the proamniotic cavity. The molecular mechanisms that link changes in cellular morphology and cellular potency are still not well-explored. GRHL2, an epithelial state inducer, has been reported to control the expression of a subset of the pluripotent network genes upon transition from naive to primed pluripotency state (Chen et al., 2018). Conversely, MCRS1, a mesenchymal state inducer (Liu et al., 2014), is required to maintain the epiblast lineage after trophectoderm and primitive endoderm specification, suggesting that the ability to retain an non-polar mesenchymal-like phenotype in the ICM is critical (Cui et al., 2020).

CELL MORPHOLOGY AND BIOMECHANICAL FORCES

Biomechanical forces in the embryo are a function of two main cellular features: cell motility and cell deformation. They play critical roles in shaping the embryo's 3-D architecture prior to gastrulation. During the process of TE and ICM segregation (Marikawa and Alarcón, 2009), mechanical forces are directly responsible for their position and fate specification through regulation of the orientation of asymmetric divisions. Cells located on the embryo's surface retain contractile abilities and differentiate into TE cells, whereas cells on the center, without contractile abilities, become the ICM (Bissiere et al., 2018). Consecutively, during blastocyst cavity formation, trophectoderm epithelial integrity associated with directional fluid transport results in the establishment of a blastocyst luminal pressure that drives further lumenogenesis and embryo growth (Wang et al., 2018; Chan et al., 2019).

Non-polarized naïve epiblast precursors at this stage do not respond to mechanical stimuli (Verstreken et al., 2019). Later on, at the peri-implantation stage, upon ECM-mediated epiblast epithelialization, the luminal pressure will induce apical surface repulsion, which contributes to the fusion of multiple rosette-like clusters and to the establishment of inverted cup shaped-morphology of the mouse embryo (Christodoulou et al., 2018; Dokmegang et al., 2020). In parallel, the progression of epiblast cells from non-polarized naïve pluripotent cells to apicobasally polarized primed cells enables biomechanical signaling to play a role in epiblast cells' fate decisions (Verstreken et al., 2019). An amniote embryo's shape at the peri-gastrulation stage exhibit species-specific variation (Sheng, 2015). As a consequence, the underlying mechanical forces and their interplay with cellular morphogenesis can also vary. In the chick embryo, for example, where the peri-gastrulation embryo's shape can be likened to a disc, a supracellular actomyosin ring located in the marginal zone, at the edge of the embryonic tissue, controls the embryo global geometry. This ring also induces cellular deformations that are transmitted locally though the epiblast epithelial structure, inducing "polonaise-like" coordinated cellular migration and initiation of the primitive streak (Saadaoui et al., 2020). The

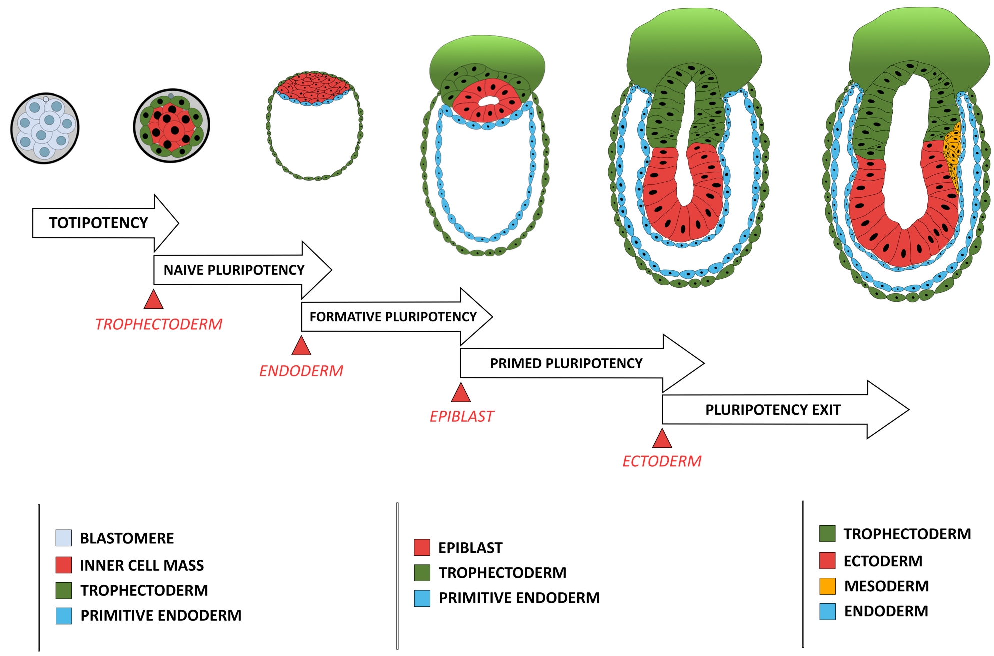

FIGURE 1 | Comparison between the developmental stage of a mouse embryo and the concomitant restriction in cellular potency. Each restriction in cellular potency is associated with the creation of an embryonic structure through an epithelialization process: the totipotency is lost when the trophectoderm epithelializes; the naïve pluripotency loss corresponds to the epithelialization of the endoderm; the formative state loss is concomitant with the epithelialization of the epiblast; and the primed pluripotency loss corresponds to the acquisition of a fully epithelial organization by the epiblast leading to pluripotency exit, a stage poised for differentiation including ectoderm-fated epithelium formation and mesendoderm induction through another round of EMT.

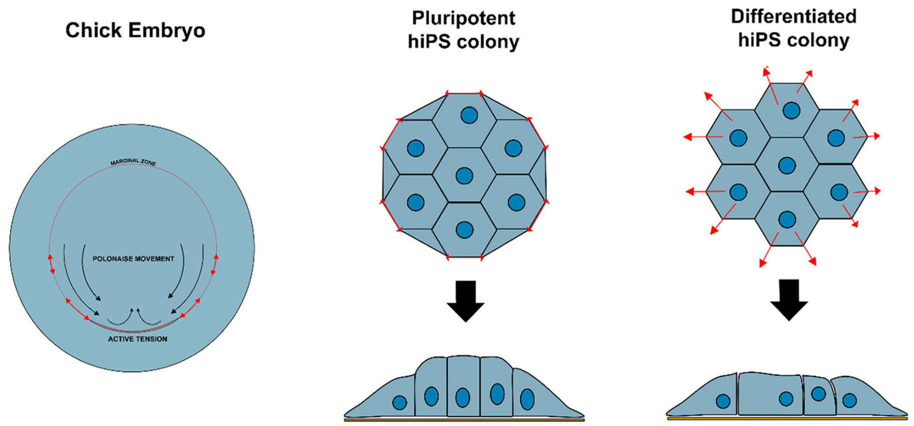

FIGURE 2 | Variation in biomechanical stress can modulate cell behavior and identity. Contractile actomyosin ring in the marginal zone of a developing chicken embryo induces cellular deformations that affect epiblast structure and promote coordinated circular cell migration and initiation of primitive streak. Similar structure is observed at the edge of hiPS cell colonies *in vitro*, resulting in tensile forces that maintain specific cellular organization and enforce pluripotency of the hiPSC colony.

"global" architecture of the pre-gastrulating chick embryo is somewhat similar to the "embryonic disc" seen in some mammalian groups, including in the human, and interestingly, a similar supracellular actin structure has also been reported to exist at the edge of disc-shaped human pluripotent stem cell (PSC) colonies *in vitro* (Närvä et al., 2017) (**Figure 2**). However, its existence *in vivo* (in the human embryo) or its causal relationship with human primitive streak initiation is unclear.

In vitro findings suggest that human PSCs can adopt a spectrum of morphological identities between fully epithelial and partially mesenchymal *in vitro*, as a consequence of differences in ECM compositions and concentrations (Hamidi et al., 2020), possibly reflecting ECM-dependent localized variations in migratory potential and epithelialization status of epiblast cells *in vivo* (Nakaya et al., 2013). It has been reported that basement membrane composition can influence PSC's epithelialization

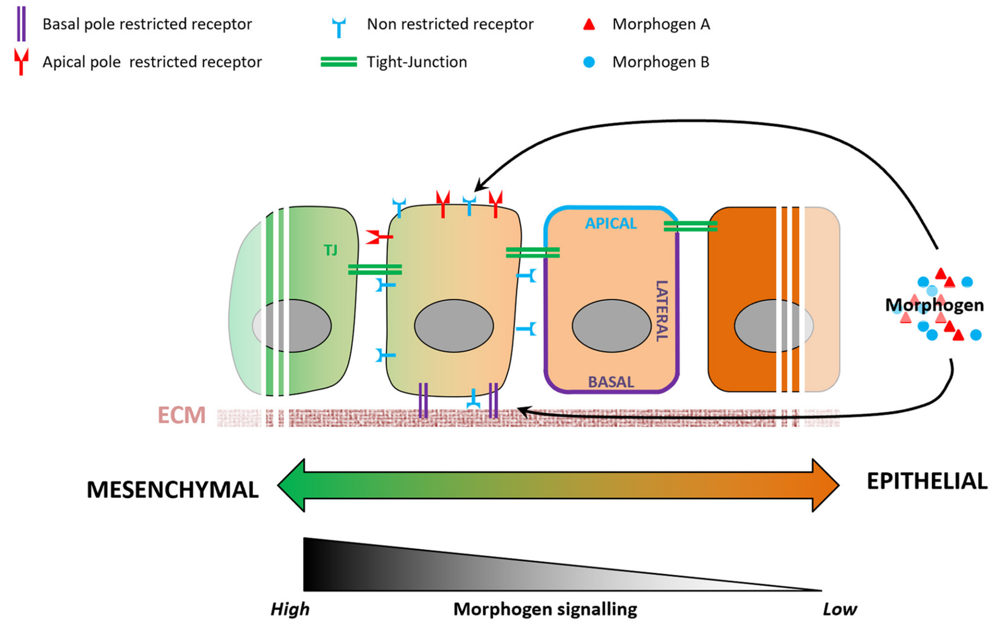

FIGURE 3 | Variations in epithelial organization can modulate levels of cellular response to a given morphogen. During the epithelialization process, tight junctions act as impermeable seals that compartmentalize the apical and basolateral membranes of a cell. As a consequence, a morphogen present at the apical pole will not be able to reach receptors localized on the basolateral membrane, and vice-versa. Some receptors are known to be localized specifically to either the apical or basolateral plasma membranes, and variations in cell's epithelial organization will result in different levels of signaling pathway activation.

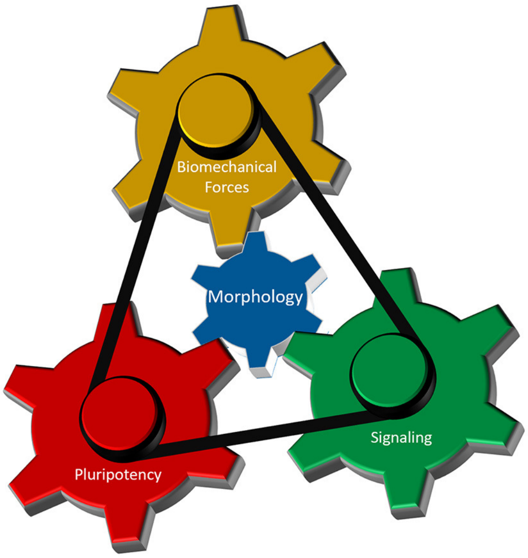

FIGURE 4 | Cellular morphology as the fundamental parameter that coordinates different regulatory components of 3-D morphogenesis. Biomechanical forces, cellular potency and molecular signaling are the main components that dictate early morphogenesis of an embryo. Cellular morphology, defined by its epithelial and/or mesenchymal status, interacts with each of those three components to induce local variations in cellular responses necessary for the formation of highly reproducible structure in an early embryo.

(Futaki et al., 2019; Hamidi et al., 2020) or induce EMT upon basement membrane breakdown (Nakaya et al., 2008), consistent with the fact that ECM's heterogeneity increases as embryonic development proceeds (Loganathan et al., 2016; Futaki et al., 2019). Spatiotemporal-specific ECM composition can be the blueprint of biomechanical force anisotropy and of an embryo's 3-D structure by providing a highly-specific local environment adequate for generating biomechanics-mediated signaling complexity (Loganathan et al., 2014).

CELL MORPHOLOGY AND RESPONSE TO MORPHOGENS

Morphogen signaling regulates many aspects of embryonic development (Tuazon and Mullins, 2015), action of which remains poorly understood. For instance, cells exposed to the same signals exhibit distinct fates depending on their spatiotemporal information in the embryo (Morgani and Hadjantonakis, 2020), and cellular geometry controls the level of response to morphogens in the mouse embryo (Zhang et al., 2019). Epithelialization-associated specification of apical and basolateral compartments of a cell involves the establishment of apical junctions as barriers to molecular diffusion. Morphogen availability and morphogen receptors are known to localize preferentially to either the apical or the basolateral membranes of the epithelium (Yin et al., 2017), resulting in a likewise compartmentalized molecular and subcellular response to a given morphogen (**Figure 3**). BMP receptors, for example, are present in mesodermal cells at levels similar to those in epiblast cells, but the BMP signaling activity is higher in the mesoderm cells (Morgani et al., 2018). Transition between epithelial and mesenchymal states of the same cell population (e.g., EMT during gastrulation) involves loss of apicobasal polarization, which may

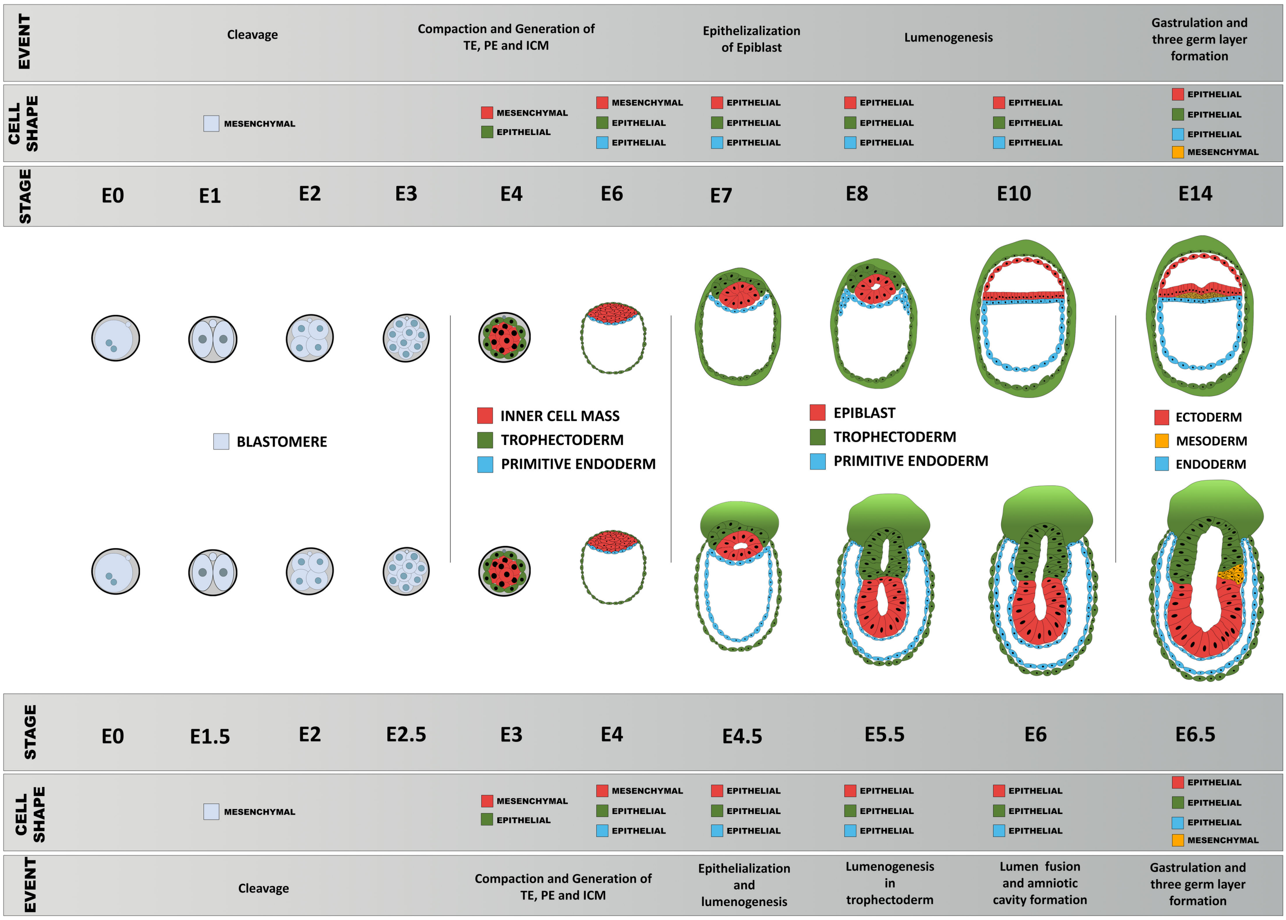

FIGURE 5 | Schematic diagram of comparison of early morphogenesis in the human and mouse. Upon fertilization, mouse and human embryos undergo a series of morphological changes, primarily as a consequence of the interplay between their epithelial and mesenchymal status, pluripotency, biomechanical forces, and morphogen signaling. Blastomeres show little apicobasal polarization before compaction between 8→16 cell stage that results in the first lineage specification: epithelialized trophoblast and non-polar inner cell mass. The primitive endoderm precursors then undergo epithelialization followed by a gradual polarization process of the epiblast precursors, resulting in formation of the proamniotic cavity and an epithelial epiblast that will be maintained until the next major transformation event during gastrulation.

lead to more BMP receptors being exposed to BMP morphogen in mesoderm cells and enhance cellular response to it. *In vitro* models of human epiblast formation and differentiation allow us to investigate this question in more detail (Warmflash et al., 2014; Williams and Solnica-Krezel, 2017; Hamidi et al., 2020). In hESC colonies, differences in receptor accessibility due to apicobasal polarization led to the establishment of a gradient of BMP signaling activation, resulting in differential commitment of PSCs to the three germ layers (Etoc et al., 2016; Hamidi et al., 2020).

Additional levels of complexity in modulating differential effect of morphogen on cellular fate specification can be achieved by ECM heterogeneity and its role in mediating morphogen availability or receptor activation at the basolateral side. In addition to controlling cells' epithelial or mesenchymal status, the ECM can also act as a filtering mesh that can slow down, concentrate or biochemically modulate the action of a given morphogen. As a consequence, cells with similar morphological characteristics and morphogen exposure can display different responses depending on their ECM composition.

WHAT CAN WE LEARN FROM THIS EMT/MET-CENTRIC MODEL?

As discussed above, interplay between cellular morphology, pluripotency, biomechanical forces, and morphogen signaling is critical for establishing proper 3-D architecture of a developing embryo (**Figure 4**). However, the mechanistic relationship between these events remains elusive. Why do cells require concurrent morphological transitions in order to achieve pluripotency changes? Do mechanical forces affect morphogen signaling and pluripotency levels, or is it the signaling that results in a specific manifestation of mechanical forces that in turn regulate cellular behavior? According to a recent model (Das et al., 2019), biomechanical forces can be a secondary consequence of short-range morphogen signaling that ensures the robustness and long-range transmission of information necessary for proper embryo-level morphogenesis. To accomplish this, cells are required to have appropriate cell-cell and cell-ECM interactions, permitting transmission of the mechanical signals. Thus, cellular morphology may act as a signal integrator that can receive, process, and send specific information among cells located in neighboring tissues.

Indeed, large-scale morphogenetic movements (e.g., during primitive streak formation) involve oriented cellular intercalation and morphology changes that can be understood from the perspective of polarized cytoskeletal organization and directional biomechanical tension (Ferro et al., 2020), associated with the supracellular organization of the actin-myosin cytoskeletal network of the epiblast epithelium (Hamidi et al., 2019; Ferro et al., 2020). However, in view of the robustness and speed of signal transduction through mechanical means, it is still unclear how cells can sense the requirement for morphological changes and effectively communicate with each other to construct elaborate, supracellular structures. A possible hypothesis, from analysis of zebrafish gastrulation, could be that there is heterogeneity in such integration and that some cells respond and relay more readily a given signal to their neighbors (Das et al., 2019).

During early embryonic development, it is unclear why cells need to undergo successive morphological transformation in order to achieve the complexity in cellular differentiation. Is it a necessity to ensure proper control over the morphogenetic process or just a direct consequence of morphology changes? The former would imply that it is necessary to restrict cellular potency as embryonic morphogenesis progresses in order to reduce potential differentiation errors. However, this paradigm seems to be contradicted by a recent study on totipotency loss and trophectoderm differentiation in which the authors showed that ICM-derived naïve PSCs retain the ability to differentiate into the trophectoderm lineage (Guo et al., 2020). The latter implies that acquisition of epithelial features is sufficient to trigger differentiation process(es) that would restrict their potency. This scenario may be a more realistic one as a recent study showed that attachment of the cellular plasma membrane to the submembrane cortex protects naïve PSCs from progressing to a primed state or further (Bergert et al., 2020). Using Ezrin mutant proteins to modulate the membrane-to-cortex attachment (MCA), the authors showed that a high MCA inhibited PSC differentiation, whereas a low MCA resulted in a permissive state that allows differentiation. Moreover, strong membrane-to-cortex attachment is known to maintain cellular polarity and protect cells from morphologic transition (Houk et al., 2012; Schneider et al., 2013). This suggests that in the case of MCA, cells are preferentially using physical forces as checkpoints to control their progression through important morphogenetic events (**Figure 5**). This and other similar hypotheses could be tested in the future by combining *in vitro* models of early epiblast-like PSC organization (Deglincerti et al., 2016) with the use of biomaterials capable of dynamic modulation of their physical properties (LeValley and Kloxin, 2019). Such approaches would enable a powerful *in vitro* platform, with high reproducibility and programmability, to investigate how mechanical signals are integrated into the biochemical network that regulates cellular specification and tissue patterning and whether cell morphological changes might be the missing link reconciling how mechanical and chemical signals influence cell identity during development.

DATA AVAILABILITY STATEMENT

The original contributions presented in the study are included in the article/supplementary material, further inquiries can be directed to the corresponding author/s.

AUTHOR CONTRIBUTIONS

GS conceived the manuscript topic. GI, SH, and GS discussed about the writing and wrote the manuscript. All authors agreed on the content of manuscript.

FUNDING

This work has been partly funded by a MEXT scholarship to GI and Kakenhi Kiban B and C, JST, and Takeda foundation research grafts to GS.

REFERENCES

Bedzhov, I., and Zernicka-Goetz, M. (2014). Self-organizing properties of mouse pluripotent cells initiate morphogenesis upon implantation. *Cell* 156, 1032–1044. doi: 10.1016/j.cell.2014.01.023

Bergert, M., Lembo, S., Sharma, S., Russo, L., Milovanović, D., Gretarsson, K. H., et al. (2020). Cell surface mechanics gate embryonic stem cell differentiation. *Cell Stem Cell*. 28, 1–8. doi: 10.1016/j.stem.2020.10.017

Bissiere, S., Gasnier, M., Alvarez, Y. D., and Plachta, N. (2018). Cell fate decisions during preimplantation mammalian development. *Curr. Top. Dev. Biol.* 128, 37–58. doi: 10.1016/bs.ctdb.2017.11.001

Chan, C. J., Costanzo, M., Ruiz-Herrero, T., Mönke, G., Petrie, R. J., Bergert, M., et al. (2019). Hydraulic control of mammalian embryo size and cell fate. *Nature* 571, 112–116. doi: 10.1038/s41586-019-1309-x

Chen, A. F., Liu, A. J., Krishnakumar, R., Freimer, J. W., DeVeale, B., and Blelloch, R. (2018). GRHL2-dependent enhancer switching maintains a pluripotent stem cell transcriptional subnetwork after exit from naive pluripotency. *Cell Stem Cell* 23, 226–238.e224. doi: 10.1016/j.stem.2018.06.005

Christodoulou, N., Kyprianou, C., Weberling, A., Wang, R., Cui, G., Peng, G., et al. (2018). Author correction: sequential formation and resolution of multiple rosettes drive embryo remodelling after implantation. *Nat. Cell Biol.* 20:1434. doi: 10.1038/s41556-018-0245-6

Cui, W., Cheong, A., Wang, Y., Tsuchida, Y., Liu, Y., Tremblay, K. D., et al. (2020). MCRS1 is essential for epiblast development during early mouse embryogenesis. *Reproduction* 159, 1–13. doi: 10.1530/REP-19-0334

Das, D., Jülich, D., Schwendinger-Schreck, J., Guillon, E., Lawton, A. K., Dray, N., et al. (2019). Organization of embryonic morphogenesis via mechanical information. *Dev. Cell* 49, 829–839.e825. doi: 10.1016/j.devcel.2019.05.014

Deglincerti, A., Croft, G. F., Pietila, L. N., Zernicka-Goetz, M., Siggia, E. D., and Brivanlou, A. H. (2016). Self-organization of the *in vitro* attached human embryo. *Nature* 533, 251–254. doi: 10.1038/nature17948

Dokmegang, J., Yap, M. H., Han, L., Cavaliere, M., and Doursat, R. (2020). Computational modelling unveils how epiblast remodelling and positioning rely on trophectoderm morphogenesis during mouse implantation. doi: 10.1101/2020.06.08.140269

Etoc, F., Metzger, J., Ruzo, A., Kirst, C., Yoney, A., Ozair, M. Z., et al. (2016). A balance between secreted inhibitors and edge sensing controls gastruloid self-organization. *Dev. Cell* 39, 302–315. doi: 10.1016/j.devcel.2016.09.016

Ferro, V., Chuai, M., McGloin, D., and Weijer, C. J. (2020). Measurement of junctional tension in epithelial cells at the onset of primitive streak formation in the chick embryo via non-destructive optical manipulation. *Development* 147:dev175109. doi: 10.1242/dev.175109

Futaki, S., Nakano, I., Kawasaki, M., Sanzen, N., and Sekiguchi, K. (2019). Molecular profiling of the basement membrane of pluripotent epiblast cells in post-implantation stage mouse embryos. *Regene. Therap.* 12, 55–65. doi: 10.1016/j.reth.2019.04.010

Ghimire, S., Van der Jeught, M., Neupane, J., Roost, M. S., Anckaert, J., Popovic, M., et al. (2018). Comparative analysis of naive, primed and ground state pluripotency in mouse embryonic stem cells originating from the same genetic background. *Sci. Rep.* 8:5884. doi: 10.1038/s41598-018-24051-5

Guo, G., Stirparo, G. G., Strawbridge, S., Spindlow, D., Yang, J., Clarke, J., et al. (2020). Human naïve epiblast cells possess unrestricted lineage potential. doi: 10.1101/2020.02.04.933812

Hamidi, S., Nakaya, Y., Nagai, H., Alev, C., Kasukawa, T., Chhabra, S., et al. (2020). Mesenchymal-epithelial transition regulates initiation of pluripotency exit before gastrulation. *Development* 147:dev184960. doi: 10.1242/dev.184960

Hamidi, S., Nakaya, Y., Nagai, H., Alev, C., Shibata, T., and Sheng, G. (2019). Biomechanical regulation of EMT and epithelial morphogenesis in amniote epiblast. *Phys. Biol.* 16:041002. doi: 10.1088/1478-3975/ab1048

Houk, A. R., Jilkine, A., Mejean, C. O., Boltyanskiy, R., Dufresne, E. R., Angenent, S. B., et al. (2012). Membrane tension maintains cell polarity by confining signals to the leading edge during neutrophil migration. *Cell* 148, 175–188. doi: 10.1016/j.cell.2011.10.050

Humiecka, M., Szpila, M., Kło,ś, P., Maleszewski, M., and Szczepańska, K. (2017). Mouse blastomeres acquire ability to divide asymmetrically before compaction. *PLoS ONE* 12:e0175032. doi: 10.1371/journal.pone.0175032

Kinoshita, M., Barber, M., Mansfield, W., Cui, Y., Spindlow, D., Stirparo, G. G., et al. (2020). Capture of mouse and human stem cells with features of formative pluripotency. *Cell Stem Cell*. doi: 10.1016/j.stem.2020.11.005

LeValley, P. J., and Kloxin, A. M. (2019). Chemical approaches to dynamically modulate the properties of synthetic matrices. *ACS Macro Lett.* 8, 7–16. doi: 10.1021/acsmacrolett.8b00808

Liu, M. X., Zhou, K. C., and Cao, Y. (2014). MCRS1 overexpression, which is specifically inhibited by miR-129*, promotes the epithelial-mesenchymal transition and metastasis in non-small cell lung cancer. *Mol. Cancer* 13:245. doi: 10.1186/1476-4598-13-245

Loganathan, R., Little, C. D., Joshi, P., Filla, M. B., Cheuvront, T. J., Lansford, R., et al. (2014). Identification of emergent motion compartments in the amniote embryo. *Organogenesis* 10, 350–364. doi: 10.4161/org.36315

Loganathan, R., Rongish, B. J., Smith, C. M., Filla, M. B., Czirok, A., Bénazéraf, B., et al. (2016). Extracellular matrix motion and early morphogenesis. *Development* 143, 2056–2065. doi: 10.1242/dev.127886

Maître, J. L., Turlier, H., Illukkumbura, R., Eismann, B., Niwayama, R., Nédélec, F., et al. (2016). Asymmetric division of contractile domains couples cell positioning and fate specification. *Nature* 536, 344–348. doi: 10.1038/nature18958

Marikawa, Y., and Alarcón, V. B. (2009). Establishment of trophectoderm and inner cell mass lineages in the mouse embryo. *Mol. Reprod. Dev.* 76, 1019–1032. doi: 10.1002/mrd.21057

Morgani, S. M., and Hadjantonakis, A. K. (2020). Signaling regulation during gastrulation: insights from mouse embryos and *in vitro* systems. *Curr. Top. Dev. Biol.* 137, 391–431. doi: 10.1016/bs.ctdb.2019.11.011

Morgani, S. M., Metzger, J. J., Nichols, J., Siggia, E. D., and Hadjantonakis, A. K. (2018). Micropattern differentiation of mouse pluripotent stem cells recapitulates embryo regionalized cell fate patterning. *Elife* 7:e32839. doi: 10.7554/eLife.32839.029

Nakaya, Y., Sukowati, E. W., and Sheng, G. (2013). Epiblast integrity requires CLASP and dystroglycan-mediated microtubule anchoring to the basal cortex. *J. Cell Biol.* 202, 637–651. doi: 10.1083/jcb.201302075

Nakaya, Y., Sukowati, E. W., Wu, Y., and Sheng, G. (2008). RhoA and microtubule dynamics control cell-basement membrane interaction in EMT during gastrulation. *Nat. Cell Biol.* 10, 765–775. doi: 10.1038/ncb1739

Närvä, E., Stubb, A., Guzmán, C., Blomqvist, M., Balboa, D., Lerche, M., et al. (2017). A strong contractile actin fence and large adhesions direct human pluripotent colony morphology and adhesion. *Stem Cell Rep.* 9, 67–76. doi: 10.1016/j.stemcr.2017.05.021

Saadaoui, M., Rocancourt, D., Roussel, J., Corson, F., and Gros, J. (2020). A tensile ring drives tissue flows to shape the gastrulating amniote embryo. *Science* 367, 453–458. doi: 10.1126/science.aaw1965

Schneider, D., Baronsky, T., Pietuch, A., Rother, J., Oelkers, M., Fichtner, D., et al. (2013). Tension monitoring during epithelial-to-mesenchymal transition links the switch of phenotype to expression of moesin and cadherins in NMuMG cells. *PLoS ONE* 8:e80068. doi: 10.1371/journal.pone.0080068

Shahbazi, M. N., Scialdone, A., Skorupska, N., Weberling, A., Recher, G., Zhu, M., et al. (2017). Pluripotent state transitions coordinate morphogenesis in mouse and human embryos. *Nature* 552, 239–243. doi: 10.1038/nature24675

Sheng, G. (2015). Epiblast morphogenesis before gastrulation. *Dev. Biol.* 401, 17–24. doi: 10.1016/j.ydbio.2014.10.003

Stumpf, P. S., and MacArthur, B. D. (2019). Machine learning of stem cell identities from single-cell expression data via regulatory network archetypes. *Front. Genet.* 10:2. doi: 10.3389/fgene.2019.00002

Thakurela, S., Sindhu, C., Yurkovsky, E., Riemenschneider, C., Smith, Z. D., Nachman, I., et al. (2019). Differential regulation of OCT4 targets facilitates reacquisition of pluripotency. *Nat. Commun.* 10:4444. doi: 10.1038/s41467-019-11741-5

Tian, T. V., Di Stefano, B., Stik, G., Vila-Casadesús, M., Sardina, J. L., Vidal, E., et al. (2019). Whsc1 links pluripotency exit with mesendoderm specification. *Nat. Cell Biol.* 21, 824–834. doi: 10.1038/s41556-019-0342-1

Tuazon, F. B., and Mullins, M. C. (2015). Temporally coordinated signals progressively pattern the anteroposterior and dorsoventral body axes. *Semin. Cell Dev. Biol.* 42, 118–133. doi: 10.1016/j.semcdb.2015.06.003

Verstreken, C. M., Labouesse, C., Agley, C. C., and Chalut, K. J. (2019). Embryonic stem cells become mechanoresponsive upon exit from ground state of pluripotency. *Open Biol.* 9:180203. doi: 10.1098/rsob.180203

Wang, X., Zhang, Z., Tao, H., Liu, J., Hopyan, S., and Sun, Y. (2018). Characterizing inner pressure and stiffness of trophoblast and inner cell mass of blastocysts. *Biophys. J.* 115, 2443–2450. doi: 10.1016/j.bpj.2018.11.008

Warmflash, A., Sorre, B., Etoc, F., Siggia, E. D., and Brivanlou, A. H. (2014). A method to recapitulate early embryonic spatial patterning in human embryonic stem cells. *Nat. Methods* 11, 847–854. doi: 10.1038/nmeth.3016

Williams, M. L., and Solnica-Krezel, L. (2017). Regulation of gastrulation movements by emergent cell and tissue interactions. *Curr. Opin. Cell Biol.* 48, 33–39. doi: 10.1016/j.ceb.2017.04.006

Yin, X., Kang, J. H., Andrianifahanana, M., Wang, Y., Jung, M. Y., Hernandez, D. M., et al. (2017). Basolateral delivery of the type I transforming growth factor beta receptor is mediated by a dominant-acting cytoplasmic motif. *Mol. Biol. Cell* 28, 2701–2711. doi: 10.1091/mbc.e17-05-0334

Zhang, Z., Zwick, S., Loew, E., Grimley, J. S., and Ramanathan, S. (2019). Mouse embryo geometry drives formation of robust signaling gradients through receptor localization. *Nat. Commun.* 10:4516. doi: 10.1038/s41467-019-12533-7

Conflict of Interest: The authors declare that the research was conducted in the absence of any commercial or financial relationships that could be construed as a potential conflict of interest.

frontiers
in Cell and Developmental Biology

ORIGINAL RESEARCH
published: 11 March 2021
doi: 10.3389/fcell.2021.653472

Three-Dimensional Architecture of Glomerular Endothelial Cells Revealed by FIB-SEM Tomography

Yuto Kawasaki[1], Yasue Hosoyamada[1,2], Takayuki Miyaki[1], Junji Yamaguchi[3], Soichiro Kakuta[3], Tatsuo Sakai[1] and Koichiro Ichimura[1,3]*

[1] Department of Anatomy and Life Structure, Juntendo University Graduate School of Medicine, Tokyo, Japan, [2] Department of Nutrition, Faculty of Health Care Sciences, Chiba Prefectural University of Health Sciences, Chiba, Japan, [3] Laboratory of Morphology and Image Analysis, Research Support Center, Juntendo University Graduate School of Medicine, Tokyo, Japan

OPEN ACCESS

Edited by:
Silvia Garagna,
University of Pavia, Italy

Reviewed by:
Nobuhiko Ohno,
Jichi Medical University, Japan
Christel Genoud,
University of Lausanne, Switzerland
Sei Saitoh,
Fujita Health University, Japan

***Correspondence:**
Koichiro Ichimura
ichimura@juntendo.ac.jp

Specialty section:
This article was submitted to
Cell Growth and Division,
a section of the journal
Frontiers in Cell and Developmental Biology

***Received:** 14 January 2021*
***Accepted:** 04 February 2021*
***Published:** 11 March 2021*

Citation:
Kawasaki Y, Hosoyamada Y, Miyaki T, Yamaguchi J, Kakuta S, Sakai T and Ichimura K (2021) Three-Dimensional Architecture of Glomerular Endothelial Cells Revealed by FIB-SEM Tomography. Front. Cell Dev. Biol. 9:653472. doi: 10.3389/fcell.2021.653472

Focused-ion beam-scanning electron microscopic (FIB-SEM) tomography enables easier acquisition of a series of ultrastructural, sectional images directly from resin-embedded biological samples. In this study, to clarify the three-dimensional (3D) architecture of glomerular endothelial cells (GEnCs) in adult rats, we manually extracted GEnCs from serial FIB-SEM images and reconstructed them on an Amira reconstruction software. The luminal and basal surface structures were clearly visualized in the reconstructed GEnCs, although only the luminal surface structures could be observed by conventional SEM. The luminal surface visualized via the reconstructed GEnCs was quite similar to that observed through conventional SEM, indicating that 3D reconstruction could be performed with high accuracy. Thus, we successfully described the 3D architecture of normal GEnCs in adult rats more clearly and precisely than ever before. The GEnCs were found to consist of three major subcellular compartments, namely, the cell body, cytoplasmic ridges, and sieve plates, in addition to two associated subcellular compartments, namely, the globular protrusions and reticular porous structures. Furthermore, most individual GEnCs made up a "seamless" tubular shape, and some of them formed an autocellular junction to make up a tubular shape. FIB-SEM tomography with reconstruction is a powerful approach to better understand the 3D architecture of GEnCs. Moreover, the morphological information revealed in this study will be valuable for the 3D pathologic evaluation of GEnCs in animal and human glomerular diseases and the structural analysis of developmental processes in the glomerular capillary system.

Keywords: FIB-SEM tomography, block-face imaging, glomerular endothelial cell, mesangial cell, autocellular junction, 3D ultrastructure

INTRODUCTION

Glomerular endothelial cells (GEnCs) form a glomerular capillary system between afferent and efferent arterioles (Kriz and Kaissling, 2000). The glomerular capillary system, together with the mesangium, creates a vascular compartment of the glomerulus. The vascular compartment is further enwrapped by an epithelial compartment, which is composed of the glomerular basement membrane (GBM) and podocytes, *en bloc* (Ichimura et al., 2007; **Figure 1A**).

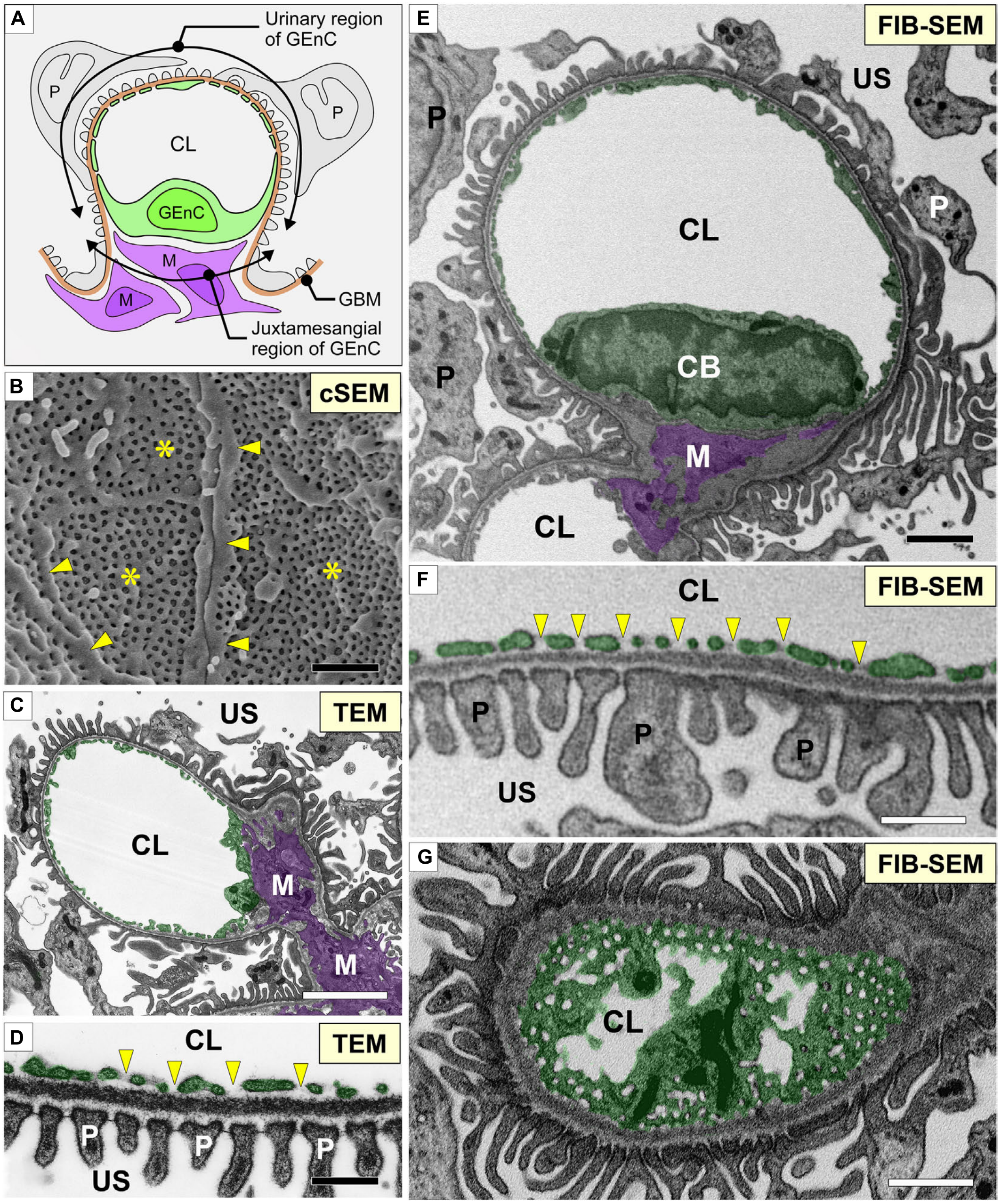

FIGURE 1 | Glomerular capillary images of conventional electron microscopy and focused-ion beam-scanning electron microscopy (FIB-SEM). **(A)** Two regions of a glomerular endothelial cell (GEnC) in relation to the surrounding structures, such as the glomerular basement membrane (brown line, GBM), mesangial cells (purple cells, M), and podocytes (gray cells, P). **(B)** Conventional SEM (cSEM) image of the luminal surface of GEnCs. Highly fenestrated sieve plates (asterisks) and cytoplasmic ridges (arrowheads) are clearly visible. **(C,D)** Conventional TEM images. **(E–G)** Contrast-inverted FIB-SEM images. Conventional TEM and FIB-SEM images showing that the transverse sections of the glomerular capillary are similar in quality **(C–F)**. **(D,F)** Magnification of glomerular capillary wall, which consists of GEnCs, the GBM, and podocyte foot processes. The fenestrae of GEnCs do not exhibit diaphragms (arrowheads in **D,F**). **(G)** Grazing section of a capillary wall showing the fenestrae without diaphragms. CB, cell body of glomerular endothelial cell; CL, capillary lumen; US, urinary space. Scale bar, 5 μm in **(C,E,G)**; 200 nm in **(B,D,F)**.

Vascular endothelial cells are structurally specialized to maintain the specific functions of individual organs. The relationship between their ultrastructure and permeability has been explored in many previous studies (Roberts and Palade, 2000). In the capillaries where the transendothelial exchange vigorously occurs, numerous transcellular pores or fenestrae form "sieve plates." Such fenestrated endothelial cells are found in the exocrine and endocrine glands, liver sinusoid, intestinal villi, and kidney (glomerular and peritubular capillaries) (Pease, 1955; Maul, 1971). In general, endothelial fenestrae are furnished with fenestral diaphragms composed of a transmembrane glycoprotein, namely, PV-1 (Stan et al., 1999a,b; Stan et al., 2004). The fenestral diaphragms function by maintaining the diameters of these structures in a specific small range (Simionescu, 1983, 2000; Ichimura et al., 2008). For efficient glomerular ultrafiltration, the GEnCs cause fenestral diaphragms to disappear and enlarge the diameter during glomerular development (Reeves et al., 1980; Ichimura et al., 2008).

Endothelial cells face the lumen of the vasculature; thus, conventional scanning electron microscopy (SEM) is useful in evaluating their luminal surface structures. GEnCs can be exposed by freeze fracture and visualized by conventional SEM; however, only limited numbers and parts of GEnCs can be exposed by freeze fracture (Miyaki et al., 2020a). Thus, conventional SEM would not be enough to examine the whole architecture of individual GEnCs.

Focused-ion beam-SEM (FIB-SEM) tomography is a powerful approach to overcome this problem. This method of electron microscopy automatically acquires the serial sectional images directly from biological samples embedded in epoxy resin (Kubota, 2015; Ohno et al., 2015; Titze and Genoud, 2016). These FIB-SEM images are comparable to conventional transmission electron microscopy (TEM) images. Moreover, three-dimensional (3D) cellular structures can be reconstructed from serial sectional images with high reliability (Miyaki et al., 2020a,b). Recently, using this approach, our group has re-evaluated the 3D ultrastructure of podocytes in the context of health (Ichimura et al., 2015), development (Ichimura et al., 2017), disease (Ichimura et al., 2019), and evolution (Ichimura and Sakai, 2017; Kawasaki et al., 2019; Miyaki et al., 2020c). The 3D reconstructed images of single podocytes enable the evaluation of surface structures of these cells from any direction and without interference by neighboring podocytes and the GBM. Furthermore, other groups found that a direct interaction was formed between podocytes and mesangial cells in human glomerular diseases using serial block-face SEM, which is an alternative SEM method for acquiring the serial sectional images directly from resin-embedded tissue samples (Takaki et al., 2019; Nagai et al., 2020).

Focused-ion beam-SEM tomography with reconstruction techniques can also reveal the 3D architecture of nephron-constituent cells other than podocytes. In the present study, using FIB-SEM tomography and reconstruction techniques, we successfully described the 3D architecture of normal GEnCs in adult rats more clearly and precisely than ever before.

MATERIALS AND METHODS

Animals

Two adult (10 weeks old, male) Wistar rats (Charles River Japan, Yokohama, Japan) were used in this study. Rats were perfused with physiological saline and subsequently 2.5% glutaraldehyde fixative buffered with 0.1 M phosphate buffer (PB) under anesthesia with pentobarbital. All procedures performed on laboratory animals were approved by the Institutional Animal Care and Use Committee of Juntendo University School of Medicine (approval no. 2020104). All animal experiments were carried out in accordance with the Guidelines for Animal Experimentation of Juntendo University School of Medicine.

Conventional TEM

Conventional TEM was performed as described previously (Ichimura et al., 2009, 2010). In brief, the slices of fixed kidney cortex were successively immersed in 0.4% osmium tetroxide (OsO_4) in 0.1 M PB for 1 h, 2% low-molecular-weight tannic acid (LMW-TA, Electron Microscopy Sciences, Hatfield, PA, United States) in 0.05 M maleate buffer for 4 h, and 1% uranyl acetate in 0.05 M maleate buffer for 3 h. The slices were then dehydrated with a graded series of ethanol and embedded in Oken Epok 812 epoxy resin (Oken-shoji, Tokyo, Japan). Ultrathin sections (90–100 nm thickness) were produced with an ultra 45° diamond knife (Diatome, Biel, Switzerland) and transferred to 50-mesh copper grids coated with a Formvar membrane. The ultrathin sections stained with lead citrate and uranyl acetate were digitally photographed with an H-7100 transmission electron microscope (Hitachi High-Technologies, Tokyo, Japan), which was equipped with a C4742-95 CCD camera (Hamamatsu Photonics, Shizuoka, Japan).

Conventional SEM

Conventional SEM was performed as described previously (Dong et al., 2010; Miyaki et al., 2020a). Small cubes of the fixed kidney cortex (approximately 4 × 4 × 2 mm) were processed with conductive staining. First, the cubes were immersed in 1% OsO_4 in 0.1 M PB for 30 min at 24°C, washed with 0.1 M PB for 5 min three times, and then immersed in 1% LMW-TA (Electron Microscopy Sciences) in distilled water (DW) for 2 h at RT. After the cubes were washed three times with DW for 5 min, the same staining procedure was repeated twice. However, OsO_4 was diluted with DW.

The stained samples were dehydrated with a graded series of ethanol and then immersed in *t*-butyl alcohol. The samples were freeze-dried using an ES-2030 freeze dryer (Hitachi High-Technologies, Tokyo, Japan). The dried specimens were mounted on aluminum stubs with carbon paste (Pelco Colloidal Graphite, Ted Pella, Inc., Redding, CA, United States). The mounted specimens were coated with osmium with an OPC80T osmium plasma coater (Filgen, Inc., Nagoya, Japan). The samples were observed with an S-4800 field emission-SEM (Hitachi High-Technologies). Regions of interest were imaged using a backscattered electron detector with an acceleration voltage of 3 kV. Individual podocytes were denoted with different transparent colors using Adobe Illustrator.

FIB-SEM Tomography

Focused-ion beam-SEM tomography was performed as described previously (Miyaki et al., 2020a,b; **Figure 2**). In brief, the cortex of the fixed kidney was cut into 250-μm-thick slices with a DTK-1000 MicroSlicers (Dosaka EM, Kyoto, Japan). The slices were successively immersed in 1% OsO_4 containing 1.5% potassium ferrocyanide [$K_4Fe(CN)_6 \cdot 3H_2O$] in 0.1 M cacodylate buffer (CB) for 1 h on ice, 1% LMW-TA (Electron Microscopy Sciences) in 0.1 M CB for 4 h at 24°C, 2% aqueous OsO_4 for 30 min at 24°C, and

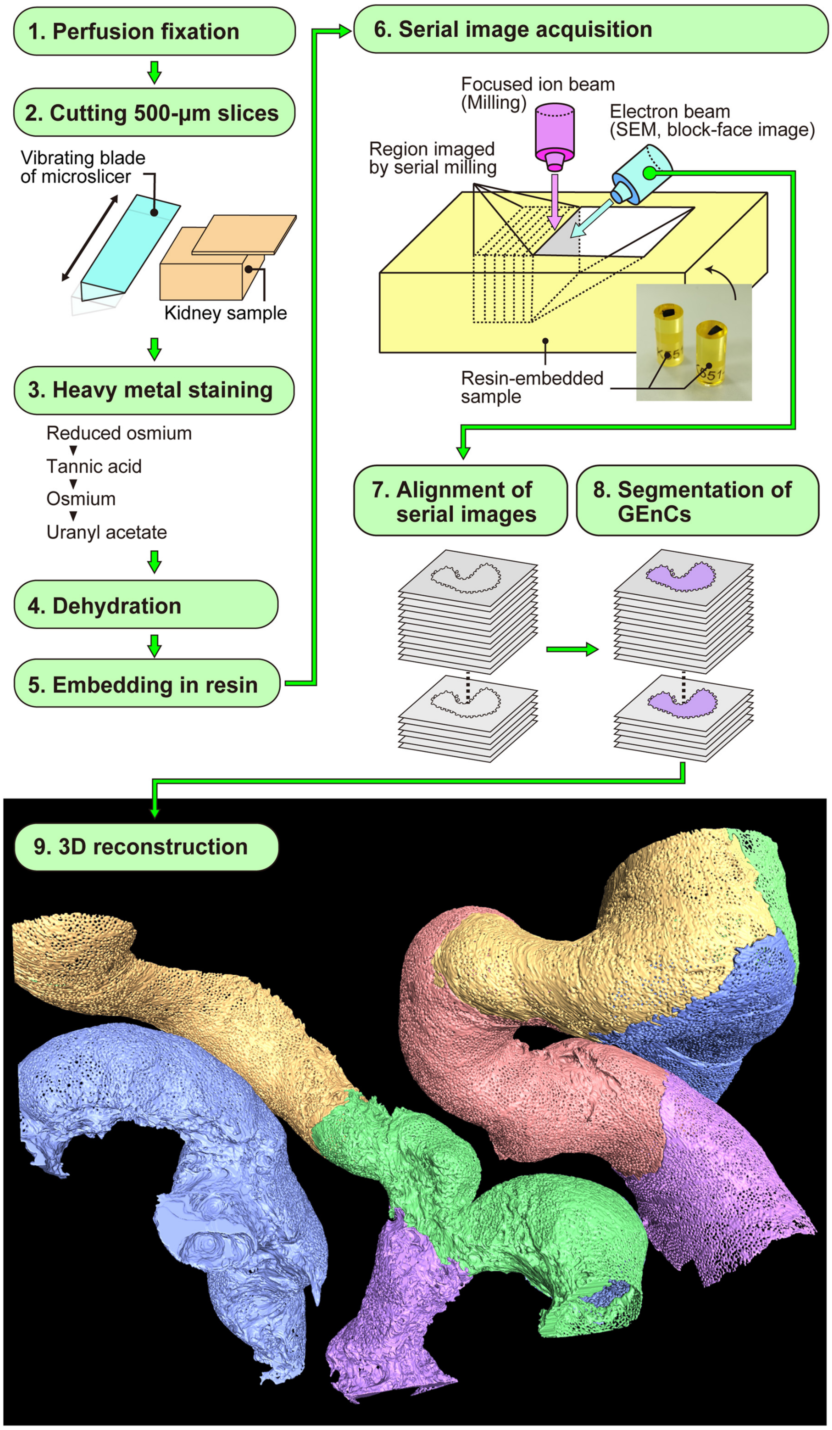

FIGURE 2 | Focused-ion beam-scanning electron microscopy (FIB-SEM) tomography and 3D reconstruction of glomerular endothelial cells (GEnCs). The series of this method is largely divided into nine steps (1–9). Finally, the color-coded 3D reconstruction images of GEnCs are produced.

1% aqueous uranyl acetate $[UO_2(CH_3COO)_2{\cdot}2H_2O]$ overnight at 24°C. The slices were washed with 0.1 M CB or DW for 5 min, three times, between each staining step.

The stained samples were then dehydrated using a graded series of ethanol. The dehydrated samples were successively immersed in propylene oxide for 5 min twice, 50% epoxy resin in propylene oxide on a rotational mixer for 3 h, and then pure epoxy resin on a rotational mixer for 12 h. Subsequently, the samples were embedded in newly made pure epoxy resin and hardened for 3 days at 60°C.

The surfaces of the resin-embedded tissues were exposed using a diamond knife on an Ultracut UCT (Leica Biosystems). The block was mounted onto an HV-8 aluminum stub (Micro Star, Tokyo, Japan). The space between the block and stub was filled with carbon paste and then coated with a thin layer of platinum–palladium, using an MC1000 ion sputter coater (Hitachi High-Technologies).

The coated surface of the block was imaged with a Helios Nanolab 660 FIB-SEM (Thermo Fisher Scientific, Waltham, MA, United States), at a high acceleration voltage of 10 kV, to determine the area of interest. To prevent beam damage, a platinum layer was deposited on the area of interest, with a 2.5 nA beam current, where a voltage of 30 kV accelerated gallium ions. To make the new block face (imaging-face), a trench was cut using FIB milling, with a 25 nA beam current, where gallium ions were accelerated by a voltage of 30 kV. Serial FIB-SEM images were acquired with Auto Slice and View imaging software (Thermo Fisher Scientific) on a Helios Nanolab 660 FIB-SEM. New surfaces for serial block-face imaging were generated using FIB milling, with a 0.77 nA beam current. Three sets of serial 850 FIB-SEM images were obtained from two adult rats every 50 nm in depth, with a backscattered electron detector at an acceleration voltage of 3.0 kV. The size of each FIB-SEM image was 41.5 × 27.7 μm (width × height). Thus, the volume of serial image acquisition was 41.5 × 27.7 × 42.5 μm (width × height × depth).

Three-Dimensional Reconstruction

After aligning serial FIB-SEM images, we manually segmented the target GEnCs on individual FIB-SEM images using AMIRA 6.1 reconstruction software (Thermo Fisher Scientific) and then reconstructed them using the same software (**Figure 2**). We used a Cintiq 27QHD large interactive pen display for the segmentation procedure (Wacom, Tokyo, Japan).

RESULTS

Sectional FIB-SEM Images of GEnCs

We obtained serial FIB-SEM images of the glomeruli of adult Wistar rats. The contrast-inverted FIB-SEM images of the glomerulus achieved a quality comparable to that of conventional TEM images (**Figures 1C,D,E–G**). In spatial relation to the surrounding structures, the glomerular capillary and GEnCs were divided into two regions, urinary and juxtamesangial regions, as previously proposed by Sakai and Kriz (1987; **Figure 1A**). The urinary region made up 70–80% of the total circumference in a GEnC and adhered to the GBM (**Figures 1E,F**). The urinary region was also highly attenuated and fenestrated (**Figures 1F,G**). The fenestrae in GEnCs were not furnished with fenestral diaphragms, unlike that in other fenestrated endothelial cells, such as peritubular capillary endothelial cells (arrows in **Figure 1F**). The juxtamesangial region made up 20–30% of the total circumference of a GEnC and was in contact with the mesangium without the GBM between them (**Figures 1A,E**). The cell bodies of GEnCs, which contained a nucleus and bulged into the capillary lumen, were usually localized at the juxtamesangial region (**Figures 1A,E**).

Three-Dimensional Architecture of GEnCs Revealed by 3D Reconstruction

We reconstructed six glomerular capillary loops containing 24 GEnCs from serial FIB-SEM images (**Figure 2**). Both the luminal and basal surface structures were clearly visualized

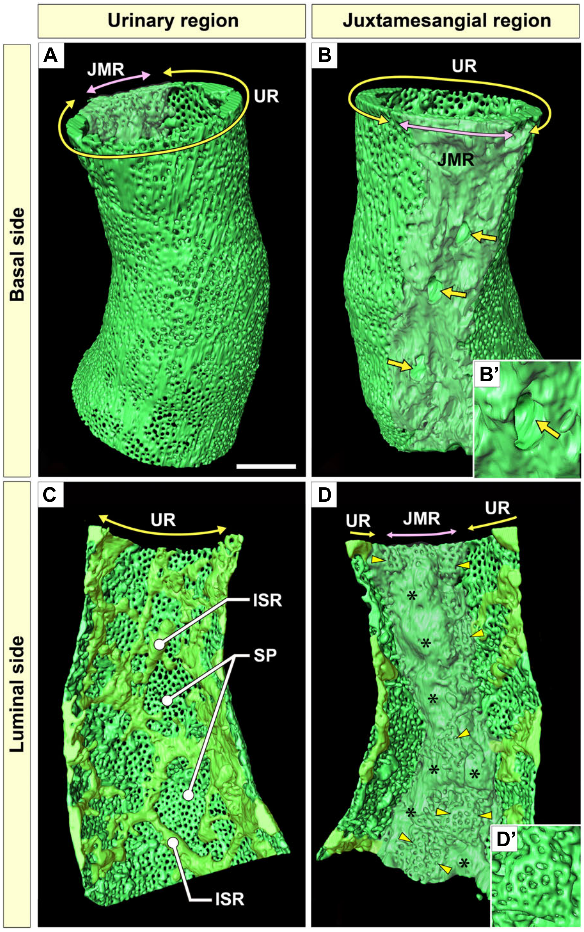

FIGURE 3 | Urinary region (UR) and juxtamesangial region (JMR) of a glomerular endothelial cell (GEnC). **(A,B)** Three-dimensional reconstruction of a single GEnC tube. The basal surfaces of the UR and JMR are predominantly shown in **(A,B)**, respectively. **(A)** In the UR, the basal surface is smooth in total despite the high fenestration. **(B)** In the JMR, the basal surface is uneven with less fenestration. The indentations for mesangial cell processes were frequently recognized (arrows). **(B′)** High magnification of an indentation created by a large non-adhesive mesangial cell process. The GEnC tube in **(A,B)** is longitudinally divided into two halves, and the luminal surfaces of the UR **(C)** and JMR **(D)** are shown. **(C)** In the UR, the sieve plates are among the fine intersieve ridges (yellowish-green). **(D)** In the JMR, the thick juxtamesangial cytoplasmic ridge could be found (asterisks, whitish-green). The reticular porous structures are frequently recognized on and beside the thick juxtamesangial ridge (arrowheads). **(D′)** High magnification of the reticular porous structure. ISR, intersieve ridge; SP, sieve plate. Scale bar, 5 μm. The reconstructed images of GEnC **(A–D)** are also shown in **Supplementary Movies 1–3**.

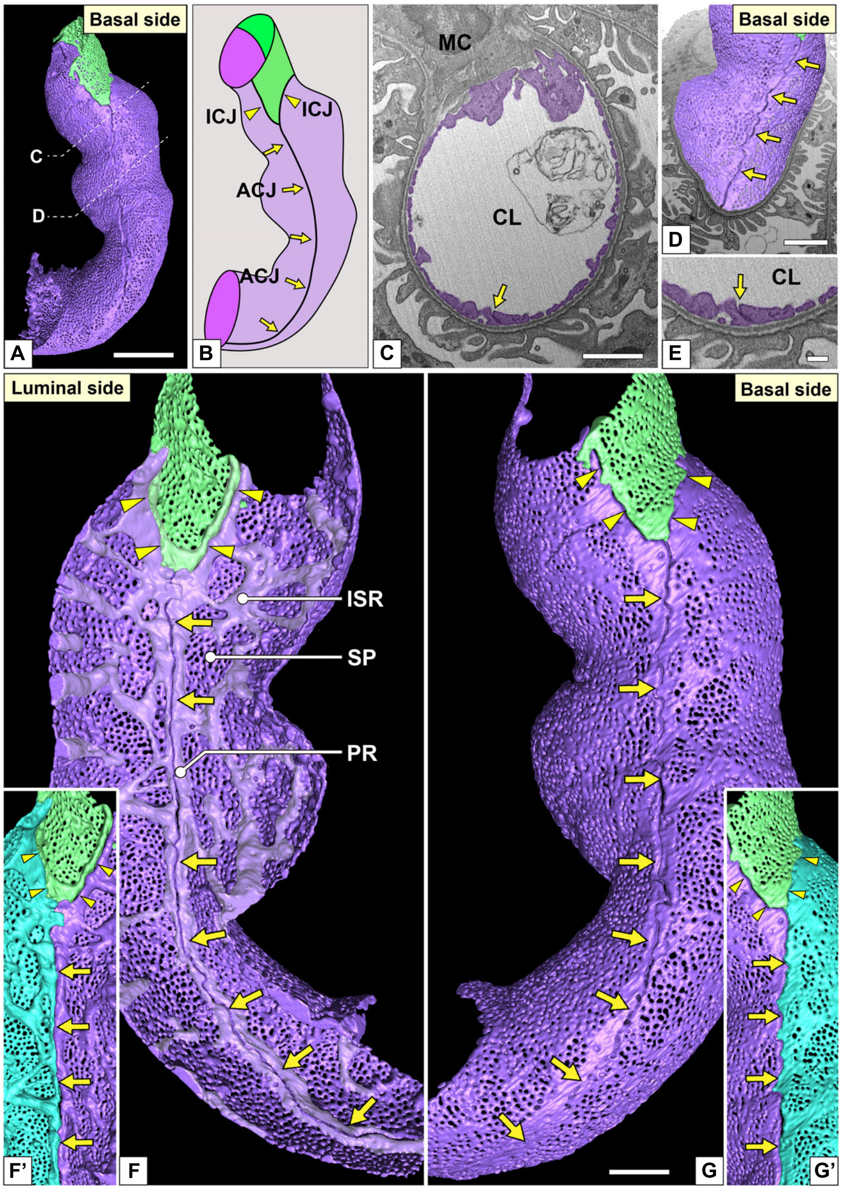

FIGURE 4 | Urinary region and autocellular junction of glomerular endothelial cells (GEnCs). **(A)** A reconstructed capillary is formed by two GEnCs (purple and green). **(B)** The location of cellular junctions in this capillary. The purple GEnC forms an autocellular junction (ACJ), which is along the longitudinal axis of the capillary. ICJ, intercellular junction between green and purple GEnCs. **(C)** The sectional focused-ion beam-scanning electron microscopy (FIB-SEM) image of the purple GEnC. CL, capillary lumen; MC, mesangial cell. **(D)** The reconstructed GEnCs are displayed on the sectional FIB-SEM image. **(E)** Magnified image of the ACJ shown in **(C)**. The luminal **(F,F′)** and basal **(G,G′)** surfaces of the urinary region. **(F)** Two peripheral ridges of the purple GEnC bulge into the capillary lumen and are aligned in parallel to form an ACJ (arrows in **F**). Between purple and green GEnCs, an intercellular junction is formed via their peripheral ridges (arrowheads in **F**). The peripheral and intersieve ridges were represented by whitish-purple. **(G)** The basal surface of these cytoplasmic ridges is smooth. **(F′,G′)** To show the location of the ACJ more clearly, a part of the purple GEnC is displayed on the right in blue. Arrows, ACJ; arrowheads, ICJ. ISR, intersieve ridge; PR, peripheral ridge; SP, sieve plate. Scale bar, 5 μm in **(A,C,D)**; 2 μm in **(G)**; and 100 nm in **(E)**. The reconstructed image of GEnCs **(F,G)** is also shown in **Supplementary Movie 4**.

in the reconstructed GEnCs (**Figures 3–5** and **Supplementary Movies 1–6**), although only the luminal surface structures could be observed by conventional SEM (**Figure 1B**). The luminal surface visualized based on the reconstructed GEnCs was quite similar to that observed by conventional SEM (**Figures 1B**, **3C**, **4F**), indicating that 3D reconstruction could be performed with high accuracy.

Urinary Region

The urinary regions of GEnCs were highly attenuated and fenestrated (**Figures 3A,C** and **Supplementary Movies 1, 2**). The basal surface of the urinary region was smooth since it adhered to the distended, smooth GBM (**Figure 3A** and **Supplementary Movie 1**). The urinary region was subdivided into sieve plates and cytoplasmic ridges. The sieve plates exhibited numerous dense

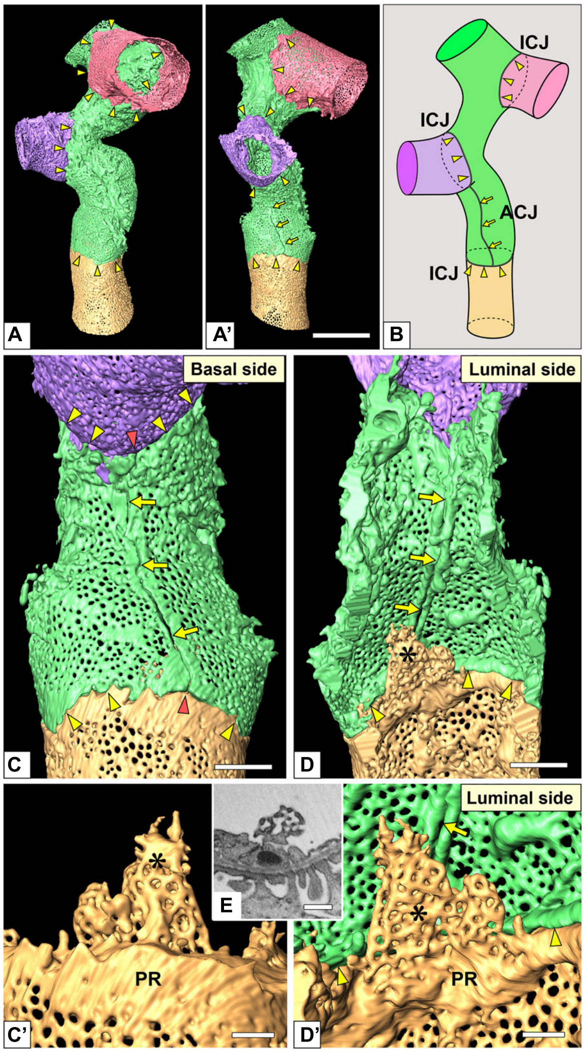

FIGURE 5 | Intercellular junction and autocellular junction (ACJ) of glomerular endothelial cells (GEnCs). **(A)** Reconstruction of a branching capillary formed by four GEnCs (purple, green, red, and yellow). **(A′)** View of the capillary shown in **(A)** from a different angle. **(B)** The location of cellular junctions in this capillary. The green GEnC forms an ACJ, which is along the longitudinal axis of the capillary. ICJ, intercellular junction between adjacent GEnCs. The basal **(C)** and luminal **(D)** surfaces of the urinary region. Two peripheral cytoplasmic ridges of the green GEnC are aligned in parallel to form an ACJ (arrows). The ACJ meets the ICJ to create "inverted T-shaped" seams (red arrowheads). Yellow arrowheads, ICJs between green and yellow GEnCs. **(C′,D′)** Magnified image of a reticular porous structure formed on the peripheral ridge (PR) of the yellow GEnC. **(C′)** The green GEnC is removed from **(C)**. **(E)** Focused-ion beam-scanning electron microscopy (FIB-SEM) image of the reticular porous structure shown in **(C′,D′)**. Asterisks, reticular porous structure. Scale bar, 10 μm in **(A′)**; 2 μm in **(C,D)**; 100 nm in **(C′,D′,E)**. The reconstructed images of GEnCs **(A,A′,C,D)** are also shown in **Supplementary Movies 5, 6**.

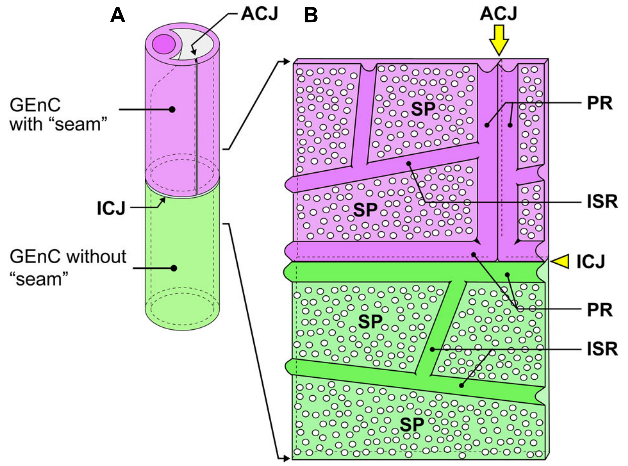

FIGURE 6 | Schematic diagram of the cytoplasmic ridges and cellular junctions in the urinary region. **(A)** A green glomerular endothelial cell (GEnC) forms a capillary tube without an autocellular tight junction. This type of capillary is the so-called "seamless capillary"; a purple GEnC makes an autocellular junction (ACJ) to form a capillary tube. The ACJ is usually along the longitudinal axis of the capillary. Two GEnCs are connected by an intercellular junction (ICJ), which is usually aligned perpendicularly to the longitudinal axis of the capillary. **(B)** Luminal view of the adhering region between purple and green GEnCs. The capillary tube shown in **(A)** is cut lengthwise and unfolded. The peripheral ridge (PR) forms the cell periphery of GEnCs; thus, two PRs of adjacent GEnCs are parallel. The intersieve ridge (ISR) is between the sieve plates (SPs), which are highly attenuated and fenestrated.

fenestrae (**Figures 3C**, **4G** and **Supplementary Movies 2, 4**), and the cytoplasmic ridges were formed between the sieve plates (as intersieve ridges; asterisks in **Figures 3C**, **4G**). The cytoplasmic ridges were also formed along the cell margin (as a peripheral ridge; arrowheads in **Figures 4F,F′**, **5D** and **Supplementary Movie 4**), and the GEnCs connected at their peripheral ridges via a tight junction (**Figures 4C–E, 6B**); thus, the two peripheral ridges ran parallel to each other (the cellular junctions of GEnCs will be described in detail later). The intersieve ridges usually continued to the peripheral ridge (**Figure 6B**) and cell body (**Figure 7F**). The reticular porous structures were frequently found on the cytoplasmic ridges, especially on the peripheral ridges (asterisks in **Figures 5C′,D,D′**).

Juxtamesangial Region

The juxtamesangial region was less fenestrated (**Figures 3B,D** and **Supplementary Movies 1, 3**). This region consisted of the cell body (**Figures 7B,D** and **Supplementary Movie 7**) and thick cytoplasmic ridges, referred to as juxtamesangial ridges (asterisks in **Figure 3D** and **Supplementary Movie 3**). The reticular porous structures were frequently found on the luminal surfaces of the cell bodies (arrowheads in **Figures 7C–E,E′**) and the juxtamesangial ridges (arrowheads in **Figures 3D,D′**). Moreover, in some GEnCs, globular protrusions were also found on the luminal surface of the cell bodies (asterisks in **Figures 7A,A′,D,E** and **Supplementary Movie 7**). The spatial arrangement of subcellular compartments was thus revealed in GEnCs (as summarized in **Figure 8**).

On the basal surface of the juxtamesangial region, indentations created by mesangial cell processes were frequently recognized (arrows in **Figures 3B**, **7B**, **9G**; arrowheads in **Figure 9H′**). Mesangial cells showed the extension of numerous

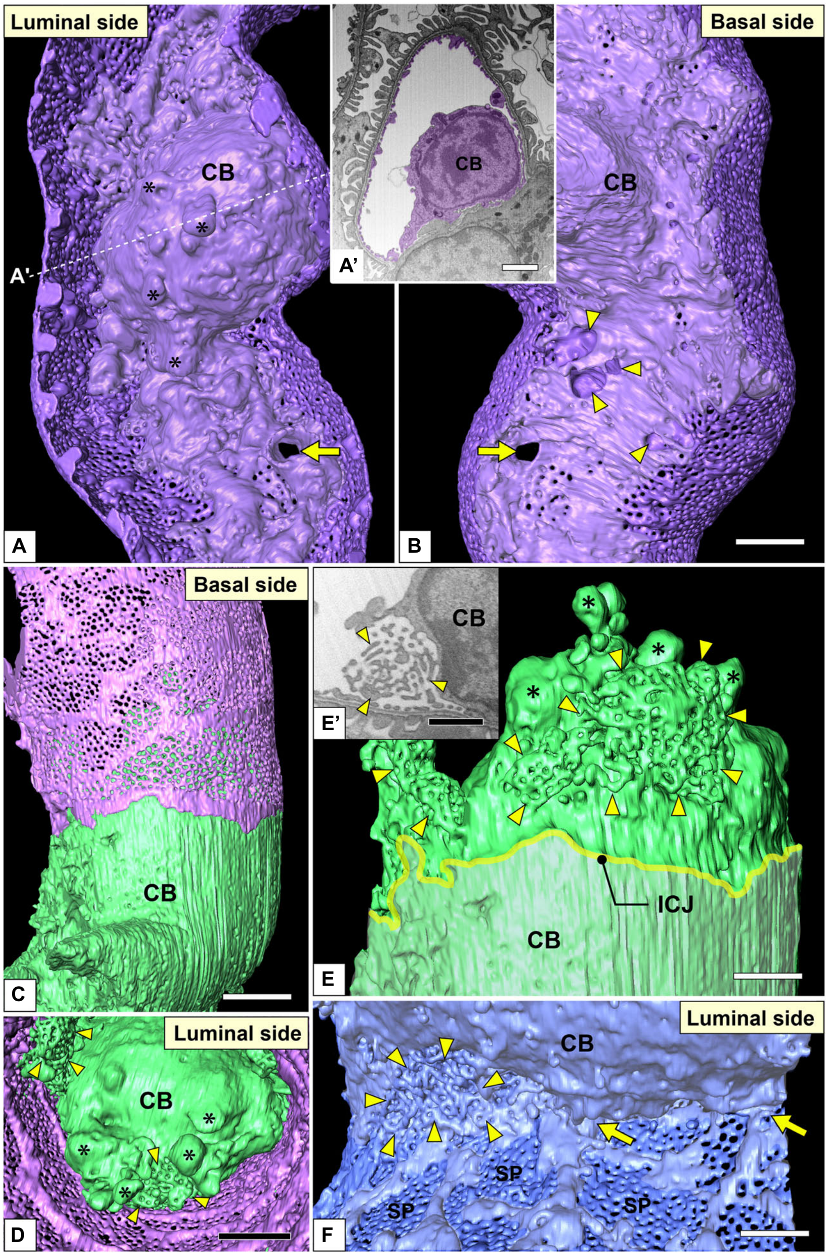

FIGURE 7 | Juxtamesangial region and cell bodies of glomerular endothelial cells (GEnCs). Luminal **(A)** and basal **(B)** views of the same juxtamesangial region. The globular protrusions (asterisks) are found on the luminal surface of the cell body. The non-adhesive mesangial cell processes create the perforation (arrow) and indentations (arrowheads) at the juxtamesangial region. **(A′)** The sectional focused-ion beam-scanning electron microscopy (FIB-SEM) image at the dotted line in **(A)**. **(C–E)** Cell body of the green GEnC. This cell body possesses reticular porous structures (arrowheads in **D,E**), in addition to globular protrusions (asterisks in **D,E**), on the luminal surface. **(E)** The purple GEnC is removed from **(C)** to show the luminal surface of the green GEnC. **(E′)** FIB-SEM image of the reticular porous structure shown in **(E)**. **(F)** Luminal view of the connecting part of urinary and juxtamesangial regions. The intersieve ridges continue the cell body (arrows), and the reticular porous structure (arrowheads) exists at the angle between urinary and juxtamesangial regions. ICJ, intercellular junction between green and purple GEnCs; CB, cell body of GEnC; SP, sieve plate. Scale bar, 5 μm in **(A′,B,D)**; 2 μm in **(E,F)**; 100 nm in **(E′)**. The reconstructed image of GEnC **(A,B)** is also shown in **Supplementary Movie 7**.

cytoplasmic processes, which were classified into two groups, adhesive and non-adhesive. The adhesive processes adhered to the GBM at their tips (red and yellow arrowheads in **Figures 9A,A′**); the non-adhesive processes extend toward the juxtamesangial regions of GEnCs (arrows in **Figures 9A,A′**).

Most of the adhesive processes were tiny spines based on their shapes (red arrowheads in **Figures 9A′,D–H** and **Supplementary Movie 8**). Some of the adhesive processes exhibited large, tongue-like shapes and were inserted into the narrow angle between the GEnC and GBM (yellow arrowheads

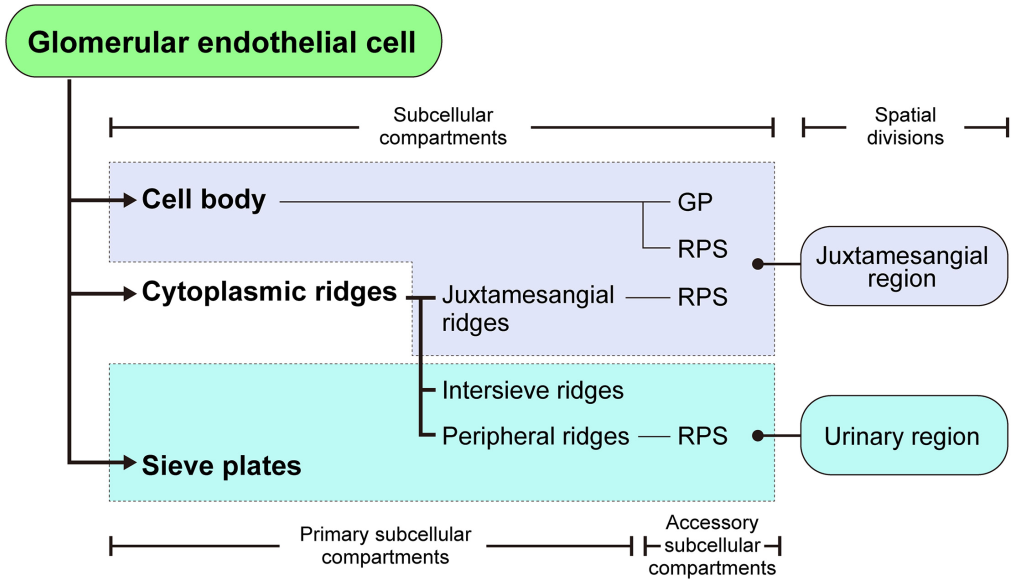

FIGURE 8 | Structural hierarchy of the subcellular compartments in a glomerular endothelial cell (GEnC). The reticular porous structures (RPSs) are formed on the cell body, juxtamesangial ridges, and peripheral ridges, with the globular protrusions (GPs) on the cell body.

in **Figures 9A,E,H**). The indentations created by the tongue-like processes were found on the basal surface of the juxtaglomerular region (yellow arrowheads in **Figure 9H′**).

The non-adhesive processes protruded toward the basal surface of the cell body and juxtamesangial ridges to make deep indentations on them (arrows in **Figures 3B**, **7B**, **9G** and **Supplementary Movie 8**). Some non-adhesive processes penetrated the juxtamesangial ridges to enter the capillary lumen (arrows in **Figures 9A–C,F,F′**). These penetrating non-adhesive processes were irregularly enlarged in the capillary lumen.

Cellular Junctions

Most of the individual GEnCs (20 of total 24 reconstructed GEnCs) were recognized to form a tubular shape, except for four GEnCs. In 17 of the 20 total tubular GEnCs, the individual GEnCs formed a tubular shape without a seam—such endothelial cell types are referred as "seamless endothelial cells" (green cell in **Figure 6A**; Wolff and Bär, 1972; Bär et al., 1984). The adjacent seamless GEnCs were connected in an end-to-end manner via the intercellular junction, structurally regarded as a tight junction. The intercellular junctions between GEnCs were generally aligned circumferentially to the longitudinal axis of the glomerular capillary (**Figures 5A,A′,B** and **Supplementary Movie 5**). At the bifurcation area of the glomerular capillary, two tubular GEnCs were typically connected in an end-to-side manner (**Figures 5A,A′**).

Three of the 20 total tubular GEnCs formed a tubular shape by forming an autocellular junction (purple cell in **Figure 6A**), which was structurally regarded as a tight junction similar to the intercellular junction (arrow in **Figure 5E**). These autocellular junctions were generally along the longitudinal axis of the capillary (arrows in **Figures 4**, **5**). They continued to the circumferential intercellular junction to form a "T-shaped" seam (red arrowheads in **Figure 5C**).

DISCUSSION

Benefits of FIB-SEM Tomography for Structural Analysis of GEnCs

The 3D ultrastructures observed on the reconstructed GEnCs based on serial FIB-SEM images could be confirmed via conventional SEM images, indicating that the reconstructed images have high accuracy. This highly accurate visibility of the 3D ultrastructures is one of the most important benefits of this approach. Conventional SEM is useful for revealing the luminal surface structures of GEnCs; however, it is almost impossible to observe their basal surface structures because the basal surface is attached to the GBM or mesangium and is difficult to expose. The 3D reconstruction ultimately resolved this problem by enabling the observation of surface structures from any direction and without interference by the neighboring GBM, mesangium, and podocytes. Furthermore, the color-coded reconstructed images are also helpful in determining the spatial relationship between GEnCs and mesangial cells, for example, the arrangement of GEnC intercellular and autocellular junctions and the penetration of mesangial non-adhesive processes into the glomerular capillary lumen.

Definition and Structural Hierarchy of Subcellular Compartments in GEnCs

The 3D reconstruction of GEnCs is also helpful in determining the structural hierarchy of their subcellular compartments (as summarized in **Figure 8**). The GEnCs were largely divided

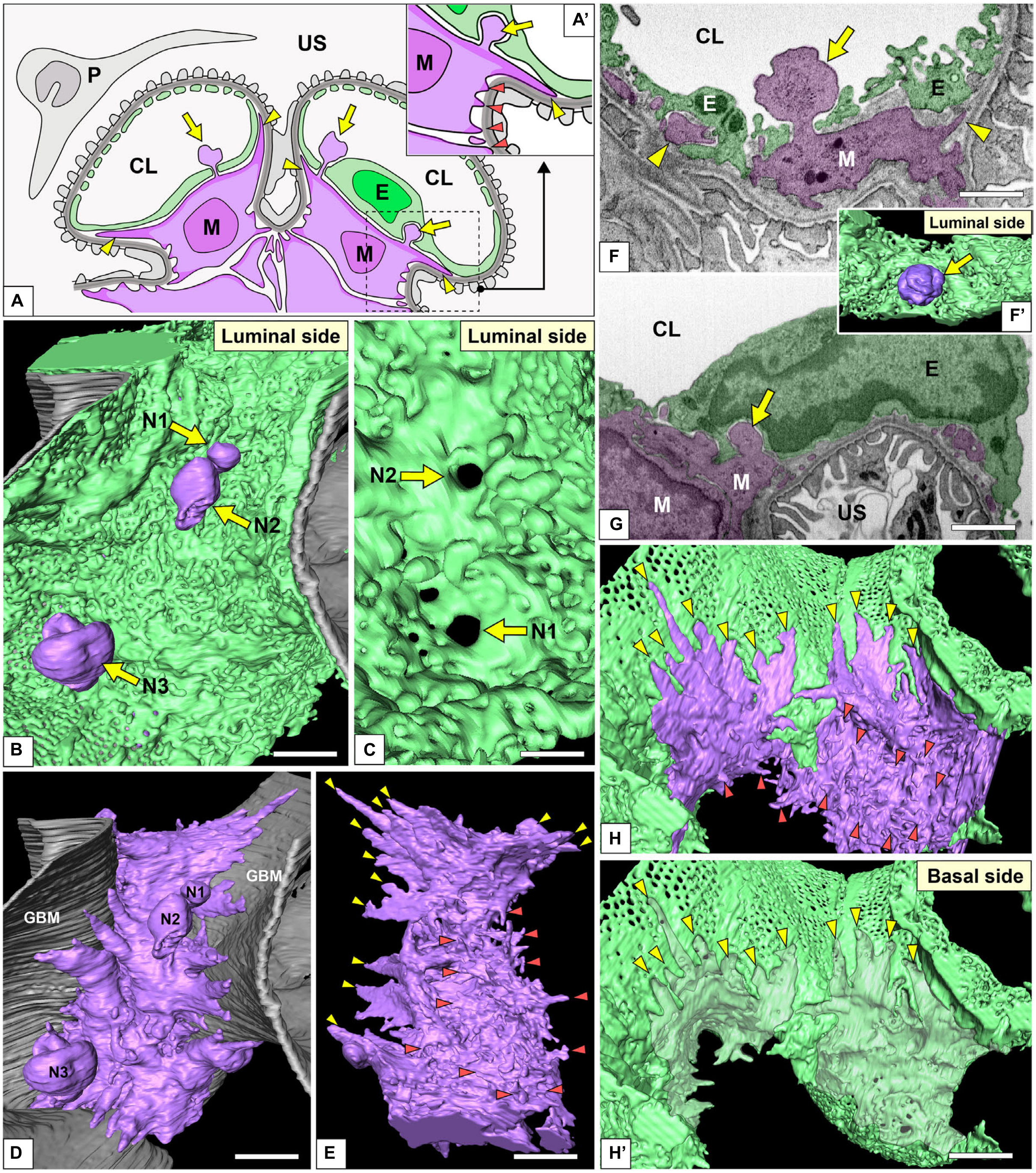

FIGURE 9 | Spatial relationship among glomerular endothelial cells (GEnCs) and mesangial cells. **(A,A′)** Schematic diagram showing the two-dimensional geometry of GEnCs (green, E), mesangial cells (purple, M), podocytes (gray, P), and the glomerular basement membrane (GBM). The non-adhesive mesangial cell processes (arrows) protrude toward the juxtamesangial region of the GEnC to form the indentation or penetrate it into the capillary lumen. Most of the adhesive mesangial cell processes are spiny cytoplasmic processes and adhere to the GBM at their tips (orange arrowheads in **A′**). Some adhesive mesangial cell processes exhibit large, tongue-like shapes and are inserted into the narrow angle between the GEnC and GBM (yellow arrowheads in **A,A′**). **(B)** Luminal view of three non-adhesive mesangial cell processes (purple, N1–N3) penetrating the green GEnC. Gray layer, GBM. **(C)** The large holes of GEnCs (arrows) for the penetration of mesangial cell processes, N1 and N2. **(D)** The spatial relationship between the mesangial cell and GBM. The green GEnC shown in **(B)** is removed to reveal the mesangial cell processes. **(E)** The mesangial cells shown in **(D)** are rotated 180° to show the spiny mesangial cell processes (orange arrowheads). Some of them develop tongue-like projections (yellow arrowheads). **(F,G)** Focused-ion beam-scanning electron microscopy (FIB-SEM) images of adhesive (arrowheads) and non-adhesive mesangial cell processes (arrows). **(F′)** Three-dimensional reconstruction of the non-adhesive process shown in **(F)**. **(H,H′)** The impression created by the tongue-like processes against the basal surface of the juxtaglomerular region (yellow arrowheads in **H′**). CL, capillary lumen; US, urinary space. Scale bar, 2 μm in **(B,D,E,H′)**; 200 nm in **(C,F,G)**. The reconstructed image of GEnC and mesangial cell **(B,E)** is also shown in **Supplementary Movie 8**.

into three kinds of primary subcellular compartment: cell body, cytoplasmic ridge, and sieve plate. The cell body contains a nucleus and bulged toward the capillary lumen. The cytoplasmic ridges form a net that exhibits coarse and irregular-shaped meshes around the cell body. The sieve plates, which are surrounded by the cytoplasmic ridges, are highly fenestrated regions for glomerular filtration. Based on the location of the presence, the cytoplasmic ridges are further divided into the juxtamesangial, intersieve, and peripheral ridges. In addition to these primary subcellular compartments, two accessory subcellular compartments, the reticular porous structure and globular protrusion, are frequently associated with the cell body and cytoplasmic ridges.

Characteristics of Cellular Junctions in GEnCs

Individual GEnCs generally make up the entire circumference of a capillary tube. Most of the individual GEnCs form a capillary tube without an autocellular junction (green GEnC in **Figure 6A**)—such endothelial cells have been called "seamless endothelial cells" (Wolff and Bär, 1972; Bär et al., 1984). Some GEnCs formed an autocellular junction to form a capillary tube (purple GEnC in **Figure 6A**). During the developmental remodeling of the capillary system in zebrafish larvae, the endothelial cells lose their autocellular junction to self-fuse and transform into a seamless endothelial cell (Lenard et al., 2015). Thus, the seamless GEnC is likely formed from the GEnC with an autocellular junction via self-fusion. However, to understand the developmental process of seamless GEnCs, it is necessary to analyze the developing glomerular capillaries in perinatal animals.

Relationship Between GEnCs and Mesangial Cells

A higher blood pressure (approximately 50 mm Hg) is loaded in the glomerular capillary, which is a driving force of glomerular ultrafiltration. To protect the glomerular structure against its higher intracapillary pressure, several mechanical protectors are supported in both the vascular and epithelial compartments (Ichimura et al., 2007; Ichimura and Sakai, 2017). Mesangial cells, mechanical protectors, adhere to the internal surface of the GBM through their adhesive processes and pull centripetally to prevent overextension of the epithelial component (Sakai and Kriz, 1987; Drenckhahn et al., 1990).

Farquhar and Palade (1962) previously reported the mesangial cell processes entering the capillary lumen, which corresponded to the non-adhesive processes presented in this study. The phenomenon that mesangial cell processes penetrate GEnCs has not been examined beyond this study. The non-adhesive mesangial cell processes were prominently enlarged at the end; thus, they were frequently found in the sectional FIB-SEM images as cytoplasmic masses. However, it is difficult to determine whether such cytoplasmic masses are derived from mesangial cells through conventional SEM and TEM, because the penetrating part of the mesangial cell is thin. This is the reason why research on this phenomenon has not proceeded. The functions of the non-adhesive processes of mesangial cells are unknown at this time, although Farquhar and Palade (1962) speculated that these mesangial cell processes serve as a sensor for the capillary lumen environment.

Further Adaptation of FIB-SEM Tomography to GEnC Research

Focused-ion beam-SEM tomography with a 3D reconstruction technique is a powerful approach used in our previous podocyte research (Ichimura et al., 2015, 2017, 2019; Kawasaki et al., 2019; Miyaki et al., 2020c). In the present study, we clearly visualized the 3D cytoarchitecture of normal GEnCs in adult rats. However, as in podocytes, this approach should help in the 3D ultrastructural analysis of GEnCs under developmental and pathological conditions.

The development of the glomerular capillary system starts from the S-shaped body stage of glomerulogenesis (Reeves et al., 1978; Ichimura et al., 2003). The growth process of the glomerular capillary system is considered to be mediated by two types of angiogenesis processes, namely, sprouting angiogenesis and intussusceptive angiogenesis. In the sprouting process, the newly formed capillary is branched from the existing capillary; in the intussusceptive process, the existing capillary is split into two daughter capillaries (Patan et al., 1992; Djonov et al., 2000; Burri et al., 2004). However, it remains unknown as to which of the two angiogenesis processes is used to develop the glomerular capillary system. Our group is currently evaluating the morphological development of the glomerular capillary system using FIB-SEM tomography and 3D reconstruction techniques and will soon report our results.

Limitations of 3D Ultrastructural Analysis Using FIB-SEM Tomography

Focused-ion beam-SEM tomography could precisely reveal the 3D architecture of GEnCs; however, there are several technical disadvantages to this approach. First, image acquisition is limited to a relatively small volume in FIB-SEM tomography; thus, it is quite challenging to obtain the total volume of a glomerulus at a high resolution to evaluate the delicate structures of GEnCs. Owing to this problem, it was impossible to analyze the entire architecture of the glomerular capillary system. Array tomography is a solution to this problem. It has been used to obtain serial images from serial ultrathin sections made by a diamond knife with specimens mounted on a base substrate, such as silicon warfare or a glass plate (Micheva and Smith, 2007; Dittmayer et al., 2018). The serial ultrathin sections on the base substrate are physically stable and repeatedly observable by SEM. Terasaki et al. (2020) visualized the 3D architecture of a normal glomerular capillary system by array tomography using an ATUMtome, which automatically collects serial ultrathin sections on a tape base (Hayworth et al., 2014). This method will be useful for evaluating 3D pathologic alterations of the glomerular capillary system, such as the hilar neovascularization in diabetic nephropathy (Min and Yamanaka, 1993; Osterby et al., 1999) and the reorganization of the capillary system in mesangioproliferative glomerulonephritis (Kriz et al., 2003; Notoya et al., 2003; Ichimura et al., 2006).

CONCLUSION

Focused-ion beam-SEM tomography was able to clearly visualize the 3D architecture of normal GEnCs. The morphological information revealed in this study will be valuable for 3D pathologic analyses of GEnCs in animal and human glomerular diseases.

DATA AVAILABILITY STATEMENT

The raw data supporting the conclusions of this article will be made available by the authors, without undue reservation.

ETHICS STATEMENT

The animal study was reviewed and approved by the Institutional Animal Care and Use Committee of Juntendo University School of Medicine (approval no. 2020104).

AUTHOR CONTRIBUTIONS

KI designed the experiments, prepared the figures, and wrote the manuscript. YK, TM, JY, SK, and KI obtained serial FIB-SEM images. YK, YH, and KI performed 3D reconstruction. YK, YH, TS, and KI analyzed the experimental data. All authors contributed to the article and approved the submitted version.

FUNDING

This study was supported, in part, by a Grant-in-Aid for Scientific Research from the Ministry of Education, Culture, Sports, Science, and Technology of Japan (Grant Nos. 15K18960 and 17K08521 to KI).

SUPPLEMENTARY MATERIAL

The Supplementary Material for this article can be found online at: https://www.frontiersin.org/articles/10.3389/fcell.2021.653472/full#supplementary-material

REFERENCES

Bär, T., Guldner, F. H., and Wolff, J. R. (1984). "Seamless" endothelial cells of blood capillaries. *Cell Tissue Res.* 235, 99–106.

Burri, P. H., Hlushchuk, R., and Djonov, V. (2004). Intussusceptive angiogenesis: its emergence, its characteristics, and its significance. *Dev. Dyn.* 231, 474–488. doi: 10.1002/dvdy.20184

Dittmayer, C., Volcker, E., Wacker, I., Schroder, R. R., and Bachmann, S. (2018). Modern field emission scanning electron microscopy provides new perspectives for imaging kidney ultrastructure. *Kidney Int.* 94, 625–631. doi: 10.1016/j.kint.2018.05.017

Djonov, V., Schmid, M., Tschanz, S. A., and Burri, P. H. (2000). Intussusceptive angiogenesis: its role in embryonic vascular network formation. *Circ. Res.* 86, 286–292. doi: 10.1161/01.res.86.3.286

Dong, H. M., Ichimura, K., and Sakai, T. (2010). Structural organization of hepatic portal vein in rat with special reference to musculature, intimal folds, and endothelial cell alignment. *Anat. Rec. (Hoboken)* 293, 1887–1895. doi: 10.1002/ar.21246

Drenckhahn, D., Schnittler, H., Nobiling, R., and Kriz, W. (1990). Ultrastructural organization of contractile proteins in rat glomerular mesangial cells. *Am. J. Pathol.* 137, 1343–1351.

Farquhar, M. G., and Palade, G. E. (1962). Functional evidence for the existence of a third cell type in the renal glomerulus: phagocytosis of filtration residues by a distinctive "third" cell. *J. Cell Biol.* 13, 55–87. doi: 10.1083/jcb.13.1.55

Hayworth, K. J., Morgan, J. L., Schalek, R., Berger, D. R., Hildebrand, D. G., and Lichtman, J. W. (2014). Imaging ATUM ultrathin section libraries with WaferMapper: a multi-scale approach to EM reconstruction of neural circuits. *Front. Neural Circuits* 8:68. doi: 10.3389/fncir.2014.00068

Ichimura, K., Kakuta, S., Kawasaki, Y., Miyaki, T., Nonami, T., Miyazaki, N., et al. (2017). Morphological process of podocyte development revealed by block-face scanning electron microscopy. *J. Cell Sci.* 130, 132–142. doi: 10.1242/jcs.187815

Ichimura, K., Kurihara, H., and Sakai, T. (2003). Actin filament organization of foot processes in rat podocytes. *J. Histochem. Cytochem.* 51, 1589–1600. doi: 10.1177/002215540305101203

Ichimura, K., Kurihara, H., and Sakai, T. (2006). Involvement of mesangial cells expressing alpha-smooth muscle actin during restorative glomerular remodeling in Thy-1.1 nephritis. *J. Histochem. Cytochem.* 54, 1291–1301. doi: 10.1369/jhc.6a7000.2006

Ichimura, K., Kurihara, H., and Sakai, T. (2007). Actin filament organization of foot processes in vertebrate glomerular podocytes. *Cell Tissue Res.* 329, 541–557. doi: 10.1007/s00441-007-0440-4

Ichimura, K., Kurihara, H., and Sakai, T. (2009). Beta-cytoplasmic actin localization in vertebrate glomerular podocytes. *Arch. Histol. Cytol.* 72, 165–174. doi: 10.1679/aohc.72.165

Ichimura, K., Kurihara, H., and Sakai, T. (2010). Primary cilia disappear in rat podocytes during glomerular development. *Cell Tissue Res.* 341, 197–209. doi: 10.1007/s00441-010-0983-7

Ichimura, K., Miyaki, T., Kawasaki, Y., Kinoshita, M., Kakuta, S., and Sakai, T. (2019). Morphological processes of foot process effacement in puromycin aminonucleoside nephrosis revealed by FIB/SEM tomography. *J. Am. Soc. Nephrol.* 30, 96–108. doi: 10.1681/asn.2018020139

Ichimura, K., Miyazaki, N., Sadayama, S., Murata, K., Koike, M., Nakamura, K. I., et al. (2015). Three-dimensional architecture of podocytes revealed by block-face scanning electron microscopy. *Sci. Rep.* 5:8993.

Ichimura, K., and Sakai, T. (2017). Evolutionary morphology of podocytes and primary urine-producing apparatus. *Anat. Sci. Int.* 92, 161–172. doi: 10.1007/s12565-015-0317-7

Ichimura, K., Stan, R. V., Kurihara, H., and Sakai, T. (2008). Glomerular endothelial cells form diaphragms during development and pathologic conditions. *J. Am. Soc. Nephrol.* 19, 1463–1471. doi: 10.1681/asn.2007101138

Kawasaki, Y., Matsumoto, A., Miyaki, T., Kinoshita, M., Kakuta, S., Sakai, T., et al. (2019). Three-dimensional architecture of pericardial nephrocytes in *Drosophila melanogaster* revealed by FIB/SEM tomography. *Cell Tissue Res* 378, 289–300. doi: 10.1007/s00441-019-03037-3

Kriz, W., Hahnel, B., Hosser, H., Ostendorf, T., Gaertner, S., Kränzlin, B., et al. (2003). Pathways to recovery and loss of nephrons in anti-Thy-1 nephritis. *J. Am. Soc. Nephrol.* 14, 1904–1926. doi: 10.1097/01.asn.0000070073.79690.57

Kriz, W., and Kaissling, B. (2000). "Structural organization of the mammalian kidney," in *The Kidney, Physiology and Pathophysiology*, eds D. W. Seldin and G. Giebisch (Philadelphia, PA: Lippincott Williams & Wilkins), 587–654.

Kubota, Y. (2015). New developments in electron microscopy for serial image acquisition of neuronal profiles. *Microscopy (Oxf)* 64, 27–36. doi: 10.1093/jmicro/dfu111

Lenard, A., Daetwyler, S., Betz, C., Ellertsdottir, E., Belting, H. G., Huisken, J., et al. (2015). Endothelial cell self-fusion during vascular pruning. *PLoS Biol* 13:e1002126. doi: 10.1371/journal.pbio.1002126

Maul, G. G. (1971). Structure and formation of pores in fenestrated capillaries. *J. Ultrastruct. Res.* 36, 768–782. doi: 10.1016/S0022-5320(71)90030-X

Micheva, K. D., and Smith, S. J. (2007). Array tomography: a new tool for imaging the molecular architecture and ultrastructure of neural circuits. *Neuron* 55, 25–36. doi: 10.1016/j.neuron.2007.06.014

Min, W., and Yamanaka, N. (1993). Three-dimensional analysis of increased vasculature around the glomerular vascular pole in diabetic nephropathy. *Virchows Arch. A Pathol. Anat. Histopathol.* 423, 201–207. doi: 10.1007/BF01614771

Miyaki, T., Kawasaki, Y., Hosoyamada, Y., Amari, T., Kinoshita, M., Matsuda, H., et al. (2020a). Three-dimensional imaging of podocyte ultrastructure using FE-SEM and FIB-SEM tomography. *Cell Tissue Res.* 379, 245–254. doi: 10.1007/s00441-019-03118-3

Miyaki, T., Kawasaki, Y., Hosoyamada, Y., Amari, T., Kinoshita, M., Matsuda, H., et al. (2020b). Volume scanning electron microscopy for 3D imaging of biological ultrastructure. *Juntendo Med. J.* 66, 108–119. doi: 10.14789/jmj.2020.66.JMJ19-R19

Miyaki, T., Kawasaki, Y., Matsumoto, A., Kakuta, S., Sakai, T., and Ichimura, K. (2020c). Nephrocytes are part of the spectrum of filtration epithelial diversity. *Cell Tissue Res.* 382, 609–625. doi: 10.1007/s00441-020-03313-7

Nagai, M., Saitoh, S., Takaki, T., Ohbayashi, T., Hotta, O., Ohno, N., et al. (2020). Glomerular cellular interactions following disruption of the glomerular basement membrane in IgA nephropathy: ultrastructural analyses by 3-dimensional serial block-face scanning electron microscopy. *Kidney Med.* 2, 222–225. doi: 10.1016/j.xkme.2019.11.003

Notoya, M., Shinosaki, T., Kobayashi, T., Sakai, T., and Kurihara, H. (2003). Intussusceptive capillary growth is required for glomerular repair in rat Thy-1.1 nephritis. *Kidney Int.* 63, 1365–1373. doi: 10.1046/j.1523-1755.2003.00876.x

Ohno, N., Katoh, M., Saitoh, Y., Saitoh, S., and Ohno, S. (2015). Three-dimensional volume imaging with electron microscopy toward connectome. *Microscopy (Oxf)* 64, 17–26. doi: 10.1093/jmicro/dfu112

Osterby, R., Asplund, J., Bangstad, H. J., Nyberg, G., Rudberg, S., Viberti, G. C., et al. (1999). Neovascularization at the vascular pole region in diabetic glomerulopathy. *Nephrol. Dial. Transplant.* 14, 348–352. doi: 10.1093/ndt/14.2.348

Patan, S., Alvarez, M. J., Schittny, J. C., and Burri, P. H. (1992). Intussusceptive microvascular growth: a common alternative to capillary sprouting. *Arch. Histol. Cytol.* 55 Suppl, 65–75. doi: 10.1679/aohc.55.Suppl_65

Pease, D. C. (1955). Electron microscopy of the vascular bed of the kidney cortex. *Anat. Rec.* 121, 701–721. doi: 10.1002/ar.1091210402

Reeves, W., Caulfield, J. P., and Farquhar, M. G. (1978). Differentiation of epithelial foot processes and filtration slits: sequential appearance of occluding junctions, epithelial polyanion, and slit membranes in developing glomeruli. *Lab. Invest.* 39, 90–100.

Reeves, W. H., Kanwar, Y. S., and Farquhar, M. G. (1980). Assembly of the glomerular filtration surface. Differentiation of anionic sites in glomerular capillaries of newborn rat kidney. *J. Cell Biol.* 85, 735–753. doi: 10.1083/jcb.85.3.735

Roberts, W. G., and Palade, G. E. (2000). "Endothelial fenestrae and fenestral diaphragms," in *Morphogenesis of Endothelium*, eds W. Risau and G. M. Rubanyi (Amsterdam: Harwood Academic Publishers), 23–42.

Sakai, T., and Kriz, W. (1987). The structural relationship between mesangial cells and basement membrane of the renal glomerulus. *Anat. Embryol. (Berl)* 176, 373–386. doi: 10.1007/BF00310191

Simionescu, M. (2000). "Structural, biochemical and functional differentiation of the vascular endothelium," in *Morphogenesis of Endothelium*, eds W. Risau and G. M. Rubanyi (Amsterdam: Harwood Academic Publishers), 1–22.

Simionescu, N. (1983). Cellular aspects of transcapillary exchange. *Physiol. Rev.* 63, 1536–1579. doi: 10.1152/physrev.1983.63.4.1536

Stan, R. V., Ghitescu, L., Jacobson, B. S., and Palade, G. E. (1999a). Isolation, cloning, and localization of rat PV-1, a novel endothelial caveolar protein. *J. Cell Biol.* 145, 1189–1198. doi: 10.1083/jcb.145.6.1189

Stan, R. V., Kubitza, M., and Palade, G. E. (1999b). PV-1 is a component of the fenestral and stomatal diaphragms in fenestrated endothelia. *Proc. Natl. Acad. Sci. U.S.A.* 96, 13203–13207. doi: 10.1073/pnas.96.23.13203

Stan, R. V., Tkachenko, E., and Niesman, I. R. (2004). PV1 is a key structural component for the formation of the stomatal and fenestral diaphragms. *Mol. Biol. Cell* 15, 3615–3630. doi: 10.1091/mbc.e03-08-0593

Takaki, T., Ohno, N., Saitoh, S., Nagai, M., and Joh, K. (2019). Podocyte penetration of the glomerular basement membrane to contact on the mesangial cell at the lesion of mesangial interposition in lupus nephritis: a three-dimensional analysis by serial block-face scanning electron microscopy. *Clin. Exp. Nephrol.* 23, 773–781. doi: 10.1007/s10157-019-01701-0

Terasaki, M., Brunson, J. C., and Sardi, J. (2020). Analysis of the three dimensional structure of the kidney glomerulus capillary network. *Sci. Rep.* 10:20334. doi: 10.1038/s41598-020-77211-x

Titze, B., and Genoud, C. (2016). Volume scanning electron microscopy for imaging biological ultrastructure. *Biol. Cell* 108, 307–323. doi: 10.1111/boc.201600024

Wolff, J. R., and Bär, T. (1972). 'Seamless' endothelia in brain capillaries during development of the rat's cerebral cortex. *Brain Res.* 41, 17–24. doi: 10.1016/0006-8993(72)90613-0

Conflict of Interest: The authors declare that the research was conducted in the absence of any commercial or financial relationships that could be construed as a potential conflict of interest.

frontiers
in Cell and Developmental Biology

ORIGINAL RESEARCH
published: 16 April 2021
doi: 10.3389/fcell.2021.632381

Two-Phase Lineage Specification of Telencephalon Progenitors Generated From Mouse Embryonic Stem Cells

Makoto Nasu[1], Shigeyuki Esumi[2], Jun Hatakeyama[3], Nobuaki Tamamaki[4] and Kenji Shimamura[3]*

[1] Department of Health Sciences, Faculty of Life Sciences, Kumamoto University, Kumamoto, Japan, [2] Department of Anatomy and Neurobiology, Graduate School of Medical Sciences, Kumamoto University, Kumamoto, Japan, [3] Department of Brain Morphogenesis, Institute of Molecular Embryology and Genetics, Kumamoto University, Kumamoto, Japan, [4] Department of Morphological Neural Science, Graduate School of Medical Sciences, Kumamoto University, Kumamoto, Japan

Proper brain development requires precisely controlled phases of stem cell proliferation, lineage specification, differentiation, and migration. Lineage specification depends partly on concentration gradients of chemical cues called morphogens. However, the rostral brain (telencephalon) expands prominently during embryonic development, dynamically altering local morphogen concentrations, and telencephalic subregional properties develop with a time lag. Here, we investigated how progenitor specification occurs under these spatiotemporally changing conditions using a three-dimensional *in vitro* differentiation model. We verified the critical contributions of three signaling factors for the lineage specification of subregional tissues in the telencephalon, ventralizing sonic hedgehog (Shh) and dorsalizing bone morphogenetic proteins (BMPs) and WNT proteins (WNTs). We observed that a short-lasting signal is sufficient to induce subregional progenitors and that the timing of signal exposure for efficient induction is specific to each lineage. Furthermore, early and late progenitors possess different Shh signal response capacities. This study reveals a novel developmental mechanism for telencephalon patterning that relies on the interplay of dose- and time-dependent signaling, including a time lag for specification and a temporal shift in cellular Shh sensitivity. This delayed fate choice through two-phase specification allows tissues with marked size expansion, such as the telencephalon, to compensate for the changing dynamics of morphogen signals.

Keywords: telencephalon, patterning, D–V axis, progenitor specification, mouse ES cells

Edited by:
Maurizio Zuccotti,
University of Pavia, Italy

Reviewed by:
Edwin S. Monuki,
University of California, Irvine,
United States
Masayuki Kobayashi,
Akita Prefectural University, Japan

****Correspondence:***
Makoto Nasu
mnas@kumamoto-u.ac.jp

Specialty section:
This article was submitted to
Cell Growth and Division,
a section of the journal
Frontiers in Cell and Developmental Biology

Received: *23 November 2020*
Accepted: *09 March 2021*
Published: *16 April 2021*

Citation:
Nasu M, Esumi S, Hatakeyama J, Tamamaki N and Shimamura K (2021) Two-Phase Lineage Specification of Telencephalon Progenitors Generated From Mouse Embryonic Stem Cells.
Front. Cell Dev. Biol. 9:632381.
doi: 10.3389/fcell.2021.632381

INTRODUCTION

The telencephalon is the most elaborate structure of the mammalian brain and is responsible for higher mental functions, such as memory, speech, value judgments, and sociality. These neural functions are achieved by complex neural networks composed of cells with distinct lineages and origins within the telencephalon. The telencephalon is roughly divided into three subregions along its dorsal–ventral (D–V) axis: (i) the dorsal midline tissues, including the hem, which appears to be lost during development; (ii) the dorsal telencephalon (pallium), mainly producing glutamatergic neurons and ultimately forming the cerebral cortex, and (iii) the ventral telencephalon (subpallium), which includes the ganglionic eminence (GE) producing mainly GABAergic neurons and the preoptic area (POA) producing GABAergic as well as cholinergic neurons (Shimamura et al., 1995; Wilson and Rubenstein, 2000; Rallu et al., 2002a; Schuurmans and Guillemot, 2002; Imayoshi et al., 2008; Medina and Abellán, 2009). The cerebral cortex is composed of cells originating both internally and externally. The main external source is the ventrally adjoining GE (Tamamaki et al., 1997; Métin et al., 2006; Wonders and Anderson, 2006). The GE is further subdivided into three parts: the rostrally located lateral and medial ganglionic eminences (LGE and MGE) and the caudal ganglionic eminence (CGE).

The development of these subregions must be precisely coordinated to achieve proper telencephalic organization. It is generally believed that secreted signaling molecules or morphogens form concentration gradients according to the spatial distance from their sources and that progenitors attain distinct identities according to the local signal intensity, termed the French flag model (Wolpert, 1969). The morphogen sonic hedgehog (Shh) and bone morphogenetic proteins (BMPs) determine the fate of the ventral and dorsal telencephalon, respectively (Marín and Rubenstein, 2001; Rallu et al., 2002a). Loss of Shh signaling in the telencephalon of Foxg1-driven Smoothened (Smo) conditional mutants, where the expression of Shh signal transducer, Smo, is missing in the whole telencephalon because of the telencephalon-specific expression of Cre recombinase in the Foxg1 locus, results in complete loss of the ventral properties (Fuccillo et al., 2004). On the other hand, the dorsal midline tissues are regulated by BMPs to form the cortical hem and choroid plexus (Hébert et al., 2002; Subramanian and Tole, 2009). Wnt proteins (WNTs) are another dorsalizing factor. Conditional loss of beta-catenin, a key mediator of canonical WNT signaling, results in loss of the dorsal telencephalon and expansion of the ventral telencephalon (Backman et al., 2005).

Recently, temporal patterning cues, in addition to spatial cues, have been recognized as critical for neural specification (Ribes and Briscoe, 2009; Rogers and Schier, 2011; Sagner and Briscoe, 2017). Patterning mechanisms may require signal dose dependence, time dependence, or both. Several *in vivo* studies have demonstrated that certain telencephalic subregional properties develop with a time lag. The expression of Nkx2-1, a marker for MGE/POA progenitors, is detected before that of Gsx2, a marker for LGE/CGE progenitors, in the ventral telencephalon. Moreover, swelling of the MGE precedes that of LGE by 1 or 2 days in mice (Corbin et al., 2000; Sousa and Fishell, 2010). The specification of dorsal midline tissues occurs before the embryonic day (E) 8.5, preceding the expression of Gsx2 at approximately E9.5 (Thomas and Dziadek, 1993). A simple morphogen concentration gradient does not well explain this temporal progression of telencephalic patterning. Two interpretations are possible. One is that the patterning of the telencephalon is achieved by a concurrent specification of multiple regions during an early phase, followed by delayed differentiation of Gsx2^{+} LGE progenitors during the later phase. The other is that each subregion in the telencephalon is specified within distinct time windows and that fate determination of Gsx2^{+} LGE progenitors occurs after Nkx2-1^{+} MGE progenitor induction. The latter scheme implies that the relevant fate determinant factor(s) act on MGE and LGE progenitors at different time points. This raises an intriguing question as to how the order of induction among subregions is determined. However, it is difficult to distinguish between these putative patterning mechanisms based on current experimental results *in vivo*. In addition, it is still unknown precisely when and for how long cells are capable of making fate choices. In the past decade, it has become possible to generate nascent telencephalon-like tissues (organoids) *in vitro* from mouse or human embryonic stem (ES) cells or induced pluripotent stem (iPS) cells using either a three-dimensional (3D) *in vitro* differentiation method or a two-dimensional (2D) method (Watanabe et al., 2005; Eiraku et al., 2008; Danjo et al., 2011; Cambray et al., 2012; Nasu et al., 2012, 2020b; Maroof et al., 2013; Arber et al., 2015; Tyson et al., 2015). *In vitro* studies have generally administered signaling cues for the entire duration of the developmental process under study, despite the potential advantages of *in vitro* experimental models for examining the temporal dependence of lineage specification signals compared with *in vivo* systems.

Here, we investigate the time-dependent specification of subregional progenitors in telencephalon using the 3D culture system, where subregional induction by morphogens can be achieved under controlled conditions. We provide evidence for time-dependent fate specification during development in which a short-lasting signal during a specific time window is sufficient to induce subregional progenitors; in other words, the timing rather than the duration of signal exposure is essential for the specification. Furthermore, the two ventral progenitors of the MGE/POA and LGE/CGE show different dose dependencies through a temporal shift in cellular responsiveness for Shh signaling. Taken together, the present study reveals novel developmental mechanisms for telencephalon patterning based on the interplay of dose and time dependence.

RESULTS

Two Specific Time Windows for Ventral Fate Induction in the Telencephalon by Sonic Hedgehog Signaling

To identify essential temporal signaling processes for patterning the telencephalon, we used a 3D culture system to investigate how the subregional lineages of the telencephalon progenitors generated from mouse ES cells were specified in a temporal manner. The day of plating was defined as day 0. First, we verified proper neural induction using our method to inhibit transforming growth factor-beta (TGFb) signal during days 0–5 and WNT signal during days 1–5. The expressions of Nestin, a marker for neural lineage-committed cells, and Sox2, a neural progenitor cell marker, were observed in most parts of the outer zone of each aggregate (**Figures 1A,B** and **Supplementary Figures 1A,B**). N-cadherin, a marker for adherens junctions located at the apical side of the neuroepithelium, was detected at its inner border, whereas pH3, a mitotic cell marker, was located inside along the border (**Figure 1C** and **Supplementary Figure 1E**). EdU-labeled proliferating cells during days 9 and 10 were widely accumulated but exclusively in the outer zone (**Figure 1D**), indicating that our method effectively induced neural lineage cells, and neurogenesis occurred in the outer zone with the apical inside polarity, which is consistent with that reported by our previous study (Nasu et al., 2012). We observed that apoptotic cells were mostly retained in the inner cavity, detected by cleaved caspase-3, the active form of caspase-3 (**Figure 1E**). Induction of four lineage fates was immunocytochemically distinguished in developing telencephalic organoids by the following marker expression patterns on day 10 *in vitro*: Pax6$^+$/Foxg1$^+$ for the dorsal telencephalon (cortex), Gsx2$^+$/Foxg1$^+$ for the dorsal half of the ventral telencephalon (LGE/CGE), Nkx2-1$^+$/Foxg1$^+$ for the ventral-most telencephalon (MGE/POA), and Lmx1a$^+$/Foxg1$^-$ for the dorsal midline tissues (**Supplementary Figures 1A–D,F,I**). These four lineages were chosen because they emerge in a specific arrangement along with the D–V axis of the telencephalon *in vivo*, and both the location and temporal sequence of emergence are well documented (Toresson et al., 2000; Yun et al., 2001; Rallu et al., 2002a,b; Schuurmans and Guillemot, 2002; Corbin et al., 2003; Nasu et al., 2012). Using Foxg1::venus ES cells expressing fluorescent Venus specifically in telencephalic cells, we found that most neural lineage cells adopted the dorsal telencephalic progenitors, defined by co-expressing Foxg1 and Pax6, in the default condition with no added cues (**Figures 1E–I**).

To investigate how long specific ES cell populations are sensitive to fate determination by signaling cues, we first focused on the known ventral fate determinant Shh. We utilized the advantage of chemical compounds to recombinant proteins, including high induction potency of signaling pathways, good stability in cell culture conditions, and less difference between manufacturing lots, to achieve tight control of the signal exposure (Chen et al., 2009; Danjo et al., 2011; Naujok et al., 2014). We examined its ventralizing effects of different durations of transient exposure to the Shh agonist SAG (3 nM) following the neural induction in the *in vitro* differentiation system (part A in **Figure 2A**). Exposure to SAG on day 5 resulted in increased ventral marker expression (Nkx2-1$^+$) concomitant with decreased dorsal marker expression (Pax6$^+$) among the Foxg1$^+$ domain on day 10 (**Figures 2B–D**). The efficiency for general telencephalon induction (Foxg1::venus$^+$ cells) was not influenced by the timing of SAG addition, indicating that telencephalic fate was maintained but ventralized by Shh signaling (**Supplementary Figures 2A–G**). Exposure on day 5 was the most effective condition for ventral marker induction, and similar numbers of Nkx2-1$^+$ cells were induced by SAG exposure starting on day 5 independent of exposure duration (2–4 days) (days 5–7, 78.91 ± 4.50%; days 5–8, 73.86 ± 7.09%; days 5–9, 73.71 ± 10.80%) (**Supplementary Figures 3A–F** and **Figure 2K**). In contrast, induction of Nkx2-1$^+$ cells (ventralization) was markedly reduced when 3 day SAG was administered starting on day 6 (day 6–9, 24.89 ± 12.24%) (**Supplementary Figures 3G–I**). Thus, SAG exposure for 2 days was sufficient to induce Nkx2-1$^+$ (MGE/POA progenitor) cells. The critical condition for Nkx2-1$^+$ cell induction is the specific timing of SAG application rather than the duration of SAG exposure.

Furthermore, Shh signaling specified distinct ventral lineage pathways depending on the timing of induction (part B in **Figure 2A**) in that the time window for the optimal induction of ventral-most MGE/POA (Nkx2-1$^+$/Foxg1$^+$) cells differed from that required for LGE/CGE (Gsx2$^+$/Foxg1$^+$) cell induction (**Figures 2B–K**). Although Nkx2-1$^+$/Foxg1$^+$ cells were efficiently induced by 2 day SAG exposure starting on day 5 but not on day 6 or 7 (days 6–8, 33.65 ± 16.92%; days 7–9, 5.01 ± 2.15%) (**Figures 2D,G,J**), Gsx2$^+$/Foxg1$^+$ cells were induced efficiently by 2 day SAG exposure starting on day 7 but poorly by exposure starting on day 5 or 6 (days 5–7, 2.85 ± 0.60%; days 6–8, 7.18 ± 6.11%; days 7–9, 20.12 ± 4.74%) (**Figures 2C,F,I**). Longer SAG exposure also slightly increased Gsx2$^+$/Foxg1$^+$ cell numbers (days 5–8, 7.90 ± 1.00%; days 5–9, 7.06 ± 3.39%; days 6–9, 12.19 ± 7.25%), but induction was clearly more sensitive to the timing of SAG exposure than the duration of exposure.

The induction rate of Pax6$^+$ cells was inversely related to the induction rate of Nkx2-1$^+$ cells, as numerous Pax6$^+$ cells were induced with and without SAG exposure from days 7–9 (**Figures 2B,E,H**). SAG addition on day 6 resulted in a mixture of the three progenitors (**Figures 2E–G** and **Supplementary Figures 3G–I**). The relative induction rates differed significantly among cultures exposed to SAG for 2 days but starting on day 5, 6, or 7 (**Figure 2L**). Collectively, these results revealed two distinct time windows for the specification of ventral telencephalic progenitors by Shh, days 5–7 for Nkx2-1$^+$ MGE/POA progenitors and days 7–9 for Gsx2$^+$ LGE/CGE progenitors.

Lateral Ganglionic Eminence/Caudal Ganglionic Eminence-Like Post-mitotic Neurons Were Produced by Late Exposure to the Sonic Hedgehog Agonist

Gsx2 is expressed mainly in LGE/CGE progenitor cells *in vivo* and also at low levels in a small number of MGE progenitors (**Supplementary Figure 1F**). To verify that the Gsx2$^+$/Foxg1$^+$ cells analyzed on day 10 were indeed LGE/CGE progenitors, we characterized neurons generated from these progenitors by extending the culture period up to the emergence of post-mitotic neurons (day 12). Under SAG exposure during days 7–9 (optimal for Gsx2$^+$/Foxg1$^+$ induction over Nkx2-1$^+$/Foxg1$^+$ induction), Gsx2$^+$/Foxg1$^+$ LGE/CGE progenitor cells were observed at the luminal side of organoids (**Figures 3A,B**), which corresponds to the apical side of the brain wall *in vivo* (Nasu et al., 2012). Post-mitotic neurons were located in the marginal zone and specifically labeled with the pan-GE neuronal markers Gad65 and Ctip2 (**Figure 3C**

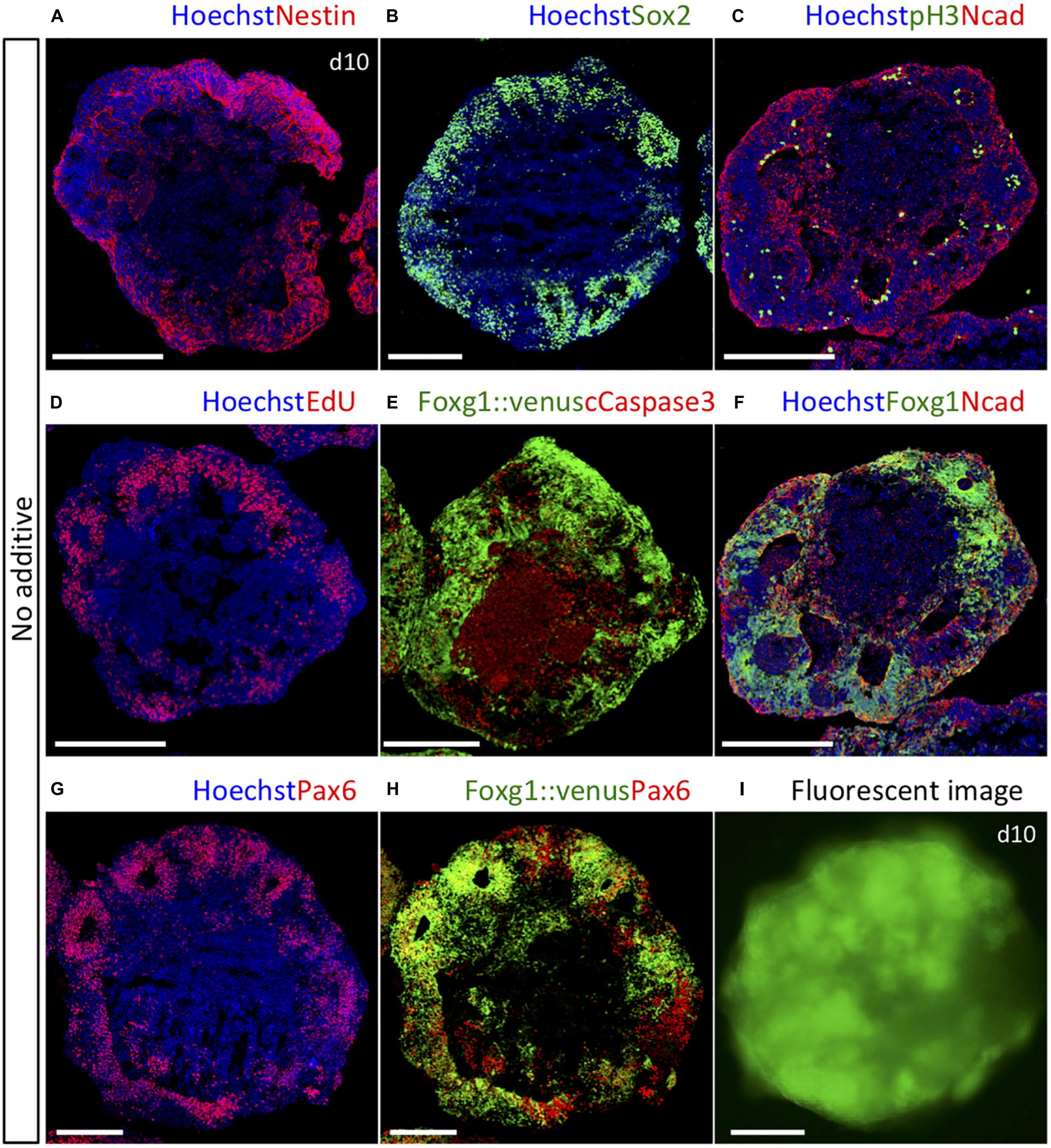

FIGURE 1 | Foxg1::venus cell aggregates cultured in the default condition with no added cues. **(A)** Nestin$^+$ neural lineage-committed cells were observed in most part of the outer zone. **(B)** Sox2$^+$ neural progenitor cells were observed in the outer zone. **(C)** N-cadherin$^+$ adherens junctions and pH3$^+$ mitotic cells were located at the inner border of the outer zone. **(D)** EdU$^+$ proliferating cells were dominantly located in the outer zone. **(E)** Cleaved caspase-3$^+$ apoptotic cells were mostly retained in the inner cavity. **(F–H)** Majority of cells co-expressed Foxg1 and Pax6, indicating cortical fate. **(I)** Whole-mount fluorescence image of a Foxg1::venus aggregate. All aggregates were analyzed on day 10. Hoechst 33342 (blue), nuclear staining. Scale bars, 200 μm.

and **Supplementary Figures 1G,H**) and the LGE/CGE-specific neuronal marker Foxp2 (**Figure 3D** and **Supplementary Figures 1F,G**). Gad65$^+$ cells, which include both post-mitotic neurons and intermediate progenitors (Wu et al., 2011), were more widely distributed than were Ctip2$^+$ or Foxp2$^+$ cells. No Foxp2$^+$ cells were observed in the vicinity of Nkx2-1$^+$/Foxg1$^+$ MGE/POA progenitor cells under SAG exposure during days 5–7 (not shown). It is thus reasonable to assume

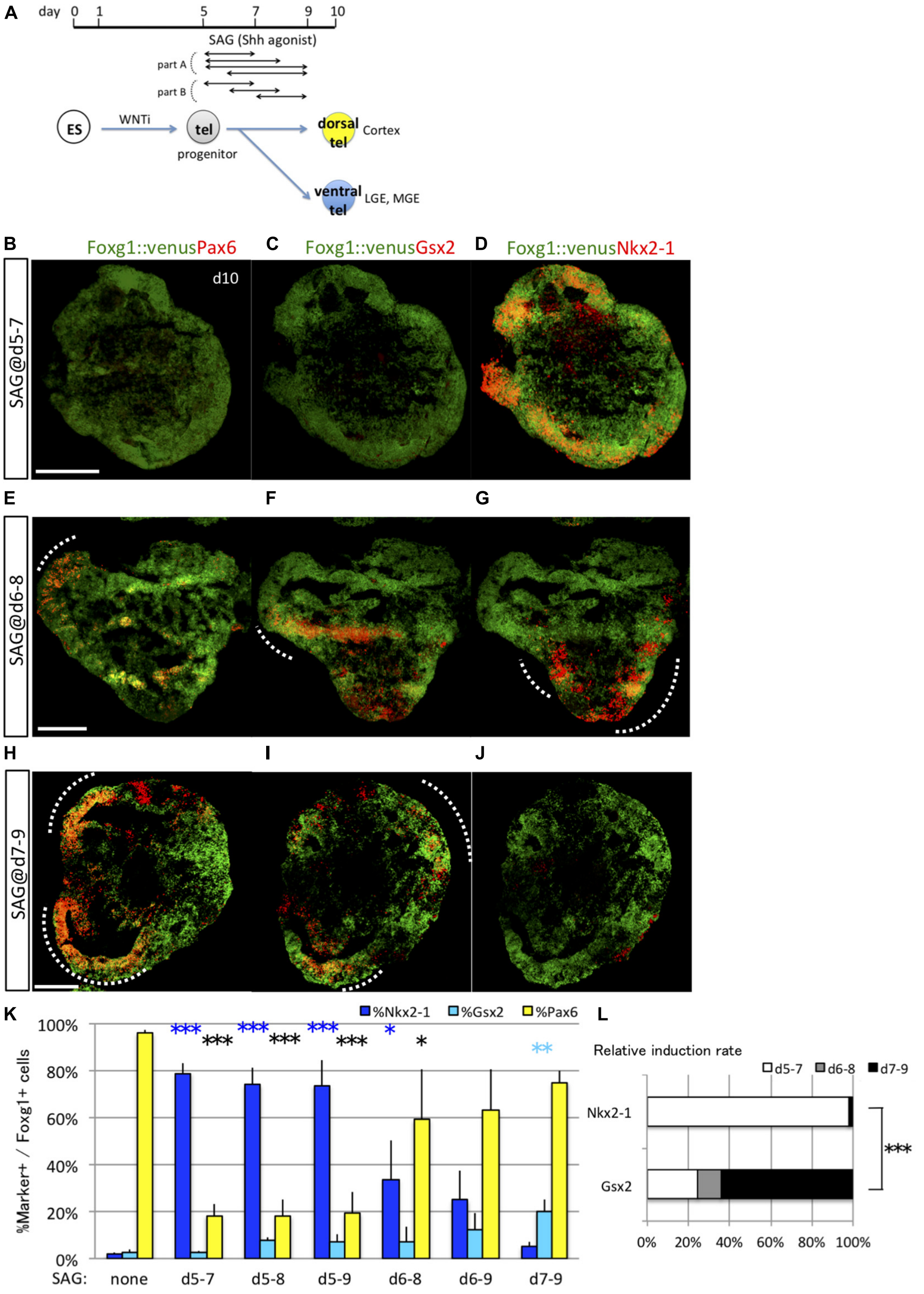

FIGURE 2 | Analyses of the optimal Shh signal time window for induction of ventral fates in telencephalic organoids. **(A)** Schematic of the differentiation strategy for dorsal and ventral telencephalon (tel) using the 3D culture model. Embryonic stem (ES) cells can be differentiated into lineages of the anterior telencephalon by Wnt inhibition (WNTi; anteriorization) and lineages of the ventral telencephalon by Shh signaling (ventralization). We determined the optimal time window of Shh signal exposure to induce ventral telencephalon using an Shh agonist (SAG). Cell aggregates (organoids) were analyzed to express the pan-telencephalic marker Foxg1 and subregional markers on day 10. **(B–J)** Fluorescence images of serial sections through Foxg1::venus (telencephalic) cell aggregates (green) co-immunostained for subregional markers (red) Pax6 **(B,E,H)**, Gsx2 **(C,F,I)**, and Nkx2-1 **(D,G,J)**. A dashed line indicates an area with dual Foxg1^{+}/subregional marker^{+} cells. Scale bars, 200 μm. **(B–D)** Aggregates cultured with 3-nM SAG during days 5–7 post-seeding expressed Nkx2-1 primarily. **(E–G)** Aggregates cultured with 3-nM SAG during days 6–8 expressed Pax6, Gsx2, and Nkx2-1. **(H–J)** Aggregates cultured with 3-nM SAG during days 7–9 expressed Pax6 and Gsx2 but little Nkx2-1. **(K)** Proportions (%) of subregional marker^{+} cells among Foxg1^{+} cells; Pax6^{+} (yellow bars), Gsx2^{+} (cyan bars), and Nkx2-1^{+} (blue bars). “d5–7,” “d6–8,” “d7–9,” “d5–8,” “d6–9,” and “d5–9” indicate SAG exposure during days 5–7, 6–8, 7–9, 5–8, 6–9, and 5–9, respectively. “None” indicates the culture condition without SAG. **(L)** Differences in relative induction rate during days 5–7 (white bars), 6–8 (gray bars), and 7–9 (black bars) indicate that the fates of Nkx2-1^{+} and Gsx2^{+} cells are determined at different times, with the early time window optimal for inducing Nkx2-1^{+} cells and the late time window optimal for inducing Gsx2^{+} cells. Values expressed as mean ± standard error of the mean (*N* = 3). *$P < 0.05$, **$P < 0.01$, ***$P < 0.001$.

that these Gsx2$^+$ progenitors produced post-mitotic neurons in the LGE/CGE. Furthermore, *in vitro*-generated Gsx2$^+$ or Nkx2-1$^+$ progenitors appear to adequately mimic lineage fate *in vivo*.

Sonic Hedgehog Dose-Dependent Induction of Nkx2-1 and Dose-Independent Induction of Gsx2

The present study revealed that specification of MGE/POA (Nkx2-1$^+$/Foxg1$^+$) progenitors and LGE/CGE (Gsx2$^+$/Foxg1$^+$) progenitors by Shh is dependent on the precise timing of first exposure (starting on days 5 and 7, respectively) but is not markedly influenced by absolute duration of Shh exposure. On the contrary, previous studies reported that the ventral properties of the telencephalon were specified by Shh in a dose-dependent manner, such that MGE/POA cells were induced by a high concentration and LGE/CGE cells by a low concentration (Danjo et al., 2011). Thus, both dose-dependent and time-dependent mechanisms may be important for ventral specification, although this issue has not been investigated under conditions in which these contributions can be clearly distinguished. To clarify this issue, we tested different concentrations of SAG, ranging from 0.3 to 10 nM, during the early (days 5–7) and late (days 7–9) time windows (**Figure 4A**). During the early time window (days 5–7), Nkx2-1$^+$ and Pax6$^+$ cell induction rates showed reciprocal SAG dose dependencies (**Figures 4B–N** and **Supplementary Figures 4A–L**). Nkx2-1$^+$ cells were efficiently induced by relatively high doses of SAG (82.96 ± 3.09% at 3 nM and 90.32 ± 7.52% at 10 nM) but sparsely by low doses (8.48 ± 2.62% at 0.3 nM and 11.66 ± 5.48% at 1 nM). Alternatively, Pax6$^+$ cells were substantially differentiated under low-dose SAG (or no SAG) but poorly induced by high-dose Shh. These results indicate that Nkx2-1$^+$ and Pax6$^+$ lineages are positively and negatively regulated by Shh signaling, respectively, in a dose-dependent manner during the early time window. In contrast to MGE/POA and cortical cells, Gsx2$^+$ cells were not efficiently induced by any dose of SAG during the early time window (below 7.7%) but were induced during the second time window by all SAG doses (15.32 ± 4.32% at 0.3 nM, 13.11 ± 3.86% at 1 nM, 22.98 ± 3.73% at 3 nM, and 25.89 ± 5.90% at 10 nM). Notably, Nkx2-1$^+$ cells were not induced during the second time window, even at high doses of SAG (below 3.2%). In summary, Nkx2-1$^+$ MGE/POA induction required both time- and dose-dependent Shh signaling mechanisms, whereas Gsx2$^+$ LGE/CGE induction was also highly dependent on the timing of the Shh signal (in a later time window) but much less sensitive to Shh dose. The efficiency for the general induction of telencephalic progenitors (Foxg1::venus$^+$ cells) was not substantially influenced by SAG concentration during either time window (**Supplementary Figures 2H–P**).

Dorsal Midline Tissues Were Induced by Timed Bone Morphogenetic Protein and WNT Exposure

The pallium (cortex) is in contact with the subpallium (the MGE in early development) at the pallial–subpallial boundary and with dorsal midline tissues at the hem–cortex boundary (HCB). Results presented in **Figures 1**, **2** suggest that pallial vs. subpallial fate at the pallial–subpallial boundary is determined by Shh signaling during a specific temporal window (days 5–7 *in vitro*). To address when the fate of hem vs. cortex progenitors at the HCB is induced by a dorsalizing signal, we focused on BMP and WNT, which are known signaling factors for dorsalization in the telencephalon and for fate choice at the HCB between dorsal midline and cortical tissues (Eiraku et al., 2008; Watanabe et al., 2012). We first examined the time window for efficient induction of Lmx1a$^+$ dorsal midline tissue by BMP signaling (exposure to recombinant BMP4) (**Figure 5A**). Similar to that in the case *in vivo*, where the Lmx1a$^+$ hem adjoins the dorsal Foxg1$^+$ cortex at the HCB within the Sox2$^+$ neuroepithelial sheet (**Supplementary Figure 1A**), *in vitro*-generated Lmx1a$^+$ cells were frequently adjacent to Foxg1::venus$^+$ cells independent of induction efficiency (**Figures 5B–F**). Consistent with a previous report (Watanabe et al., 2012), early BMP signaling starting on day 5 or 6 (but not day 7 or 8) efficiently induced Lmx1a$^+$ cells at the cost of Foxg1::venus$^+$ cells (days 5–7, 1.85 ± 0.42%; days 6–8, 1.93 ± 0.29%; days 7–9, 1.09 ± 0.39%; days 8–10, 0.76 ± 0.16%, no BMP, 0.44 ± 0.21%; expressed as a percentage of all Foxg1::venus$^+$ cells in aggregates) (**Figure 5G**), indicating that BMP is a key signal for the fate choice between midline and cortical lineages at the HCB *in vitro*. Next, we examined the time window for efficient induction of Lmx1a$^+$ dorsal midline tissue by WNT signaling using the Wnt agonist CHIR99021 (**Figure 5A**). WNT signaling alone did not markedly induce Lmx1a$^+$ cells, although numbers were numerically higher with stimulation starting on day 5 (days 5–7 or 5–10) compared with day 7 or 8 (**Figure 5H**). WNT signal had weaker dorsalizing effects than did BMP signal; however, WNT-containing conditions were strongly negative for Foxg1 expression (**Figure 5H**), which contrasts with the modest decrease of Foxg1 by BMP signal (**Figure 5G**). Earlier or longer WNT exposure resulted in fewer Foxg1$^+$ cells, possibly because of the caudalizing effects of the WNT signal.

Subsequently, we investigated whether BMP and WNT signals acted synergistically to induce the dorsal midline fate (Lmx1a$^+$) when present for 2 or 5 days starting on day 5 (**Figure 6A**). Foxg1 expression was negatively regulated by both BMP and WNT, whereas WNT had a greater negative effect on Foxg1 expression (**Supplementary Figures 5A,B**). To focus on the fate determination of the dorsal midline vs. cortical cells, this analysis was limited to Sox1$^+$ neural progenitor cells because both Foxg1$^+$ cells and Lmx1a$^+$ cells co-expressed Sox2 (**Figures 6B–J**). Similar to the ventralizing signal, a short period of BMP4 and/or CHIR99021 exposure (2 days) was of Lmx1a$^+$/Sox2$^+$ dorsal midline cells, although a longer exposure (5 days) might be more effective (**Figure 6K**). BMP and WNT synergistically induced more than 10% of dorsal midline cells. Thus, the fates of cortical cells and dorsal midline tissues were determined by both BMP and WNT signals, mainly during days 5–8. Collectively, cortical fate was negatively influenced by a dorsalizing and a ventralizing factor during the same period.

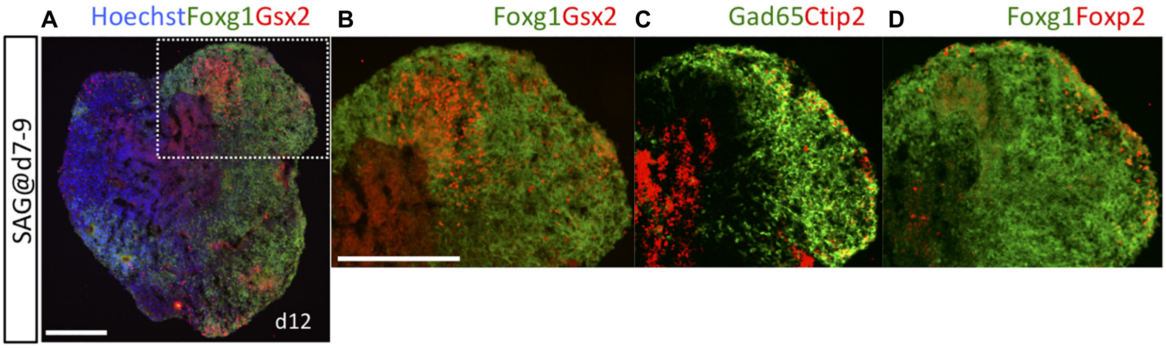

FIGURE 3 | Post-mitotic LGE neurons were detected on day 12. Cell aggregates were cultured with 3-nM SAG during days 7–9 and analyzed on day 12. **(A)** Fluorescence image of an entirely Foxg1::venus^{+} aggregate (green) immunostained for Gsx2 (red) to show the induction of LGE progenitors. Hoechst 33342 (blue), nuclear staining. White dotted rectangular area is magnified in **(B–D)**. **(B)** Gsx2^{+}/Foxg1^{+} LGE progenitors are located at the inner side within an area of Foxg1^{+} cells. **(C)** Expression of the pan-GE post-mitotic neuron markers Gad65 and Ctip2. **(D)** Expression of the LGE-specific post-mitotic neuron marker Foxp2. Foxp2^{+} neurons and Ctip2^{+} neurons are localized in the marginal areas of Gad65^{+} and Foxg1^{+} zones. Scale bars, 200 μm.

Gsx2^{+} Lateral Ganglionic Eminence/Caudal Ganglionic Eminence Induction Required Subthreshold Levels of Sonic Hedgehog and Wnt Signal During the Early Phase

The fates of the two ventral subregions, MGE/POA and LGE/CGE, were determined through a two-phase specification process dependent on distinct mechanisms; early progenitors produced ventral cells (MGE/POA) through strongly dose-dependent Shh signaling, whereas late progenitors required Shh signaling for ventral specification (LGE/CGE) but with much lower dose sensitivity. Importantly, early progenitors had little competence for differentiating into Gsx2^{+} cells and late progenitors for differentiating into Nkx2-1^{+} cells, implying that the Shh signaling response shifts from the early to late phase. For the induction of the LGE/CGE fate, progenitors must first remain resistant to both ventralizing and dorsalizing signals during early development to avoid the ventral-most (MGE/POA) and the dorsal (cortex) fate and must then respond to a later Shh signal.

Some endogenous signals may be responsible for this shift in specification competency (Sasai et al., 2014). We thus examined how progenitors change signal dependence *in vitro*. To clarify whether an endogenous early signal is involved, we examined expression dynamics of the above D–V patterning factors—Wnt3a, BMP4, and Shh— and Tgfb1 as a reference from an ES cell maintenance state (day 0) through neural differentiation using quantitative polymerase chain reaction (qPCR). Consistent with the previous study, we detected quite low but certain expressions of Wnt3a, Shh, and Tgfb1 and a high expression of Bmp4 in ES cells (day 0), where BMP4 signaling might be distinct from differentiation stages (**Supplementary Figures 6A–D**; Bertacchi et al., 2015; Morikawa et al., 2016). We confirmed that those expressions were sustained and dynamically changed in the course of neural differentiation. Next, we examined inhibiting the activity of selective inhibitors of Shh, WNT, BMP, and TGFb signaling pathway (termed SHHi, WNTi, BMPi, and TGFi, respectively) during the early phase of culture under baseline conditions (i.e., no Shh, BMP, or Wnt agonists). SHHi significantly downregulated its downstream target, Gli1, but not Patched 1 (Ptc1) (**Supplementary Figures 6E,F**). WNTi efficiently reduced the amount of beta-catenin, a downstream target in the WNT pathway (**Supplementary Figures 6H,K**). Although BMPi and TGFi slightly but not significantly reduced the number of phosphorylated Smad1/5 (pSmad1/5) and phosphorylated Smad2 (pSmad2), a downstream target in the BMP pathway and the TGFb pathway, respectively (**Supplementary Figures 6I,J,L,M**), it might be partially due to the activity of BMP4 and TGFb signal transduction that was still low under baseline conditions (**Supplementary Figures 6B,D**). Then, we applied SHHi, WNTi, BMPi, and TGFi during the early phase, followed by late exposure to the Shh agonist (**Figure 7A**). Both SHHi and WNTi treatment, but not BMPi and TGFi treatment, during days 5–7 dramatically reduced Gsx2 + cell induction in response to late Shh agonist exposure and modified fate determination (**Figures 7B–K** and **Supplementary Figures 7A–F**). SHHi basically induced the cortical fate, and WNTi drastically increased Nkx2-1^{+} cell numbers. These findings indicated that both Shh and WNT signals during days 5–7 are a prerequisite for later LGE/CGE induction by Shh. Given that early Shh and WNT signals are induction factors for ventral-most (MGE/POA) and dorsal midline tissues, respectively, they must be at subthreshold levels to evoke the temporal shift in specification competency. Gene expression state of environmental factors, such as Shh, Wnt3a, and Bmp4, but not Tgfb1, were different between days 5 and 7, which should be derived from their own cell aggregates (**Supplementary Figures 6A–D**). Two target genes of the Shh signaling pathway, Gli1 and Ptc1, remained unchanged during days 5–7 (**Supplementary Figures 6E,F**), whereas Smoothened (Smo), one of the essential Shh signaling components, was downregulated from days 5 to 6 and 7 (**Supplementary Figure 6G**). These indicated that neuronal progenitors change

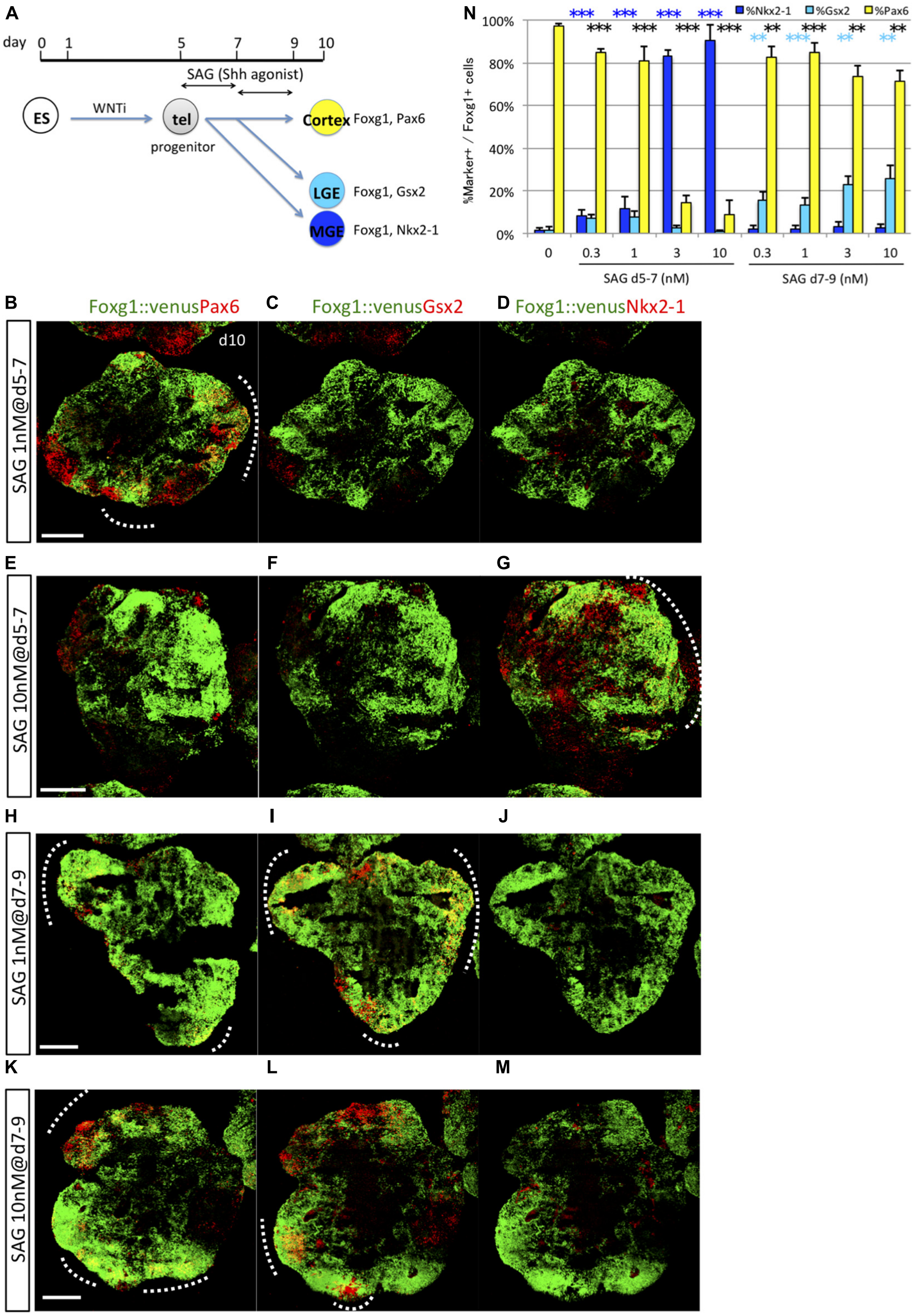

FIGURE 4 | Dose-dependent induction of Nkx2-1 and dose-independent induction of Gsx2. **(A)** Schematic of the 3D culture used to investigate dose-dependent subregional marker expression in two time windows, days 5–7 and 7–9. **(B–M)** Fluorescence images of serial sections through Foxg1::venus (telencephalic) cell aggregates (green) co-immunostained for subregional markers (red) Pax6 **(B,E,H,K)**, Gsx2 **(C,F,I,L)**, and Nkx2-1 **(D,G,J,M)**. A dashed line indicates an area with dual Foxg1$^+$/subregional marker$^+$ cells. Scale bars, 200 μm. **(B–D)** Aggregates cultured with 1-nM SAG during days 5–7 post-seeding expressed Pax6 primarily. **(E–G)** Aggregates cultured with 10-nM SAG during days 5–7 expressed Nkx2-1 primarily. **(H–M)** Aggregates cultured with 1-nM (**H–J**) and 10-nM (**K–M**) SAG during days 7–9 expressed Pax6 and Gsx2 but little Nkx2-1. **(N)** Proportion (%) of subregional marker$^+$ cells among Foxg1$^+$ cells; Pax6$^+$ (yellow bars), Gsx2$^+$ (cyan bars), and Nkx2-1$^+$ (blue bars). SAG was added to the culture during days 5–7 or 7–9 at the following concentrations: 0 (none), 0.3, 1, 3, and 10 nM. Results expressed as mean ± SEM (*N* = 4). $^{**}P < 0.01$, $^{***}P < 0.001$.

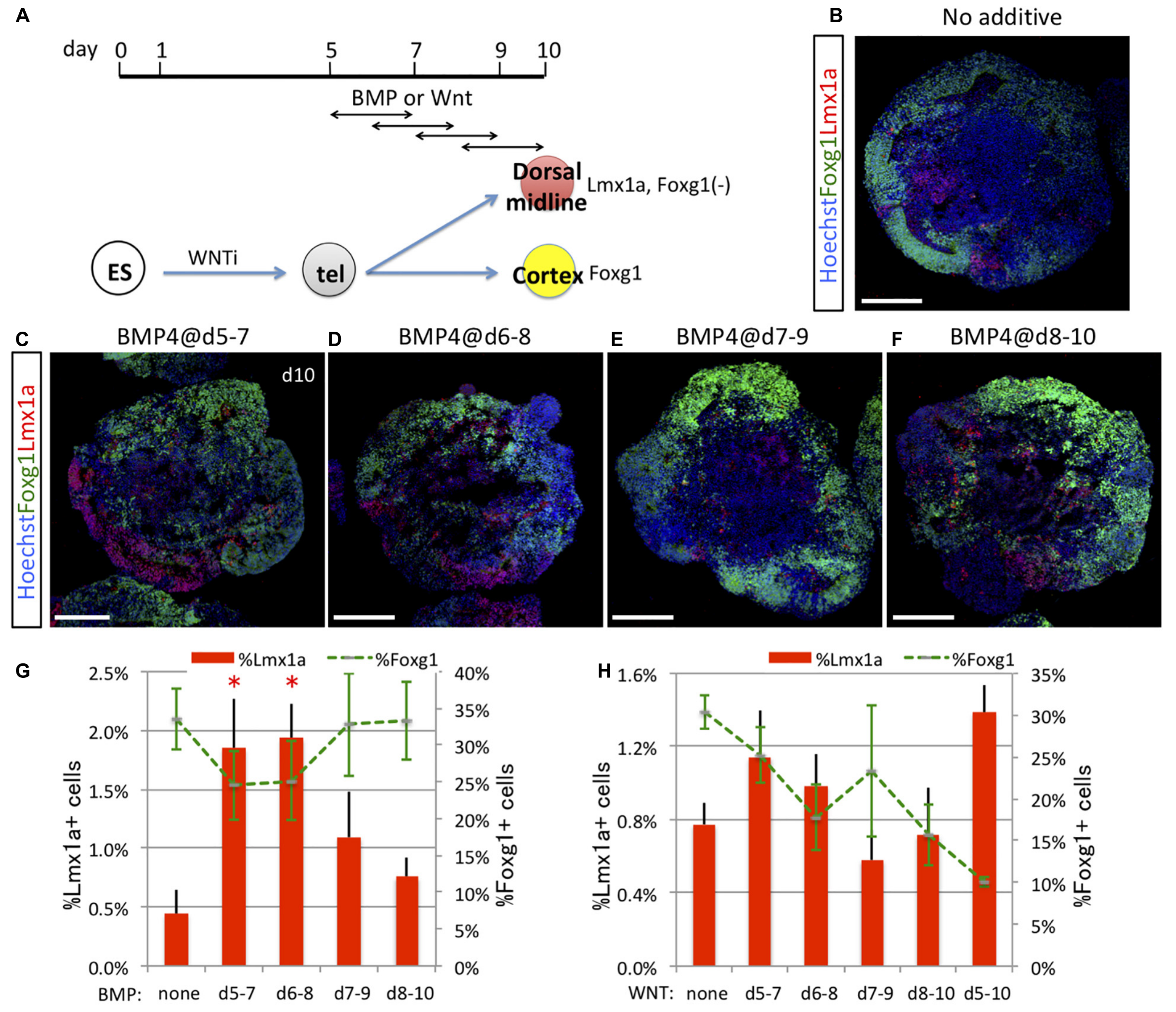

FIGURE 5 | Dorsal midline tissues were induced by timed BMP and WNT exposure. **(A)** Schematic of differentiation strategy for dorsal midline tissues and cortex. ES cells differentiated into Pax6$^+$/Foxg1$^+$ cells (cortex) under the default condition (no additional cues) or into Lmx1a$^+$ dorsal midline cells by BMP or WNT signaling (dorsalization). **(B–F)** Using the 3D culture, we assessed the optimal time window for 2 days of BMP signal (BMP4 recombinant protein) exposure to induce dorsal midline tissues. Foxg1::venus cell aggregates cultured without BMP4 **(B)** or with BMP4 during days 5–7 **(C)**, 6–8 **(D)**, 7–9 **(E)**, or 8–10 **(F)**. Images show Foxg1::venus fluorescence (green) and immunostaining for Lmx1a (red). Lmx1a$^+$ cells (red) were induced in restricted patches but in contiguous arrangement with Foxg1$^+$ cortical cells (green) as *in vivo*. Hoechst 33342 (blue), nuclear staining. Scale bars, 200 μm. **(G)** Proportion (%) of subregional marker$^+$ cells among the whole aggregate; Lmx1a$^+$ (red bars) and Foxg1$^+$ (green dashed line). **(H)** We analyzed the optimal time window for 2 or 5 days of WNT signal exposure to induce dorsal midline tissues using the WNT agonist CHIR99021. Proportion (%) of subregional marker$^+$ cells in aggregates; Lmx1a$^+$ (red bars) and Foxg1$^+$ (green dashed line). Expressed as mean ± SEM ($N = 3$). $^*P < 0.05$.

their expressional profiles during their lineage commitment and temporally modify cellular responsiveness for the Shh signaling pathway and the environmental signaling state.

Taken together, our data propose the two-phase specification model to explain the delayed specification of LGE/CGE progenitors relative to MGE/POA and cortical progenitors (**Figure 8**). The model postulates that whole tissue organization is achieved in two phases. In the early phase, the fates of subregions close to signal sources are determined by exposure to high morphogen concentrations (a dominant morphogen), whereas the fate of subregions receiving multiple signals remains pending. In the late phase, all the pending fates were determined based on temporal changes in environmental cues or progenitor competence. The present study demonstrates that the changes in signal dependence for progenitor specification are essential for fate determination during the late phase and are rendered by subthreshold Shh and WNT signals during the early phase.

DISCUSSION

In the present study, we highlight the concerning points and topics of telencephalon patterning. We verified the critical contributions of three key signaling factors for lineage specification of subregions in the telencephalon, ventralizing Shh

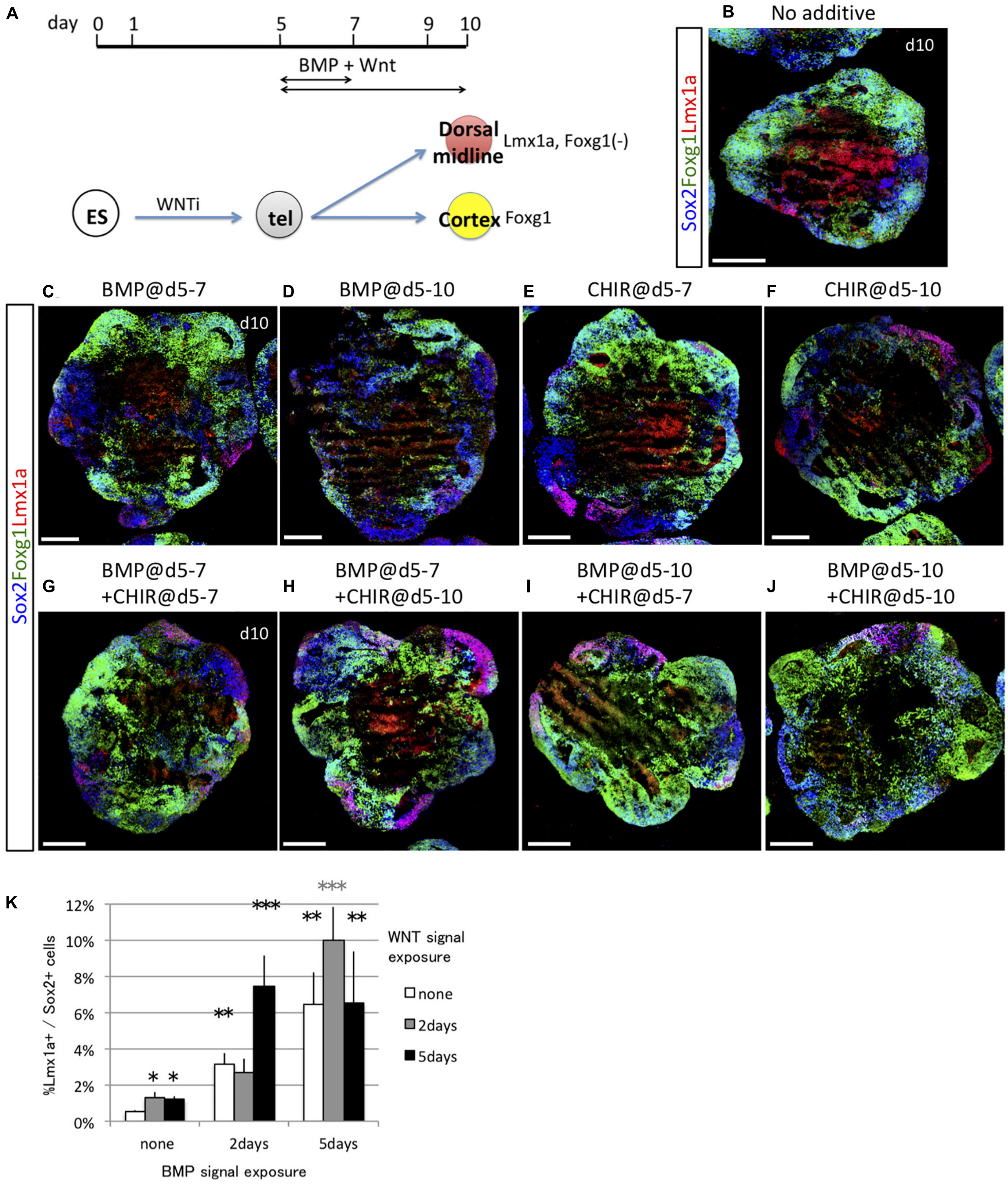

FIGURE 6 | Dorsal midline tissues were induced by timed BMP and WNT exposure. **(A)** Schematic of differentiation strategy for dorsal midline tissues and cortex. **(B–F)** Using the 3D culture, we assessed the optimal time window for 2 days (days 5–7) or 5 days (days 5–10) of BMP signal (BMP4 recombinant protein) or WNT signal (CHIR) exposure to induce dorsal midline tissues. Foxg1::venus cell aggregates cultured with no cues **(B)** or with BMP4 during days 5–7 and days 5–10 **(C,D)**, with CHIR during days 5–7 and 5–10 **(E,F)**. Images show Foxg1::venus fluorescence (green) and immunostaining for Lmx1a (red) and Sox2 (blue). **(G–J)** We examined the synergistic effect of BMP and WNT signals in combination for 2 days (days 5–7) or 5 days (days 5–10). Scale bars, 200 μm. **(K)** Proportion (%) of Lmx1a$^+$ cells among Sox2$^+$ cells. Greater proportion (%) of Lmx1a$^+$ cells among Sox2$^+$ cells indicates that WNT signaling enhances the dorsalizing effect of BMP. Expressed as mean ± SEM (*N* = 3). **P* < 0.05, ***P* < 0.01, ****P* < 0.001.

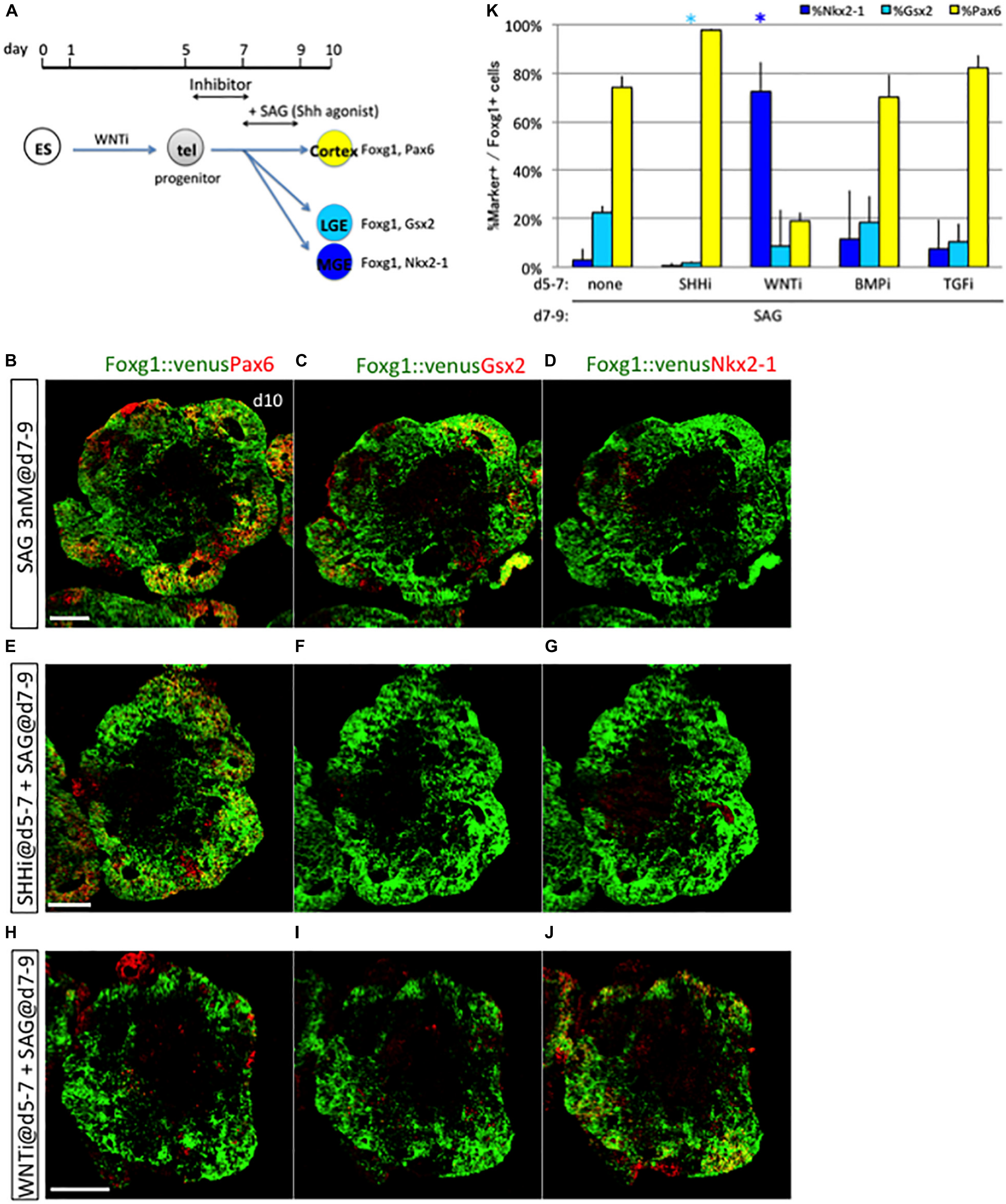

FIGURE 7 | Prerequisite condition for subsequent LGE/CGE induction. **(A)** Schematic of the 3D culture used to identify the signaling pathway responsible for LGE/CGE induction. Disruption of LGE/CGE induction by Shh signal exposure during days 7–9 due to the absence of any endogenous signal during days 5–7 indicates the need for a prerequisite condition. Inhibitors for Shh signal (cyclopamine), WNT signal (WNTi), BMP signal (LDN193189), and TGFb signal (SB 431542) were added to the culture during days 5–7 with subsequent Shh signal exposure (SAG) during days 7–9. **(B–J)** Aggregates cultured without any inhibitor **(B–D)** or with inhibitors for the SHH **(E–G)** and WNT **(H–J)** signaling pathway during days 5–7 and then treated with SAG during days 7–9. Scale bars, 200 μm. **(K)** Proportion (%) of subregional marker$^+$ cells among Foxg1$^+$ cells; Pax6$^+$ (yellow bars), Gsx2$^+$ (cyan bars), and Nkx2-1$^+$ (blue bars). Early treatment with Shh and WNT signaling inhibitors reduced Gsx2$^+$ cell induction by later SAG exposure. Results expressed as mean ± SEM (N = 3). *P < 0.05.

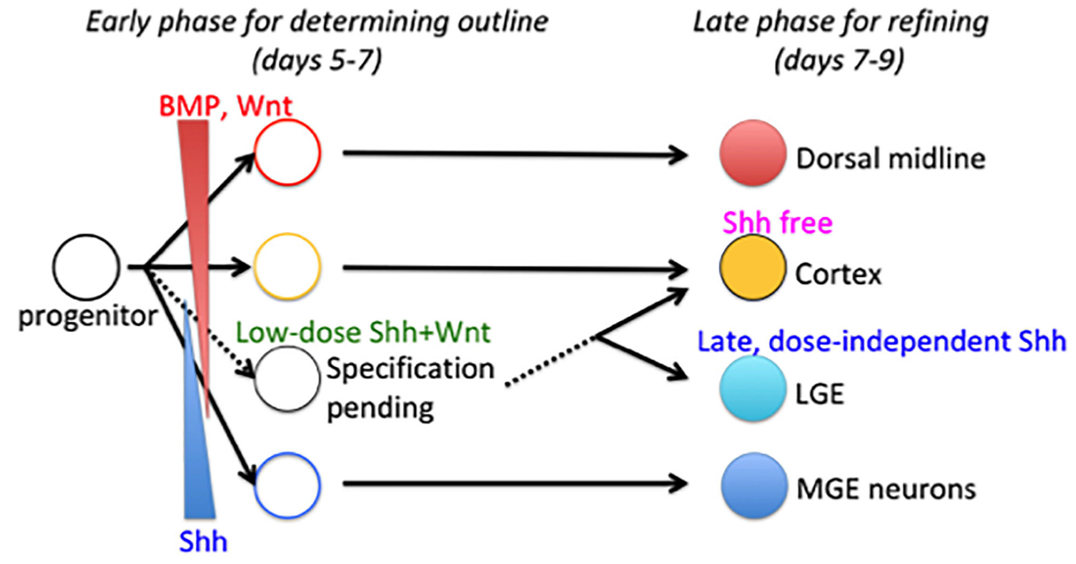

FIGURE 8 | Two-phase specification model for telencephalon patterning. Fate of dorsal midline telencephalic cells is determined by BMP/WNT signaling, whereas the fate of ventral-most telencephalon (MGE) cells is determined by a high dose of Shh signal during the early phase (shown by solid lines). Fate determination of intermediate subregions is conditional (shown by dashed lines). LGE is specified by a dose-independent Shh signal during the late phase through a temporal shift in progenitor states for the Shh response.

and dorsalizing BMP and WNT. By applying these factors at different concentrations and time points, we achieved selective induction of subregional progenitors from mouse ES cells. According to the accepted patterning model based on positional information, the dose is a key determinant of morphogen response, such that tissues at short or long distances from a signal source are differentially induced or are both induced but by high and low doses of the signal, respectively (Wolpert, 1969; Campbell, 2003; Medina and Abellán, 2009). Our results appear consistent with this model in that cells were induced to express Nkx2-1 (MGE/POA lineage) by a high Shh dose, Gsx2 (LGE/CGE lineage) by a low Shh dose, and Lmx1a (the dorsal midline tissue lineage) by BMP and WNT. In addition, we also found that the timing of signal exposure for efficient induction was specific to each lineage; early exposure to Shh efficiently induces MGE/POA progenitors, whereas late exposure to Shh induces LGE/CGE progenitors, and early BMP/WNT signal exposure induces dorsal midline tissues. Cortical fate (Pax6$^+$/Foxg1$^+$) was a default (signal-independent) state in the early stage. These suggest that the fate of most telencephalic cells is determined concurrently, whereas that of a small group, the LGE/CGE progenitors, is delayed (for 2 days in mice). Our results provide evidence that both the appropriate dose and correct timing are critical for telencephalic patterning by morphogens.

The early patterning field may be so small that the middle domain receives multiple morphogens derived from distinct signal sources. Three possible mechanisms could allow cells within this domain to respond selectively or correctly interpret multiple patterning cues as a fate determinant: (i) one morphogen is the dominant fate determinant (i.e., due to a higher concentration or greater sensitivity of the cell), (ii) multiple morphogens work together (i.e., the cell requires the synergistic actions of multiple morphogens for fate determination), and (iii) fate determination is conditional (e.g., contingent on a prior priming signal). In the third case, cellular changes are required to prepare the cell for subsequent fate determination. Considering our results showing delayed specification of LGE/CGE progenitors relative to MGE/POA and cortical progenitors, the latter two-phase specification model is favored (**Figure 8**). The early phase determines an outline of the tissue subdivision, and the late phase refines the pattern.

Although morphogens continue to be produced throughout the expansion of the telencephalon, the size of the prospective patterning field changes up to several folds, and some distinct regional characteristics emerge progressively. When the patterning field expands with tissue growth, signal-receiving cells must decode the spatiotemporally changing status of signals. In addition to positional information underlying the classic model, temporal information may be a critical signaling domain of patterning cues for neural specification (Ribes and Briscoe, 2009). Several possible mechanisms could confer dose dependence, time dependence, or both to fate-determining signals (Sagner and Briscoe, 2017). (i) For dose dependence and time independence, progenitors could convert a transient graded signal into a sustained molecular change through induction of an autoregulatory feed-forward loop before extensive tissue growth. The specification should be contemporaneously completed within a relatively short period and before the onset of planar expansion of the neuroepithelial tissue. In this way, the progenitor could recognize the morphogen at an early stage as a pre-patterning signal (Moore et al., 2013). Such progenitors would exhibit robustness for the change in tissue size and a consequent change in signal dose. (ii) For time dependence and dose independence, the mechanism could involve sequential signal transduction or a signal-relay system in which signal recipient cells first react to the signal and then transfer it to other neighboring cells (van Boxtel et al., 2015). This sequential signal transduction would result in a temporal gradient of the signal. In this case, the timing of the input is the primary cue for fate determination, and signal transduction in the following cell population would be little affected by changes in absolute dose associated with tissue growth. (iii) Finally, a dose- and time-dependent mechanism is represented by two distinct cases. (iii-a) The integrated intensity of intracellular signal transduction could be important for some progenitors (Dessaud et al., 2007; Ribes and Briscoe, 2009). These progenitors would decode the cumulative amount of signal received during a certain period. In this case, the initial dose, the rate of change, and the exposure time would all be essential factors for establishing cell identity. When an ultrasensitive switch-like response to a morphogen signal occurs in an intracellular signaling pathway, a graded signal is converted to a transcriptional code, which is composed of Pax6, Gsx2, and Nkx2-1 in the telencephalon (Lek et al., 2010; Rogers and Schier, 2011; Shindo et al., 2016). When progenitors are exposed to subthreshold signals, they keep a graded response to the incremental signals, and graded induction will take time to be achieved (Zhang et al., 2006). In the case of (ii) and (iii-a), the signal duration is a key factor, and fate should differ depending on the length of signal exposure time. (iii-b) In the other case, to adopt the demand for a definite signal input with attenuation as the tissue size increases, progenitors may change competence for signal responsiveness as development proceeds (Rogers and Schier, 2011). A subthreshold signal or another signaling input may trigger the shift in signal dependence (Lek et al., 2010; Sasai et al., 2014; Srinivasan et al., 2014). In this case, recipient cells respond depending on their competence at that time and would be unaffected by both the initial dose and the rate of change. Our data demonstrate novel developmental mechanisms for telencephalon patterning based on both dose dependence in the early phase and time dependence, including a temporal shift in cellular Shh sensitivity, to induce ventral fate in response to Shh signaling. This delayed fate choice allows tissues with marked size expansion, such as the telencephalon or other tissues, to cope with the changing dynamics of patterning cues.

Conditions for the induction of $Gsx2^+$ LGE/CGE had an adverse effect on $Nkx2\text{-}1^+$ MGE/POA induction and *vice versa*, implying a repressive interaction between Nkx2-1 and Gsx2 or associated signaling pathways. It is compatible with previous findings in mutant mice (Rallu et al., 2002a,b; Schuurmans and Guillemot, 2002; Corbin et al., 2003). For instance, $Shh^{-/-}$; $Gli3^{-/-}$ double mutants and Nestin–Cre-driven Shh null mutants that lose Shh expression around E10–12 retained all telencephalic subdivisions but failed to express Nkx2-1 in the MGE and exhibit a concomitant expansion of Gsx2 expression into the MGE-like subdivision (Rallu et al., 2002b; Xu et al., 2005). Fate conversion of the MGE to LGE was also observed in $Nkx2\text{-}1^{-/-}$ mutant mice (Sussel et al., 1999; Corbin et al., 2003), whereas mild mutants (Six3–Cre driving Smo mutants) exhibited a mosaic reduction of Nkx2-1 expression in the MGE with ectopic Gsx2 expression in the Nkx2-1-negative patches (Xu et al., 2010). Nkx2-1-Cre-mediated recombinant cells are not detected in LGE/CGE, indicating that Gsx2 and Nkx2-1 lineages are derived from different progenitors (Xu et al., 2008). The expression of Nkx2-1 comes before that of Gsx2 (Corbin et al., 2003). These findings strongly suggest that Nkx2-1 represses Gsx2, although it is currently unclear if this transcriptional regulation is direct. It also remains to be determined how presumptive LGE/CGE progenitors change competence in a time-dependent manner or how LGE/CGE progenitor specification is delayed relative to other telencephalic tissues. Possible explanations include slow accumulation of *de novo* synthesized proteins or degradation of existing proteins dependent on genetic or epigenetic regulation (Hirabayashi et al., 2009; Aldiri et al., 2017). The induction rate of LGE/CGE fate was still low under our conditions with a later phase of the Shh signal. Considering that the antibody used in this study did not detect the majority of MGE/POA progenitors, some of which expressed Gsx2 at a low level (**Supplementary Figure 1F**), it might fail to detect some LGE/CGE progenitors expressing Gsx2 at a low level, resulting in underestimation of the induction of LGE/CGE. Additional cues, such as FGF15/19 and Activin A, may be required for more effective induction of LGE/CGE fate (Danjo et al., 2011; Cambray et al., 2012). As MGE-derived neurons produce Shh (Nery et al., 2001; Sousa and Fishell, 2010), MGE-derived Shh may act as the subthreshold delay signal for subsequent LGE cell induction. Further studies are required to reveal the precise molecular signaling mechanisms underlying the delayed induction of LGE/CGE cells.

MATERIALS AND METHODS

ES Cell Culture and Treatment With Soluble Factors

Mouse ES cells [Foxg1::venus (Eiraku et al., 2008)] were maintained as described previously (Watanabe et al., 2005). Briefly, ES cells were cultured on feeder-free, gelatin-coated dishes with a maintenance medium composed of Glasgow minimum essential medium supplemented with 10% Knockout Serum Replacement (Thermo Fisher Scientific), 1% fetal calf serum, 1 mM pyruvate (Sigma-Aldrich), 0.1 mM non-essential amino acids (Thermo Fisher Scientific), 0.1 mM 2-mercaptoethanol (Sigma-Aldrich), and leukemia inhibitory factor. The *in vitro* differentiation conditions for the 3D culture were as described in our previous study with minor modifications (Nasu et al., 2012). Briefly, ES cells were dissociated in 0.25% trypsin and quickly re-aggregated by plating on 96-well low cell-adhesion plates (Sumilon) in differentiation medium (5,000 cells per 100 μl/well). The differentiation medium was a growth factor-free chemically defined medium (gfCDM) composed of Iscove's modified Dulbecco's medium (Fujifilm Wako)/Ham's F12 medium (Fujifilm Wako) 1:1, 1 × Chemically Defined Lipid Concentrate (Thermo Fisher Scientific), 450 μM monothioglycerol (Sigma-Aldrich), 5 mg/ml purified bovine serum albumin, 5.5 μg/ml apo-transferrin, 6.7 ng/ml selenium, and 10 μg/ml insulin. The day of ES cell seeding was defined as differentiation day 0. On day 5, cell aggregates were transferred to bacterial-grade, non-coated dishes with Dulbecco's modified Eagle medium/Ham's F12 medium supplemented with N2 and apo-transferrin (Fujifilm Wako). The TGF inhibitor SB 431542 (Cayman, 13031, IC50 = 94 nM) was added at a final concentration of 5 μM on day 0. The Wnt inhibitors IWP2 (Cayman, 13951, IC50 = 27 nM) and IWR1e (Cayman, 13659, IC50 = 180 nM) (WNTi) (Chen et al., 2009) were freshly prepared in 100 μl of gfCDM and added at final concentrations of 1 and 2 μM, respectively, on day 1. Matrigel (BD Biosciences) was prepared in 100 μl of gfCDM at a final concentration of 100 μg/ml and added on day 1. Human recombinant FGF8 (humanzyme, HZ-1104) was added at a final concentration of 50 ng/ml during days 5–7. The concentration, timing, and duration of SAG (Cayman, 11914, EC50 = 3 nM) exposure are described in the text and figures. The timing and duration of 1 ng/ml of BMP4 (humanzyme, HZ-1045) or 1 nM Wnt agonist CHIR99021 (Cayman, 13122, IC50 = 6.7 nM) exposure are described in the text and figures. The Shh antagonist cyclopamine (Cayman, 11321, IC50 = 24 nM) was added at 1 nM and the BMP inhibitor LDN193189 (Cayman, 11802, IC50 = 4.9 nM) at 10 nM on days 5–7 as indicated.

Tissue Preparation

Jcl:ICR mice were killed at embryonic day 12 (E12) (purchased from CLEA Japan). All mice were anesthetized with medetomidine/midazolam/butorphanol tartrate/phosphate-buffered saline (PBS) (final dose, 0.3 mg/kg of body weight; 4 mg/kg of body weight; and 5 mg/kg of body weight, respectively) and perfused from the left ventricle with iced 4% paraformaldehyde (PFA)/PBS (pH 7.2). Extracted brain tissues were postfixed with 4% PFA/PBS (pH 7.2) for 1 h. Cell aggregates were harvested on day 10 or 12 and fixed with 4% PFA/PBS (pH 7.2) for 20 min. Fixed tissues and cell aggregates were cryoprotected in 15% sucrose/PBS overnight at 4℃ and embedded in Tissue-Tek O.C.T. compound (Sakura Finetek). Frozen tissues were sliced at 12 μm. All animal experiments were performed in accordance with institutional (Kumamoto University) guidelines and were approved by the Animal Care and Use Committee of Kumamoto University.

Immunostaining

Immunohistochemistry and immunocytochemistry were performed as described previously (Nasu et al., 2020a). Briefly, sections were rinsed with 0.3% Triton-X100/PBS three times and incubated overnight at 4℃ with primary antibodies diluted in incubation buffer (5% donkey serum/0.3% Triton-X100/PBS) after pretreatment with incubation buffer for 30 min. The following primary antibodies were used at the indicated dilutions: anti-cCaspase3 (rabbit, 1:50; Cell signaling, 9664), anti-Ctip2 (rat monoclonal, 1:3,000; Abcam, ab18465), anti-Foxg1 (rabbit, 1:2,000; TaKaRa, M227), anti-Foxp2 (goat, 1:100; Santa Cruz, sc-21069), anti-Gad65 (mouse monoclonal, 1:200; BD Pharmingen, 559931), anti-Gsx2 (rabbit, 1:500; Millipore, ABN162), anti-Lmx1a (goat, 1:100; Santa Cruz, sc-54273), anti-N-cadherin (mouse, 1:1,000; BD Pharmingen, 610920), anti-Nestin (mouse, 1:200; BD Pharmingen, 611658/611659), anti-Nkx2-1 (mouse, 1:500; Leica, NCL-L-TTF-1), anti-Pax6 (rabbit, 1:2,000; BioLegend, PRB-278P), anti-pH3 (rabbit, 1:1,000; Millipore, 06-570), and anti-Sox2 (rabbit, 1:1,000; Millipore, AB5603). Hoechst 33342 was used for counterstaining of nuclei. Proliferating cells were labeled by EdU for 24 h from day 9 and detected chemically according to the manufacturer's instructions (Thermo Fisher Scientific). Images were obtained using a BZ-X700 fluorescence microscope (Keyence) and laser-scanning confocal microscope (FV-1200, FV-1000, or FV-300; Olympus) and analyzed using BZ-X700 software and ImageJ. The percentage of Pax6$^+$, Gsx2$^+$, Nkx2-1$^+$ fractions among Foxg1$^+$ area was calculated. The expression of Pax6, Gsx2, and Nkx2-1 is based on nuclear staining, whereas the fluorescence of venus protein, corresponding to Foxg1 expression, localizes a whole cell. To revise underestimation caused by comparing nuclear staining fractions to a whole cell, the total percentage of three lineages was regarded as 100% because the telencephalon is subdivided by a transcriptional code, which is composed of Pax6, Gsx2, and Nkx2-1 (Rallu et al., 2002a,b; Schuurmans and Guillemot, 2002; Corbin et al., 2003). The percentage of Lmx1a$^+$ and Foxg1$^+$ positive fractions was calculated among whole aggregates (**Figure 5**) or among nuclear staining Sox2$^+$ area (**Figure 6**). Five to eight aggregates from three or four biological replicates were analyzed.

Quantitative Polymerase Chain Reaction

qPCR was performed using the ViiA7 Real-Time PCR System (Thermo Fisher Scientific). ES cells under maintenance culture (referred to as day 0) or cell aggregates under differentiation culture on days 3, 4, 5, 6, and 7 were harvested, and total RNAs were sampled for the qPCR study. Cell aggregates treated with SHHi during days 5–7 were harvested on days 6 and 7. Expression levels of target genes were obtained from duplicated, three biological replicates and shown as relative values, based on the expression of beta-actin (as an internal control). Primers used were as follows: beta-actin, forward 5′-AAGGCCAACC GTGAAAAGAT-3′, reverse 5′-GTGGTACGACCAGAGGCAT AC-3′; Bmp4, forward 5′-GCTGGAATGATTGGATTGTG-3′, reverse 5′-CATGGTTGGTTGAGTTGAGG-3′; Shh, forward 5′-TTCTGTGAAAGCAGAGAACTCC-3′, reverse 5′-GGGAC GTAAGTCCTTCACCA-3′; Tgfb1, forward 5′-TACCATGCC AACTTCTGTCTGGGA-3′, reverse 5′-ATGTTGGACAACTGC TCCACCTTG-3′; Wnt3a, forward 5′-GAACCGTCACAAC AATGAGG-3′, reverse 5′-CTTCACAGCTGCCAGATAGC-3′; Gli1, forward 5′-CCAAGCCAACTTTATGTCAGGG-3′, reverse 5′-AGCCCGCTTCTTTGTTAATTTGA-3′; Ptc1, forward 5′-CG AGACCAACGTGGAGGAGC-3′, reverse 5′-GGAGTCTGTA TCATGAGTTGAGG-3′; Smo, forward 5′-GGAGGGTTCCC AGGGTTGAA-3′, reverse 5′-GCCCCTCGACTCCCAACTT-3′.

Western Blotting

Cell aggregates treated with or without inhibitors from day 5 were dissociated using TrypLE Express Enzyme (Thermo Fisher Scientific) on day 6 and lysed in radioimmunoprecipitation assay buffer containing 50-mM Tris hydrochloride (pH 7.6), 150-mM sodium chloride, 1% Nonidet P40, 0.5% sodium deoxycholate, and 0.1% sodium dodecyl sulfate with protease inhibitor cocktail (Nacalai) and ethylenediaminetetraacetic acid-free phosphatase inhibitor cocktail (Nacalai). A total of 2.7–9.0 μg of protein extracts were separated by 10% sodium dodecyl sulfate–polyacrylamide gel electrophoresis and blotted onto polyvinylidene fluoride membrane (Merck, Immobilon). Three biological replicates were analyzed. The following primary antibodies were used at the indicated dilutions: anti-beta-actin (rabbit, 1:1,000; Cell Signaling, 4970), anti-beta-catenin (rabbit, 1:1,000; Cell Signaling, 8480), anti-phospho-Smad1/5 (rabbit, 1:1,000; Cell Signaling, 9516), and anti-phospho-Smad2 (rabbit, 1:1,000; Cell Signaling, 3108). Anti-rabbit IgG, HRP-linked antibody (rabbit, 1:2,000; Cell Signaling, 7074) was used as a secondary antibody. The blocking buffer used was Western BLoT Immuno Booster (TaKaRa). The chemiluminescent substrate used was Western BLoT Ultra-Sensitive HRP Substrate (TaKaRa). The chemiluminescent signal was detected using LAS 4000mini (Cytiva) and analyzed using ImageJ.

Statistical Analyses

All statistical tests were conducted using R. Multiple-group means were compared by one-way ANOVA with *post hoc* Dunnett's test (**Figures 2**, **5**, **7**) or Williams' tests (**Figure 4**) for pairwise comparisons or by two-way ANOVA with *post hoc* Dunnett's test (**Figure 6**). Frequencies were compared by Fisher's exact test (**Figure 2**). A $P < 0.05$ (two-tailed) was considered significant for all tests.

DATA AVAILABILITY STATEMENT

The original contributions presented in the study are included in the article/**Supplementary Material**, further inquiries can be directed to the corresponding author/s.

ETHICS STATEMENT

The animal study was reviewed and approved by the Animal Care and Use Committee of Kumamoto University.

AUTHOR CONTRIBUTIONS

MN conceived and designed the research, performed all experiments and analyses, and wrote the manuscript. SE, JH, and NT helped to perform the experiments. KS contributed to finalizing the manuscript. All authors contributed to the article and approved the submitted version.

FUNDING

This work was supported by the JSPS KAKENHI Grant Number JP15K18957 (MN) and MEXT KAKENHI Grant Numbers 17H05771 and 19H04784 (JH) and funded by the Center for Metabolic Regulation of Healthy Aging, Kumamoto University.

ACKNOWLEDGMENTS

We are grateful to Dr. Haruka Sato for her valuable comments. We would like to thank Hiromi Kitahara for technical assistance. We would like to thank Enago (www.enago.jp) for the English language review.

SUPPLEMENTARY MATERIAL

The Supplementary Material for this article can be found online at: https://www.frontiersin.org/articles/10.3389/fcell.2021.632381/full#supplementary-material

REFERENCES

Aldiri, I., Xu, B., Wang, L., Chen, X., Hiler, D., Griffiths, L., et al. (2017). The dynamic epigenetic landscape of the retina during development, reprogramming, and tumorigenesis. *Neuron* 94, 550–568.e10. doi: 10.1016/j.neuron.2017.04.022

Arber, C., Precious, S. V., Cambray, S., Risner-Janiczek, J. R., Kelly, C., Noakes, Z., et al. (2015). Activin A directs striatal projection neuron differentiation of human pluripotent stem cells. *Development* 142, 1375–1386. doi: 10.1242/dev.117093

Backman, M., Machon, O., Mygland, L., Van Den Johannes, C. J., Zhong, W., et al. (2005). Effects of canonical Wnt signaling on dorso-ventral specification of the mouse telencephalon. *Dev. Biol.* 279, 155–168. doi: 10.1016/j.ydbio.2004.12.010

Bertacchi, M., Pandolfini, L., D'Onofrio, M., Brandi, R., and Cremisi, F. (2015). The double inhibition of endogenously produced bmp and wnt factors synergistically triggers dorsal telencephalic differentiation of mouse es cells. *Dev. Neurobiol.* 75, 66–79. doi: 10.1002/dneu.22209

Cambray, S., Arber, C., Little, G., Dougalis, A. G., de Paola, V., Ungless, M. A., et al. (2012). Activin induces cortical interneuron identity and differentiation in embryonic stem cell-derived telencephalic neural precursors. *Nat. Commun.* 3:841. doi: 10.1038/ncomms1817

Campbell, K. (2003). Dorsal-ventral patterning in the mammalian telencephalon. *Curr. Opin. Neurobiol.* 13, 50–56. doi: 10.1016/S0959-4388(03)00009-6

Chen, B., Dodge, M. E., Tang, W., Lu, J., Ma, Z., Fan, C., et al. (2009). Small molecule-mediated disruption of Wnt-dependent signaling in tissue regeneration and cancer. *Nat. Chem. Biol.* 5, 100–107. doi: 10.1038/nchembio.137

Corbin, J. G., Gaiano, N., Machold, R. P., Langston, A., and Fishell, G. (2000). The Gsh2 homeodomain gene controls multiple aspects of telencephalic development. *Development* 127, 5007–5020.

Corbin, J. G., Rutlin, M., Gaiano, N., and Fishell, G. (2003). Combinatorial function of the homeodomain proteins Nkx2.1 and Gsh2 in ventral telencephalic patterning. *Development* 130, 4895–4906. doi: 10.1242/dev.00717

Danjo, T., Eiraku, M., Muguruma, K., Watanabe, K., Kawada, M., Yanagawa, Y., et al. (2011). Subregional specification of embryonic stem cell-derived ventral telencephalic tissues by timed and combinatory treatment with extrinsic signals. *J. Neurosci.* 31, 1919–1933. doi: 10.1523/JNEUROSCI.5128-10.2011

Dessaud, E., Yang, L. L., Hill, K., Cox, B., Ulloa, F., Ribeiro, A., et al. (2007). Interpretation of the sonic hedgehog morphogen gradient by a temporal adaptation mechanism. *Nature* 450, 717–720. doi: 10.1038/nature06347

Eiraku, M., Watanabe, K., Matsuo-Takasaki, M., Kawada, M., Yonemura, S., Matsumura, M., et al. (2008). Self-organized formation of polarized cortical tissues from ESCs and its active manipulation by extrinsic signals. *Cell Stem Cell* 3, 519–532. doi: 10.1016/j.stem.2008.09.002

Fuccillo, M., Rallu, M., McMahon, A. P., and Fishell, G. (2004). Temporal requirement for hedgehog signaling in ventral telencephalic patterning. *Development* 131, 5031–5040. doi: 10.1242/dev.01349

Hébert, J. M., Mishina, Y., and McConnell, S. K. (2002). BMP signaling is required locally to pattern the dorsal telencephalic midline. *Neuron* 35, 1029–1041. doi: 10.1016/S0896-6273(02)00900-5

Hirabayashi, Y., Suzki, N., Tsuboi, M., Endo, T. A., Toyoda, T., Shinga, J., et al. (2009). Polycomb limits the neurogenic competence of neural precursor cells to promote astrogenic fate transition. *Neuron* 63, 600–613. doi: 10.1016/j.neuron.2009.08.021

Imayoshi, I., Shimogori, T., Ohtsuka, T., and Kageyama, R. (2008). Hes genes and neurogenin regulate non-neural versus neural fate specification in the dorsal telencephalic midline. *Development* 135, 2531–2541. doi: 10.1242/dev.021535

Lek, M., Dias, J. M., Marklund, U., Uhde, C. W., Kurdija, S., Lei, Q., et al. (2010). A homeodomain feedback circuit underlies step-function interpretation of a Shh morphogen gradient during ventral neural patterning. *Development* 137, 4051–4060. doi: 10.1242/dev.054288

Marín, O., and Rubenstein, J. L. R. (2001). A long, remarkable journey: tangential migration in the telencephalon. *Nat. Rev. Neurosci.* 2, 780–790.

Maroof, A. M., Keros, S., Tyson, J. A., Ying, S.-W., Ganat, Y. M., Merkle, F. T., et al. (2013). Directed differentiation and functional maturation of cortical interneurons from human embryonic stem cells. *Cell Stem Cell* 12, 559–572. doi: 10.1016/j.stem.2013.04.008

Medina, L., and Abellán, A. (2009). Development and evolution of the pallium. *Semin. Cell Dev. Biol* 20, 698–711. doi: 10.1016/j.semcdb.2009.04.008

Métin, C., Baudoin, J.-P., Rakiæ, S., and Parnavelas, J. G. (2006). Cell and molecular mechanisms involved in the migration of cortical interneurons. *Eur. J. Neurosci.* 23, 894–900. doi: 10.1111/j.1460-9568.2006.04630.x

Moore, S., Ribes, V., Terriente, J., Wilkinson, D., Relaix, F., and Briscoe, J. (2013). Distinct regulatory mechanisms act to establish and maintain pax3 expression in the developing neural tube. *PLoS Genet.* 9:e1003811. doi: 10.1371/journal.pgen.1003811

Morikawa, M., Koinuma, D., Mizutani, A., Kawasaki, N., Holmborn, K., Sundqvist, A., et al. (2016). BMP sustains embryonic stem cell self-renewal through distinct functions of different krüppel-like factors. *Stem Cell Reports* 6, 64–73. doi: 10.1016/j.stemcr.2015.12.004

Nasu, M., Shimamura, K., Esumi, S., and Tamamaki, N. (2020a). Sequential pattern of sublayer formation in the paleocortex and neocortex. *Med. Mol. Morphol.* 53, 168–176. doi: 10.1007/s00795-020-00245-7

Nasu, M., Shimamura, K., Esumi, S., and Tamamaki, N. (2020b). Formation of dorsal–ventral axis of the pallium derived from mouse embryonic stem cells. *Biochem. Biophys. Res. Commun.* 524, 117–122. doi: 10.1016/j.bbrc.2020.01.070

Nasu, M., Takata, N., Danjo, T., Sakaguchi, H., Kadoshima, T., Futaki, S., et al. (2012). Robust formation and maintenance of continuous stratified cortical neuroepithelium by laminin-containing matrix in mouse ES cell culture. *PLoS One* 7:e53024. doi: 10.1371/journal.pone.0053024

Naujok, O., Lentes, J., Diekmann, U., Davenport, C., and Lenzen, S. (2014). Cytotoxicity and activation of the Wnt/beta-catenin pathway in mouse embryonic stem cells treated with four GSK3 inhibitors. *BMC Res. Notes* 7:273. doi: 10.1186/1756-0500-7-273

Nery, S., Wichterle, H., and Fishell, G. (2001). Sonic hedgehog contributes to oligodendrocyte specification in the mammalian forebrain. *Development* 128, 527–540.

Rallu, M., Corbin, J. G., and Fishell, G. (2002a). Parsing the prosencephalon. *Nat. Rev. Neurosci.* 3, 943–951. doi: 10.1038/nrn989

Rallu, M., Machold, R., Gaiano, N., Corbin, J. G., and Mcmahon, A. P. (2002b). Dorsoventral patterning is established in the telencephalon of mutants lacking both Gli3 and Hedgehog signaling. *Development* 129, 4963–4974.

Ribes, V., and Briscoe, J. (2009). Establishing and interpreting graded Sonic Hedgehog signaling during vertebrate neural tube patterning: the role of negative feedback. *Cold Spring Harb. Perspect. Biol.* 1:a002014. doi: 10.1101/cshperspect.a002014

Rogers, K. W., and Schier, A. F. (2011). Morphogen gradients: from generation to interpretation. *Annu. Rev. Cell Dev. Biol.* 27, 377–407. doi: 10.1146/annurev-cellbio-092910-154148

Sagner, A., and Briscoe, J. (2017). Morphogen interpretation: concentration, time, competence, and signaling dynamics. *Wiley Interdiscip. Rev. Dev. Biol.* 6:e271. doi: 10.1002/wdev.271

Sasai, N., Kutejova, E., and Briscoe, J. (2014). Integration of signals along orthogonal axes of the vertebrate neural tube controls progenitor competence and increases cell diversity. *PLoS Biol.* 12:e1001907. doi: 10.1371/journal.pbio.1001907

Schuurmans, C., and Guillemot, F. (2002). Molecular mechanisms underlying cell fate specification in the developing telencephalon. *Curr. Opin. Neurobiol.* 12, 26–34. doi: 10.1016/S0959-4388(02)00286-6

Shimamura, K., Hartigan, D. J., Martinez, S., Puelles, L., and Rubenstein, J. L. (1995). Longitudinal organization of the anterior neural plate and neural tube. *Development* 121, 3923–3933.

Shindo, Y., Iwamoto, K., Mouri, K., Hibino, K., Tomita, M., Kosako, H., et al. (2016). Conversion of graded phosphorylation into switch-like nuclear translocation via autoregulatory mechanisms in ERK signalling. *Nat. Commun.* 7:10485. doi: 10.1038/ncomms10485

Sousa, V. H., and Fishell, G. (2010). Sonic hedgehog functions through dynamic changes in temporal competence in the developing forebrain. *Curr. Opin. Genet. Dev.* 20, 391–399. doi: 10.1016/j.gde.2010.04.008

Srinivasan, S., Hu, J. S., Currle, D. S., Fung, E. S., Hayes, W. B., Lander, A. D., et al. (2014). A BMP-FGF morphogen toggle switch drives the ultrasensitive expression of multiple genes in the developing forebrain. *PLoS Comput. Biol.* 10:e1003463. doi: 10.1371/journal.pcbi.1003463

Subramanian, L., and Tole, S. (2009). Mechanisms underlying the specification, positional regulation, and function of the cortical hem. *Cereb. Cortex.* 19, 90–95. doi: 10.1093/cercor/bhp031

Sussel, L., Marin, O., Kimura, S., and Rubenstein, J. L. R. (1999). Loss of Nkx2 . 1 homeobox gene function results in a ventral to dorsal molecular respecification within the basal telencephalon: evidence for a transformation of the pallidum into the striatum. *Development* 126, 3359–3370.

Tamamaki, N., Fujimori, K. E., and Takauji, R. (1997). Origin and route of tangentially migrating neurons in the developing neocortical intermediate zone. *J. Neurosci.* 17, 8313–8323.

Thomas, T., and Dziadek, M. (1993). Capacity to form choroid plexus-like cells in vitro is restricted to specific regions of the mouse neural ectoderm. *Development* 117, 253–262.

Toresson, H., Potter, S. S., and Campbell, K. (2000). Genetic control of dorsal-ventral identity in the telencephalon: opposing roles for Pax6 and Gsh2. 127, 4361–4371.

Tyson, J. A., Goldberg, E. M., Maroof, A. M., Xu, Q., Petros, T. J., and Anderson, S. A. (2015). Duration of culture and sonic hedgehog signaling differentially specify PV versus SST cortical interneuron fates from embryonic stem cells. *Development* 142, 1267–1278. doi: 10.1242/dev.111526

van Boxtel, A. L., Chesebro, J. E., Heliot, C., Ramel, M. C., Stone, R. K., and Hill, C. S. (2015). A temporal window for signal activation dictates the dimensions of a nodal signaling domain. *Dev. Cell.* 35, 175–185. doi: 10.1016/j.devcel.2015.09.014

Watanabe, K., Kamiya, D., Nishiyama, A., Katayama, T., Nozaki, S., Kawasaki, H., et al. (2005). Directed differentiation of telencephalic precursors from embryonic stem cells. *Nat. Neurosci.* 8, 288–296. doi: 10.1038/nn1402

Watanabe, M., Kang, Y.-J., Davies, L. M., Meghpara, S., Lau, K., Chung, C.-Y., et al. (2012). BMP4 sufficiency to induce choroid plexus epithelial fate from embryonic stem cell-derived neuroepithelial progenitors. *J. Neurosci.* 32, 15934–15945. doi: 10.1523/JNEUROSCI.3227-12.2012

Wilson, S. W., and Rubenstein, J. L. R. (2000). Induction and dorsoventral patterning of the telencephalon. *Neuron* 28, 641–651. doi: 10.1016/S0896-6273(00)00171-9

Wolpert, L. (1969). Positional information and the spatial pattern of cellular differentiation. *J. Theor. Biol.* 25, 1–47. doi: 10.1016/S0022-5193(69)80016-0

Wonders, C. P., and Anderson, S. A. (2006). The origin and specification of cortical interneurons. *Nat. Rev. Neurosci.* 7, 687–696. doi: 10.1038/nrn1954

Wu, S., Esumi, S., Watanabe, K., Chen, J., Nakamura, K. C., Nakamura, K., et al. (2011). Tangential migration and proliferation of intermediate progenitors of

GABAergic neurons in the mouse telencephalon. *Development* 138, 2499–2509. doi: 10.1242/dev.063032

Xu, Q., Guo, L., Moore, H., Waclaw, R. R., Campbell, K., and Anderson, S. A. (2010). Sonic hedgehog signaling confers ventral telencephalic progenitors with distinct cortical interneuron fates. *Neuron* 65, 328–340. doi: 10.1016/j.neuron.2010.01.004

Xu, Q., Tam, M., and Anderson, S. A. (2008). Fate mapping Nkx2.1-lineage cells in the mouse telencephalon. *J. Comp. Neurol.* 506, 16–29. doi: 10.1002/cne.21529

Xu, Q., Wonders, C. P., and Anderson, S. A. (2005). Sonic hedgehog maintains the identity of cortical interneuron progenitors in the ventral telencephalon. *Development* 132, 4987–4998. doi: 10.1242/dev.02090

Yun, K., Potter, S., and Rubenstein, J. L. R. (2001). Gsh2 and Pax6 play complementary roles in dorsoventral patterning of the mammalian telencephalon. *Development* 128, 193–205.

Zhang, Q., Andersen, M. E., and Conolly, R. B. (2006). Binary gene induction and protein expression in individual cells. *Theor. Biol. Med. Model.* 3:18. doi: 10.1186/1742-4682-3-18

Conflict of Interest: The authors declare that the research was conducted in the absence of any commercial or financial relationships that could be construed as a potential conflict of interest.

frontiers
in Cell and Developmental Biology

PERSPECTIVE
published: 14 June 2021
doi: 10.3389/fcell.2021.679226

Perspective: Extending the Utility of Three-Dimensional Organoids by Tissue Clearing Technologies

Etsuo A. Susaki[1,2]* *and Minoru Takasato*[3,4]

[1] Department of Biochemistry and Systems Biomedicine, Graduate School of Medicine, Juntendo University, Tokyo, Japan, [2] Laboratory for Synthetic Biology, RIKEN Center for Biosystems Dynamics Research, Osaka, Japan, [3] Laboratory for Human Organogenesis, RIKEN Center for Biosystems Dynamics Research, Kobe, Japan, [4] Laboratory of Molecular Cell Biology and Development, Department of Animal Development and Physiology, Graduate School of Biostudies, Kyoto University, Kyoto, Japan

An organoid, a self-organizing organ-like tissue developed from stem cells, can exhibit a miniaturized three-dimensional (3D) structure and part of the physiological functions of the original organ. Due to the reproducibility of tissue complexity and ease of handling, organoids have replaced real organs and animals for a variety of uses, such as investigations of the mechanisms of organogenesis and disease onset, and screening of drug effects and/or toxicity. The recent advent of tissue clearing and 3D imaging techniques have great potential contributions to organoid studies by allowing the collection and analysis of 3D images of whole organoids with a reasonable throughput and thus can expand the means of examining the 3D architecture, cellular components, and variability among organoids. Genetic and histological cell-labeling methods, together with organoid clearing, also allow visualization of critical structures and cellular components within organoids. The collected 3D data may enable image analysis to quantitatively assess structures within organoids and sensitively/effectively detect abnormalities caused by perturbations. These capabilities of tissue/organoid clearing and 3D imaging techniques not only extend the utility of organoids in basic biology but can also be applied for quality control of clinical organoid production and large-scale drug screening.

Keywords: organoid, tissue clearing technique, 3D imaging, light-sheet fluorescence microscopy, omics

OPEN ACCESS

Edited by:
Silvia Garagna,
University of Pavia, Italy

Reviewed by:
Rajprasad Loganathan,
Johns Hopkins University,
United States
Giulia Fiorentino,
University of Pavia, Italy

****Correspondence:***
Etsuo A. Susaki
suishess-kyu@umin.ac.jp

Specialty section:
This article was submitted to Cell Growth and Division, a section of the journal Frontiers in Cell and Developmental Biology

Received: *11 March 2021*
Accepted: *11 May 2021*
Published: *14 June 2021*

Citation:
Susaki EA and Takasato M (2021) Perspective: Extending the Utility of Three-Dimensional Organoids by Tissue Clearing Technologies. Front. Cell Dev. Biol. 9:679226. doi: 10.3389/fcell.2021.679226

INTRODUCTION

Directed differentiation of human pluripotent stem cells (PSCs) to generate target organ cells is currently the most promising method to create artificial organs for regenerative medicine. To date, various cell types of target organs have been induced, including those of the blood, myocardium, lung, pancreas, liver, intestine, brain, and kidney (Wang et al., 2007; Davis et al., 2008; Yang et al., 2008; Xia and Zhang, 2009; Spence et al., 2011; Pagliuca et al., 2014; Takasato et al., 2014). However, reproducing the original function of organs with the use of differentiated cells remains a significant challenge, as correct replication of the three-dimensional (3D) structures of the original organ is essential.

A method to create 3D mini-organs from human PSCs has continued to attract attention in recent years. When organ-specific progenitor cells derived from human PSCs are aggregated and cultured under 3D culture conditions, the progenitor cells undergo self-organization within the aggregate to form organ-specific tissues in the same manner that occurs during ontogenesis. Such aggregates are called *organoids*. Ocular organoids were the first to be generated, which was followed by the creation of gastric, liver, brain, intestinal, and renal organoids (Eiraku et al., 2011; Lancaster et al., 2013; Takebe et al., 2013; McCracken et al., 2014; Takasato et al., 2015). Organoids can potentially contribute to various fields of research, including tissue physiology, stem cell biology, developmental biology, disease modeling, drug discovery, and regenerative medicine (Foglietta et al., 2020; Grenier et al., 2020; Li et al., 2020; Bock et al., 2021).

Due to the intrinsic 3D organ-like architecture of organoids with random coordinates in contrast to the corresponding native tissues, 3D observation is essential to obtain accurate structural information of dynamic 3D events (Rios and Clevers, 2018). However, the intense scattering of light within organoids limits 3D observation to the sub-millimeter range from the surface. In addition, 3D reconstitution by serial sectioning is arduous due to the fragility of organoids, which leads to deformation and fracturing of the sample, resulting in insufficient resolution, low contrast, and lack of internal 3D characterization (Pampaloni et al., 2013; Renner et al., 2017). A biased sampling of two-dimensional sections may result in inaccurate quantitative data with large standard deviations (Albanese et al., 2020).

Recent tissue clearing and 3D imaging technologies have the potential to solve these problems and provide system-level single-cell analysis of whole multicellular structures. 3D imaging of large tissue samples of whole organs and bodies has already been established by combining efficient tissue clearing protocols and optical microscopy, which provides useful information of the unique 3D structures of biological tissues by collecting images of the entire sample (Susaki and Ueda, 2016; Ueda et al., 2020a,b). In addition, tissue clearing protocols for spheroids and organoids have been developed and even applied in recent studies (Costa et al., 2019). Although each tissue clearing protocol has unique advantages and disadvantages, optimization of relatively small organoid samples is easier than that of large and complicated animal tissues. Besides, detailed 3D analysis of a single organoid can expedite the clearing and 3D imaging framework for a large-scale multi-organoid screening approach to assess genetic or pharmacological perturbations. Therefore, the aim of this perspective is to summarize recent adaptations and prospects of tissue clearing and 3D imaging frameworks in organoid research.

Brief Overview of Modern Tissue Clearing Technologies

Tissue clearing is basically an extension of the conventional histology technique that literally makes tissue "transparent" by suppressing light scattering and light absorption in the fixed tissue sample. Since Lundvall and Spalteholz initialized clearing of human tissues with the use of organic solvents more than 100 years ago (Lundvall, 1905; Spalteholz, 1914), the field has achieved dramatic innovations in the last few decades, as dozens of protocols, categorized as organic solvent (hydrophobic reagent)-based protocols, hydrophilic reagent-based protocols, and hydrogel-tissue chemistry (Ueda et al., 2020a,b), have been recently established.

Optical clearing generally involves exchanging the surrounding medium (e.g., phosphate-buffered saline) with a solvent with optical properties similar to those of the biomaterial. This step is called refractive index (RI) matching because the RI is a preferred indicator of optical properties. However, this process is relatively complex physicochemically and not necessarily limited to RI homogenization, as dispersion of the fibrous structures of the extracellular matrix and the affinity (infiltration) of compounds into living tissues may also have significant effects (Ueda et al., 2020a; Yu et al., 2021). RI matching can also be combined with other processes to remove light-scattering and light-absorbing substances from the biological tissue, such as lipids (delipidation), the bone matrix (decalcification), and pigments (decolorization or bleaching). The requirement of incorporating these steps is dependent on the experimental purpose and target tissue type. Tissue clearing protocols incorporate these steps by combining various compounds and physical techniques (e.g., electrophoresis).

Organic solvent-based tissue clearing protocols originating from the Spalteholz reagent are represented by the benzyl alcohol/benzyl benzoate (BABB) method, 3D imaging of solvent-cleared organs (3DISCO), and the ethyl-cinnamate (ECi) method (Dent et al., 1989; Becker et al., 2012; Ertürk et al., 2012; Klingberg et al., 2017). Generally, these protocols have very strong clearing abilities over relatively short periods of time. However, it is necessary to understand the characteristics of the reagents regarding tissue shrinkage, signal retention of fluorescent proteins, safety, and compatibility with the microscope system.

The hydrophilic reagent-based clearing technique was initially tested with the use of several hydrophilic chemicals (e.g., sugars and alcohols) to transluce human skin and sclera in medical applications (Bakutkin et al., 1995; Zimnyakov et al., 1996; Tuchin et al., 1997). Since then, a wide variety of hydrophilic reagent protocols have been proposed with the advantages of ease of handling, safety, and preservation capacity of biomaterials, which include FocusClear$^{\mathrm{TM}}$ (Chiang et al., 2001), Sca*l*e (Hama et al., 2011, 2015), *Clear^{T}* (Kuwajima et al., 2013), SeeDB (Ke et al., 2013, 2016), FRUIT (Hou et al., 2015), CUBIC (clear, unobstructed brain/body imaging cocktail and computational analysis) (Susaki et al., 2014; Tainaka et al., 2018), FUnGI (fructose, urea, and glycerol for imaging) (Rios et al., 2019), RTF (rapid clearing method based on triethanolamine and formamide) (Yu et al., 2018), Ce3D (clearing-enhanced 3D) (Li et al., 2017), and TDE (2,2′-thiodiethanol) immersion (Aoyagi et al., 2015).

Hydrogel-tissue chemistry involves the preparation of a tissue-hydrogel scaffold by cross-linking hydrogel monomers to native biomolecules (Gradinaru et al., 2018). The initial formulation, called CLARITY (and its variations), uses acrylamide, while later versions, SWITCH (Murray et al., 2015) and SHIELD (Park et al., 2018), utilize glutaraldehyde and a polyepoxide, respectively. Due to the increased tissue rigidity caused by transformation, these protocols can be combined with harsh delipidation or re-probing procedures with sodium dodecyl sulfate (SDS) and physical electrophoresis. Furthermore, the use of a water-absorbing polymer for Expansion Microscopy (ExM) enables high-resolution imaging with a general microscopy setup (Chen et al., 2015; Ku et al., 2016). The expansion can also contribute to the final transparency of the sample. Other hydrophilic clearing reagents have also applied the same strategy (Kim et al., 2018; Murakami et al., 2018; Tainaka et al., 2018).

Although limited to fixed samples, tissue clearing facilitates observation of the 3D architecture of biological tissues with a light microscope at the cellular or higher resolution, thereby providing a powerful analytical approach for complex biological systems.

Tissue Clearing Technologies in Organoid Studies

Clearing of cell reaggregates (spheroids and organoids) for whole-mount imaging was recommended in early protocols (Timmins and Nielsen, 2007). More recently, many of the clearing methods introduced in the previous section have been tested from simple whole-mount observations to advanced phenotyping of 3D cultured reaggregates (Costa et al., 2019; **Table 1**). Since most current clearing protocols are optimized for animal tissues and organs, clearing cell reaggregates with the use of any of these procedures is, in principle, much simpler. Although tissue clearing methods have been adopted at least to some extent, experience is required for further applications in broader organoid research.

A side-by-side comparison of protocols would be helpful to identify the clearing method that is most appropriate for a particular application. Boutin and Hoffman-Kim compared early phase hydrophilic clearing protocols (*Clear*^{T2}, Sca*l*eA2, and SeeDB) and concluded that *Clear*^{T2} is the most effective for clearing neural spheres (Boutin and Hoffman-Kim, 2015). However, in a later study, the authors also applied an updated Sca*l*e protocol (Sca*l*eS) for clearing of cancer cell spheroids (Boutin et al., 2018b). Cheung and colleagues compared SeeDB, *Clear*^{T2}, and Sca*l*eSQ for adaptation to an on-chip spheroid processing system and concluded that SeeDB and Sca*l*eSQ were more effective to clear a sample than *Clear*^{T2}, although there were some drawbacks of increased autofluorescence and sample expansion (Grist et al., 2016). Schöler, Bruder and colleagues compared the performance of the organic solvent reagent BABB with several other types of clearing reagents and found that BABB-based clearing proved to be both the fastest and most efficient for clearing of human midbrain organoids (Renner et al., 2020). Garfa-Traoré and colleagues compared several clearing methods (TDE, CUBIC, and RapiClear®) for murine intestinal organoids and obtained the best clearing and staining results with RapiClear® (Lallemant et al., 2020). Rudolf and colleagues tested several hydrophilic reagents and mounting media (glycerol, Sca*l*eS, *Clear*^{T2}, and CytoVista) for clearing of various spheroids and found that Sca*l*eS and a high concentration of glycerol (88% $RI = 1.459$) provided the best clearing results, while preserving the fluorescent signals and maintaining sample integrity, although various factors (i.e., size, complexity, and composition) affected the clearing results (Nürnberg et al., 2020). Another study suggested similar performance of glycerol ($>85\%$) and RapiClear® for clearing of pancreatic tumor spheroids (Steinberg et al., 2020). Lorenzo and colleagues demonstrated the effectiveness of both CUBIC and CLARITY for clearing of tumor cell spheroids (Masson et al., 2015).

These mixed results indicate that there is no "gold-standard" protocol for clearing of all cell reaggregates. As with the clearing of large tissue samples, it is necessary to choose an appropriate protocol in consideration of the pros and cons. The complexity of a reaggregate can affect the efficiency of optical clearing (Nürnberg et al., 2020) and thus may occasionally require delipidation. For example, Paşca and colleagues clearly and quantitatively reproduced cortico-striatal projections in human induced PSC (iPSC)-derived cortico-striatal assembloids with the use of the latest CUBIC-L/R procedure (Miura et al., 2020). Chung and colleagues applied SHIELD technology to single-cell and cytoarchitecture combined with multiple labeling methods for analysis of organoids (Albanese et al., 2020). ExM (Chen et al., 2015) enables super-resolution imaging together with improved clearing and staining results. Brismar and colleagues applied ExM to probe labeling and for high-resolution imaging of tumor cell spheroids, and found that as compared to simpler clearing protocols, ExM improved antibody penetration and image resolution in deeper regions (Edwards et al., 2020).

Tailoring of key parameters (e.g., compound type, concentration, immersion time, and temperature) in the original protocol should also be taken into account. Correia and colleagues found that the molecular weight of polyethylene glycol in *Clear*^{T2} reagent can affect clearing and imaging quality (Costa et al., 2018b). Molley et al. (2020) used the Sca*l*eCUBIC-2 protocol for clearing of Matrigel-embedded microtumors with some modifications to timing, washing, and handling. Dekkers et al. (2019) designed a fructose-glycerol immersion method as a simple, non-toxic, optical clearing step for complete 3D imaging of fragile organoids. Later, the authors cleared human colonic organoids with their FUnGI clearing reagent that was originally developed for clearing of human cancer specimens (Rios et al., 2019; van Ineveld et al., 2020). Our group modified the delipidation stringency of our CUBIC protocol for clearing of large kidney organoids (**Figure 1**).

Other than clearing performance, the compatibility of the cell-labeling/probing methods and microscopy setup should also be considered, as discussed in the following sections.

Labeling of Spheroids and Organoids With Fluorescent Proteins and Probes

Since tissue clearing alone cannot label objects in a 3D structure, appropriate cell/structure labeling with a fluorescent protein (FP) or histological staining is also required for observation. Therefore, it is crucial to consider the compatibility of the tissue clearing technique with various labeling methods.

Conventional organic solvents show weak retention of FP signals. When using reagents in this category with FP labeling, more FP-compatible protocols (Schwarz et al., 2015; Pan et al., 2016; Qi et al., 2019) should be considered. Tanaka and colleagues recently improved the ECi method for clearing of FP-labeled organoids (Masselink et al., 2019). Alternatively, clearing

TABLE 1 | Recent tissue clearing applications in organoid research.

Method category	Protocol	Chemical	Applied reaggregates	References
Organic solvent-based method	BABB	Ethanol Hexane Benzyl benzoate Benzyl alcohol	Cultured cancer cell spheroids	Wenzel et al., 2014 Smyrek and Stelzer, 2017 Schmitz et al., 2017 Desmaison et al., 2018 Messal et al., 2021
			Human midbrain organoids	Renner et al., 2020
	3DISCO	Tetrahydroflurane Dichloromethane Dibenzylether	Human iPSC-derived retinal organoids	Reichman et al., 2017 Garita-Hernandez et al., 2018
	ECi method	Ethyl cinnamate	Human cerebral organoids	Masselink et al., 2019
			Human brain organoids co-cultured with patient-derived glioblastoma cells	Goranci-Buzhala et al., 2020
			Vascularized tumor and neural organoids	Wörsdörfer et al., 2019
Hydrophilic reagent-based method	Single chemical	Urea	Tumor cell spheroids	Wei et al., 2019
		Glycerol	Tumor cell spheroids	Timmins and Nielsen, 2007
			Various human cell spheroids	Nürnberg et al., 2020
			Pancreatic tumor cell spheroids	Steinberg et al., 2020
		TDE	Tissue spheroids	Paiè et al., 2016
	Clear^{T}	Formamide Polyethylene glycol	Rat neural cell and glioma cell spheroids	(Boutin and Hoffman-Kim, 2015; Boutin et al., 2018a)
			Human cell spheroids	Kabadi et al., 2015
			Human dermal fibroblast spheroids	Costa et al., 2018b
			Human Dermal Fibroblast spheroids	Costa et al., 2018a
	Sca*l*e	Urea Glycerol Triton X-100	Neural cell spheres	Boutin and Hoffman-Kim, 2015
	Sca*l*eS Sca*l*eSQ	Urea Sorbitol Glycerol DMSO Triton X-100	Various human cell spheroids	Nürnberg et al., 2020
			Cancer cell spheroids	Boutin et al., 2018b
			patient-derived lung tumor organoid	Takahashi et al., 2019
			Breast cancer spheroids	Grist et al., 2016
	SeeDB	D(-)-fructose	Breast cancer spheroids	Grist et al., 2016
	FUnGI	D(-)-fructose Glycerol Urea	Human colonic organoids	van Ineveld et al., 2020
	FRUIT	D(-)-fructose Urea	iPSC-derived human cerebral organoids co-cultured with Patient-derived glioblastoma cells	Krieger et al., 2020
	Fructose-glycerol (FG)	D-(-)-Fructose Glycerol	Human colonic organoids	Dekkers et al., 2019
	Sca*l*eCUBIC-1/2 (1st gen. CUBIC)	(Delipidation) Quadrol Urea Triton X-100 (RI matching) Triethanolamine Urea Sucrose	Tumor cell spheroids	Masson et al., 2015
			Cancer cell spheroids	Kang et al., 2020
			Human iPSC-derived ureteric bud organoids	Mae et al., 2020
			Matrigel-embedded tumor cell spheroids	Molley et al., 2020
	CUBIC-L/R (2nd gen. CUBIC)	(Delipidation) N-butyldiethanolamine Triton X-100 (RI matching) Nicotinamide N-methylnicotinamide Antipyrine	Human iPSC-derived cortico-striatal assembroids	Miura et al., 2020

(Continued)

TABLE 1 | Continued

Method category	Protocol	Chemical	Applied reaggregates	References
	RTF	Triethanolamine Formamide	Brain organoids	Rakotoson et al., 2019
	FocusClear$^{\mathrm{TM}}$*	Diatrizoic acid Tween 20	Human intestinal crypt organoids	Chen et al., 2013
	PROTOS**	Diatrizoic acid N-methyl-D-glucamine Iodixanol	Murine intestinal organoids	Serra et al., 2019
	RapiClear®***		Murine intestinal organoids Pancreatic tumor cell spheroids Human iPSC-derived brain spheroids	Lallemant et al., 2020 Steinberg et al., 2020 Govindan et al., 2021
Hydrogel-tissue chemistry	CLARITY/PACT	Hydrogel embedding (Delipidation) SDS (RI matching) Histodenz$^{\mathrm{TM}}$ Glycerol	Tumor cell spheroids Murine/human cell spheroids Adipose-derived stem cell spheroids Human ESC-derived cerebral organoids Human iPSC-derived retinal organoids	Masson et al., 2015 Chen et al., 2016 Silva Santisteban et al., 2017 Sakaguchi et al., 2019 Cora et al., 2019
	SWITCH	Glutaraldehyde cross-linking (Delipidation) SDS (RI matching) Diatrizoic acid N-methyl-D-glucamine Iodixanol	Human ESC-derived cerebral organoids	Renner et al., 2017
	SHIELD	Polyepoxy cross-linking (Delipidation) SDS (RI matching) Diatrizoic acid N-methyl-D-glucamine Iodixanol	Human iPSC-derived cerebral organoids	Albanese et al., 2020
	ExM	Hydrogel embedding (RI matching) Expansion in water	Tumor cell spheroids	Edwards et al., 2020

**A commercialized proprietary reagent provided by CelExplorer Labs Co. (Hsinchu, Taiwan). **This reagent was initially developed for samples prepared by hydrogel-tissue chemistry. ***A commercialized proprietary reagent provided by SunJin Lab Co. (Hsinchu, Taiwan).*

with hydrophilic reagents or tissue-hydrogel chemistry methods that generally retain FP signals should be considered. In this regard, some methods strictly compared the performance of keeping FP protein signals with other clearing protocols. For example, Ce3D has a superior ability to FP preservation when compared to major clearing methodologies (BABB, DISCO, Scal*e*, Scal*e*CUBIC, SeeDB, *Clear*^{T}, CLARITY, PACT, and SWITCH) (Li et al., 2017).

Whole-mount labeling of organoids with molecular probes (antibodies and small chemical dyes) has also been widely applied in many organoid studies. However, probe diffusion in 3D specimens is generally problematic, even in "small" cell reaggregates. For example, Smyrek and Stelzer investigated multiple whole-mount spheroid immunostaining parameters, including permeabilization, incubation time, and temperature, based on classical immunostaining procedures and proposed parameter guidelines (Smyrek and Stelzer, 2017). However, the signal intensity and homogeneity were varied and dependent on the antibody type and treatment protocol. Schöler, Bruder and colleagues very recently reported staining, clearing, and quantification analysis of relatively large (> 800 μm diameter) organoids (Renner et al., 2020). While the procedure was successfully automated, the protocol required a long incubation time (total 12 days for primary and secondary antibody staining) with multiple renewals of the staining reagents.

Various tissue clearing methods for large-scale 3D staining have been developed with improved efficiency and homogeneity. Recent developments of improved and more versatile 3D staining protocols, such as iDISCO, AbScal*e*/ChemScal*e*, SWITCH, and CUBIC-HistoVIsion (Renier et al., 2014, 2016; Hama et al., 2015; Murray et al., 2015; Susaki et al., 2020), have enabled large-scale 3D tissue staining. iDISCO, with optimized permeabilization and staining steps, enables immunostaining of whole mouse embryos and brains. AbScal*e*/ChemScal*e* utilizes urea to facilitate probe penetration via Scal*e* clearing technology. SWITCH modulates the kinetics of probe binding to tissue by two procedures: SWITCH-off

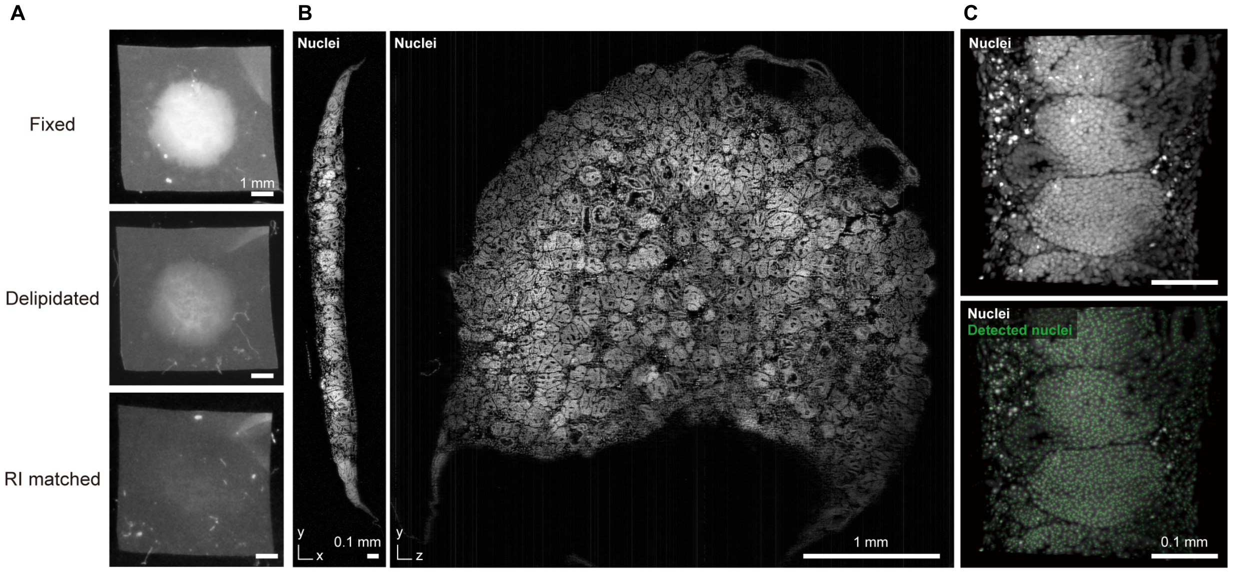

FIGURE 1 | CUBIC-clearing and 3D imaging of a whole human kidney organoid. **(A)** A human iPSC-derived large kidney organoid ($\varphi \sim 4$ mm, thickness $> 300\ \mu\text{m}$) (Takasato et al., 2016) is delipidated and RI-matched with a modified CUBIC-L/R protocol. **(B)** The cleared and propidium iodide-stained kidney organoid was imaged with a custom-built macrozoom LSFM (GEMINI system, Susaki et al., 2020) with a voxel resolution of $\sim 2.5\ \mu\text{m}^3$. **(C)** A part of the organoid image was subjected to nuclear coordinate detection (3D Maxima analysis, modified from our previously reported method (Susaki et al., 2020), which can be used for further 3D analysis of the cell architecture.

(inhibits probe binding) and SWITCH-on (facilitates probe binding). In our latest study on CUBIC-HistoVIsion, biological tissue was modeled as an electrolyte gel for screening of multiple essential 3D staining conditions that provides highly optimized 3D staining of cleared specimens of an entire organ and the whole body. However, the current protocol is not applicable to multiplex immunolabeling. Alternative protocols (e.g., Ce3D, SWITCH) can be considered to avoid this drawback. The incorporation of these recent 3D staining strategies can overcome the drawbacks of labeling entire organoids.

Several studies have applied these recent 3D staining protocols for labeling of whole organoids. For example, Takagi and colleagues applied AbSca*le* immunostaining together with Sca*le*S clearing to patient-derived tumor organoids for *in vitro* evaluation of molecularly targeted drugs (Takahashi et al., 2019). Another study employed AbSca*le* and Sca*le*S for staining and clearing of various human cell spheroids (Nürnberg et al., 2020). In addition, Ergun and colleagues applied an iDISCO-based whole-organoid procedure to stain vascularized tumors and neural organoids (Wörsdörfer et al., 2019). Moreover, for staining of human cerebral organoids, Chung and colleagues applied a modified eFLASH protocol that enables homogeneous staining of 8–10 whole organoids simultaneously in 1–2 days (Yun et al., 2019). The versatile staining ability of their SCOUT method further supports system-level analysis of the framework of 3D organoids (Albanese et al., 2020).

As in the case of FP, it should be noted that retention of the stained signals is dependent on the clearing reagents, as some may remove a portion of the staining target, while others may alter the binding affinity or antigenicity (Lallemant et al., 2020; Matryba et al., 2020). For example, the intensive comparison by Li et al. (2017) showed that the preservation degree of antigenicity toward major cell type markers in the lymph node is varied among tested methods. Antigen retrieval methods have been incorporated in some 3D staining and clearing protocols (Messal et al., 2021). After staining, cross-linking is occasionally required to preserve binding of the probe when clearing a specimen (Susaki et al., 2020).

3D Imaging of Cleared Spheroids and Organoids

The acquisition of whole-organoid information requires a proper 3D imaging setup. Besides conventional line-scan imaging, such as confocal and two-photon microscopy, light-sheet fluorescence microscopy (LSFM) is especially useful for 3D observation of cleared whole specimens. LSFM excites the fluorescent signals within the cleared sample with a sheet-shaped illumination and acquires section images with a vertically positioned complementary metal-oxide semiconductor (cMOS) or charge-coupled device (CCD) camera. This setup enables collection of high-throughput 3D images of the entire sample with minimal photodamage. LSFM has thus been proposed as the optimal modality for high-speed, high-quality 3D imaging of cleared samples, including spheroids and organoids (Dodt et al., 2007; Pampaloni et al., 2007; Keller and Stelzer, 2008; Santi, 2011; Keller and Dodt, 2012; Costa et al., 2019). As compared with confocal and two-photon microscopy, experimental studies have reported the superior speed and depth of LSFM for imaging of 3D organoids (Lallemant et al., 2020).

Custom-built LSFM systems have been reported in earlier studies. For example, a series of studies reported organoid/spheroid clearing with LSFM imaging using a monolithic digital scanned laser light-sheet-based fluorescence microscope (mDSLM) (Keller et al., 2008; Schmitz et al., 2017; Smyrek and Stelzer, 2017) and a millimeter-scaled optofluidic lab-on-a-chip device, which integrates light-sheet illumination and a microfluidic channel, for imaging of cell spheroids (Paiè et al., 2016). Moreover, Lorenzo and colleagues improved the resolution of 3D spheroid images using a light-sheet setup with adaptive optics (Masson et al., 2015). A specific light-sheet setup, such as a dual-view inverted selective plane illumination microscope (Kumar et al., 2014; Eismann et al., 2020), open-top LSFM (Glaser et al., 2019), and single-objective LSFM (Li et al., 2014; Bouchard et al., 2015), have the potential to enable large-scale imaging for screening purposes owing to the compatibility of these systems for imaging of multiple organoids cultured in multi-well plates.

With the commercialization of LSFMs, the opportunities of 3D organoid imaging with clearing are beginning to expand. The ZEISS Lightsheet Z.1 has been one of the most popular commercial LSFMs so far, enabling high-throughput multi-view 3D imaging with an easy-to-use operation (Cora et al., 2019; Dekkers et al., 2019; Sakaguchi et al., 2019; Lallemant et al., 2020; Molley et al., 2020; Preusser et al., 2020). However, the RI range of the equipped objective lens is up to 1.48, which is incompatible with some transparent reagents with an RI of > 1.5 and thus can cause the formation of spherical aberrations when imaging large samples at higher magnifications. The recently released Lightsheet 7 improves this issue with an RI range of 1.33–1.58, allowing the imaging of samples up to 2 cm in size with the use of almost any clearing reagent.

Regardless of the type of microscope used, the design of the entire experimental workflow should be optimized by selecting an appropriate clearing method, microscope setup, objective lens specification, and image resolution. Compatibility of some organic solvents (e.g., dibenzyl ether in iDISCO) with a commercialized LSFM should be taken into account, due to their corrosive effects such as dissolution of glues used in the construction of objective lenses (McKey et al., 2020). A proper optical resolution should also be set to meet the experimental and analytical objectives while avoiding oversampling. A high numerical aperture (NA) objective lens with a short working distance can also interfere with volume imaging. RI discrepancies between objective lens coverage and clearing reagents can reduce imaging quality due to spherical aberrations.

Whole imaging of a large kidney organoid that was generated from human iPS cells is depicted in **Figure 1** (Takasato et al., 2016). The sample was cleared with CUBIC reagent (final $RI = 1.52$) and 3D data were collected at a voxel resolution of 2.5 μm^3 to detect cell coordinates for subsequent cellular architecture analysis. Low magnification macro-objectives (NA $\sim$ 0.1) provide reasonable image quality and data size (15.5 GB for raw 16-bit TIFF data, 1.6 GB for processed 8-bit TIFF data) for this purpose. Oversampling microscopic images with excessive magnification and higher NA objectives will produce redundant data sets. For example, if an image is captured at 2.5 times the voxel resolution, the data size will be an order of magnitude larger ($2.5^3 = 15.625$), thereby burdening data storage and subsequent image analysis.

DISCUSSION: PROSPECTS OF ORGANOID RESEARCH WITH TISSUE CLEARING TECHNOLOGY

Any organoid application requires sensitive and accurate phenotyping. Here, organoid models of human diseases are discussed. For example, regarding the use of organoids to recapitulate microcephaly caused by the Zika virus (ZIKV), forebrain organoid size and neuronal proliferation have been assessed (Dang et al., 2016; Qian et al., 2016). That platform also showed an upregulation of the innate immune receptor Toll-like receptor 3 (TLR3) after ZIKV infection of human organoids. A pharmacological administration with a TLR3 competitive inhibitor reduced the phenotypic effects of ZIKV infection (Dang et al., 2016). A model of polycystic kidney disease was also replicated *in vitro* with the use of kidney organoids, where multiple cysts actually formed within the organoids generated from patient-derived iPSCs (Cruz et al., 2017; Low et al., 2019; Shimizu et al., 2020). Several drugs, such as thapsigargin, a non-competitive inhibitor of the sarco/endoplasmic reticulum Ca^{2+} ATPase, and CFTRinh–172, a selective CFTR channel inhibitor, are reported to inhibit the number and size of cysts in the disease model.

A recent study proposed that 3D information relevant to the pathophysiological processes and responses to perturbations (e.g., drug administration) is needed for further quantitative and comprehensive analysis of these *in vitro* disease models. Chung and colleagues developed a prominent SCOUT framework for whole 3D organoid phenotyping by clearing- and LSFM imaging-based multiple feature acquisition and atlas-independent analysis (Albanese et al., 2020). The use of SCOUT successfully extracted multiple features from the 3D dataset relevant to the developmental stages of the organoid and differences in protocols. Finally, SCOUT was applied to the ZIKV infection model to quantify the multiscale impact of ZIKV infection on brain development in the 3D datasets. The analysis produced a comprehensive quantification of the pathology, including cell loss, reduction of ventricles, and overall change in tissue reorganization. Assessment of other complex information, such as the 3D neural network structure, will potentially be integrated into future studies of cerebral organoids or cortico-striatal assembroids (Renner et al., 2017; Miura et al., 2020).

Apart from these disease models, imaging-based classification and clustering analysis of multiple organoid phenotypes for large-scale screening has also been proposed (Pampaloni et al., 2013) with a final aim to achieve classification and clustering

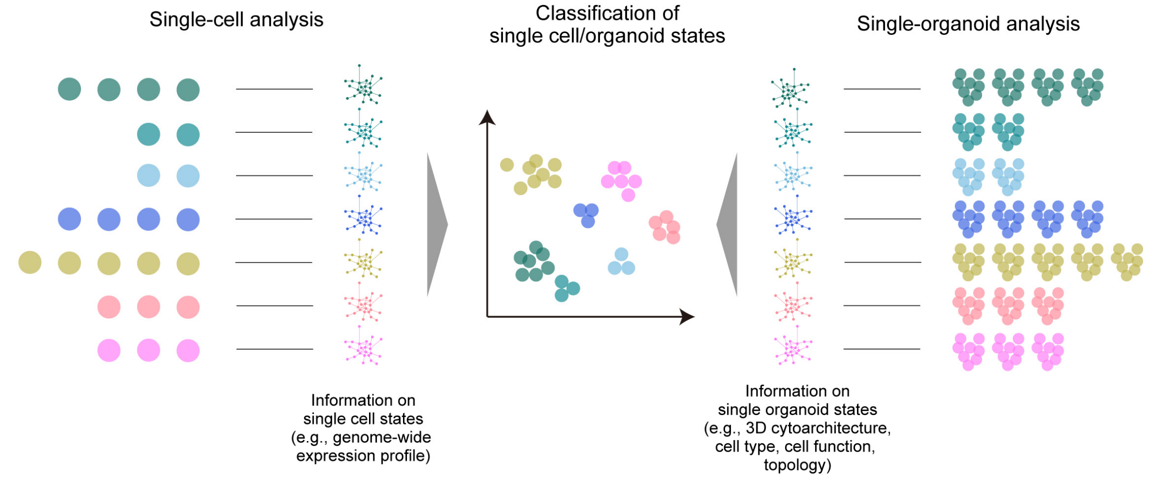

FIGURE 2 | A large-scale multi-organoid analysis. As in the case of single-cell analysis, in which various omics data (e.g., a genome-wide expression profile) are collected to determine the cell type or state, the states of multiple single organoids can be analyzed by collecting data of the 3D cytoarchitecture, distributions of identified cell types, or topological features. This information can be finally used for the classification and clustering of the organoid population.

of organoids based on the phenotype (i.e., organoid states), as with other omics analyses (**Figure 2**). Most studies so far have relied on the collection of various biological data within the organoids. As a representative approach, high-content imaging allows for high-throughput and multi-channel imaging data collection and analysis (Wenzel et al., 2014; Schmuck et al., 2017; Czerniecki et al., 2018; Durens et al., 2020). Recently, Lukonin et al. (2020) devised an imaging-based drug screening assay of approximately 450,000 intestinal organoids by extracting several features from the image (e.g., signal intensities of marker proteins, area, and circularity of the reaggregates) and clustering the organoids into 15 groups related to seven major phenotypes affected by the screened drugs. Tissue clearing techniques are beginning to be incorporated into such large-scale automated procedures for organoid screening (Silva Santisteban et al., 2017; Boutin et al., 2018b; Grenier et al., 2020; Renner et al., 2020; Rybin et al., 2021), which have been useful for the collection of comprehensive information across organoids and to improve screening accuracy. Histo-cytometry or proteomic imaging by multiplex and multi-modal labeling together with clearing can scale the amount of information (Murray et al., 2015; Li et al., 2017; Park et al., 2018).

The considerable data size and calculation throughput for clustering organoid phenotypes are possible drawbacks to large-scale screening with multi-modal information. Instead, organoid 3D data with less modality (e.g., a single channel of nuclear staining) may also provide sensitive information about the internal state. A simple topological analysis of all cell distribution within the 3D organoid by graph representation is a promising approach (Poli et al., 2019). A pioneering study by Stelzer and colleagues demonstrated multiscale analysis of individual and neighboring cells to the global topologies of optically cleared spheroids, and employed an analytical scheme inspired by graph theory and computational topology, in which all cell nuclei are segmented and represented as a cell graph for feature extraction (e.g., the relative position of each cell nucleus, the number of neighboring cells, and the distances to neighboring cells) (Schmitz et al., 2017). They also presented the possibility of multi-organoid clustering analysis based on the identified features. This proposed analytical scheme can alternatively offer an opportunity to classify the structural phenotypes (structural states) of multiple organoids based on mathematical topology analysis or machine learning-based feature extraction, which are occasionally independent of biological meanings. This scheme can, for example, enhance multi-organoid drug screening, which is currently dependent on classical dose-response curves (Broutier et al., 2017; Yan et al., 2018; Kopper et al., 2019; Takahashi et al., 2019). This 3D architecture-based classification and clustering methodology can also be readily combined with biological analyses of marker gene expression profiles, omics approaches, or physiological readout, further facilitating the extraction of essential molecular mechanisms. Tissue clearing technologies can fully support such large-scale, high-throughput topological analysis of multiple organoids in the future.

CONCLUSION

The examples described here provide a clear perspective of tissue clearing techniques as excellent tools for organoid research to facilitate the collection of biological profiles using organoids, understanding of pathophysiological processes, and the development of new therapeutic tools. 3D spatial interrogation of organoids can also be applied in larger projects, such as the Organoid Cell Atlas of the Human Cell Atlas

Project by providing references and workflows for comparing molecular expression patterns between organoids and cell populations in actual tissues/organs (Bock et al., 2021). Further accumulation of technical tips and applications will be needed in future efforts.

DATA AVAILABILITY STATEMENT

The raw data supporting the conclusions of this article will be made available by the authors, without undue reservation.

AUTHOR CONTRIBUTIONS

MT generated the kidney organoid. ES cleared and imaged the sample. Both authors contributed to the conception, writing, and review of the manuscript.

FUNDING

This work was supported by Grants-in-Aid for Scientific Research (B) (JSPS KAKENHI grant 19H03413 to ES), Grants-in-Aid for Scientific Research on Innovative Areas (JSPS KAKENHI grant 17H06328 to ES, 18H05108 to MT), and UTEC-UTokyo FSI Research Grant (to ES).

ACKNOWLEDGMENTS

We thank all of the laboratory members of The University of Tokyo and the RIKEN Center for Biosystems Dynamics Research (Dr. Hiroki Ueda lab); particularly, Y. Saito for her support in sample preparation and imaging. We also thank Oxford Instruments/Bitplane for instruction in operating the Imaris software. We also would like to thank Enago (www.Enago.jp) for the English language review.

REFERENCES

Albanese, A., Swaney, J. M., Yun, D. H., Evans, N. B., Antonucci, J. M., Velasco, S., et al. (2020). Multiscale 3D phenotyping of human cerebral organoids. *Sci. Rep.* 10:21487. doi: 10.1038/s41598-020-78130-7

Aoyagi, Y., Kawakami, R., Osanai, H., Hibi, T., and Nemoto, T. (2015). A rapid optical clearing protocol using 2,2'-thiodiethanol for microscopic observation of fixed mouse brain. *PLoS One* 10:e0116280. doi: 10.1371/journal.pone.0116280

Bakutkin, V. V., Maksimova, I. L., Semyonova, T. N., Tuchin, V. V., and Kon, I. L. (1995). "Controlling optical properties of sclera," in *Proceedings of the Ophthalmic Technologies V*, Vol. 2393, San Jose, CA. doi: 10.1117/12.209841

Becker, K., Jährling, N., Saghafi, S., Weiler, R., and Dodt, H. U. (2012). Chemical clearing and dehydration of GFP expressing mouse brains. *PLoS One* 7:e33916. doi: 10.1371/annotation/17e5ee57-fd17-40d7-a52c-fb6f86980def

Bock, C., Boutros, M., Camp, J. G., Clarke, L., Clevers, H., Knoblich, J. A., et al. (2021). The Organoid Cell Atlas. *Nat. Biotechnol.* 39, 13–17. doi: 10.1038/s41587-020-00762-x

Bouchard, M. B., Voleti, V., Mendes, C. S., Lacefield, C., Grueber, W. B., Mann, R. S., et al. (2015). Swept confocally-aligned planar excitation (SCAPE) microscopy for high speed volumetric imaging of behaving organisms. *Nat. Photonics* 9, 113–119. doi: 10.1038/nphoton.2014.323

Boutin, M. E., and Hoffman-Kim, D. (2015). Application and assessment of optical clearing methods for imaging of tissue-engineered neural stem cell spheres. *Tissue Eng. Part C Methods* 21, 292–302. doi: 10.1089/ten.tec.2014.0296

Boutin, M. E., Kramer, L. L., Livi, L. L., Brown, T., Moore, C., and Hoffman-Kim, D. (2018a). A three-dimensional neural spheroid model for capillary-like network formation. *J. Neurosci. Methods* 299, 55–63. doi: 10.1016/j.jneumeth.2017.01.014

Boutin, M. E., Voss, T. C., Titus, S. A., Cruz-Gutierrez, K., Michael, S., and Ferrer, M. (2018b). A high-throughput imaging and nuclear segmentation analysis protocol for cleared 3D culture models. *Sci. Rep.* 8:11135. doi: 10.1038/s41598-018-29169-0

Broutier, L., Mastrogiovanni, G., and Verstegen, M. M. A. (2017). Human primary liver cancer–derived organoid cultures for disease modeling and drug screening. *Nat. Med.* 23, 1424–1435. doi: 10.1038/nm.4438

Chen, F., Tillberg, P. W., and Boyden, E. S. (2015). Expansion microscopy. *Science* 347, 543–548. doi: 10.1126/science.1260088

Chen, Y. Y., Silva, P. N., Syed, A. M., Sindhwani, S., Rocheleau, J. V., and Chan, W. C. W. (2016). Clarifying intact 3D tissues on a microfluidic chip for high-throughput structural analysis. *Proc. Natl. Acad. Sci. U.S.A.* 113, 14915–14920. doi: 10.1073/pnas.1609569114

Chen, Y., Tsai, Y.-H., Liu, Y.-A., Lee, S.-H., Tseng, S.-H., and Tang, S.-C. (2013). Application of three-dimensional imaging to the intestinal crypt organoids and biopsied intestinal tissues. *Sci. World J.* 2013, 624342. doi: 10.1155/2013/624342

Chiang, A., Liu, Y., Chiu, S., Hu, S., Huang, C., and Hsieh, C. (2001). Three−dimensional mapping of brain neuropils in the cockroach, *Diploptera punctata*. *J. Comp. Neurol.* 440, 1–11. doi: 10.1002/cne.1365

Cora, V., Haderspeck, J., Antkowiak, L., Mattheus, U., Neckel, P. H., Mack, A. F., et al. (2019). A cleared view on retinal organoids. *Cells* 8:391. doi: 10.3390/cells8050391

Costa, E. C., Moreira, A. F., de Melo-Diogo, D., and Correia, I. J. (2018a). ClearT immersion optical clearing method for intact 3D spheroids imaging through confocal laser scanning microscopy. *Opt. Laser Technol.* 106, 94–99. doi: 10.1016/j.optlastec.2018.04.002

Costa, E. C., Moreira, A. F., de Melo-Diogo, D., and Correia, I. J. (2018b). Polyethylene glycol molecular weight influences the Clear^{T2} optical clearing method for spheroids imaging by confocal laser scanning microscopy. *J Biomed. Opt.* 23:055003. doi: 10.1117/1.JBO.23.5.055003

Costa, E. C., Silva, D. N., Moreira, A. F., and Correia, I. J. (2019). Optical clearing methods: an overview of the techniques used for the imaging of 3D spheroids. *Biotechnol. Bioeng.* 116, 2742–2763. doi: 10.1002/bit.27105

Cruz, N. M., Song, X., Czerniecki, S. M., Gulieva, R. E., Churchill, A. J., Kim, Y. K., et al. (2017). Organoid cystogenesis reveals a critical role of microenvironment in human polycystic kidney disease. *Nat. Mater.* 16, 1112–1119. doi: 10.1038/nmat4994

Czerniecki, S. M., Cruz, N. M., Harder, J. L., Menon, R., Annis, J., Otto, E. A., et al. (2018). High-throughput screening enhances kidney organoid differentiation from human pluripotent stem cells and enables automated multidimensional phenotyping. *Cell Stem Cell* 22, 929–940. doi: 10.1016/j.stem.2018.04.022

Dang, J., Tiwari, S. K., Lichinchi, G., Qin, Y., Patil, V. S., Eroshkin, A. M., et al. (2016). Zika virus depletes neural progenitors in human cerebral organoids through activation of the innate immune receptor TLR3. *Cell Stem Cell* 19, 258–265. doi: 10.1016/j.stem.2016.04.014

Davis, R. P., Ng, E. S., Costa, M., Mossman, A. K., Sourris, K., Elefanty, A. G., et al. (2008). Targeting a GFP reporter gene to the MIXL1 locus of human embryonic stem cells identifies human primitive streak-like cells and enables isolation of primitive hematopoietic precursors. *Blood* 111, 1876–1884. doi: 10.1182/blood-2007-06-093609

Dekkers, J. F., Alieva, M., Wellens, L. M., Ariese, H. C. R., Jamieson, P. R., Vonk, A. M., et al. (2019). High-resolution 3D imaging of fixed and cleared organoids. *Nat. Protoc.* 14, 1756–1771. doi: 10.1038/s41596-019-0160-8

Dent, J. A., Polson, A. G., and Klymkowsky, M. W. (1989). A whole-mount immunocytochemical analysis of the expression of the intermediate filament protein vimentin in Xenopus. *Development* 105, 61–74. doi: 10.1242/dev.105.1.61

Desmaison, A., Guillaume, L., Triclin, S., Weiss, P., Ducommun, B., and Lobjois, V. (2018). Impact of physical confinement on nuclei geometry and cell division dynamics in 3D spheroids. *Sci. Rep.* 8:8785. doi: 10.1038/s41598-018-27060-6

Dodt, H. U., Leischner, U., Schierloh, A., Jährling, N., Mauch, C. P., Deininger, K., et al. (2007). Ultramicroscopy: three-dimensional visualization of neuronal networks in the whole mouse brain. *Nat. Methods* 4, 331–336. doi: 10.1038/nmeth1036

Durens, M., Nestor, J., Williams, M., Herold, K., Niescier, R. F., Lunden, J. W., et al. (2020). High-throughput screening of human induced pluripotent stem cell-derived brain organoids. *J. Neurosci. Methods* 335:108627. doi: 10.1016/j.jneumeth.2020.108627

Edwards, S. J., Carannante, V., Kuhnigk, K., Ring, H., Tararuk, T., Hallböök, F., et al. (2020). High-resolution imaging of tumor spheroids and organoids enabled by expansion microscopy. *Front. Mol. Biosci.* 7:1405. doi: 10.3389/fmolb.2020.00208

Eiraku, M., Takata, N., Ishibashi, H., Kawada, M., Sakakura, E., Okuda, S., et al. (2011). Self-organizing optic-cup morphogenesis in three-dimensional culture. *Nature* 472, 51–56. doi: 10.1038/nature09941

Eismann, B., Krieger, T. G., Beneke, J., Bulkescher, R., Adam, L., Erfle, H., et al. (2020). Automated 3D light-sheet screening with high spatiotemporal resolution reveals mitotic phenotypes. *J. Cell Sci.* 133:jcs245043. doi: 10.1242/jcs.245043

Ertürk, A., Becker, K., Jährling, N., Mauch, C. P., Hojer, C. D., Egen, J. G., et al. (2012). Three-dimensional imaging of solvent-cleared organs using 3DISCO. *Nat. Protoc.* 7, 1983–1995. doi: 10.1038/nprot.2012.119

Foglietta, F., Canaparo, R., Muccioli, G., Terreno, E., and Serpe, L. (2020). Methodological aspects and pharmacological applications of three-dimensional cancer cell cultures and organoids. *Life Sci.* 254:117784. doi: 10.1016/j.lfs.2020.117784

Garita-Hernandez, M., Guibbal, L., Toualbi, L., Routet, F., Chaffiol, A., Winckler, C., et al. (2018). Optogenetic light sensors in human retinal organoids. *Front. Neurosci.* 12:789. doi: 10.3389/fnins.2018.00789

Glaser, A. K., Reder, N. P., Chen, Y., Yin, C., Wei, L., Kang, S., et al. (2019). Multi-immersion open-top light-sheet microscope for high-throughput imaging of cleared tissues. *Nat. Commun.* 10:2781. doi: 10.1038/s41467-019-10534-0

Goranci-Buzhala, G., Mariappan, A., Gabriel, E., Ramani, A., Ricci-Vitiani, L., Buccarelli, M., et al. (2020). Rapid and efficient invasion assay of glioblastoma in human brain organoids. *Cell Rep.* 31:107738. doi: 10.1016/j.celrep.2020.107738

Govindan, S., Batti, L., Osterop, S. F., Stoppini, L., and Roux, A. (2021). Mass generation, neuron labeling, and 3D imaging of minibrains. *Front. Bioeng. Biotechnol.* 8:1436. doi: 10.3389/fbioe.2020.582650

Gradinaru, V., Treweek, J., Overton, K., and Deisseroth, K. (2018). Hydrogel-tissue chemistry: Principles and applications. *Annu. Rev. Biophys.* 47, 355–376. doi: 10.1146/annurev-biophys-070317-032905

Grenier, K., Kao, J., and Diamandis, P. (2020). Three-dimensional modeling of human neurodegeneration: brain organoids coming of age. *Mol. Psychiatry* 25, 254–274. doi: 10.1038/s41380-019-0500-7

Grist, S. M., Nasseri, S. S., Poon, T., Roskelley, C., and Cheung, K. C. (2016). On-chip clearing of arrays of 3-D cell cultures and micro-tissues. *Biomicrofluidics* 10:044107. doi: 10.1063/1.4959031

Hama, H., Hioki, H., Namiki, K., Hoshida, T., Kurokawa, H., Ishidate, F., et al. (2015). ScaleS: an optical clearing palette for biological imaging. *Nat. Neurosci.* 18, 1518–1529. doi: 10.1038/nn.4107

Hama, H., Kurokawa, H., Kawano, H., Ando, R., Shimogori, T., Noda, H., et al. (2011). Scale: a chemical approach for fluorescence imaging and reconstruction of transparent mouse brain. *Nat. Neurosci.* 14, 1481–1488. doi: 10.1038/nn.2928

Hou, B., Zhang, D., Zhao, S., Wei, M., Yang, Z., Wang, S., et al. (2015). Scalable and DiI-compatible optical clearance of the mammalian brain. *Front. Neuroanat.* 9:19. doi: 10.3389/fnana.2015.00019

Kabadi, P. K., Vantangoli, M. M., Rodd, A. L., Leary, E., Madnick, S. J., Morgan, J. R., et al. (2015). Into the depths: techniques for in vitro three-dimensional microtissue visualization. *Biotechniques* 59, 279–286. doi: 10.2144/000114353

Kang, W., Ferruzzi, J., Spatarelu, C.-P., Han, Y. L., Sharma, Y., Koehler, S. A., et al. (2020). Tumor invasion as non-equilibrium phase separation. *bioRxiv* [Preprint]. doi: 10.1101/2020.04.28.066845

Ke, M.-T., Fujimoto, S., and Imai, T. (2013). SeeDB: a simple and morphology-preserving optical clearing agent for neuronal circuit reconstruction. *Nat. Neurosci.* 16, 1154–1161. doi: 10.1038/nn.3447

Ke, M.-T., Nakai, Y., Fujimoto, S., Takayama, R., Yoshida, S., Kitajima, T. S., et al. (2016). Super-resolution mapping of neuronal circuitry with an index-optimized clearing agent. *Cell Rep.* 14, 2718–2732. doi: 10.1016/j.celrep.2016.02.057

Keller, P. J., and Dodt, H. U. (2012). Light sheet microscopy of living or cleared specimens. *Curr. Opin. Neurobiol.* 22, 138–143. doi: 10.1016/j.conb.2011.08.003

Keller, P. J., and Stelzer, E. H. K. (2008). Quantitative in vivo imaging of entire embryos with Digital scanned laser light sheet fluorescence microscopy. *Curr. Opin. Neurobiol.* 18, 624–632. doi: 10.1016/j.conb.2009.03.008

Keller, P. J., Schmidt, A. D., Wittbrodt, J., and Stelzer, E. H. K. (2008). Reconstruction of zebrafish early embryonic development by scanned light sheet microscopy. *Science* 322, 1065–1069. doi: 10.1126/science.1162493

Kim, J. H., Jang, M. J., Choi, J., Lee, E., Song, K.-D., Cho, J., et al. (2018). Optimizing tissue-clearing conditions based on analysis of the critical factors affecting tissue-clearing procedures. *Sci. Rep.* 8:12815. doi: 10.1038/s41598-018-31153-7

Klingberg, A., Hasenberg, A., Ludwig-Portugall, I., Medyukhina, A., Männ, L., Brenzel, A., et al. (2017). Fully automated evaluation of total glomerular number and capillary tuft size in nephritic kidneys using lightsheet microscopy. *J. Am. Soc. Nephrol.* 28, 452–459. doi: 10.1681/ASN.2016020232

Kopper, O., de Witte, C. J., Lõhmussaar, K., Valle-Inclan, J. E., Hami, N., Kester, L., et al. (2019). An organoid platform for ovarian cancer captures intra- and interpatient heterogeneity. *Nat. Med.* 25, 838–849. doi: 10.1038/s41591-019-0422-6

Krieger, T. G., Tirier, S. M., Park, J., Jechow, K., Eisemann, T., Peterziel, H., et al. (2020). Modeling glioblastoma invasion using human brain organoids and single-cell transcriptomics. *Neuro. Oncol.* 22, 1138–1149. doi: 10.1093/neuonc/noaa091

Ku, T., Swaney, J., Park, J. Y., Albanese, A., Murray, E., Cho, J. H., et al. (2016). Multiplexed and scalable super-resolution imaging of three-dimensional protein localization in size-adjustable tissues. *Nat. Biotechnol.* 34, 973–981. doi: 10.1038/nbt.3641

Kumar, A., Wu, Y., Christensen, R., Chandris, P., Gandler, W., McCreedy, E., et al. (2014). Dual-view plane illumination microscopy for rapid and spatially isotropic imaging. *Nat. Protoc.* 9, 2555–2573. doi: 10.1038/nprot.2014.172

Kuwajima, T., Sitko, A. A., Bhansali, P., Jurgens, C., Guido, W., and Mason, C. (2013). ClearT: a detergent- and solvent-free clearing method for neuronal and non-neuronal tissue. *Development* 140, 1364–1368. doi: 10.1242/dev.091844

Lallemant, L., Lebreton, C., and Garfa-Traoré, M. (2020). Comparison of different clearing and acquisition methods for 3D imaging of murine intestinal organoids. *J. Biol. Methods* 7:e141. doi: 10.14440/jbm.2020.334

Lancaster, M. A., Renner, M., Martin, C.-A., Wenzel, D., Bicknell, L. S., Hurles, M. E., et al. (2013). Cerebral organoids model human brain development and microcephaly. *Nature* 501, 373–379. doi: 10.1038/nature12517

Li, T., Ota, S., Kim, J., Wong, Z. J., Wang, Y., Yin, X., et al. (2014). Axial plane optical microscopy. *Sci. Rep.* 4, 7253. doi: 10.1038/srep07253

Li, W., Germain, R. N., and Gerner, M. Y. (2017). Multiplex, quantitative cellular analysis in large tissue volumes with clearing-enhanced 3D microscopy (Ce3D). *Proc. Natl. Acad. Sci. U.S.A.* 114, E7321–E7330. doi: 10.1073/pnas.1708981114

Li, Y., Tang, P., Cai, S., Peng, J., and Hua, G. (2020). Organoid based personalized medicine: from bench to bedside. *Cell Regen* 9:21.

Low, J. H., Li, P., Chew, E. G. Y., Zhou, B., Suzuki, K., Zhang, T., et al. (2019). Generation of human PSC-derived kidney organoids with patterned nephron segments and a de novo vascular network. *Cell Stem Cell* 25, 373–387. doi: 10.1016/j.stem.2019.06.009

Lukonin, I., Serra, D., Challet, M. L., Volkmann, K., Baaten, J., Zhao, R., et al. (2020). Phenotypic landscape of intestinal organoid regeneration. *Nature* 586, 275–280. doi: 10.1038/s41586-020-2776-9

Lundvall, V. H. (1905). "Veiteres iiber demonstration embryonaler skelette," in *Anatomischer Anzeiger*, ed. K. von Bardeleben (Jena: Verlag von Gustav Fischer).

Mae, S.-I., Ryosaka, M., Sakamoto, S., Matsuse, K., Nozaki, A., Igami, M., et al. (2020). Expansion of human iPSC-derived ureteric bud organoids with repeated branching potential. *Cell Rep.* 32:107963. doi: 10.1016/j.celrep.2020.107963

Masselink, W., Reumann, D., Murawala, P., Pasierbek, P., Taniguchi, Y., Bonnay, F., et al. (2019). Broad applicability of a streamlined ethyl cinnamate-based clearing procedure. *Development* 146:dev166884. doi: 10.1242/dev.166884

Masson, A., Escande, P., Frongia, C., Clouvel, G., Ducommun, B., and Lorenzo, C. (2015). High-resolution in-depth imaging of optically cleared thick samples using an adaptive SPIM. *Sci. Rep.* 5:16898. doi: 10.1038/srep16898

Matryba, P., Sosnowska, A., Wolny, A., Bozycki, L., Greig, A., Grzybowski, J., et al. (2020). Systematic evaluation of chemically distinct tissue optical clearing techniques in murine lymph nodes. *J. Immunol.* 204, 1395–1407. doi: 10.4049/jimmunol.1900847

McCracken, K. W., Catá, E. M., Crawford, C. M., Sinagoga, K. L., Schumacher, M., Rockich, B. E., et al. (2014). Modelling human development and disease in pluripotent stem-cell-derived gastric organoids. *Nature* 516, 400–404. doi: 10.1038/nature13863

McKey, J., Cameron, L. A., Lewis, D., Batchvarov, I. S., and Capel, B. (2020). Combined iDISCO and CUBIC tissue clearing and lightsheet microscopy for in toto analysis of the adult mouse ovary†. *Biol. Reprod.* 102, 1080–1089. doi: 10.1093/biolre/ioaa012

Messal, H. A., Almagro, J., Zaw, T. M., Tedeschi, A., Ciccarelli, A., Blackie, L., et al. (2021). Antigen retrieval and clearing for whole-organ immunofluorescence by FLASH. *Nat. Protoc.* 16, 239–262. doi: 10.1038/s41596-020-00414-z

Miura, Y., Li, M.-Y., Birey, F., Ikeda, K., Revah, O., Thete, M. V., et al. (2020). Generation of human striatal organoids and cortico-striatal assembloids from human pluripotent stem cells. *Nat. Biotechnol.* 38, 1421–1430. doi: 10.1038/s41587-020-00763-w

Molley, T. G., Wang, X., Hung, T.-T., Jayathilaka, P. B., Yang, J.-L., and Kilian, K. A. (2020). Geometrically structured microtumors in 3D hydrogel matrices. *Adv Biosyst* 4:e2000056. doi: 10.1002/adbi.202000056

Murakami, T. C., Mano, T., Saikawa, S., Horiguchi, S. A., Shigeta, D., Baba, K., et al. (2018). A three-dimensional single-cell-resolution whole-brain atlas using CUBIC-X expansion microscopy and tissue clearing. *Nat. Neurosci.* 21, 625–637. doi: 10.1038/s41593-018-0109-1

Murray, E., Cho, J. H., Goodwin, D., Ku, T., Swaney, J., Kim, S. Y., et al. (2015). Simple, scalable proteomic imaging for high-dimensional profiling of intact systems. *Cell* 163, 1500–1514. doi: 10.1016/j.cell.2015.11.025

Nürnberg, E., Vitacolonna, M., Klicks, J., von Molitor, E., Cesetti, T., Keller, F., et al. (2020). Routine optical clearing of 3D-cell cultures: simplicity forward. *Front. Mol. Biosci.* 7:20. doi: 10.3389/fmolb.2020.00020

Pagliuca, F. W., Millman, J. R., Gürtler, M., Segel, M., Van Dervort, A., Ryu, J. H., et al. (2014). Generation of functional human pancreatic β cells in vitro. *Cell* 159, 428–439. doi: 10.1016/j.cell.2014.09.040

Paiè, P., Bragheri, F., Bassi, A., and Osellame, R. (2016). Selective plane illumination microscopy on a chip. *Lab. Chip.* 16, 1556–1560. doi: 10.1039/C6LC00084C

Pampaloni, F., Ansari, N., and Stelzer, E. H. K. (2013). High-resolution deep imaging of live cellular spheroids with light-sheet-based fluorescence microscopy. *Cell Tissue Res.* 352, 161–177. doi: 10.1007/s00441-013-1589-7

Pampaloni, F., Reynaud, E. G., and Stelzer, E. H. K. (2007). The third dimension bridges the gap between cell culture and live tissue. *Nat. Rev. Mol. Cell Biol.* 8, 839–845. doi: 10.1038/nrm2236

Pan, C., Cai, R., Quacquarelli, F. P., Ghasemigharagoz, A., Lourbopoulos, A., Matryba, P., et al. (2016). Shrinkage-mediated imaging of entire organs and organisms using uDISCO. *Nat. Methods* 13, 859–867. doi: 10.1038/nmeth.3964

Park, Y. G., Sohn, C. H., Chen, R., McCue, M., Yun, D. H., Drummond, G. T., et al. (2018). Protection of tissue physicochemical properties using polyfunctional crosslinkers. *Nat. Biotechnol.* 37, 73–83. doi: 10.1038/nbt.4281

Poli, D., Magliaro, C., and Ahluwalia, A. (2019). Experimental and computational methods for the study of cerebral organoids: a review. *Front. Neurosci.* 13:162. doi: 10.3389/fnins.2019.00162

Preusser, F., dos Santos, N., Contzen, J., Stachelscheid, H., Costa, ÉT., Mergenthaler, P., et al. (2020). FRC-QE: A robust and comparable 3D microscopy image quality metric for cleared organoids. *bioRxiv* [Preprint]. doi: 10.1101/2020.09.10.291286

Qi, Y., Yu, T., Xu, J., Wan, P., Ma, Y., Zhu, J., et al. (2019). FDISCO: Advanced solvent-based clearing method for imaging whole organs. *Sci Adv* 5:eaau8355. doi: 10.1126/sciadv.aau8355

Qian, X., Nguyen, H. N., Song, M. M., Hadiono, C., Ogden, S. C., Hammack, C., et al. (2016). Brain-Region-specific organoids using mini-bioreactors for modeling ZIKV exposure. *Cell* 165, 1238–1254. doi: 10.1016/j.cell.2016.04.032

Rakotoson, I., Delhomme, B., Djian, P., Deeg, A., Brunstein, M., Seebacher, C., et al. (2019). Fast 3-D imaging of brain organoids with a new single-objective planar-illumination two-photon microscope. *Front. Neuroanat.* 13:77. doi: 10.3389/fnana.2019.00077

Reichman, S., Slembrouck, A., Gagliardi, G., Chaffiol, A., Terray, A., Nanteau, C., et al. (2017). Generation of storable retinal organoids and retinal pigmented epithelium from adherent human iPS Cells in xeno-free and feeder-free conditions. *Stem Cells* 35, 1176–1188. doi: 10.1002/stem.2586

Renier, N., Adams, E. L., Kirst, C., Wu, Z., Azevedo, R., Kohl, J., et al. (2016). Mapping of brain activity by automated volume analysis of immediate early genes. *Cell* 165, 1789–1802. doi: 10.1016/j.cell.2016.05.007

Renier, N., Wu, Z., Simon, D. J., Yang, J., Ariel, P., and Tessier-Lavigne, M. (2014). iDISCO: a simple, rapid method to immunolabel large tissue samples for volume imaging. *Cell* 159, 896–910. doi: 10.1016/j.cell.2014.10.010

Renner, H., Grabos, M., Becker, K. J., Kagermeier, T. E., Wu, J., Otto, M., et al. (2020). A fully automated high-throughput workflow for 3D-based chemical screening in human midbrain organoids. *Elife* 9:e52904. doi: 10.7554/eLife.52904.sa2

Renner, M., Lancaster, M. A., Bian, S., Choi, H., Ku, T., Peer, A., et al. (2017). Self−organized developmental patterning and differentiation in cerebral organoids. *EMBO J.* 17:e201694700. doi: 10.15252/embj.201694700

Rios, A. C., and Clevers, H. (2018). Imaging organoids: a bright future ahead. *Nat. Methods* 15, 24–26. doi: 10.1038/nmeth.4537

Rios, A. C., Capaldo, B. D., Vaillant, F., Pal, B., van Ineveld, R., Dawson, C. A., et al. (2019). Intraclonal plasticity in mammary tumors revealed through large-scale single-cell resolution 3D imaging. *Cancer Cell* 35:e6. doi: 10.1016/j.ccell.2019.05.011

Rybin, M. J., Ivan, M. E., Ayad, N. G., and Zeier, Z. (2021). Organoid models of glioblastoma and their role in drug discovery. *Front. Cell. Neurosci.* 15:4. doi: 10.3389/fncel.2021.605255

Sakaguchi, H., Ozaki, Y., Ashida, T., Matsubara, T., Oishi, N., Kihara, S., et al. (2019). Self-organized synchronous calcium transients in a cultured human neural network derived from cerebral organoids. *Stem Cell Rep.* 13, 458–473. doi: 10.1016/j.stemcr.2019.05.029

Santi, P. A. (2011). Light sheet fluorescence microscopy: a review. *J. Histochem. Cytochem.* 59, 129–138. doi: 10.1369/0022155410394857

Schmitz, A., Fischer, S. C., Mattheyer, C., Pampaloni, F., and Stelzer, E. H. (2017). Multiscale image analysis reveals structural heterogeneity of the cell microenvironment in homotypic spheroids. *Sci. Rep.* 7:43693. doi: 10.1038/srep43693

Schmuck, M. R., Temme, T., Dach, K., de Boer, D., Barenys, M., Bendt, F., et al. (2017). Omnisphero: a high-content image analysis (HCA) approach for phenotypic developmental neurotoxicity (DNT) screenings of organoid neurosphere cultures in vitro. *Arch. Toxicol.* 91, 2017–2028. doi: 10.1007/s00204-016-1852-2

Schwarz, M. K., Scherbarth, A., Sprengel, R., Engelhardt, J., Theer, P., and Giese, G. (2015). Fluorescent-protein stabilization and high-resolution imaging of cleared, intact mouse brains. *PLoS One* 10:e0124650. doi: 10.1371/journal.pone.0124650

Serra, D., Mayr, U., Boni, A., Lukonin, I., Rempfler, M., Challet, M. L., et al. (2019). Self-organization and symmetry breaking in intestinal organoid development. *Nature* 569, 66–72. doi: 10.1038/s41586-019-1146-y

Shimizu, T., Mae, S.-I., Araoka, T., Okita, K., Hotta, A., Yamagata, K., et al. (2020). A novel ADPKD model using kidney organoids derived from disease-specific human iPSCs. *Biochem. Biophys. Res. Commun.* 529, 1186–1194. doi: 10.1016/j.bbrc.2020.06.141

Silva Santisteban, T., Rabajania, O., Kalinina, I., Robinson, S., and Meier, M. (2017). Rapid spheroid clearing on a microfluidic chip. *Lab Chip.* 18, 153–161. doi: 10.1039/C7LC01114H

Smyrek, I., and Stelzer, E. H. K. (2017). Quantitative three-dimensional evaluation of immunofluorescence staining for large whole mount spheroids with light sheet microscopy. *Biomed. Opt. Exp.* 8, 484–499. doi: 10.1364/BOE.8.000484

Spalteholz, W. (1914). *Über das Durchsichtigmachen Von Menschlichen Und Tierischen Präparaten*. Leipzig: S. Hirzel.

Spence, J. R., Mayhew, C. N., Rankin, S. A., Kuhar, M. F., Vallance, J. E., Tolle, K., et al. (2011). Directed differentiation of human pluripotent stem cells into intestinal tissue in vitro. *Nature* 470, 105–109. doi: 10.1038/nature09691

Steinberg, E., Orehov, N., Tischenko, K., Schwob, O., Zamir, G., Hubert, A., et al. (2020). Rapid clearing for high resolution 3D imaging of ex vivo pancreatic cancer spheroids. *Int. J. Mol. Sci.* 21, 7703. doi: 10.3390/ijms21207703

Susaki, E. A., and Ueda, H. R. (2016). Whole-body and whole-organ clearing and imaging techniques with single-cell resolution: toward organism-level systems biology in mammals. *Cell Chem. Biol.* 23, 137–157. doi: 10.1016/j.chembiol.2015.11.009

Susaki, E. A., Shimizu, C., Kuno, A., Tainaka, K., Li, X., Nishi, K., et al. (2020). Versatile whole-organ/body staining and imaging based on electrolyte-gel properties of biological tissues. *Nat. Commun.* 11:1982. doi: 10.1038/s41467-020-15906-5

Susaki, E. A., Tainaka, K., Perrin, D., Kishino, F., Tawara, T., Watanabe, T. M., et al. (2014). Whole-brain imaging with single-cell resolution using chemical cocktails and computational analysis. *Cell* 157, 726–739. doi: 10.1016/j.cell.2014.03.042

Tainaka, K., Murakami, T. C., Susaki, E. A., Shimizu, C., Saito, R., Takahashi, K., et al. (2018). Chemical landscape for tissue clearing based on hydrophilic reagents. *Cell Rep.* 24, 2196–2210. doi: 10.1016/j.celrep.2018.07.056

Takahashi, N., Hoshi, H., Higa, A., Hiyama, G., Tamura, H., Ogawa, M., et al. (2019). An in vitro system for evaluating molecular targeted drugs using lung patient-derived tumor organoids. *Cells* 8:481. doi: 10.3390/cells8050481

Takasato, M., Er, P. X., Becroft, M., Vanslambrouck, J. M., Stanley, E. G., Elefanty, A. G., et al. (2014). Directing human embryonic stem cell differentiation towards a renal lineage generates a self-organizing kidney. *Nat. Cell Biol.* 16, 118–126. doi: 10.1038/ncb2894

Takasato, M., Er, P. X., Chiu, H. S., and Little, M. H. (2016). Generation of kidney organoids from human pluripotent stem cells. *Nat. Protoc.* 11, 1681–1692. doi: 10.1038/nprot.2016.098

Takasato, M., Er, P. X., Chiu, H. S., Maier, B., Baillie, G. J., Ferguson, C., et al. (2015). Kidney organoids from human iPS cells contain multiple lineages and model human nephrogenesis. *Nature* 526, 564–568. doi: 10.1038/nature15695

Takebe, T., Sekine, K., Enomura, M., Koike, H., Kimura, M., Ogaeri, T., et al. (2013). Vascularized and functional human liver from an iPSC-derived organ bud transplant. *Nature* 499, 481–484. doi: 10.1038/nature12271

Timmins, N. E., and Nielsen, L. K. (2007). Generation of multicellular tumor spheroids by the hanging-drop method. *Methods Mol. Med.* 140, 141–151. doi: 10.1007/978-1-59745-443-8_8

Tuchin, V. V., Maksimova, I. L., Zimnyakov, D. A., Kon, I. L., Mavlyutov, A. H., and Mishin, A. A. (1997). Light propagation in tissues with controlled optical properties. *J. Biomed. Opt.* 2, 401–417. doi: 10.1117/12.281502

Ueda, H. R., Dodt, H. U., Osten, P., Economo, M. N., Chandrashekar, J., and Keller, P. J. (2020a). Whole-brain profiling of cells and circuits in mammals by tissue clearing and light-sheet microscopy. *Neuron* 106, 369–387. doi: 10.1016/j.neuron.2020.03.004

Ueda, H. R., Erturk, A., Chung, K., Gradinaru, V., Chedotal, A., Tomancak, P., et al. (2020b). Tissue clearing and its applications in neuroscience. *Nat. Rev. Neurosci.* 21, 61–79. doi: 10.1038/s41583-019-0250-1

van Ineveld, R. L., Ariese, H. C. R., Wehrens, E. J., Dekkers, J. F., and Rios, A. C. (2020). Single-cell resolution three-dimensional imaging of intact organoids. *J. Vis. Exp.* 160:e60709. doi: 10.3791/60709

Wang, D., Haviland, D. L., Burns, A. R., Zsigmond, E., and Wetsel, R. A. (2007). A pure population of lung alveolar epithelial type II cells derived from human embryonic stem cells. *Proc. Natl. Acad. Sci. U.S.A.* 104, 4449–4454. doi: 10.1073/pnas.0700052104

Wei, M., Shi, L., Shen, Y., Zhao, Z., Guzman, A., Kaufman, L. J., et al. (2019). Volumetric chemical imaging by clearing-enhanced stimulated Raman scattering microscopy. *Proc. Natl. Acad. Sci. U.S.A.* 116, 6608–6617. doi: 10.1073/pnas.1813044116

Wenzel, C., Riefke, B., Grundemann, S., Krebs, A., Christian, S., Prinz, F., et al. (2014). 3D high-content screening for the identification of compounds that target cells in dormant tumor spheroid regions. *Exp. Cell Res.* 323, 131–143. doi: 10.1016/j.yexcr.2014.01.017

Wörsdörfer, P., Dalda, N., Kern, A., Krüger, S., Wagner, N., Kwok, C. K., et al. (2019). Generation of complex human organoid models including vascular networks by incorporation of mesodermal progenitor cells. *Sci. Rep.* 9:15663. doi: 10.1038/s41598-019-52204-7

Xia, X., and Zhang, S.-C. (2009). Differentiation of neuroepithelia from human embryonic stem cells. *Methods Mol. Biol.* 549, 51–58. doi: 10.1007/978-1-60327-931-4_4

Yan, H. H. N., Siu, H. C., Law, S., Ho, S. L., Yue, S. S. K., Tsui, W. Y., et al. (2018). A Comprehensive human gastric cancer organoid biobank captures tumor subtype heterogeneity and enables therapeutic screening. *Cell Stem Cell* 23, 882–897. doi: 10.1016/j.stem.2018.09.016

Yang, L., Soonpaa, M. H., Adler, E. D., Roepke, T. K., Kattman, S. J., Kennedy, M., et al. (2008). Human cardiovascular progenitor cells develop from a KDR+ embryonic-stem-cell-derived population. *Nature* 453, 524–528. doi: 10.1038/nature06894

Yu, T., Zhu, J., Li, D., and Zhu, D. (2021). Physical and chemical mechanisms of tissue optical clearing. *iScience* 21:102178. doi: 10.1016/j.isci.2021.102178

Yu, T., Zhu, J., Li, Y., Ma, Y., Wang, J., Cheng, X., et al. (2018). RTF: a rapid and versatile tissue optical clearing method. *Sci. Rep.* 8:1964. doi: 10.1038/s41598-018-20306-3

Yun, D. H., Park, Y.-G., Cho, J. H., Kamentsky, L., Evans, N. B., Albanese, A., et al. (2019). Ultrafast immunostaining of organ-scale tissues for scalable proteomic phenotyping. *bioRxiv* [Preprint]. doi: 10.1101/660373

Zimnyakov, D. A., Tuchin, V. V., Michin, A. A., Kon, I. L., and Serov, A. N. (1996). In-vitro human sclera structure analysis using tissue optical immersion effect. *Int. Soc. Opt. Photon. Ophthal. Technol. VI* 2673, 233–243. doi: 10.1117/12.240070

Conflict of Interest: RIKEN and CUBICStars Co. have filed patents regarding this work, in which ES. was a co-inventor. ES was also a senior researcher employed by CUBICStars Co.

The remaining author declares that the research was conducted in the absence of any commercial or financial relationships that could be construed as a potential conflict of interest.

frontiers
in Cell and Developmental Biology

REVIEW
published: 26 July 2021
doi: 10.3389/fcell.2021.698315

Ovary Development: Insights From a Three-Dimensional Imaging Revolution

Bikem Soygur and Diana J. Laird*

Department of Obstetrics, Gynecology & Reproductive Sciences, Center for Reproductive Sciences, Eli and Edythe Broad Center of Regeneration Medicine and Stem Cell Research, University of California, San Francisco, San Francisco, CA, United States

Edited by:
Silvia Garagna,
University of Pavia, Italy

Reviewed by:
Kazuhiro Kawamura,
International University of Health and Welfare (IUHW), Japan
Joshua Johnson,
University of Colorado Denver, United States

****Correspondence:***
Diana J. Laird
diana.laird@ucsf.edu

Specialty section:
This article was submitted to Cell Growth and Division, a section of the journal Frontiers in Cell and Developmental Biology

Received: *21 April 2021*
Accepted: *02 July 2021*
Published: *26 July 2021*

Citation:
Soygur B and Laird DJ (2021) Ovary Development: Insights From a Three-Dimensional Imaging Revolution.
Front. Cell Dev. Biol. 9:698315.
doi: 10.3389/fcell.2021.698315

The ovary is an indispensable unit of female reproduction and health. However, the study of ovarian function in mammals is hindered by unique challenges, which include the desynchronized development of oocytes, irregular distribution and vast size discrepancy of follicles, and dynamic tissue remodeling during each hormonal cycle. Overcoming the limitations of traditional histology, recent advances in optical tissue clearing and three-dimensional (3D) visualization offer an advanced platform to explore the architecture of intact organs at a single cell level and reveal new relationships and levels of organization. Here we summarize the development and function of ovarian compartments that have been delineated by conventional two-dimensional (2D) methods and the limits of what can be learned by these approaches. We compare types of optical tissue clearing, 3D analysis technologies, and their application to the mammalian ovary. We discuss how 3D modeling of the ovary has extended our knowledge and propose future directions to unravel ovarian structure toward therapeutic applications for ovarian disease and extending female reproductive lifespan.

Keywords: ovary, folliculogenesis, tissue clearing, microscopy, 3D analysis

INTRODUCTION

Female reproduction hinges on the development of the ovary, the organ which generates mature oocytes and produces hormones to regulate reproductive functions. The ovary harbors the oocyte reserve which supplies mature eggs for the duration of reproductive lifespan and concludes with the cessation of ovulation at menopause. The loss of ovarian function and subsequent drop in gonadal hormones has been associated with enhanced risk for cardiovascular disease (Atsma et al., 2006), osteoporosis, bone fractures (Van Der Voort et al., 2003), neurologic diseases, and adverse impact on quality of life compared to age-matched pre-menopausal controls (Broekmans et al., 2009; Parker et al., 2009; Rocca et al., 2009). Thus, the ovary may play a regulatory role in healthy aging beyond its indispensable function in female fertility.

The multifaceted functions of the ovary are accomplished by the coordination of diverse cell populations. The operational unit of the mammalian ovary is the follicle, which consists of an oocyte surrounded by granulosa and theca cells. The maturation of follicles from the non-growing or primordial stage toward large antral or ovulatory follicles is governed by signaling between follicles, within the supportive cells of the follicles, and the greater ovarian microenvironment (McGee and Hsueh, 2000; Da Silva-Buttkus et al., 2009). In addition, the function of follicles (and ultimately ovarian health) depends on hormones transported through blood vessels, signals received by nerve fibers, and homeostasis regulated by lymphatic vessels (Domínguez and Se, 2011; Brown and Russell, 2014). Understanding the dynamic and complex interactions between these different structures within the ovary has proven to be challenging.

In the past, the primary method for evaluating organs at the tissue and cellular level consisted of histological sectioning and immunostaining; however, three-dimensional, irregular, and dynamic biological structures are difficult to interpret by two-dimensional analysis. *In vivo* imaging methods such as ultrasound and tomography provide 3D visualization [reviewed in Feng et al. (2018) and Fiorentino et al. (2021)], however, only larger follicles can be detected. A newly developed imaging approach using optimized X-ray micro-Computed Tomography (microCT) detects secondary and later stage follicles (Fiorentino et al., 2020), however, imaging of small structures including primordial and primary follicles remains challenging. Three-dimensional (3D) imaging technologies were first developed to trace extensive nerve processes in the brain, which revealed the intricate structural and functional relationships (Dodt et al., 2007). 3D approaches have since been applied to structural and molecular features of developing as well as pathological organs. Initial 3D studies emphasized the importance of *in toto* analysis of ovaries (Cordeiro et al., 2015; Faire et al., 2015; Malki et al., 2015) however, the field of ovarian research has not widely adopted such approaches as fully as other organs. Despite the relatively small size of the ovary compared to other organs and ease of optical clearing, understanding of its 3D structure has lagged owing to its dynamic organization and extensive remodeling which occurs with each menstrual or estrus cycle.

The diagnosis of ovarian diseases is limited by our still evolving understanding of how the ovary changes during adulthood and undergoes aging. Defining the spatial relationships between components– including the vasculature, nerve fibers, and follicles– will enhance understanding of ovarian function and pathologies, and lay the foundation for identifying therapeutics for fertility preservation, ovarian cancer, and premature menopause. 3D modeling of the ovary can help demystify one of the earliest organs to undergo aging, which earned the title “canary in the coal mine” (Quinn and Cedars, 2017); apart from advancing reproductive medicine, the study of aging in the ovary may provide broader insight into the process of aging across and serve as a model of early detection for aging pathologies.

In this review, we outline the development and activity of mammalian ovarian compartments, discuss traditional methods of 2D ovarian analysis and their limitations. We summarize historical clearing techniques, recent advances and their facilitation of 3D imaging and quantitative analysis. Finally, we enumerate future directions for 3D analysis, specific applications to deepen understanding of ovarian development, as well as elucidate pathologic conditions of the ovary.

OVARIAN COMPARTMENTS AND THEIR DEVELOPMENT

Oocytes

Germ cell precursors in mice are segregated from somatic lineages around embryonic day 7.25 (E7.25) as a group of about 40 primordial germ cells (PGCs) located in the primitive streak near embryonic endoderm of the embryo (Ginsburg et al., 1990; McLaren, 2003). Diploid and sexually-undetermined PGCs transit through developing hindgut and dorsal mesentery before settling in the gonad primordium, or genital ridge, beginning at E10.5. PGCs expand by proliferation during their migration (Cantu et al., 2016), however, upon reaching the fetal gonads, their mitotic divisions involve incomplete cytokinesis, which leads to the formation of stable intercellular bridges that connect germ cells in cysts (Pepling and Spradling, 1998; Greenbaum et al., 2007, 2009). In the fetal ovary, extrinsic and intrinsic signals nudge germ cells in the anterior region to initiate meiotic machinery at ∼E13.5, which is followed by a wave-like propagation of meiotic initiation toward the posterior region (Menke et al., 2003; Bullejos and Koopman, 2004; Bowles et al., 2006; Koubova et al., 2006; Kumar et al., 2011; Arora et al., 2016; Vernet et al., 2020). As germ cells progress through different stages of meiotic prophase I (MPI), cyst breakdown begins, somatic support cells known as Granulosa cell precursors begin to encapsulate individual oocytes around E17.5. These structures, known as primordial follicles, are formed asynchronously and in a stereotyped pattern, beginning around birth at the center (or medulla region) of the ovary, followed by the outer surface (or cortex) and concluding by postnatal day 5 (PN5) (Pepling and Spradling, 2001; Pepling et al., 2010). The growth of follicles (to primary stage) similarly begins predominantly in the anterior-dorsal region of mouse ovaries around PN4 (Cordeiro et al., 2015) and continues thereafter, regulated by a combination of activator and suppressor signals that remains incompletely understood (Chen et al., 2020). Initial follicle growth continuously proceeds through stages that have been categorized morphologically as primary (a layer of cuboidal granulosa cells surrounds the oocyte) and secondary (multiple layers of granulosa cells and outer steroidogenic theca cells surround the oocyte); follicle death occurs at this stage until the onset of puberty, at which point the cyclic waves of follicle stimulating hormone and luteinizing hormone sustain the maturation of a subset of follicles to the antral stage (growing follicle with antral cavity). Although the default pathway for most antral follicles is atresia, a subset escape from that degenerative process. Among those, only dominant follicle(s) complete the final growth phase and get ovulated (McGee and Hsueh, 2000; Edson et al., 2009). After follicular rupture and ovulation, remaining supporting cells transform to progesterone-secreting cells and form the corpus luteum. Despite the foundational discoveries through decades of histological studies, the spatiotemporal dynamics and regulation of later follicle maturation, ovulation, and corpus luteum are still poorly understood.

Somatic Cells

Ovarian fate depends on the differentiation and development of somatic lineages from bipotential precursors in the fetal gonads. These support cells eventually form what has been considered a supportive niche for the oocyte. The earliest gonad precursor cells originate from a thickening of the mesenchyme on the ventromedial side of the embryonic kidney (mesonephros), to which a cohort of coelomic epithelial cells migrate and proliferate; these two precursors establish the supporting steroidogenic and interstitial cells of the genital ridges [reviewed in Estermann et al. (2020)]. 'Pre-granulosa' cell populations emerge at different stages of ovarian development and contribute to the formation of distinct pools of follicles. The first group of pre-granulosa cells express *Foxl2* in early fetal stages, develop to granulosa cells in the medulla, and contribute to initial follicle formation during early stages of reproduction (Mork et al., 2012; Zheng et al., 2014). A second group of *Lgr5* expressing pre-granulosa cells are predominantly in the ovarian cortex and contribute to formation of cortical follicles (Ng et al., 2014; Rastetter et al., 2014; Niu and Spradling, 2020). Another somatic component of ovarian follicles, the theca cell layer, has two origins: from $Wt1^+$ stromal cells of developing ovary and from Gli^+ mesenchymal cells that migrate from the mesonephros (Liu et al., 2015). Signals from both granulosa cells and oocytes are required for the differentiation of theca cells to functional steroidogenic cells (theca interna) as well as to the fibrous, connective tissue layer (theca externa) (Liu et al., 2015).

Vessel Network and Innervation

The vascular network transports gases, nutrients, and macromolecules required for the growth and maintenance of ovarian follicles. Blood vessels and lymphatics also remove metabolic waste and drain extracellular fluids from tissues, transporting proteins and lipids back to the bloodstream while controlling immune cell trafficking (Olszewski, 2003; Brown and Russell, 2014). Most organs do not undergo active remodeling of the vasculature, except during wound healing and pathological conditions such as cancers. However, the ovary is an exception, as dynamic changes occur in the vasculature during each hormonal cycle (Fraser, 2006). Time-lapse microscopy analysis and lineage tracing of *Tie2*-expressing endothelial cells revealed that small branches from the vessels at the border of the mesonephros and gonad extend into the primordial gonad at E11.5. With subsequent sex differentiation of the gonads, distinct vascular structures become evident in developing ovaries; without further endothelial cell migration from the mesonephros, blood vessels grow by branching morphogenesis, penetrate the developing ovaries and undergo local organization and remodeling within (Brennan et al., 2002; Coveney et al., 2008). In adult ovaries, anatomical and histological studies describe the morphology of the main vasculature entering the ovarian hilum and speculate that it functions to provide blood supply required for ovarian function; however, our knowledge of 3D vessel architecture and its relationship to normal ovarian function and diseases remains limited.

Peripheral nerves grow along blood vessels in most organs; however, this is not the case in the fetal ovary, as sympathetic nerves do not invade synchronously with vasculature, but rather innervate later than vasculature. Although neural projections in the medulla of fetal and adult mammalian ovary were identified through 2D histologic analyses (D'Albora et al., 2002; Dees et al., 2006), the spatial resolution of peripheral innervation together with vessel networks had to await the advent of 3D imaging and will be discussed later.

HISTOLOGIC METHODS FOR ANALYSIS OF THE OVARY

The field of anatomy was founded upon the meticulous description of macroscopic structures and inference of organ function. The dawn of the microscope moved anatomy into the cellular realm but necessitated the slicing of organs into thin pieces to view tissue structure. To parse most organs like the ovary, histologic approaches relied on sectioning specimens into 6 or 8 μm thick slices in meticulous order, staining with dyes or antibodies, and examining every fifth to every tenth section (Bucci et al., 1997; Flaws et al., 1997, 2001; Tilly, 2003; Sarma et al., 2020). Follicle quantification was carried out multiplying by a correction factor to the representative counts, which was not constant but changing based on the age of the ovary. This approach is labor intensive, and results vary considerably due to the accuracy of thickness of each slice, the number of slides counted, and the correction factor used in each study. Another technique to access follicle count is stereology, whereby objects of interest are counted in a known fraction of an organ (Gundersen, 1986; Gundersen et al., 1988). In this method, the ovary is uniformly and systematically cut into smaller pieces and a fraction of randomly-selected pieces are embedded, cut into thick (∼25 μm) sections, and follicles are counted by optical disector fractionator. In this algorithm, the raw count is multiplied by the inverse of the sampling fractions to calculate the total number of follicles in the ovary (Myers et al., 2004; Charleston et al., 2007; Sarma et al., 2020). Although stereology is deemed more accurate, the requirement for special equipment and expertise makes this technique less widely used.

With the development and implementation of machine learning technologies in biomedical sciences, quantitative analysis of various structures in biological samples can be expedited. New methods for automatic detection and counting of ovarian follicles on histological slides rely upon a deep learning algorithm known as Convolution Neuronal Networks (CNN) (Sonigo et al., 2018; Inik et al., 2019). Although machine learning provides unparalleled speed for analyzing samples, the information obtained at the cellular level derives from two-dimensional histological sections, which may be distorted or non-adjacent.

While spatial and temporal asynchrony of early ovarian development reflect the complexities of ovarian function and ultimately related diseases, the number of studies addressing spatiotemporal dynamics during later stages of ovarian development is limited by its opacity. In the fetal and neonatal mouse ovary, Cordeiro et al. (2015) used reporter proteins driven by stage-specific oocyte-specific promoters *Mvh*, *Gdf9*, and *Zp3* to reveal spatiotemporal dynamics of the first wave of folliculogenesis in 3D. *Mvh*-EGFP was detected earliest in the fetus, persisted in primordial follicles in postnatal ovaries, and extinguished in later stages of folliculogenesis. *Gdf9*-mCherry positive oocytes were detected starting at PN0. Zp3-AmCyan expression was first seen in oocytes located in the anterior-dorsal region of PN4 ovary, suggesting formation of primary follicles initially occurs in the anterior-dorsal part of the ovary (**Figure 1A**). Similarly, growing follicles were mainly detected in the dorsal region of postnatal ovaries. Although a powerful tool, endogenous reporter proteins must be visualized immediately after dissection, since the fluorescent signal drops dramatically after sample fixation. This constraint prevented optical clearing of the ovaries and limited analysis to structures positioned within 80 μm of the sample edge.

OBSTACLES TO VISUALIZATION OF THE INTACT OVARY

3D imaging of whole embryos, organs and even adult bodies has exploded over the past decade due to advances in computational analysis, optical clearing, and image rendering. The challenges of combining macro and micro anatomy in intact organs include: (*1*) the need for appropriate microscopes and objectives with long working distances to accommodate large samples, (*2*) computation and storage required for big data sets, and (*3*) the opacity of most organs. The invention of confocal microscopy (Minsky, 1988), optical sectioning techniques (Conchello and Lichtman, 2005; Paddock and Eliceiri, 2014), and increased computational power, together with strategies for image data management (Wallace et al., 2015; Zhu et al., 2017; Bajcsy et al., 2018), overcame the first two challenges. In this review, we focus on the last: how opacity limits imaging of organs and how the ovary can be made transparent with different approaches.

Similar to other organs, ovaries are composed of epithelial, connective tissues, vasculature and nerve fibers with varying components (e.g., membranes, nuclei, lipids, proteins, collagens, blood, tissue fluid, water etc.) that have different refraction indices, meaning that the light propagates through them at different speeds. Thus, light waves passing through the ovary scatter heterogeneously between different tissue layers, conferring an opaque or milky appearance. The underlying mechanisms of light scattering in biological samples and different clearing techniques are explained in detail by others (Richardson and Lichtman, 2015; Tian et al., 2021). To increase transparency, optical clearing methods aim to reduce the heterogeneity in refractive indices of different organ compartments by removing some tissue components (like lipids). This removal is performed in addition to immersing the sample in a solution with a refractive index more closely matched to the tissue or alternatively embedding it in hydrophilic polymers. Different clearing techniques are often combined, using active or passive removal of tissue components, followed by bathing the sample in refractive index-matched solution. Optical clearing methods were initially developed to elucidate complex neuronal circuits, brain structure, and function in the brain (Dodt et al., 2007). Later, the same techniques were applied to different organs, including ovaries; here, we summarize the underlying rationales, main advantages and drawbacks of those protocols in the field of ovarian research (**Table 1** and **Figure 2**).

CLEARING TECHNIQUES AND QUANTITATIVE APPROACHES USED FOR ASSESSMENT OF OVARIES IN 3D

More than a century ago, Spalteholz (1914) developed the first clearing method by immersing large organs in the organic solvents benzyl alcohol and methyl salicylate. Although this method was detrimental to the tissue structure and only applicable for large samples (Steinke and Wolff, 2001), it formed the basis for almost all solvent-based clearing protocols to date.

Imaging Oocytes and Follicles

Organic Solvent-Based Clearing

The main steps of solvent-based protocols are tissue dehydration, removing lipids, and impregnating the sample with clearing solution to homogenize the refractive index of remaining structures (**Figure 2A**). Zucker and Jeffay (2006) revived a solvent-based clearing approach by dehydrating late fetal mouse ovaries and immersing them in benzyl alcohol and benzyl benzoate (BABB). They stained intact fresh mouse ovaries with LysoTracker Red (LT) to label apoptotic cells. Subsequent fixation with 4% paraformaldehyde and 1% glutaraldehyde preserved tissue morphology as well as boosting background fluorescence signal that was advantageous for visualization of overall morphology. Imaging the intact ovary with a confocal microscope revealed that apoptosis occurs in individual granulosa cells or groups of granulosa cells located near an oocyte or antrum, which is the fluid-filled cavity in large follicles (Zucker and Jeffay, 2006). Although only fluorescent signal from dye and aldehyde-induced background signal were visualized, this first demonstrated that ovaries can be made transparent and visualized in 3D and provided a basis for future studies.

The first 3D visualization of oocytes *in situ* relied upon organic solvent-based clearing in BABB to render mouse ovaries transparent after immunostaining (Faire et al., 2015). Following fixation and permeabilization in Methanol:DMSO, immunolabeling was performed with nuclear markers NOBOX and GCNA to facilitate object segmentation, particularly for more densely packed primordial follicles. Based on the fortuitous observation that the oocyte nucleus increases in volume with follicle growth, primordial could be distinguished from growing follicles to produce the most accurate and direct quantification to date. Primordial follicles were counted in the intact ovary for the first time, showing a gradual drop in the total number from ∼5,000 at PN5 to ∼3,000 at PN7 and ∼800 at 6 months. Beyond quantification of the ovarian reserve, 3D imaging enabled analysis of the spatial organization of follicles revealing the

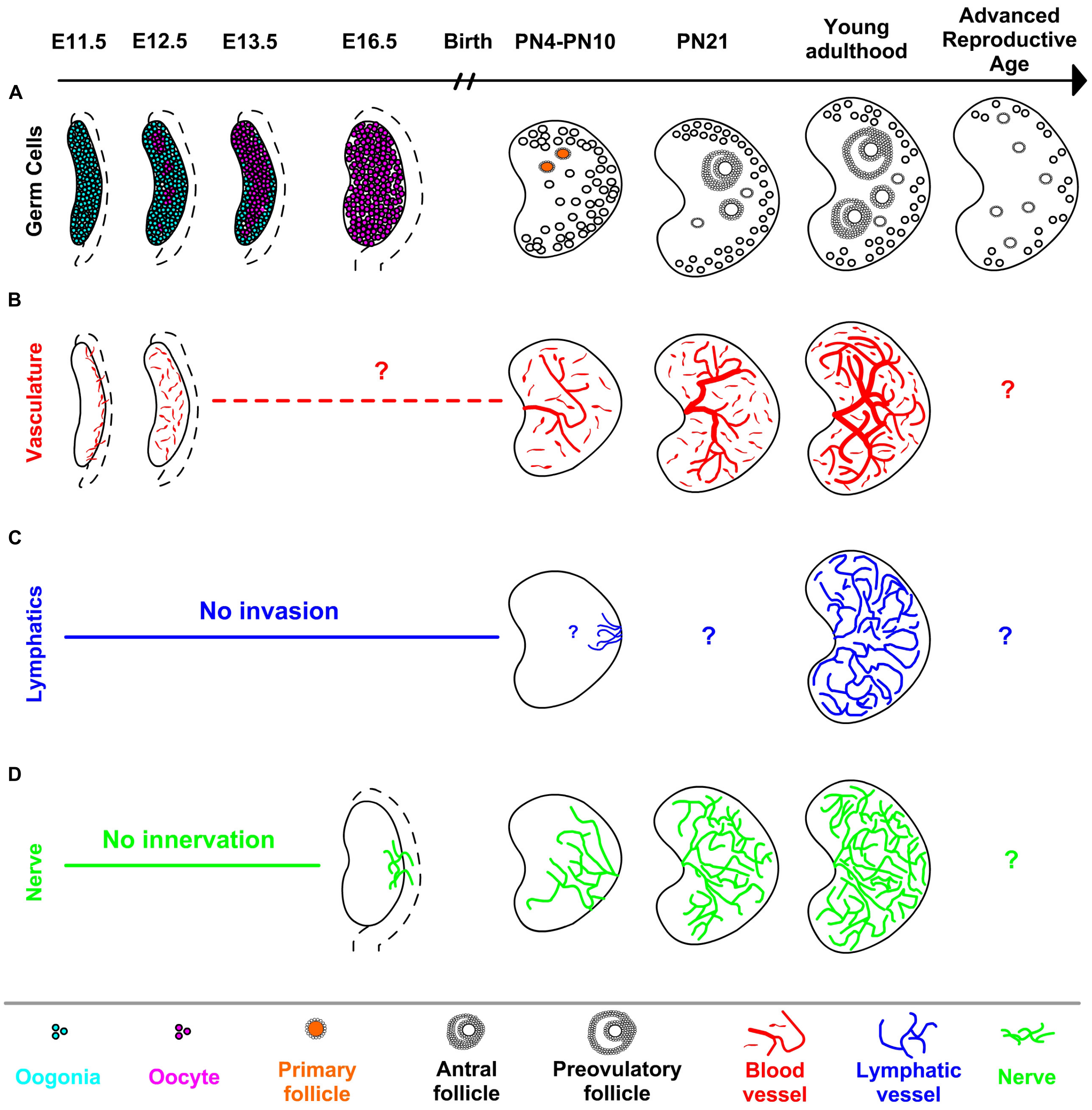

FIGURE 1 | Main developmental events of the ovary organogenesis uncovered by 3D imaging in mice. **(A)** Following the localization in the gonad, germ cells undergo meiosis (in magenta) asynchronously starting as early as E12.5 in the anterior-medial region of the ovary. Germ cells located in the peripheral-posterior part of the ovary maintain their pluripotency (cyan) and initiate the meiosis later and by E16.5, all germ cells enter meiosis. Formation of primary follicles (in orange) and the first activation of follicular growth occur in the anterior-dorsal region of the postnatal ovary. While the number of follicles decreases with advanced maternal age, aged ovaries harbor mostly primordial and primary follicles due to the decreased number of later stage follicles. **(B)** Blood vessels (in red) at the gonad-mesonephros border expand into the gonad at E11.5 and proliferate to establish the blood vessel network of the developing ovary. Although further development of the vascular network in late fetal ovaries is unclear, blood vessels in the postnatal ovaries enter from the hilum and blood vessel diameters and branching increase by adulthood. **(C)** Lymphatic vessels (in blue) invade the ovary as early as PN10, however, the first point of contact inside the PN10 ovary is unclear with the resolution of micrographs. Similar to blood vessels, the adult ovary contains a complex network of lymphatic vessels. **(D)** Nerve fibers (in green) in the mesonephros innervate the ovary first from the dorsal side at E16.5, neural projections expand to medulla then cortex by PN4 and the neural network further increases with age. Dashed lines adjacent to fetal ovaries illustrate mesonephros. Question marks in **(B–D)** refer unidentified geography of related structures at given developmental points in 3D.

precise borders of the medullary region in the neonatal ovary where the follicle growth starts.

In addition to advantages in quantitation and spatial analysis, whole-mount imaging is ideal for visualizing rare events. Given the controversy over oogonial stem cells, Faire et al. (2015) examined oocyte proliferation in the postnatal ovary by incorporation of the thymidine analog Bromodeoxyuridine (BrdU) and phospho-histone H3 (pHH3)

TABLE 1 | Studies that applied different 3D visualization and analysis approaches in mouse ovaries.

	Clearing reagent	**Stage**	**Fixative**	**Immunolabeling applied (Y/N)**	**Microscope used**	**Structures analyzed**	**Quantitative analysis**	**References**
Organic solvent based	BABB	Embryonic, postnatal, and adult	4% PFA	Yes	Confocal microscope and optical projection tomography	3D geography of lymphatic and blood vessels	N/A	Svingen et al., 2012
	BABB	Embryonic	4% PFA	Yes	Confocal microscope	Spatiotemporal characteristics of meiotic initiation in germ cells	Imaris and Matlab	Soygur et al., 2021
	BABB	Postnatal	4% PFA and 1% Glut	No (stained with a fluorescent dye, LysoTracker)	Confocal microscope	Apoptotic granulosa cells in follicles	N/A	Zucker and Jeffay, 2006
	BABB	Postnatal and adult	MeOH:DMSO	Yes	Confocal microscope	The numbers and spatial distribution of follicles	Volocity and Matlab	Faire et al., 2015
	iDISCO	Adult	4% PFA	Yes	Spinning disk confocal microscope	Growing follicles and interstitial compartment	N/A	McKey et al., 2020
Aqueous based	Sca*l*eA2	Embryonic	4% PFA	Yes	Confocal microscope	Total germ cell numbers	Imaris	Malki et al., 2015
	CUBIC	Embryonic	4% PFA	Yes (endogenous mCerulean, mCherry, and mOrange are also visualized)	Confocal microscope	Synchrony of meiotic onset and cytoplasmic sharing in germ cell clones	Imaris	Soygur et al., 2021
	CUBIC	Postnatal and adult	4% PFA	Yes	Light-sheet microscope	Follicle numbers, 3D modeling of ovarian innervation and vasculature	Imaris	Tong et al., 2020
	CUBIC	Adult	4% PFA	No (endogenous GFP signal is visualized)	Confocal and light-sheet microscopes	3D visualization of all cells in the ovary	N/A	Kagami et al., 2018
	CUBIC	Adult	4% PFA	Yes (endogenous Tomato signal is also visualized)	Light-sheet microscope	Growing follicles, vasculature, and interstitial compartment	N/A	McKey et al., 2020
Hydrogel embedding	CLARITY	Postnatal, adult, and aged	4% PFA	Yes	Confocal microscope	Dynamics of follicles, 3D structure and role of vasculature	Imaris and Matlab	Feng et al., 2017
	CLARITY	Adult	4% PFA	Yes	Light-sheet microscope	Follicle numbers and vasculature	Imaris	Ma et al., 2018
Combined	iDISCO and CUBIC	Adult	4% PFA	Yes	Light-sheet microscope and spinning disk confocal microscope	Growing follicles, oocytes, vasculature, and interstitial compartment	N/A	McKey et al., 2020
	CLARITY and Sca*l*eA2	Adult	4% PFA	Yes (endogenous td Tomato signal is also visualized)	Light-sheet microscope	Blood and lymphatic vessels	Ilastik and Imaris	Oren et al., 2018

PFA, paraformaldehyde; Glut, glutaraldehyde; MeOH, methanol; DMSO, dimethyl sulfoxide; N/A, not applied.

immunostaining. However, coincidence of proliferation markers with NOBOX was exceedingly rare: 0.03% of oocytes at PN7. Proliferation markers could not be visualized during later ovarian development due to technical limitations. These results corroborate the definitive ovarian reserve and its decrease during aging. Although this study was the first to quantitatively analyze the intact ovary in 3D, the approach was limited in imaging, analysis, and technical capabilities. Ovaries older than 6-months could not be processed due to insufficient antibody penetration, clearing and/or elevated background. Accuracy was restricted to primordial follicles due to dim fluorescent signal of follicles at later stages, particularly antral. Finally, use of methanol as a fixative limited selection of antibodies since many epitopes are masked.

A recent study used 3D imaging to map the transition of germ cells in the fetal ovary from mitosis to meiosis (Soygur et al., 2021). Paraformaldehyde-fixed mouse ovaries were labeled with various nuclear markers and cleared in BABB. To determine the 3D distribution of germ cells, embryonic ovaries were computationally divided into seven segments along the longitudinal as well as transverse planes and germ cell numbers were quantified by using custom MATLAB scripts in Imaris analysis software. This revealed an earlier

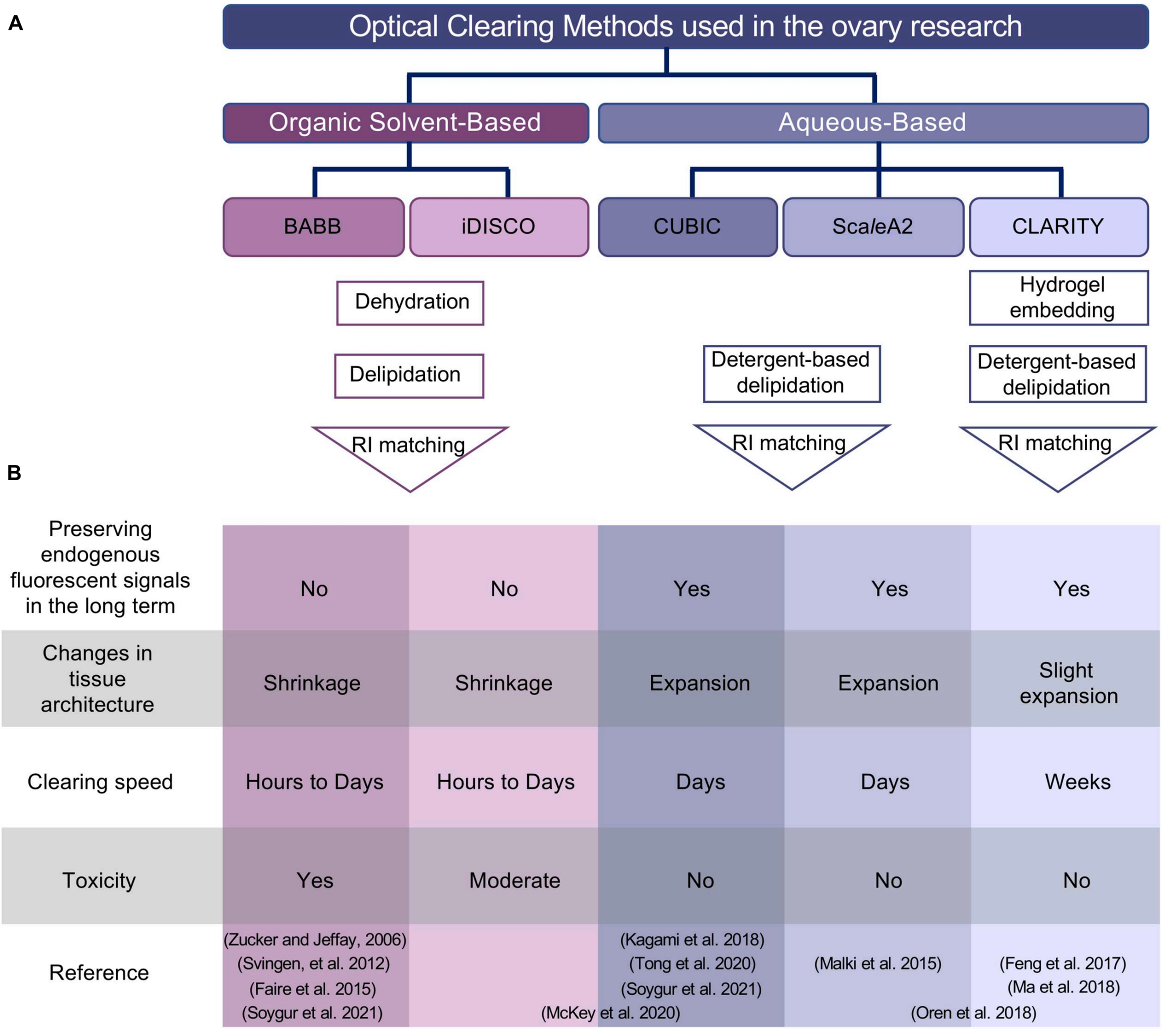

Preserving endogenous fluorescent signals in the long term	No	No	Yes	Yes	Yes
Changes in tissue architecture	Shrinkage	Shrinkage	Expansion	Expansion	Slight expansion
Clearing speed	Hours to Days	Hours to Days	Days	Days	Weeks
Toxicity	Yes	Moderate	No	No	No
Reference	(Zucker and Jeffay, 2006) (Svingen, et al. 2012) (Faire et al. 2015) (Soygur et al. 2021)	(McKey et al. 2020)	(Kagami et al. 2018) (Tong et al. 2020) (Soygur et al. 2021)	(Malki et al. 2015) (Oren et al. 2018)	(Feng et al. 2017) (Ma et al. 2018)

FIGURE 2 | Summary of optical clearing methods applied to the ovary. **(A)** Outline of organic solvent-based and aqueous-based clearing approaches. Despite the use of different reagents in two different (BABB and iDISCO) organic solvent-based clearing methods, both protocols involve dehydration, delipidation, and a final RI matching step. Aqueous-based approaches (CUBIC and Sca*l*eA2) use high concentrations of detergents to remove lipids, while hydrogel embedding of the sample in CLARITY protocol maintains tissue and protein structure before incubation with high concentration of detergents to remove lipids. **(B)** Comparison of different methods based on experimental specifications. Studies used combined approaches are placed spanning the columns for iDISCO and CUBIC or Sca*l*eA2 and CLARITY in the reference column. BABB, benzyl alcohol and benzyl benzoate; iDISCO, immunolabeling-enabled three-dimensional imaging of solvent-cleared organs; CUBIC, clear, unobstructed brain/body imaging cocktails and computational analysis; CLARITY, clear lipid-exchanged acrylamide-hybridized rigid imaging/immunostaining/*in situ*-hybridization-compatible tissue hydrogel; RI, refractive index.

appearance of the earliest SYCP3+ meiotic cells as clusters in the core anterior ovary as early as E12.5. This radial geometry of meiotic initiation which precedes the anterior-posterior meiotic wave is orchestrated by intercellular bridges between developing germ cells (**Figure 1A**). Although the transition from mitotic to SYCP3+ leptotene and zygotene stage occurs asynchronously in a spatially-defined pattern, progression to the SYCP1+ pachytene stage was by contrast observed to be rapid and synchronous, suggesting that the time spent in the early stages of MPI differs amongst germ cells. By taking advantage of the well-established solvent-based clearing method, this study revealed spatiotemporal differences between critical developmental events in germ cells in mice, the functional consequence of which remains to be tested.

Although BABB was the first organic solvent used to clear mouse organs, it was not sufficient to clear bigger samples and alcohol-based dehydration rapidly quenched fluorescence signals. These limitations were overcome by replacing BABB with the combination of dibenzyl ether (DBE) and tetrahydrofuran (THF), known as 3DISCO solvent-based clearing (Erturk et al., 2012, 2014), or iDISCO in combination with immunolabeling (Renier et al., 2014). A major advantage of this method is the preservation of fluorescent signal longer, in addition to clearing large tissues, notably a whole adult mouse body with ultimate DISCO (uDISCO) (Pan et al., 2016). This protocol was improved

TABLE 2 | Possible future applications of 3D imaging.

What is known	Current unknown	Questions that can be answered using 3D visualization
Mature oocytes can be generated by co-culturing mESCs-derived PGCLCs and fetal ovarian somatic cells (rOvaries) *in vitro*.	Why is the efficiency of *in vitro* oocyte derivation relatively low and how can it be improved?	Identifying *in vivo* oocyte-niche (supporting cells, vasculature, and neuronal) interactions in 3D and comparing 3D architecture of rOvaries with *in vivo* structure can lead to the development of better culture systems (for instance, recapitulating *in vivo* development by enrichment of the vasculature and neuronal progenitors in the culture systems).
Ovarian cancer organoids are generated by using patient-derived tumor cells to study the progression and treatment of ovarian tumors.	How closely do ovarian organoids mimic 3D structure of *in vivo* ovarian cancers?	Validation of ovarian cancer organoids against ovarian tumors in 3D and identifying cellular heterogeneity in intact tumors at single cell resolution. 3D evaluation of organoids can be advantageous for more accurate and rapid evaluation of drug response studies for personalized treatments in the future.
Cryopreservation of human ovarian tissue pieces aims to preserve fertility in patients.	What is the 3D composition of ovarian strips and what is the best cryopreservation protocol that maintains the tissue structure?	Mapping complex ovarian structures to advance our understanding of the human ovary and providing a valuable tool to compare the effects of different cryopreservation protocols on the 3D structural integrity of the ovarian follicles, vasculature, and stroma.
Follicle numbers and ovarian microenvironment (increased fibrosis, stiffness, and inflammation) change with aging.	How do the hallmarks of ovarian aging affect tissue structure?	Newly developed probes can provide better labeling for aged ovaries. 3D visualization can reveal complex vascular and neuronal network, and fine details of ovarian aging that potentially affects the function of the ovary.

mESC, mouse embryonic stem cells; PGCLCs, primordial germ cell-like cells; rOvaries, reconstituted ovaries; 3D, three-dimensional.

with shortened processing times and increased fluorescent preservation by combined adjustment of temperature and pH in DISCO with superior fluorescence-preserving capability (FDISCO) (Qi et al., 2019). Among these variations, iDISCO was used to clear adult ovaries, achieving efficient fluorescent signal as well as successful antibody penetration to visualize follicular structures and the ovarian interstitial compartment in adult mice (McKey et al., 2020).

Aqueous-Based Clearing

Despite advances in organic solvent-based clearing techniques, the instability of endogenous fluorescent signals that resulted from the removal of water molecules during dehydration created a need for aqueous-based clearing approaches. Sucrose (Tsai et al., 2009), fructose/thioglycerol (SeeDB) (Ke et al., 2013), and formamide (ClearT) (Kuwajima et al., 2013) are aqueous solutions with high refractive indices that approximate that of tissues. Simple immersion in such aqueous clearing solutions preserves lipid structures, however, it is not sufficient to clear thick samples containing connective tissue such as ovaries. Sca*l*eA2 is an aqueous-based clearing approach that uses detergents instead of hydrophobic solvents to remove lipids while maintaining tissue hydration with urea and glycerol (Hama et al., 2011) (**Figure 2A**). Samples in Sca*l*eA2 undergo expansion due to hyperhydration, however, transparency is improved with a lower cost of reagents compared to some other aqueous-based solutions. Sca*l*eA2 was combined with sucrose preincubation to image oocytes with TRA98 in fetal ovaries during meiosis and fetal oocyte attrition (Malki et al., 2015). After manually correcting the image segmentation for a representative single z stack, the actual percentage of the error of automatic germ cell detection was calculated as 9–14%, which can be further improved with higher quality image acquisition. The total germ cell number decreased about 27% between E15.5 and E18.5, which is less than the almost twofold loss reported by histological sampling (Malki et al., 2014). Sca*l*eA2 with TRA98 immunofluorescence was also used to study right/left ovarian asymmetry. Earlier studies showed inequalities between right and left ovaries in function as the ovulation rate in mice (Wiebold and Becker, 1987). Similar to results presented by Faire et al. (2015) in adult ovaries, precise analysis of germ populations demonstrated no significant difference between right and left ovaries at E15.5 and E18.5. The work of Malki et al. (2015) laid the groundwork for 3D analysis of embryonic ovaries by providing a detailed analysis pipeline, error rate of the technique, and direct comparison between sampling and whole-mount methods.

Even greater transparency with aqueous clearing came from a chemical screen of mouse brain based on components of Sca*l*eA2. The Clear, Unobstructed Brain/Body Imaging Cocktails and Computational analysis (CUBIC) protocol (Susaki et al., 2014, 2015) can be applied as simple immersion or perfusion. The first reagent contains polyhydric alcohol (Quadrol), detergent (Triton-X 100), and urea and removes lipids. The second reagent, consisting of triethanolamine polyhydric alcohol, sucrose and urea, matches the refractive index of the tissue and provides improves transparency over Sca*l*eA2and preservation of endogenous fluorescent signals (**Figure 2**). CUBIC has been used to understand 3D structures of ovaries using endogenous fluorescent reporter proteins and immunolabeled structures. A modified CUBIC protocol was employed by Kagami et al. (2018) to visualize ubiquitous EGFP in adult mouse ovary as a proof of principle. Incubation in Sca*l*eA2-CUBIC-1 solution alone sufficiently cleared fetal mouse ovaries for visualization of endogenous fluorescent signals and immunolabeling (Soygur et al., 2021). 3D imaging of inducible multicolored reporters revealed clonal structure of germ cells; during cyst formation, 3D analysis provided quantitative evidence that cytoplasmic sharing occurs via germ cell intercellular bridges. While CUBIC clearing is sufficient to visualize endogenous proteins in fetal ovaries, McKey et al. (2020) reported that it did not provide optimal results in adults. However, this discrepancy may be attributable to minor differences in clearing protocols in these two studies. Combining two clearing approaches, iDISCO and CUBIC, improved clearing efficiency and allowed imaging of various cell populations: follicles, vasculature, interstitial cells, and neurons in adult ovaries (McKey et al., 2020). While this study is the first to combine two different clearing methods to visualize immunolabeled structures in adult mouse ovaries, immunolabeled structures could not be analyzed quantitatively in adult ovaries due to high background or inaccurate segmentation of image analysis software.

Hydrogel Embedding

Hydrogel embedding of tissues is used with aqueous clearing methods to help maintain biological/cellular structures through providing structural support. In the method dubbed CLARITY (Clear Lipid-exchanged Acrylamide-hybridized Rigid Imaging/Immunostaining/*in situ*-hybridization-compatible Tissue hYdrogel) (Chung et al., 2013), hydrogel monomers are infused during tissue fixation, and the polymerization of hydrogel mesh is initiated with heat to form a tissue-hydrogel hybrid. Subsequently, lipids are removed from the tissue-hydrogel hybrid with highly concentrated detergents, either passively or aided by electrophoresis, before immersing the tissue in a refractive index-matched clearing solution (**Figure 2A**). Feng et al. (2017) implemented a passive CLARITY protocol to render mouse ovaries transparent over 4–8 weeks. They were able to quantify follicles and their spatial distribution throughout development and aging (from PN3 to 12-months old). The volume of follicles increased $\sim 3 \times 10^5$-fold from primordial to pre-ovulatory follicle whereas, follicle roundness decreased, reflecting massive follicle growth and dynamic tissue remodeling in the ovaries (Feng et al., 2017). Spatial analysis of follicle distribution within the ovary demonstrated that follicles tend to localize toward the center as folliculogenesis progresses (from primordial to antral follicles) and ovary undergoes active remodeling at each cycle as observed previously (Hirshfield and DeSanti, 1995). Within the ovary, follicles aggregated with similarly staged follicles, however, pre-ovulatory follicles had fewer primordial, primary, and secondary follicle neighbors compared to later follicular stages, suggesting that estrogen or other factors secreted by pre-ovulatory follicles may inhibit earlier stage of folliculogenesis.

Imaging Vasculature in the Ovary

In addition to changes in the organization of follicles, whole-mount imaging revealed the dynamics of the vasculature in mouse ovaries. Organic solvent-based clearing was applied to mouse ovaries that express GFP under *Prox1* promoter in order to characterize the spatiotemporal development of the lymphatic network in the ovary (Svingen et al., 2012). *Prox*1-EGFP ovaries were fixed in 4% paraformaldehyde, immunolabeled with GFP and lymphatic vascular markers followed by embedding in agarose. BABB cleared ovaries were imaged with confocal microscope or optical projection tomography, and visually presented by using Imaris software. Previously, the presence of lymphatic vessels was reported in ovaries just before birth by *X*-gal staining of *Prox1*$^{+/\mathrm{lacZ}}$ mice (Brennan et al., 2002) however, 3D visualization of lymphatic vessels in *Prox*1-EGFP ovaries at higher magnification revealed that the first lymphatic vessels invade the ovary at PN10. This later development of ovarian lymphatics contrasts with other adjacent structure such as the uterus and ovarian ligaments in which lymphangiogenesis occurs during fetal development. 3D visualization of the lymphatic network using Prox1-GFP revealed expansion through the ovarian medulla and cortex during adulthood (**Figure 1C**). The lymphatic network mostly overlapped with endoglin-positive blood vessels, but by contrast, LYE1-positive small lymphatic capillaries were predominantly localized in ovarian and extraovarian rete. Enabled by 3D imaging and clearing, this first qualitative description of the complex network of lymphatic vessels (Svingen et al., 2012) lays the foundation for future studies to probe function of lymphangiogenesis by examining interactions with follicles in healthy, advanced age, as well as diseased ovaries.

CLARITY also enabled the mapping of dynamic changes in ovarian blood vessels during folliculogenesis, which would be difficult or impossible to visualize with traditional histology. Work by Feng et al. (2017) revealed that the largest vasculature originating from ovarian hilum was expanded 40% from PN3 to adulthood. At the follicle level, PECAM1+ endothelial cells were absent or sparse in primordial and primary follicles but became prominent in the thecal layer of secondary follicles, and remained through the antral, preovulatory follicles and the corpus luteum. Inducing follicular growth by hormone treatment at PN21 dramatically increased the diameter of the main vessel and revealed a structured organization of follicles around main vascular tree (**Figure 1B**). In mice with a heterozygous deletion of vascular endothelial growth factor A (*Vegfa*$^{+/-}$), the same hormone treatment contributed to defects in ovarian vasculature, and ultimately decreased ovarian weight and reduced number of oocytes ovulated compared to wild-type; this functionally demonstrated the dependence of follicle maturation and successful ovulation upon vascular remodeling.

Further driven by the need to visualize the elaborate structure of the vascular systems, CLARITY and Sca*le*A2 were combined to establish the Whole Organ Blood and Lymphatic Vessel Imaging (WOBLI) technique (Oren et al., 2018). This optimization replaced the costly FocusClear clearing reagent in the CLARITY protocol with Sca*le*A2 to improve efficiency of tissue clearing in combination with immunolabeling. For high-resolution 3D structural resolution of blood vessels in the ovary and other organs, transgenic mice expressing tdTomato under the *Ve-cadherin* promoter were processed by WOBLI and imaged with light sheet microscopy. Although immersion of the sample in WOBLI clearing solution expanded the tissue (∼1.7- 2-fold), the broad morphology and follicular structures were maintained in the ovary. In pubertal mice, this protocol allowed for quantification of total vessel length, vessel diameter, vessel straightness and total number of branching points within the ovary (Oren et al., 2018). As blood vessels and lymphatics are responsible for homeostasis and immune function, 3D mapping of their dynamics provides valuable information toward targeted drug delivery for ovarian cancers or fertility treatment.

Imaging Peripheral Nerves in the Ovary

The Capel group first charted peripheral innervation in the developing and neonatal ovary and using whole-mount imaging with combined iDISCO and CUBIC clearing techniques (McKey et al., 2019). Detailed 3D analysis of the intact gonad and adjacent mesonephros uncovered the spatiotemporal dynamics of innervation of the ovary and its striking sexual dimorphism with the developing testis. Immunofluorescence revealed that the neuronal network in the ovary is established by TH+ projections in the mesonephros that first invade the dorsal side of the ovary before birth, reaching the ventral side by passing through medulla (**Figure 1D**). While the innervation of the ovary begins during fetal development, the testis is recalcitrant to neural projections at the same timepoint, is likely due to repressive signals which are upregulated during male but not female somatic differentiation. Although this study was the first to identify patterns of innervation of the developing ovary, functional interactions between nerve fibers and somatic cells of the ovary during fetal development remain to be tested.

In a recent 3D study of innervation in postnatal and adult mouse ovaries using CUBIC-clearing Tong et al. (2020) showed that each follicle is innervated by a single neural fiber; furthermore, peripheral nerve branching around follicles increases at later stages of folliculogenesis (**Figure 1D**). They further showed that PMSG-induced follicular growth contributed to a visible increase in TH-positive neuronal fibers in the ovary within 48-h. Tracing the long and circuitous routes of nerve fibers could not be accomplished through traditional histology, but is ripe for 3D techniques. The growth and regeneration of nerve fibers in the ovary warrant further study, particularly focused on various pathologies related to neural network of the ovary.

3D MODELING OF THE AGING OVARY

Although the age-related decline in ovarian function has long been recognized, the structural and functional changes occurring in the ovary during aging are not well defined. Feng et al. (2017) applied the CLARTIY protocol to visualize 12-month-old mouse ovaries and quantified follicle numbers by using Imaris software. Consistent with prior reports, they demonstrated a decrease in the number of total follicles at this age of reproductive senescence, however, the percentage of primordial and primary follicles was found to increase in aged ovaries due to decreased numbers of secondary and later stage follicles (Feng et al., 2017). In addition to diminished follicle numbers, other studies have described dramatic changes that occur in the ovarian microenvironment with aging, and their potential impact ovarian function and follicle development (Duncan et al., 2018). More recently increased ovarian stiffness was associated with elevated collagen and decreased hyaluronan in 2D histological examination of aged ovaries (Amargant et al., 2020). Further insight into tissue properties in the ovary came from a 3D analysis of adult mouse ovaries which demonstrated that sphericity of follicles decreased in later stages of folliculogenesis due to the changes in ovarian rigidity; interestingly this change was not observed when folliculogenesis was artificially induced by hormone treatment in prepubertal mice (Feng et al., 2017). This result suggests that changes in the ovarian stroma over time regulate the stiffness of the ovary and affect the shape of follicles. Possible functional outcomes of altered physical properties of follicles remain to be tested.

Conventional histological analysis showed increased accumulation of extracellular matrix, particularly collagen I and III, leads fibrosis in the stroma with aging. Age-related fibrosis appears to be connected with infiltration of multinucleated macrophage giant cells in ovaries at advanced aged (Briley et al., 2016). Detailed transcriptome analysis revealed changes in the macrophage populations in aged ovaries that may contribute to the aging-associated chronic inflammation (known as inflammaging) in the ovaries (Zhang et al., 2020). Despite the detailed characterization of inflammation in ovarian aging, the location and dynamics of immune cells in ovaries has not been reported. 3D imaging will help to define the hallmarks of ovarian aging as well as the changes in tissue structure (follicles, vasculature, and nerve fibers) caused by age-induced fibrosis and inflammation.

3D ANALYSIS OF THE OVARY IN DIFFERENT SPECIES

The majority of 3D analysis techniques were initially developed for studies in mice because they are widely used mammalian models for human physiology and disease, while their small size increases clearing efficiency. Improvements in clearing and imaging technologies have allowed researchers to image intact human embryos as well as fetal organs. Using the 3DISCO protocol, gestational week 10.5 ovaries and the surrounding extensive vascular network were successfully visualized for the 3D human cell atlas (Belle et al., 2017).

More recently, a number of studies applied 3D modeling to different species to study ovarian diseases in rats. Ma et al. (2018) used CLARITY and 3D imaging to investigate follicle dynamics and the vessel structure in rat ovaries following the induction of Polycystic Ovary Syndrome (PCOS) by 5α-dihydrotestosterone (DHT). Despite the similar follicle numbers in both groups during the early stages of folliculogenesis, pre-ovulatory follicles were completely absent in PCOS-like ovaries. The authors performed low-frequency electro-acupuncture (EA), which positively increases ovulation and pregnancy success rates in humans with PCOS (Smith et al., 2016), and showed a quantitative restoration pre-ovulatory follicles in PCOS-like rats. In addition to the poor ovulatory response, the vascular architecture in PCOS-like rat ovaries was impaired. EA treatment partially rescued the PCOS-like phenotype by increasing total vascular area and volume, particularly in mature follicles, suggesting that elevated blood flow allows mature follicles to receive signals required for ovulation. The role of innervation in PCOS pathology and its possible treatment via EA therapy were also studied in rat ovaries using CUBIC clearing and 3D analysis (Tong et al., 2020). EA treatment reversed the increased innervation in the ovarian stroma and the diminished neuronal network around individual follicles in PCOS-like ovaries. Denervation studies suggested that EA treatment of this model of PCOS in rats is regulated through the superior ovarian nerve (SON). The 3D techniques applied in these studies uncovered intricate relationships between follicles, vasculature and nerve fibers in PCOS, which affects as many as 18% of women during their childbearing years (Ding et al., 2017). The expanded use of 3D analysis will grant more comprehensive view of PCOS as well as other complex pathologies.

Clearing and 3D imaging of ovaries in fish has proved to be challenging due to the high concentration of lipids in teleost oocytes. A recent study compared several clearing methods in medaka ovaries: (*i*) simple immersion in high-refractive index matching solutions, (*ii*) iDISCO, (*iii*) CUBIC, (*iv*) Ethyl cinnamate 'ECi,' and (*v*) combined CUBIC and ECi 'C-ECi' (Lesage et al., 2020). Solvent-based ECi and iDISCO techniques provided better transparency for paraformaldehyde-fixed medaka ovaries however, methyl green counterstaining produced high background with ECi clearing. To reduce the background staining that potentially arose from the remaining lipid in ECi-cleared ovaries, the authors varied pH, temperature, and combined CUBIC and Ethyl cinnamate 'C-ECi' techniques. Among all parameters tested, the combined C-ECi protocol (pH7, 50°C) best preserved the methyl green fluorescent signal. 3D analysis showed that medaka ovaries predominantly contain small follicles whereas post-vitellogenic (maturation) stage follicles comprise 2,3% of total follicles and localize on the ventral side of the ovary. Direct comparison of follicle numbers determined by 3D versus 2D analysis revealed that the prior 2D estimations lead to overcounting of intermediate follicles and undercounting of small and larger follicles. The same analysis pipeline was also applied to trout ovaries that contain bigger oocytes, yielding a similar predominance of small follicles. This study by Lesage et al. (2020) serves as a guide for clearing and analysis of ovaries with high lipid content and guide for future developmental studies in various species.

FUTURE DIRECTIONS

3D visualization and analysis of the ovary at single cell resolution has great potential to reveal higher-order biological structure, while also holding promise for improving *in vitro* approaches. Until a few years ago, the generation of mature oocytes by *in vitro* reconstitution of oogenesis was a major challenge in the field of reproductive biology. A major breakthrough came with the recognition that mouse embryonic stem cell-derived primordial germ cell-like cells (PGCLCs) could be induced to initiate meiosis by co-culture with fetal ovarian somatic cells, which lead to the formation of reconstituted ovaries (rOvaries) and ultimately the generation of healthy offspring from these *in vitro* derived oocytes (Hikabe et al., 2016). While this model offers a unique platform for studying the regulatory mechanisms of oogenesis and paves the way for future human-focused studies, the relatively low efficiency of *in vitro* oocyte derivation would likely be improved by studies aimed at understanding the complex interactions between the oocyte and its niche (supporting cells, vasculature, and neuronal) in 3D. The comprehensive view of the ovary provided by 3D analyses highlights the dynamic changes occurring during development and will inform the roadmap for generating oocytes outside of the body (**Table 2**).

Insights gained from structural and functional 3D mapping of the ovary will aid in studying the progression and treatment of ovarian disease through novel organoid technologies. As *in vitro*-produced model organ structures containing several cell types of the target organ, organoids can be used to recapitulate tissue organization and structure, and to study cellular and tissue function in the context of diseases *in vitro* (Clevers, 2016). Although traditional 2D cell culture is the backbone of *in vitro* studies, development of 3D organoids more closely mimics the physiological composition of tissues and is gaining traction for understanding diseases and developing drugs as well as cell therapies. 3D ovarian cancer organoids were generated using patient-derived tumor cells and used to establish experimental models, perform drug response assays, and subsequently to develop personalized treatment strategies for ovarian cancers (Kopper et al., 2019; Maru et al., 2019; Nanki et al., 2020). Despite the efforts spent for their generation, these 3D ovary organoid structures were analyzed in 2D using conventional histological preparations. A direct comparison of the 3D structure of ovarian cancer organoids to tumors as well as ovary tissue would validate this model and potentially provide useful insights. More widespread adoption of techniques for clearing and 3D analysis will be important for improving ovarian cancer organoids, precisely mapping cell-cell interactions, and identifying cellular heterogeneity within tumors, particularly during drug responses (**Table 2**).

The application of 3D technologies to human ovaries will also augment current knowledge and practices of fertility preservation treatments. Cryopreservation of human ovarian cortical strips is becoming increasingly common as a means of preserving fertility. This procedure aims to protect fertility in cancer patients, particularly in pre-pubertal girls who lose their ovarian function as a result of chemotherapy or radiation (Wallace et al., 2014; Rivas Leonel et al., 2019). The success of fertility preservation treatment depends on the number of follicles maintained in cryopreserved tissue pieces, which is a function of the cryopreservation technique. The efficiency of cryopreservation has been compared by assessing follicle numbers and structure before and after using 2D conventional histology (Nisolle et al., 2000; Kagawa et al., 2009; Silber et al., 2010). With a different approach, Soleimani et al. (2006) took visualized human ovarian tissue strips in 3D after staining with a vital dye, Rhodamine 123 (R123) that would enable analysis without compromising transplantability. However, the absence of a clearing step in live tissue limits analysis to samples that are thinner than 0.5 mm. New developments in clearing techniques and 3D analysis of human ovary pieces will enable the mapping of complex ovarian structures such as follicles, vasculature and nerves at the single cell level, providing fundamentally new basic information about human ovarian follicle development. Careful examination of human cortical ovarian strips will also provide a valuable tool to compare the impacts of different cryopreservation protocols on the 3D structural integrity of the ovarian follicles, vasculature, and stroma in order to establish the least harmful protocol for clinical specimens (**Table 2**).

Although different clearing approaches greatly extend the limits of high-resolution analysis of intact organs (and even entire intact organisms), the field of 3D ovary modeling has adopted a limited number of these techniques. Despite the relative ease of clearing the fetal and adult ovaries, increased fibrosis and stiffness of the ovary with aging (Briley et al., 2016; Amargant et al., 2020) make the visualization and downstream analysis more challenging. To increase labeling efficiency and enhance subcellular protein identification in aged ovaries, recently developed probes and fluorophores provide promising alternatives to conventional immunoglobulin G (IgG) antibodies. Nanobodies are monomeric (heavy chain only) antibody fragments with the advantages of small size (15 kDa compared to 150 kDa for IgGs) allowing deeper and more effective penetration into tissue, higher binding affinity for their targets, and increased fluorescence intensity, thus providing better visualization of samples (de Beer and Giepmans, 2020). A nanobody based approach, along with an improved clearing protocol, was implemented in whole-body immunolabeling and visualization of mice, enabling Cai et al. (2019) to map neuronal projections in adult mice, and simultaneously to uncover short vascular connections in the brain which had previously not been visualized. Accordingly, improving the clearing and labeling efficiency of the aged ovary by applying these recent developments in the 3D modeling era will elucidate potential mechanisms contributing to the age-related decline in fertility as well as other pathologies (**Table 2**).

CONCLUSION

The pioneering studies of the last 15 years paved the way for deciphering the 3D structure and function of the mammalian ovary. In the longer term, the development of non-toxic clearing reagents would enable 3D visualization of specimens for downstream analysis and manipulation in the lab or treatments in the clinic. With the evolution and widespread adoption and combination of tissue clearing technologies, imaging and analysis tools with other cutting edge genomic and machine learning technologies, the field will be poised to unravel the complexity of the mammalian ovary, and ultimately to advance female reproductive health and aging.

AUTHOR CONTRIBUTIONS

BS and DJL conceived and wrote the review. Both authors contributed to the article and approved the submitted version.

FUNDING

BS was supported by the Global Consortium for Reproductive Longevity and Equality at the Buck Institute (Grant Number GCRLE-1620), made possible by the Bia-Echo Foundation. DJL was supported by P30-ES030284, R01ES028212, and R01GM122902, the W. M. Keck Foundation, and the UCSF Program for Breakthrough Biomedical Research.

ACKNOWLEDGMENTS

We thank Rebecca G. Jaszczak, Steven A. Cincotta, Eliza Gaylord, Mariko Foecke, and Jing Li for comments on the manuscript.

REFERENCES

Amargant, F., Manuel, S. L., Tu, Q., Parkes, W. S., Rivas, F., Zhou, L. T., et al. (2020). Ovarian stiffness increases with age in the mammalian ovary and depends on collagen and hyaluronan matrices. *Aging Cell* 19:e13259.

Arora, R., Abby, E., Ross, A. D., Cantu, A. V., Kissner, M. D., Castro, V., et al. (2016). Meiotic onset is reliant on spatial distribution but independent of germ cell number in the mouse ovary. *J. Cell Sci.* 129, 2493–2499.

Atsma, F., Bartelink, M. L., Grobbee, D. E., and Van Der Schouw, Y. T. (2006). Postmenopausal status and early menopause as independent risk factors for cardiovascular disease: a meta-analysis. *Menopause* 13, 265–279. doi: 10.1097/01.gme.0000218683.97338.ea

Bajcsy, P., Chalfoun, J., and Simon, M. (2018). "Introduction to big data microscopy experiments," in *Web Microanalysis of Big Image Data*, (Cham: Springer), 1–15. Available online at: https://doi.org/10.1007/978-3-319-63360-2_1

Belle, M., Godefroy, D., Couly, G., Malone, S. A., Collier, F., Giacobini, P., et al. (2017). Tridimensional visualization and analysis of early human development. *Cell* 169, 161–173.e12.

Bowles, J., Knight, D., Smith, C., Wilhelm, D., Richman, J., Mamiya, S., et al. (2006). Retinoid signaling determines germ cell fate in mice. *Science* 312, 596–600. doi: 10.1126/science.1125691

Brennan, J., Karl, J., and Capel, B. (2002). Divergent vascular mechanisms downstream of Sry establish the arterial system in the XY gonad. *Dev. Biol.* 244, 418–428. doi: 10.1006/dbio.2002.0578

Briley, S. M., Jasti, S., Mccracken, J. M., Hornick, J. E., Fegley, B., Pritchard, M. T., et al. (2016). Reproductive age-associated fibrosis in the stroma of the mammalian ovary. *Reproduction* 152, 245–260. doi: 10.1530/rep-16-0129

Broekmans, F. J., Soules, M. R., and Fauser, B. C. (2009). Ovarian aging: mechanisms and clinical consequences. *Endocr. Rev.* 30, 465–493. doi: 10.1210/er.2009-0006

Brown, H. M., and Russell, D. L. (2014). Blood and lymphatic vasculature in the ovary: development, function and disease. *Hum. Reprod. Update* 20, 29–39. doi: 10.1093/humupd/dmt049

Bucci, T. J., Bolon, B., Warbritton, A. R., Chen, J. J., and Heindel, J. J. (1997). Influence of sampling on the reproducibility of ovarian follicle counts in mouse toxicity studies. *Reprod. Toxicol.* 11, 689–696. doi: 10.1016/s0890-6238(97)00034-8

Bullejos, M., and Koopman, P. (2004). Germ cells enter meiosis in a rostro-caudal wave during development of the mouse ovary. *Mol. Reprod. Dev.* 68, 422–428. doi: 10.1002/mrd.20105

Cai, R., Pan, C., Ghasemigharagoz, A., Todorov, M. I., Forstera, B., Zhao, S., et al. (2019). Panoptic imaging of transparent mice reveals whole-body neuronal projections and skull-meninges connections. *Nat. Neurosci.* 22, 317–327. doi: 10.1038/s41593-018-0301-3

Cantu, A. V., Altshuler-Keylin, S., and Laird, D. J. (2016). Discrete somatic niches coordinate proliferation and migration of primordial germ cells via Wnt signaling. *J. Cell Biol.* 214, 215–229. doi: 10.1083/jcb.201511061

Charleston, J. S., Hansen, K. R., Thyer, A. C., Charleston, L. B., Gougeon, A., Siebert, J. R., et al. (2007). Estimating human ovarian non-growing follicle number: the application of modern stereology techniques to an old problem. *Hum. Reprod.* 22, 2103–2110. doi: 10.1093/humrep/dem137

Chen, Y., Yang, W., Shi, X., Zhang, C., Song, G., and Huang, D. (2020). The factors and pathways regulating the activation of mammalian primordial follicles in vivo. *Front. Cell Dev. Biol.* 8:575706. doi: 10.3389/fcell.2020.575706

Chung, K., Wallace, J., Kim, S. Y., Kalyanasundaram, S., Andalman, A. S., Davidson, T. J., et al. (2013). Structural and molecular interrogation of intact biological systems. *Nature* 497, 332–337.

Clevers, H. (2016). Modeling development and disease with organoids. *Cell* 165, 1586–1597. doi: 10.1016/j.cell.2016.05.082

Conchello, J. A., and Lichtman, J. W. (2005). Optical sectioning microscopy. *Nat. Methods* 2, 920–931.

Cordeiro, M. H., Kim, S. Y., Ebbert, K., Duncan, F. E., Ramalho-Santos, J., and Woodruff, T. K. (2015). Geography of follicle formation in the embryonic mouse ovary impacts activation pattern during the first wave of folliculogenesis. *Biol. Reprod.* 93:88.

Coveney, D., Cool, J., Oliver, T., and Capel, B. (2008). Four-dimensional analysis of vascularization during primary development of an organ, the gonad. *Proc. Natl. Acad. Sci. U.S.A.* 105, 7212–7217. doi: 10.1073/pnas.0707674105

Da Silva-Buttkus, P., Marcelli, G., Franks, S., Stark, J., and Hardy, K. (2009). Inferring biological mechanisms from spatial analysis: prediction of a local inhibitor in the ovary. *Proc. Natl. Acad. Sci. U.S.A.* 106, 456–461. doi: 10.1073/pnas.0810012106

D'Albora, H., Anesetti, G., Lombide, P., Dees, W. L., and Ojeda, S. R. (2002). Intrinsic neurons in the mammalian ovary. *Microsc. Res. Tech.* 59, 484–489. doi: 10.1002/jemt.10231

de Beer, M. A., and Giepmans, B. N. G. (2020). Nanobody-Based probes for subcellular protein identification and visualization. *Front. Cell. Neurosci.* 14:573278. doi: 10.3389/fncel.2020.573278

Dees, W. L., Hiney, J. K., Mcarthur, N. H., Johnson, G. A., Dissen, G. A., and Ojeda, S. R. (2006). Origin and ontogeny of mammalian ovarian neurons. *Endocrinology* 147, 3789–3796. doi: 10.1210/en.2006-0394

Ding, T., Hardiman, P. J., Petersen, I., Wang, F. F., Qu, F., and Baio, G. (2017). The prevalence of polycystic ovary syndrome in reproductive-aged women of different ethnicity: a systematic review and meta-analysis. *Oncotarget* 8, 96351–96358. doi: 10.18632/oncotarget.19180

Dodt, H. U., Leischner, U., Schierloh, A., Jahrling, N., Mauch, C. P., Deininger, K., et al. (2007). Ultramicroscopy: three-dimensional visualization of neuronal networks in the whole mouse brain. *Nat. Methods* 4, 331–336. doi: 10.1038/nmeth1036

Domínguez, R., and Se, C.-M. (2011). The ovarian innervation participates in the regulation of ovarian functions. *Endocrinol. Metabol. Syndrome* S4:001.

Duncan, F. E., Cofino, R., and Pavone, M. E. (2018). "Female reproductive aging: from consequences to mechanisms, markers, and treatments," in *Conn's Handbook of Models for Human Aging*, eds J. L. Ram and P. M. Conn (Cambridge, MA: Elsevier Academic Press).

Edson, M. A., Nagaraja, A. K., and Matzuk, M. M. (2009). The mammalian ovary from genesis to revelation. *Endocr. Rev.* 30, 624–712. doi: 10.1210/er.2009-0012

Erturk, A., Becker, K., Jahrling, N., Mauch, C. P., Hojer, C. D., Egen, J. G., et al. (2012). Three-dimensional imaging of solvent-cleared organs using 3DISCO. *Nat. Protoc.* 7, 1983–1995. doi: 10.1038/nprot.2012.119

Erturk, A., Lafkas, D., and Chalouni, C. (2014). Imaging cleared intact biological systems at a cellular level by 3DISCO. *J. Vis. Exp.* 89:51382.

Estermann, M. A., Major, A. T., and Smith, C. A. (2020). Gonadal sex differentiation: supporting versus steroidogenic cell lineage specification in mammals and birds. *Front. Cell Dev. Biol.* 8:616387. doi: 10.3389/fcell.2020.616387

Faire, M., Skillern, A., Arora, R., Nguyen, D. H., Wang, J., Chamberlain, C., et al. (2015). Follicle dynamics and global organization in the intact mouse ovary. *Dev. Biol.* 403, 69–79. doi: 10.1016/j.ydbio.2015.04.006

Feng, Y., Cui, P., Lu, X., Hsueh, B., Moller Billig, F., Zarnescu Yanez, L., et al. (2017). CLARITY reveals dynamics of ovarian follicular architecture and vasculature in three-dimensions. *Sci. Rep.* 7:44810.

Feng, Y., Tamadon, A., and Hsueh, A. J. W. (2018). Imaging the ovary. *Reprod. Biomed. Online* 36, 584–593.

Fiorentino, G., Parrilli, A., Garagna, S., and Zuccotti, M. (2020). Three-Dimensional micro-computed tomography of the adult mouse ovary. *Front. Cell Dev. Biol.* 8:566152. doi: 10.3389/fcell.2020.566152

Fiorentino, G., Parrilli, A., Garagna, S., and Zuccotti, M. (2021). Three-dimensional imaging and reconstruction of the whole ovary and testis: a new frontier for the reproductive scientist. *Mol. Hum. Reprod.* 27:gaab007.

Flaws, J. A., Abbud, R., Mann, R. J., Nilson, J. H., and Hirshfield, A. N. (1997). Chronically elevated luteinizing hormone depletes primordial follicles in the mouse ovary. *Biol. Reprod.* 57, 1233–1237. doi: 10.1095/biolreprod57.5.1233

Flaws, J. A., Hirshfield, A. N., Hewitt, J. A., Babus, J. K., and Furth, P. A. (2001). Effect of bcl-2 on the primordial follicle endowment in the mouse ovary. *Biol. Reprod.* 64, 1153–1159. doi: 10.1095/biolreprod64.4.1153

Fraser, H. M. (2006). Regulation of the ovarian follicular vasculature. *Reprod. Biol. Endocrinol.* 4:18.

Ginsburg, M., Snow, M. H., and Mclaren, A. (1990). Primordial germ cells in the mouse embryo during gastrulation. *Development* 110, 521–528. doi: 10.1242/dev.110.2.521

Greenbaum, M. P., Iwamori, N., Agno, J. E., and Matzuk, M. M. (2009). Mouse TEX14 is required for embryonic germ cell intercellular bridges but not female fertility. *Biol. Reprod.* 80, 449–457. doi: 10.1095/biolreprod.108.070649

Greenbaum, M. P., Ma, L., and Matzuk, M. M. (2007). Conversion of midbodies into germ cell intercellular bridges. *Dev. Biol.* 305, 389–396. doi: 10.1016/j.ydbio.2007.02.025

Gundersen, H. J. (1986). Stereology of arbitrary particles. A review of unbiased number and size estimators and the presentation of some new ones, in memory of William R. Thompson. *J. Microsc.* 143, 3–45. doi: 10.1111/j.1365-2818.1986.tb02764.x

Gundersen, H. J., Bagger, P., Bendtsen, T. F., Evans, S. M., Korbo, L., Marcussen, N., et al. (1988). The new stereological tools: disector, fractionator, nucleator and point sampled intercepts and their use in pathological research and diagnosis. *APMIS* 96, 857–881. doi: 10.1111/j.1699-0463.1988.tb00954.x

Hama, H., Kurokawa, H., Kawano, H., Ando, R., Shimogori, T., Noda, H., et al. (2011). Scale: a chemical approach for fluorescence imaging and reconstruction of transparent mouse brain. *Nat. Neurosci.* 14, 1481–1488. doi: 10.1038/nn.2928

Hikabe, O., Hamazaki, N., Nagamatsu, G., Obata, Y., Hirao, Y., Hamada, N., et al. (2016). Reconstitution in vitro of the entire cycle of the mouse female germ line. *Nature* 539, 299–303. doi: 10.1038/nature20104

Hirshfield, A. N., and DeSanti, A. M. (1995). Patterns of ovarian cell proliferation in rats during the embryonic period and the first three weeks postpartum. *Biol. Reprod.* 53, 1208–1221. doi: 10.1095/biolreprod53.5.1208

Inik, O., Ceyhan, A., Balcioglu, E., and Ulker, E. (2019). A new method for automatic counting of ovarian follicles on whole slide histological images based on convolutional neural network. *Comput. Biol. Med.* 112:103350. doi: 10.1016/j.compbiomed.2019.103350

Kagami, K., Shinmyo, Y., Ono, M., Kawasaki, H., and Fujiwara, H. (2018). Three-dimensional evaluation of murine ovarian follicles using a modified CUBIC tissue clearing method. *Reprod. Biol. Endocrinol.* 16:72.

Kagawa, N., Silber, S., and Kuwayama, M. (2009). Successful vitrification of bovine and human ovarian tissue. *Reprod. Biomed. Online* 18, 568–577. doi: 10.1016/s1472-6483(10)60136-8

Ke, M. T., Fujimoto, S., and Imai, T. (2013). SeeDB: a simple and morphology-preserving optical clearing agent for neuronal circuit reconstruction. *Nat. Neurosci.* 16, 1154–1161. doi: 10.1038/nn.3447

Kopper, O., De Witte, C. J., Lohmussaar, K., Valle-Inclan, J. E., Hami, N., Kester, L., et al. (2019). An organoid platform for ovarian cancer captures intra- and interpatient heterogeneity. *Nat. Med.* 25, 838–849.

Koubova, J., Menke, D. B., Zhou, Q., Capel, B., Griswold, M. D., and Page, D. C. (2006). Retinoic acid regulates sex-specific timing of meiotic initiation in mice. *Proc. Natl. Acad. Sci. U.S.A.* 103, 2474–2479. doi: 10.1073/pnas.0510813103

Kumar, S., Chatzi, C., Brade, T., Cunningham, T. J., Zhao, X., and Duester, G. (2011). Sex-specific timing of meiotic initiation is regulated by Cyp26b1 independent of retinoic acid signalling. *Nat. Commun.* 2:151.

Kuwajima, T., Sitko, A. A., Bhansali, P., Jurgens, C., Guido, W., and Mason, C. (2013). ClearT: a detergent- and solvent-free clearing method for neuronal and non-neuronal tissue. *Development* 140, 1364–1368. doi: 10.1242/dev.091844

Lesage, M., Thomas, M., Bugeon, J., Branthonne, A., Gay, S., Cardona, E., et al. (2020). C-ECi: a CUBIC-ECi combined clearing method for three-dimensional follicular content analysis in the fish ovarydagger. *Biol. Reprod.* 103, 1099–1109. doi: 10.1093/biolre/ioaa142

Liu, C., Peng, J., Matzuk, M. M., and Yao, H. H. (2015). Lineage specification of ovarian theca cells requires multicellular interactions via oocyte and granulosa cells. *Nat. Commun.* 6:6934.

Ma, T., Cui, P., Tong, X., Hu, W., Shao, L. R., Zhang, F., et al. (2018). Endogenous ovarian angiogenesis in polycystic ovary syndrome-like rats induced by low-frequency electro-acupuncture: the CLARITY three-dimensional approach. *Int. J. Mol. Sci.* 19:3500. doi: 10.3390/ijms19113500

Malki, S., Tharp, M. E., and Bortvin, A. (2015). A whole-mount approach for accurate quantitative and spatial assessment of fetal oocyte dynamics in mice. *Biol. Reprod.* 93:113.

Malki, S., Van Der Heijden, G. W., O'donnell, K. A., Martin, S. L., and Bortvin, A. (2014). A role for retrotransposon LINE-1 in fetal oocyte attrition in mice. *Dev. Cell* 29, 521–533. doi: 10.1016/j.devcel.2014.04.027

Maru, Y., Tanaka, N., Itami, M., and Hippo, Y. (2019). Efficient use of patient-derived organoids as a preclinical model for gynecologic tumors. *Gynecol. Oncol.* 154, 189–198. doi: 10.1016/j.ygyno.2019.05.005

McGee, E. A., and Hsueh, A. J. (2000). Initial and cyclic recruitment of ovarian follicles. *Endocr. Rev.* 21, 200–214. doi: 10.1210/er.21.2.200

McKey, J., Bunce, C., Batchvarov, I. S., Ornitz, D. M., and Capel, B. (2019). Neural crest-derived neurons invade the ovary but not the testis during mouse gonad development. *Proc. Natl. Acad. Sci. U.S.A.* 116, 5570–5575. doi: 10.1073/pnas.1814930116

McKey, J., Cameron, L. A., Lewis, D., Batchvarov, I. S., and Capel, B. (2020). Combined iDISCO and CUBIC tissue clearing and lightsheet microscopy for in toto analysis of the adult mouse ovarydagger. *Biol. Reprod.* 102, 1080–1089. doi: 10.1093/biolre/ioaa012

McLaren, A. (2003). Primordial germ cells in the mouse. *Dev. Biol.* 262, 1–15. doi: 10.1016/s0012-1606(03)00214-8

Menke, D. B., Koubova, J., and Page, D. C. (2003). Sexual differentiation of germ cells in XX mouse gonads occurs in an anterior-to-posterior wave. *Dev. Biol.* 262, 303–312. doi: 10.1016/s0012-1606(03)00391-9

Minsky, M. (1988). Memoir on inventing the confocal scanning microscope. *Scanning* 10, 128–138. doi: 10.1002/sca.4950100403

Mork, L., Maatouk, D. M., Mcmahon, J. A., Guo, J. J., Zhang, P., Mcmahon, A. P., et al. (2012). Temporal differences in granulosa cell specification in the ovary reflect distinct follicle fates in mice. *Biol. Reprod.* 86:37.

Myers, M., Britt, K. L., Wreford, N. G., Ebling, F. J., and Kerr, J. B. (2004). Methods for quantifying follicular numbers within the mouse ovary. *Reproduction* 127, 569–580. doi: 10.1530/rep.1.00095

Nanki, Y., Chiyoda, T., Hirasawa, A., Ookubo, A., Itoh, M., Ueno, M., et al. (2020). Patient-derived ovarian cancer organoids capture the genomic profiles of primary tumours applicable for drug sensitivity and resistance testing. *Sci. Rep.* 10:12581.

Ng, A., Tan, S., Singh, G., Rizk, P., Swathi, Y., Tan, T. Z., et al. (2014). Lgr5 marks stem/progenitor cells in ovary and tubal epithelia. *Nat. Cell Biol.* 16, 745–757. doi: 10.1038/ncb3000

Nisolle, M., Casanas-Roux, F., Qu, J., Motta, P., and Donnez, J. (2000). Histologic and ultrastructural evaluation of fresh and frozen-thawed human ovarian xenografts in nude mice. *Fertil. Steril.* 74, 122–129. doi: 10.1016/s0015-0282(00)00548-3

Niu, W., and Spradling, A. C. (2020). Two distinct pathways of pregranulosa cell differentiation support follicle formation in the mouse ovary. *Proc. Natl. Acad. Sci. U.S.A.* 117, 20015–20026. doi: 10.1073/pnas.2005570117

Olszewski, W. L. (2003). The lymphatic system in body homeostasis: physiological conditions. *Lymphat. Res. Biol.* 1, 11–21; discussion 21-14.

Oren, R., Fellus-Alyagor, L., Addadi, Y., Bochner, F., Gutman, H., Blumenreich, S., et al. (2018). Whole organ blood and lymphatic vessels imaging (WOBLI). *Sci. Rep.* 8:1412.

Paddock, S. W., and Eliceiri, K. W. (2014). "Laser scanning confocal microscopy: history, applications, and related optical sectioning techniques," in *Confocal Microscopy: Methods and Protocols*, ed. S. W. Paddock (New York, NY: Springer New York), 9–47. doi: 10.1007/978-1-60761-847-8_2

Pan, C., Cai, R., Quacquarelli, F. P., Ghasemigharagoz, A., Lourbopoulos, A., Matryba, P., et al. (2016). Shrinkage-mediated imaging of entire organs and organisms using uDISCO. *Nat. Methods* 13, 859–867. doi: 10.1038/nmeth.3964

Parker, W. H., Jacoby, V., Shoupe, D., and Rocca, W. (2009). Effect of bilateral oophorectomy on women's long-term health. *Womens Health (Lond.)* 5, 565–576. doi: 10.2217/whe.09.42

Pepling, M. E., and Spradling, A. C. (1998). Female mouse germ cells form synchronously dividing cysts. *Development* 125, 3323–3328. doi: 10.1242/dev.125.17.3323

Pepling, M. E., and Spradling, A. C. (2001). Mouse ovarian germ cell cysts undergo programmed breakdown to form primordial follicles. *Dev. Biol.* 234, 339–351. doi: 10.1006/dbio.2001.0269

Pepling, M. E., Sundman, E. A., Patterson, N. L., Gephardt, G. W., Medico, L. Jr., and Wilson, K. I. (2010). Differences in oocyte development and estradiol sensitivity among mouse strains. *Reproduction* 139, 349–357. doi: 10.1530/rep-09-0392

Qi, Y., Yu, T., Xu, J., Wan, P., Ma, Y., Zhu, J., et al. (2019). FDISCO: advanced solvent-based clearing method for imaging whole organs. *Sci. Adv.* 5:eaau8355. doi: 10.1126/sciadv.aau8355

Quinn, M. M., and Cedars, M. I. (2017). A canary in the coal mine: reproductive health and cardiovascular disease in women. *Semin. Reprod. Med.* 35, 250–255. doi: 10.1055/s-0037-1603097

Rastetter, R. H., Bernard, P., Palmer, J. S., Chassot, A. A., Chen, H., Western, P. S., et al. (2014). Marker genes identify three somatic cell types in the fetal mouse ovary. *Dev. Biol.* 394, 242–252. doi: 10.1016/j.ydbio.2014.08.013

Renier, N., Wu, Z., Simon, D. J., Yang, J., Ariel, P., and Tessier-Lavigne, M. (2014). iDISCO: a simple, rapid method to immunolabel large tissue samples for volume imaging. *Cell* 159, 896–910. doi: 10.1016/j.cell.2014.10.010

Richardson, D. S., and Lichtman, J. W. (2015). Clarifying tissue clearing. *Cell* 162, 246–257. doi: 10.1016/j.cell.2015.06.067

Rivas Leonel, E. C., Lucci, C. M., and Amorim, C. A. (2019). Cryopreservation of human ovarian tissue: a review. *Transfus. Med. Hemother.* 46, 173–181.

Rocca, W. A., Shuster, L. T., Grossardt, B. R., Maraganore, D. M., Gostout, B. S., Geda, Y. E., et al. (2009). Long-term effects of bilateral oophorectomy on brain aging: unanswered questions from the Mayo Clinic Cohort Study of Oophorectomy and Aging. *Womens Health (Lond.)* 5, 39–48. doi: 10.2217/17455057.5.1.39

Sarma, U. C., Winship, A. L., and Hutt, K. J. (2020). Comparison of methods for quantifying primordial follicles in the mouse ovary. *J. Ovarian Res.* 13:121.

Silber, S., Kagawa, N., Kuwayama, M., and Gosden, R. (2010). Duration of fertility after fresh and frozen ovary transplantation. *Fertil. Steril.* 94, 2191–2196. doi: 10.1016/j.fertnstert.2009.12.073

Smith, C. A., Armour, M., and Ee, C. (2016). Complementary therapies and medicines and reproductive medicine. *Semin. Reprod. Med.* 34, 67–73.

Soleimani, R., De Vos, W., Van Oostveldt, P., Lierman, S., Van Den Broecke, R., De Sutter, P., et al. (2006). Two novel techniques to detect follicles in human ovarian cortical tissue. *Hum. Reprod.* 21, 1720–1724. doi: 10.1093/humrep/del057

Sonigo, C., Jankowski, S., Yoo, O., Trassard, O., Bousquet, N., Grynberg, M., et al. (2018). High-throughput ovarian follicle counting by an innovative deep learning approach. *Sci. Rep.* 8:13499.

Soygur, B., Jaszczak, R. G., Fries, A., Nguyen, D. H., Malki, S., Hu, G., et al. (2021). Intercellular bridges coordinate the transition from pluripotency to meiosis in mouse fetal oocytes. *Sci. Adv.* 7:eabc6747. doi: 10.1126/sciadv.abc6747

Spalteholz, W. (1914). *Über das Durchsichtigmachen von Menschlichen und Tierischen Präparaten*. Leipzig: S. Hirzel.

Steinke, H., and Wolff, W. (2001). A modified spalteholz technique with preservation of the histology. *Ann. Anat.* 183, 91–95. doi: 10.1016/s0940-9602(01)80020-0

Susaki, E. A., Tainaka, K., Perrin, D., Kishino, F., Tawara, T., Watanabe, T. M., et al. (2014). Whole-brain imaging with single-cell resolution using chemical cocktails and computational analysis. *Cell* 157, 726–739. doi: 10.1016/j.cell.2014.03.042

Susaki, E. A., Tainaka, K., Perrin, D., Yukinaga, H., Kuno, A., and Ueda, H. R. (2015). Advanced CUBIC protocols for whole-brain and whole-body clearing and imaging. *Nat. Protoc.* 10, 1709–1727. doi: 10.1038/nprot.2015.085

Svingen, T., Francois, M., Wilhelm, D., and Koopman, P. (2012). Three-dimensional imaging of Prox1-EGFP transgenic mouse gonads reveals divergent modes of lymphangiogenesis in the testis and ovary. *PLoS One* 7:e52620. doi: 10.1371/journal.pone.0052620

Tian, T., Yang, Z., and Li, X. (2021). Tissue clearing technique: recent progress and biomedical applications. *J. Anat.* 238, 489–507. doi: 10.1111/joa.13309

Tilly, J. L. (2003). Ovarian follicle counts–not as simple as 1, 2, 3. *Reprod. Biol. Endocrinol.* 1:11.

Tong, X., Liu, Y., Xu, X., Shi, J., Hu, W., Ma, T., et al. (2020). Ovarian innervation coupling with vascularity: the role of electro-acupuncture in follicular maturation in a rat model of polycystic ovary syndrome. *Front. Physiol.* 11:474. doi: 10.3389/fphys.2020.00474

Tsai, P. S., Kaufhold, J. P., Blinder, P., Friedman, B., Drew, P. J., Karten, H. J., et al. (2009). Correlations of neuronal and microvascular densities in murine cortex revealed by direct counting and colocalization of nuclei and vessels. *J. Neurosci.* 29, 14553–14570. doi: 10.1523/jneurosci.3287-09.2009

Van Der Voort, D. J. M., Van Der Weijer, P. H. M., and Barentsen, R. (2003). Early menopause: increased fracture risk at older age. *Osteoporos. Int.* 14, 525–530. doi: 10.1007/s00198-003-1408-1

Vernet, N., Condrea, D., Mayere, C., Feret, B., Klopfenstein, M., Magnant, W., et al. (2020). Meiosis occurs normally in the fetal ovary of mice lacking all retinoic acid receptors. *Sci. Adv.* 6:eaaz1139. doi: 10.1126/sciadv.aaz1139

Wallace, C. T., St Croix, C. M., and Watkins, S. C. (2015). Data management and archiving in a large microscopy-and-imaging, multi-user facility: problems and solutions. *Mol. Reprod. Dev.* 82, 630–634. doi: 10.1002/mrd.22538

Wallace, W. H., Smith, A. G., Kelsey, T. W., Edgar, A. E., and Anderson, R. A. (2014). Fertility preservation for girls and young women with cancer: population-based validation of criteria for ovarian tissue cryopreservation. *Lancet Oncol.* 15, 1129–1136. doi: 10.1016/s1470-2045(14)70334-1

Wiebold, J. L., and Becker, W. C. (1987). Inequality in function of the right and left ovaries and uterine horns of the mouse. *J. Reprod. Fertil.* 79, 125–134. doi: 10.1530/jrf.0.0790125

Zhang, Z., Schlamp, F., Huang, L., Clark, H., and Brayboy, L. (2020). Inflammaging is associated with shifted macrophage ontogeny and polarization in the aging mouse ovary. *Reproduction* 159, 325–337. doi: 10.1530/rep-19-0330

Zheng, W., Zhang, H., Gorre, N., Risal, S., Shen, Y., and Liu, K. (2014). Two classes of ovarian primordial follicles exhibit distinct developmental dynamics and physiological functions. *Hum. Mol. Genet.* 23, 920–928. doi: 10.1093/hmg/ddt486

Zhu, J., Liu, A.-A., Chen, M., Tasdizen, T., and Su, H. (2017). Special issue on biomedical big data: understanding, learning and applications. *IEEE Trans. Big Data* 3, 375–377. doi: 10.1109/tbdata.2017.2772930

Zucker, R. M., and Jeffay, S. C. (2006). Confocal laser scanning microscopy of whole mouse ovaries: excellent morphology, apoptosis detection, and spectroscopy. *Cytometry A* 69, 930–939. doi: 10.1002/cyto.a.20315

Conflict of Interest: The authors declare that the research was conducted in the absence of any commercial or financial relationships that could be construed as a potential conflict of interest.

frontiers
in Cell and Developmental Biology

ORIGINAL RESEARCH
published: 29 July 2021
doi: 10.3389/fcell.2021.692617

3D Reconstruction of the Clarified Rat Hindbrain Choroid Plexus

Paola Perin[1]*, Riccardo Rossetti[2], Carolina Ricci[2], Daniele Cossellu[2], Simone Lazzarini[2], Philipp Bethge[3,4], Fabian F. Voigt[3,4], Fritjof Helmchen[3,4], Laura Batti[5], Ivana Gantar[5] and Roberto Pizzala[2]

[1] Department of Brain and Behavioral Sciences, University of Pavia, Pavia, Italy, [2] Department of Molecular Medicine, University of Pavia, Pavia, Italy, [3] Brain Research Institute, University of Zurich, Zurich, Switzerland, [4] Neuroscience Center Zurich, Zurich, Switzerland, [5] Wyss Center for Bio and Neuroengineering, Geneva, Switzerland

OPEN ACCESS

Edited by:
Elisa Cebral,
CONICET Institute of Biodiversity and Experimental and Applied Biology (IBBEA), Argentina

Reviewed by:
Jeppe Praetorius,
Aarhus University, Denmark
Serge Weis,
Kepler University Hospital GmbH, Austria
Neil Dani,
Boston Children's Hospital and Harvard Medical School, United States

***Correspondence:**
Paola Perin
pperin@unipv.it

Specialty section:
This article was submitted to Cell Growth and Division, a section of the journal Frontiers in Cell and Developmental Biology

Received: *08 April 2021*
Accepted: *12 July 2021*
Published: *29 July 2021*

Citation:
Perin P, Rossetti R, Ricci C, Cossellu D, Lazzarini S, Bethge P, Voigt FF, Helmchen F, Batti L, Gantar I and Pizzala R (2021) 3D Reconstruction of the Clarified Rat Hindbrain Choroid Plexus. Front. Cell Dev. Biol. 9:692617. doi: 10.3389/fcell.2021.692617

The choroid plexus (CP) acts as a regulated gate between blood and cerebrospinal fluid (CSF). Despite its simple histology (a monostratified cuboidal epithelium overlying a vascularized stroma), this organ has remarkably complex functions several of which involve local interaction with cells located around ventricle walls. Our knowledge of CP structural organization is mainly derived from resin casts, which capture the overall features but only allow reconstruction of the vascular pattern surface, unrelated to the overlying epithelium and only loosely related to ventricular location. Recently, CP single cell atlases are starting to emerge, providing insight on local heterogeneities and interactions. So far, however, few studies have described CP spatial organization at the mesoscale level, because of its fragile nature and deep location within the brain. Here, using an iDISCO-based clearing approach and light-sheet microscopy, we have reconstructed the normal rat hindbrain CP (hCP) macro- and microstructure, using markers for epithelium, arteries, microvasculature, and macrophages, and noted its association with 4th ventricle-related neurovascular structures. The hCP is organized in domains associated to a main vessel (fronds) which carry a variable number of villi; the latter are enclosed by epithelium and may be flat (leaf-like) or rolled up to variable extent. Arteries feeding the hCP emerge from the cerebellar surface, and branch into straight arterioles terminating as small capillary anastomotic networks, which run within a single villus and terminate attaching multiple times to a large tortuous capillary (LTC) which ends into a vein. Venous outflow mostly follows arterial pathways, except for the lateral horizontal segment (LHS) and the caudal sagittal segment. The structure of fronds and villi is related to the microvascular pattern at the hCP surface: when LTCs predominate, leaflike villi are more evident and bulge from the surface; different, corkscrew-like villi are observed in association to arterioles reaching close to the CP surface with spiraling capillaries surrounding them. Both leaf-like and corkscrew-like villi may reach the 4th ventricle floor, making contact points at their tip, where no gap is seen between CP epithelium and ependyma. Contacts usually involve several adjacent villi and may harbor epiplexus macrophages. At the junction between medial (MHS) and lateral (LHS) horizontal segment, arterial supply is connected to the temporal bone subarcuate fossa, and venous outflow drains to a ventral vein which exits through the cochlear nuclei at the Luschka foramen. These vascular connections stabilize the hCP overall structure within the 4th ventricle but make MHS-LHS joint particularly fragile and very easily damaged when removing the brain from the skull. Even in damaged samples, however, CP fronds (or isolated villi) often remain strongly attached to the dorsal cochlear nucleus (DCN) surface; in these fronds, contacts are still present and connecting "bridges" may be seen, suggesting the presence of real molecular contacts rather than mere appositions.

Keywords: choroid plexus, vascular network, brain ventricle, iDISCO+, tissue clarification

INTRODUCTION

The choroid plexus (CP) acts as a regulated gate between blood and cerebrospinal fluid (CSF). This role involves several functions, such as immune cell trafficking, water and solute transport, and secretion of endogenously produced macromolecules (Neman and Chen, 2016) that are involved in neural metabolism, neuroendocrine signaling, and neurogenic niche regulation (Kaiser and Bryja, 2020). Despite its simple histology (a monostratified cuboid epithelium overlying a connective stroma vascularized by fenestrated capillaries) many aspects of CP functions are still unknown, especially because of its fragility, convoluted shape, and deep location within the brain. So far, the studies observing CP cellular responses *in situ* have shown its interactions with factors in blood and CSF (Cui et al., 2020; Shipley et al., 2020); however, within a single CP, epithelial cells are heterogeneous in their developmental origin (reviewed in Lun M. et al., 2015) and protein expression (Lun M. P. et al., 2015; Dani et al., 2021), especially in relation to intercellular contact (Lobas et al., 2012), and it is not clear whether this heterogeneity translates into spatial differences in CP function. It is known that within ventricles there are CSF currents (Faubel et al., 2016) which would differentially expose the various parts of the ventricular surface to substances released into the CSF (Kreeger et al., 2018), and points of contact of the CP fronds to the ventricular surface have sporadically been described (Terr and Edgerton, 1985). CSF currents and direct contacts would modulate periventricular responses to factors present or released at the apical side of the CP epithelium. For example, macrophages have been observed to cross the CP epithelium upon inflammatory insults (Cui et al., 2020), and CP-derived Otx2 is able to reach neurons influencing their plasticity in the adult (Spatazza et al., 2013). In both cases, CSF currents or proximity could allow the CP to influence a region of the brain without the surrounding tissue being affected.

The recently discovered link between CP geometrical features and human brain pathologies (Lizano et al., 2019) has fueled the interest in a better understanding of the morphology of this somewhat neglected part of the brain. The need for advancing the current knowledge about CP geometry is paradoxically higher in rodents, especially in rat, where standardized anatomical atlases are less complete than for humans (Barrière et al., 2019), despite it being the model of choice for many functional studies of physiology and pathology. So far, few studies have focused on the spatial organization of the organ *in situ*, because of its poor contrast in MRI or CT (Hubert et al., 2019), fragile nature and deep location, which make it difficult to preserve 3D details. Scanning electron microscopy of CP vascular casts from various animals and ventricles have given an overview of vascular network arrangement (Meunier et al., 2013). A recent single-cell and single-nucleus RNA sequencing study has provided a cellular atlas of developing, adult and aging mouse CP across all brain ventricles, and displayed the spatial distribution of specific RNAs and proteins (Dani et al., 2021). However, these studies do not yield enough spatial details to fully reconstruct the connection topology of CP vascular networks and, due to CP isolation from the brain, are unable to assess correlations between vascular patterns, epithelial folding, and ventricular localization.

Using an iDISCO+-based approach and light-sheet microscopy, we have observed in a recent study in the rat hindbrain, the association of CP lateral expansion with auditory system structures, such as cochlear nuclei and endolymphatic sac (Perin et al., 2019). In this work, we employ the same approach to reconstruct the hindbrain CP (hCP) and its components.

MATERIALS AND METHODS

Experiments were performed on inbred Wistar rats ($n = 20$: 10 males and 10 females; average age: 116 ± 41 days; mean ± SD). Animals were housed with 12 h/12 h light/dark cycle, food and water provided *ad libitum*; sacrifices were performed during the light phase. This study was carried out in accordance with the recommendations of Act 26/2014, Italian Ministry of Health. The protocol (number 155/2017-PR) was approved by the Italian Ministry of Health and University of Pavia Animal Welfare Office (OPBA). All efforts were made to minimize number of animals used and animal suffering.

Sample Preparation

For all experiments, animals were anesthetized, sacrificed and fixed as in Perin et al. (2019). Samples were postfixed overnight in 4% PFA and then cryoprotected in 30% sucrose solution until sinking. Although no freezing step was present in the protocol, we found that sucrose cryoprotection greatly enhanced tissue transparency in comparison to non-cryoprotected samples (not shown). In two cases, each half of the hindbrain was imaged separately with different markers, for a total of 22 samples. In nine samples, temporal and basisphenoid bones were left attached to the brain; for better penetration of antibodies, using a rongeur the skull was opened dorsally by removing the parietal and occipital bones, and the tympanic bullae were opened ventrally. Samples including bone were decalcified with buffered 10% EDTA in PBS (pH 7.4, mild shaking, daily changed) until softening of the squamous temporal bone (3–4 weeks at room temperature or 2 weeks at 37°C). Decalcified samples were cleared as in Perin et al. (2019), and immunolabeled using rabbit anti-Iba1 (WAKO, 1:200) for macrophages/microglia, sheep anti-transthyretin (TTR; Abcam n. ab9015, 1:250) or goat anti-Notch-2 (ThermoFisher n. PA547091, 1:50) for CP epithelium, goat anti-rat IgG (ThermoFisher, 1:200) or rabbit anti-collagen IV (ColIV; Abcam n. ab6586, 1:200) for blood vessels, and mouse-anti smooth muscle actin (SMA; Abcam n. ab7817, 1:200) for arteries and veins. Species-matched Alexa-conjugated donkey secondary antibodies (Life Technology) or AttoFluor-conjugated nanobodies (Synaptic Systems) were used at 1:200. Incubations with nanobodies required half the time than with regular antibodies. TO-PRO labeling (2 h, ThermoFisher, 1:2500) was used in some samples to stain cell nuclei at the end of secondary antibody incubation.

Light-Sheet Imaging

Light-sheet imaging was performed on mesoSPIM microscopes[1] (Voigt et al., 2019) at the Brain Research Institute, University of Zurich and the Wyss Center for Bio and Neuroengineering in Geneva, Switzerland. Higher resolution scans of two samples were made on a CLARITY-optimized light-sheet microscope (COLM) at the Wyss Center for Bio and Neuroengineering in Geneva, Switzerland.

For mesoSPIM: After staining and clearing, brains were attached to a custom 3D-printed holder, then submerged in a 40 × 40 × 40 mm quartz cuvette (Portmann Instruments) filled with dibenzyl ether (DBE, nd = 1.562) and imaged using a home-built mesoscale single-plane illumination microscope (mesoSPIM). The microscope consists of a dual-sided excitation path using a fiber-coupled multiline laser combiner (405, 488, 515, 561, 594, and 647 nm, Omicron SOLE-6) and a detection path comprising an Olympus MVX-10 zoom macroscope with a 1× objective (Olympus MVPLAPO 1×), a filter wheel (Ludl 96A350), and a scientific CMOS (sCMOS) camera (Hamamatsu Orca Flash 4.0 V3). The excitation paths also contain galvo scanners (GCM-2280-1500, Citizen Chiba) for light-sheet generation and reduction of shadow artifacts due to absorption of the light-sheet. In addition, the beam waist is scanned using electrically tunable lenses (ETL; Optotune EL-16-40-5D-TC-L) synchronized with the rolling shutter of the sCMOS camera. This axially scanned light-sheet mode (ASLM) leads to a uniform axial resolution across the field-of-view (FOV) of 4–10 μm (depending on zoom and wavelength). Image acquisition is controlled using custom software written in Python[2]. Field of view sizes ranged from 16.35 mm at 0.8× (pixel size 8.23 μm) 6.54 mm at 2× (pixel size: 3.3 μm), 3.27 mm at 4× (pixel size: 1.6 μm) to 2.62 mm at 5× (pixel size: 1.28 μm). Z-stacks were acquired at 1, 3, 5, or 8 μm spacing. The laser/filter combinations were: Autofluorescence: 488 nm excitation and a 520/35 bandpass filter (BrightLine HC, AHF); Alexa 555: 561 nm excitation and 561 nm longpass (561LP Edge Basic, AHF); Alexa 633: 647 nm excitation and multiband emission filter (QuadLine Rejectionband ZET405/488/561/640, AHF).

For COLM: Light-sheet imaging was performed using a customized version of the Clarity Optimized Light-sheet Microscope (COLM; Tomer et al., 2014) at the Wyss Center Advanced Light-sheet Imaging Center, Geneva. Briefly, the sample was illuminated by one of the two digitally scanned light sheets, using a 488, 561, and 633 nm wavelength laser. Emitted fluorescence was collected by a 10X XLFLUOR4X N.A. 0.6, filtered (525/50, 609/54, and 680/42 nm Semrock BrightLine HC) and imaged on an Orca-Flash 4.0 LT digital CMOS camera, in rolling shutter mode. A self-adaptive positioning system of the light sheets across z-stacks acquisition ensured optimal image quality over the large z-stack. Images were reconstructed in 3D using the Grid Collection Stitching plugin tool in TeraStitcher (BMC Bioinformatics, Italy). Z-stacks were acquired at 3 μm spacing and pixel size was 0.59 μm

Image Processing and Analysis

In order to optimize thresholding and segmentation, bubble artifacts were removed manually in Fiji (Schindelin et al., 2012), and striping artifacts were minimized with the VSNR V2 plugin for Fiji (Fehrenbach et al., 2012).

Vascular Reconstruction

Vessels were classified as arteries if SMA++ ColIV+, veins if SMA+− ColIV+, with a diameter >50 μm, and an irregular (i.e., not circular) section. Segmentation of arteries and veins (n = 7 samples) could be performed with Fiji by Otsu thresholding and binarization of SMA-labeled low-resolution images (pixel size: 3 μm or more). Given that CP arteries and veins are limited in number, branch sparsely and do not taper appreciably, their diameters were measured manually at the CP entering point. Segmented stacks with vessels were skeletonized with the Skeletonize3D FIJI plugin and then the Analyze Skeleton plugin (Arganda-Carreras et al., 2010) was used to extract average branch length, tortuosity (measured as ratio between branch length and endpoint distance) and longest shortest path.

For capillaries, since our non-chain specific anti-Col IV antibody labeled the basal lamina of both blood vessels and CP epithelium (Urabe et al., 2002), leading to the appearance of connecting threads (corresponding to thin stroma between capillaries in a frond), and IgG was also distributed in the stroma, giving similar patterns as Col-IV with connecting threads between vessels (see **Figure 8C**), capillary segmentation was performed manually by limiting selection to circular or ellipsoid structures (n = 4 samples). Capillary tracing was performed on MesoSPIM 5× image stacks or COLM stacks.

Frond Reconstruction

The choroid plexus epithelium was labeled either with Notch2 or TTR (n = 5 samples from four animals). Epithelial outline was segmented with the "snakes" segmentation of ITK-SNAP (Yushkevich et al., 2006) or by Otsu thresholding with Fiji.

---

[1] http://mesospim.org/

[2] https://github.com/mesoSPIM/mesoSPIM-control

Contacts with 4th ventricle parenchyma were annotated following Paxinos atlas (Paxinos and Watson, 2013). Given that iDISCO+ dehydration shrinks tissues, we considered tight contacts to be present when tissues adhered (i.e., no gap was evident) and loose contacts to be present when distance was $<10\ \mu$m and overall frond shape was complementary to adjacent brain surface. Since not all samples were preserving the entire CP (most samples without bone had damage at the MHS-LHS junction, and samples divided in two sagittally had damage at the SS), number of contacts was compared per section rather than per entire CP.

For macrophages, Iba1 signal ($n = 8$ samples) was thresholded and cells were counted either manually with the ImageJ Cell Counter function or automatedly with the Connected Object function. In samples where an epithelial marker was also present ($n = 3$ samples), stromal and epiplexus populations were counted separately. Macrophages were considered at contact sites when they touched both CP epithelium and ependyma.

3D Reconstruction

Three-dimensional reconstruction was performed with Fiji (Schindelin et al., 2012), ITK-SNAP (Yushkevich et al., 2006), and ParaView (Ahrens et al., 2005; Ayachit, 2015). Briefly, the structures of interest were manually segmented using the Selection Brush tool in FIJI. Segmented stacks were filtered with Gaussian Blur 3D (0.5 pixel for x and y, 2 pixels for z), converted to NRRD and imported in ITK-SNAP, where segmentation was refined using edge-based snakes. Segmented volume was saved as a NIFTI file and surface mesh exported to ParaView for 3D visualization.

Statistics

Capillary diameters were measured by hand with Fiji using the ColIV or IgG signal on six random-picked high-resolution optical sections; the resulting dataset was fitted with MATLAB function fitgmdist with $k = 2$ in to extract mean sizes of the two capillary populations. Average tortuosity of small and large capillaries was compared using t-test assuming unequal variances.

RESULTS

Overall CP Shape

As described in other mammals, the rat hCP is composed of four parts on each side (**Figure 1**). We decided to adopt the human nomenclature (Sharifi et al., 2005), thus dividing the plexus in rostral and caudal sagittal segments (RSS, CSS, located medially) and medial (MHS) and lateral (LHS) horizontal segments. Whereas rostral and caudal SS do not show a clear division between them, clear boundaries are instead observed between RSS and MHS and between MHS and LHS.

The hCP is dorsally attached to the cerebellum. In the rat, the RSS emerges from the ventral side of the cerebellar nodulus and the MHS from its lateral side (**Figure 2A**). The RSS emerges as a bilateral expansion on the ventral side of the nodulus, but the two sides merge while going posteriorly, and detach from the nodulus because of the interposition of the tela choroidea (**Figure 2B**). At the caudal end of the ventricle, the CSS is anchored to the area postrema (**Figure 2B**). The MHS nodulus expansions extends in the latero-posterior direction showing a partial overlap with a different expansion coming from the paraflocculus (**Figure 2C**), which reaches the opening of the subarcuate fossa and curves anteriorly surrounding the dorsal cochlear nucleus (**Figure 2D**), emerging from the Luschka foramen at the junction between the dorsal and ventral cochlear nucleus, and ending in association to the ventromedial side of the flocculus (**Figure 2E**). The convolute structure of the hCP follows that of the cerebellum, with the HS following the lateral expansion of the flocculonodular lobe and the SS extending backward. The overall shape of CP and its association with brain structures are also shown in **Supplementary Video 1**.

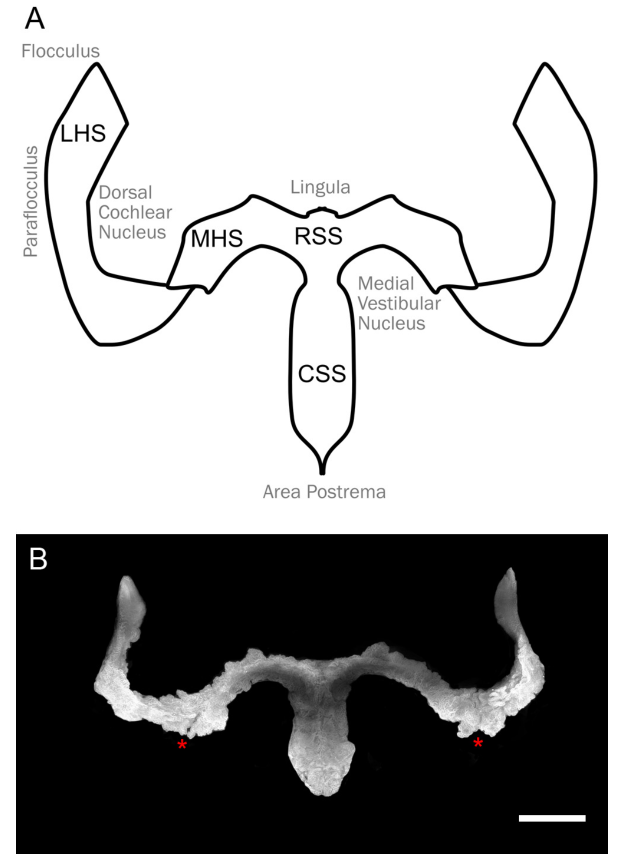

FIGURE 1 | Overall shape of the hindbrain CP. **(A)** Schema of the hindbrain CP with relative hindbrain surrounding areas. RSS, rostral sagittal segment; CSS, caudal sagittal segment; MHS, medial horizontal segment; LHS, lateral horizontal segment. **(B)** Overall CP shape obtained from segmentation of the Notch2 signal Z-stack maximal projection of the light-sheet 3D dataset of a female rat cleared brain. Notice the presence of an incisure between MHS and LHS (asterisks). Scale bar: 1 mm.

Fronds

The epithelial surface of the hCP is folded in a complex way. We will call “frond” a 3D region of the CP related to a parent

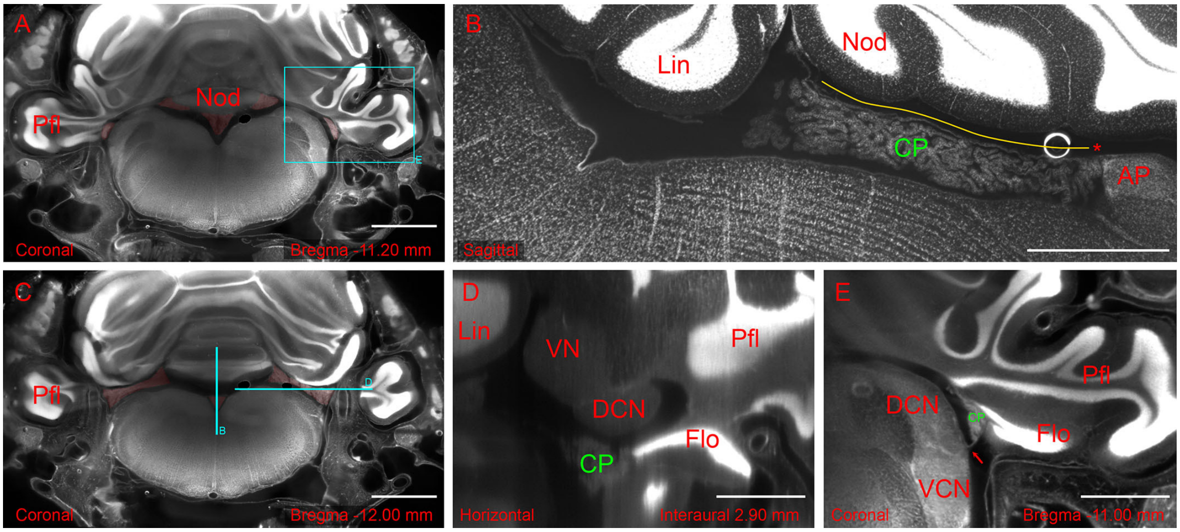

FIGURE 2 | Hindbrain slices from light-sheet 3D dataset of the whole-mount brain-bone preparation showing the extent and association of the CP. **(A)** Coronal slice showing CP attachment (highlighted in red) at the nodulus and paraflocculus. Scale bar: 2 mm. **(B)** Sagittal slice (different animal from **A**) showing the CSS with overlying tela coroidea (yellow line) and attachment to area postrema (asterisk). Scale bar: 1 mm. **(C)** Coronal slice showing the MHS (highlighted in red). Same animal as in **(A)**. Scale bar: 2 mm. **(D)** Horizontal slice detail (reslice of stack in **A,C**) showing the dorsal cochlear nucleus (DCN) and flocculus (FL). Scale bar: 1 mm. **(E)** Coronal slice detail from animal in **(A)** showing the foramen of Luschka (arrow) with the associated CP. Scale bar: 1 mm. All sections were stained with TOPRO for cell nuclei. Autofluorescence signal is also visible. Cyan rectangle on panel **(A)** and cyan lines on panel **(C)** indicate *x*, *y* positions of panels **(B,D,E)**.

vessel, which appears separable from the adjacent CP when labeled with an epithelial marker, and "villus" a (usually) sheet-like projection containing two layers of epithelial cells and the related capillaries (**Figure 3A**). Frond geometry changes depending on CP region, and flat, compact regions alternate with looser configurations, with thin, convoluted fronds and villi (**Figure 3B**). Frond exact shape and position are poorly conserved among individuals, but they may form physical contact points with several structures located at the ventricular surface (**Figure 3C**); in particular, the dorsal cochlear nucleus (**Figure 3D**), medial vestibular nucleus/prepositus hypoglossi (**Figure 3E**) cerebellar lingula (**Figure 3F**) and nucleus of the solitary tract (**Figures 3G,H**). Sporadic frond contacts are also seen around the arterial entry points at the cerebellar surface (not shown). At these contact points, villi touch the brain surface. Although isolated villi may make contact points, at most sites adjacent or close villi form multiple contact points (**Figures 3C,H**), and the resulting structure may follow the brain surface for 100–200 μm or more: the largest contact seen (**Figure 3I**) covered an area of 2×10^5 μm^2 overall. Although CP epithelium was labeled and observed at high resolution in four animals only (two males and two females), it is interesting to note, as a preliminary observation, that epithelial contacts measured in females appeared more numerous than in males (27 ± 7 per segment, vs 11 ± 2) and tighter (loose contacts were 13 ± 0.2% in females vs 45 ± 4% in males).

Because of its loose configuration and attachment points with surrounding structures, the junction between MHS and LHS appears to be the most fragile part of the plexus, and in preparations where the brain has been taken out of the skull it may be frayed or entirely missing (**Figures 4A,B**). This region is also often damaged in available published atlases. In samples where the bone was removed preserving the CP MHS-LHS junction, contacts were still found in this region, often displaying ripped vascular connections (**Figure 4C**); interestingly, at high resolution, ependyma displayed surface indents corresponding to overlying villi, and points where small connecting bridges were seen between ependyma and CP villi (**Figure 4D**), suggesting the presence of molecular bonds (rather than just loose apposition) between the CP epithelium and ependyma.

In samples where the epithelium was co-labeled with Iba-1 ($n = 2$, one male and one female), the large majority (92 ± 2%, $n = 1914$) of macrophages were stromal and spaced in a regular way (**Figure 5**); epiplexus macrophages were observed in all positions around the epithelium, including contacts with the ventricular surface, located between the CP foot and the ependyma (**Figure 5B**). Half of contact points ($n = 36$) displayed epiplexus macrophages, usually a single one (see **Figure 3C**).

Vascular Network

The CP artery supply (**Figure 6**) is mainly derived from the AICA (a minor contribution from SCA was seen in one rat). At CP attachment points to the cerebellum, arteries running on the cerebellar surface periodically bifurcate forming thin and scarcely branching arteries which enter the CP. At entry points (which are only broadly conserved among animals, **Supplementary Figure 1A**) a single artery, a small cluster, or a branch of a parent artery coasting the CP may be found. The SS arteries run dorsoventrally from the nodulus, with a straight course in the RSS (**Figure 6A**), and a more branched distribution in the CSS (**Figure 6B**).

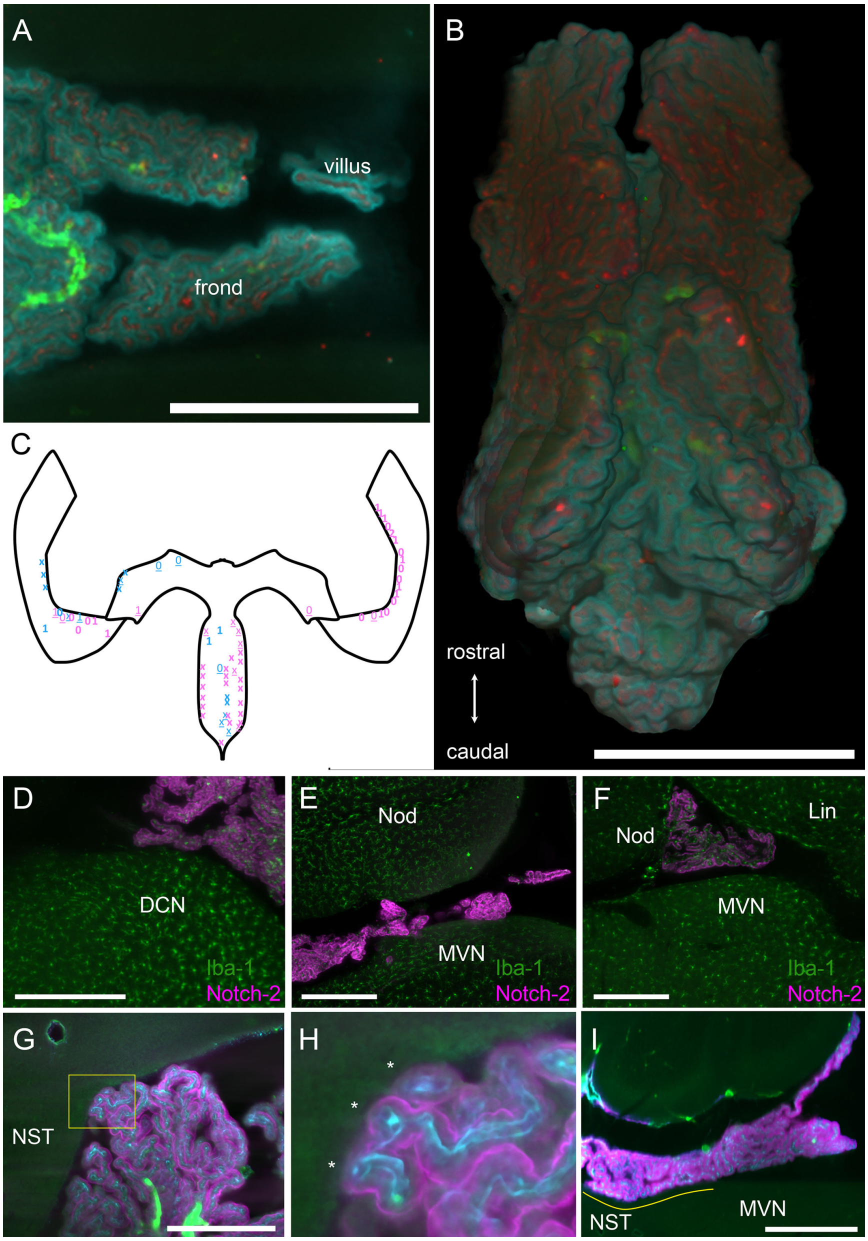

FIGURE 3 | Structure of hCP fronds and villi. **(A)** Example of frond and villus from the CSS. Z-stack maximal projection over 50 μm z-range (5 μm steps, 10 planes). Cyan, Notch-2; red, CollV; green, autofluorescence and SMA. Scale bar: 1 mm. **(B)** Three-dimensional rendering of the ventral view of the whole SS segmented from the same sample in **(A)**. Scale bar: 1 mm. **(C)** Schema of the CP as in **Figure 1A**, with indications of location and approximate size of contacts (each symbol indicates a single villus). Blue, males; pink, females. Numbers indicate macrophages at contact site for two animals. Xs indicate two different animals where macrophages were not labeled. Bold symbols indicate tight contacts, underlined symbols indicate loose contacts. In female samples, one was without bone, so only HS was considered, whereas the other was cut in half sagittally, so only HS was considered. In both male samples, right HS was damaged and was not considered. **(D)** Example of foot contacting the DCN. Z-stack maximal projection over 60 μm z-range (2 μm steps). Green, Iba-1 labeling; magenta, Notch-2. **(E)** Foot contacting the MVN. Z-stack maximal projection over 60 μm z-range (2 μm steps). Green, Iba-1 labeling; magenta, Notch-2. **(F)** Foot contacting the lingula. Single 2 μm optical slice. Green, Iba-1 labeling; magenta, Notch-2. Scale bar for **(D–F)**: 400 μm. **(G)** Foot contacting the nucleus of the solitary tract. Single 3 μm optical slice. Green, autofluorescence and SMA; cyan, CollV; magenta, Notch2 labeling. Scale bar: 500 μm. **(H)** Magnification of COLM image of the contact shown in G (yellow box). Three fronds (asterisks) each containing a capillary are seen contacting the ependyma. **(I)** Single sagittal 5 μm optical plane showing the extent of the largest observed contact area (yellow line). NST, nucleus of the solitary track. Scale bar: 1 mm.

Arteries for the MHS emerge periodically from the flocculonodular lobe of the cerebellum, starting from the nodulus side and running at the dorsal side or in the center of the MHS core (**Figure 6C**). Arteries deriving from the paraflocculus are fed by the AICA through an artery loop within the subarcuate fossa, which exits the fossa to reach the

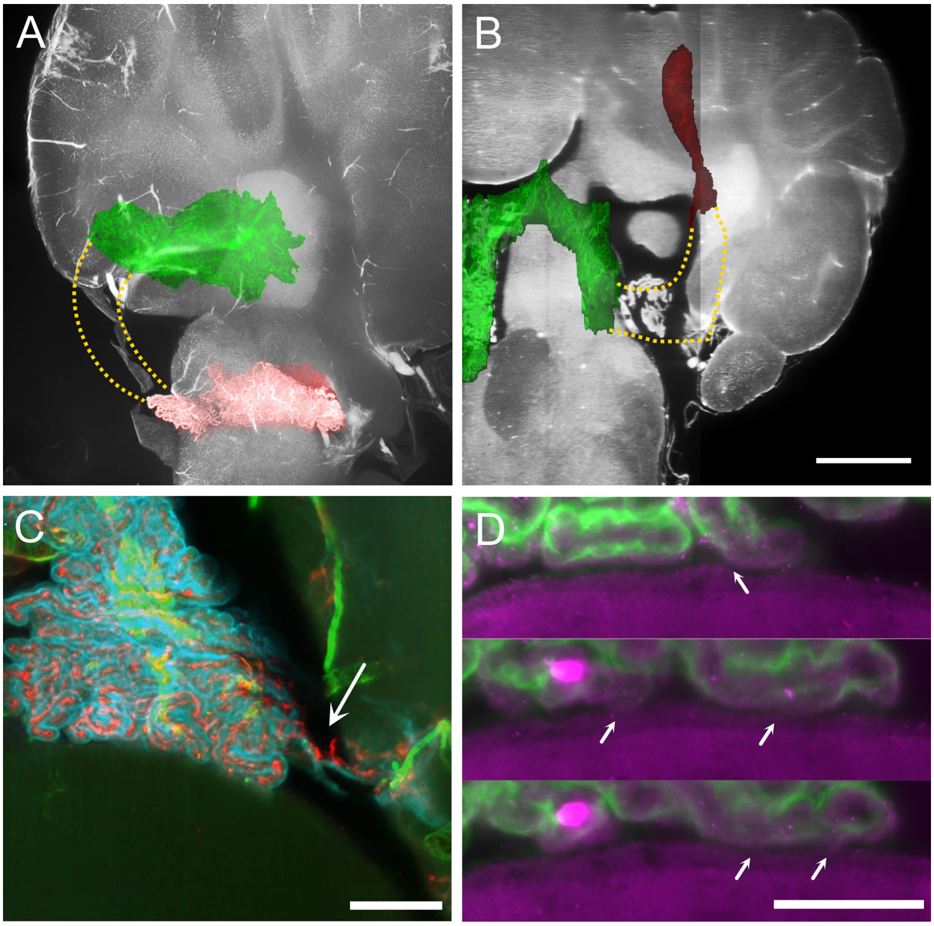

FIGURE 4 | MHS-LHS junction after removal of temporal bone. **(A)** Overlay of plexus vascular segmentation with a substack of unsegmented hindbrain. Red, LHS; green, SS and MHS. The stippled area in yellow corresponds to the location of the missing part of the CP. Sagittal view. **(B)** Similar to **(A)**, resliced to horizontal plane. Scale bar: 1 mm. **(C)** COLM image of a contact region between CP and DCN in a sample where temporal bone has been removed. The plexus appears ripped (arrow) but contact with DCN is not removed. Scale bar: 200 μm. **(D)** Magnification of the CP-DCN contact (same animal as in **C**) showing the indentation marks left by CP villi on DCN ependymal surface. In some positions (arrows) the CP appears connected to the DCN surface. Scale bar: 100 μm.

CP (**Figure 6D**). A final arterial entry point is seen at the LHS anterior tip (see **Figure 6A** or later in **Figure 7F**), which is independent from the parafloccular loop. CP arteries are usually quite thin (37.7 ± 13.6 μm at CP entry point, $n = 77$), straight (tortuosity index = 0.81 ± 0.11), and branch with low complexity (on average, the maximal branching order from CP limit to SMA disappearance is 1.6 ± 0.5) after entering the CP.

Venous drainage (**Figure 7**) is carried by vessels which are much larger (average diameter: 106 ± 39 μm, $n = 18$) but less numerous (**Supplementary Figure 1B**) than arteries. The RSS and MHS drain dorsally into veins running to the cerebellum (**Figures 7A,B**).The CSS drains laterally into a vein passing through the solitary tract (**Figures 7C,D**), which enters the plexus through the tela choroidea and joins dorsal arterial supply upon entry. The LHS is instead drained by ventral veins (**Figures 7E,F**) which converge into a larger vein running under the DCN and exiting the brain parenchyma at the foramen of Luschka, where it associates with the meningeal rim. The same vein receives blood from the cochlear nuclei: directly from the DCN and indirectly, through short tributaries, from the VCN.

Differently from arteries and veins, CP microcirculation (**Figure 8**) displays a peculiar organization. Measured capillary sizes were fit with two gaussian-distributed populations: large (average diameter 31.5 ± 4 μm) and small (average diameter: 15.6 ± 3 μm). The spatial pattern of the two capillary types is very different (**Figure 8**). Large capillaries display high tortuosity (tortuosity index: 0.58 ± 0.18, $n = 10$), and little branching into other large capillaries (**Figure 8A**). Small capillaries are significantly less tortuous (tortuosity index: 0.83 ± 0.09, $n = 255$, $p = 0.01$), and connect to large tortuous capillaries (LTCs) forming bidimensional anastomotic networks (SCANs, small capillary anastomotic networks, containing interconnected segments with a mean length of 60 ± 30 μm) (**Figures 8A,B**) which fill single villi (**Figure 8A** and **Supplementary Videos 2A–D**). A quantification of the two populations' proportions and positions relative to the edge of the villi of large and small capillaries in a single frond will require segmentation of the

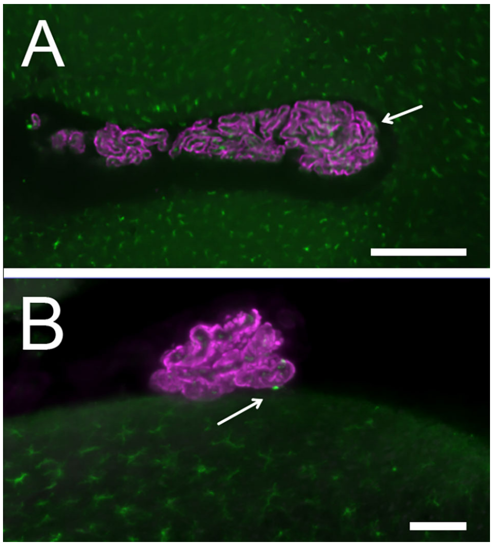

FIGURE 5 | CP macrophage distribution: Epithelium is labeled with Notch2, macrophages with Iba1. **(A)** LHS. Arrows point to epiplexus cells. Scale bar: 400 μm. **(B)** RSS: an epiplexus cell is seen at the contact point with brainstem. Scale bar: 100 μm.

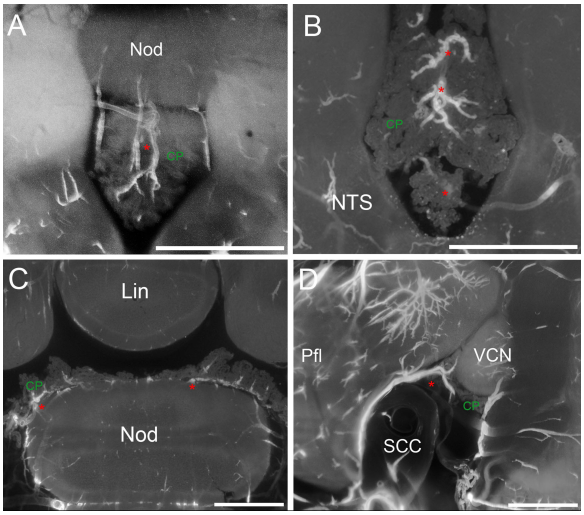

FIGURE 6 | CP arteries. **(A)** Z-stack maximal projection over 90 μm z-range (3 μm steps) showing arteries (red asterisk) penetrating the RSS. **(B)** Z-stack maximal projection over 50 μm z-range (5 μm steps) showing the star-like pattern of arteries entering the CSS. **(C)** Single optical slice showing CP "mounds" around arteries in the MHS and RSS. **(D)** Z-stack maximal projection over 90 μm z-range (3 μm steps) slices showing the artery (red asterisk) penetrating the MHS lateral side from the subarcuate fossa of the paraflocculus. Pfl, paraflocculus; SCC, semicircular canal, VCN, ventral cochlear nucleus. Scale bars: 1 mm. Signal: autofluorescence and SMA.

whole vascular network at high resolution. However, it is well apparent that the distribution of small and large capillaries is not homogeneous even in adjacent fronds (**Figure 8C**), and therefore extreme caution must be exerted when measuring effects of a treatment on CP capillary diameter. As discussed later, part of the heterogeneity is regionalized within CP segments.

Although we did not, in the present work, reconstruct the whole artery-to-vein vascular network, in high-resolution samples we could observe and reconstruct junctions among all vascular elements. Large capillaries were seen connecting to veins (**Figure 8D**), and appeared large and tortuous until the end, draining into the principal vein or one of its short branches (**Figure 8E**). Therefore, these large capillaries may be considered venules. Arterioles, recognized by their SMA+ muscle layer, were straight, thin, and gave origin to small capillaries (**Figure 8F**), usually with a short SMA+ segment emerging at an angle (**Figure 8G**).

Microvascular patterns were associated with frond structure (**Figure 9**). When both large and small capillaries are found within a single leaflike villus (**Figures 9A,B**), the large capillary usually followed the free margin. However, connections from the venular end of the villus to the arteriolar end often followed a global spiral pathway (see **Supplementary Video 3**). In the loose part of CSS (shown at low-res in **Figure 3B**), single capillaries could instead be seen spiraling in association with their feeder arterioles (**Figure 9D**; see also **Figure 8B1**); the spiral was covered by epithelium with little or no interposing stroma (**Figure 9E**). Leaflike villi covering SCANs were also present in the loose CSS, both associated to arterioles (**Figure 9F**) and venules (e.g., the one in **Figure 8A**); in these cases, villi were usually folded around the main vessel. In the loose part of LHS, capillaries defined flat leaflike villi, whereas in compact fronds, no protruding structure was observed on the free surface, which displayed ordered rows of capillaries (**Figures 9A,F**, see also **Figure 8C**). A tentative schematic reconstruction of the CP vascular network is depicted in **Figure 9G**.

DISCUSSION

The CP performs a multitude of important functions including CSF production, development, and maintenance of the periventricular neurogenic zones, neuroimmune communication, and delivery of micronutrients, growth factors, hormones and neurotrophins to the brain *via* the CSF, either from systemic blood through the leaky microvasculature or from the CP epithelium (Ghersi-Egea et al., 2018; Kaiser and Bryja, 2020) or mesenchymal components (Dani et al., 2021). The association between CP vascular, stromal, and epithelial components appears essential for CP functioning, also due to the presence of local signaling between epithelial cells, mesenchymal cells, and blood vessels. Given that molecular heterogeneity in the roof plate precursors of hCP appears to persist in the adult, with the segregation of cell lineages that do not intermingle (reviewed in Lun M. et al., 2015), and that Shh-dependent production of CP epithelial cells and blood vessels is also regionalized (Huang et al., 2009), it appears likely that some spatial variations of epithelial features would correlate with those of vascular network. A recent work characterizing RNA expression at cell level and mapping the expression of selected RNAs and proteins has shown that several genes are expressed along a rostrocaudal

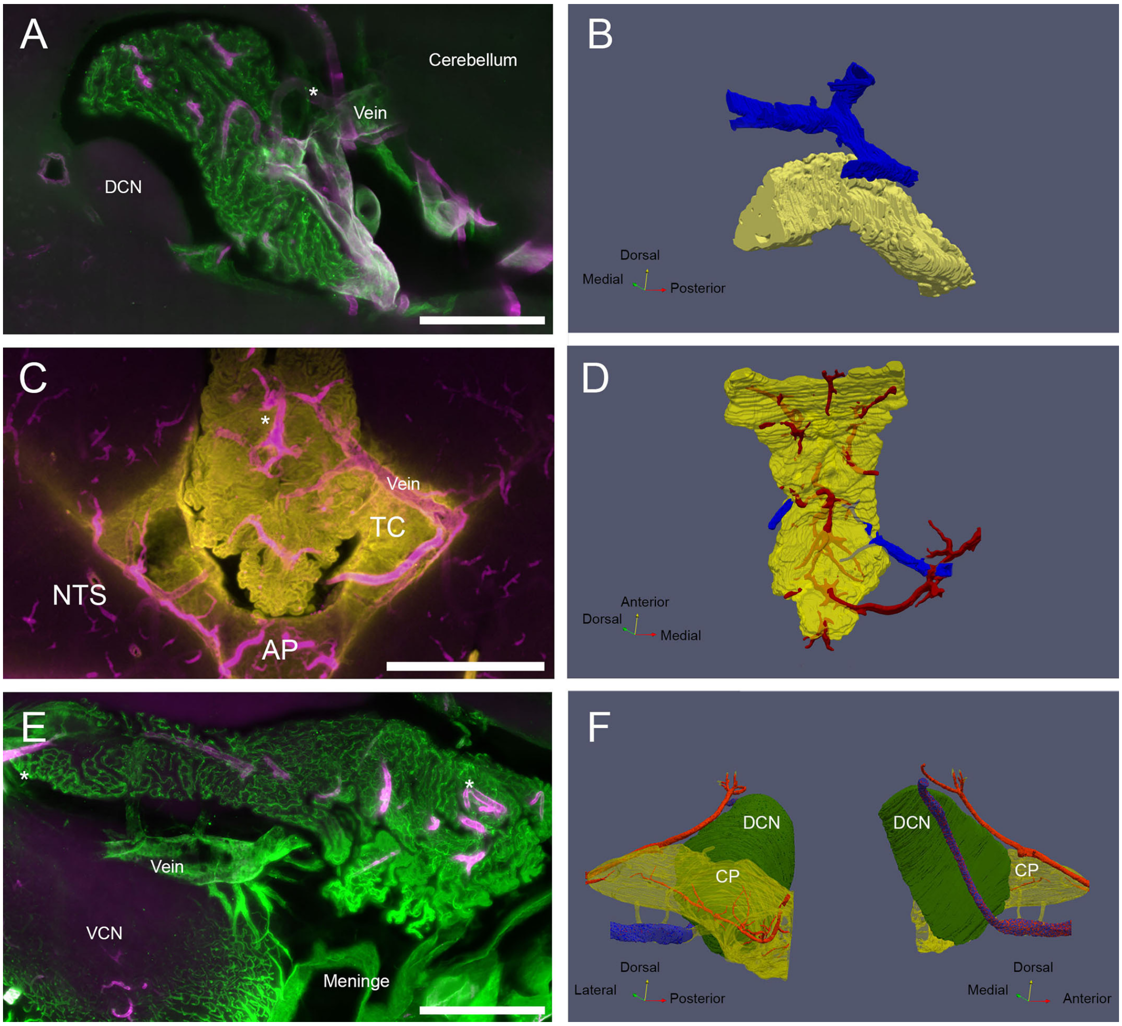

FIGURE 7 | CP veins. **(A)** View of the MHS vascular arrangement. SMA, magenta; CollV, green. Scale bar: 500 μm. **(B)** Reconstruction of MHS-associated vein. Vein is blue, CP is yellow. **(C)** View of the CSS venous outflow. SMA, magenta; Notch-2, yellow. Note that Notch-2 labels both CP epithelium and tela choroidea (TC). Scale bar: 1 mm. **(D)** Reconstruction of CSS-associated vein. Veins are blue, arteries red, CP yellow (semitransparent). **(E)** View of the LHS vascular arrangement. SMA, magenta; CollV, green. Scale bar: 500 μm. **(F)** Reconstruction of the vein passing under the DCN and emerging associated with Luschka foramen. Vein is shown in stippled blue. Connections to the CP (shown as semitransparent) are shown in yellow. Arteries (red) feeding the DCN and CP LHS are also shown. Both medial and lateral views are shown for clarity.

gradient. Interestingly, Shh appears more expressed in the rostral part, and may be involved in the heterogeneity of frond compactness we observed in the present work, which also follows a rostrocaudal distribution.

In recent years, several vascular atlases of rodent brains (Quintana et al., 2019; Kirst et al., 2020; Todorov et al., 2020) have been produced at capillary detail. However, the most detailed atlases focus on brain parenchyma, whereas CP is usually overlooked or just mentioned in passing. The CP capillary bed is however very different from those of the brain parenchyma (Cserr, 1971; Parab et al., 2021), and in the hCP these differences are carried to the extreme (Gomez and Gordon-Potts, 1981; Weiger et al., 1986; Scala et al., 1994). Moreover, the rodent hCP presents as an additional challenge its association with the paraflocculus in its most lateral region, which makes it extremely easy to damage when removing the brain from the skull. This work sets a primer for further morphological analysis of the hCP on clarified rat preparations.

In the rat, lateral CP vascular casts show parallel arteries feeding a flat, highly anastomosed capillary network draining into parallel veins that follow artery courses (Sangiorgi et al., 2003), and in mouse immunolabeling shows tight straight arteries expressing claudin-5 and vWF+ veins following arteries and also coasting the CP free edge (Dani et al., 2021). On the other hand, in the rat hCP venules were observed to be tortuous, but their connections to capillaries were not explored (Sun and Hashimoto, 1991).

Our reconstruction of the vascular architecture suggests that in the rat hCP there are two microvascular compartments, namely, SCANs and LTCs. The regularity of arteriolar sprouting

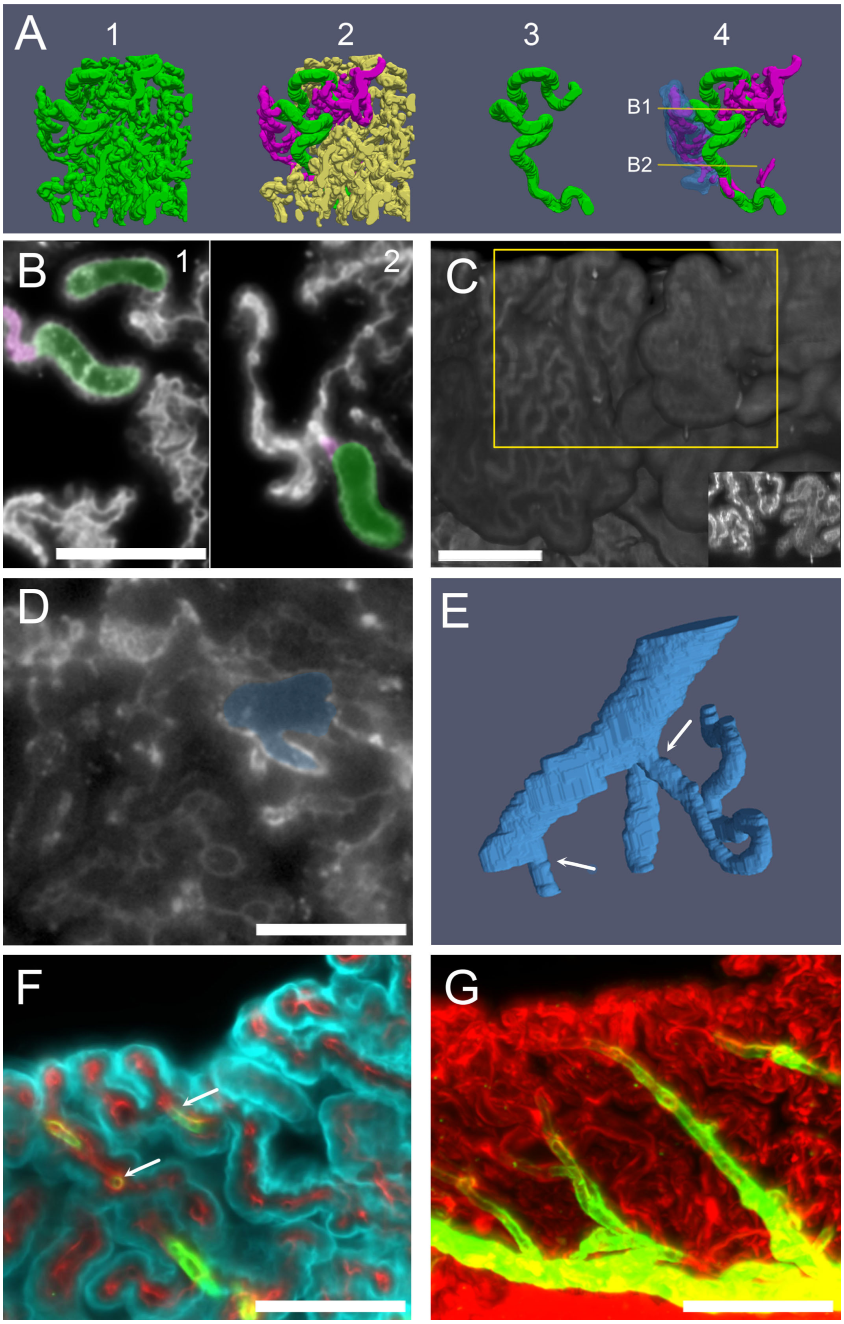

FIGURE 8 | Capillaries. **(A)** Three-dimensional reconstruction of capillaries from a male rat CSS labeled with anti-IgG. Capillaries have been segmented from a cube of CSS CP. 1: All vessels shown together, displaying the full vascular density of the segmented volume. 2: A single large capillary (green) and the small capillaries connected to it (magenta) are evidenced. 3: The large capillary shown in isolation. No branches are present in most large capillaries, which follow a very tortuous path. 4: The large capillary and its connected small capillaries are shown: the epithelium overlying a small capillary anastomotic network (SCAN) is shown in blue (semitransparent). SCANs branch within single villi, which may be folded, making the network appear more complex. Lines and arrows mark the planes and attachment points shown in **(B)**. **(B)** Single optical sections (labeled with anti-IgG) of the stack used for the reconstruction in **(A)**, showing that the SCAN (highlighted magenta) is attached to the same large capillary (highlighted green) at several levels (arrows). Scale bar: 100 μm. **(C)** Three-dimensional reconstruction of the ventral surface of CP CSS labeled with IgG. Villi from two adjacent fronds display only small (left) or only large capillaries (right) on the surface. Scale bar: 200 μm. Inset: Z-stack maximal projection from 10 optical sections from the region highlighted by the yellow box. **(D)** Single optical section (labeled with anti-IgG) showing the junction between a large tortuous capillary and a vein. Scale bar: 100 μm. **(E)** Three-dimensional reconstruction of the capillary-venous junction. Arrows point at the two capillaries entering the vein branches. One of the capillaries is cut short for clarity. **(F)** COLM image of a CP frond showing the arteriole junctions: a straight arteriole (labeled with SMA, green) contacts capillaries (labeled with Col-IV) with the same initial diameter (arrow). Cyan, Notch-2. Since ColIV also labels CP epithelial basal lamina, connections are seen between vessels. **(G)** Z-stack maximal projection of the same sample as **(F)**, showing the whole course of the arteriole (30 μm z-range; 3 μm steps, 10 planes). Red, ColIV; green, SMA. Scale bar: 100 μm.

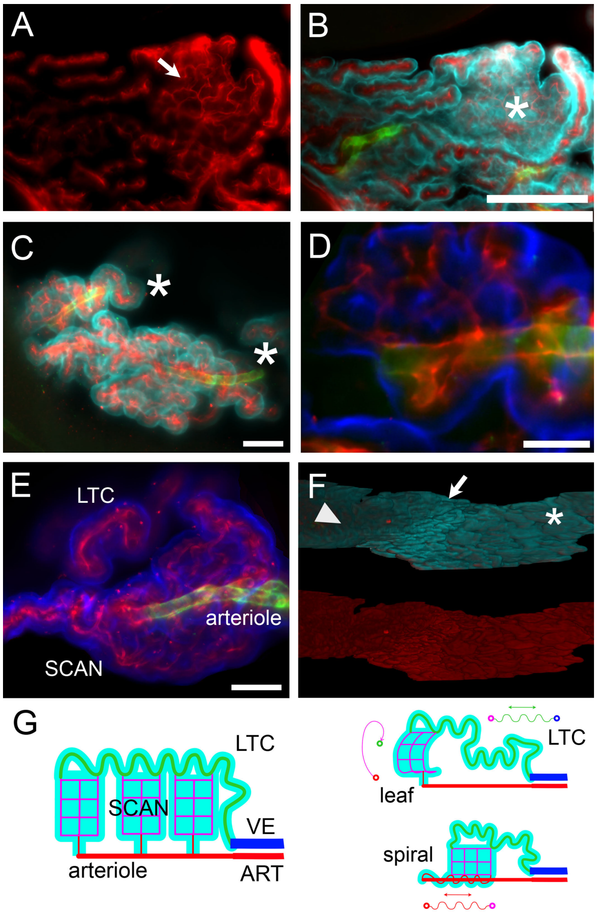

FIGURE 9 | Microvascular network and frond structure. **(A)** SCAN within a single villus in the loose part of LHS of a female rat. The anastomotic pattern of the small capillary network (arrow) is evident. Collagen IV labeling. **(B)** Same section as in **(A)**, additionally labeled for CP epithelium (Notch2, cyan) and arterioles (SMA, green). One flat villus is *en face* in this section (asterisk), and its whole lateral surface is visible. The distribution of large capillaries at the periphery and small capillary (SCAN) in the center is evident. This SCAN attaches to its parent arteriole following a loose spiral course (see **Supplementary Video 6**). Scale bar: 200 μm. **(C)** Terminal region of corkscrew-like villi from the loose part of CSS. Arterioles are seen in the middle, associated with spiraling capillaries. Asterisks mark the direction of the parent artery. Green, SMA; red, CollV; cyan, Notch-2. Scale bar: 100 μm. **(D)** Single optical slice with a magnification of a portion of the top villus in **(C)**, showing that the arteriole is associated with capillaries running within the same villus. Scale bar: 50 μm. Green, SMA; red, CollV; blue, Notch-2. **(E)** Z-stack maximal projection from 50 optical sections (3 μm steps) displaying a SCAN associated with its arteriole and LTC. Scale bar: 100 μm. **(F)** Three-dimensional reconstruction of the LHS surface of a female rat facing the DCN. Top: Notch-2 (cyan) + CollV (red) + SMA (green) labeling. Bottom: collV labeling (red). Notice the passage from leaflike villi (asterisk) to digitiform villi (arrow) to flat surface (arrowhead) passing from the caudal to the rostral part of LHS. Scale bar: 500 μm. **(G)** Schema of hCP vascular network. Arteries (ART) divide into arterioles, which give rise to SCANs (magenta) through divergent connections. At their other end, SCANs contact LTCs (green) which course back to reach veins (VE). Since LTCs are very long, a single capillary may fill an entire frond, and SCANs are attached *via* multiple outlets to a single LTC. Probably due to growth with spatial constraints, both SCANs and LTCs may display a tortuous pathway; differential growth of SCANs and LTCs (and possibly pre-SCAN vessels) may produce all microvascular patterns observed.

could suggest the presence of SCAN "modules" that can be interposed between arterioles and LTCs (which are venular in position). Although SCANs contain vessels of smaller diameter than LTCs, anastomoses between them would make parallel channels, increasing the total area for blood flow. Simulations employing the actual geometry of the CP vascular network will be needed to understand blood flow features in SCANs and LTCs. Several questions arise from the present data: 1- is the permeability similar in SCANs and LTCs? Single-cell expression in the mouse did not evidence distinct endothelial populations. Moreover, our IgG data suggest that both small and large capillaries are permeable to proteins, since both displayed outer IgG rings. Consistently, arterioles [which have been found to display tight walls (Dani et al., 2021)] were clearly observed in SMA-labeled samples but no straight vessels with a diameter similar to SMA+ arterioles were seen in IgG-labeled samples. 2- are SCANs dynamically regulated as modules? SCAN confinement within single villi could allow local interactions between endothelium, stromal components, and epithelium, such as what has been evidenced in Dani et al. (2021). 3- is there any feedback between LTCs and feeder arterioles? Our images evidenced the presence of SMA+ sphincters at SCAN sprouting from arterioles, but we could not clearly identify arteriovenous shunts. However, since CSF production is highly regulated, the dynamic diversion of flow to large capillaries *via* arteriolar vasoconstriction, and the modular organization of small capillaries (which may be optimized in number and size *via* vascular remodeling) suggest interesting hypotheses for functional regulation.

During development, both angiogenesis and epitheliogenesis are regulated by Shh in the hCP but not telencephalic CPs (Nielsen and Dymecki, 2010). In the adult animal, the CP epithelium has been found to be postmitotic (Huang et al., 2009) or dividing at a much slower rate than during development (Dani et al., 2021), and therefore vascular growth in a fixed-volume villus or frond would be expected to induce tortuosity. Although the action of Shh appears restricted to development in normal animals (Nielsen and Dymecki, 2010), it is likely that physiological or pathological stimuli activate angiogenesis in the adult: for instance, VEGF is released from CP epithelial cells and affects both CP endothelium and ependyma (Maharaj et al., 2008), and redundant VEGF signaling pathways, both cell-autonomous and non-autonomous, are involved in the formation of fenestrated endothelium in zebrafish CP (Parab et al., 2021). Dynamical vascular remodeling would be particularly expected in the hCP, since a differential transcriptome analysis (Lun M. P. et al., 2015) displayed that angiogenesis-related genes are more highly expressed in it than in telencephalic CP. Moreover, the localization of dividing cells mostly close to CP attachment (Dani et al., 2021), where veins are found, could suggest that LTC tortuosity comes from vascular growth at the venous end, pushing the vessel toward CP distal villi.

In regards to rat hCP macroanatomy, the observed peculiar arrangements of arteries and veins most likely reflect development of the cerebellum and related structures. In fact, the rodent paraflocculus extends laterally, reorients during development, and ends surrounded by temporal bone

(Panezai et al., 2020); on the other hand, the dorsal cochlear nucleus is a paracerebellar nucleus that shares a similar (though not identical) developmental origin with the cerebellum (Farago et al., 2006), and therefore association of CP-related vasculature to cochlear nuclei may reflect rhombic lip rearrangements during development.

Since the overall CP structure is stabilized by the macrovascular connections, our finding that villi may differentially extend up to the ventricular surface suggests the presence of an additional factor able to modulate local concentrations of CSF factors, by directly increasing local CP secretions or by affecting CSF flow.

Geometrically, it is known that some hCP regions appear more "ordered" (i.e., the epithelium and underlying stroma form a continuous sheet or a compact 3D structure), whereas other regions appear "disordered" with long, irregularly ramified fronds. The distribution of ordered and disordered CP regions appears to be maintained in a species- and ventricle-related way (Gomez and Gordon-Potts, 1981; Weiger et al., 1986; Scala et al., 1994; Marinković et al., 2005; Zagorska-Swiezy et al., 2008) and is likely to follow gradients of morphogen expression as found in Dani et al. (2021). Although no roles have been found for these geometrical differences yet, it is interesting to note that CP volumes may vary within the human population, physiologically for some regions, such as Bochdalek's flower basket (Horsburgh et al., 2012; Barany et al., 2017) or pathologically (with a connection to psychosis) for lateral CP (Lizano et al., 2019). In humans, the glomus of the lateral ventricles CP contains extremely tortuous capillary beds (Marinković et al., 2005) (defined "chaotic" in Zagorska-Swiezy et al., 2008), strikingly differing from the rest of CP. It would be interesting to see whether a similar organization is found as the one presented here.

Changes in the growth or positioning of different CP regions and fronds would modulate the exchange of signals with the periventricular brain tissue. CP contacts with brain parenchyma are characterized by exchange of vesicles (Terr and Edgerton, 1985) similar to those released through apocrine secretion by CP epithelium (Balusu et al., 2016); moreover, macrophages are found to exit the CP at "hotspots" at the distal end of fronds upon CCL2 signaling (Cui et al., 2020). This suggests that these contacts are not a product of chance. Furthermore, the structures where we observed CP contacts overlap with those in the 4th ventricle that display adult neurogenesis (Tighilet et al., 2007, 2016; González-González et al., 2017), suggesting a role for the hCP in neurogenesis and plasticity, as is known for the lateral ventricle CP (Kaiser and Bryja, 2020), and as would be suggested by the expression of Otx2 in both lateral and hCP (Spatazza et al., 2013). At present, mechanisms responsible for contact formation are not clear, and may involve CSF flow [which creates "currents" (Faubel et al., 2016) that may direct the flexible fronds to precise spots], developmental patterns where certain fronds are induced to grow longer by intrinsic signals and/or chemoattractants (Nielsen and Dymecki, 2010; Cui et al., 2020; Dani et al., 2021), and complementary adhesion proteins on the ependyma and CP epithelium (see for example, Lobas et al., 2012) that may induce adhesion of the CP epithelium of different villi (thereby keeping them compact) or anchor CP villi to ventricular surface spots. Developmental and molecular studies on these contacts will be needed to help clarify the issue. The present observations on microvascular pattern suggest a mechanism whereby local adult angiogenesis would modulate the structure of villi and fronds, by differentially lengthening of microvascular network compartments, and may therefore also regulate CP relations with the ventricular surface. In this context, although more observation will be needed, the preliminarily observed gender difference in number and type of contacts could underlie some of the gender-related functional CP differences, such as TTR effects (Vancamp et al., 2019).

Several clearing techniques are known to induce size changes. In particular, iDISCO+ reduces mouse brain size about 10% (Renier et al., 2016) but does not affect the size of bones (Wang et al., 2019). Although such limited shrinking does not cause bulk damage, and therefore vascular connectivity should not be distorted, several of our measured parameters are likely to be affected. In particular, connecting structures between brain regions (such as CP fronds) will be stretched, and weak connection could detach. The finding that, despite this stretch, connections are still consistently observed between CP and ventricle floor, suggests that at contact points there may be mechanisms for cell adhesion, and not simple juxtaposition of CP and ependyma; our technique would actually lead us to an underestimation of contact points. On the other hand, CP volume shrinking will certainly bias densities (e.g., of macrophages) toward slightly higher values, and would also affect local curvature of fronds and capillaries, therefore biasing tortuosity measures. Therefore, comparisons of measurements taken with iDISCO+ and vascular cast reconstruction (e.g., Quintana et al., 2019) must take this factor into account.

DATA AVAILABILITY STATEMENT

The raw data supporting the conclusions of this article will be made available by the authors, without undue reservation.

ETHICS STATEMENT

The animal study was reviewed and approved by the OPBA – University of Pavia and Ministry of Public Health, Rome, Italy.

AUTHOR CONTRIBUTIONS

PP ideated the experiments, performed the surgeries, clearing, and image analysis, wrote the manuscript, and made figures. RR, CR, DC, SL, and RP performed the clearing, image analysis, and made videos. PB, FV, FH, LB, and IG performed the light-sheet scans. All authors contributed to discussion, revised and approved the article.

FUNDING

This work was supported by Universitiamo crowdfunding campaign "Silence 2.0" and Associazione Italiana Tinnitus (AIT) Onlus donations.

ACKNOWLEDGMENTS

The authors thank Stefano Scarpa, M.Sc. for help in image segmentation.

SUPPLEMENTARY MATERIAL

The Supplementary Material for this article can be found online at: https://www.frontiersin.org/articles/10.3389/fcell.2021.692617/full#supplementary-material

Supplementary Figure 1 | (A) Schema of the CP as in **Figure 1A**, with indications of arterial points of entry. Symbols and colors indicate samples. **(B)** Schema of the CP as in **Figure 1A**, with indications of venous points of entry. Symbols and colors indicate samples.

Supplementary Video 1 | Z-stack progression of light-sheet 3D dataset of the whole-mount brain-bone preparation of **Figure 2A**, showing the extent and association of the CP (highlighted in red). Scale bar: 2 mm.

Supplementary Video 2 | (A) 360° rotation on *y*-axis of reconstruction shown in **Figure 8A1**. **(B)** 360° rotation on *y*-axis of reconstruction shown in **Figure 8A2**. **(C)** 360° rotation on *y*-axis of reconstruction shown in **Figure 8A3**. **(D)** 360° rotation on *y*-axis of reconstruction shown in **Figure 8A4**.

Supplementary Video 3 | Z-stack progression of light-sheet 3D dataset of the region shown in **Figure 9B**. Scale bar: 200 μm.

REFERENCES

Ahrens, J., Geveci, B., and Law, C. (2005). *ParaView: An End-User Tool for Large Data Visualization*, Visualization Handbook. Amsterdam: Elsevier.

Arganda-Carreras, I., Fernández-González, R., Muñoz-Barrutia, A., and Ortiz-De-Solorzano, C. (2010). 3D reconstruction of histological sections: Application to mammary gland tissue. *Microsc. Res. Tech.* 73, 1019–1029. doi: 10.1002/jemt.20829

Ayachit, U. (2015). *The ParaView Guide: A Parallel Visualization Application*. New York, NY: Kitware.

Balusu, S., Van Wonterghem, E., De Rycke, R., Raemdonck, K., Stremersch, S., Gevaert, K., et al. (2016). Identification of a novel mechanism of blood-brain communication during peripheral inflammation via choroid plexus-derived extracellular vesicles. *EMBO Mol. Med.* 8, 1162–1183. doi: 10.15252/emmm.201606271

Barany, L., Baksa, G., Patonay, L., Ganslandt, O., Buchfelder, M., and Kurucz, P. (2017). Morphometry and microsurgical anatomy of Bochdalek's flower basket and the related structures of the cerebellopontine angle. *Acta Neurochir.* 159, 1539–1545. doi: 10.1007/s00701-017-3234-9

Barrière, D. A., Magalhães, R., Novais, A., Marques, P., Selingue, E., Geffroy, F., et al. (2019). The SIGMA rat brain templates and atlases for multimodal MRI data analysis and visualization. *Nat. Commun.* 10:5699. doi: 10.1038/s41467-019-13575-7

Cserr, H. F. (1971). Physiology of the choroid plexus. *Physiological. Rev.* 51, 273–311. doi: 10.1152/physrev.1971.51.2.273

Cui, J., Frederick, B., Shipley, M. L., Shannon, O. A., Neil, D., Mya, D., et al. (2020). Inflammation of the Embryonic Choroid Plexus Barrier following Maternal Immune Activation. *Dev. Cell* 2020:55. doi: 10.1016/j.devcel.2020.09.020

Dani, N., Herbst, R. H., McCabe, C., Green, G. S., Kaiser, K., Head, J. P., et al. (2021). A cellular and spatial map of the choroid plexus across brain ventricles and ages. *Cell* 184, 3056.e–3074.e. doi: 10.1016/j.cell.2021.04.003

Farago, A. F., Awatramani, R. B., and Dymecki, S. M. (2006). Assembly of the brainstem cochlear nuclear complex is revealed by intersectional and subtractive genetic fate maps. *Neuron* 50, 205–218. doi: 10.1016/j.neuron.2006.03.014

Faubel, R., Westendorf, C., Bodenschatz, E., and Eichele, G. (2016). Cilia-based flow network in the brain ventricles. *Science* 353, 176–178. doi: 10.1126/science.aae0450

Fehrenbach, J., Weiss, P., and Lorenzo, C. (2012). Variational algorithms to remove stationary noise: applications to microscopy imaging. *IEEE Trans. Image Proc.* 21, 4420–4430. doi: 10.1109/TIP.2012.2206037

Ghersi-Egea, J. F., Strazielle, N., Catala, M., Silva-Vargas, V., Doetsch, F., and Engelhardt, B. (2018). Molecular anatomy and functions of the choroidal blood-cerebrospinal fluid barrier in health and disease. *Acta Neuropathol.* 135, 337–361. doi: 10.1007/s00401-018-1807-1

Gomez, D. G., and Gordon-Potts, D. (1981). The lateral, third, and fourth ventricle choroid plexus of the dog: a structural and ultrastructural study. *Ann. Neurol.* 10, 333–340. doi: 10.1002/ana.410100404

González-González, M., Gómez-González, G., and Becerra-González, M. (2017). Identification of novel cellular clusters define a specialized area in the cerebellar periventricular zone. *Sci. Rep.* 7:40768. doi: 10.1038/srep40768

Horsburgh, A., Kirollos, R. W., and Massoud, T. F. (2012). Bochdalek's flower basket: applied neuroimaging morphometry and variants of choroid plexus in the cerebellopontine angles. *Neuroradiology* 54, 1341–1346. doi: 10.1007/s00234-012-1065-1

Huang, X., Ketova, T., Fleming, J. T., Wang, H., Dey, S. K., Litingtung, Y., et al. (2009). Sonic hedgehog signaling regulates a novel epithelial progenitor domain of the hindbrain choroid plexus. *Development* 136, 2535–2543. doi: 10.1242/dev.033795

Hubert, V., Chauveau, F., Dumot, C., Ong, E., Berner, L. P., Canet-Soulas, E., et al. (2019). Clinical Imaging of Choroid Plexus in Health and in Brain Disorders: A Mini-Review. *Front. Mole. Neurosci.* 12:34. doi: 10.3389/fnmol.2019.00034

Kaiser, K., and Bryja, V. (2020). Choroid Plexus: The Orchestrator of Long-Range Signalling Within the CNS. *Int. J. Mol. Sci.* 21:4760. doi: 10.3390/ijms21134760

Kirst, C., Skriabine, S., Vieites-Prado, A., Topilko, T., Bertin, P., Gerschenfeld, G., et al. (2020). Mapping the Fine-Scale Organization and Plasticity of the Brain Vasculature. *Cell* 180, 780.e–795.e. doi: 10.1016/j.cell.2020.01.028

Kreeger, P. K., Strong, L. E., and Masters, K. S. (2018). Engineering Approaches to Study Cellular Decision Making. *Annu. Rev. Biomed. Eng.* 20, 49–72. doi: 10.1146/annurev-bioeng-062117-121011

Lizano, P., Lutz, O., Ling, G., Lee, A. M., Eum, S., Bishop, J. R., et al. (2019). Association of Choroid Plexus Enlargement With Cognitive, Inflammatory, and Structural Phenotypes Across the Psychosis Spectrum. *Am. J. Psychiatry* 176, 564–572. doi: 10.1176/appi.ajp.2019.18070825

Lobas, M. A., Helsper, L., Vernon, C. G., Schreiner, D., Zhang, Y., Holtzman, M. J., et al. (2012). Molecular heterogeneity in the choroid plexus epithelium: the 22-member γ-protocadherin family is differentially expressed, apically localized, and implicated in CSF regulation. *J. Neurochem.* 120, 913–927. doi: 10.1111/j.1471-4159.2011.07587.x

Lun, M., Monuki, E., and Lehtinen, M. (2015). Development and functions of the choroid plexus–cerebrospinal fluid system. *Nat. Rev. Neurosci.* 16, 445–457. doi: 10.1038/nrn3921

Lun, M. P., Johnson, M. B., Broadbelt, K. G., Watanabe, M., Kang, Y. J., Chau, K. F., et al. (2015). Spatially heterogeneous choroid plexus transcriptomes encode positional identity and contribute to regional CSF production. *J. Neurosci.* 35, 4903–4916. doi: 10.1523/JNEUROSCI.3081-14.2015

Maharaj, A. S., Walshe, T. E., Saint-Geniez, M., Venkatesha, S., Maldonado, A. E., Himes, N. C., et al. (2008). VEGF and TGF-beta are required for the maintenance of the choroid plexus and ependyma. *J. Exp. Med.* 205, 491–501. doi: 10.1084/jem.20072041

Marinković, S., Gibo, H., Filipović, B., Dulejić, V., and Piscević, I. (2005). Microanatomy of the subependymal arteries of the lateral ventricle. *Surg. Neurol.* 63, 451–458. doi: 10.1016/j.surneu.2004.06.013

Meunier, A., Sawamoto, K., and Spassky, N. (2013). "Chapter 42 Ependyma Choroid," in *Patterning and Cell Type Specification in the Developing CNS and PNS*, eds L. R. John and P. R. Rubenstein (New York, NY: Academic Press), 819–833. doi: 10.1016/B978-0-12-397265-1.00086-1

Neman, J., and Chen, T. (eds) (2016). *The Choroid Plexus and Cerebrospinal Fluid*. New York, NY: Academic Press, doi: 10.1016/C2014-0-00275-4

Nielsen, C. M., and Dymecki, S. M. (2010). Sonic hedgehog is required for vascular outgrowth in the hindbrain choroid plexus. *Dev. Biol.* 340, 430–437.

Panezai, S. K., Luo, Y., Vibulyaseck, S., Sarpong, G. A., Nguyen-Minh, V. T., Nedelescu, H., et al. (2020). Reorganization of longitudinal compartments in the laterally protruding paraflocculus of the postnatal mouse cerebellum. *J. Comp. Neurol.* 528, 1725–1741. doi: 10.1002/cne.24849

Parab, S., Quick, R. E., and Matsuoka, R. L. (2021). Endothelial cell-type-specific molecular requirements for angiogenesis drive fenestrated vessel development in the brain. *Elife* 10:e64295. doi: 10.7554/eLife.64295

Paxinos, G., and Watson, C. (2013)*The Rat Brain in Stereotaxic Coordinates*, 7th Edn. Cambridge, MA: Academic Press.

Perin, P., Voigt, F. F., Bethge, P., Helmchen, F., and Pizzala, R. (2019). iDISCO+ for the Study of Neuroimmune Architecture of the Rat Auditory Brainstem. *Front. Neuroanat.* 13:15. doi: 10.3389/fnana.2019.00015

Quintana, D. D., Lewis, S. E., Anantula, Y., Garcia, J. A., Sarkar, S. N., Cavendish, J. Z., et al. (2019). The cerebral angiome: High resolution MicroCT imaging of the whole brain cerebrovasculature in female and male mice. *NeuroImage* 2019, 202. doi: 10.1016/j.neuroimage.2019.116109

Renier, N., Adams, E. L., Kirst, C., Wu, Z., Azevedo, R., Kohl, J., et al. (2016). Mapping of Brain Activity by Automated Volume Analysis of Immediate Early Genes. *Cell* 165, 1789–1802. doi: 10.1016/j.cell.2016.05.007

Sangiorgi, S., Picano, M., Manelli, A., Peron, S., Tomei, G., and Raspanti, M. (2003). The microvasculature of the lateral choroid plexus in the rat: a scanning electron microscopy study of vascular corrosion casts. *Eur. J. Morphol.* 41, 155–160.

Scala, G., Mirabella, N., Paino, G., and Pelagalli, G. V. (1994). Sur la microvascularisation des plexus choroïdes des ventricules latéraux chez la Chèvre (Capra hircus) [The microvascularization of the choroid plexus of the lateral ventricles in the goat (Capra hircus)]. *Anat. Histol. Embryol.* 23, 93–101.

Schindelin, J., Arganda-Carreras, I., Frise, E., Kaynig, V., Longair, M., Pietzsch, T., et al. (2012). Fiji: an open-source platform for biological-image analysis. *Nat. Methods* 9, 676–682. doi: 10.1038/nmeth.2019

Sharifi, M., Ciołkowski, M., Krajewski, P., and Ciszek, B. (2005). The choroid plexus of the fourth ventricle and its arteries. *Folia Morphol.* 64, 194–198.

Shipley, F. B., Dani, N., Xu, H., Deister, C., Cui, J., Head, J. P., et al. (2020). Tracking Calcium Dynamics and Immune Surveillance at the Choroid Plexus Blood-Cerebrospinal Fluid Interface. *Neuron* 108, 623.e–639.e. doi: 10.1016/j.neuron.2020.08.024

Spatazza, J., Lee, H. H., Di Nardo, A. A., Tibaldi, L., Joliot, A., Hensch, T. K., et al. (2013). Choroid-plexus-derived Otx2 homeoprotein constrains adult cortical plasticity. *Cell Rep.* 3, 1815–1823. doi: 10.1016/j.celrep.2013.05.014

Sun, S. Q., and Hashimoto, P. H. (1991). Venous microvasculature of the pineal body and choroid plexus in the rat. *J. Electron. Microsc.* 40, 29–33.

Terr, L. I., and Edgerton, B. J. (1985). Physical effects of the choroid plexus on the cochlear nuclei in man. *Acta Otolaryngol.* 100, 210–217. doi: 10.3109/00016488509104783

Tighilet, B., Brezun, J. M., Sylvie, G. D., Gaubert, C., and Lacour, M. (2007). New neurons in the vestibular nuclei complex after unilateral vestibular neurectomy in the adult cat. *Eur. J. Neurosci.* 25, 47–58. doi: 10.1111/j.1460-9568.2006.05267.x

Tighilet, B., Dutheil, S., Siponen, M. I., and Noreña, A. J. (2016). Reactive Neurogenesis and Down-Regulation of the Potassium-Chloride Cotransporter KCC2 in the Cochlear Nuclei after Cochlear Deafferentation. *Front. Pharmacol.* 7:281. doi: 10.3389/fphar.2016.00281

Todorov, M. I., Paetzold, J. C., Schoppe, O., Tetteh, G., Shit, S., Efremov, V., et al. (2020). Machine learning analysis of whole mouse brain vasculature. *Nat. Methods* 17, 442–449. doi: 10.1038/s41592-020-0792-1

Tomer, R., Ye, L., Hsueh, B., and Deisseroth, K. (2014). Advanced CLARITY for rapid and high-resolution imaging of intact tissues. *Nat. Protoc.* 9, 1682–1697. doi: 10.1038/nprot.2014.123

Urabe, N., Naito, I., Saito, K., Yonezawa, T., Sado, Y., Yoshioka, H., et al. (2002). Basement membrane type IV collagen molecules in the choroid plexus, pia mater and capillaries in the mouse brain. *Arch. Histol. Cytol.* 65, 133–143. doi: 10.1679/aohc.65.133

Vancamp, P., Gothié, J. D., Luongo, C., Sébillot, A., Le Blay, K., Butruille, L., et al. (2019). Gender-specific effects of transthyretin on neural stem cell fate in the subventricular zone of the adult mouse. *Sci. Rep.* 9:19689. doi: 10.1038/s41598-019-56156-w

Voigt, F. F., Kirschenbaum, D., Pagès, P. E. S., Campbell, R. A. A., and Kästli, R. (2019). The mesoSPIM initiative: open-source light-sheet microscopes for imaging cleared tissue. *Nat. Methods* 16, 1105–1108. doi: 10.1038/s41592-019-0554-0

Wang, Q., Liu, K., Yang, L., Wang, H., and Yang, J. (2019). BoneClear: whole-tissue immunolabeling of the intact mouse bones for 3D imaging of neural anatomy and pathology. *Cell Res.* 29, 870–872. doi: 10.1038/s41422-019-0217-9

Weiger, T., Lametschwandtner, A., Hodde, K. C., and Adam, H. (1986). The angioarchitecture of the choroid plexus of the lateral ventricle of the rabbit. A scanning electron microscopic study of vascular corrosion casts. *Brain Res.* 378, 285–296. doi: 10.1016/0006-8993(86)90931-5

Yushkevich, P. A., Piven, J., Cody Hazlett, H., Gimpel Smith, R., Ho, S., Gee, J. C., et al. (2006). User-guided 3D active contour segmentation of anatomical structures: Significantly improved efficiency and reliability. *Neuroimage* 31, 1116–1128.

Zagorska-Swiezy, K., Litwin, J. A., Gorczyca, J., Pitynski, K., and Miodonski, A. J. (2008). The microvascular architecture of the choroid plexus in fetal human brain lateral ventricle: a scanning electron microscopy study of corrosion casts. *J. Anat.* 213, 259–265. doi: 10.1111/j.1469-7580.2008.00941.x

Conflict of Interest: The authors declare that the research was conducted in the absence of any commercial or financial relationships that could be construed as a potential conflict of interest.